DYNAMIC MECHANICAL AND FAILURE PROPERTIES OF SOLDER JOINTS

LIU JIANFEI

(*M.Eng., University of Science and Technology of China*)

A THESIS SUBMITTED

FOR THE DEGREE OF DOCTOR OF PHILOSOPHY

DEPARTMENT OF MECHANICAL ENGINEERING

NATIONAL UNIVERSITY OF SINGAPORE

2010

ACKNOWLEDGEMENTS

THANKS. PROF. V.P.W. Shim

THANKS. PROF. V.B.C. Tan

AND

THANKS. MY FAMILY

SINCERELY ! NO MORE WORDS NEEDED !

JUNE 2010

TABLE OF CONTENTS

SUMMARY

Solders are widely used in interconnections in electronic components. Their unique and remarkable properties have facilitated many developments in advanced electronic packaging - e.g., recent flip-chip techniques for ball grid arrays (BGA). Solder joints serve as electrical and mechanical connectors between electronic components and printed circuit boards; fracture/failure of a solder joint would result in the breakdown of an electrical device. Thus, solder joint reliability is a critical issue in electronic packaging technology. Recent investigations have examined many areas such as the influence of thermal variations, mechanical loading, as well as the formation of intermetallic compounds; theoretical, experimental and numerical approaches have been adopted. Arising from growing environmental consciousness, manufacturers are moving towards lead (Pb) free solders for electronic devices and components; this poses new challenges in assessing solder joint reliability for various lead-free solder candidates.

Cyclic loading or thermal variations can generate fatigue failure in solder joints; shock or impact usually produces brittle fracture. Arising from the continuous push for device miniaturization and new applications in portable electronics, solder joint failure under drop or shock conditions is becoming a critical issue. Like most materials, it has been discovered that the mechanical properties of eutectic Sn-Pb solder alloy is quite rate-dependent. However, studies of solder joints under dynamic or impact conditions are limited, especially for lead-free solders. An actual solder joint in an IC package has a barrel-like profile and this profile exhibits slight variations among individual joints;

moreover, a solder bump fused into a joint is not exactly the same as the alloy before it is melted to form the joint – i.e. intermetallic compounds form between the solder and the copper pad, and impurities, voids, etc, are generated in actual solder joints. Thus, it is envisaged that the overall behavior of an actual solder joint is better defined by experimentally-measured responses, rather than to derive it from the material properties of individual components of the solder alloy (prior to melting to form the joint), the copper pad and the substrate. Therefore, this study investigates the load-deformation response and failure characteristics of lead-free solder joints in BGA packages under quasi-static and dynamic/impact loading. The objectives are to explore appropriate experimental methods for testing single solder joint specimens, formulate a failure force envelope that incorporates sensitivity to deformation rate, and establish finite element models of solder joints that utilize the experimentally-obtained mechanical properties for numerical simulation of solder joint behavior in IC packages.

Chapter 1 introduces some background information on advanced surface mount technologies and common issues related to the reliability of IC packages; studies on rate-dependent mechanical properties of solder alloys and the trend towards Pb-free soldering are reviewed. The literature survey shows that in terms of mechanical reliability of solder joints, considerable research has been undertaken in the area of thermally-induced or mechanic cyclic loading, taking into consideration the presence of intermetallic compounds; theoretical, experimental and numerical approaches have been employed. It appears that studies involving the measurement of load-

deformation response and strength of actual solder joints are limited, and investigations in the area of impact loading are scarce. These motivate the current study on the mechanical response of solder joints subjected to quasi-static and impact loading. Chapter 2 describes the test methodology employed and experimental results for solder joint specimens subjected to quasi-static loading. These include the preparation of solder joint specimens and an evaluation of solder joint specimen configuration to be adopted for tests (i.e., multi-joint or single-joint specimen). Special fixtures designed to accommodate small solder joint specimens for combined tension-shear and compression-shear loading. Chapter 3 describes impact test methodology for single solder joint specimen and corresponding dynamic tests together with the results obtained. This effort includes numerical and experimental evaluation of dynamic test methods using an impact bar system (based on one-dimensional stress wave theory), and devising of a miniature impact tester for very small specimens. The experimental results substantiate the feasibility and accuracy of this miniature impact tester, and show the rate-sensitivity of solder joint deformation. Chapter 4 describes characterization of the rate-dependent mechanical properties of solder joints and finite element models for a single solder joint specimen. Numerical simulations are performed to identify the force-deformation response of a single solder joint subjected to laterally unconstrained loading or laterally constrained loading. From the experimental results, failure force envelope is proposed for single solder joint specimens, incorporating rate-sensitivity. As an actual solder joint has a barrel-like profile; the experimentally-obtained force-deformation responses of solder joints could only be converted to idealized stress-strain

relationships by assuming a normalized specimen length and cross-sectional area. Numerical simulations are subsequently performed to investigate the feasibility and accuracy of approximating an actual barrel-like solder geometry by a cylinder, and finally an equivalent beam. The idealized stress-strain responses are then related to strain-rate and incorporated into a beam model to describe single solder joints. An ABAQUS subroutine is established, whereby a field variable is used to capture strain rate sensitivity and facilitate the input of mechanical properties to simulation. Chapter 5 describes test and simulation results of IC package subjected to three-point bending induced quasi-statically and by drop impact. This is to investigate the response of IC packages under static and dynamic loading and to examine the validity of numerical simulations employing the beam model developed. Strain values at several locations on the surface of IC package specimens were measured using strain gauges and corresponding values extracted from numerical simulation, for comparison and evaluation.

The final Chapter (6) summarizes the main achievements of this study and describes briefly possible future work.

LIST OF TABLES

LIST OF FIGURES

CHAPTER 1 BACKGROUND AND LITERATURE REVIEW

The failure/fracture of solder joints in electronic packaging is a major issue in electrical products. It is a complicated problem and related to many factors such as type of packaging, mechanical properties of solders or the environment of use. This chapter first introduces developments relating to surface mount technologies in integrated circuit (**IC**) packaging and some common failures observed in IC assemblies. The movement from lead-tin solder alloy (e.g., eutectic Sn63Pb37) towards lead-free soldering, and the rate-dependent mechanical properties of solder alloys are then described. The formation of a solder joint in BGA packages and the intermetallic compound (**IMC**) formed between the solder bump and copper pad is highlighted; the non-uniform geometry of solder joints and the IMC increase the complexity of defining mechanical properties and FEM modeling. Finally, the literature review indicates that extensive research has been conducted at the area of solder joint behavior and reliability under thermal or mechanical cyclic loading conditions. There have been some investigations on solder joint strength under monotonic loading (tension, shear, etc.), but studies on response to impact loading are relatively few, particularly for lead-free solder joints. Studies on solder joint strength are mostly related to electronic packages and researches on small solder joints are quite scarce. This motivates the current study, which involves investigation of the quasi-static and dynamic mechanical properties of single solder joint specimens based on new generation of lead-free solder.

1.1 Advanced IC packages and issues of reliability

(1) Developments in surface mount technologies

Soldering technologies for attaching electrical components to printed circuit boards (PCB) have undergone many developments in recent years. Surface mount technology (SMT) was implemented in the early 1980s and is now important in integrated circuit (IC) packaging and assembly. The inherent merits of surface mount technology can be summarized as: “increased circuit density; decreased component size; decreased board size; reduced weight; shorter leads; shorter interconnections; improved electrical performance; facilitation of automation and lower cost in volume production” (Hwang, 1996). As early as 1996, it was estimated that around 50 to 60 percent of total IC packages will be surface mount configurations, which will surpass through-hole packages (THT) (Fig.1-1).

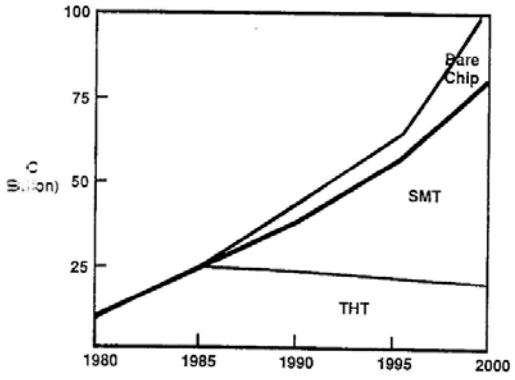

Fig.1-1 Evolution of IC packaging (Hwang, 1996)

Attaching IC packages to PCBs employ different packaging technologies, depending on the package types and their applications. With respect to

JEDEC (Joint Electronic Device Engineering Council) and IPC (Institute for Interconnecting and Packaging Electronic Circuits) standards, conventional surface mount technologies for IC packages are illustrated in Fig.1-2,

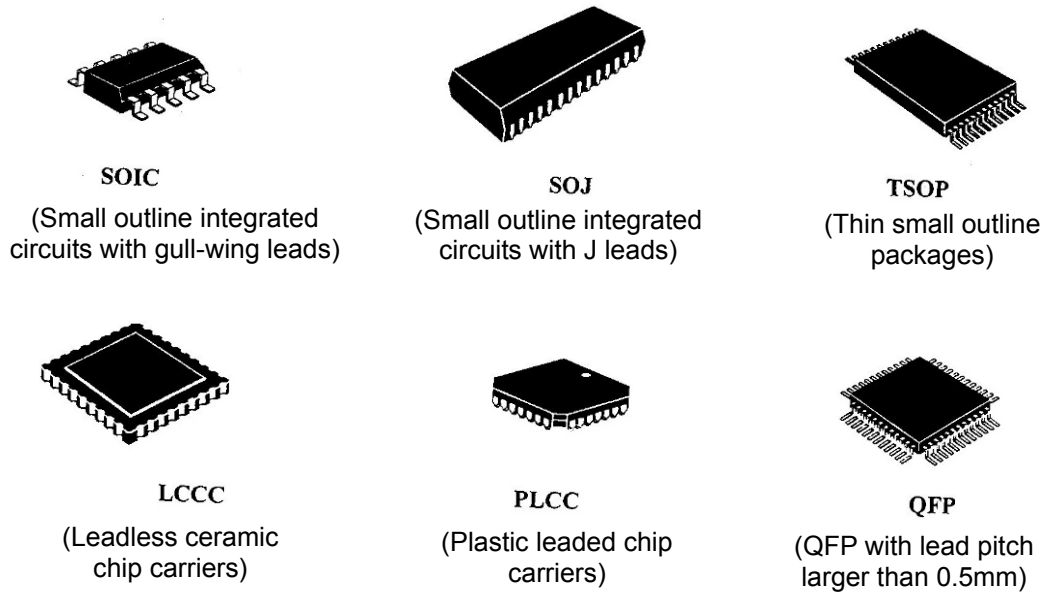

Fig.1-2 Conventional configurations of surface mount IC packages (Hwang, 1996)

In recent years, the use of integrated circuits has increased rapidly, as electronic product manufacturers seek to build smaller, lighter and more reliable products. This has propelled the development of advanced surface mount technologies. Advanced surface mount packages and chip-attachment methods include tape automated bonding (TAB), chip-on-board (COB), flip-chip technology and ball grid array (BGA), as well as pad array carrier (PAC) and multi-chip module (MCM) technologies (Fig.1-3). There are special books that provide detailed descriptions of surface mount technology (e.g., Strauss 1994), multichip module design (e.g., Licari 1995) and popular BGA technologies (e.g., Lau 1995).

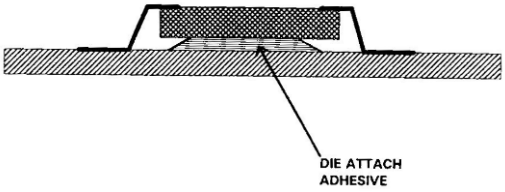

Tape Automated Bonding Technology

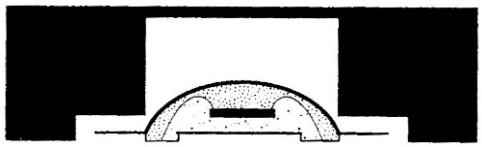

Chip-on-Board Technology

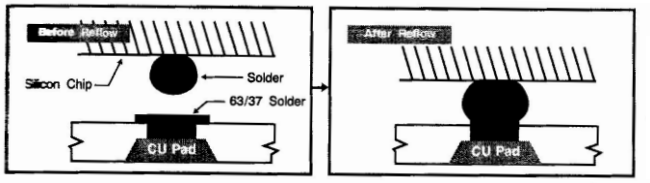

Flip-chip technology

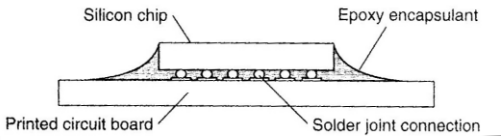

Ball Grid Array package

Plastic molded pad array MCM

Flip-chip MCM-L

Fig.1-3 Schematic illustration of advanced IC packages (Hwang, 1996)

(2) Reliability of advanced IC packages

As a result of the compact designs of advanced IC packages, reliability is a challenge and a major concern for manufacturers. Failure in electronic devices may be caused by cracking and delamination in IC packages. For example, a model based on the assumption of perfect linear elastic crack tip fields was developed by Yao and Qu (2002) to determine the amount of cohesive failure at polymer-metal interfaces. A review of reliability prediction methods for electronic devices has been presented by Foucher et al. (2002). The dominant issue in component level reliability is delamination and cracks initiated at the interface between dissimilar materials; in board level reliability, solder joint integrity is a primary issue (Amagai, 2002). Research has been

conducted on the topics of silicon die, underfill and solder properties, as well as environmental conditions (moisture, temperature and loading mode) that affect the reliability of advanced IC packages. The following describes some of these factors.

Han (2001) applied fracture mechanics together with finite element analysis (FEA) to study cracking on the rear of dies in flip-chip BAG packages (Fig.1-4). The effects of crack location/length and some key material properties on the reliability of flip chip BGA package were analyzed; the stress intensity factor and strain energy release rate calculated from FEA were taken as design indices. Three-point bend tests (e.g., Wu, et al., 2003) and four-point bend tests (e.g., Cotterell, et al., 2003) have also been conducted to measure the strength of silicon dies, and it was found that die strength depends on the grinding pattern, and is affected by defects introduced through surface grinding and edge dicing. Tsai et al. (2006) proposed two test methods (point-loaded circular plate with simple supports and point-loaded plate on an elastic foundation) to measure silicon die strength; the test results were compared with the widely used four-point bending test.

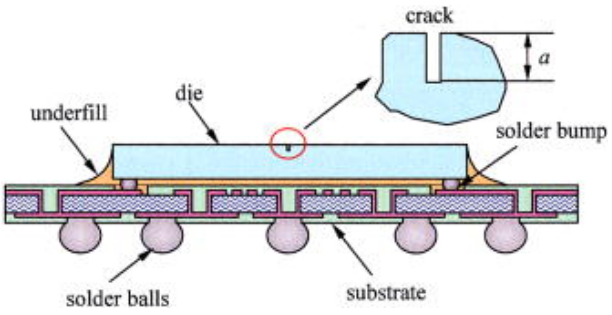

Fig.1-4 Schematic cross sectional view of die cracking in flip chip BGA package (Han, 2001)

Underfill materials consist of epoxy or cyanate ester resins, catalyst, crosslinker, wetting agent, pigment and fillers; the key material properties affecting underfill flow are viscosity and surface tension as experimentally measured by Wang (2002). The application of underfill in an IC package reduces the stress to solder bumps and enhances the reliability of solder joints; however, the adhesion properties of underfill material are critical to the thermo-mechanical reliability of underfilled flip chips. When the interfaces between the die and the underfill or between the underfill and solder mask on the board are not completely bonded, the solder joint fatigue life for a flip chip package will be affected. Xu et al. (2004) used a fracture mechanics approach to study underfill delamination in flip chips subjected to thermal cycling or thermal shock testing via the J-integral method. Kuo et al. (2004) studied the time and temperature-dependent mechanical behavior of underfill materials in electronic packaging; numerical simulations (Larson and Verges, 2003; Park, et al., 2003) were conducted to investigate how stress and fracture at chip/underfill interfaces are influenced by the thermo-mechanical properties of the underfill and the structure of the flip-chip assembly due to temperature changes.

Studies of moisture failure mechanisms have been conducted for chip scale packages. Okura et al. (2002) investigated the effect of constant temperature and humidity environments on the durability of interconnects in underfilled flip-chip-on-board assemblies, and found that new failure modes may be created due to hygromechanical swelling; Pseudo 3-D finite element analyses have been undertaken to quantify moisture absorption and diffusion through the

polymeric underfill, and the resulting hygromechanical viscoplastic stress history. Tee et al. (2003) applied various types of modeling to analyze moisture distribution, hygroswelling behavior and thermo-mechanical stresses in FCBGA with no-flow underfill subjected to moisture preconditioning, reflow and pressure cooker tests (PCT). Modeling of interfacial delamination in plastic IC packages under hygrothermal loading has also been conducted by Tay (2005). Fig.1-5 illustrates the progress of delamination at the interface between the die attach material and die backside under PCT conditions (121^0C, 2atm, 100RH% and 168hours) (Chung, et al. 2002).

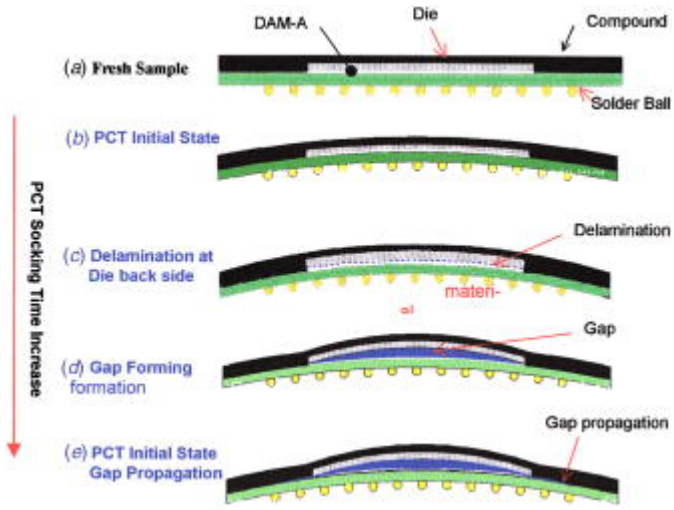

Fig.1-5 Illustration of delamination due to moisture under PCT conditions (Chung, et al. 2002)

Thermal loading arises from the presence of dissimilar materials that are combined together. Because of mismatch between their thermal expansion coefficients, high stresses may be generated at the interfaces between different materials during fabrication and assembly or operation. For example, delamination between copper and epoxy molding compounds in IC packages may occur during manufacturing processes or operation. Also, in the

operation of many electrical devices, power dissipation is very high, thus generating heat and causing temperature variations. Therefore, interfacial fracture caused by thermal loading is one of the primary concerns in electronic package design. Koguchi et al. (2003) investigated numerically and experimentally, deflections in chip scale packages using a thermo-viscoelastic analysis based on multi-layer plate theory. Vandevelde et al. (2003) conducted parameterized modeling of the thermo-mechanical reliability of chip scale package (CSP) assemblies with respect to several factors - the PCB parameters, chip dimensions and the parameters defining solder joint geometry. Cai et al. (2003) studied thermal fatigue failure of SnPb solder joints in flip-chip packages and found that mismatch of thermal expansion resulted in overall warpage of the assembly for packages with underfill. There has been extensive research on the reliability of IC packages subjected to thermally induced loading.

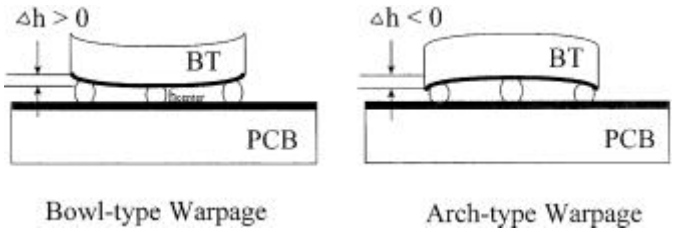

Fig.1-6 Representation of warpage of substrate in BGA assembly (Chan et al., 2002)

Failure and fracture of solder joints in advanced IC packages are major issues that affect the reliability of electrical devices, and have generated much research in this area. Factors such as insufficient heating in the solder melting phase, poor thermal stability of PCBs, insufficient printing solder paste, type of pad surface finishing and diffusion barriers affect soldering performance and

result in fatigue failure of solder joints (Alam et al., 2002; Fan et al., 2003; Steenberge, et al, 2007). Substrate flexibility was found to have significant effect on solder joint thermal fatigue reliability. Yang et al. (2005) examined the influence of residual warpage and consequent residual stress after reflow on the reliability of large flip-chips using lead-free solder; several effective experimental approaches to accurately measure residual warpage (Moiré interferometry, shadow Moiré, and image processing schemes) have been employed. Chan et al. (2002) studied the effect of warpage of the substrate on the reliability of ball grid array assemblies (Fig.1-6); warpage changes the shape of solder joints and will reduce joint fatigue life. Liu et al. (2002) investigated the thermal mechanical flexibility of substrate to improve solder joint thermal fatigue life. Thermal stresses and strains in solder joints can be reduced as flexible substrates can absorb energy that would otherwise be concentrated in solder joints during temperature cycling (Chen et al., 2005). With an increase in power dissipation and a decrease of package size, the heat generated by electric currents becomes severe. Mismatch in the coefficients of thermal expansion (CTE) between a silicon die and a PCB will induce stresses in solder joints; this may decrease the reliability of flip-chip packages. For example, Su et al. (2003) studied cracking at the interface of an In60Pb40 solder joint on a brittle die when the joint was subjected to a temperature change; a fracture initiation criterion based on critical values of the stress intensities was applied and validated. Shakya et al. (2004) developed an improved time-dependent analytical model for predicting the maximum shear displacement in an area-array electronic assembly under global thermal mismatch loading. Experiments and finite element analysis

studies on the thermo-mechanical durability of solder joints in IC assemblies have also been conducted (e.g., Zhang, et al., 2005; Obaid, et al., 2005); some modified Coffin-Manson equations have been developed to predict solder joint fatigue life reliability (e.g., Shohji, et al., 2004).

There have been quite a lot of research on thermo-mechanical behavior and reliability of solder joints. Apart from thermally-induced stresses in solder joints, mechanical loading is also a major cause of solder joint failures in IC packages. With the trend towards lead-free solders, the reliability of lead-free solder joints has prompted increasing research in this area in recent years (Lau, 2006). For example, monotonic and cyclic four-point bend tests have been undertaken for reliability assessment of solder joints (Sn63Pb37, SnAg3.0Cu0.5 and SnAg4.0Cu0.5) in flip chip BGA components (Chen, et al., 2007). The present research investigates the mechanical properties and reliability of lead-free solder joints in BGA package subjected to quasi-static and dynamic loading. A detailed literature review of previous studies on the mechanical properties of solder joints is presented following this.

1.2 Solder alloys and solder joints

1.2.1 Solder alloys and rate-dependent mechanical properties

(1) Types of solder alloys and the trend to lead-free soldering

Solders are commonly used in electronic packaging and assemblies as interconnecting material; they serve electrical, thermal and mechanical functions. As prevention of failure/fracture in solder joints is critical, understanding the mechanical properties of solder material is important in determining solder joint strength and reliability. A general definition of a solder is a fusible alloy which liquefies at temperatures below 400^{o}C. Various alloy systems can be used as solder materials, such as Sn-Pb, Sn-Ag, Sn-Sb, Sn-Bi, Sn-In, Sn-Pb-Ag, Sn-Pb-Sb, Sn-Pb-Bi, Sn-Pb-In, Sn-Ag-Sb, Pb-In, Pb-Ag and Pb-Sb (Hwang, 1996). This makes the physical properties of a solder complex because they depend on the alloy components and proportions (Table 1-1). Moreover, factors such as temperature and loading speed can affect solder alloy strength, depending on the alloy system, as illustrated in Fig.1-7.

Table 1-1 Fourteen solder alloy systems and their corresponding phase transition temperatures (Hwang, 1996)

Alloy composition	Solidus °C	Solidus °F	Liquidus °C	Liquidus °F	Plastic range °C	Plastic range °F
Sn-Pb System						
100 Sn	232	450	232	450	0	0
80 Sn/20 Pb	183	361	199	390	0	0
70 Sn/30 Pb	183	361	193	380	10	19
63 Sn/37 PB (E)	183	361	183	361	0	0
60 Sn/40 Pb	183	361	190	375	7	14
50 Sn/50 Pb	183	361	216	420	33	59
40 Sn/60 Pb	183	361	238	460	55	99
30 Sn/70 Pb	185	365	255	491	70	126
25 Sn/75 Pb	183	361	266	511	83	150
15 Sn/85 Pb	183	361	288	550	105	189
10 Sn/90 Pb	268	514	302	575	34	61
5 Sn/95 Pb	308	586	312	594	4	8
100 Pb	328	620	328	620	0	0
Sn-Ag System						
100 Ag	961	1761	961	1762	0	0
96.5 Sn/3.5 Ag (E)	221	430	221	430	0	0
95 Sn/5Ag	221	430	240	464	19	34
Sn-Sb System						
100 Sb	630.5	1167	630.5	1167	0	0
99 Sn/1 Sb (E)	235	456	235	456	0	0
95 Sn/5 Sb	235	455	240	464	5	9
Sn-Bi System						
100 Bi	271.5	520	271.5	520	0	0
42 Sn/58 Bi (E)	138	281	138	281	0	0
Sn-In System						
100 In	156.6	313	156.6	313	0	0
70 Sn/30 In	117	241	175	346	58	105
52 Sn/48 In	118	244	131	268	13	24
60 Sn/40 In	113	235	122	252	9	17
48 Sn/52 In (E)	117	241	117	241	0	0
Pb-In System						
70 Pb/30 In	240	464	253	488	13	24
50 Pb/50 In	180	256	209	408	29	52
40 Pb/60 In	174	345	185	365	11	20
30 Pb/70 In	160	320	174	345	14	25

Pb-Sb System						
95 Pb/5 Sb	252	485	295	563	43	78
90 Pb/10 Sb	252	485	260	500	8	15
88.9 Pb/11.1 Sb (E)	252	485	252	486	0	0
Sn-Au System						
100 Au	1063	1945	1063	1945	0	0
80 Au/20 Sn (E)	280	536	280	536	0	0
Pb-Ag System						
97.5 Pb/2.5 Ag (E)	303	578	303	578	0	0
Sn-Pb-Ag System						
62 Sn/36 Pb/2 Ag (E)	179	355	179	355	0	0
15 Sn/82.5 Pb/2.5 Ag	275	527	280	537		
10 Sn/88 Pb/2 Ag	268	514	290	554	22	40
5 Sn/90 Pb/5 Ag	292	558	292	558	0	0
5 Sn/92.5 Pb/2.5 Ag	287	549	296	564	9	15
5 Sn/93.5 Pb/1.5 Ag	296	564	301	574	5	10
2 Sn/95.5 Pb/2.5 Ag	299	570	304	579	5	9
1 Sn/97.5 Pb/1.5 Ag	309	588	309	588	0	0
Sn-Pb-Bi System						
60 Sn/14.5 Pb/25.5 Bi	96	205	180	356	84	151
43 Sn/43 Pb/14 Bi	144	291	163	325	19	34
34 Sn/20 Pb/46 Bi (E)	100	212	100	212	0	0
16 Sn/32 Pb/52 Bi (E)	96	205	96	205	0	0
Sn-Pb-Sb System						
85 Sn/10 Pb/5 Sb	188	370	230	447	42	76
5 Sn/85 Pb/10 Sb	245	473	255	491	10	18
5 Sn/92 Pb/3 Sb	239	462	285	545	46	83
Sn-Pb-In System						
70 Sn/18 Pb/12 In (E)	162	324	162	324	0	0
Pb-In-Ag System						
92.5 Pb/5 In/2.5 Ag (E)	300	572	300	572	0	0
90 Pb/5 In/5 Ag	290	554	310	590	20	36

NOTE: (E) = eutectic alloy.

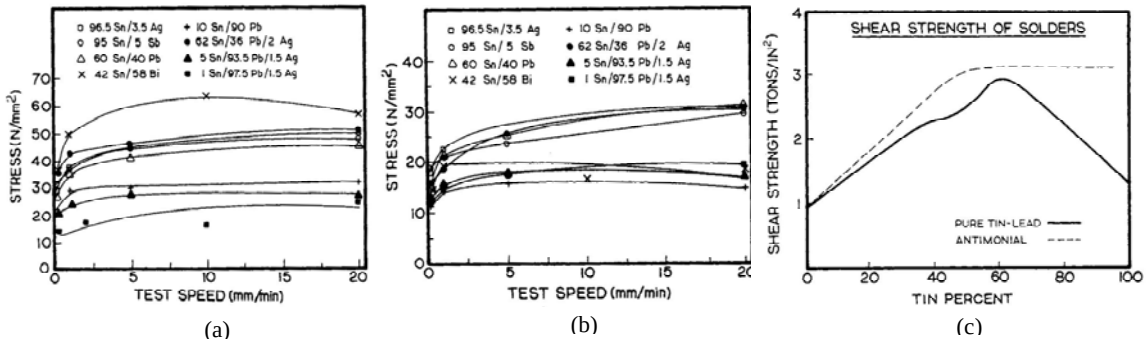

(a) (b) (c)

Fig.1-7 Shear strength of solder alloys corresponding to (a) 20°C (b) 100°C and (c) Sn-Pb composition (Hwang, 1996)

Among these compositions of solder alloys, eutectic Sn-Pb solder (Sn63Pb37) has been widely used in electrical devices. However, there is a global trend to lead-free soldering. For instance, Fig.1-8 shows a 1657CCGA (ceramic column grid array) package, which was developed by IBM, as one of the best packaging candidates for housing IC chips in high-end computers. Like all other IC packages, the CCGA used to be soldered onto PCBs using Sn-Pb solder. However, because of regulations against the use of lead, implemented from July 1st 2006, CCGA packages now have to be soldered using lead-free solders (Lau et al, 2004).

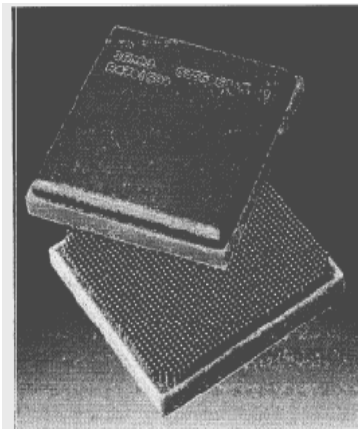

Fig.1-8 IBM's 1657 CCGA (Lau, et al., 2004)

Lead (Pb) is a heavy toxic substance used in many electrical appliances, and the lead in solder constitutes about 3% of the world's total consumption. Arising from today's trend towards 'green' products, environmentally-conscious manufacturers are moving to lead-free schemes for electronic devices and components, and this trend towards complete lead-free products is gathering momentum. Following the lead-free roadmaps developed by the Japanese Electronics Industries Association (JEIDA) (1998) and the National Electronics Manufacturing Initiative (NEMI) (1999), the European Union has published a directive (2002/95/EC) in January 2003, restricting the use of certain hazardous substances in electrical and electronic equipment (RoHS) by July 2006 (Gupta, et al., 2004).

Table 1-2 Lead-free solder candidate alloys in use and their cautions (Suganuma, 2004)

Processes	Alloys	Notes
Wave soldering	*Sn–Ag family*	Compatibility with Sn–Pb plated components.
	Sn–3.5Ag	Fillet-lifting and land-lifting.
	Sn–(3–3.9)Ag–(0.5–0.8)Cu	For one-sided PWBs, Bi can be added, although the compatibility with 42 alloy should be noted.
	Sn–Cu family	
	Sn–0.7Cu	
	With some additions: Ag, Au, Ni, Ge, In, etc.	
Reflow soldering		
High temperature	*Sn–Ag family*	Heat resistance of components and PWBs. One needs to control temperature distribution on PWBs.
	Sn–3.5Ag	Compatability of Bi with Sn-Pb plating.
	Sn–(3–3.9)Ag–(0.5–0.8)Cu	
	Sn–(2–4)Ag–(1–6)Bi	
	With 1–3%In	
Intermediate temperature	*Sn–Zn family*	Corrosion should be noted, especially for chlorine and for humidity.
	Sn–9Zn, Sn–7Zn–Al	Barrier plating such as Au/Ni can improve high-temperature stability.
	Sn–8Zn–3Bi	

	Sn–Ag–In family Sn–3.5Ag–(6–8)In–0.5Bi	Compatibility with certain kind of plating.
Low temperature	*Sn–Bi family* Sn–57Bi–(0.5–1)Ag	Compatibility with Sn–Pb plated components.
Hand and robot soldering	*Sn–Ag family* Sn–3Ag–0.5Cu Sn–Cu, Sn–Bi families	Compatibility among different solders and fluxes.

As Pb-free solders come in various compounds with distinctive components, experimental data and simulation results related to them are still limited, compared to information on conventional Sn-Pb solder. New challenges lie in determining their reliability and failure/fracture mechanisms as well as selection of appropriate Pb-free alloys to maximize product life, in addition to the considerations on toxicity, cost, abundance, wetability and melting temperature etc. For example, Kim et al. (2003) studied the effects of precipitates (i.e. ~0.1 wt.% Fe, Ni, Co, Mn or Ti) on micro-structural features, undercooling characteristics and monotonic quasi-static tensile properties of lead-free (Sn96.5Ag3Cu0.5) solder alloys and joints. Table 1-2 lists some current lead-free solders, together with their compositions and characteristics. Among these, it has been stated that “the Sn-Ag-Cu family of solder is the strongest candidate to become the standard lead-free solder. Research in Japan, Europe and the United States indicates that this alloy is extremely stable and is considered capable of meeting globally acknowledged standards. However, the compositions being recommended in Japan, Europe, and the United States have slight differences” (Suganuma, 2004).

Some research has shown that some types of SnAgCu lead-free solder joints showed better reliability under the conditions investigated than SnPb solder

joints (Nurmi, et al., 2004; Keser, et al., 2004). Spraul et al. (2007) tested the reliability of SnPb and Pb-free flip-chips under temperature cycling conditions (-40^0C to 125^0C) and found that the components soldered with SnAg4Cu0.5 solder exhibited a significantly longer life before electrical breakdown. A microstructural perspective may explain this; Xiao et al. (2004) experimentally studied the aging effects on the microstructure and tensile properties of Sn95.5Ag3.9Cu0.6 solder alloy; the aging behavior of lead-free alloy was different and more complex than that of eutectic SnPb solder alloy. Peng et al. (2006) found that a Sn-Ag solder system can lower the intermetallic compound (IMC) diffusion rate hence result in a better resistance to solder bump strength degradation. A comparative study between SnPb and SnAgCu solder joint reliability under thermal cycling was also conducted by Vandevelde et al. (2007) using non-linear finite element analysis. Early thermal cycling tests by Ratchev et al. (2004) showed a different crack propagation for SnAgCu solder connections (web-like cracking linking brittle particles through the bulk of the solder instead of cracks along Sn and Pb grain interfaces) (Fig.1-9). Wiese and Wolter (2007) investigated experimentally the creep of thermally aged SnAg and SnAgCu solders via three types of specimens (flip-chip, PCB joint and bulk specimens), and found that Cu and Au intermetallics are able to significantly strengthen SnAg and SnAgCu solders and that this strengthening effect depends on the undercooling of the solder.

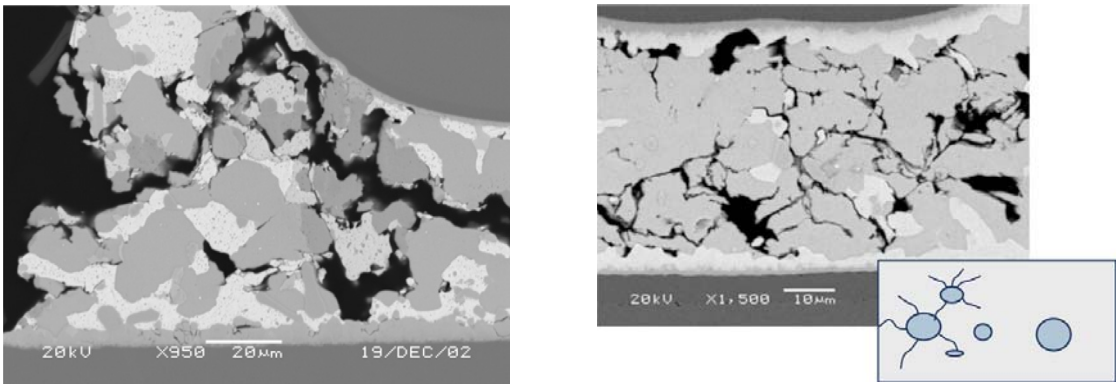

(a) (b)

Fig.1-9 Low magnification SEM pictures of (a) a SnPbAg solder connection and (b) a corner SnAgCu solder connection (Vandevelde, et al., 2007)

Increasing research has been initiated with the movement to Pb-free soldering in IC assemblies, and many more studies of the Sn-Ag-Cu family have been carried out with respect to the thermo-mechanical analysis of solder alloys and solder joints. For example, Lau et al. (2002) examined the creep behavior of lead free solder joints (96.5Sn3.5Ag) using ANSYS. Wei, et al. (2004) investigated the behavior of Sn95.5Ag3.9Cu0.6 solder alloy under thermo-mechanical loading, and proposed a constitutive model to characterize tensile and cyclic behavior of this lead-free alloy. Korhonen and Lehman (2007) conducted isothermal fatigue tests on near-eutectic Sn-Ag-Cu alloys between -25^0C and 125^0C. Research on the dynamic mechanical properties of Sn-Ag-Cu soldering is still limited. In this study, solder joints comprising Sn96.5Ag3.0Cu0.5 are examined through quasi-static and impact loading to identify their rate-dependent mechanical properties (solder ball specimens are provided by Micron Semiconductor Asia Pte Ltd).

(2) Rate-dependent mechanical properties of solder alloys

In order to obtain a fuller understanding of the mechanical response of solder joints, it is instructive to determine the possibility of rate sensitivity in solder alloys; this is because a solder joint in an IC package constitutes a connection between a solder bump and a pad. Experimental tests have showed that Sn-Pb solder alloys are strain-rate and temperature dependent. Hwang (1996) presented a diagram showing the effect of shearing rate on the strength of Sn63Pb37 solder; the shearing rate is very small (10^{-7}~10^{-1}/s), as shown in Fig.1-10a. Peng et al. (2004) demonstrated that the shear strength of a solder bump varies with the speed of shearing - a higher speed results in a higher shear strength, although the shear speeds examined were still relatively low (0.01mm/s ~ 0.2mm/s), as shown in Fig.1-10b.

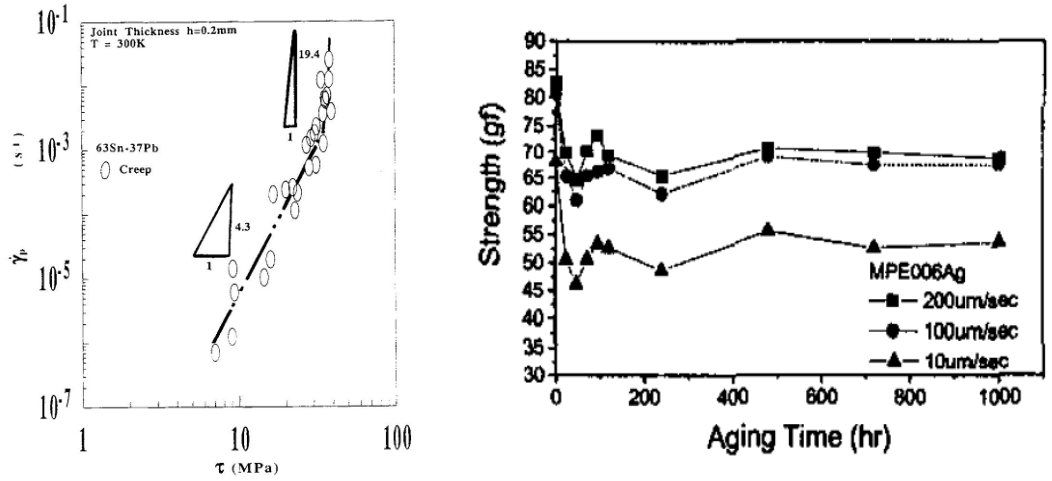

(a) (b)

Fig.1-10 (a) Variation of plastic shear strain rate with stress for Sn63Pb37 solder (Hwang, 1996), and (b) effect of shear speed and aging time on shear strength of Sn-Pb solder (Peng, et al., 2004)

Sasaki et al. (2001) conducted tension tests on Sn60Pb40 solder materials,

and the stress-strain results showed strain rate dependence (from 0.001%~0.1%s^{-1}) and temperature dependence (303K ~ 343K), as depicted in Fig.1-11a. Nose et al. (2003) measured the tensile strength of six types of Sn-Pb solder alloys (5Sn-95Pb, 10Sn-90Pb, 40Sn-60Pb, 60Sn-40Pb, 63Sn-37Pb and 62Sn-36Pb-2Ag) at strain rates of 0.001/s to 0.1/s, in the temperature range of 313K and 398K. Dog-bone shaped tensile specimens were machined from a 25mm diameter solid bar. The tensile strength was found to increase with strain rate, and the stress-strain curves are also related to temperature and Sn content (Fig.1-11b, illustrates the response of 60Sn40Pb solder alloy).

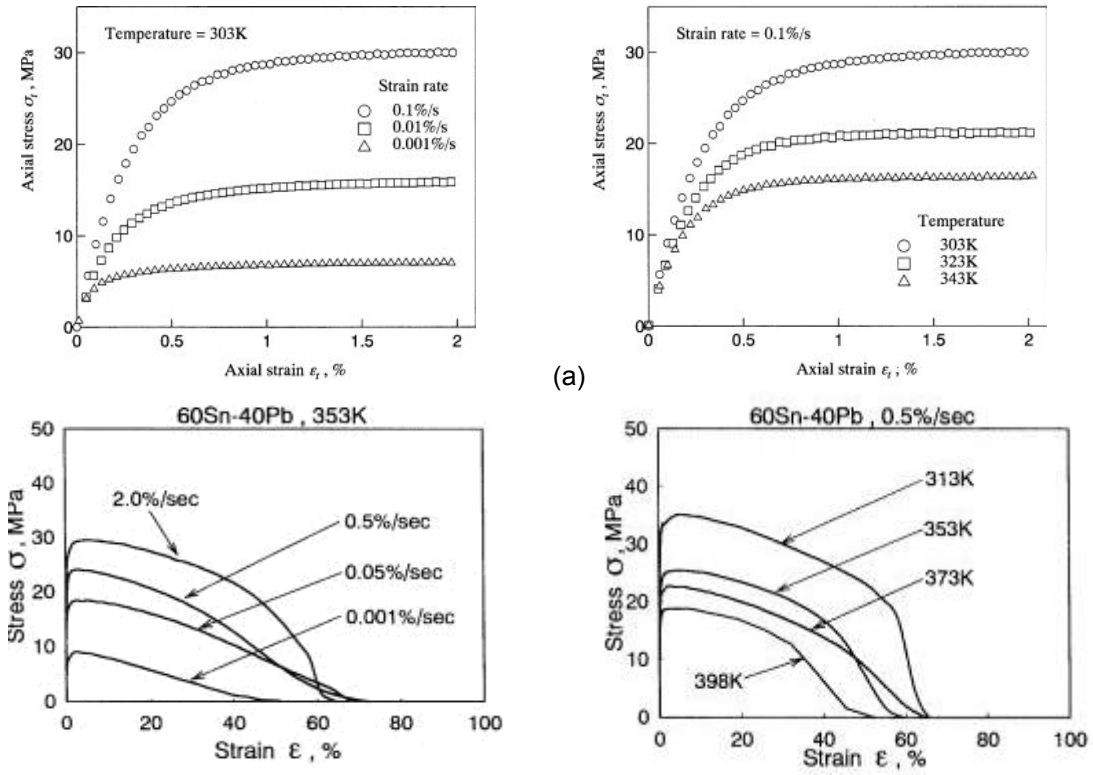

Fig.1-11 Illustration of effect of strain rate and temperature on tensile stress-strain response of 60Sn40Pb solder alloy (a) from Sasaki, et al., 2001 and (b) from Nose et al., 2003)

A simple constitutive equation for creep was assumed by Nose et al. (2003),

$$\dot{\varepsilon}_c = \alpha\sigma^{\beta} \tag{1-1}$$

Sasaki et al. (2001) assumed that the limiting stress $\sigma_{\lim}$ (i.e. ultimate stress) of solder alloy under pure tension can be expressed as a power function of the strain rate $\dot{\varepsilon}$,

$$\dot{\varepsilon} = A_0\sigma_{\lim}^{n} \tag{1-2}$$

where A_0 is a material constant. From tensile tests on 60Sn40Pb solder alloy (Fig.1-12), the relationship between strain rate (from 0.1%~0.001%/s) and limiting stress was identified for various temperatures:

$$\begin{cases} \ln\dot{\varepsilon} = 3.08\ln\sigma_{\lim} - 12.9 & \text{at } 303\text{K} \\ \ln\dot{\varepsilon} = 3.11\ln\sigma_{\lim} - 11.9 & \text{at } 323\text{K} \\ \ln\dot{\varepsilon} = 3.16\ln\sigma_{\lim} - 11.0 & \text{at } 343\text{K} \end{cases} \tag{1-3}$$

Vandevelde et al. (2003) described the elastic modulus E (*MPa*) of the solder alloy investigated as a function of temperature T (Celsius),

$$E = 35366 - 151T \tag{1-4}$$

and the yield stress σ_y (*MPa*) as a function of temperature T (Celsius),

$$\sigma_y = 33.9 - 0.145T \tag{1-5}$$

Work-hardening, which defines the increase in flow stress due to plastic deformation of the solder material, was described by,

$$\sigma_y = G\left(\frac{\varepsilon_{pl}}{6.1\times10^{11}}\right)^{1/5.6} \tag{1-6}$$

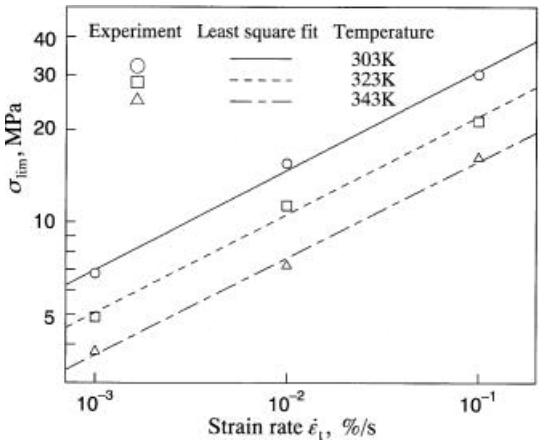

Fig.1-12 Variation of strain rate with limiting stress at 303, 323 and 343K for 60Sn40Pb solder alloys under tension (Sasaki et al., 2001)

There are a limited number of reports on strain rate sensitivity of solder that encompasses high rates. Clyens and Campbell (1974) derived stress–strain curves for 61.9Sn38.1Pb solder for the strain rate range 200~4000/s. Wang and Yi (2002) conducted compression tests at strain rates of 0.001~1200/s on 63Sn–37Pb solder with a grain size of 15μm. The normalized yield stress was characterized by the Cowper–Symonds model to define the strain rate effect,

$$\sigma/\sigma_0 = 1 + (\dot{\varepsilon}/D)^{1/q} \qquad (1\text{-}7)$$

Siviour et.al (2005) measured the compressive mechanical properties of solders (Sn-Pb, Sn-Ag, Sn-Ag-Cu) at high strain rates (500–3000/s) using a split Hopkinson bar, and found that the solder alloys are strain rate and temperature dependent, and a linear fit was applied to the variation of stress (at 2% strain) with strain rate or temperature for Sn63Pb37 solder alloy (Fig.1-13).

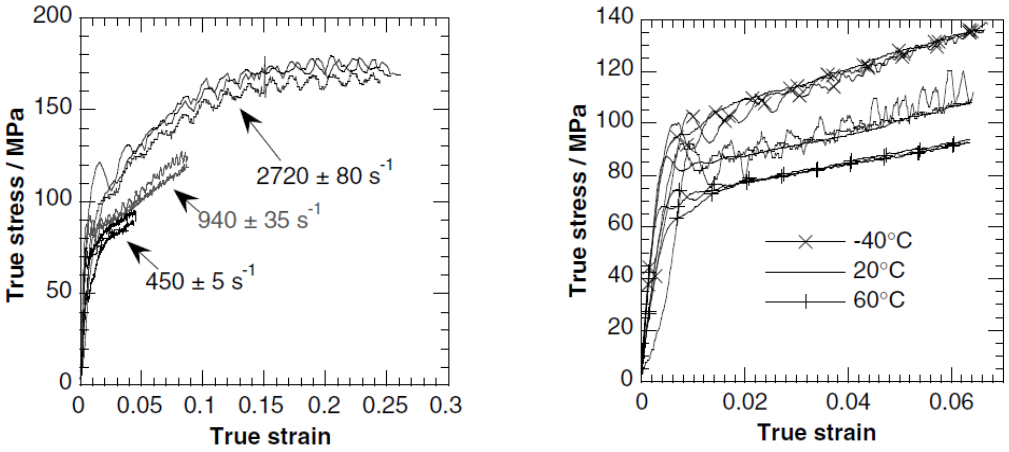

(a) Stress-strain curves for Sn63Pb37 solder alloy at three strain rates (at 20^{0}C), and at three different temperatures (at 950 ± 50s^{-1})

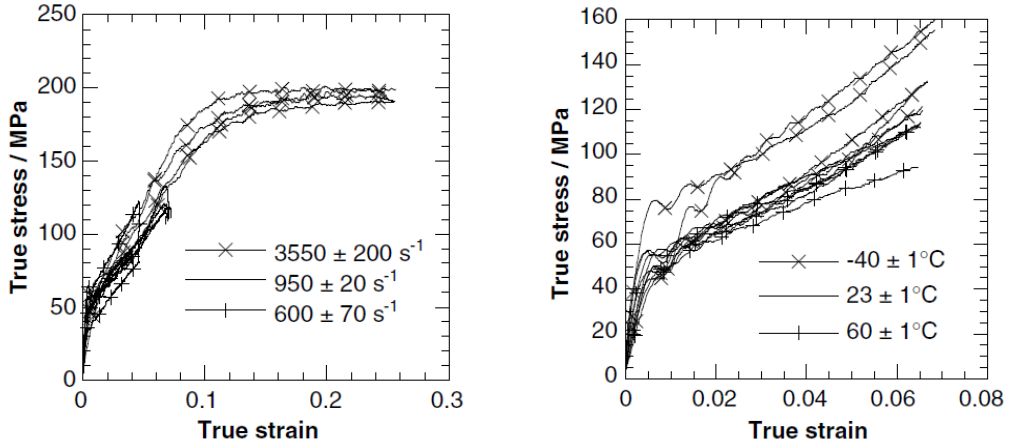

(b) Stress-strain curves for Sn96.5Ag3.0Cu0.5 solder alloy at three strain rates (at 20^{0}C), and three temperatures (at 990 ± 70s^{-1})

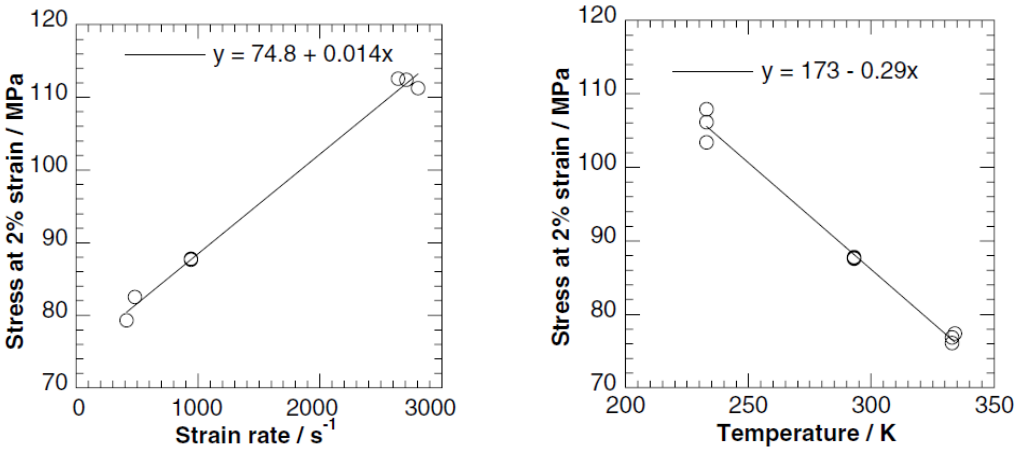

(c) The dependence of stress at 2% strain on strain rate for Sn63Pb37 solder at 20^{0}C, and on temperature at 950 ± 50s^{-1})

Fig.1-13 Mechanical properties of SnPb and lead-free solder alloys at high strain rates (Siviour, et al., 2005)

Constitutive relationships have been developed to describe rate-dependant properties of solder alloys, taking into account both strain-rate and temperature dependences. A flow rule for creep-plasticity in solder alloy was proposed by McDowell et al. (1994), whereby the inelastic rate of deformation tensor is defined by

$$\mathrm{D}_{in} = \sqrt{3/2}A\left[\left\langle s_v \right\rangle / D\right]^n \exp\left(B\left[\left\langle s_v \right\rangle / D\right]^{n+1}\right)\exp(-Q/RT)\mathrm{N} \qquad (1\text{-}8)$$

where A, B and n are material constants, Q is the activation energy for inelastic flow, R the universal gas constant, T the absolute temperature and N the direction of inelastic strain rate; $\left\langle s_v \right\rangle$ is a yield function with a von Mises form in terms of the viscous overstress (i.e. $\left\langle s_v \right\rangle = s_v$ if $s_v \geq 0$ and $\left\langle s_v \right\rangle = 0$ otherwise). By applying Eq.(1-8) to Sn63Pb37 solder material, Stolkarts et al. (2001) found, that a simplified flow equation can yield a more satisfactory fit for experimental data collected with temperatures that vary from 25~100^{o}C and strain rates ranging from 0.000025~0.01s^{-1}, over a strain of 0.3% to 1%,

$$\mathrm{D}_{in} = \sqrt{3/2}A\left[\left\langle s_v \right\rangle / D\right]^n \exp(-Q/RT)\mathrm{N} \qquad (1\text{-}9)$$

This model is “simpler than a typical creep-plasticity model due to the fact that no isotropic or kinematic hardening was observed over the experimental ranges examined”, the authors stated. Since no kinematic hardening was observed, then $s_v = \sqrt{3/2}\|\mathrm{s}\| - \sigma_y$; therefore the rate of inelastic strain for uniaxial loading was defined by

$$\dot{\varepsilon}_{in} = A\left[\left\langle \sigma - \sigma_y \right\rangle / D\right]^n \exp(-Q/RT) \qquad (1\text{-}10)$$

where σ_y, D and Q can be taken as constants over the ranges examined. From the results of creep tests, Wiese and Wolter (2004) found that the

general creep behavior of eutectic SnAg/SnAgCu solder follows a double power law,

$$\dot{\varepsilon} = A_1\left[\sigma/\sigma_N\right]^{n_1}\exp\left(-Q_1/RT\right)+A_2\left[\sigma/\sigma_N\right]^{n_2}\exp\left(-Q_2/RT\right) \qquad (1\text{-}11)$$

The first term corresponds to creep behavior at low stresses, and the second term corresponds to the response at high stresses.

An Arrhenius-type power-law constitutive model to describe the steady-state shear strain rate $\dot{\gamma}$ of solder in terms of the applied shear stress τ is

$$\dot{\gamma} = C\tau^n \exp\left(-\frac{Q}{RT}\right) \qquad (1\text{-}12)$$

where n is the stress exponent, Q is activation energy for creep, R Boltzmann's constant, T the absolute temperature and C is a constant. Shi et al. (2002) point out that this simple Arrhenius model does not consider the difference in dislocation creep mechanisms at low and high temperatures, as it employs only one power-law creep process for the whole temperature range. Based on a dislocation controlled creep mechanism and Gibbs's free-energy theory, a more parameter creep constitutive model for eutectic solder was proposed,

$$\dot{\gamma} = C_1\frac{G}{T}\left(\frac{\tau}{G}\right)^n\left[1+C_2\exp\left(-\frac{\left(Q_c-Q_l\right)-\left(\alpha-\beta\right)\left(\tau/G\right)}{RT}\right)\right]\exp\left(-\frac{Q_l-\alpha\left(\tau/G\right)}{RT}\right) \qquad (1\text{-}13)$$

where Q_c and Q_l are the respective activation energies for core-diffusion and lattice-diffusion; α and β represent the slopes of the activation energy versus normalized shear stress curves at low and high temperatures respectively.

The constitutive theory of Darveaux for isotropic thermo-viscoplasticity has attracted wide use for modeling the strain rate and temperature dependence of solder alloys; the steady state creep rate is defined by

$$\frac{d\varepsilon_{steadystate}}{dt} = A_1 \frac{E}{T}\left[\sinh\left(\beta\frac{\sigma}{E}\right)\right]^n \exp\left(\frac{-Q}{kT}\right) \qquad (1\text{-}14)$$

This type of constitutive model has been employed in a number of studies to describe the behavior of solder alloy (as well as solder joints) under thermo-cyclic loading and thermal-creep behavior (e.g., Amagai, et al., 2002; Xiao and Armstrong, 2005; Vandevelde, et al., 2003).

There are some other constitutive models that have been proposed to describe visocoplasticity of Sn-Pb or Pb-free solder alloys. Stolkarts et al. (2001) proposed a constitutive model for Sn63Pb37 solder alloy (strain rates of 0.000025~0.01s^{-1}) based on simplification of a creep-plasticity model, and assumed that micro-crack density is the only internal variable for the elastic properties of a solid damaged by cyclic loading. Sasaki et al. (2001) proposed a viscoplastic constitutive model for Sn-Pb solder alloys which independently incorporates equations for elastic, plastic and creep strains (i.e., Hooke's law for elastic strain, a flow law based on a von Mises type yield criterion for plastic strain and a modified Norton's law for creep). Yi et al. (2002) also proposed a viscoplastic constitutive model to describe the thermo-mechanical behavior of Sn63Pb37 solders, based on a combination of grain boundary sliding and matrix dislocation deformation mechanisms. Basaran et al. (2005) presented a viscoplastic model unified with a thermodynamics-based damage concept for Sn63Pb37 solder alloy; the model takes into account isotropic and

kinematic hardening and grain size coarsening evolution. For lead-free solder alloy, Fossum et al. (2006) proposed an internal viscoplastic damage variable to characterize Sn95.5Ag3.9Cu0.6 solder alloy under cyclic thermo-mechanical loading conditions; Yang et al. (2007) proposed a constitutive model to describe the time-dependent cyclic deformation behavior of Sn96.5Ag3.5 solder alloy under cyclic multi-axial straining.

1.2.2 Solder joints in BGA packages and intermetallic compounds

(1) Solder joints in BGA packages

Among advanced IC packages, ball grid array (BGA) packages assembled by flip-chip technology have been widely used in electronic devices in recent years, due to their high I/O density, short electrical connections and low cost (Fig.1-14). During reflow, the solder balls collapse and surface tension between solder balls and associated pad creates a strong self-centering property to compensate for any placement offsets (Kim, et al., 2004; Kim, et al., 2005). This BGA technology also has specialized techniques; depending on the substrate employed, there are ceramic (CBGA), plastic (PBGA), tape automated bonding (TBGA), metal (MBGA) and dimple grid arrays (DBGA) (Daya Perera, 1999). Consumer demand for smaller, lower cost devices with more functionality has driven the use of BGA packages in many applications, and new BGA chip scale packages continue to be developed, such as the micro-ball grid array, mini-ball grid array and micro-SMT. Solder joint arrays in

BGA packages enable compact interconnections between electrical components and circuit boards; solder joint strength and their mechanical behavior are critical issues in reliability of BGA packages.

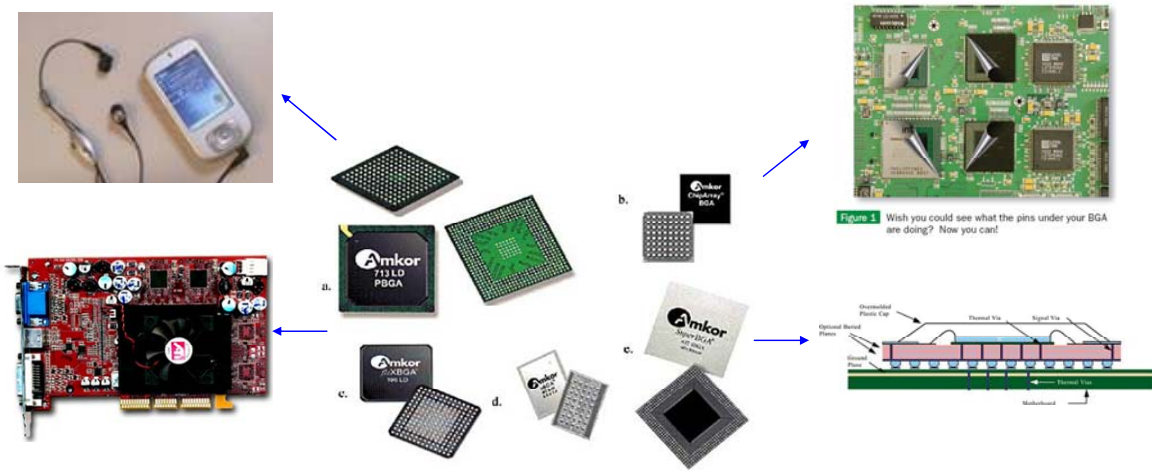

Fig.1-14 BGA packages in electronic devices

It should be pointed out that the solder joint geometry after a reflow process using flip-chip technology is related to many parameters, such as solder volume, pad thickness, pad size, surface tension, contact angle, as well as design factors such as whether solder mask defined (SMD) and non-solder mask defined (NSMD) approaches are adopted (solder mask opening is a key factor in SMD). Experimental measurements on eutectic lead-tin solder joints in flip-chip packages were performed by Josell et al. (2002) to study the relationship between solder joint stand-off height, lateral offset with applied force (normal and shear), solder volume and pad diameter. Theoretical approaches for predicting the geometric shape of a solder joint have also been investigated via energy-based methods and a force balance approach. For example, finite element formulations based on energy-based approach have been developed to study the effect of variation in design parameters

(vertical loading, solder joint volume and pad radius) on the geometrical shape of a joint under quasi-static loading (Salalha et al., 2004). By ignoring the influence of gravity, the force balance in a molten solder joint can be classified into three portions: surface tension of the liquid-atmosphere interface, surface tension of the liquid-solid interface and the force from pressure (Fig.1-15); a method to predict solder joint geometry after a reflow process for solder and non-solder mask defined BGA packages has been presented by Chen, et al. (2002). Chen et al. (2006) also described an analytical geometric method to determine liquid formation in solder joints in flip chip technology by a force balance approach. Besides these major solder joint shape prediction methods, Ahmad et al. (2005) estimated solder joint shapes by a modified Perzyna viscoplastic model; large deformation viscoplastic finite element analysis was used to simulate incompressible fluid flow. Multiformity of solder joint geometry in flip-chip IC packages increases the diversity of solder joint mechanical behavior, and also increases the complexity of FEM models.

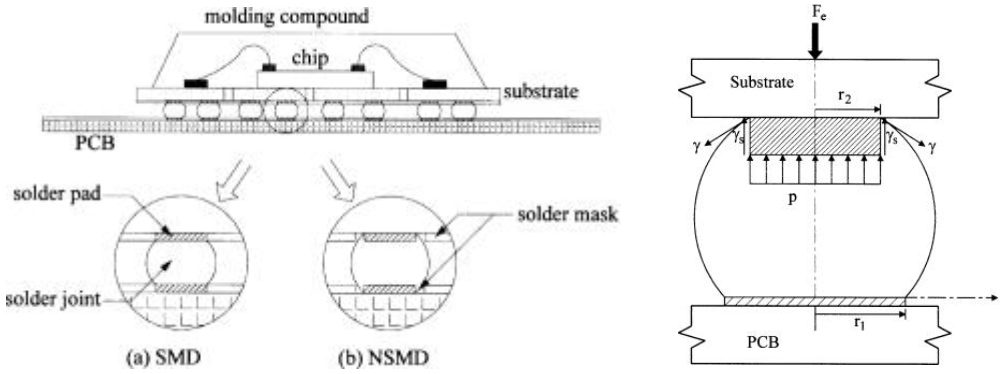

Fig.1-15 Configuration of BGA package and force balance for the upper pad of a NSMD-SMD solder joint (Chen, et al., 2002)

Defects induced in solder joints remain hidden until in-circuit or functional

testing is performed on an electrical device. Direct measurement of deformation of individual solder joint in an IC package is still difficult and measurement of force in a solder joints is nearly impossible in practice. There are some preliminary studies in these areas. Liu and Ume (2002) proposed a vibration approach for the inspection of flip-chip solder joint quality; finite element modeling showed that solder joint defects (such as solder joint disconnection) will change the vibration frequencies and responses of a flip chip. Pendse and Zhou (2002) used digital image correlation metrology to experimentally detect solder joint strain in BGA package assemblies; in this technique, deformation is obtained by the matching of pre- and post-deformation image patterns; the sensitivity of this technique is limited by the resolution of the image capturing tool (Fig.1-16a). Ham and Lee (2003) used high sensitivity moiré interferometry to measure shear deformation of Sn63Pb37 solder joints in wafer-level CSP assemblies and warpage of the assembly during thermal loading (Fig.1-16b); these showed that the creep behavior of solder reduces warpage of packages and increases shear deformation in solder bumps. The moiré interferometry technique was also used by other researchers to monitor real time strain evolution in solder joints (Ye, et al., 2003; Shi, et al., 2004, Joo, et al., 2005; Cho, et al. 2004). Xie et al. (2002) used an atomic force microscope (AFM) moiré method to measure the shear strain induced by thermal deformation for solders in BGA packages, and found that their results are consistent with that derived from electron beam moiré methods.

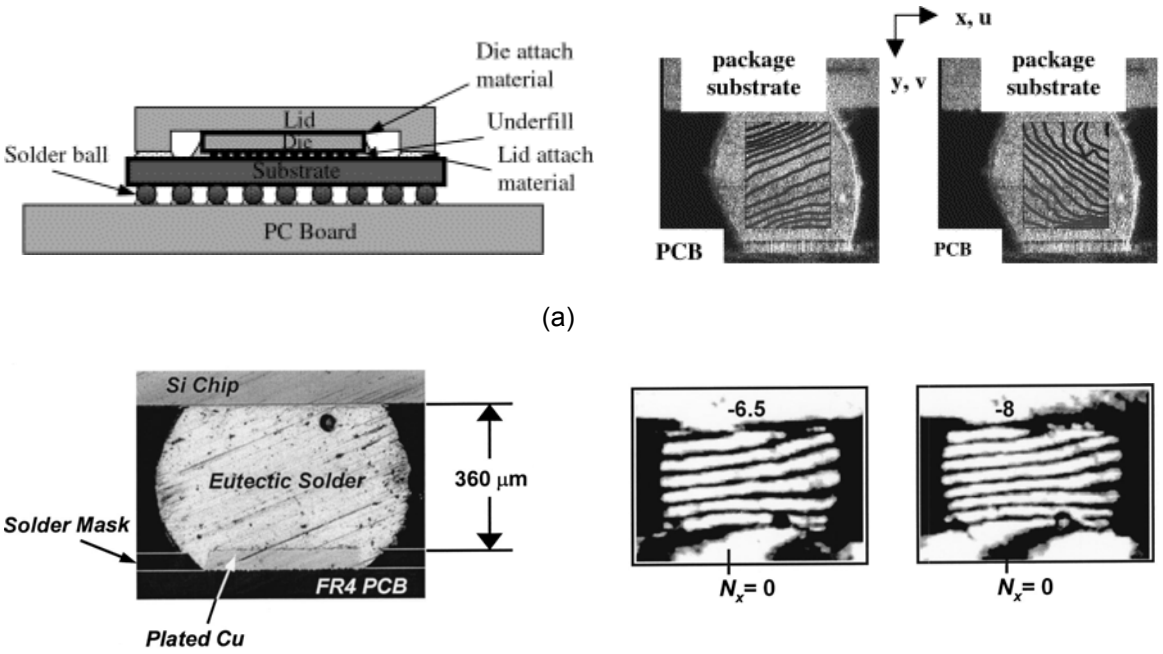

Fig.1-16 (a) Typical structure of a ceramic BGA package with a flip chip die and the graphical presentation of the u and v contours for the solder joint (Pendse and Zhou, 2002); (b) moiré fringes showing U displacement fields of the solder bump induced by the thermal loading; the contour interval is 417 nm per fringe (Ham and Lee, 2003)

These approaches in deformation and failure detection in solder joints are still not applicable in actual manufacturing operations. Characterization of solder joint mechanical properties and reliability remain based on conventional approaches employing thermo or mechanical tests on solder alloys and packages or board level IC specimens. Numerical simulations are often used to analyze solder joint behavior under thermal or mechanical loading, and to predict failures and the reliability of IC packages. It is noted that it may not be accurate to use the properties of a solder alloy as inputs for numerical simulation of solder bumps in a solder joint. This is because after the solder alloy is melted and bonded to pads, their metallic compositions as well as microstructure will change with temperature and aging, etc. Many researchers have proposed models for bulk scale metals, not micro-scale BGA solder balls.

The microstructure of solders in microelectronics IC components changes over time. The phase growth process in solder bumps arises from elevated temperatures during reflow and operation of the component. Moreover, mechanical stresses and strains due to intrinsic thermal mismatch between the various materials will occur and promote micro structural changes. Three different phase growth models for BGA solder balls (Sn63Pb37) in a real-life electronic package have been investigated experimentally and the quadratic power phase growth model fits the test data best (Basaran and Wen, 2003). Müller (2004) studied experimentally and simulated numerically the micro structural development and change in solder joints as well as growth of the intermetallic phases. Microstructural coarsening (phase growth) is considered to be closely related to thermo-mechanical fatigue failure. Intermetallic compounds formed between a solder bump and a pad are known to have distinct microstructure and affect the mechanical behavior of a solder joint.

(2) Formation and influence of intermetallic compounds

An intermetallic compound (IMC) is a thin layer of compound that is formed between the solder bump and the pad in a solder joint. The IMC growth process is strongly dependent on aging time and can lead to progressive weakening or damage along the bonding interface. Intermetallic compounds in solder joints increase the complexity of the solder joint properties; hence, understanding the effects of extensive distribution of IMC in solder joints is crucial to assessing solder joint reliability. It has aroused great interest in the

formation of IMC in solder joints. Observations from such investigations may help provide an understanding of fracture, shear strength and electrical resistance in solder joints.

Huang et al. (2002) examined the Cu-Sn IMC layer thickness in Sn63Pb37 solder paste as a function of reflow time and temperature, and its effect on IMC reliability. For traditional Sn63Pb37 solder, it was found that Cu_6Sn_5 forms in the IMC between Cu and Sn-Pb solders at 283^0C. Li and Chan (2002) studied intermetallic formation between a Pd-Ag metallization conductor and 62Sn-36Pb-2Ag solder using transmission electron microscopy (TEM), X-ray diffraction; energy-dispersive X-Ray (EDX) analysis and Selected Area Electron Diffraction (SAED) analysis to identify the formation of intermetallic compounds. The IMC formed between Pb-free solder bumps and a pad on a PCB are different from those in Pb-Sn solder joints. Chiu el al. (2004) investigated the effect of IMC growth for Pb-free solders (SnAgCu) under thermal aging (125^0C) for BGA package reliability under drop impact. The key finding is that Kirkendall voids formed at the interface between the bulk solder and the bare Cu pad of a package as a result of aging at a relatively low temperature of 100^0C. Fig.1-17a illustrates the coalescing of voids resulting in an almost complete crack separation at the interface after 40 days of aging. Void formation and coalescence were shown to be the dominant mechanisms for solder joint strength and board level drop reliability degradation. Islam et al. (2003) investigated the dissolution kinetics of electrolytic Ni and electroless Ni-P in solder joints between Cu/Ni/Au and Cu/NiP/Au finished copper pads and molten Sn96.5Ag3.5Cu0.5 solder alloy; it was found that after 180

minutes of molten reaction, the P-rich Ni layer is broken and creates more channels which results from coalescence of the kirkindal voids formed during the diffusion process (Fig.1-17b); shear tests showed that brittleness of the solder joint increases with an increase in reflow time, and fracture occurs within the IMC and P-rich Ni layer.

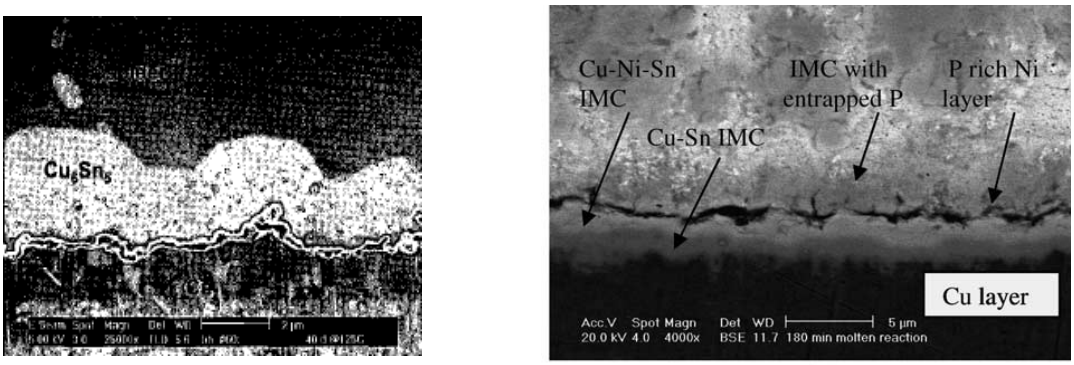

(a) (b)

Fig.1-17 Void growth and coalescence at pad-solder joint interface (a) after 40 days of aging at 125^{0}C, resulting in dramatically weakened interfacial strength (Chiu et. al, 2004) (b) after 180min reaction in molten condition at 250^{0}C (Islam et al, 2003).

In the studies of Sn-Pb and Sn-Ag solders, it was found that the thickness of the intermetallic compound grows with aging time roughly according to $t^{1/2}$. Based on diffusion-controlled growth theory, the isothermal growth of an intermetallic layer can be approximated by $d = d_0 + (Dt)^{1/2}$, where *d* is the total thickness of the intermetallic compound, d_0 the initial thickness of the layer, *D* the diffusion coefficient and *t* the isothermal aging time (Peng et al., 2004). Gupta et al. (2004) compared the IMC growth and morphology of Sn-Ag-Cu solder with four kinds of substrate pad finishes, at different thermal aging time, and tested the interconnection shear strength. Dunford et al. (2004) studied intermetallic compound formation in Pb-free solder joints (Sn3.5Ag and

Sn3.8Ag0.7Cu) on organic preservative and electroless nickel-immersion gold surface finishes, and described the solder microstructure, IMC formation and damage mechanisms. Islam et al. (2005) investigated the dissolution kinetics of Sn96.5Ag3.5 solder on electrolytic Ni and electroless NiP layer flexile substrates. Arulvanan et al. (2007) examined the microstructure evolution at intermetallic interfaces in SnAgCu solder joints subjected to thermal cycling tests (-40^0C/$+125^0$C); crack initiation and crack propagation during the test were studied. Lu et al. (2006) investigated lead free Sn-Ag-y%Cu (y=0, 0.5, 1 and 2) interconnect interfacial microstructures and the microstructure evolution under isothermal thermal treatment (150^0C/1000h). Intermetallic growth and microstructure evolution in Pb-free (e.g. Sn-Ag, Sn-Ag-Cu) solder joint have received increasing attention in recent years (Pang, et al. 2004; Vianco, et al. 2004; Sharif and Chan, 2005; Fix, et al. 2005; Islam, et al. 2005; Dariavach, et al. 2006; Jang, et al., 2006; Jang and Duh, 2006; Jiang, et al., 2006; Huang, et al. 2006; Sundelin, et al. 2006)

Lau et al. (2004) conducted thermal cycling tests on 1657CCGA packages assembled using solder ball arrays (95.5Sn3.9Ag0.6Cu and 63Sn37Pb) on PCBs with different pad surface finishes (CuSn, NiAu and Entek OSP). Test data for more than 7500 cycles between 0 and 100^0C in 40 minute cycles were collected and compared. The properties and thickness of the intermetallic compounds formed at the solder/pad interfaces are factors that directly affect the reliability of solder joints. Nanoindentation on SnAgCu solder joints and IMC interfaces were also conducted to determine the hardness and Young's modulus (Ogawa, et al. 2005; Xu and Pang, 2006; Xu,

et al., 2006). Studies showed that the tensile or shear strength of a solder joint decreases with the growth of the IMC with aging time (Amagai, et al., 2002; Duan, et al., 2003, Kim, et al., 2005, Chen, et al., 2006; Lu, et al., 2006). As a conclusion, intermetallic compounds are brittle in nature compared to the solder bump, and have significant effects on solder joint strength in BGA IC packages.

1.3 Reliability and strength of solder joints

According to classical fracture mechanics, failure may be associated with pre-cracks of certain shapes and sizes. However, in actual electronic packages, the size and location of a crack cannot be predicted. This increases the difficulties in employing traditional fracture criteria to address complicated actual problems. Some failure criteria have been developed to assess solder joint strength and to predict interconnection fracture in IC packages based on maximum normal and shear stress, maximum effective stress, energy release rate or strain energy density. In experimental approaches, criteria based on resistance measurements of daisy-chained solder joints monitored in situ have also been explored to determine electrical failure during accelerated testing of flip chip joints (e.g. Stepniak, 2002). This section describes some failure studies of solder joints in IC packages. From a review of literature, it is found that a large number of studies have been conducted on the fatigue failure of solder joints subjected to temperature variation or cyclic bending, and on FEM simulations incorporating viscous constitutive models for solder

bumps. Few investigations on solder joint strength under quasi-static loading are available and reports on dynamic loading are even fewer; this is particularly so scarce for direct measurement relating to single solder joint specimens.

1.3.1 Fatigue failure induced by cyclic loading

Fatigue failure is most common in ball grid arrays in a flip chip package. In recent years, the trend for electronic devices (such as IT devices) is to become ever lighter, thinner and smaller; this motivates more research in this area. There are probably two major sources of fatigue failure in solder joints in IC packages. One is fatigue cycle loading due to thermal variations, and the other is direct mechanical cyclic loading that flexes PCB boards and induces solder joint detachment. The following sections constitute a literature review of aspects of thermo-mechanical behavior of solder joint and reliability of IC packages under mechanical cyclic loading as well as prediction of fatigue life.

(1) Fatigue failure by thermally cyclic loading

Thermal stresses arise from the presence of dissimilar materials that are combined together and undergo a change in temperature. During the assembly of electronic packaging, thermal expansion mismatch between a chip and the substrate occurs due to temperature cycling, and also thermal expansion of solder joints. In the operation of many electrical devices, power dissipation is very high, thus generating heat and causing temperature

variations. Thermal fatigue failure may be induced in solder joint interconnections due to thermal variation as a result of operation of the device. Therefore, solder joint fracture from thermal loading is one of the primary concerns in electronic package design. Many studies have been conducted on the reliability of solder joints and their fracture/failure modes under such loading.

Experimental studies of thermal-cycling have been conducted to analyze solder joint reliability and the effect of microstructure on joint reliability (e.g., Nurmi, et al., 2004). It is customary to test packages to failure using temperature cycling tests to establish solder joint reliability. For example, Lau et al. (2002) used an empirical equation to predict the thermal fatigue life of solder joints (Sn63Pb37) on PCBs, and measured the crack lengths after different thermal cycles in solder joints (Fig.1-18); finite element simulation was used to calculate the average strain energy density around the crack tip. There have been researches on accelerated cycling approaches. For example, Chen et al. (2005) developed thermoelectric cooler based rapid temperature cycling testing methodology and applied this to advanced tap BGA packages for long-term reliability assessment. Pucha et al. (2004) presented a field-use induced damage mapping methodology in which field-use thermal conditions are mapped to develop accelerated thermal cycling guidelines to qualify microelectronic packages.

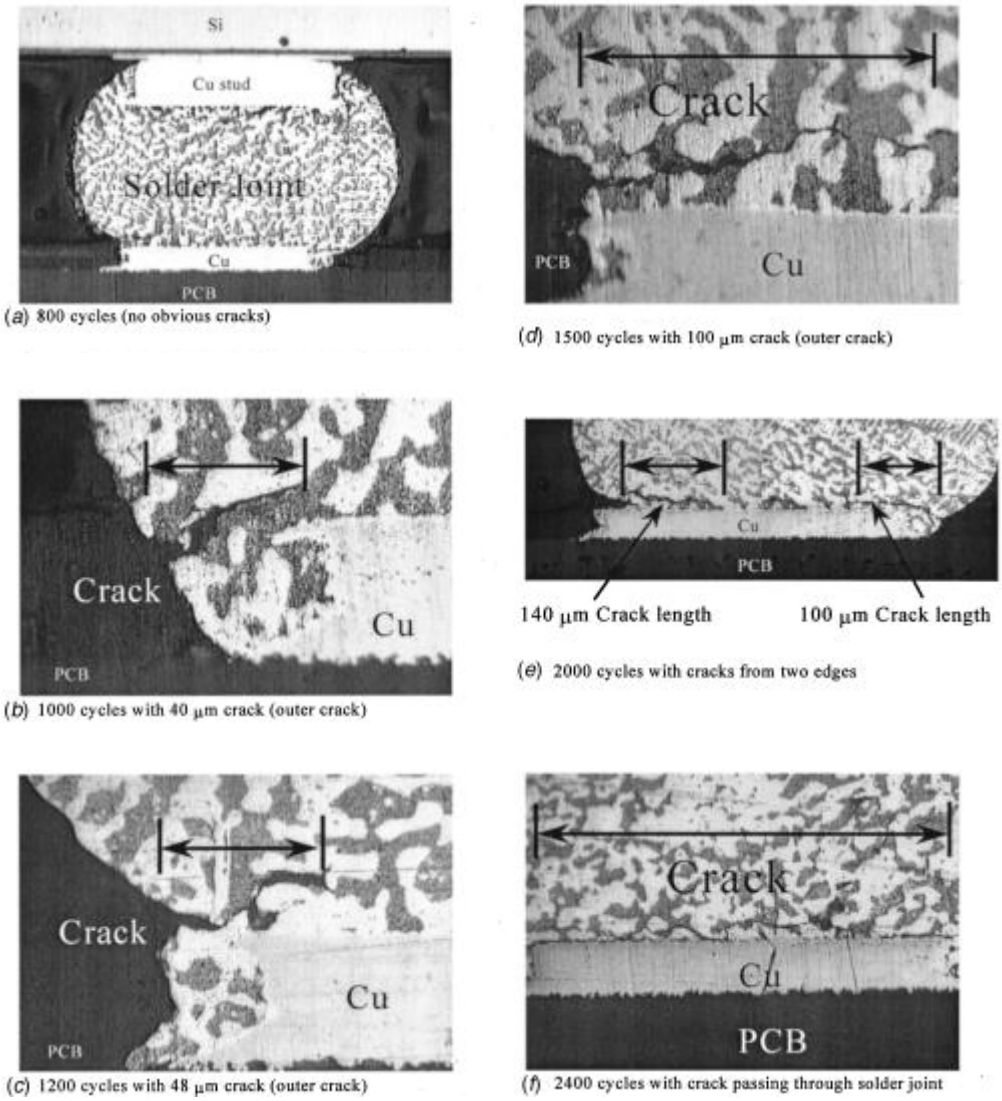

Fig.1-18 Cross sections of the corner solder joint (Sn63Pb37) after different thermal cycles (Lau et al., 2002)

Solder joints usually operate at relatively high temperatures when a device is powered. Thermal vibration gives rise to mechanical response that is strain rate and temperature dependent. There has been much work in recent years on predicting solder joint reliability using theoretical or semi-empirical approaches in conjunction with finite element modeling, together with a constitutive law or hypothesis that governs failure in solder by fatigue. Creep-plasticity theories are constitutive models that intrinsically take into account time-dependent inelastic deformations. Lau et al. (2002) conducted a time-

temperature-dependent nonlinear analysis of lead free solder (Sn65Pb36Ag2, Sn96.5Ag3.5 and In100) subjected to thermal cycling conditions on wafer level chip scale package. The shear stress and shear creep strain hysteresis loops, shear stress history, and shear creep strain history at the corner solder joint were presented. Finite element modeling was carried out via ANSYS (release 5.6.1), which can solve boundary-value problems that involve the Garofalo-Arrhenius steady-state creep constitutive equation expressed by,

$$\frac{d\gamma}{dt} = C\left(\frac{G}{\Theta}\right)\left[\sinh\left(\omega\frac{\tau}{G}\right)\right]^n \exp\left(-\frac{Q}{k\Theta}\right) \qquad (1\text{-}15)$$

where γ is the creep shear strain, $d\gamma/dt$ the creep shear strain rate, t is time, C a material constant, G the temperature dependent shear modulus, Θ the absolute temperature (K); ω defines the stress level at which the power law stress dependence breaks down, τ is the shear stress, n the stress exponent, Q the activation energy for a specific diffusion mechanism (e.g., dislocation diffusion, solute diffusion, lattice self-diffusion, and grain boundary diffusion), and k the Boltzmann's constant ($8.617\text{x}10^{-5}$eV/^{0}K). For specified solder alloys, the material constants in Eq.(1-15) can be determined experimentally, resulting in a single hyperbolic sine function,

$$\frac{d\gamma}{dt} = A\left[\sinh\left(\frac{\tau}{B}\right)\right]^n \exp\left(-\frac{Q}{kT}\right) \qquad (1\text{-}16)$$

If the solder material obeys the von Mises criterion, then the predicting equation can be expressed as,

$$\frac{d\varepsilon}{dt} = C_1\left[\sinh\left(C_2\sigma\right)\right]^{C_3} \exp\left(-\frac{C_4}{T}\right) \qquad (1\text{-}17)$$

where there are four constants for each type of solder alloy; this corresponds to the input for the implicit creep model (TBOPT=8) in ANSYS, release 5.6.1.

This steady-state creep constitutive equation has been widely used by many researchers for simulation of the thermo-mechanical behavior of solder joints (Guilbault, et al., 2002; Dudek, et al., 2003; Tee, et al., 2003; Wiese and Meusel, 2003; Yang, et al., 2004, Kim, et al., 2006; Lu, et al., 2006; Chen, et al. 2006; Roellig, et al. 2007; Heffes and Nied, 2004).

In addition to elasto-plastic strains, Lau et al. (2002) assumed that the creep strain for Sn63Pb37 follows Norton's steady-state creep law,

$$\frac{d\gamma_{crp}}{dt} = B\tau^n \exp\left(-\frac{\Delta H}{kT}\right) \qquad (1\text{-}18)$$

where γ_{crp} is the steady-state creep shear strain, τ the shear stress, and ΔH the activation; thermal cycling test on IC assemblies were performed and numerical simulations were conducted to calculate the distribution of the maximum von Mises stress and maximum equivalent plastic strain in the corner solder. In modeling the thermo-mechanical durability of high I/O BGA package, Davuluri et al. (2002) used Weertman's power law to model steady state creep deformation in a Sn63Pb37 solder joint,

$$\dot{\varepsilon} = 0.2557\left(\sigma_{equ}\right)^{6.28} \exp\left(-\frac{0.7036}{8.617\times10^{-5}T}\right) \qquad (1\text{-}19)$$

where $\dot{\varepsilon}$ is the equivalent creep strain rate, σ_{equ} the equivalent stress in MPa and T the temperature in Kelvin. In the study by Lau and Dauksher (2005), both Sn95.5SnAg3.9Cu0.6 and Sn63Pb37 solders were assumed to follow a sinh law, while Sn10Pb90 solder is modeled by a power law.

(2) Fatigue failures induced by mechanical cyclic loading

Most reliability studies have focused on thermal cycle fatigue life, and relatively less attention has been devoted to failure from mechanical fatigue of solder joints. Although thermal fatigue is a constant issue, electronic devices are also frequently subjected to high cycle mechanical fatigue induced by vibration during shipping, handling and operation. For example, mechanical fatigue reliability is especially critical for portable products where key pad actuation often induces repeated bending in the printed circuit board. Due to the market-driven demand for miniaturization and more functionality in portable microelectronic products such as cellular phones, the development of IC package has been directed towards smaller, thinner, lighter and higher density package configurations. As a result, pad sizes become smaller, the ball pitch becomes finer, and ball size is reduced. To address this trend, failure/fracture in solder joints induced by mechanical cyclic loading has attracted increased attention in recent years; a greater number of studies on bend/vibration fatigue life and associated fracture modes of interconnects have been carried out.

Daya Perera (1999) evaluated the reliability of BGA solder joints by twisting and bending the PCB boards of mobile phones; cracks in solder joints were found at the interface between solder bump and pads in most cases, and solder joint connection failure arose from propagation of cracks under fatigue loading. Wu et al. (2002) conducted three-point cyclic bending on a stacked chip scale package and observed brittle facture in the IMC (Fig.1-19a); the

fatigue life was characterized by a two-parameter Weibull model. Jonnalagadda (2002) examined mechanical flexure of a PCB board containing a via-in-pad structure by experimentally and numerically approaches to study the mechanical cycling fatigue reliability of solder joints in a BGA package. Plastic strain was generally used to identify locations of potential damage. Zheng et al. (2003) conducted experimental studies to investigate board level solder joint reliability and fatigue life through mechanical cyclic loading. Mercado et al. (2004) presented images of the cross-section of a failed package after cyclic bending with a 4mm deflection amplitude at 1Hz; the solder joint failure modes corresponded to fatigue cracks at the package side or pad cratering, as shown in Fig.1-19b. Lai et al. (2007) conducted both experimental and numerical studies to investigate board-level reliability of wafer-level chip-scale packages subjected to four-point cyclic bending that combine different deflection amplitudes and excitation frequencies.

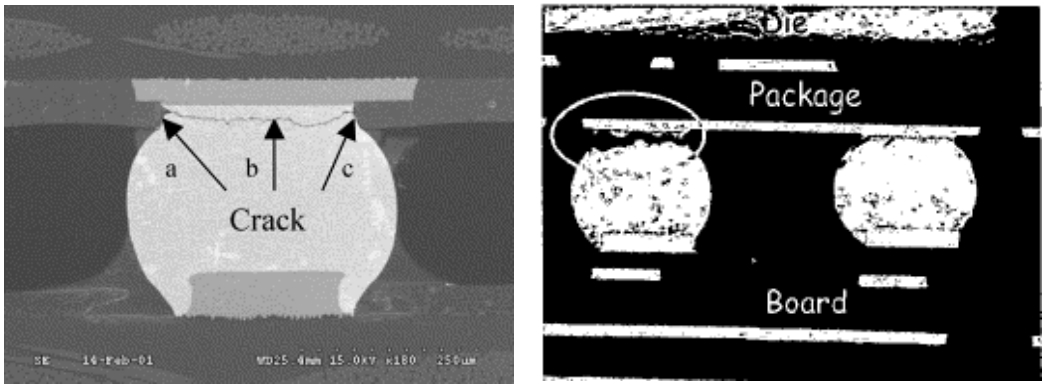

(a) (b)

Fig.1-19 (a) Solder joint fracture at the substrate side (Wu et al., 2002); (b) solder joint cracks and pad cratering (Mercado et al., 2004)

The stress and strain fields around crack tips of different length cracks in

solder joints were examined via FEM simulation, and J-integral values were calculated along contours around the crack tip (Lau, 1996). A fatigue crack growth model akin to the Paris law was proposed to predict the number of cycles to failure for single cracked interconnect which undergoes cyclic Mode-II shear loading in conjunction with either a constant crack opening force (Mode-I) or a constant crack closing force; the model predicts that forces of the order of only one Newton can significantly impede or accelerate the propagation of a fatigue crack (Larson and Verges, 2003)

(3) Fatigue life prediction

Fatigue failure of solder joints in electric packaging is of serious concern and development of estimation methods for the fatigue life of solder joints has been attempted. These include recent evaluation of solder joint reliability and fatigue life prediction under thermal and mechanical loading. The majority of these use plastic strain energy as the criterion for life prediction (Lau, et al., 2002; Guven, et al., 2004; Zhang, et al., 2004; Liu, et al., 2006; Roellig, et al., 2007).

The generalized Coffin-Manson equation is used to estimate the mean number of cycles to failure,

$$\overline{N}_f = \frac{D}{\gamma^n} \qquad (1\text{-}20)$$

where D and n are related to individual type of solder and depend on the model assumptions; γ is the strain per cycle and could be the total strain, plastic strain, matrix creep strain, integrated matrix creep strain, the Von

Mises strain for multiaxial stress/strain states or the strain of a particular mode (Mirman, 2002; Lee, et al., 2007). In the simulation of creep behavior in eutectic solder joints, Shi et al. (2002) found that the maximum cumulative equivalent inelastic strain occurred at the corner underneath the corner of the silicon die, and stated that “since the point with maximum cumulative equivalent inelastic strain has the highest possibility for cracking, its inelastic strain energy density was taken to predict the fatigue life of the solder joint”.

Darveaux (2002) utilized finite element analysis to calculate the inelastic strain energy density accumulated per cycle during thermal or power cycling. The strain energy density is then combined with crack growth data to calculate the number of cycles to initiate a crack, and the number of cycles to propagate cracks through a joint. Strain energy density values were calculated by an average across all the elements at the joint interface, and could be fitted in relation to the measured crack growth data in the form of *a modified Coffin-Manson equation*

Crack Initiation: $$N_0 = K_1 \Delta W_{ave}^{K_2} \quad (1\text{-}21)$$

Crack Growth: $$\frac{da}{dN} = K_3 \Delta W_{ave}^{K_4} \quad (1\text{-}22)$$

Alander et al. (2002) defines ΔW_{ave} as the average plastic work accumulated in Sn62Pb36Ag2 solder in BGA package during a temperature cycle. Akay et al. (2003) used a similar relationship between creep dissipation energy and fatigue life,

$$N_{f(50\%)} = \left(\frac{\Delta W_{total}}{W_0} \right)^{1/k} \quad (1\text{-}23)$$

where $N_{f(50\%)}$ is the mean number of cycles to failure, while k and W_0 are fatigue coefficients; ΔW_{total} represents the total creep dissipation energy in one stabilized cycle,

$$\Delta W_{total} = \sum_e \Delta w^e \cdot V^e = \sum_e \oint \sigma_{ij}^e d\varepsilon_{ij}^e \cdot V^e \qquad (1\text{-}24)$$

where Δw^e is the creep dissipation energy density in element e, and V^e is the volume of that element. Chan et al. (2002) used inelastic strain energy density as a failure indicator for fatigue failure analysis, this being the sum of the plastic and creep strain energy densities,

$$\Delta W = \int_c \tau_{ij} d\varepsilon_{ij}^P + \int_c \tau_{ij} \dot{\varepsilon}_{ij} dt \qquad (1\text{-}25)$$

where $\dot{\varepsilon}_{ij}$ are the creep strain rate components and c denotes the cycle at steady state.

Variyam et al. (2003) used Anand's viscoplastic material model for solder ball properties and Darveaux's methodology to generate an empirical fatigue model based on FEM simulation employing ANSYS. The plastic work density calculated from simulation results was averaged and used as the input parameter in Darveaux's formulae

$$N_1 = K_1 \Delta W^{K_2} \;\; ; \;\; da/dN = K_3 \Delta W^{K_r} \;\; ; \;\; N_{total} = N_1 + \int \frac{da}{K_3 \Delta W^{K_4}} \qquad (1\text{-}26)$$

where N_1 is the number of cycles to initiate damage, N_{total} is the total number of cycles to failure, ΔW is the increment in average plastic work density in the most highly stressed solder region for one complete temperature cycle, a is the crack length, taken as the solder ball diameter, and $K_1 \sim K_4$ are empirical constants obtained from test data.

Some other modified Coffin-Manson equations were also developed to predict solder joint fatigue life reliability (Shohji, et al., 2004). Tang and Basaran (2003) developed a thermo-mechanical fatigue life prediction model based on damage mechanics, whereby damage evolution corresponding to material degradation under cyclic thermo-mechanical loading is based on the second law of thermodynamics and uses entropy as a damage metric. Towashiraporn et al. (2004) systematically explored various errors in fatigue life prediction models; these errors include those in geometry representation, material behavior, load history, boundary condition application, and in numerical solution procedures.

1.3.2 Solder joint strength under monotonic mechanical loading

The present literature review shows that quite a number of studies have been conducted to study the mechanical reliability of solder joints under cyclic loading, induced by thermal variation or external forces. Experimental tests on package level or board level specimens and numerical modeling (FEM) incorporating constitutive models (e.g., visco-plastic models etc.) for solder bumps have been performed. It is noted that a solder joint is a connection between a chip and a substrate/PCB; its mechanical strength is related not only to the solder bump but also to the bond strength between the solder bump and copper pad, or between the copper pad and the substrate/PCB. The influence of the microstructure and IMC on solder joint reliability is

significant. Therefore, the force-deformation response to the ultimate strength point measured on an actual solder joint specimen subjected to monotonic loading is useful in characterizing the actual strength of a solder joint under tensile, compression or shear conditions. This section describes a review of monotonic mechanical loading on solder joint subjected to quasi-static and dynamic impact loading. Most of these studies related to shear testing of solder bumps, and work on dynamic testing is quite limited.

(1) Quasi-static loading

There are several texts that describe common practical analysis methods; e.g. “Mechanical analysis of electronic packaging systems” (Mekeown, 1999), describes evaluation methods and analysis procedures related to thermal, mechanical and life environments. “Lead-free soldering in electronics”, by Suganuma (2004), some test methods to examine structural integrity in microelectronics are illustrated schematically (Fig.1-20).

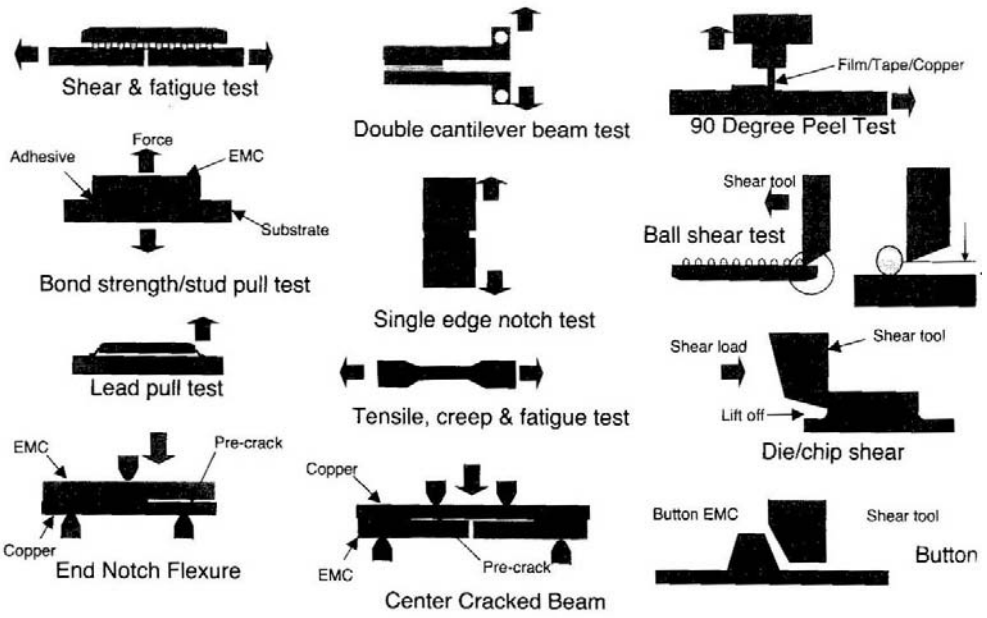

Fig.1-20 Overview of mechanical tests for microelectronic applications (Suganuma 2004)

For solder joints in IC packages, three-point and four-point bend tests are used to evaluate solder joint mechanical reliability based on package level specimens. Peel tests of package specimens have also been conducted by Wang et al. (2004), from which low cost metrology for evaluating solder joint strength has been proposed. These tests can only ascertain when a solder joint breaks under monotonic bending or peeling, but values of solder joint strength cannot be obtained. Obaid et al. (2005) conducted shear tests on solder joints using package level specimens, and determined the stress from dividing the total applied load by the total cross-section area of the solder joints. However, the average strength for a solder joint derived may be underestimated, as the solder joints do not break simultaneously.

There have been research on single solder bumps; with respect to bond strength between solder balls and die surfaces, the JEDEC standard (BGA

Ball Shear, JESD22-B117) specifies shear test methods for BGA balls. Fig.1-21 shows six typical solder joint failure modes classified by this standard; the maximum shear load depends on the solder type, ball size and pad size.

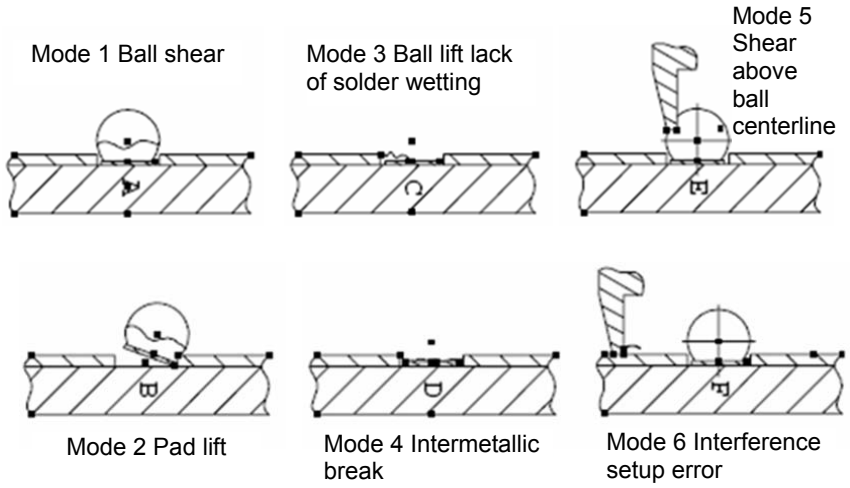

Fig.1-21 Shear failure modes of a BGA solder ball (Fig 2A-2F of JESD22-B117)

Following this test methodology, Chen and Chiang (2003) conducted shear tests at a shear speed of 0.1~0.5mm/s on eutectic solder joints between a die and a substrate, and also on solder bump bonded on a chip. Islam et al. (2003) studied the formation and morphology of IMC of Sn96.5Ag3.5Cu0.5 lead-free solder joints and tested the interfacial shear strength at a speed of 0.55mm/s. There are also studies involving quasi-static ball shear tests and numerical simulation (e.g. Gonzalez, et al., 2004; Kim, et al. 2004; Liu et al., 2004; Chen, et al., 2006; Kim, et al., 2006,). From such ball shear tests, the solder bump is bonded just to one piece of substrate, unlike an actual solder joint that connects two surfaces. As a result, the geometry of the solder bump is not the same as that of an actual solder joint. In addition, an actual solder joint in IC packages will experience both shear and normal forces when subjected to external loading. Therefore, the testing of solder joint strength in uniaxial

loading (tension, compression or shear) as well as combined shear/normal loading is necessary to characterize their strength and reliability. Such studies appear to be limited.

Bbased on interfacial loading, Shah and Mello (2004) developed a failure envelope that incorporates combined tension/compression and shear forces, similar to the Mohr-Coulomb criteria for brittle materials such as rock. The expected failure of a solder joint is described by a nonlinear envelope in the normal and shear force space according to,

$$F_x - a\sqrt{F_{N\max} - F_N} = 0 \qquad (1\text{-}27)$$

where $F_{N\max}$ is the tensile strength of the solder ball and the constant a is an empirical parameter with units of $force^{1/2}$, F_x and F_N are the normal and shear force components respectively. The shear strength of the solder ball is $a\sqrt{F_{N\max}}$. An illustration of this failure envelope for the force combinations is in Fig.1-22. The failure envelope expressed in terms of normal and shear force defines the occurrence of cracking. This study illustrates that simple criteria can be established in the form of a failure force envelope based on shear and normal forces or stresses.

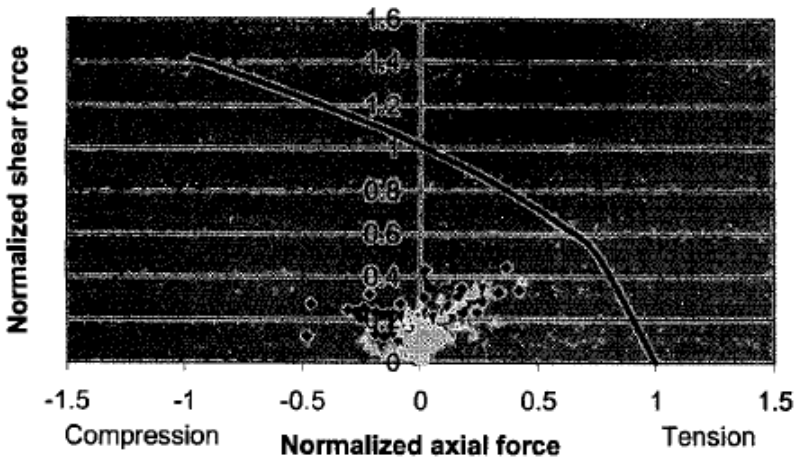

Fig.1-22 Failure envelope in terms of normal and shear force components (Shah and Mello, 2004)

In the simulation code *ABAQUS*, there is a mechanical contact property - breakable bonds - that can be defined for the nodes on the slave surface of a pure master-slave contact pair to simulate contact such as spot welds between surfaces. “The breakable bonds are designed to provide a simple simulation of spot weld failure under relatively monotonic straining, such as occurs during an impact of a vehicle structure. ABAQUS assumes that a spot weld carries a force normal to the surface onto which the node is welded, F^n , and two orthogonal shear forces tangent to the surface, F_α^s , $\alpha = 1, 2$. The magnitude of the resultant shear force, F^s , is defined as $\sqrt{\left(F_1^s\right)^2 + \left(F_2^s\right)^2}$. The normal force is positive in tension. A spot weld is assumed to be so small that it carries no moments or torque. As a result, spot welds do not impose any constraints on rotational degrees of freedom”. The failure criterion for a spot weld is

$$\left(\frac{\max(F^n,0)^2}{F_f^n}\right)+\left(\frac{F^s}{F_f^s}\right)\le 1 \qquad (1\text{-}28)$$

where F_f^n is the force required for failure in tension (Mode I loading), F_f^s is the

force for failure in pure shear (Mode II loading), and a typical yield surface for spot welds is shown in Fig.1-23.

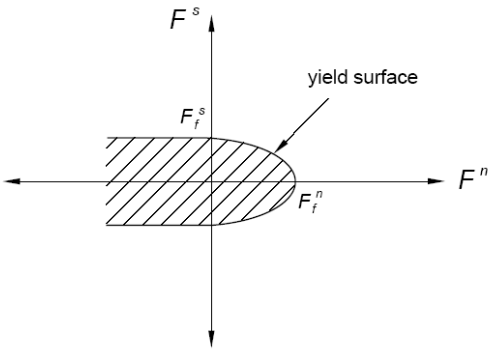

Fig.1-23 Typical yield surface for spot welds (*ABAQUS analysis menu*)

In addition, similar characterization of bond failure can be found in ANSYS; the tie-break nodes-to-surface contact links adjacent meshes and confines the movements of nodes until the bond breaks.

$$\left(\frac{|f_n|}{S_n}\right)^{C_n}+\left(\frac{|f_s|}{S_s}\right)^{C_s}\geq 1 \qquad (1\text{-}29)$$

where the subscripts n and s denote normal and shear force respectively, and f and S are respectively the calculated nodal force and the prescribed ultimate nodal force at which the bond breaks.

A study related to such a failure envelope has been undertaken by Tan et al. (2006; 2009), in which the specimens are in the form of single solder joints connecting two surfaces; they were subjected to combined tension-shear and compression-shear tests to determine the force-displacement response and failure load, using an Instron micro-tester. Typical force-displacement responses for tension/shear and compression/shear tests are illustrated in

Fig.1-24a, where the profiles are displayed separately at intervals of 0.2-0.3 mm instead of being directly overlayed for clarity. Rapid degradation of the tension/shear force for 0^0 and 30^0 loading directions was found to be associated with pad peel-off failure, while 60^0 and 90^0 tests displayed a gradual force reduction corresponding to solder yield. Failure for tension/shear is defined as the peak force experienced by the solder joint. As compression does not cause separation of a joint, failure in these tests is defined by the force causing yield. This is obtained by locating the point where the curve begins to deviate from initial linearity. The failure envelope for a single solder joint connection is obtained by plotting the normal force component against the shear component at the failure load. The envelope was found to be elliptical (Fig.1-24b), and is fitted by an empirical equation,

$$\frac{(F_T - 0.5)^2}{10^2} + \frac{(F_S)^2}{4.65^2} = 1 \qquad (1\text{-}30)$$

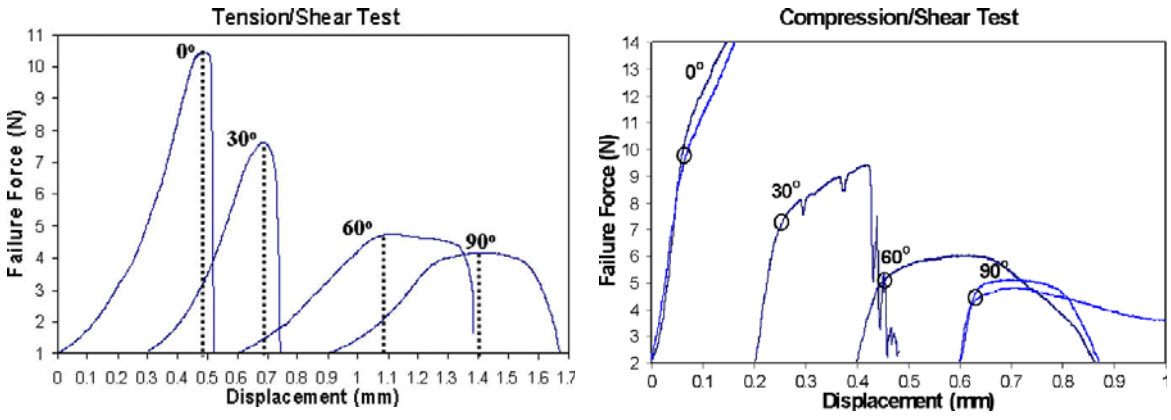

(a) Typical force-displacement profiles for tension/shear and compression/shear test for single solder joint specimens

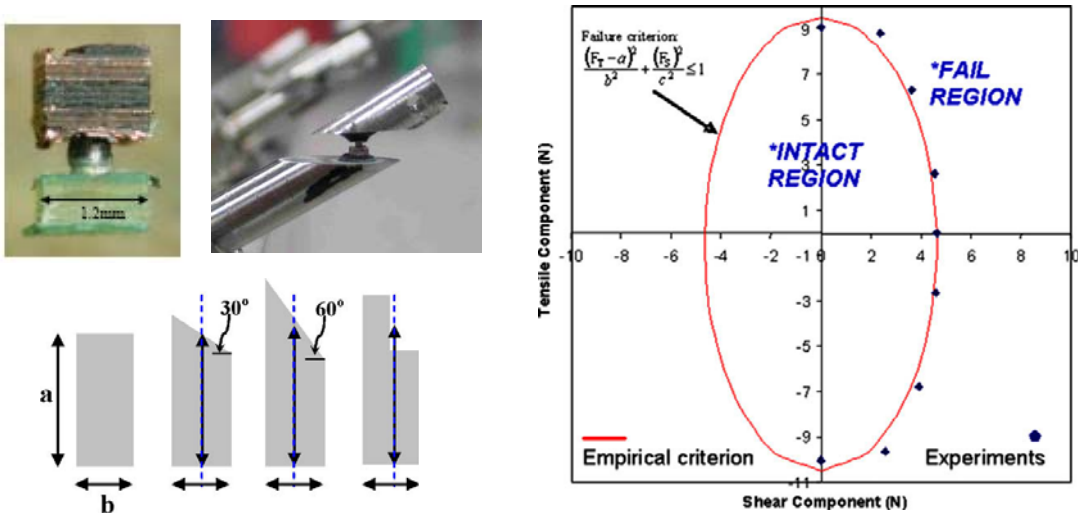

(b) Single solder joint specimen subjected to inclined testing and failure force envelope

Fig.1-24 Force-displacement response and failure envelope for a single solder joint specimen subjected to quasi-static loading (Tan, et al., 2009)

(2) Dynamic loading

Potable electronic devices in the course of use risk being subjected to drop and dynamic loading. The move towards reduction in weight and size results in finer pitch and high density packages, making products susceptible to failures induced by drop or impact. Crack/fracture can be generated at solder joint interfaces and cause loss of electrical contact during drop impact or shock loading.

Drop tests are usually undertaken to evaluate the reliability of solder joints in package or board level specimens in shock or impact loading conditions. Mishiro et al. (2002) conducted drop tests on BGA packages mounted onto a motherboard; correlation between solder joint stresses and motherboard strains was confirmed by numerical analysis and the strains were measured

by strain gauges on the motherboard; it was found that the stress at a solder joint depends on the package structure, even if the motherboard strain is the same. The present of an underfill eases the motherboard strain and disperses stress concentration at a solder joint. Saha et al. (2004) performed reliability risk tests via board level drop testing (PCB mounted with IC packages and dropped from a prescribed height) to study the effect of the intermetallic phases in Pb-free solder joints (Sn96.5Ag3.5). Jang et al. (2007) also conducted drop impact tests on BGA packages with lead-free SnAg3.8Cu0.7 and analyzed the failure morphology in solder joints. At present, manufacturers of hand-held electronic devices use the JEDEC JESD22-B104B standard for mechanical drop testing. The drop-durability of portable electronic products is quantified and ranked by the number of drops to failure. The test vehicle recommended by the JEDEC Standard JESD22-B111 for studying Interconnect durability is a daisy-chained Printed Wiring Assembly (PWA) of standard form with a standard fixture (i.e., standard boundary conditions). Mattila and Kivilahti (2005) conducted drop tests on lead-free chip scale packages by employing a 0.82m drop height. This induced a peak deceleration of 1500g over a 0.5ms duration as required by the standard. Failure was considered to have occurred when the resistance through the daisy chain network exceeded the threshold resistance for 200ns three times in a sequence of five drops.

Other testing methods have also been explored; shock tests were studied as substitutes for drop tests to qualify microelectronic products. In shock tests, a specially designed and appropriately tuned shock tester is used to impose a

short term load of given magnitude and duration on the electrical device. Suhir (2002) developed simple analytical predictive models for the dynamic response (characterized by maximum induced curvature and acceleration) of a simply supported elongated rectangular plate to an impact load applied. He concluded “that although it is possible to ‘tune’ the shock tester, so that the drop test conditions are adequately reproduced, actual drop tests should be conducted, whenever possible”. Varghese and Dasgupta (2007) presented a generic methodology to determine the durability of surface mount interconnects in electronic assemblies under drop loading condition. An impact test setup was designed for in-plane and out-of-plane impact tests (Fig.1-25). For out-of-plane impact, the sphere impacts the center of the printed wiring assembly (PWA), causing out-of-plane displacement; for in-plane impact, the specimen is oriented horizontally and the two edges orthogonal to the impact axis are guided with leaf springs to remain the impact plane. Wu et al. (2002) employed a split Hopkinson bar to perform dynamic three point impact bending tests on surface mount joints. Each specimen consisted of a small PCB section with a single resistor surface mounted by isotropic conductive adhesive. Shear tests were also performed to examine the degradation in shear strength of the joints after impact damage (Fig.1-25). In this kind of testing, the specimen size is actually limited by the diameter of bars.

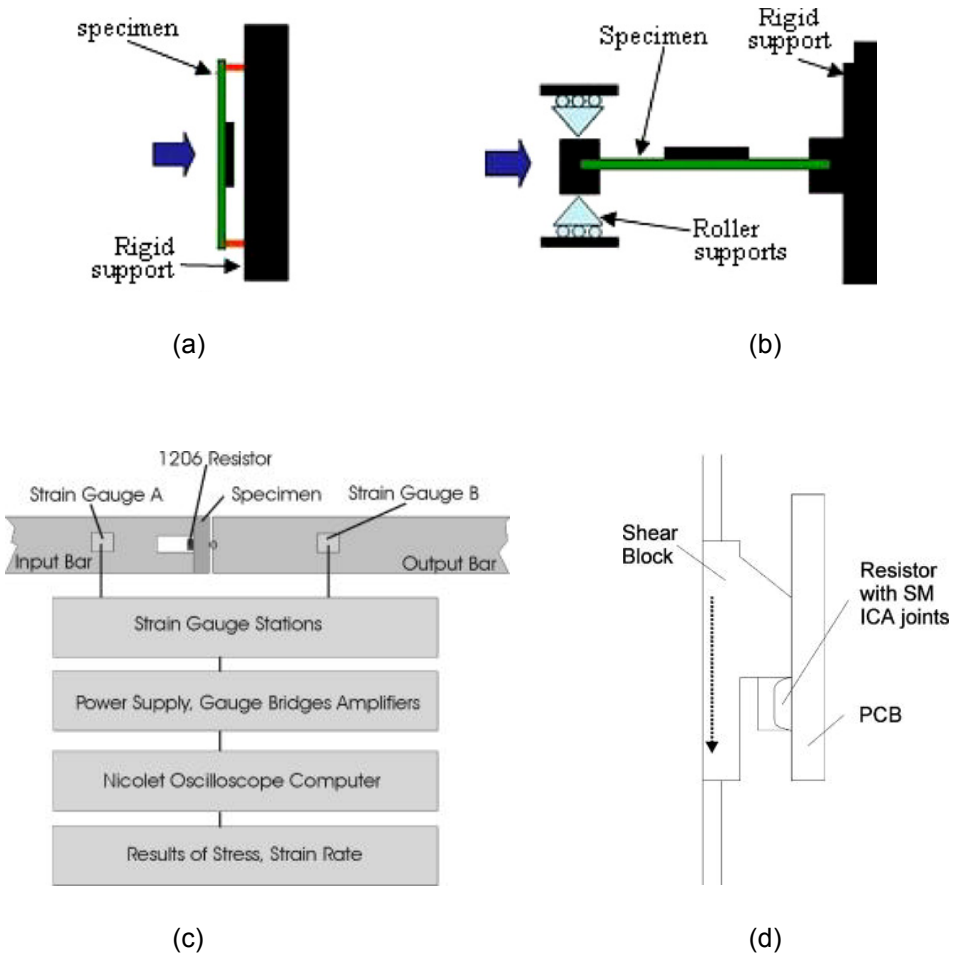

Fig.1-25 Schematic diagram of (a) the out-of-plane impact fixture, (b) in-plane impact fixture (Varghese and Dasgupta, 2007), and (c) Schematic diagram of three-point impact bending test using a the split Hopkinson bar, (d) pure shear of single joint after impact testing (Wu et al. 2002)

Direct impact on solder bumps instead of package or board level testing has been undertaken by some researchers, to identify the effect of loading rate on bond strength. Date et al. (2004) evaluated the impact toughness of solder joints quantitatively by means of a miniature Charpy test (Fig.1-26), inducing a shear rate of approximately 1m/s. Three Pb-free (near eutectic SnAgCu, eutectic SnZn and SnZnBi) and eutectic SnPb solder balls in conjunction with Cu or Ni-P pads were studied. The impact toughness, J, was calculated as the kinetic energy absorbed by the bump during fracture,

$$J = \frac{1}{2} m_p (v_1 - v_2) \qquad (1\text{-}31)$$

where m_p is the mass of the pendulum, and v_1 and v_2 are the respective velocities of the pendulum immediately before and after impact. Results showed that the impact toughness and fracture mode/location (within the bulk solder and at the interface) vary with solder composition, pad material and aging time.

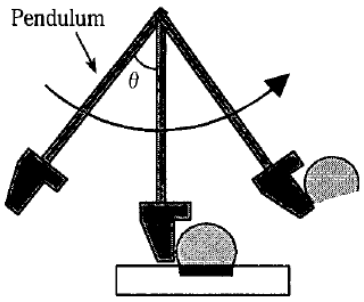

Fig.1-26 Miniature Charpy test (Date, et al., 2004)

Yeh and Lai (2006) used an MTS 858 servohydraulic test system with a flat-head pin mounted on the actuator of the tester (Fig.1-27a). The pin can be driven to reach a crosshead speed of 0.3m/s and strike a single package level solder joint, 0.3mm diameter Sn95.5Ag4Cu0.5 solder balls were mounted on the substrate pad. However, they reported that “unfortunately, due to the heavy weight of the actuator and the limitation of data acquisition sampling rate of the MTS test system, we are unable to measure reasonable impact force profiles. A numerical treatment for this particular test methodology is therefore sought”. Three-dimensional finite element analysis incorporating contact, fracture and fragmentation mechanisms was undertaken to predict transient structural responses and failure modes of the solder joint. The effect of impact angle is illustrated in (Fig.1-27b), “On the interface between the solder joint and the pad, as the pin moves from left to right, the tensile normal

stress arises on the left side of the interface while the compressive normal stress on the right side". Loading paths of shear force f_s versus normal force f_n with respect to impact angle for an impact velocity of 2m/s are illustrated in Fig.1-27c. These were extracted from the region at the left end of the interface immediately beneath the impact area. The maximum impact force and strain rate experienced by the solder joint with respect to impact angle are shown in Fig.1-27d. The author states "We notice that for impact angles varying form 0^0 to 15^0, f_n is about 1.5 times greater than f_s which implies that the impact test in reality does not represent a shear-dominant test condition even when the impact angle is 0^0. Furthermore, the loading path of f_n and f_s changes only slightly with respect to different impact angles ranging from 0^0 to 15^0. This feature indicates that the impact test itself is not sufficient to determine the four failure envelope parameters (S_n, S_s, C_n, C_s described in tiebreak nodes-to-surface contact in ANSYS). Supplementary tests that create loading paths of which are significantly different from those from the impact test are in need".

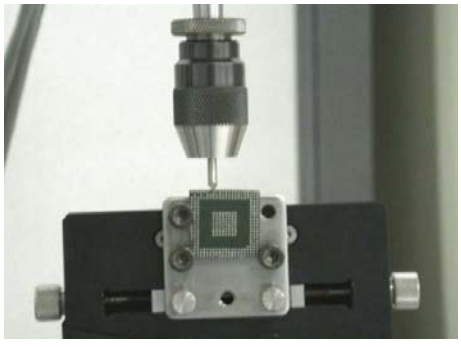

(a)

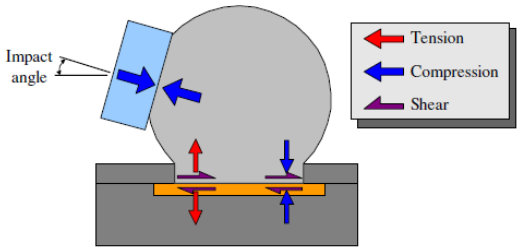

(b)

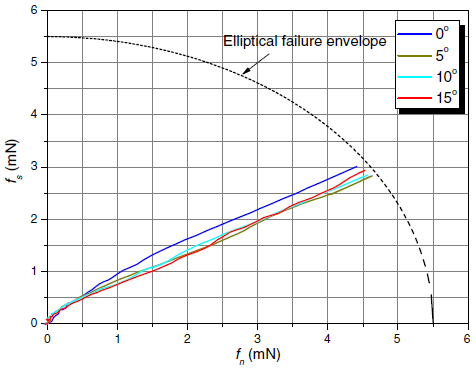

(c)

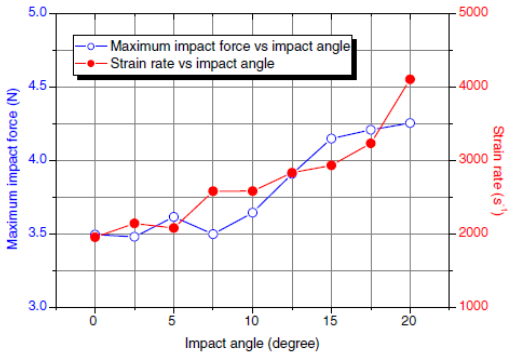

(d)

Fig.1-27 (a) MTS impact test fixture; (b) Schematic of stress distribution on the test vehicle; (c) Loading paths for different impact angles; (d) Maximum impact force and strain rate vs. impact angle ((b)-(d) refer to simulation outputs) (Yeh and Lai, 2006)

In conventional quasi-static ball shear tests, the crosshead speed is generally low. However, this mechanism has been utilized to develop devices for dynamic testing (i.e., ball impact test), whereby the crosshead speed increases to 0.5~2m/s to yield an impact force. A ball impact test apparatus must be carefully designed to suppress structural resonance in order to obtain reliable measurements. Yeh and Lai (2007) analyzed the test process using classical structural dynamics principles in order to provide insights into the transient characteristics of this test methodology. To measure the impact force response, a load cell or force meter is needed and can be placed on the target side (Fig.1-28a) or attached to the pin (Fig.1-22b). Simplified spring-and-mass structural systems corresponding to these designs are also shown, where *m* is the lumped mass, *k* the spring constant, *c* the damping coefficient and *u* the displacement. To simplify the analysis, it is assumed that the k_1 spring is far more flexible than others, so that both the systems can be further simplified as one with a single degree of freedom (Fig.1-22c). For different structural parameters (Fig.1-29a), the results for $F_0(t)$ (corresponding to the

load cell reading) is compared to the actual input load profile $F_i(t)$ which is 1N in amplitude and 30μs (Fig.1-29b), 100μs (Fig.1-29c) and 500μs (Fig.1-29d) in duration. The results show clearly that for a pulse with a duration longer than 500μs, the force profiles measured by the load cell are not sensitive to the structural parameters of the test apparatus and close to the actual loading profile (i.e., quasi-static ball shear tests). However, for a ball impact test, where the pulse duration may be less than 100μs due to fracture in the brittle IMC, accuracy of the impact force profile measured by the load cell does depend substantially on the structural design of the test apparatus. This study shows that a distorted impact force profile generated by a poorly designed ball impact test apparatus leads to unreliable and inconclusive reliability evaluation.

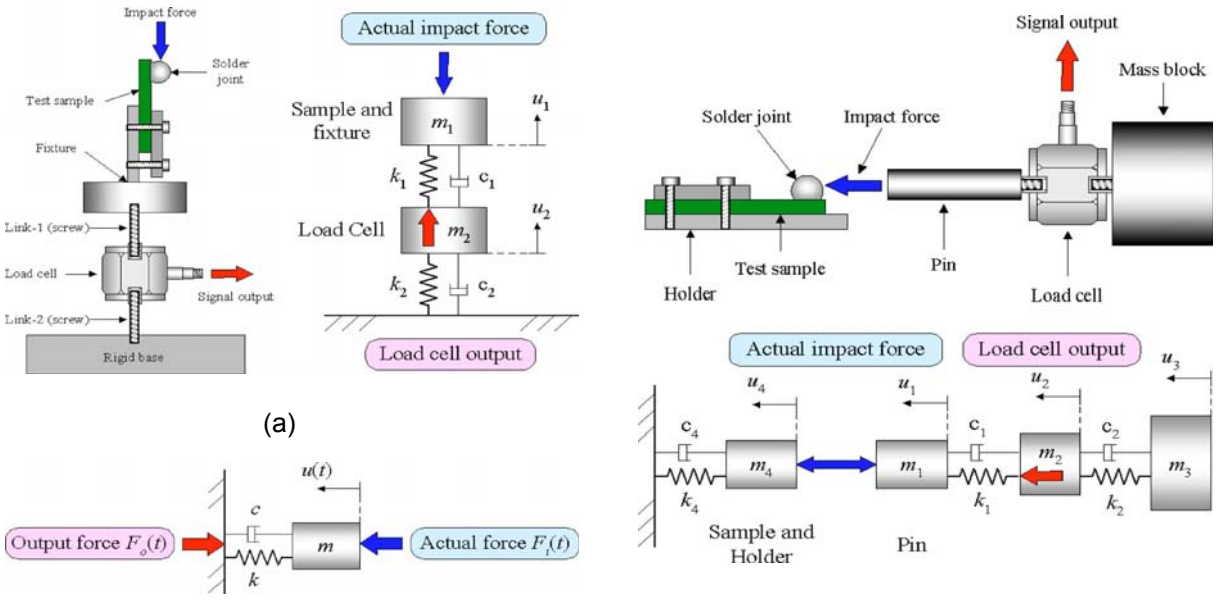

Fig.1-28 Configurations of ball impact tester (BIT) (a) load cell placed on target side (b) Load cell attached to pin (c) simplified single degree of freedom structural system (Yeh, et al. 2007)

Structure	m (g)	k (GN/m)	f (kHz)	T (μs)
A	90	0.83	15.3	65.3
B	45	0.83	21.6	46.2
C	4	0.5	56.5	17.7
D	4	5	179	5.6

(a) Structural parameters for BIT apparatus, f and T stand for the natural frequency and period of the structural system (A and B for BIT in Fig.1-28a and C and D for BIT Fig.1-28b

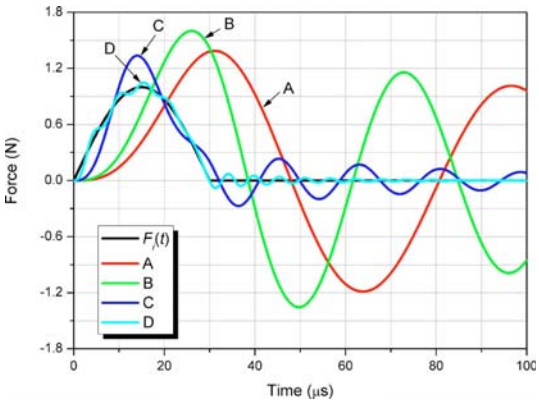

(b) Impact force profile for 30μs pulse duration

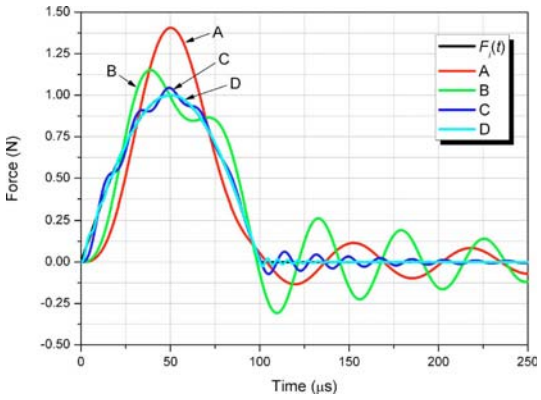

(c) Impact force profile for 100μs pulse duration

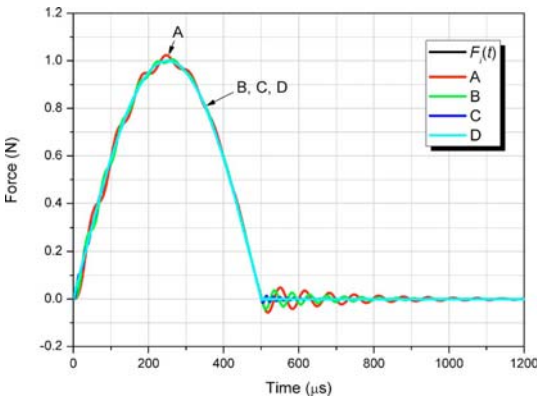

(d) Impact force profile for 500μs pulse duration

Fig.1-29 Comparison of load cell force profiles with input force profiles (Yeh, et al. 2007)

1.4 Research motivation and scope of investigation

(1) Research motivation

In advanced electronic packaging (e.g., BGAs), solder joints serve as electrical and mechanical connectors between electronic chips and printed circuit boards. Consequently, fracture or failure in solder joints results in breakdown of such electrical devices and therefore solder joint reliability is a significant concern. Most investigations in this area focus on the effects of

mechanical or thermal-induced cyclic loading on solder joint reliability, with respect to the composition in the intermetallic zone. In recent years, the effects of impact loading on electrical devices have attracted increasing concern from electrical product manufacturers. For instance, commonly-used portable electronic devices such as mobile phones and PDAs experience accidental drops onto hard floors. Tests on a pager dropped from 1.22m onto a concrete surface show that shock levels of around 2000g and 5000g can be induced in the PCB board and housing respectively (e.g., Nagaraj, 1997). The survivability of a portable device subjected to drops reflects its reliability and this affects brand loyalty by customers - a major concern of manufacturers. Therefore, demands for physical robustness have propelled research into solder joint failure under dynamic or shock loading conditions.

Failure of solder joints under dynamic or shock loads may arise from greater vulnerability associated with device miniaturization and new solder applications in portable electronic devices. The sizes of solder balls in IC packages decrease with increased circuit density, making them more prone to failure when dropped accidentally. Drop testing is commonly used to assess the dynamic response and reliability of IC packages mounted on PCB boards, but such tests do not ascertain the strength of a solder joint. With regard to the possibility of rate sensitivity of the solder alloy material, some studies have investigated the strength of bulk solder with respect to loading speeds. A solder joint in an IC package is somewhat complex, comprising a solder bump, copper pads and substrates. Intermetallic compounds as well as voids, etc, are commonly generated at solder-copper interfaces and in the solder

bump. The bond strength between the pad and substrate also influences the tensile/shear strength of an actual solder joint. Therefore, the mechanical properties of a solder joint may not be well described based primarily on the properties of bulk solder. Studies that investigate the rate dependence of solder joints have also been conducted (e.g., Williamson, et al., 2007; Yeh and Lai, 2007). However, studies on solder joint strength under dynamic or impact loads are still limited, especially for Pb-free solders.

It is also noted from a review of literature, that reports of experimental tests on single solder joint specimens are few. Some “single joint” specimens were not based on actual solder joints (Fig.1-30). For example, Kang et al. (2002) performed fatigue tests on single lap-joint specimens to obtain fatigue crack growth data for 63Sn37Pb solder joints under mode-II loading. Tropea and Botsis (2003) studied tensile deformation and carried out microscopic observations of damage in copper-solder (Sn63Pb37) joints of 1mm thickness, 1mm length and 20mm width between pure copper plates. Similar specimens were also used in cyclic tests (Desai, et al., 2004; Zhang, et al., 2005), and tensile strength tests (Chuang, et al. 2004; Chen, et al., 2006; Chen, et al. 2007). Some tests have been conducted on package specimens with a reduced number of solder joints. For example, Maveety (2004) tested the shear strength of a package with 9 solder joints at strain rates of 10^{-5}~10^{-1}/s; Specimens consisting of two silicon chips (3.3x3.3mm^2) bounded by 4 flip chip joints (one at each corner) were investigated in term of creep and crack propagation (Wiese and Meusel, 2003) and cyclic shear (Wiese and Rzepka, 2004); Chen and Lin (2006) conducted quasi-static tensile and shear tests at

0.6mm/min on BGA specimens containing 4 solder joints. In some studies, ball shear tests were conducted on single solder bumps, but with shapes different from that of an actual solder joint in an IC packages. Few reports of research on single solder joint specimens exist, e.g. quasi-static tests by Tan et al. (2006; 2009). As mentioned previously, an actual solder joint has distinct geometry that is related to many factors arising from flip-chip manufacturing technique, and the formation of intermetallic compounds also has effects on solder joint strength. Therefore, measurement of joint strength using actual solder joint specimens is necessary. Tests on package specimens may underestimate solder joint strength, as the joints in a package may not break simultaneously; therefore, testing of single solder joints is prefered.

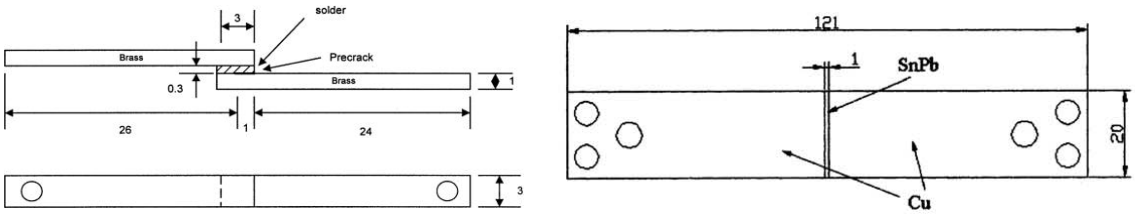

(a) (b)

Fig.1-30 Configuration of single-lap-joint specimen (Kang, et al., 2002) and copper-solder joint (Tropea and Botsis, 2003)

There are other issues related to FEM modeling of solder joints. In an actual IC package, the solder joint is small and has a barrel-like profile; this requires a fine mesh to represent it. Such FEM modeling is costing as a PCB board may contain many solder joints in the mounted IC packages. The need for detail in a finite element mesh needs to be balanced by consideration of simulation time and available computational resources. There are methods to reduce cost in modeling IC packages with solder joints. One way to reduce

FEM cost without sacrificing the 3D nature of the structure is the micro-macro methodology, whereby a relatively coarse macro model of the overall deformation between the module and PCB is used to identify critical solder joints; the outputs of macro-level modeling are then used as input boundary conditions to a much more detailed micro-model to provide the strain distribution within particular solder joints (Corbin, 1993; Gu and Nakamura, 2004). In thermo-mechanical modeling of ceramic ball grid array packages, a "modified micro-macro" methodology has been proposed, where only the critical solder joint is modeled in detail, while other connections are replaced by equivalent connections (Vandevelde, et al., 2003). Alternatively, a beam model has been employed as a substitute in place of the detailed 3-D barrel-like geometry of an actual solder joint. For example, Chan et al. (2002) used equivalent beams to represent hundreds of solder joints in ball grid array assembly, for reliability modeling of fatigue life during temperature cycling. Tan, et al. (2005) simplified solder joints via single beam elements in FE modeling of a BGA package subjected to drop impact. The beam in the FEM is a wire connection, so that the number of elements can be significantly reduced compared to 3-D models.

The preceding review related to motivation for the present investigation – a study of the quasi-static and dynamic mechanical response of single solder joint specimens subjected to tension cum shear and compression cum shear loading. The study encompasses: (1) establishment of appropriate experimental methodology for quasi-static and dynamic testing, (2) characterization of rate-dependent mechanical properties and failure criteria,

and (3) validation and implementation of beam model based on experimentally obtained solder joint properties into finite element modeling of IC packages.

(2) Scope of investigation

This study investigates the mechanical response and failure characteristics of Pb-free solder joints in IC packages under quasi-static and impact loading. The scope comprises:

(1) Establishing appropriate single solder joint specimens

As the failure force of a single solder joint is very small, accidental initial loads will degrade or damage it during specimen preparation. Therefore, an appropriate method for specimen preparation must be established.

(2) Formulation of suitable methods for quasi-static tension plus shear and compression plus shear tests

Fixtures must be designed to accommodate specimens and impose loading at various angles of incline to the axial of a solder joint. As the deformation and failure force is very small, the techniques devised should ensure no pre-load on initial-damage when mounting specimens for testing. Quasi-static tests at 7 specimen inclinations to obtain force-deformation at two deformation rates are undertaken.

(3) Establishment of appropriate impact tests

Dynamic testing is again a challenge because of the small size of the solder joint. An approach based on one-dimensional stress wave theory is to be employed. The assumption of one-dimensional wave propagation will be verified. A miniature dynamic testing machine using thin bars is designed. Performance of the device is examined via FEM modeling.

(4) Characterization of rate-dependent mechanical and failure response of single solder joint specimen

Rate-dependent mechanical characteristics of single solder joint specimens are analyzed based on experimental results. A failure criterion based on the failure/yield force is proposed and related to the normal and shear force components. This is defined by a failure envelope in terms of these force components. The effect of deformation rate is also examined.

(5) Assessment of validity of conversion of experimental load-deformation curves to equivalent stress-strain curves

As an actual solder joint has a barrel-like profile, experimental measurements can only produce load-deformation curves. To implement such information into FEM modeling, a numerical study is undertaken to evaluate the validity of simplification of a barrel geometry by a cylindrical one. This will facilitate

conversion of load-deformation data into equivalent stress-strain curves for use in FEM modeling.

(6) Establishment and validation of simplified beam model for solder joints

An equivalent beam model in conjunction with the equivalent stress-strain properties derived will be established. Validation of the model will be done through comparisons with a 3D cylindrical model and experimental results.

(7) Application of beam model for solder joints in FEM simulation of board-level specimens subject to quasi-static bending and drop impact loading.

Ultimately, quasi-static bending and dynamic drop tests are conducted on board level specimen, whereby an IC package is mounted on a PCB board. The mechanical responses (load, deflection and PCB strain) are recorded and analyzed. The solder joint beam model is implemented in FEM modeling to simulate the quasi-static and dynamic response and simulation outputs are compared with experimental results.

CHAPTER 2 QUASI-STATIC TEST METHODOLOGY AND RESULTS

2.1 Fabrication of solder joint specimens

The solder joint specimens in this study were not cut from actual BGA chip packages. This is because the mechanical properties of solder joints in BGA packages are actually determined by many factors associated with different types of chip sets, as well as the geometry and size of the joints. The objectives of this study include exploring appropriate experimental methods and FEM simulation to investigate the mechanical response of solder joints. Therefore, it is not necessary to extract specimens from actual chip sets, which is both expensive and difficult in terms of ensuring consistent quality.

It is noted that a solder joint specimen resembling an actual joint in a chip set, especially in terms of the solder bump shape and size, is sufficient for the current research. Therefore, the specimen preparation technique adopted is based on a pair of substrates bonded by solder joints. BT substrates are widely used in advanced IC packages; BT is a high heat resistant thermosetting resin with two main components, B (Bismaleimide) and T (Triazine). These are employed to fabricate solder joint specimens. The substrate plates supplied by *Micron Semiconductor Pte Ltd* (Singapore) are around 0.3mm thick, with 350μm diameter copper pads at a pitch distance of

800μm (Fig.2-1a). The copper pads are symmetrically aligned in a pattern within six small squares. Therefore, solder joints can be produced by subjecting a pair of parallel substrates to a reflow process with solder balls sandwiched between them. The solder balls used are Pb-free (Sn96.5Ag3.0Cu0.5) with a spherical geometry, 0.42mm in diameter.

It was found that the substrate plates are not perfectly flat; this resulted in inconsistent solder joint heights. Measurements of the overall thickness of the substrate assemblies at the solder joint locations verified this. The variation of solder joint height affected specimen consistency and increased the scatter in experimental results. To minimize the effects of substrate warpage, the substrate plate was cut into six squares according to the pad pattern to reduce the size, and reflow was applied to these reduced sized substrate pairs sandwiching solder balls; this is shown in Fig.2-1b. Four solder balls were mounted on one of the square substrates and thermally reflowed to bond them to the pad locations. After that, it is placed facing downwards and aligned with a matching square substrate to undergo another reflow. Through this, four solder joints are formed between a pair of substrates. Measurements of the overall thickness of these soldered square substrate showed consistent heights at the solder joints.

The preceding description details the method to fabricate solder joint specimens similar to actual ones in IC packages. Such specimen are named “package specimens”, which correspond to pairs of square substrate (around 11.3x13.3mm) bonded by several solder joints. These also constitutes

package specimens for subsequent package level tests in the form of quasi-static three-point bend and dynamic drop tests (described in *Chapter 5*), to explore their response for comparison with FEM simulation.

The fabrication of single solder joint specimens without damaging them is an even greater challenge than preparation of package specimens. As a solder joint is much smaller in size, preparation of single solder joint specimens one at a time is not feasible, as it is difficult to ensure that the substrates are parallel, and the time required by this approach is excessive. It has been emphasized that test specimens are easily degraded or damaged by any accidental load, because of their small failure force. Therefore, single solder joint specimens were fabricated by using a laser to cut the soldered square substrates into four pieces, each about 5×5mm in size, as shown in Fig.2-1c. This non-contact cutting method ensures no physical damage to the solder joints prior to testing. Fig.2-1d shows a microscopic examination of a single solder joint specimen. Parallel alignment between the substrates demonstrates that the specimen preparation procedure adopted is acceptable. (As the solder ball is located a distance from the edges of the squares, its image is not very sharp.)

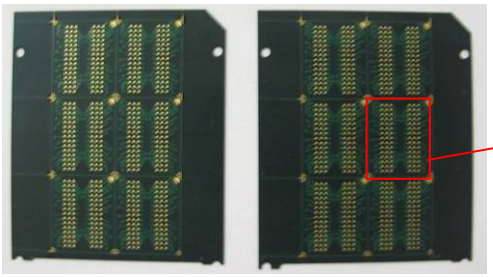

(a) Substrate plates supplied by *Micron Semiconductor Pte Ltd*

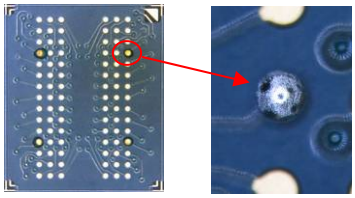

(b) A square cut from the substrate, and a solder ball mounted onto the substrate after the first reflow.

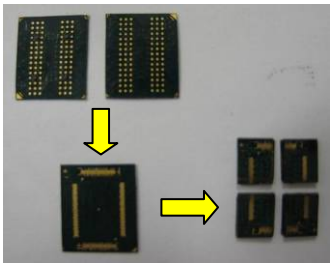

(c) Alignment of a pair of substrate squares to form four solder connections after reflow; individual single solder joint specimens separated by laser cutting.

(d) Microscopic observation of single solder joint specimen.

Fig.2-1 Preparation of solder joint specimens

2.2 Testing method and fixtures for inclined loading

2.2.1 Testing method for single solder joint specimen

In this study, the test specimens are solder joints that have two special features - a very small size and a very low failure force. These introduce difficulties in measuring their force-displacement responses, even for quasi-static loading. There is also no extensometer that can be mounted onto such tiny specimens (less than 0.5mm in size) to measure the deformation directly. Optical methods are not suitable because a solder joint in a chip package is

not easily visible and its small size increases optical resolution demands. Care must be taken in mounting a solder joint specimen because its brittleness and low failure force make it vulnerable to any accidental load, which can affect the initial integrity of the specimen.

Taking into consideration the preceding factors, an Instron micro-tester (model 5548) was found to be appropriate for loading the solder joint specimens studied (Fig.2-2). This tester can apply tensile, compressive, flexural, cyclic, and shear loading on miniature specimens. Its position control resolution is as fine as 0.02 microns and the position measurement accuracy is +/-2.5 micros over 10mm of travel. The system has a stiff frame (8.32kN/mm) to minimize system compliance and specimen deformation can be derived directly from the crosshead displacement if the specimen stiffness is relatively small. The load measurement accuracy is also high (+/-0.4%). A 1KN load cell was used in this study.

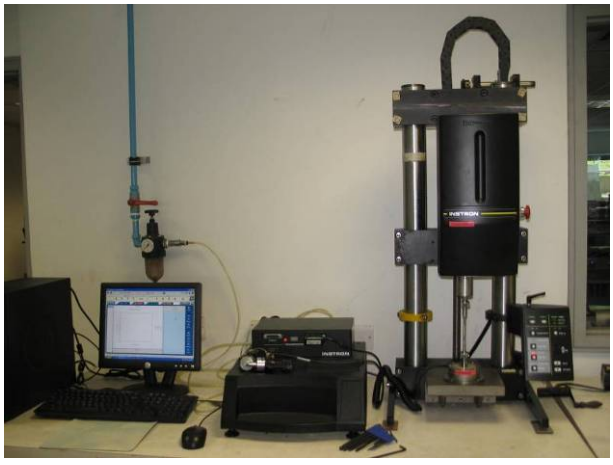

Fig.2-2 Instron materials testing system (micro-tester, model 5548)

The small yield load of a solder joint (only few Newtons) means that care must

be taken in the mounting of specimens on the micro-tester to avoid unwanted pre-loading. As shown in Fig.2-3 (a), a specimen is glued to the upper (movable) and fixed (lower) rods of the Instron micro-tester, for tension/compression/shear loading, and load is applied by movement of the upper rod. Cyanoacrylate adhesive was used and a small compressive load must be applied to the specimen during curing of the adhesive. Because of the small size of the solder joint, this small initial compression may induce a load on the solder bump sufficient to cause yield. It was found that a small movement of the upper rod via actuation of the tester can generate a load of a few Newtons during mounting of a specimen. This may affect the specimen even before a test starts. Moreover, it was found that a tensile force on the specimen is generated when the adhesive solidifies due to cure shrinkage. To prevent such undesirable pre-loading, the upper rod is allowed to move freely during specimen fixation. A special fixture was designed to facilitate this.

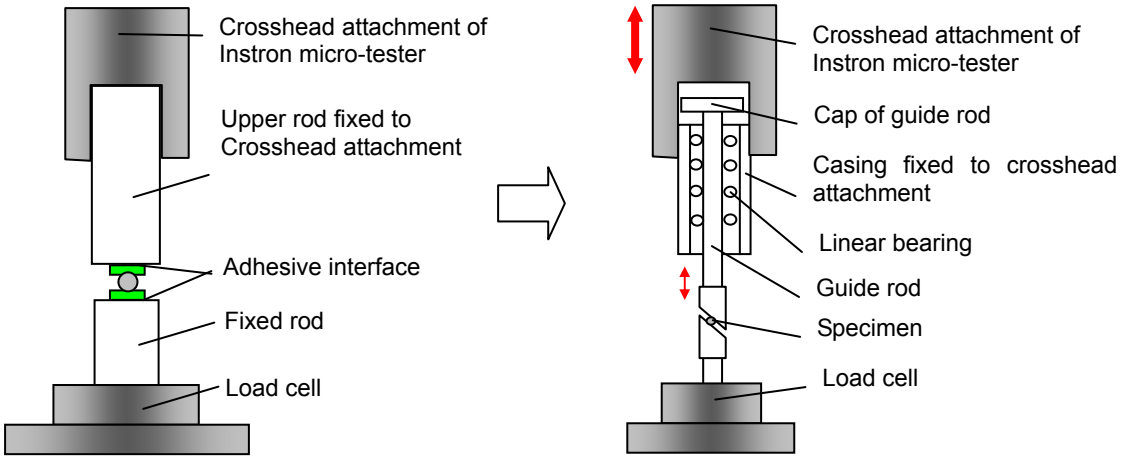

Fig.2-3 Schematic illustration of fixture for mounting a solder joint specimen on Instron micro-tester

A schematic illustration of the fixture is shown in Fig.2-3 (b). The upper

surface of the specimen is bonded to a guide rod instead of directly to the upper load actuating rod of the tester. A precision linear bearing is employed to minimize friction against the guide rod. The casing of the linear bearing is fixed to the crosshead attachment. When the crosshead attachment moves upwards to the point when the casing makes contact with the lower surface of the cap of the guide rod, tension is imposed on the specimen. Conversely, when the crosshead attachment moves downwards until it touches the upper surface of the cap, compression of the specimen commences.

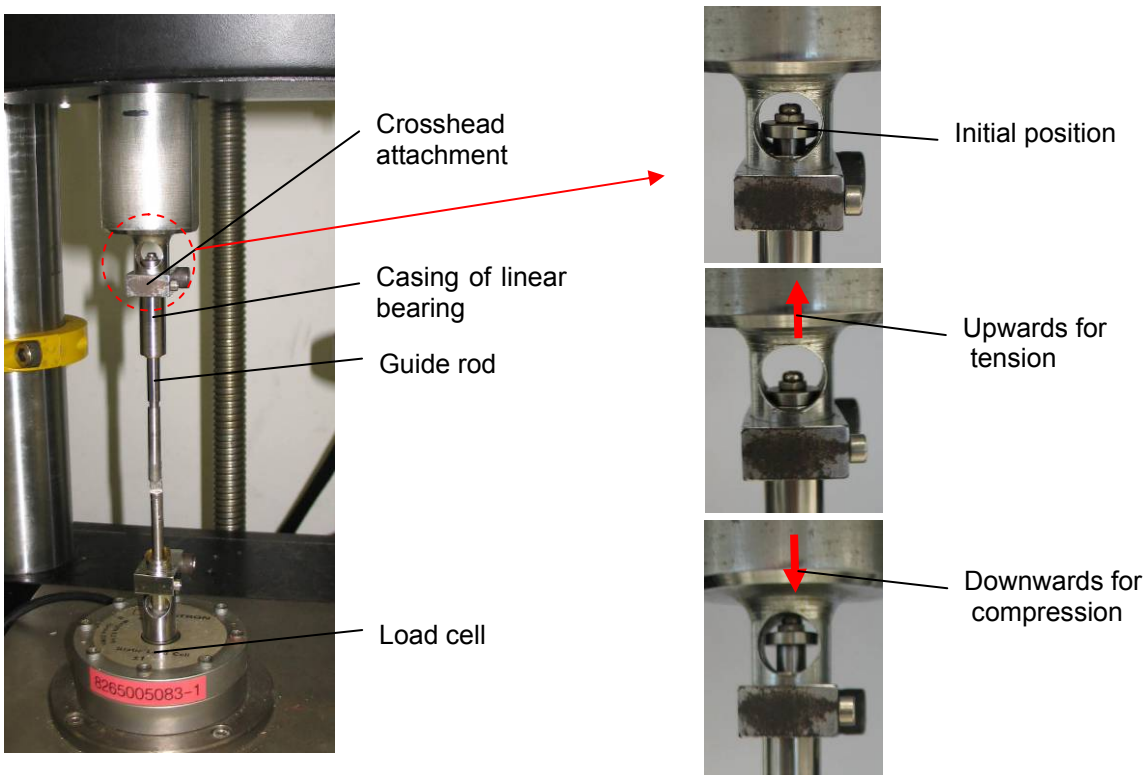

Fig.2-4 Experimental arrangement for static tensile and compression tests, and adapters to load specimens at various angles

Fig.2-4 illustrates the fixture designed to facilitate the mounting of solder joint specimens. The initial compressive load on a specimen is only the weight of the guide rod (20 grams), sufficient to ensure complete interfacial contact

between the specimen and the rods during curing of the adhesive, but too small to affect the solder joints. An example of raw data from the micro-tester is shown in Fig.2-5, where the initial load for compression or tension is 0.2N (the weight of the guide rod) and this is maintained until the initial gap between the cap of guide rod and the crosshead attachment is eliminated. This approach ensures that the initial loading condition is consistent for all tests and the specimen is not affected during its mounting.

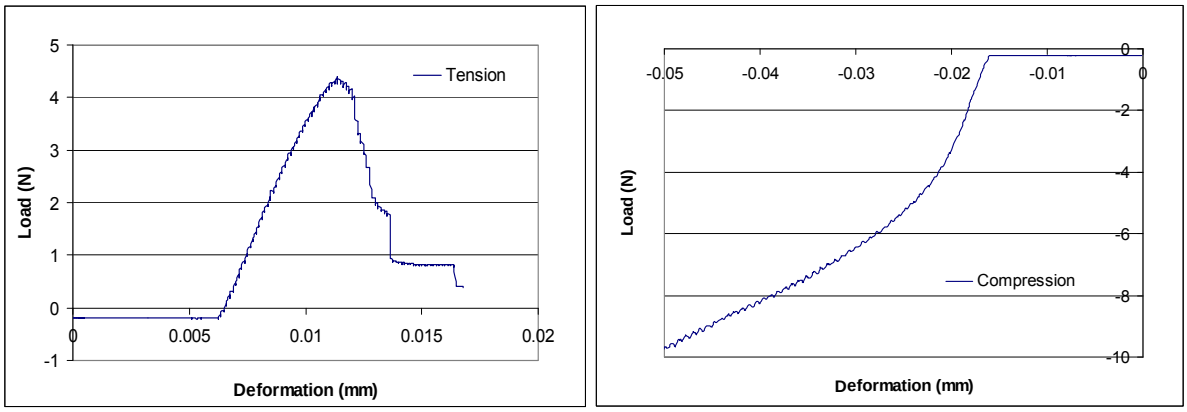

Fig.2-5 Raw tension/compression force-displacement curves from Instron micro-tester

2.2.2 Fixtures for inclined loading

In this study, a failure envelope for combined normal and shear loading is also sought to define a solder joint failure criterion. This is done by inclining the surfaces that the specimen is attached to (Fig.2-6). For different angles of inclination α, the axial load (F) on the rod will generate both normal (F_N) and shear (F_S) forces on the specimen

$$F_N = F \cdot \cos(\alpha) \quad \text{and} \quad F_S = F \cdot \sin(\alpha) \qquad (2\text{-}1)$$

The failure force components are then used to construct a failure/fracture envelope. To apply loads at different angles, threaded steel adaptors with inclined surfaces are connected to the guide and fixed rods. The use of linear bearing between casing and guide rod also facilites alignment of the pair of adaptors. Seven pairs of adaptors were used with angles of inclination of 0^0 (for pure tension or compression), 15^0, 30^0, 45^0, 60^0, 75^0 and 90^0 (for pure shear).

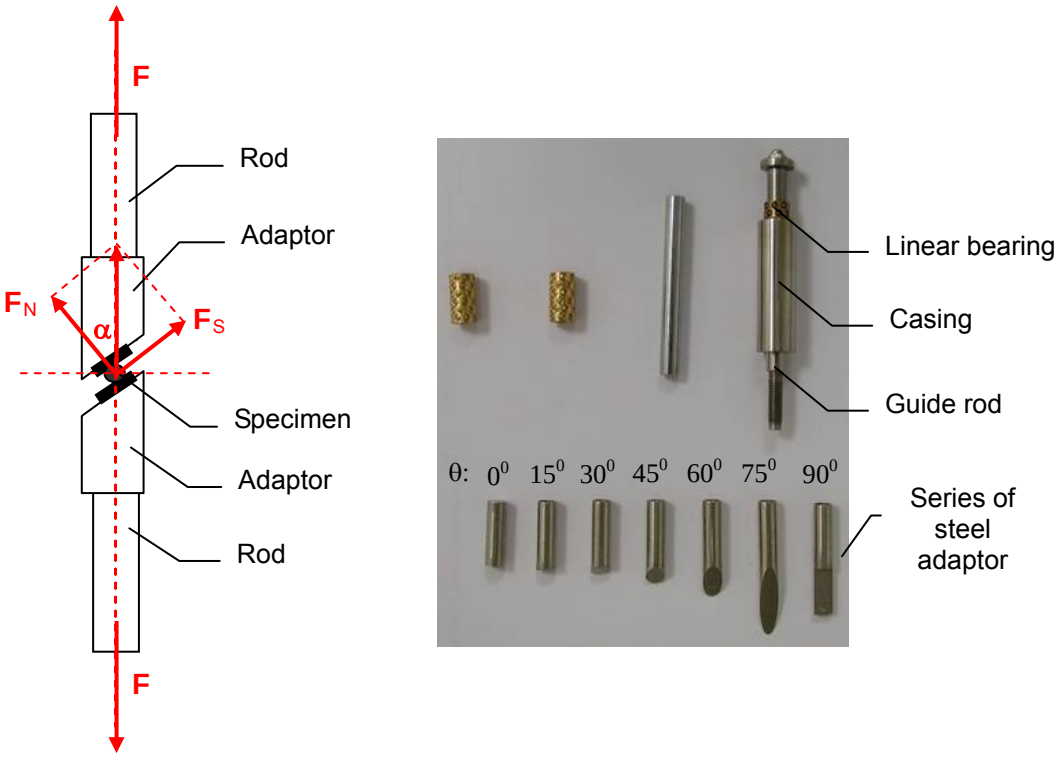

Fig.2-6 Application of combined normal and shear loading using adaptors with different angles of inclination

When attaching a solder joint specimen to the adaptors, liquid cyanoacrylate adhesive may flow down to the specimen, invalidating the test because the specimen has been reinforced by the adhesive. To prevent this, a specimen is first glued to the upper adaptor, and then connected the adaptor to the guide rod. Subsequently, the specimen is glued to the lower adaptor on the fixed rod.

The free of the guide rod within the fixture facilitates this installation procedure and maintains contact between the specimen and the adaptors via a constant small compressive force during solidification of the adhesive.

For a pure shear test, the surfaces of the upper and lower adaptors are vertical and parallel to each other. However, the fixed gap between the parallel surfaces cannot fit every specimen exactly - this will induce undesired compression or tension on a specimen. An additional adaptor is designed for use in conjunction with the shear adaptors (Fig.2-7). The additional adaptor is first positioned between the shear adaptors. Following this, one surface of the specimen is glued to the additional adaptor; then the other surface of the specimen is bonded to the shear adaptor. Finally, the other end of the additional adaptor is bonded to the other shear adaptor. The picture on the left in Fig.2-7 shows the configuration for a shear test on the Instron micro-tester, and the right picture illustrates the installation process for dynamic testing (using a miniature impact tester, which will be described in the next chapter).

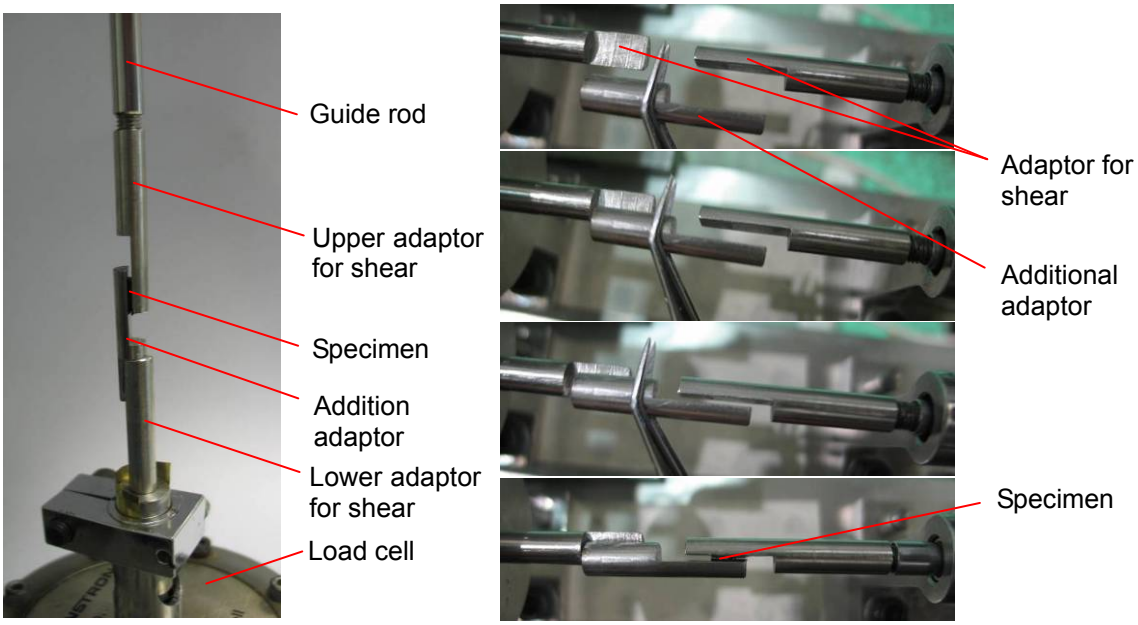

Fig.2-7 Mounting a specimen for pure shear testing

2.3 Evaluation of mechanical response of solder joint specimens

The preceding sections describe the methods adopted to fabricate single and multi-solder joint (package) specimens and to conduct the quasi-static tests for inclined loading. To determine the mechanical response of a solder joint, experiments may be conducted on package specimens, whereby the strength of a single joint is derived by averaging the total load by the number of solder joints in the package. Alternatively, tests can be carried out on single solder joint specimens. Compared to single joint specimens, package specimens are larger and stronger, making them easier to fabricate and mount on the tester. However, under tension, the solder joints are not likely to break simultaneously, which results an underestimation of the joint strength.

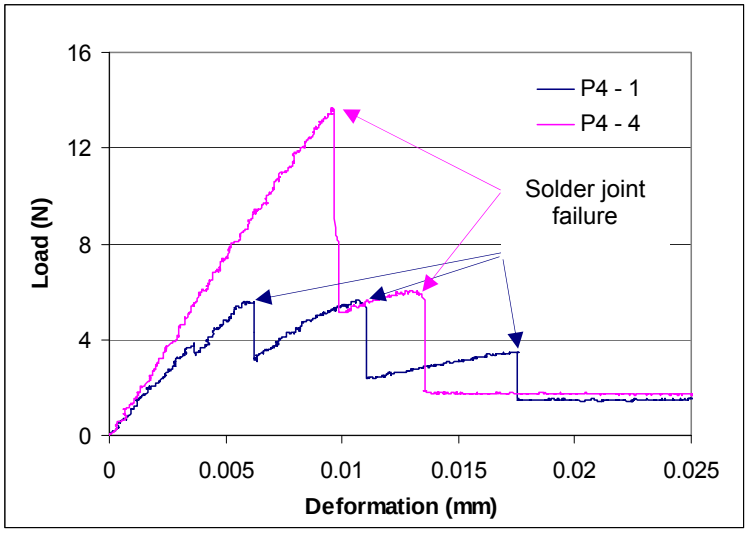

Fig.2-8 Tensile load-deformation response for non-simultaneous breakage of solder joints in a package specimen

To evaluate which type of specimen is more suitable for eliciting the mechanical properties of a single solder joint, a series of tensile tests on single and package solder joint specimens were performed at a speed of 0.00015mm/s using the Instron micro-tester. Single joint specimens are denoted by P1, while package specimens with 4, 8, 16 and 24 solder joints are denoted by P4, P8, P16 and P24. During tests, it was observed that the instant of joint failure is accompanied by a cracking sound, and a corresponding drop in load. Fig.2-8 illustrates two load-deformation curves from tests on 4-joint package specimens (specimen, P4-1 and P4-4), where a sudden drop in load indicates a solder joint breaking. It shows that the force-deformation responses are not consistent even for identical number and locations of solder joints. The earlier a solder joint breaks, the less the overall stiffness and strength.

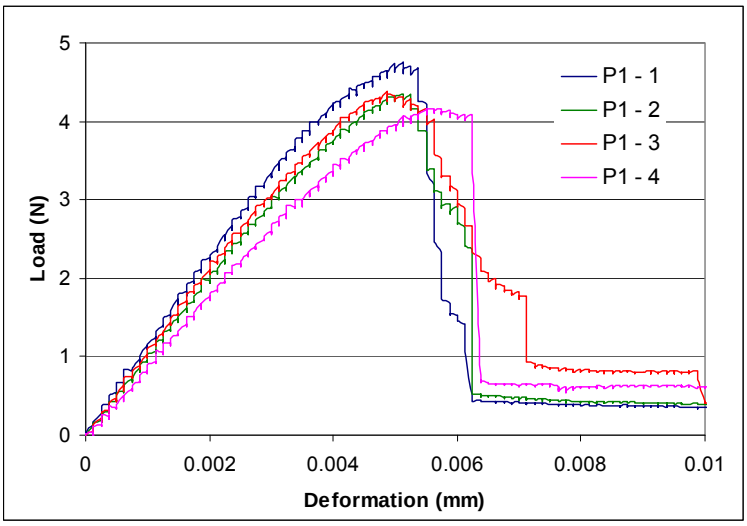
Load (N)
Deformation (mm)
P1 - 1
P1 - 2
P1 - 3
P1 - 4
0
1
2
3
4
5
0
0.002
0.004
0.006
0.008
0.01

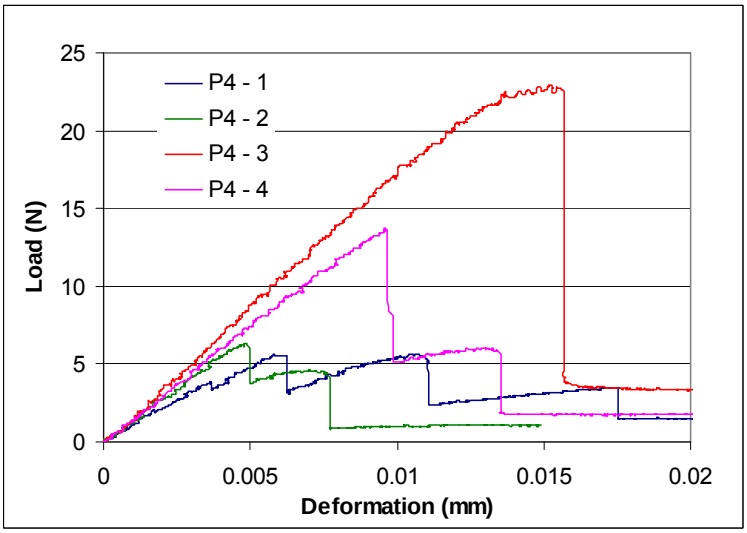
Load (N)
Deformation (mm)
P4 - 1
P4 - 2
P4 - 3
P4 - 4
0
5
10
15
20
25
0
0.005
0.01
0.015
0.02

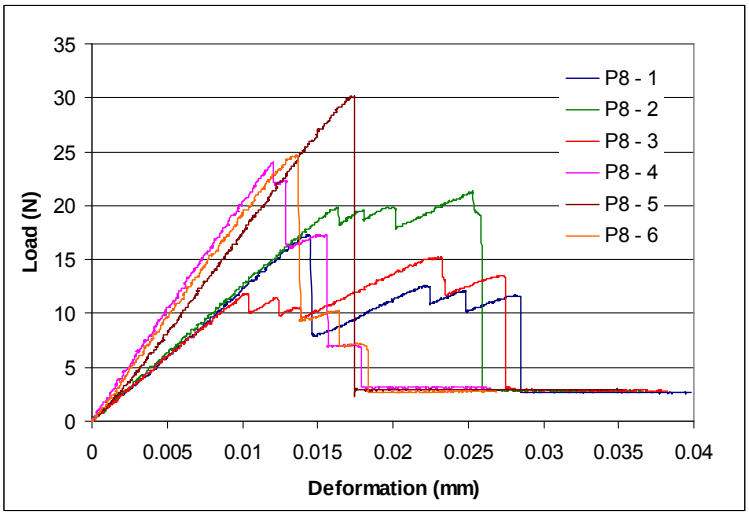
Load (N)
Deformation (mm)
P8 - 1
P8 - 2
P8 - 3
P8 - 4
P8 - 5
P8 - 6
0
5
10
15
20
25
30
35
0
0.005
0.01
0.015
0.02
0.025
0.03
0.035
0.04

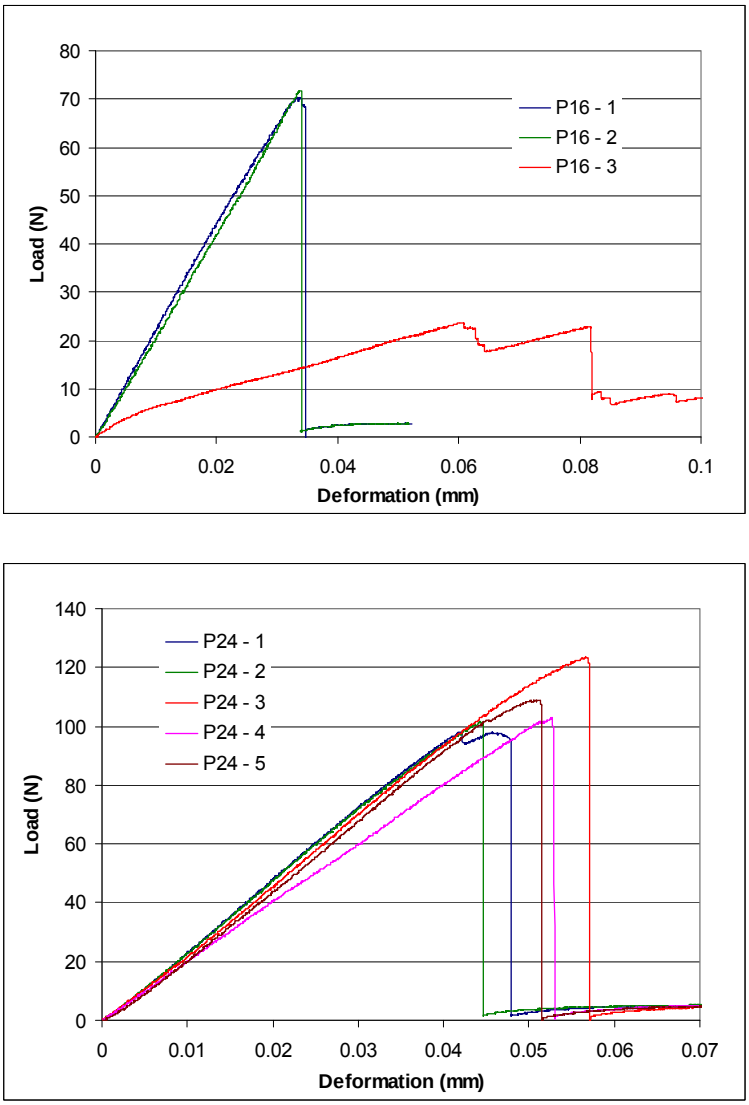

Fig.2-9 Raw load-deformation curves of package specimens containing one (P1), four (P4), eight (P8), sixteen (P16) and twenty four (P24) solder joints from 0.00015mm/s tensile tests via Instron micro-tester

Fig.2-9 shows all the tensile load-deformation curves from tensile tests on single (P1) and multiple solder joint specimens (P4, P8, P16 and P24). A curve with more than one sharp load drop demonstrates that the solder joints in a specimen are not broken simultaneously. Therefore, if the load averaged by the number of solder joints is taken to represent the response of one joint, the resulting load-deformation curve will be erroneous and the failure strength underestimated. It is noted that the number of valid tests for P4 and P8

package specimens is relatively low - one out of 4 for P8 specimens and one out of 6 for P16 specimens. When the number of solder joints in a package is increased, the overall load-deformation profiles tend to become more stable and consistent, as shown by the results for P16 and P24 specimens.

The load-deformation curves from tests on single joint specimens (P1) show an increase to the point of failure; however, there is some scatter. The degree of data scatter for single solder joint specimens cannot be compared directly with that for multi-joint specimens such as P24, based on the diagrams in Fig.2-9, as their load magnitudes are quite different (around 4.5N for P1 and 110N for P24 specimens).

With more solder joints, the stiffness of a package specimen increases correspondingly. Therefore, the compliance of the micro-tester as well as the mounting fixture cannot be ignored. The size of a multi-joint package specimen is around 11x13mm, and large ϕ20mm adaptors were used to mount the specimens on the micro-tester, which increases the compliance of fixture. Measurement of tester compliance was undertaken with the adaptors installed but without a specimen. The adaptors were glued together using cyanoacrylate adhesive and the tensile load-displacement response is repeatable, as shown in Fig.2-10. The machine compliance derived was then used to correct the raw deformation data (i.e., the curves in Fig.2-9).

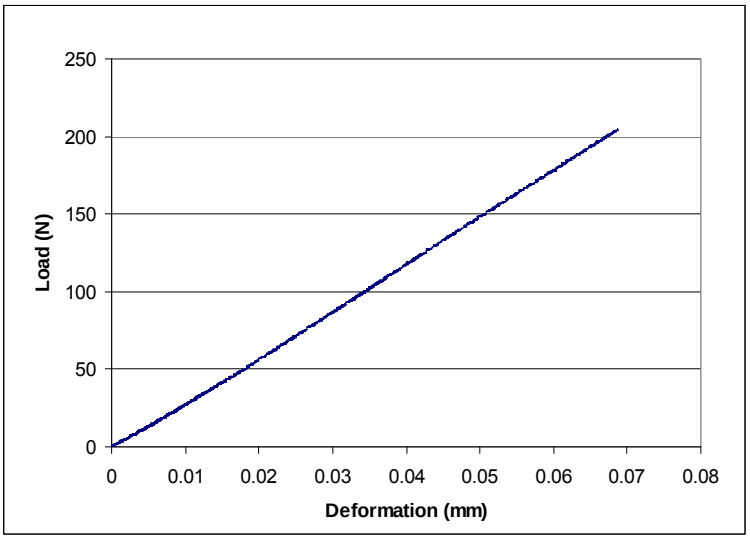

Fig.2-10 Measurement of tester compliance for tensile tests of package specimens

Fig.2-11 shows load-deformation responses for one solder joint, derived from tests on single and multi solder joint specimens. The deformation has been corrected by incorporating the tester compliance and the load averaged by the number of solder joints in a specimen. Although the elastic portion of the force-deformation curves of valid tests on P16 and P24 specimens appear straight and coincident (Fig.2-9), differences become more apparent when the curves are converted to that of one solder joint. It is noted that the derived stiffness of one solder joint tends to increase with a decrease in the number of solder joints in a package. This shall be the reason that machine compliance affects the stronger specimens more, in addition of result of non-simultaneous degradation of individual solder joints in a multi-joint specimen. The curves from tests on single solder joint specimens display the highest stiffness, and each starts with a linear phase followed by a decrease in stiffness until failure occurs. The curve from the valid test on P4 shows a similar stiffness and initial response as the curves for P1 specimens. However, the number of acceptable tests is too small (1 valid out of 4 tests). The load-deformation

responses of single solder joint specimens exhibit some scatter; this is expected, as the specimens are not totally identical.

From the preceding description of experimental results, it is concluded that single solder joint specimens are more suitable for deriving the load-deformation curves for one solder joint. As highlighted previously, special care must be excised in preparing single solder joint specimens and mounting them on the tester, to ensure consistency of test results.

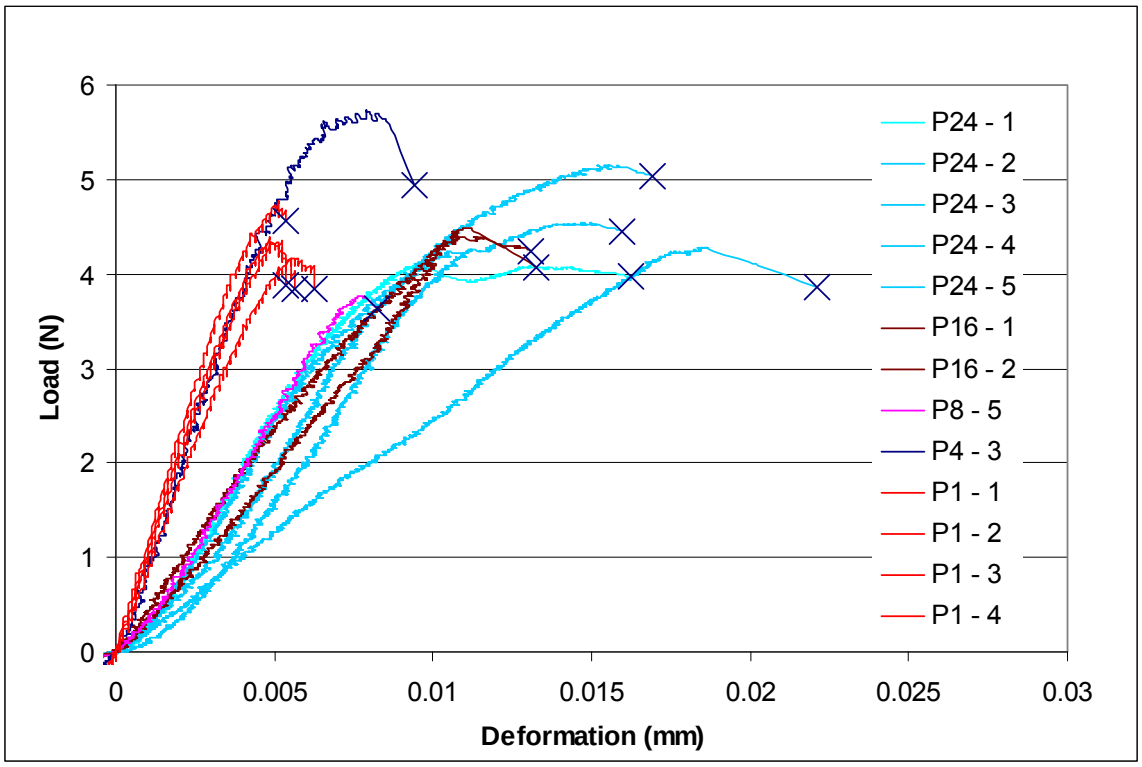

Fig.2-11 Tensile load-deformation curves of one solder joint derived from tests on package specimens containing one (P1), four (P4), eight (P8), sixteen (P16) and twenty four (P24) solder joints at a speed of 0.00015mm/s via Instron micro-tester.

2.4 Experimental results of quasi-static tests on single solder joint specimens

Quasi-static tests were carried out on single solder joint specimens comprising two parallel 5×5mm BT substrates linked by a solder joint melted from a ϕ0.42mm Pb-free (Sn96.5-Ag3.0-Cu0.5) solder ball. Pairs of steel adaptors with inclined surfaces were employed to facilitate oblique loading of the specimens. The angles of inclination were varied from 0^0 to 90^0 at increments of 15^0; these correspond to pure tension or compression for 0^0, combined normal-shear loading and pure shear for 90^0. The various angles facilitate more data points for construction of the solder joint failure force envelope.

Quasi-static tests at two deformation rates are undertaken to investigate possible rate dependence of the joint properties. One is a very low rate of 0.00015mm/s and the other is determined from the capability of the micro-tester. The highest displacement speed is 25mm/s, and the fastest data logging rate is 2ms per point. Failure of a single solder joint specimen in tension occurs at a displacement of around 0.006mm; therefore, to obtain adequate data points for the load-deformation curve, the other quasi-static deformation rate was set at 0.15mm/s. This yields around 20 data points before the solder joint breaks, sufficient to define the load-deformation curve.

Fig.2-12 shows load-deformation curves for single solder joint specimens for a deformation rate of 0.00015mm/s; Fig.2-13 shows the corresponding results

for deformation rate at 0.15mm/s. Each figure depicts the responses for tension and compression, corresponding to angles of loading ranging from 0^0 to 90^0.

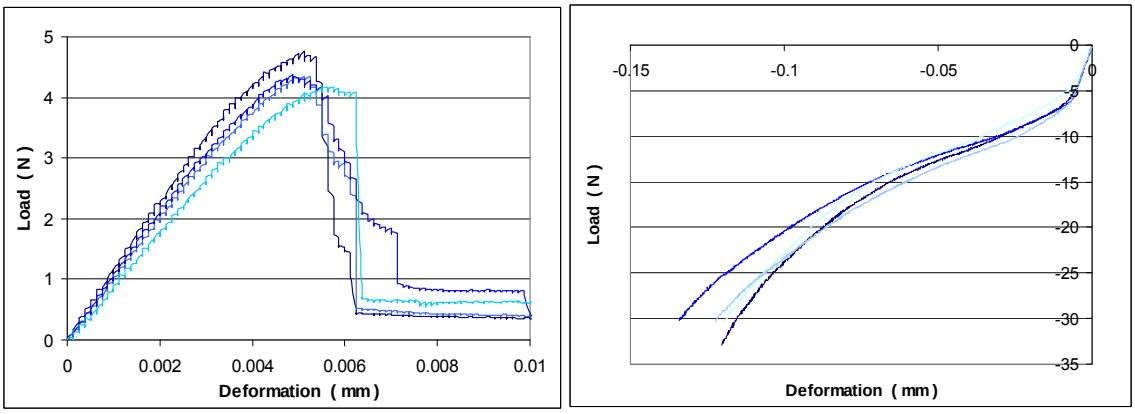

(a) Tensile and compressive load-deformation curves for loading at 0 degrees

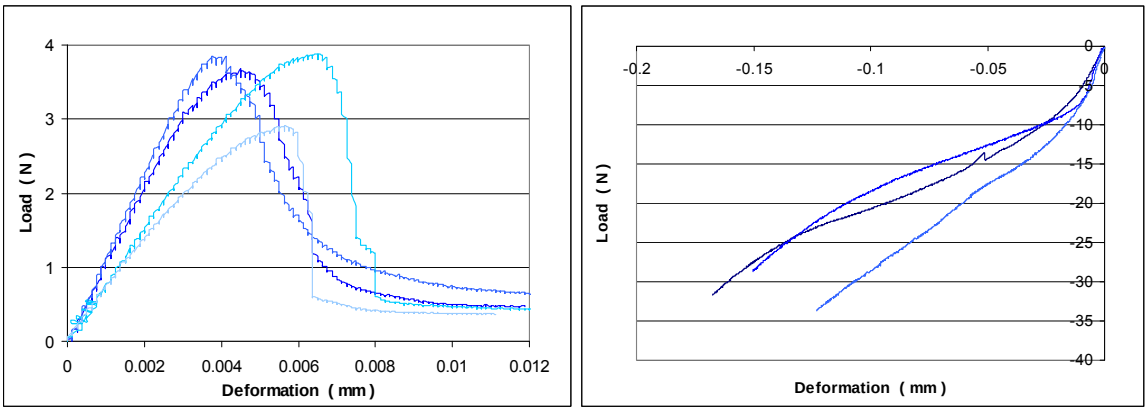

(b) Tensile and compressive load-deformation curves for loading at 15 degrees

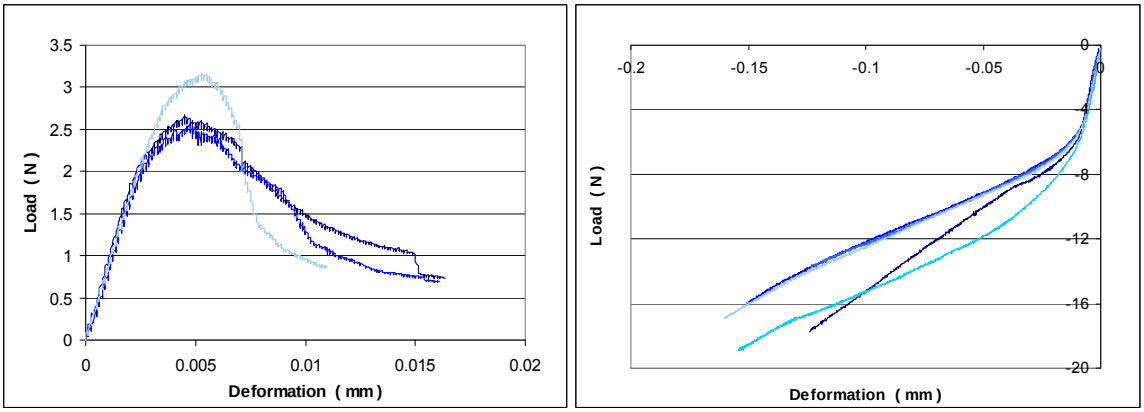

(c) Tensile and compressive load-deformation curves for loading at 30 degrees

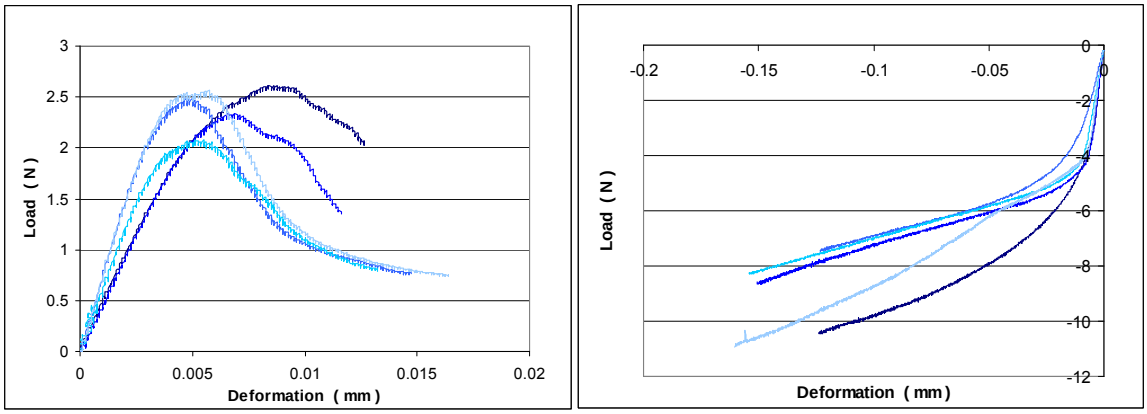

(d) Tensile and compressive load-deformation curves for loading at 45 degrees

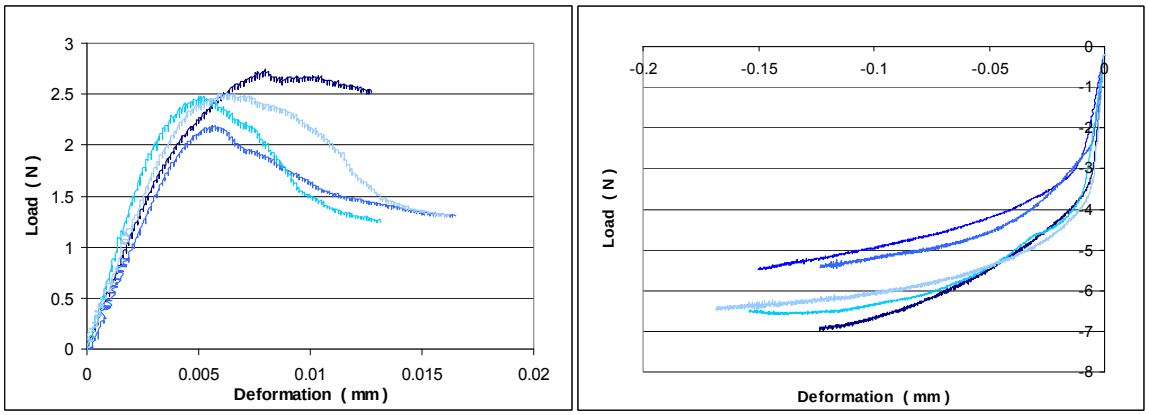

(e) Tensile and compressive load-deformation curves for loading at 60 degrees

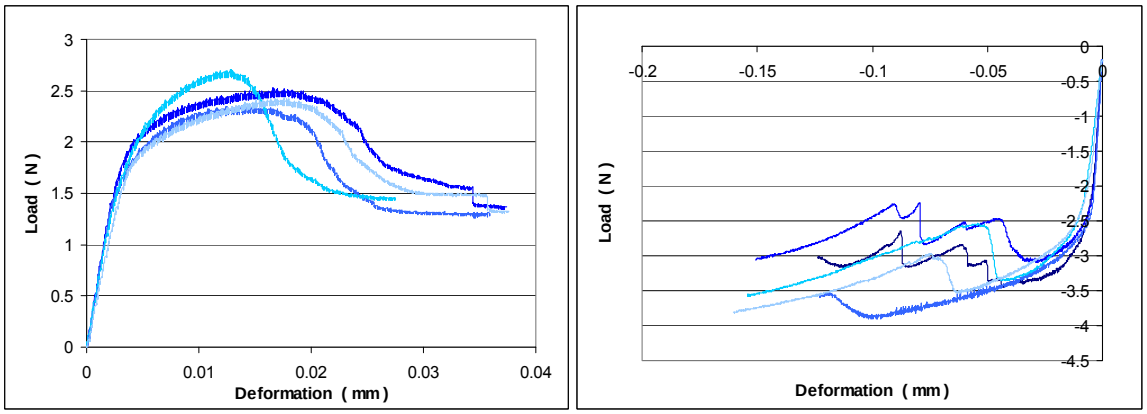

(f) Tensile and compressive load-deformation curves for loading at 75 degrees

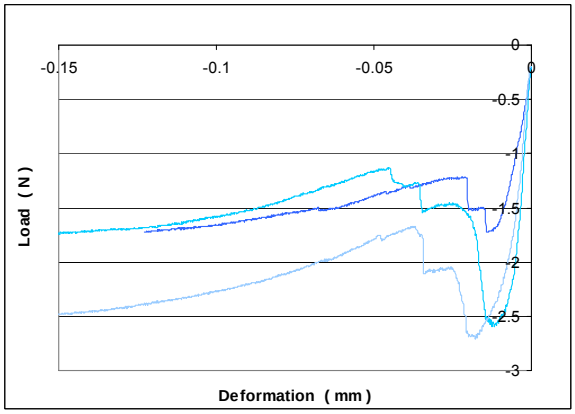

(g) Load-deformation curves for shear (90 degrees)

Fig.2-12 Quasi-static tensile and compressive load-deformation curves for single solder joint specimens loaded at a deformation rate of 0.00015mm/s.

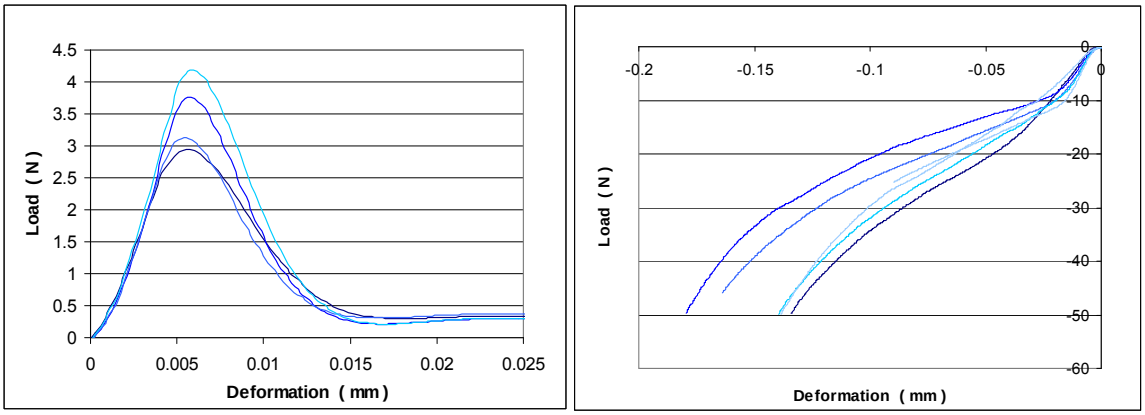

(a) Tensile and compressive load-deformation curves for loading at 0 degrees

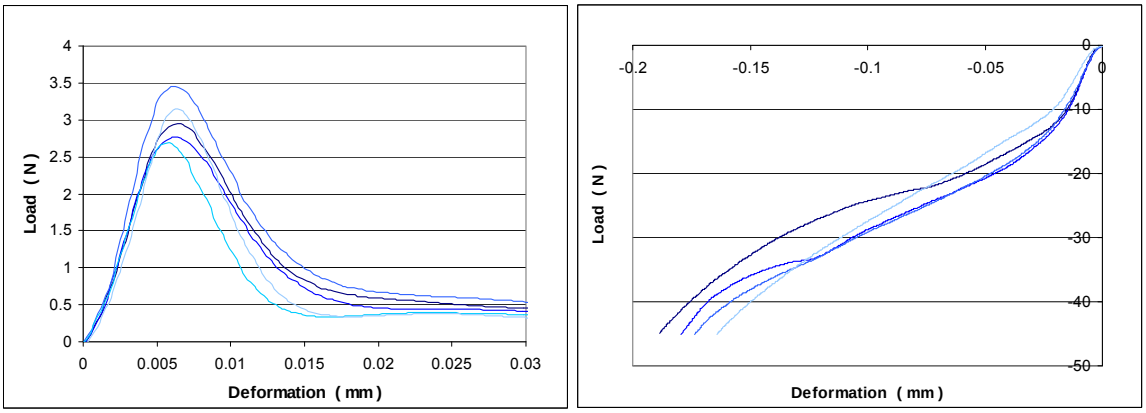

(b) Tensile and compressive load-deformation curves for loading at 15 degrees

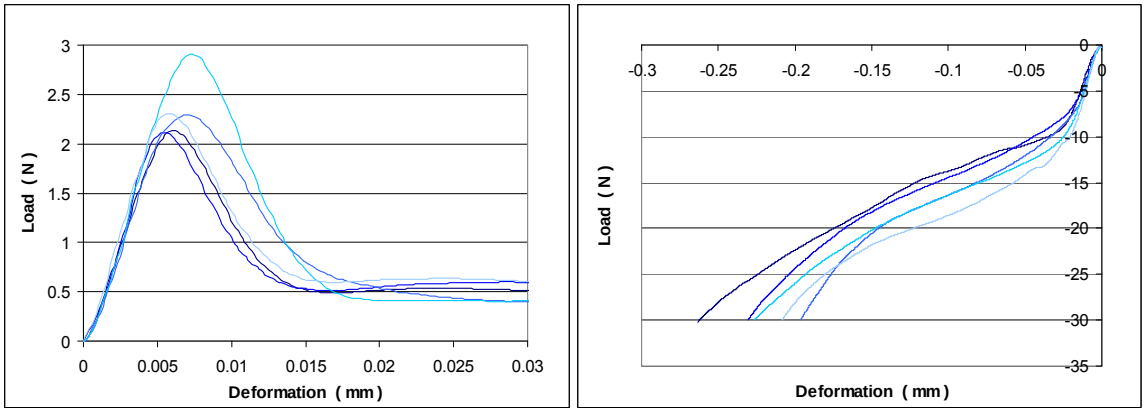

(c) Tensile and compressive load-deformation curves for loading at 30 degrees

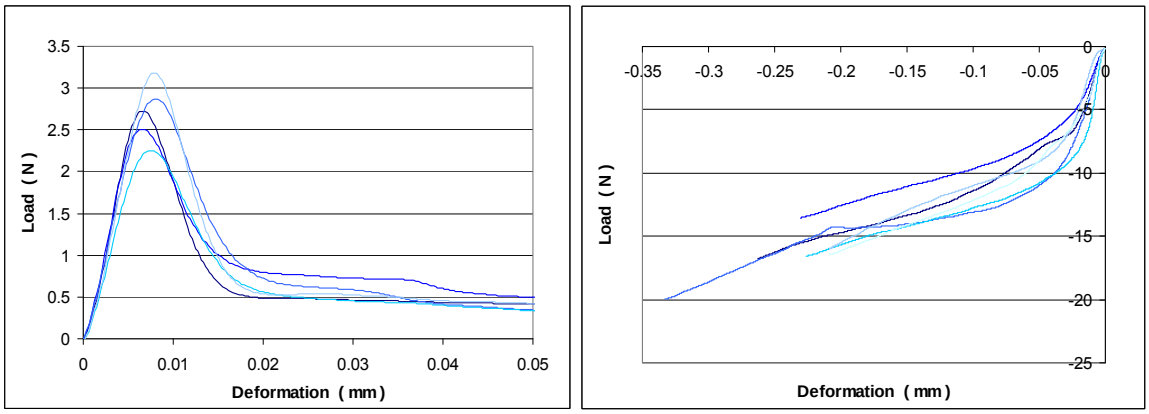

(d) Tensile and compressive load-deformation curves for loading at 45 degrees

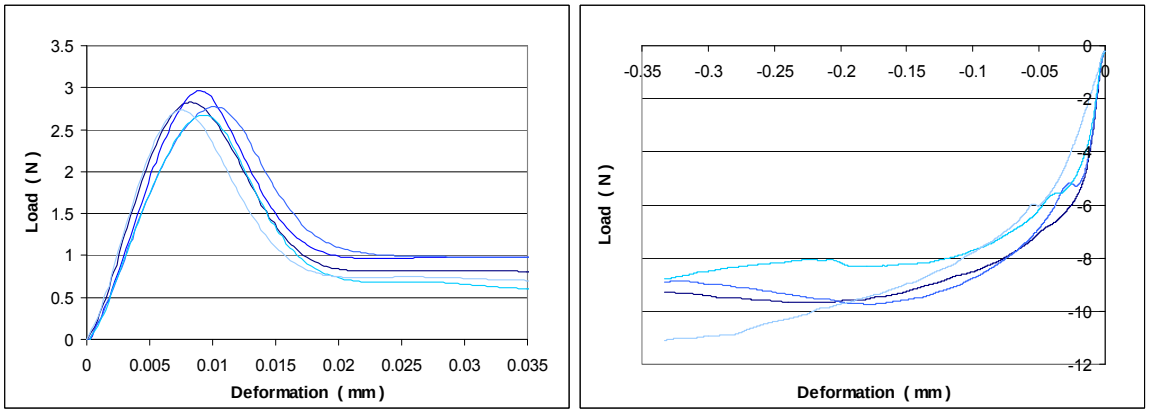

(e) Tensile and compressive load-deformation curves for loading at 60 degrees

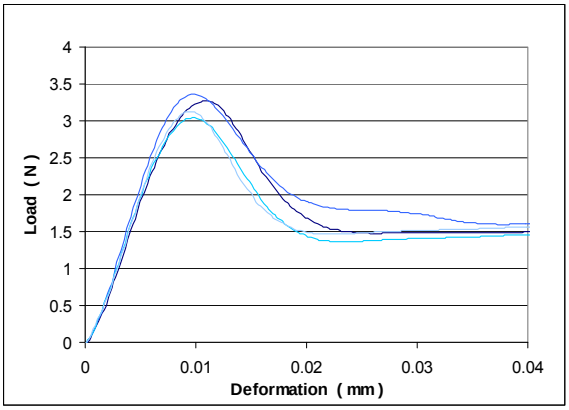

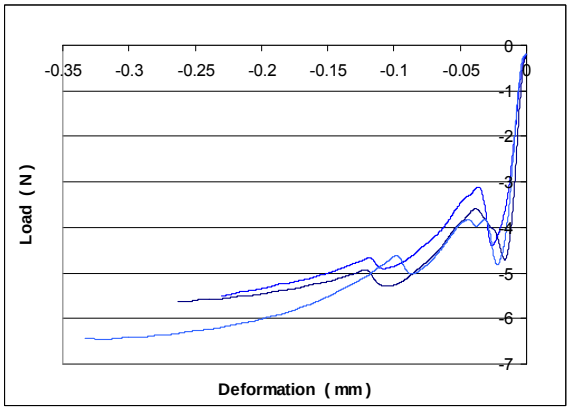

(f) Tensile and compressive load-deformation curves for loading at 75 degrees

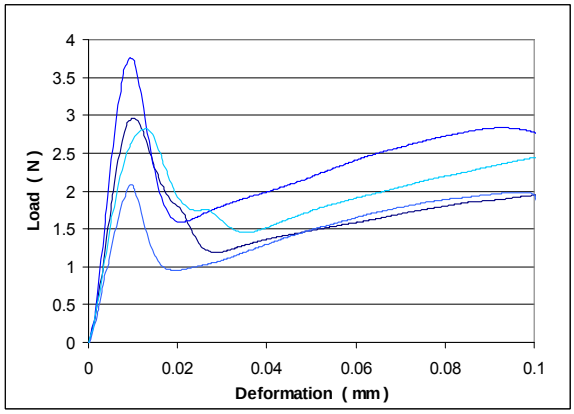

(g) Load-deformation curves for shear (90 degrees)

Fig.2-13 Quasi-static tensile and compressive load-deformation curves for single solder joint specimens loaded at a deformation rate of 0.15mm/s.

The load-deformation curves of single solder joint specimens exhibit an initial linear response followed by a phase of nonlinearity, after which the load drops for tensile loading or yields and enters a hardening phase for compression. Fig.2-14 illustrates a combined tensile/shear and a combined compressive/shear load-deformation curve corresponding to a deformation rate of 0.00015mm/s and loading at 45^0. A straight line offset from the elastic response by 0.2% strain (based on solder joint height) is drawn and its intersection with the load-deformation curve is taken to define the yield point.

The load-deformation response of a solder joint under combined tension and shear differs from that for combined compression and shear. For combined tension/shear and pure shear, there is generally an ultimate point in the load-deformation curve after which the load drops quickly, indicating solder joint breakage. However, for combined compression and shear, a solder joint can still sustain a load after yield. As a solder joint is not only an electrical but also a mechanical connection in an IC package; any physical degradation in solder joint quality may result in electrical malfunction. Therefore, in this study, deviation of a load-deformation curve from initial linearity for combined compression and shear (around yield) is deemed indicative of commencement of solder joint degradation.

It is noted that for combined tensile and shear, the yield point is close to the ultimate load (which corresponds to breakage of a joint). But for combined compression and shear, taking the yield point to indicate commencement of degradation seems somewhat conservative, as a solder joint can still sustain load and its stiffness decreases more markedly later during the transition to the strain hardening phase.

Failure of a solder joint under pure tension or combined tension and shear is defined by the ultimate load. For pure compression or combined compression and shear, failure is defined by the mid-point of the transition from the linear elastic response to the strain hardening phase. This is determined by the first intersection identifying point between the tangents to the linear elastic and approximately linear strain-hardening segments. The angle between these

two lines is then bisected and the point where the bisector meets the load-deformation curve is taken to be the point of failure (Fig.2-14).

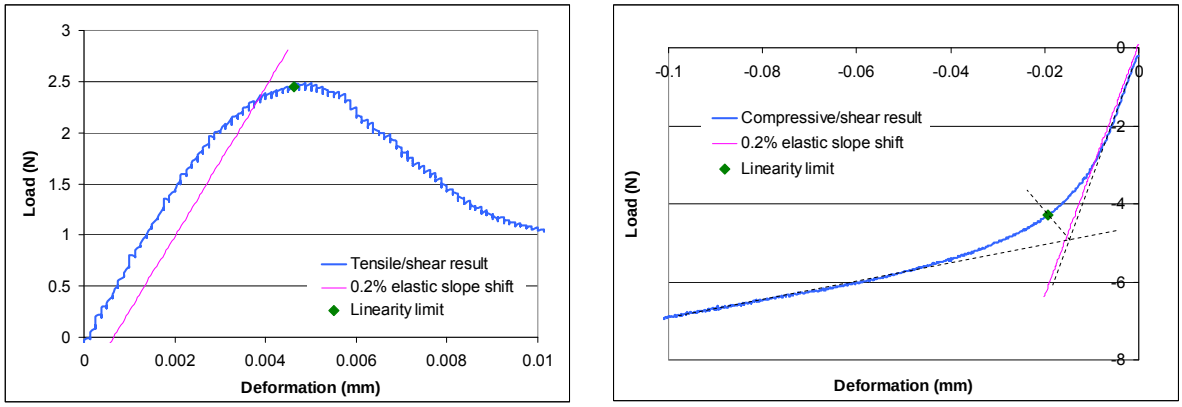

Fig.2-14 Illustration of failure points on tensile and compressive load-deformation curves

From the load-deformation curves in each group of tests, the initial stiffness and load/deformation values at failure were obtained. These are presented in *Appendix A* (Table A-1 and Table A-2). The stiffness corresponding to the linear elastic portion is calculated and the failure load is decomposed into normal (perpendicular) and shear (parallel to inclined surface) components

From the values of the normal and shear components of the failure load, failure force envelopes for a single solder joint were obtained and plotted in Fig.2-15 (a) and (b) for deformation rates of 0.00015mm/s and 0.15mm/s respectively; a comparison between the two envelopes is shown in Fig.2-15 (c). The shapes of the two envelopes are similar; with the failure envelope for a 0.15mm/s deformation rate being slightly larger. However, the difference in the tensile region is less obvious.

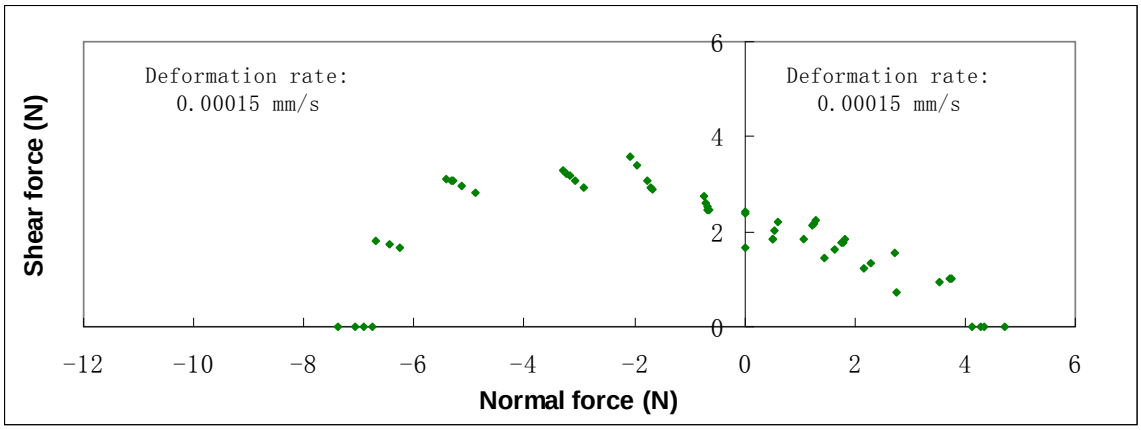

(a)

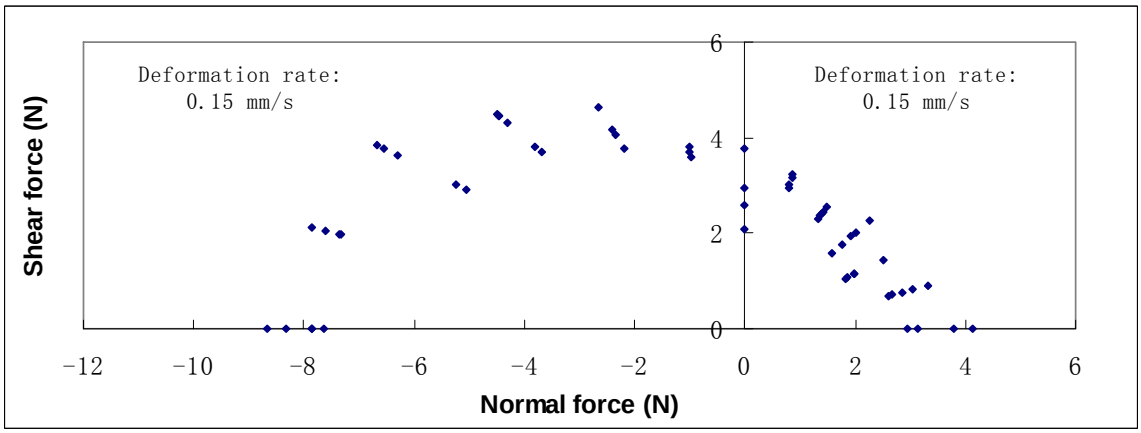

(b)

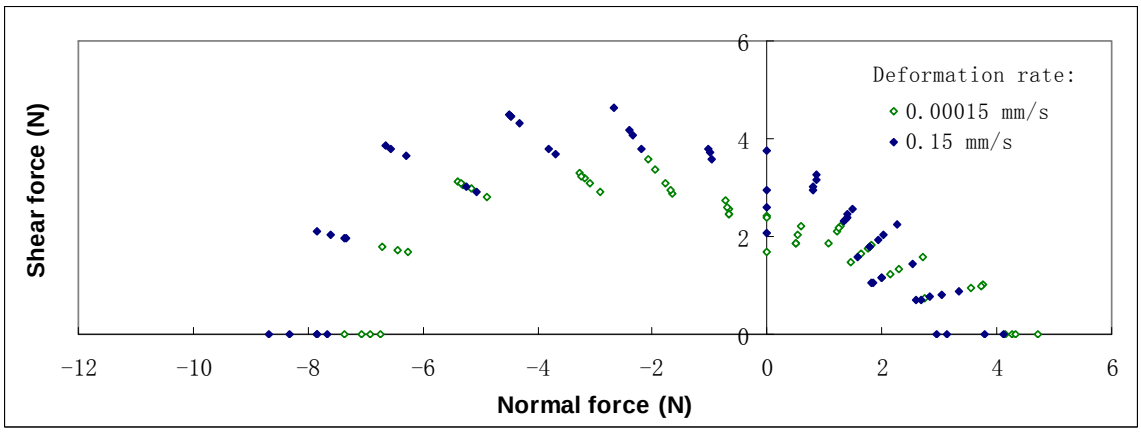

(c)

Fig.2-15 Failure force envelopes for a solder joint at deformation rates of 0.00015mm/s and 0.15mm/s.

Quasi-static tests on single solder joint specimens were undertaken, and load-deformation curves at two deformation rates obtained experimentally for

different loading angles. Data scatter can be seen in the load-deformation responses (Fig.2-12 and Fig.2-13) as well as the failure force envelopes (Fig.2-15). This scatter arises from structural complexity of a solder joint specimen, compared to a solder alloy specimen with a uniform geometry. The bond strength of a solder joint depends on many factors - the adhesion strength among components such as the solder bump, copper pads and BT substrates, as well as the material micro structure and actual solder bump profile.

For example, voids in solder joints have been considered as a defect in electronic assembly. Mechanical cyclic torsion and thermal cycling (-40^0C/125^0C) of IC assemblies have shown that voids in solder joints reduce their life, depending on void size, frequency and location (Fig.2-16). Yunus et al. (2003) reported that, “The factors that affect void formation are complex and involve the interaction of many factors. There are no established standards for void size and void area in a solder joint for it to be deemed defective. Inspection criteria have been very subjective. The effect of voids on the reliability of solder joint may depend not only on the size, but also on frequency and location”.

Wang and Panton (2005) undertook experimental research on the formation of void bubbles within molten solder bumps in flip chip connections and showed that heat flux direction plays a significant role in the formation and distribution of void bubbles in molten solder. From their experimental study of void formation in eutectic (Sn63Pb37) and lead-free (Sn3.5Ag0.75Cu) solder

bumps in flip-chip assemblies, Wang and Panton (2006) also found that eutectic solder has a slightly smaller void volume and percentage of defective bumps compared to lead-free solder.

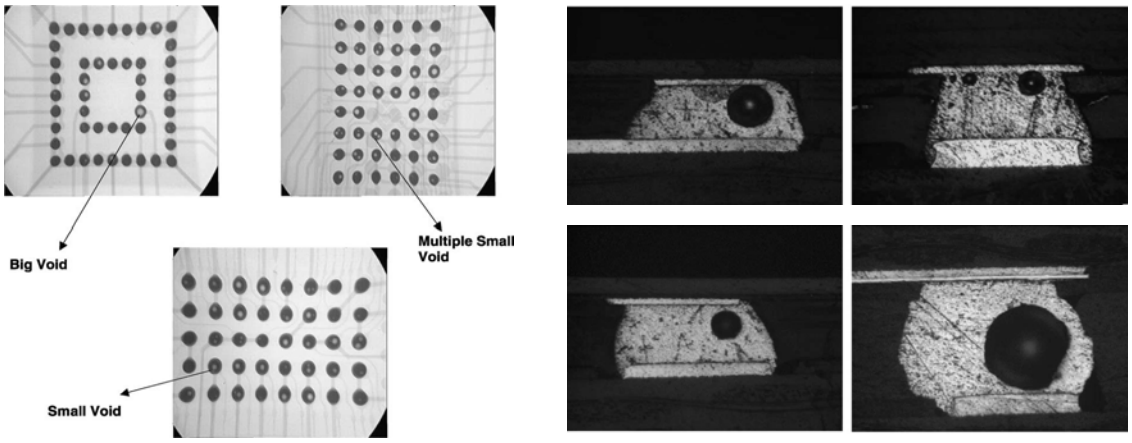

Fig.2-16 (a) X-ray images of solder joints with no voids, small voids, multiple small voids and big voids, (b) cross sectional images of solder joints with voids. (Yunus, et al. 2003)

Factors such as circuit board warpage, component warpage and solder volume variation also affect the shape of solder joints in IC packages. Rayasam (2006) measured that when the volume of eutectic solder joint in a row is 0.232 mm^3, 0.134 mm^3 and 0.368mm^3, the solder joint heights are 0.294mm, 0.360mm and 0.443mm (Fig.2-17). Rayasam and Subbarayan (2006) also proposed a solder joint shape prediction model that can handle inclination and misalignment of the upper pad of the solder joint relative to the lower pad when warped substrates are used.

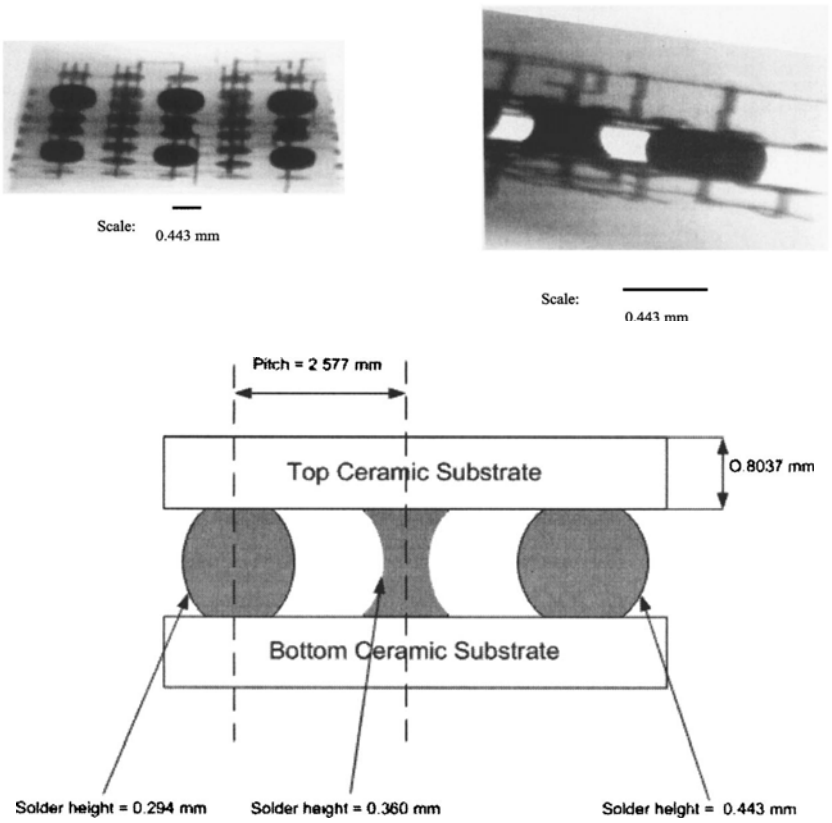

Fig.2-17 X-ray images of solder joint shapes and schematic diagram based on experimentally measured solder heights (Rayasam, 2006)

CHAPTER 3 DYNAMIC TEST METHODOLOGY AND RESULTS

3.1 Introduction

Experimental measurements of the force-displacement or stress-strain responses of specimens are necessary for characterizing the mechanical properties of a material, and to formulate constitutive relationships to serve as inputs to FEM modeling. Appropriate equipment is needed for accurate data measurements at different loading speeds. The response of a specimen subjected to quasi-static loading can be determined using a universal testing machine; inertial and wave propagation effects in specimens or the testing device need not be considered. In contrast, the testing of a specimen under impact or dynamic loading is generally based on stress wave concepts; for example, the commonly used split Hopkinson bar system was founded on one-dimensional wave theory (e.g., Kolsky, 1949; Ogawa, 1984; Li, et al., 1993; Bragov and Lomunov, 1995).

A split Hopkinson bar system comprises a cylindrical striker and two straight slender bars that are supported such that they are coaxial so that one-dimensional wave propagation in the bars can be assumed. The specimen is sandwiched between the two bars and usually has size similar or comparable to the bar diameter. However, there are small specimens such as solder joints in IC packages that have aroused interest in understanding their dynamic

mechanical behavior (e.g., Siviour et al., 2005; Tan et al., 2005; Lai et al., 2006; Lai and Yeh, 2006; Luan et al., 2007). The specimens in this study are single solder joint specimens, which belong to this category, as they measure only about 0.43mm in diameter, posing potential difficulties in dynamic testing. Even if thin bars (ϕ5mm) are employed, their cross-sectional area is still significantly larger than that of a solder joint. Testing of bulk solder alloy specimens is easier, as such specimens can be made large enough to fit the split Hopkinson bar system used. However, the stress-strain curves obtained cannot be used to describe the mechanical response of a solder joint. As highlighted earlier, a solder joint is a complex structure and its mechanical properties are determined by many factors such as the properties of the solder bump, copper pad, substrate and intermetallic compound (IMC), as well as the strengths of the interconnections between these components. Therefore, dynamic testing of actual single solder joint specimens is necessary to obtain their force-deformation responses.

In this Chapter, a detailed analysis is undertaken to evaluate the dynamic testing of a small specimen (the size of a solder joint) by a split Hopkinson bar system. FEM simulations using ABAQUS are carried out to verify the assumption of one-dimensional wave propagation and the validity of the stress-strain curve derived from strain readings corresponding to the mid-points of the bars (simulatively the strain gauge signals recorded in an actual test is examined). Subsequently, new method for impact testing is proposed; this involves the fabrication of a portable miniature impact tester for testing single solder joint specimens in tension or compression. The relevant

equations for calculating the force-deformation response of a specimen are derived. FEM modeling and experiments are also undertaken to evaluate the validity of dynamic test results obtained using this miniature tester. Finally, the dynamic force-deformation responses of a single solder joint specimen are analyzed, based on dynamic tests at two loading speeds.

3.2 Issues in effective use of split Hopkinson bar for small specimens

The split Hopkinson bar system is commonly used for determining the dynamic stress-strain properties of a material. It is based on one-dimensional wave analysis, and the overall loading history and deformation rate experienced by the specimen can often be obtained with reasonable accuracy. A typical split Hopkinson bar system is illustrated in Fig.3-1; it comprises two long cylindrical bars – an input bar and an output bar. Another shorter striker bar, propelled by compressed air, impinges on the input bar, generating an incident wave defined by the strain $\varepsilon_i(x,t)$ in the input bar. The incident wave propagates along the input bar to the interface with the specimen. Part of the incident wave is reflected back into input bar; this is defined by $\varepsilon_r(x,t)$, while part of it transmits through the specimen into the output bar as $\varepsilon_t(x,t)$. The stress and velocity at the interface x_1 of the input bar can be derived from algebraic summation of $\varepsilon_i(x_1,t)$ and $\varepsilon_r(x_1,t)$ at x_1,

$$\sigma(x_1,t) = \left[\sigma_i(x_1,t) + \sigma_r(x_1,t)\right] = E_0\left[\varepsilon_i(x_1,t) + \varepsilon_r(x_1,t)\right] \qquad (3\text{-}1)$$

$$v(x_1,t) = v_i(x_1,t) + v_r(x_1,t) = C_0[\varepsilon_i(x_1,t) - \varepsilon_r(x_1,t)] \quad (3\text{-}2)$$

The stress or velocity at the interface x_2 of the output bar is derived from the transmitted wave $\varepsilon_t(x_2,t)$.

$$\sigma(x_2,t) = \sigma_t(x_2,t) = E_0\varepsilon_t(x_2,t) \quad (3\text{-}3)$$

$$v(x_2,t) = v_t(x_2,t) = C_0\varepsilon_t(x_2,t) \quad (3\text{-}4)$$

where E_0 and C_0 are the elastic modulus and wave velocity of the bar respectively. The loading history of the specimen can be determined from Eqs. (3-1) and (3-3) in terms of the bar cross-sectional area A_0, while the deformation history can be obtained from Eqs. (3-2) and (3-4). If the specimen is uniform in cross-section, then the engineering stress-strain response of the specimen can then be derived. In SHB testing, the strain gauge locations are generally at the mid-points of the input/output bars.

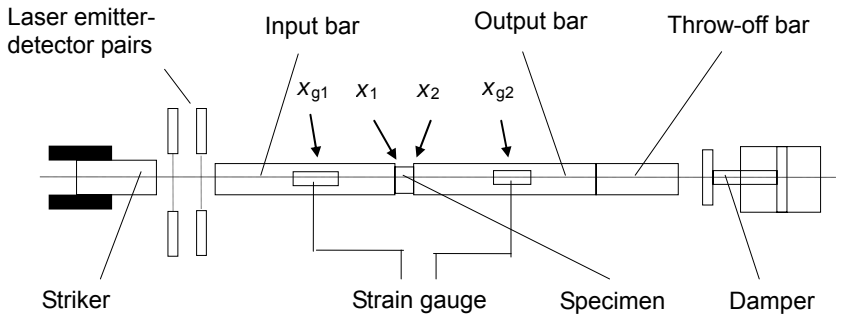

Fig.3-1 Configuration of a traditional split Hopkinson pressure bar system

In Hopkinson bar testing, the diameter of the specimen is often only somewhat slightly smaller than the input/output bar diameter. However, for tests on single solder joint specimens, the solder bump between the substrates is extremely small – less than 0.5mm in diameter – and its cross-

sectional area is only about 1% of that of the input/output bar if 5mm diameter bars are used. The stress at the interface between the solder joint and the input/output bars will be extremely localized. Consequently, the bar-specimen interfaces do not satisfy the assumption of a flat plane during wave transmission. Such contact generates three-dimensional spherical waves in the bars instead of one-dimensional plane waves. Therefore, the accuracy of the results based on one-dimensional wave propagation theory corresponding to Eqs.(3-1)~(3-4), must be investigated. In this study, numerical validation is undertaken using the finite element code ABAQUS-Explicit to simulate dynamic testing of a small specimen the size of the solder bump in a solder joint. The aims of the simulation are to verify: (1) when the stress waves attain an approximate one-dimensional stress state in the bars; (2) whether the waves recorded subsequently can yield the stress-strain properties of the specimen with reasonable accuracy using one-dimensional stress wave theory. As an additional verification, the mechanical response derived from strains associated with the mid-points of the bars, using Eqs.(3-1)~(3-4), are compared to values extracted directly from the specimen. A cylindrical specimen is assumed for the simulations.

As shown in Fig.3-2, the cylindrical specimen in simulations is assigned a diameter and length of 0.42mm. It is subjected to dynamic compression between two 1.2m long steel input bar and output bars. A constant input velocity v_0 is assigned to the input bar interface as the boundary condition (this corresponds to a striker impacting the input bar at $2v_0$). The input velocity is set to correspond to a trapezoidal pulse 200μs in total duration with

a linear rising slope of 10μs to preclude significant oscillation in the input wave arising from wave dispersion. Three cases were simulated in order to study the effect of impact intensity and bar diameter D_0 on the accuracy of the results; the cases are denoted by A (v_0=0.5m/s, D_0=5mm), B (v_0=1.0m/s, D_0=5mm) and C (v_0=1.0m/s, D_0=2.5mm). The specimen is finely meshed and the mesh size in the input/output bars is reduced gradually along the bar axis to about 0.05mm in the vicinity of the interfaces with the specimen. As indicated in Fig.3-2, the outputs at 13 nodes along a radius of the cross-sections of the input/output bar and the specimen were monitored to study the development of equilibrium.

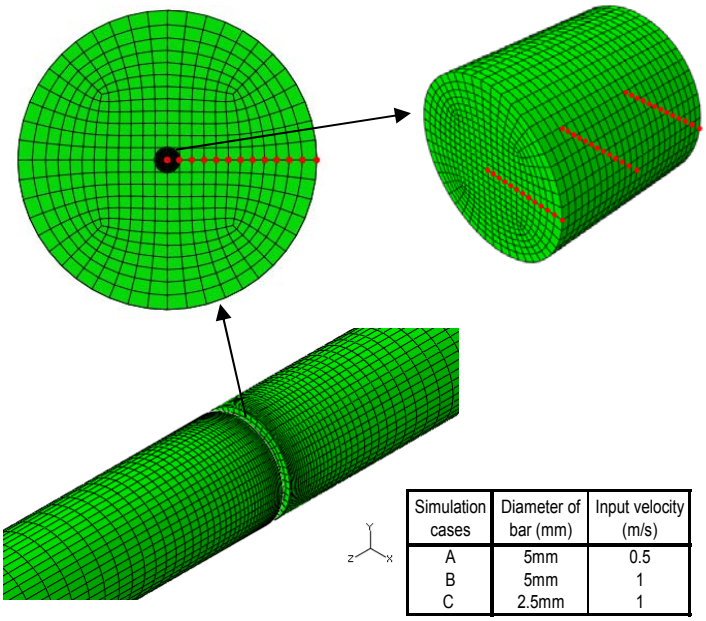

Simulation cases	Diameter of bar (mm)	Input velocity (m/s)
A	5mm	0.5
B	5mm	1
C	2.5mm	1

Fig.3-2 FEM model of dynamic test arrangement

As the objective of the simulations is to validate the testing of small specimens using a Hopkinson bar, a simple bi-linear true stress-strain curve was prescribed for the specimen material properties, as shown in Fig.3-3. The

initial linear and post-yield response, up to 7% true strain, is based on experimental results on Pb-free solder (Sn96.5-Ag3.0-Cu0.5) reported in literature (Siviour, et al. 2005); the curve is subsequently extrapolated to a true strain of 1.0 assuming constant hardening. The true stress-strain response of the specimen, derived from simulations, was also obtained from average values of the longitudinal stress and strain at nodes along the radius of the two end faces, as well as the radius of a cross-section mid-way between them. These are plotted together with the prescribed material properties for all the cases (A, B and C); the maximum point in each of the curves corresponds to the commencement of unloading. The average stress-strain responses extracted directly from the specimen coincides with the prescribed material properties, indicating that numerical processing does not introduce any noticeable spurious effects.

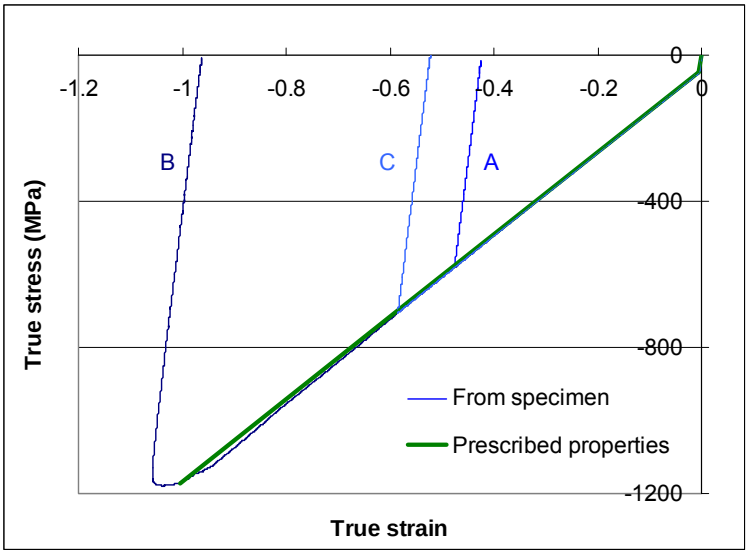

Fig.3-3 Comparison between average true stress-strain responses, exacted directly from the specimen, and specimen material properties prescribed to ABAQUS

As a result of the significant difference in cross-sectional area between the bars and specimen, contact at the bar-specimen interface is localized and somewhat similar to point indentation. This can be clearly seen from plots of the von Mises stress contours associated with the interface regions, as shown in Fig.3-4; these correspond to the instants of yielding and ultimate load on the specimen in simulation B (v_0 =1.0m/s, D_0 =5mm). The contour pattern shows that the regions of direct contact between the specimen and the bars experience much larger stresses than the other regions in the vicinity of the interface, throughout the entire duration of loading. However, this non-uniform stress distribution at the bar interfaces does not extend far. In order to examine when a state of plane wave propagation is established, for one-dimensional stress wave analysis to hold, the strain distribution across the bar cross-section was examined. As the incident stress is partially reflected and partially transmitted at the specimen-bar interfaces, the longitudinal strains at nodes along a radius in successive cross-sections 75mm apart in the input and outputs bars were extracted and examined. Fig.3-5 shows the true longitudinal strain histories extracted from 13 nodes on each radius of the cross sections – two at the bar/specimen interfaces and two 75mm away. The diagrams show that the longitudinal strain at the two interfaces are identical and exhibit a large variation in amplitude from the central axis to the outer radius. This is because only 1% of the bar surface was in contact with the specimen and this area exhibits very large compressive strains. Also shown are results for positions 75mm away from the interfaces; there are actually 13 curves in each graph, but they essentially coincide with one another, demonstrating that the longitudinal strain distribution across the bar cross-

section becomes uniform at these locations. Distributions of longitudinal strain at other cross-sections farther away were also examined and uniformity of longitudinal strain in cross-sections was maintained. Therefore, the conclusion is that the stress state in the bars becomes approximately one-dimensional 75mm from the specimen-bar interfaces in this case.

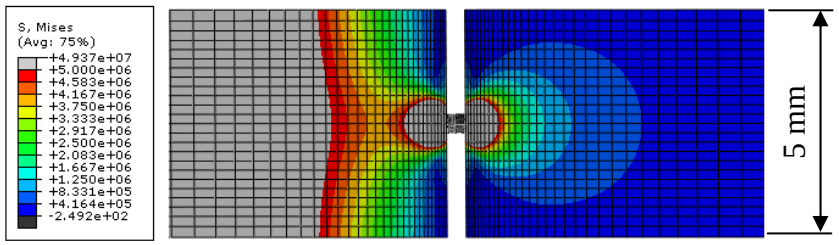

(a)

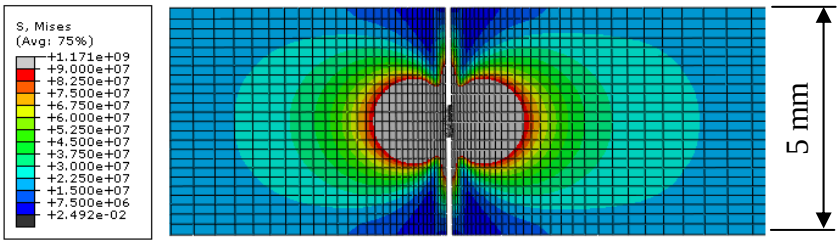

(b)

Fig.3-4 von Mises stress distribution in vicinity of bar-specimen interface at (a) the instant of yielding and (b) point of ultimate stress of the specimen (input velocity 1m/s, bar diameter 5mm)

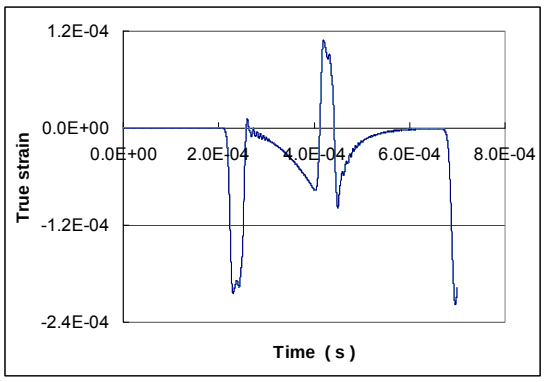

(a) Strain at input bar cross section 75mm away from interface x_1

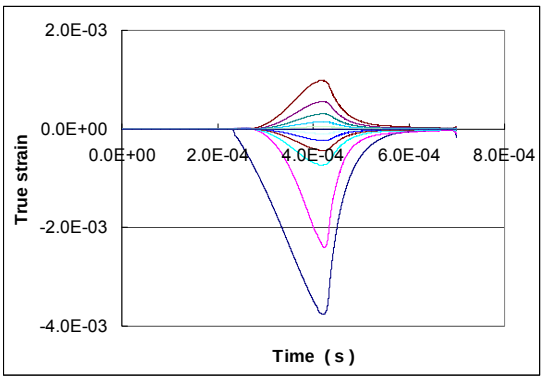

(b) Strain at interface x_1 of input bar

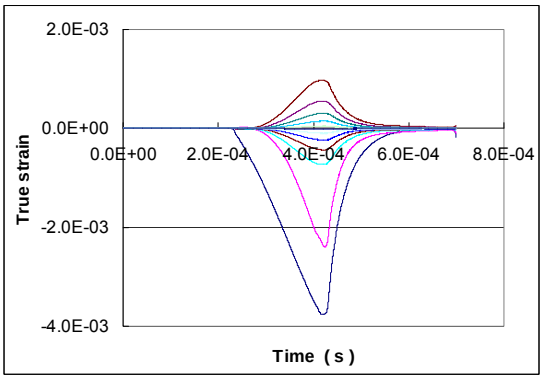

(c) Strain at interface x_2 of output bar

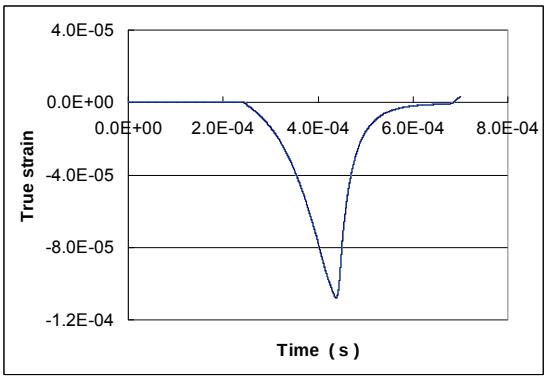

(d) Strain at output bar cross section 75mm away from interface x_2

Fig.3-5 Strain histories extracted from 13 nodes on a radius of the bar cross-section

The preceding analysis has established that the reflected and transmitted waves undergo transition from a three-dimensional to a one-dimensional state as they propagate from the specimen-bar interfaces. The validity of obtaining the stress-strain properties of a small specimen from strain signals recorded

after stress uniformity across the bar cross-section is achieved is now examined via a simulation approach. Fig.3-6 (case B: input velocity 1m/s, bar diameter 5mm) shows simulation results for the incident, reflected and transmitted strain waves, defined by the axial strain associated with the surface node at the mid-point of the bars (x_{g1} and x_{g2}) – indicative of a Hopkinson bar test. There are slight oscillations in the input wave, which indicates some dispersion as the wave travels along the bar. From the three strain waves ($\varepsilon_i(x_{g1},t)$, $\varepsilon_r(x_{g1},t)$ and $\varepsilon_t(x_{g2},t)$), the load on and deformation of the specimen can be derived using Eqs.(3-1)~(3-4). In an actual Hopkinson-bar test, it is usually assumed that the forces on the two ends of a specimen are identical, leading to the relationship $\varepsilon_i(x_{g1},t)+\varepsilon_r(x_{g1},t)=\varepsilon_t(x_{g2},t)$ and eliminating the need to employ the reflected wave $\varepsilon_r(x_{g1},t)$. However, whether this assumption still holds for small specimens is now examined based on the three waves ($\varepsilon_i(x_{g1},t)$, $\varepsilon_r(x_{g1},t)$ and $\varepsilon_t(x_{g2},t)$) generated by FEM simulations. Fig.3-6 shows curves of $\varepsilon_i(x_{g1},t)+\varepsilon_r(x_{g1},t)$ and $\varepsilon_t(x_{g2},t)$; a comparison reveals that they are almost identical, except that the curve $\varepsilon_i(x_{g1},t)+\varepsilon_r(x_{g1},t)$ contains some small oscillations arising from superposition of the incident and reflected waves. Therefore, the use of two waves instead of three in Hopkinson-bar calculations, as defined by Eqs. (3-5) and (3-6) (a positive value indicates tension while a negative value signifies compression) is still applicable for the testing of small specimens.

$$D(t)=\int_0^t[v(x_1,t)-v(x_2,t)]dt=2C_0\int_0^t[\varepsilon_i(x_{g1},t)-\varepsilon_t(x_{g2},t)]dt \qquad (3\text{-}5)$$

$$F(t)=A_0\cdot[\sigma(x_1,t)+\sigma(x_2,t)]/2=E_0\cdot\varepsilon_t(x_{g2},t) \qquad (3\text{-}6)$$

The specimen deformation $D(t)$ is derived from $\varepsilon_i(x_{g1},t)$ and $\varepsilon_t(x_{g2},t)$, and the axial load $F(t)$ from $\varepsilon_t(x_{g2},t)$; this precludes oscillations in the force profile by excluding $\varepsilon_r(x_{g1},t)$ from the calculations.

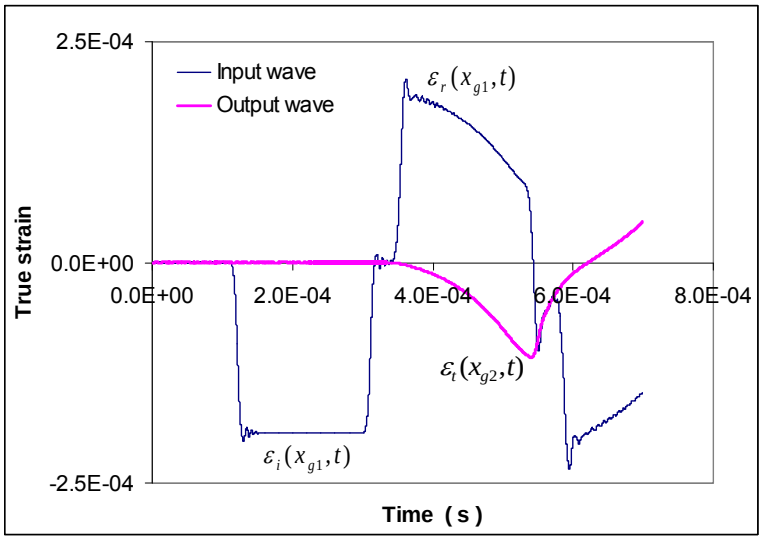

(a)

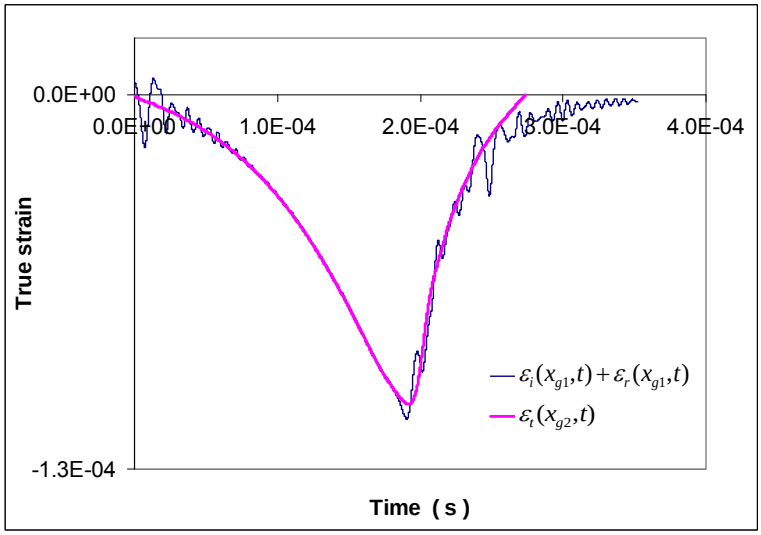

(b)

Fig.3-6 (a) Incident, reflected and transmitted strain histories at mid-points of input and output bars (i.e. strain gauge positions); (b) comparison between summation of incident and reflected waves with transmitted wave

Fig.3-7 shows the engineering stress-strain responses of the specimen derived from simulations for cases A, B and C using Eqs.(3-5)~(3-6), factoring in the specimen initial cross-sectional area and length. For comparison, the average engineering stress-strain responses of the specimen are also plotted (these are derived from the true stress-strain curves in Fig.3-3). The stress-strain curves, up to 10% engineering strain, shows the initial portion of the responses; small differences around the yield point are present in the results derived calculated using Eqs.(3-5)~(3-6), because of wave dispersion. For input/output bars of the same diameter but subjected to different input pulse velocities (cases A and B), the stress and strain values around the yield point differ somewhat, but the trend is similar; this illustrates that the magnitude of the input pulse does not affect the overall results (i.e. wave dispersion effects and stress equilibrium in the specimen). For bars with different diameters but subjected to a common input pulse (cases B and C), the resulting curves are actually identical, even their fluctuations; this indicates that when the stress attains uniformity across the bar cross-section, a decrease in bar diameter from 5mm to 2.5mm does not improve the results. Finally, the plots clearly show that soon after the yield point, the stress-strain curves derived from one-dimensional wave theory match the average engineering stress-strain curve based on nodal values from the specimen. This correlation continues up to about 30% strain, after which some divergence between the values obtained directly from the specimen and that calculated from one-dimensional wave theory become evident, as shown in the extended stress-strain plots (the reason for this is not obvious). As the average stress-strain responses extracted directly from the specimen still coincide with the prescribed material

properties (Fig.3-3), numerical processing does not seem to be the cause of the discrepancy, although there may be possible small errors accumulated from integration of the data to obtain strain values from the incident and transmitted waves. Another possible reason is wave dispersion in the bars. The waves described by Eqs.(3-1)~(3-4) refer to the bar-specimen interfaces at x_1 and x_2 (Fig.3-1); however, the incident and reflected waves at interface x_1 cannot be separated in practice, so signals recorded by the strain gauges at locations x_{g1} and x_{g2} are employed in calculations, based on the assumption that the stress waves maintain their profiles during propagation. Wave dispersion could therefore affect this assumption and generate cumulative errors. As shown in Fig.3-7, the stress-strain curves derived from one-dimensional wave theory (using strain values corresponding to the mid-point of the bars) for cases A, B and C, follow the same trend, except that the final compression is different. These responses are compared with the stress-strain values extracted directly from the specimen, and similarity is observed. This again demonstrates that the intensity of the input pulse and the bar diameter do not have a significant effect on the simulation results for the current test arrangement.

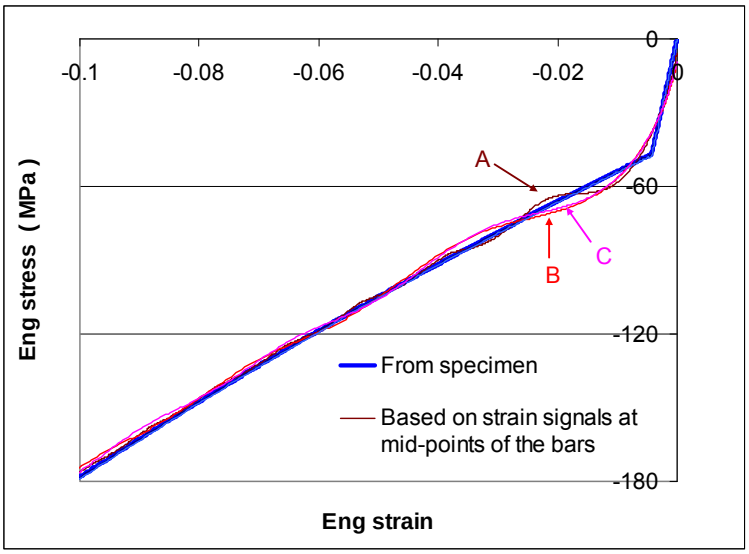

(a)

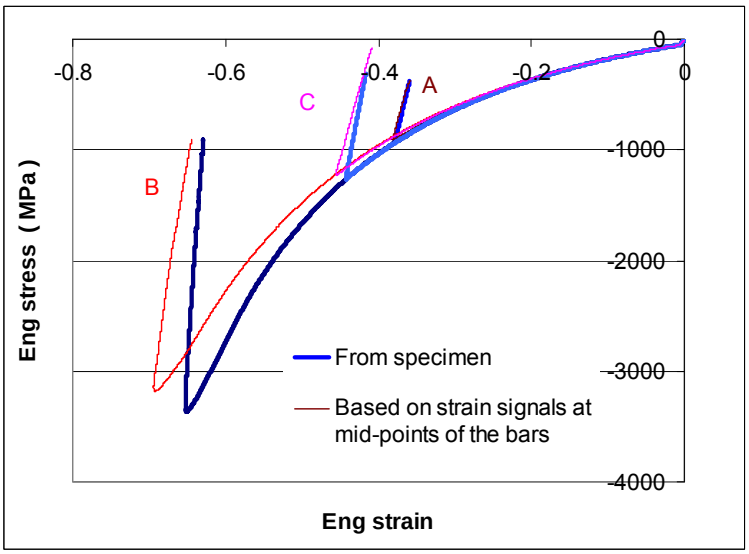

(b)

Fig.3-7 FEM results of engineering stress-strain responses, extracted directly from the specimen and comparison with calculations using strain values corresponding to the mid-point of the input/output bars, for three cases. (a) initial responses; (b) complete responses.

The simulations demonstrate the feasibility of using 5mm diameter steel input/output bars for dynamic testing of solder specimens 0.42mm in size, and to obtain acceptable results for a reasonable range of final engineering strains, based on the assumption of one-dimensional wave propagation. In actual dynamic tests, the failure force for small single solder joints is in the

order of only a few Newtons. Hence, the stress transmitted to the output bar is too small to be recorded by common foil strain gauges because of inherent background electrical noise levels. The use of copper and aluminum input/output bar systems has been explored, because their lower elastic modulus results in discernible strains even when the force in the bars is small. However, thin bars made of such materials are not physically robust, as bending of the input bar at the impacted end was observed after several tests. Therefore, 5mm diameter steel bars were finally adopted and highly sensitive semiconductor gauges employed to measure the transmitted strain in the output bar.

Before conducting tests on single solder joint specimens, an experimental examination of the effectiveness of applying the Hopkinson-bar technique to testing small specimens was undertaken. As actual solder joint specimens are not identical and it is extremely difficult to prepare cylindrical specimens less than 0.5mm in size, solder balls were therefore employed to identify rate sensitivity and verify test repeatability. Commercially eutectic solder ball specimens 0.24mm in diameter were obtained and microscopic observation showed that their profiles are consistently approximately spherical, as shown in Fig.3-8a. It was therefore assumed that these specimens should also exhibit consistent load-deformation responses. This was confirmed by quasi-static tests using an Instron micro-tester, where the load-deformation curves from multiple tests coincided with each other. Repeated dynamic tests on spherical solder ball specimens were carried out at two striker velocities, resulting in two specimen deformation rates (1m/s and 2.7m/s). The incident

wave was recorded by foil-type strain gauges (gauge factor of 2) and the transmitted wave was recorded by semiconductor gauges (gauge factor of 121). Fig.3-8a depicts actual oscilloscope traces from a test corresponding to a deformation rate of around 1m/s, showing that the transmitted wave signal is relatively free of noise. As the amplitude of the transmitted wave is very small compared to the incident wave, Eqs. (3-5) implies that the deformation rate experienced by the solder ball should follow the profile of the incident wave, which is approximately constant. The load-deformation curves derived from the strain gauge signals are relatively consistent, and Fig.3-8b shows that strain rate sensitivity is not significant between these two deformation rates. Although the scatter for the dynamic test results is larger compared to that for the quasi-static tests, the results are generally repeatable and accurate. Rate sensitivity of the solder specimens is evident, as a higher strength is observed for dynamic compression.

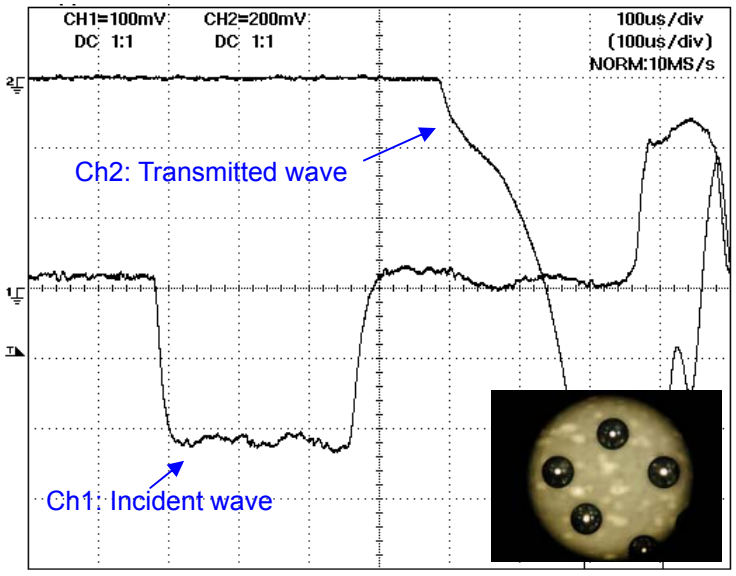

(a)

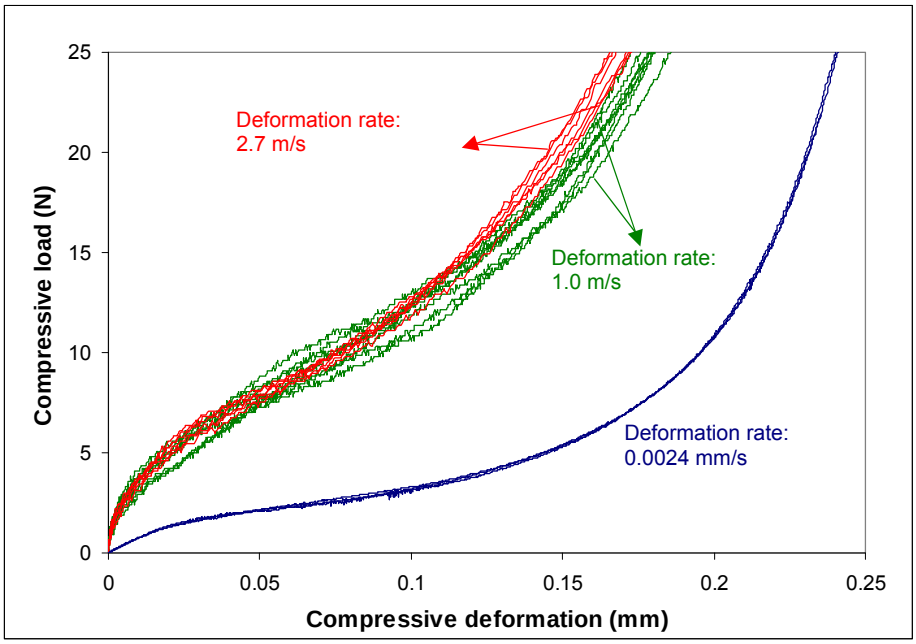

(b)

Fig.3-8 (a) Incident and transmitted strain (voltage) signals from typical Hopkinson bar test, together with microscopic image of 0.24mm diameter spherical eutectic solder balls; (b) quasi-static and dynamic compressive load-deformation curves derived from Instron micro-tester and Split Hopkinson bar.

The simulation undertaken has verified the assumption of one-dimensional wave propagation in split Hopkinson bar system for tests of small specimens, and demonstrates numerically that it is capable of producing acceptable results. However, as a solder joint is very small (0.2~ 0.5mm in diameter), tests using a Hopkinson bar system may encounter some difficulties in practice. For example, the striker, input and output bars cannot be made too thin, otherwise supporting these bars to achieve straightness and good alignment is difficult. In the case where dynamic testing at relatively low strain rates is desired, long bars are required to accommodate a long loading pulse. In addition, for high rate tests, dynamic bending of long slender bars caused by flexural waves can also be a problem.

Arising from the considerations listed, a new dynamic testing device, in the form of a miniature impact tester, was designed and fabricated for dynamic testing of single solder joint specimens. The governing theory of this tester is similar to that of the split Hopkinson bar system, i.e. one-dimensional wave propagation. However, the configuration of the miniature impact tester differs from that of a split Hopkinson bar system, in order to mitigate difficulties associated with testing small specimens. The miniature impact tester devised is portable and convenient to set up for tensile or compressive testing.

3.3 Establishment of a miniature impact tester for dynamic testing of small specimens

3.3.1 Problems associated with specimen deformation using direct impact

From a review of literature, it is noted that some devices used for dynamic tests on solder joint specimens employ load cells (e.g., Gonzalez, et al. 2004; Chen and Chiang, 2003). However, the loading rate is limited because of the frequency response of such devices (Yeh, et al. 2007). To overcome this limitation, a method is to replace the load cell by a solid cylindrical bar bonded with strain gauges. A schematic drawing is illustrated in Fig.3-9, which shows a direct impact approach for compression or tension. A striker that impacts a specimen directly corresponds to a compression test, while impacting against an impact plate generates tension in the specimen which is connected with the impact plate.

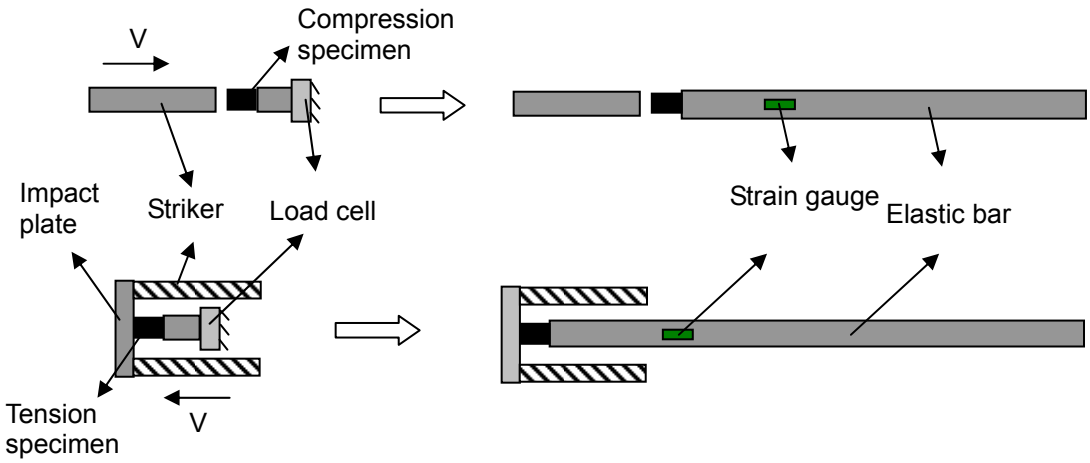

Fig.3-9 Replacement of load cell by an elastic bar to record the loading pulse

The loading history experienced by the specimen can be derived from the strain gauge readings – similar to that for a split Hopkinson bar system. The measurable duration of the loading wave is determined by the length of the bar; a long bar can accommodate a long loading pulse which is required for dynamic tests at relatively low strain-rates. The overall average deformation of a specimen can be calculated from the speeds of the two contact interfaces between the specimen and the bar/plate; one is equal to the speed of the striker/plate, while the other can be derived from the strain gauge readings. Obviously, accuracy of the deformation history derived will depend on accurate measurement of the striker/plate speed.

In this direct impact mode, the initial velocity of a striker (just before impact commences) is used to calculate the deformation history; however, this may not be accurate for a compliant specimen. To demonstrate this, a tensile test was performed whereby a 570 gram steel striker was propelled to impact a 40 gram steel impact plate at a speed of 2.69m/s (no specimen was mounted). A

high speed camera was used to capture the impact between the striker and the impact plate at a framing rate of 10000fps (Fig.3-10). It shows that soon after the striker makes contact with the plate, the plate separates and moves away from the striker at a higher speed. From the images, there appears to be no discernible separation between the striker and the plate within the initial 100μs after commencement of impact. However, separation is obvious at around 300μs. From careful examination of the images, it was observed that the separation gap is about 0.96mm at 700μs, and about 2.4mm at 2000μs. The residual speeds after separation were measured and found to be 2.25m/s for the striker and 3.44m/s for the plate. This can be explained from the law of conversation of momentum of the striker and the plate, from which the residual speed is 2.33m/s for the striker and 5.02m/s for the impact plate. The small discrepancy is acceptable, as friction was not taken into account in the calculations.

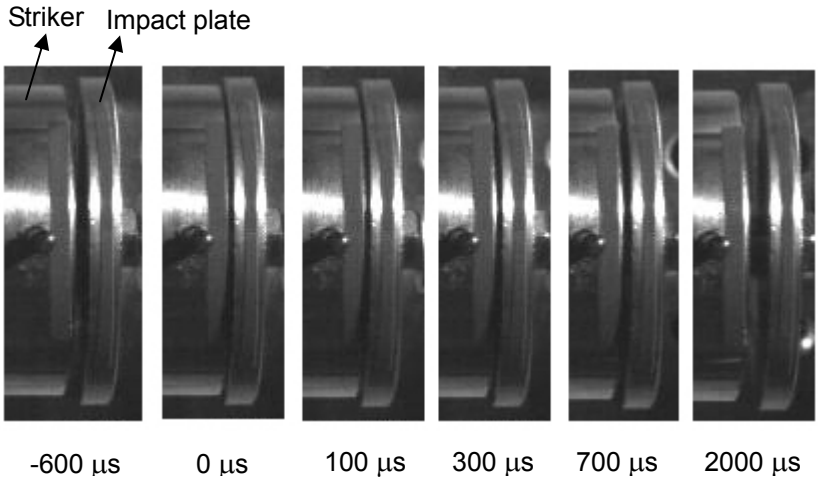

Fig.3-10 High speed camera footage at 10000 fps showing impact between the striker and the impact plate

This phenomenon reveals that when a striker impinges an impact plate

instead the specimen directly, the speed of the specimen-plate interface is different from the initial speed of striker and varies according to the compliance of the specimen. Hence, this configuration involving an impact plate is not suitable for dynamic tensile tests; it is also unsuitable for tests where the deformation history of a specimen needs to be measured accurately.

A solder joint specimen is very small and experiences brittle fracture under tension. This requires the test equipment to have a high sensitivity and frequency response to capture short loading pulses as well as small deformations. Therefore, in this study, a miniature impact tester is proposed. It is capable of both compressive and tensile testing, and the deformation or strain history is derived from the wave signals recorded by strain gauges, instead of the velocity of the striker. The configuration of this tester is somewhat different from a conventional split Hopkinson bar system. It contributes an alternative approach to impact testing and has some special features that make it convenient for extension to an ultra long-thin bar system for testing very small specimens.

3.3.2 Principles governing the miniature impact tester

In a split Hopkinson bar system, a specimen is mounted between an input and an output bar. A striker impacts the other end of the input bar and generates a loading wave which travels along the entire input bar before loading the

specimen. Similarly, the miniature impact tester also comprises an input and an output bar with a specimen sandwiched between them. However, as shown in Fig.3-11, an impact plate is connected to the end of the input bar; a hollow striker is propelled to impinge the impact plate.

With this configuration, two loading waves are initiated at the impact plate and propagate in opposite directions along the two bars. Therefore, the strain gauges on the bars can be mounted close to the specimen once the stress in the bar cross section becomes uniform, because only the input and output bar waves are used in calculation of the specimen load and deformation. Compared to a conventional split Hopkinson bar system, the short distance between the specimen and the strain gauges decreases the degree of discrepancy between recorded signals and the actual loading pulse applied on the specimen (e.g. by wave dispersion or attenuation, Gong, et al. 1990; Wang, et al. 1994). In a split Hopkinson bar, straightness and alignment between the striker and the bars is a strict requirement. However, with the miniature impact tester, waves that propagate away from the strain gauges are not involved in calculations. This implies that good alignment between the striker and the bars is only strictly required within a small vicinity of the specimen, i.e., between the positions of strain gauges. These characteristics make the miniature impact tester more convenient for use with long and thin bars. Another advantage of this tester is that it can induce both compression and tension via a simple rearrangement of the impact plate; i.e. by detaching the impact plate from input bar and connecting it to the output bar, a compressive mode is converted to a tensile one, as shown in Fig.3-11.

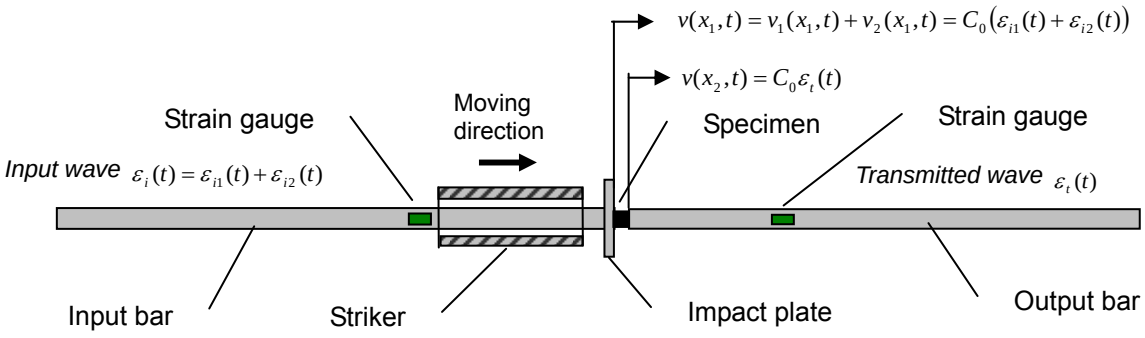

(a)

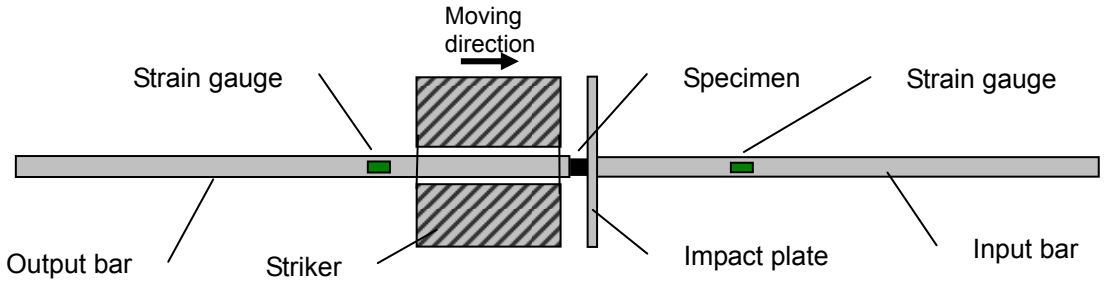

(b)

Fig.3-11 Arrangement of miniature impact tester for (a) compression and (b) tensile tests

A conventional split Hopkinson bar system is based on one-dimensional wave theory and assumes equilibrium of stress in the specimen, thus making it possible to employ only the incident and transmitted waves to calculate the strain, stress and strain-rate history of the specimen. These principles are also adopted for the miniature impact tester. The governing equations for this tester are derived with reference to the schematic diagrams in Fig.3-11a for a compression configuration. Denoting the speeds of the specimen-bar interfaces at position x_1 and x_2 as $v(x_1,t)$ and $v(x_2,t)$, the average strain rate of a specimen with initial length L_s is,

$$\dot{\varepsilon}_s(t) = \big(v(x_2,t) - v(x_1,t)\big)/L_s \qquad (3\text{-}7)$$

where $v(x_2,t)$ corresponds to the transmitted strain signal $\varepsilon_t(t)$ recorded by the strain gauges on the output bar,

$$v(x_2,t) = C_0\varepsilon_t(t) \tag{3-8}$$

where C_0 is the elastic wave velocity in the bars. The particle velocity $v(x_1,t)$ on the input bar-specimen interface is the resultant of two components ($v(x_1,t) = v_1(x_1,t) + v_2(x_1,t)$) corresponding to two sources, i.e. the impact of striker on the impact plate and the resistance of the specimen. When the striker makes contact with the impact plate (without taking into account the resistance of the specimen), it causes the plate to attain a common particle velocity $v_1(x_1,t)$. $v_1(x_1,t)$ corresponds to the tensile wave traveling towards the free end of the input bar, and is recorded by the strain gauge which yields the signal $\varepsilon_{i1}(t)$. On the other hand, resistance from the specimen is generated when compression commences. This induces the particle velocity $v_2(x_1,t)$ at the interface with the impact plate, and this corresponds to a compressive pulse propagating in the same direction as $\varepsilon_{i1}(t)$. The wave is defined as $\varepsilon_{i2}(t)$ and is also recorded by the strain gauge on the input bar. Thus, the input wave $\varepsilon_i(t)$ recorded by the strain gauge on the input bar is actually a superposition of the two pulses, i.e. $\varepsilon_i(t) = \varepsilon_{i1}(t) + \varepsilon_{i2}(t)$. As the impact plate is thin and positioned at the input bar–specimen interface, it is acceptable to make the assumption that $v_1(x_1,t)$ and $v_2(x_1,t)$ are generated simultaneously at the interface. Therefore, the velocity $v(x_1,t)$ at the input bar-specimen interface is obtained from the superposition of these two waves:

$$v(x_1,t) = v_1(x_1,t) + v_2(x_1,t) = C_0\left[\varepsilon_{i1}(t) + \varepsilon_{i2}(t)\right] = C_0\varepsilon_i(t) \tag{3-9}$$

By substituting Eq.(3-8) and Eq.(3-9) into Eq.(3-7), the average strain rate in the specimen can be obtained, and thus the corresponding average specimen strain is derived from integration of the strain rate.

$$\dot{\varepsilon}_s(t) = \big(v(x_2,t) - v(x_1,t)\big)/L_0 = C_0\big(\varepsilon_t(t) + \varepsilon_i(t)\big)/L_s \qquad (3\text{-}10)$$

Since it is difficult to separate $\varepsilon_{i2}(t)$ from $\varepsilon_{i1}(t)$, the force at the input bar-specimen interface (= $A_0 E_0 \varepsilon_{i2}(t)$, where A_0 is the bar cross sectional area) cannot be obtained. This is not a problem, since stress equilibrium in the specimen is assumed. Thus, the average stress history $\sigma_s(t)$ experienced by the specimen with cross sectional area A_s can be obtained solely from the transmitted wave $\varepsilon_t(t)$,

$$\sigma_s(t) = \frac{A_0}{A_s} E_0 \varepsilon_t(t) \qquad (3\text{-}11)$$

If the material and cross sectional area of the striker are same as that of the input bar, then the component of the input wave $v_1(x_1,t)$ should correspond to a rectangular profile with a length twice that of the striker. As a sufficiently long loading duration is necessary to deform the solder joint to the point of failure for loading at relatively low impact speeds (less than 1m/s), another technique is employed for the miniature impact tester - use of a heavy striker. The miniature tester has the advantage that it is convenient to be constructed as an ultra long thin bar system for moderate speed testing, whereby a long loading wave is generated by a short thick heavy striker with a large radius-length ratio made of a dense material, as illustrated in Fig.3-11b.

This technique of employing a heavy striker to impact a light input bar has been used previously to generate an extended input wave, and the wave

profile can be theoretically estimated as described by Shim et al. (2006). In a split Hopkinson bar, the mechanical impedances of the striker and the input bar are usually made equal through similarity in cross-sectional area and material. This results in the striker coming to rest after the stress wave generated upon impact travels to the other end of the striker and back. In contrast, if a thick, heavy tubular striker is used to impact a light, thin input bar, impact of the striker on the input bar and the resulting elastic wave propagation can be described by a Lagrange and force-velocity diagram (Fig.3-12). The integer *n* denotes instants on the time axis that there is a change in the stress and velocity at the striker-bar interface (*n* = 1, 2, 3 …). The sustained loading (corresponding to subsequent reduced striker velocities of V_3, V_5, …) will persist until the interfacial stress reduces to zero. Loading of the input bar would thus comprise several steps of decreasing amplitude, defined by σ_{2n}; i.e. σ_2, σ_4 …, with the duration of each step being twice the time for the wave to traverse the striker length. The amplitude of the load has been calculated by (Shim, 2006) to be:

$$\sigma_{2n} = V_1 \cdot \left(1 - \frac{2Z_i}{Z_i + Z_s}\right)^{n-1} \cdot \frac{Z_i Z_s}{Z_i + Z_s} \qquad (3\text{-}12)$$

where Z_s and Z_i are the mechanical impedance (ρCA) of the striker and the input bar respectively, and V_1 is the initial striker impact velocity. With a heavy striker, an input wave with a duration of a few thousand microseconds can be obtained, something not possible with a traditional Hopkinson bar system unless a striker a few meters long is employed.

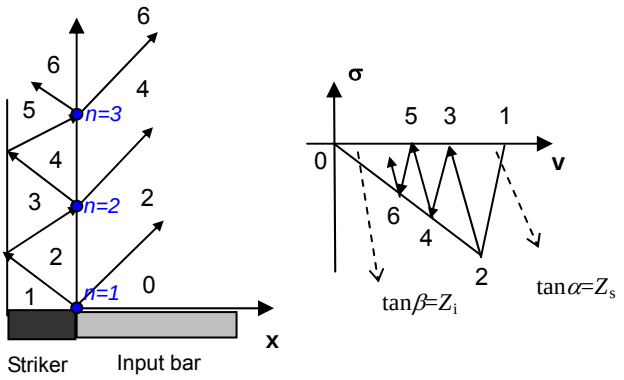

Fig.3-12 Lagrange and force-velocity diagram for impact of a heavy striker on a slender input bar (Shim, 2006).

Two steel strikers of different size were fabricated for the miniature impact tester. The corresponding input waves in elastic bar were predicted based on Eq.(3-12), and illustrated in Fig.3-13. It is seen that the amplitude of input wave generated by the 2.5kg striker is higher than that by 0.5kg striker. Currently a two-meter long input bar is employed in the miniature impact tester – this corresponds to an input wave of about 800μs in duration before superposition with the reflected wave occurs.

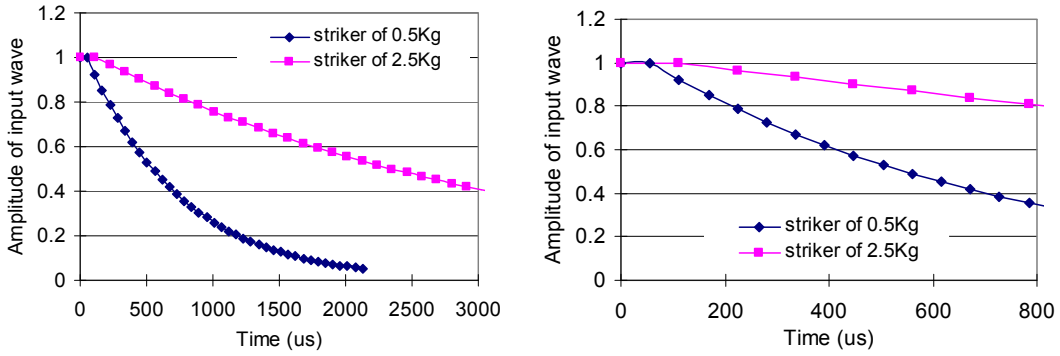

Fig.3-13 Predicted profile of the input wave generated by two heavy strikers of different mass

Fig.3-14 shows pictures of the miniature impact tester designed; detailed

descriptions are presented in *Appendix B*. A series of laser emitter-receiver pairs are sited along the axis of the bar to measure the speed of the striker before impact. The two ends of the input and output bars are supported through two precisely aligned supports, to ensure coaxiality during impact. A linear bearing is incorporated into the end support of the output bar; this minimizes friction with the output bar end to improve test accuracy. Two typical input waves generated by this tester are illustrated in Fig.3-14, for a low and a high speed impact test. The input wave (700μs) was generated by a 28cm long 2.5kg steel striker against a ϕ5mmx2m steel bar; the decrease at the fall of the wave is caused by superposition of the input and reflected waves due to limited input bar length. As the cross sectional area of the striker is much larger than that of the bar, the particle velocity induced in the input bar is close to the value of the striker velocity. This is different from a split Hopkinson bar system, whereby the amplitude of the input wave is approximately half the striker velocity when the bar and striker have same cross sectional area and material. The relatively constant amplitudes of both curves demonstrate the feasibility of imposing a constant deformation speed on solder ball specimens. The relatively smooth signals with little noise also shows that waves generated in the thin bar can be obtained, even for very low striker impact speeds.

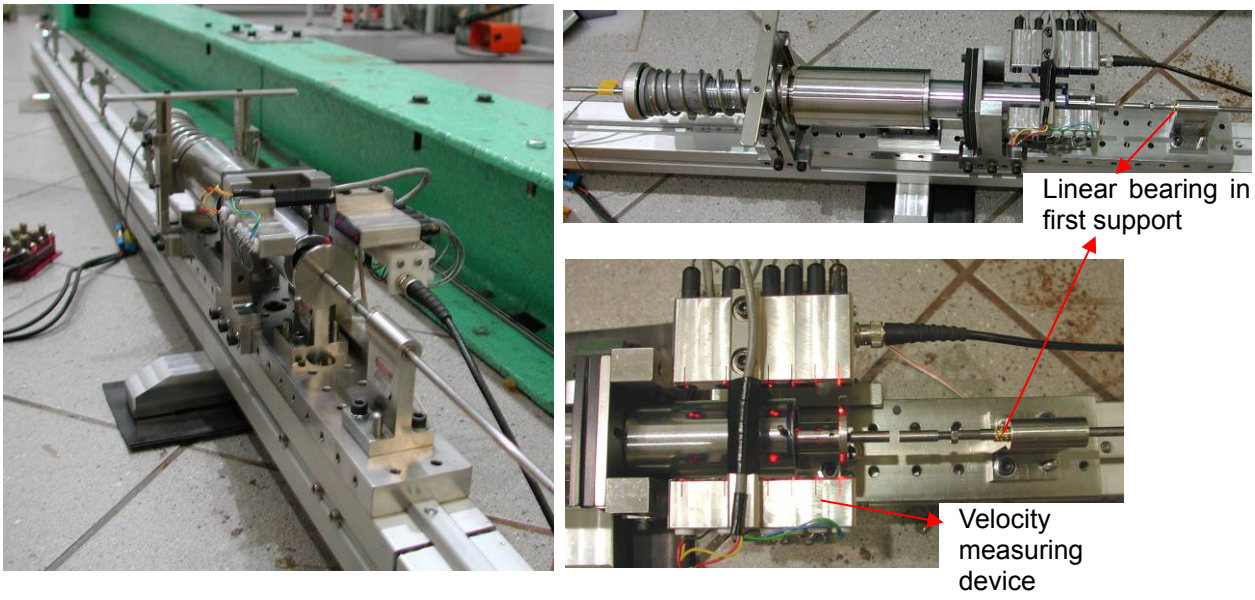

(a)

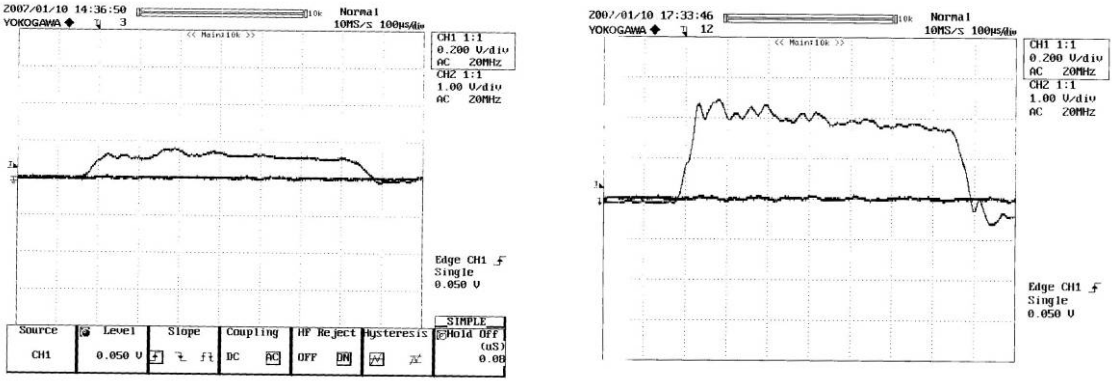

(b)

Fig.3-14 (a) Miniature impact tester and (b) input waves corresponding respectively to low and high speed impact.

3.3.3 Numerical and experimental validation

As a new experimental technique, analysis and validation of the miniature impact tester are necessary to assess its feasibility for dynamic testing, and for its optimal design to produce accurate experimental results. For this tester, the loading wave is generated by the impact of a striker on the plate that is

initially in contact with the specimen. This may cause two immediate concerns about the validity of the test. The first is whether planar contact between the impact plate and the specimen is maintained during testing, as this will affect the uniformity of loading on the specimen. The second is whether the stress wave generated at the bar/specimen interface is uniform across the bar cross section and maintains its profile during propagation. To investigate these issues, an experiment may be not able to elicit sufficient information. Hence numerical modeling using ABAQUS was performed to examine some details.

FEM modeling was carried out to simulate an input steel bar (diameter 5*mm* and length 2*m*) connected to a steel plate (diameter 40*mm* and thickness 5*mm*) that is subjected to an impact. The magnitude of the stress wave in an elastic bar is directly related to the particle velocity $v(t)$ and the bar density ρ_0 and elastic wave speed C_0 (i.e., $\sigma(t) = \rho_0 C_0 v(t)$). A velocity boundary condition comprising a 400μs trapezoidal pulse with a 20μs rising slope to a velocity of 2.5m/s) was imposed on the steel plate to simulate the impact of a striker against it. As shown in Fig.3-15, three configurations (denoted by A, B and C) were studied to investigate how the contact between the striker and the plate affects the profile of the wave generated in the input bar; this will help in the design of an optimal configuration for the impact tester. Configuration A corresponds to application of the velocity boundary condition to the annular area between a radius of 5mm and 10mm on the steel plate; in configuration B the area from a radius 15mm to R20mm is loaded, and configuration C, the radius of the loaded area is between 5mm and 20mm. The specimen and output bar are not composed in the simulation because

they do not influence the two concerns about the validity of the test, as mentioned above. The wave studied in this simulation corresponds to $v_1(x_1,t)$ as denoted by Eq.(3-9).

Fig.3-15 shows the thirteen nodes along a radius of the steel plate studied to examine how deformation of the plate affects contact with the specimen. The first six nodes near the center are 0.5mm from each other and the rest are spaced at intervals of 2.5mm. The respective nodal displacements relative to the center of the plate, as well as the nodal velocities along the bar axis are plotted in Fig.3-16a, Fig.3-16b and Fig.3-16c for contact configurations A, B and C respectively. The relative nodal displacements reflect the profile of the impact plate surface when it is loaded. The positive means in front of the plate surface. In configuration A, the impact region is located close to the ϕ5mm input bar; this induces relatively large vibrations at regions farther away during loading. Consequently, the velocity of the nodes outside the contact zone oscillates significantly, while the velocity of nodes within the contact zone exhibit slight oscillations. Conversely, if impact is applied to the outer region (configuration B), deformation of the plate stabilizes after about 50μs. This can be seen from the relative displacement profiles, where all curves coincide with each other after 50μs. The corresponding velocity profiles show that nodes close to the center display somewhat vibration at the beginning of impact contact, while nodes farther out have a more uniform profile in terms of the velocity history. The most desirable response corresponds to configuration C, where all the relative displacement curves quickly converge and there is less vibration; the profile of the plate remains constant during loading. The velocity

profiles of all nodes on the impact plate are consistent and represented by a trapezoid with a 20μs rising slope, which is similar to the the input boundary condition prescribed to the steel plate. With regard to the flatness of the impact plate during loading, the most important region is within the ϕ5mm circle (diameter of input bar). This is because the cross-sectional area a specimen is required to be less than that of the input bar. From the relative displacement values of the first six nodes in each curve (Fig.3-16), it is found that the maximum unevenness is only 0.251μm for configuration A, 0.436μm for configuration B and 0.266μm for configuration C. These small values should have negligible effects on the test results.

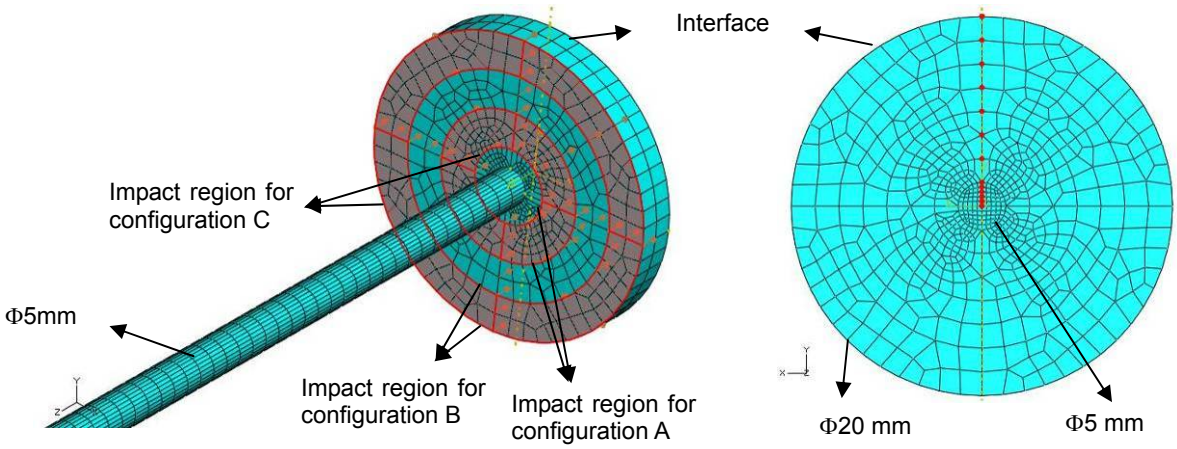

Fig.3-15 Three impact contact areas in numerical simulations

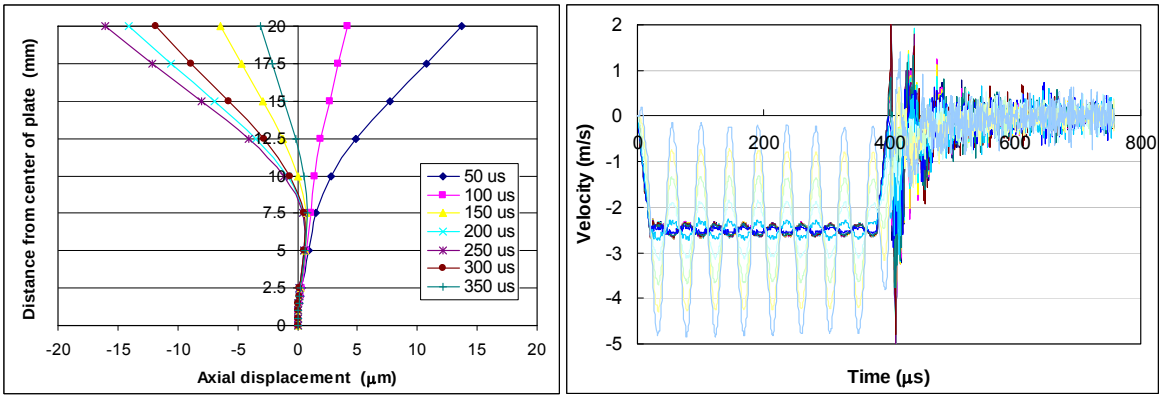

(a) Configuration A

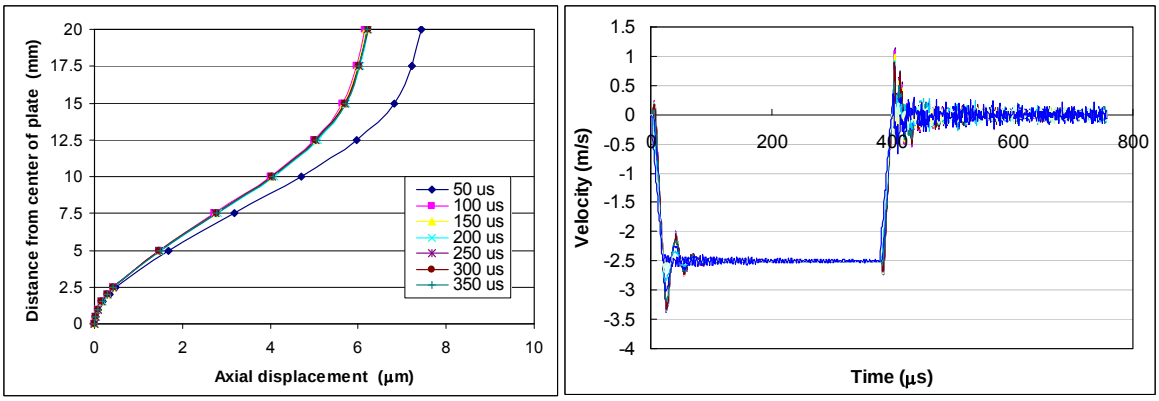

(b) Configuration B

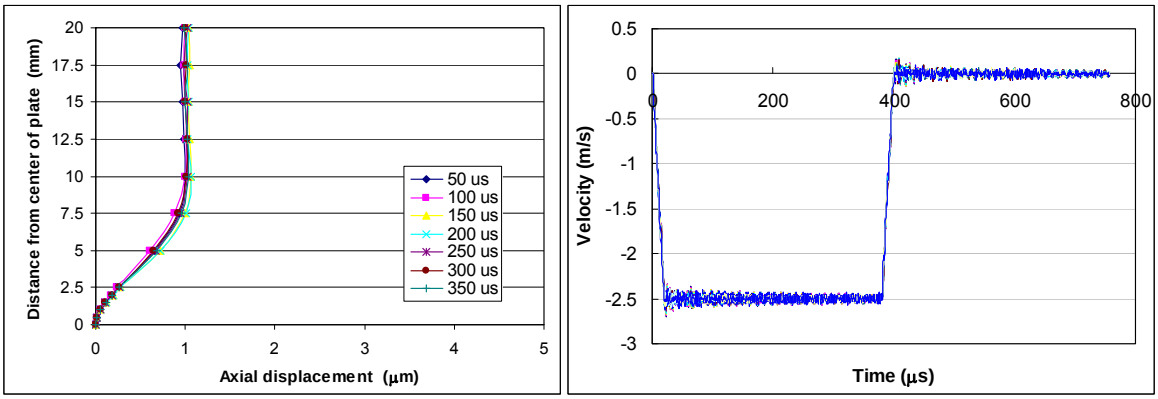

(c) Configuration C

Fig.3-16 (Left) nodal displacement relative to center and (right) nodal velocity histories, along radius of impact plate

The next objective is to examine whether the stress generated is uniform across the cross section of the bar and propagates without distortion. Nodal velocities along a 2.5mm radius at the face surface of the impact plate are

plotted in Fig.3-16. However, the resolution is reduced as they are plotted together with nodes outside the 2.5mm radius. Therefore these curves are re-plotted separately in Fig.3-17, together with the corresponding radius at bar cross sections 25cm and 50cm away from the impact plate. Coincidence of the six curves at each position clearly shows that the particle velocity in cross-sections along the bar is quite uniform, even at the interface between the impact plate and the specimen. This is maintained as the wave travels along the bar. All these input waves are acceptable in dynamic testing, and the input wave for configuration C is the best with less oscillation than the other two.

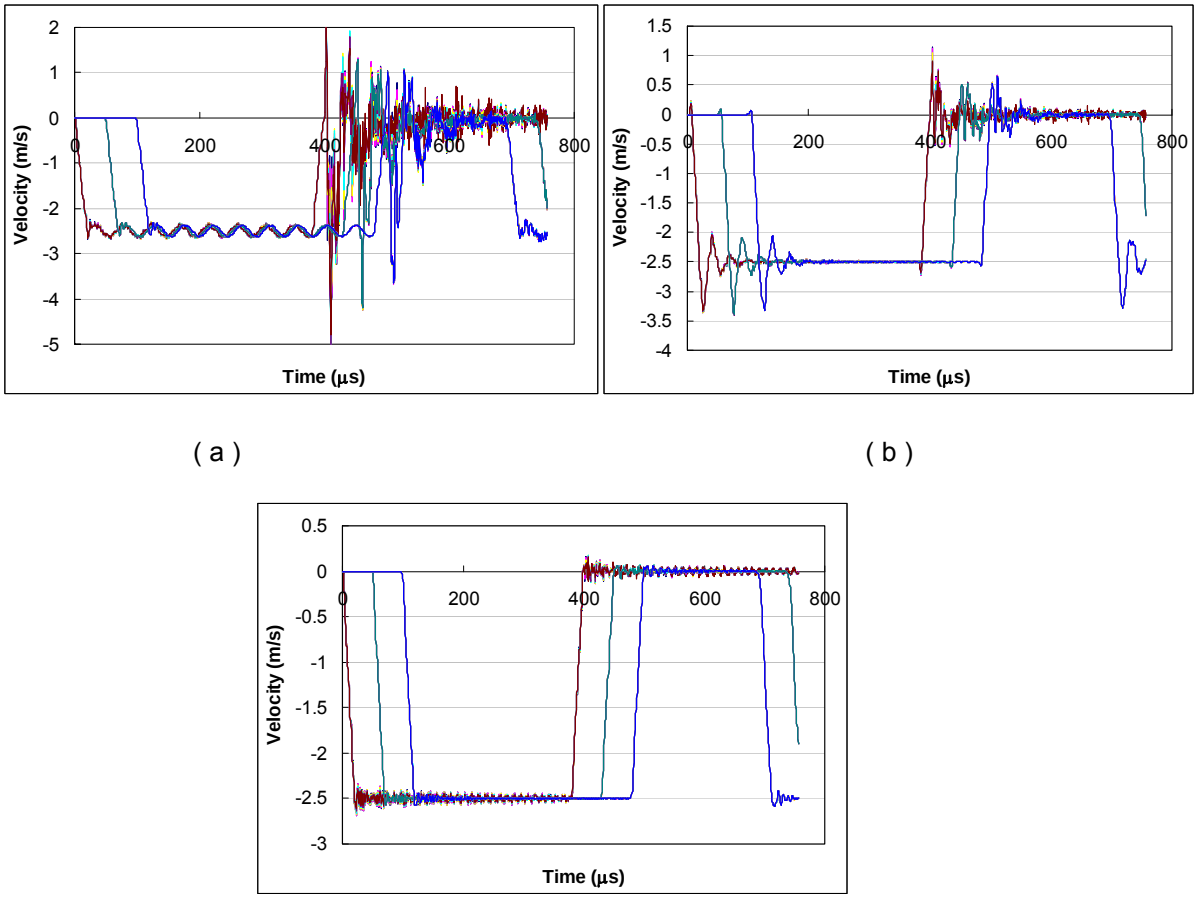

Fig.3-17 Velocity histories extracted from nodes along a radius at bar cross-sections located at the face end, and 25cm and 50cm away from the end, for (a) configuration A, (b) configuration B and (c) configuration C.

To experimentally validate the applicability of the miniature impact tester, tests on commercially available aluminum alloy were conducted. This was done to verify whether the miniature tester can produce results with comparable accuracy to that from a traditional Hopkinson bar system. Small cylindrical specimens of aluminum alloy (2.4mm in diameter and length) were fabricated and subjected to dynamic compression using a traditional Hopkinson bar system (with ϕ12mm steel bars) at two striker speeds. Dynamic tests were also carried out using the miniature impact tester (with ϕ5mm steel bars) at a striker speed of around 0.5m/s (corresponding to a test on a split Hopkinson bar system with striker speed around 1m/s). Static compression tests were also performed. Fig.3-18 shows that the results obtained using the miniature impact tester are comparable to those from the traditional Hopkinson bar system, demonstrating that the newly devised approach is capable of effecting dynamic testing. The discrepancy in the initial portion of these curves could have been caused by variation in the specimen-bar contact, as well as limitations in deriving early response from Hopkinson bars. The results from the traditional Hopkinson bar system showed slightly larger oscillations, especially in the region of yielding - this could be due to the large difference in the cross sectional area between the bar (ϕ12mm) and the specimen (ϕ2.5mm), demonstrating the need for a thin bar for small specimens (Liu, et al., 2007).

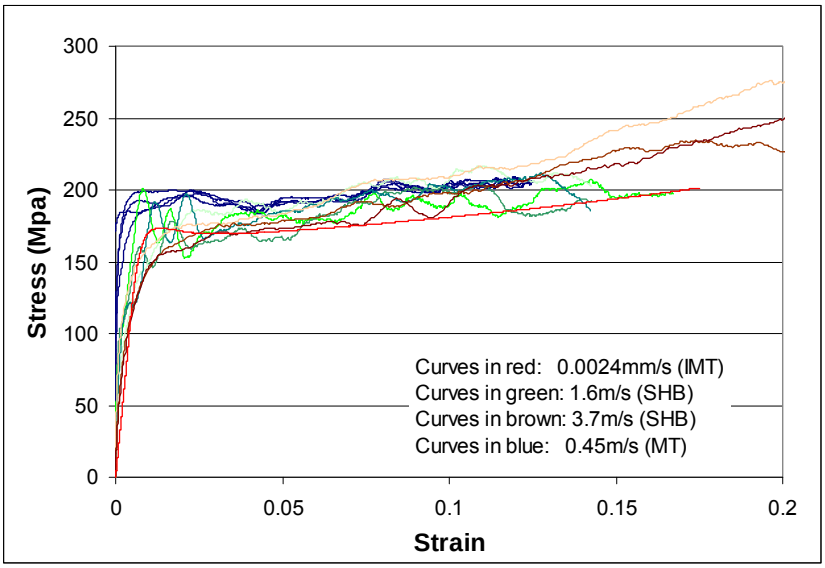

Fig.3-18 Results of tests on aluminum specimens (IMT – Instron micro tester; SHB – Split Hopkinson bar; MT – Miniature tester)

In summary, a new dynamic test methodology has been proposed. The motivation for this comes from the need to handle small specimens, whereby the load on and deformation of the specimen must be measured accurately because of their small amplitudes. This is not easy with a traditional split Hopkinson bar system, where straight alignment between the striker, input and output bars is critical. With the miniature impact tester, the region that requires precise coaxial alignment is between the striker, the impact plate and the two surfaces in contact with the specimen; this is a short region compared to a split Hopkinson bar system. The strain gauges on both the input and output bars can be mounted close to the specimen-bar interfaces. Consequently, supporting the very slender bars is less of a concern and wave dispersion or attenuation in the bars has minimal influence on the results for the miniature impact tester. Stress waves are used to derive the force and deformation response of a specimen. The proposed miniature impact tester also has the advantage that it can impose either compression or tension

simply through attachment of the impact plate to the input or output bar. These features facilitate establishment of a portable dynamic compression cum tension tester which has test accuracy comparable to a split Hopkinson bar system.

The theoretical derivation and interpretation of the governing equations have been presented, with respect to calculation of results from recorded wave signals. FEM simulation was also performed to evaluate the validity for dynamic testing. Experimental tests on aluminum specimens showed results comparable with that from a split Hopkinson bar system. The portable miniature impact tester fabricated for dynamic compression and tension testing is illustrated in Fig.3-19 and details are presented in *Appendix B*. It is relatively compact and based on a spring to propel a tubular striker. Alternative designs that use compressed gas to drive cylindrical striker are possible. An important requirement for achieving a good input wave is that the striker cross-section should cover as much of the impact plate as possible.

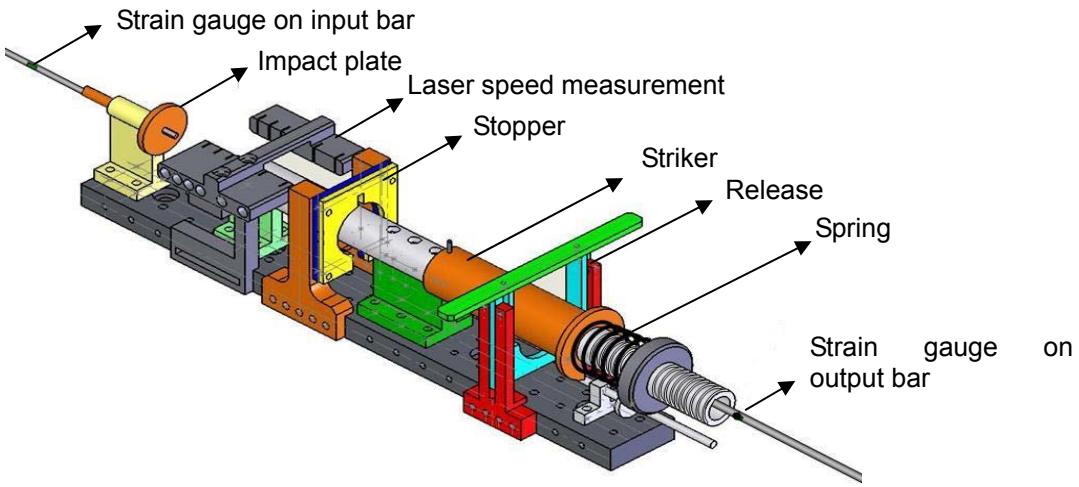

Fig.3-19 Portable miniature impact tester for dynamic compression and tension testing

3.4 Experimental results of dynamic tests on single solder joint specimens

Single solder joint specimens similar to those used in quasi-static tests were tested dynamically. They comprise two parallel 5x5mm BT substrates linked by a solder joint formed by melting a 0.42mm diameter lead free (Sn96.5-Ag3.0-Cu0.5) solder ball. Solder joint specimens were bonded to the ends of the input/output bars using a fast curing adhesive (cyanoacrylate). Dynamic tensile and compression tests corresponding to two striker speeds (around 0.3m/s and 3m/s) were conducted using the miniature impact tester. Adaptors for inclined loadings are same as that used in quasi-static testing (Fig.2-7), where an additional adaptor is employed in conjunction with the shear adaptors for pure shear testing. Foil strain gauges were used to capture the input wave and semiconductor strain gauges were for the transmitted wave. Fig.3-20 and Fig.3-21 show the load-deformation curves for loading at different angles of specimen inclination for the two dynamic test speeds; positive values denote tension. Rate sensitivity is obvious upon comparison of dynamic test results with the quasi-static responses. The average response based on this group curves is indicative of the overall force-deformation behavior of a single solder joint. The data shows that the degree of rate sensitivity is related to the mode of loading, whereby the compressive load increases significantly with loading speed, particularly at higher speeds. For tensile tests, the maximum point on the load-deformation curve signifies fracture of the joint (which is primarily separation between the Cu pad and the substrate)

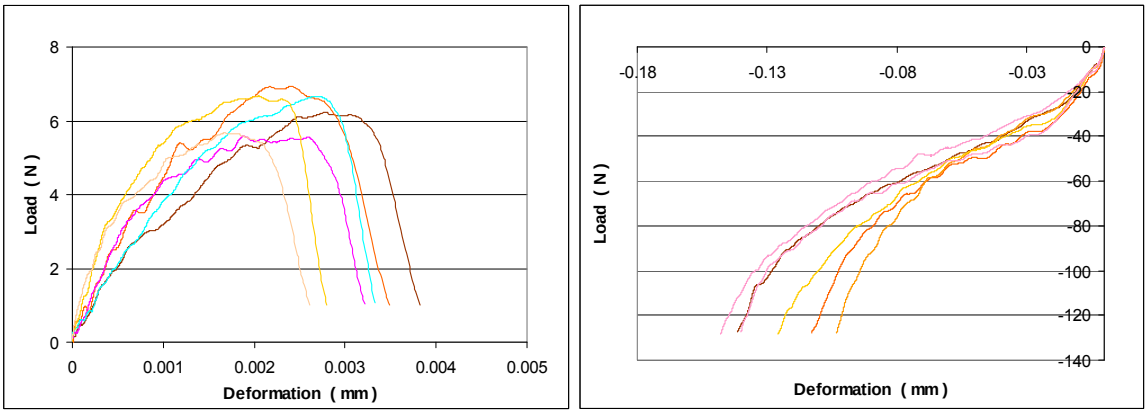

(a) Tensile and compressive load-deformation curves for loading at 0 degrees

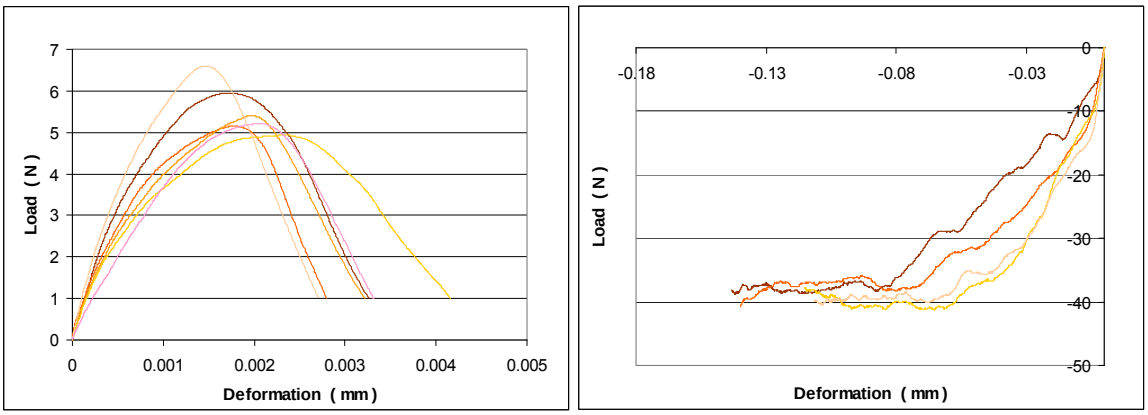

(b) Tensile and compressive load-deformation curves for loading at 15 degrees

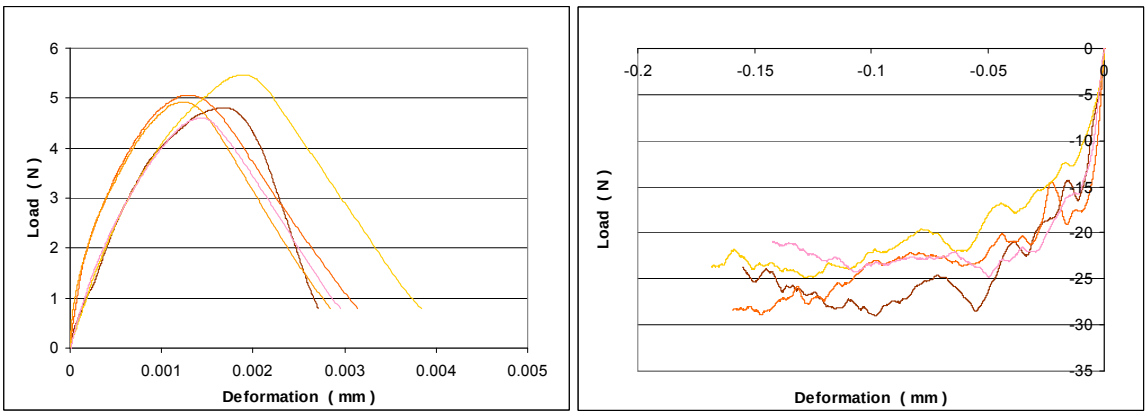

(c) Tensile and compressive load-deformation curves for loading at 30 degrees

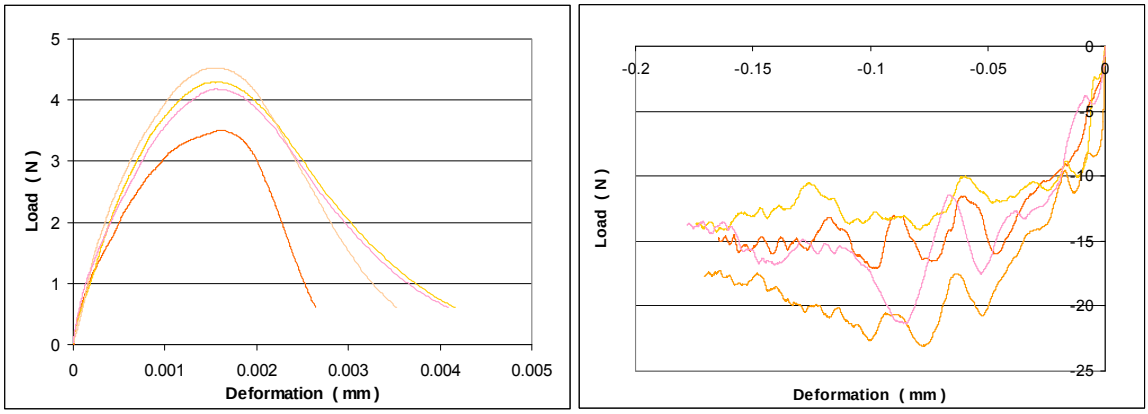

(d) Tensile and compressive load-deformation curves for loading at 45 degrees

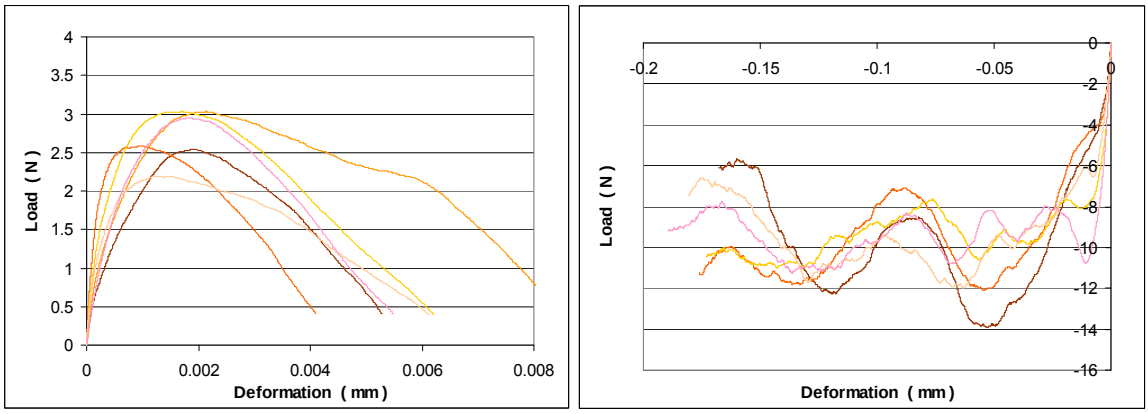

(e) Tensile and compressive load-deformation curves for loading at 60 degrees

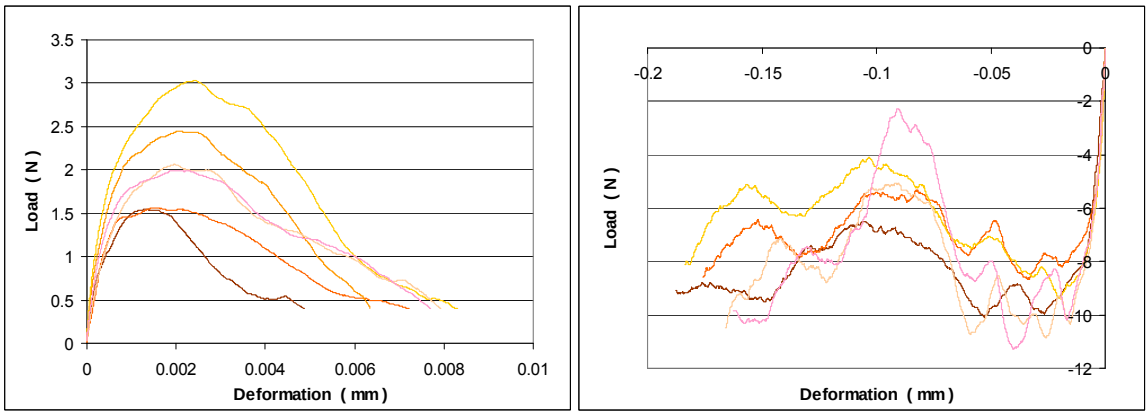

(f) Tensile and compressive load-deformation curves for loading at 75 degrees

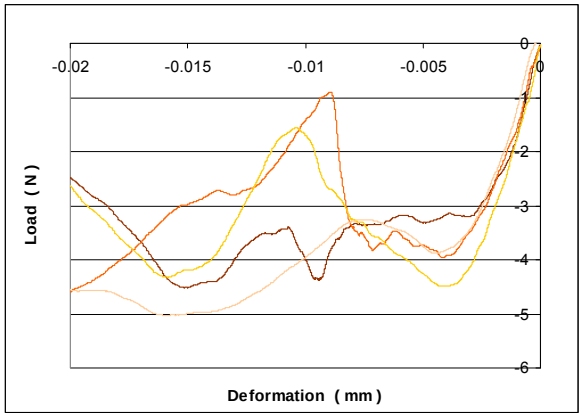

(g) Load-deformation curves for shear (90 degrees)

Fig.3-20 Dynamic tensile and compressive load-deformation responses for single solder joint specimens loaded at a deformation rate around 0.3m/s.

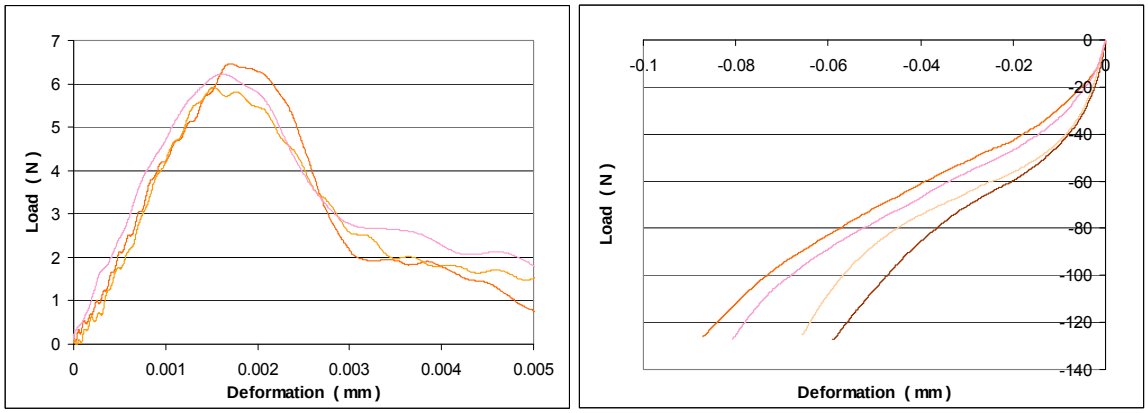

(a) Tensile and compressive load-deformation curves for loading at 0 degrees

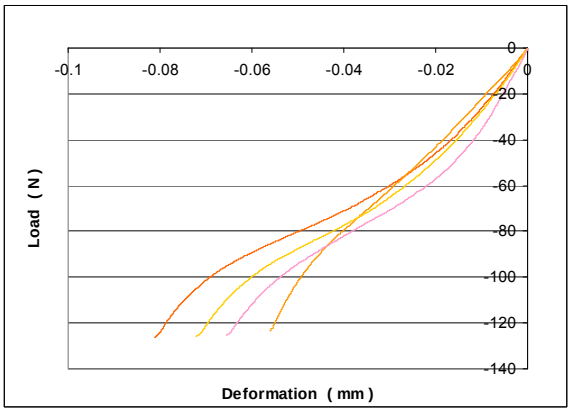

(b) Compressive load-deformation curves for loading at 15 degrees

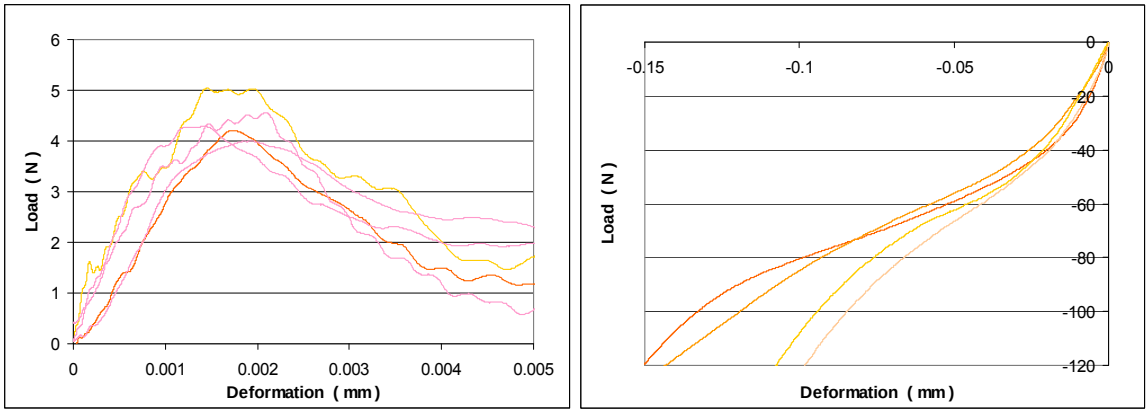

(c) Tensile and compressive load-deformation curves for loading at 30 degrees

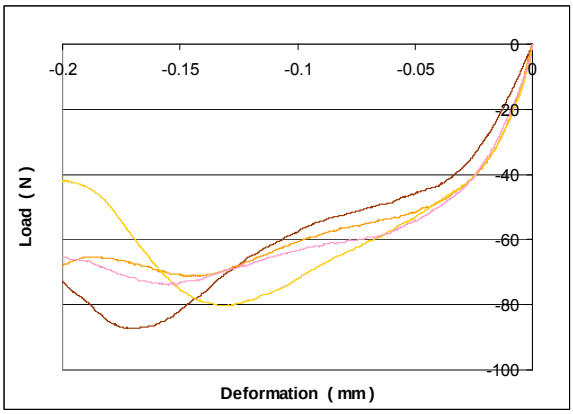

(d) Compressive load-deformation curves for loading at 45 degrees

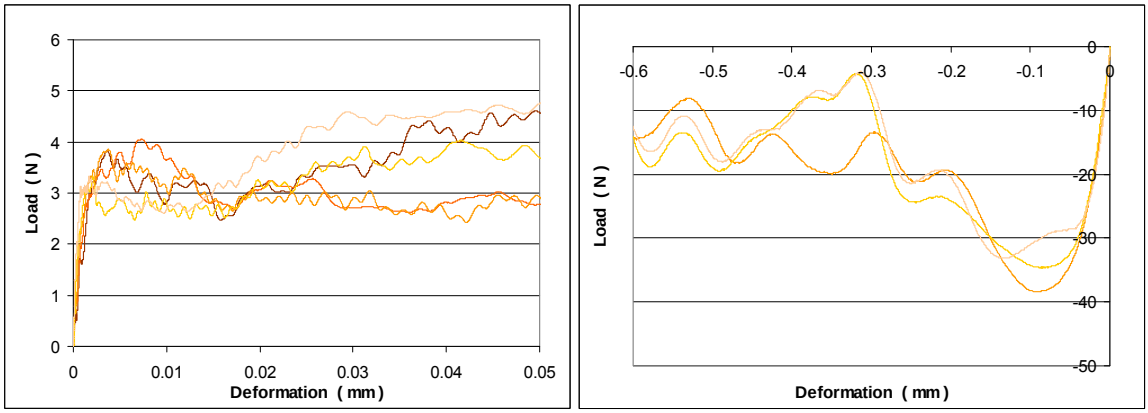

(e) Tensile and compressive load-deformation curves for loading at 60 degrees

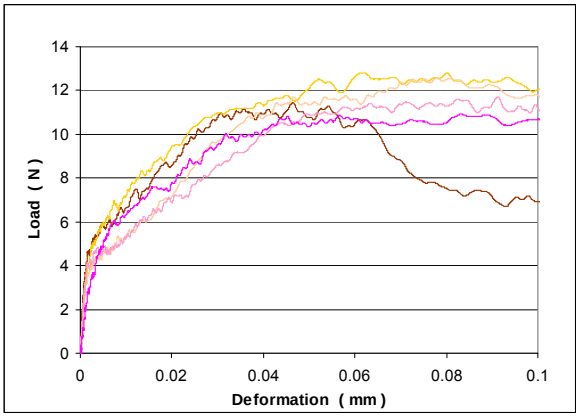

(f) Load-deformation curves for shear (90 degrees)

Fig.3-21 Dynamic tensile and compressive load-deformation curves for single solder joint specimens loaded at a deformation rate around 3m/s.

As joint specimens comprise a complex combination of the substrate, copper pad and solder material, they are not as consistent as samples of individual spherical solder balls. Therefore, the load-deformation responses of solder joint specimens exhibit more scatter compared to that of solder balls (presented in Fig.3-8). From the load-deformation curves in each group of tests, the initial stiffness and load/deformation values at failure were obtained. These are presented in Tables A-3 and A-4 in *Appendix A*, for the two dynamic testing speeds. The stiffness corresponding to the linear elastic portion is calculated and the failure load decomposed into normal (perpendicular to the inclined surface) and shear (parallel to the inclined surface) components.

From the values of the normal and shear components of the failure load, the force envelopes for a single solder joint are obtained and plotted in Fig.3-22 (a) and (b); the average deformation rates are also indicated. For the dynamic tests, the deformation rates for tension and compression are not same and also not equal to the speed of the striker. A comparison between the

envelopes is shown in Fig.3-22 (c), which shows that rate sensitivity of the failure load is more obvious in the compressive region than in the tensile region.

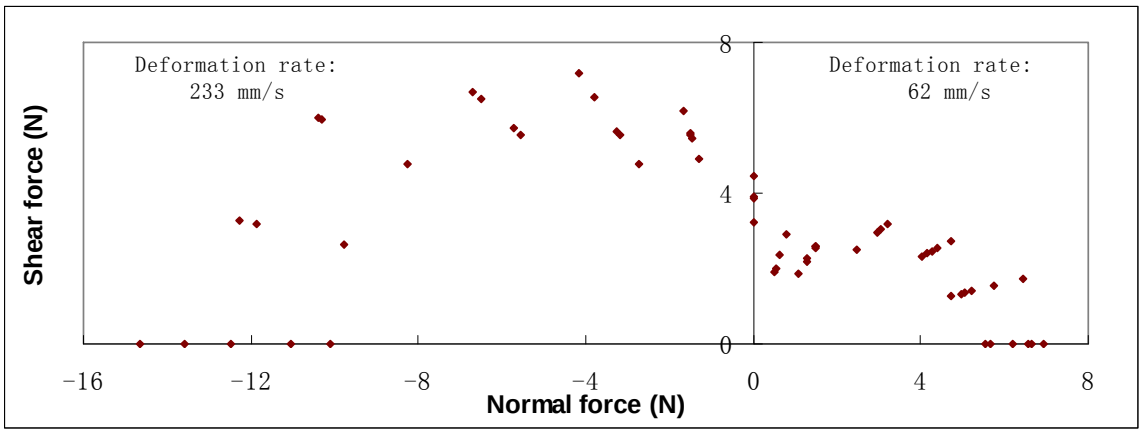

(a)

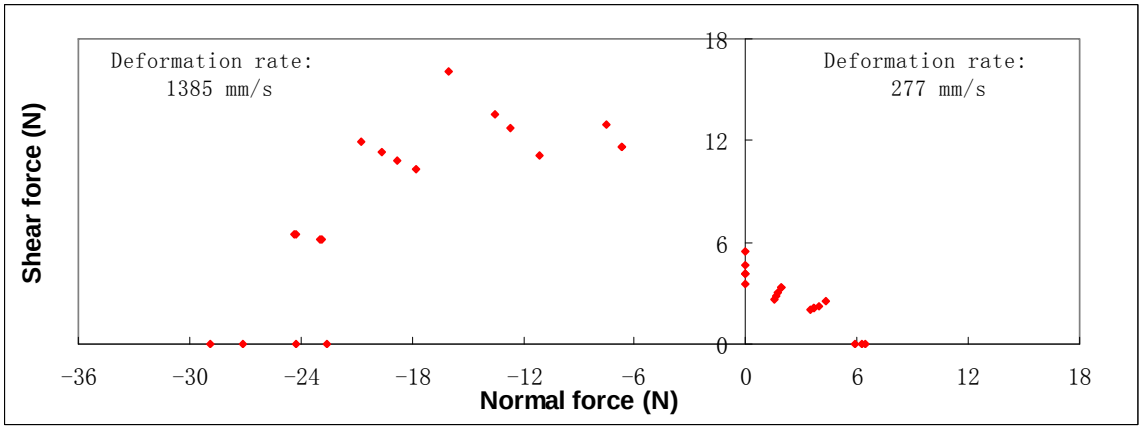

(b)

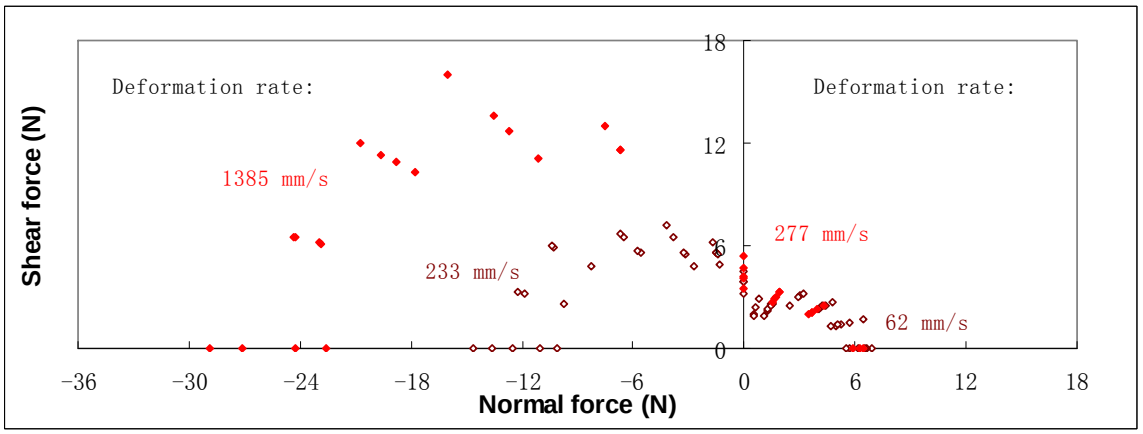

(c)

Fig.3-22 Dynamic failure force envelopes for a solder joint

CHAPTER 4 CHARACTERIZATION AND COMPUTATIONAL MODELLING OF SINGLE SOLDER JOINTS

4.1 Solder joint features and geometry

4.1.1 Microscopic measurement of solder joint dimensions

In this study, solder joints were fabricated between two BT substrates. In order to build an FEM model for numerical simulation, the solder joints were examined under a microscope. Fig.4-1 is a schematic drawing showing the profile and characteristic dimensions of a solder joint, where H1, H2 and H3 are respectively the substrate thickness, copper pad thickness and solder joint standoff height. The diameter of the copper pad is denoted by D1, while the diameters of the solder flange, solder mask and solder bump are denoted by D2, D3 and D4 respectively.

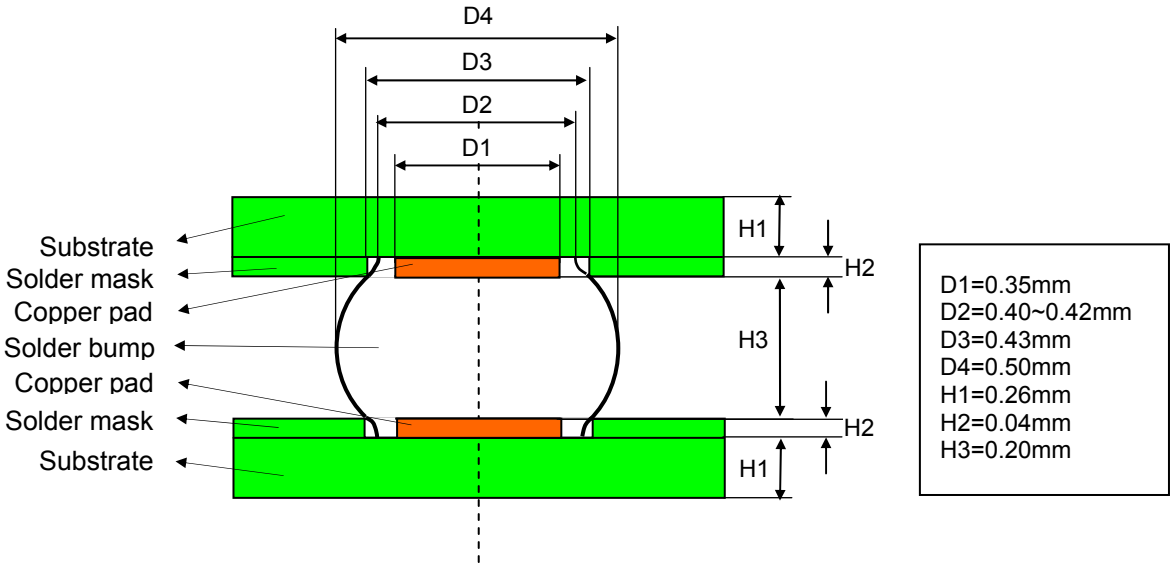

Fig.4-1 Schematic drawing and characteristic dimensions of a solder joint in present study

Fig.4-2 and Fig.4-3 are images of substrates and solder joints captured via a ZEISS microscope. A scale bar is embedded in the digital images, using the accompanying software (Axiovision 4.7). The measured values display a slight variation among the specimens and mean values were used in the creation of an FEM model.

Fig.4-2(a) shows the BT substrate sectioned across the copper pads. The thickness of the copper pad H2 is about 40μm, and the overall thickness of the substrate is 300μm, so the substrate thickness excluding the copper pad (H1) is around 260μm. Two images showing pits resulting from copper pad peel off demonstrate that the copper pad-substrate interface strength is important in the characterization of the solder joints in the current study, and provides possible evidence for the discrepancy in mechanical behavior obtained from actual experimental and simulation results. The diameters of the copper pad and solder mask cannot be measured from these pictures, as the cross sections may not correspond to the appropriate location. Therefore, the copper pad and solder mask diameters were measured from the surface of the substrates, as shown in Fig.4-2(b); the diameter of copper pad D1 is around 350μm, and the diameter of solder mask D3 is around 430μm.

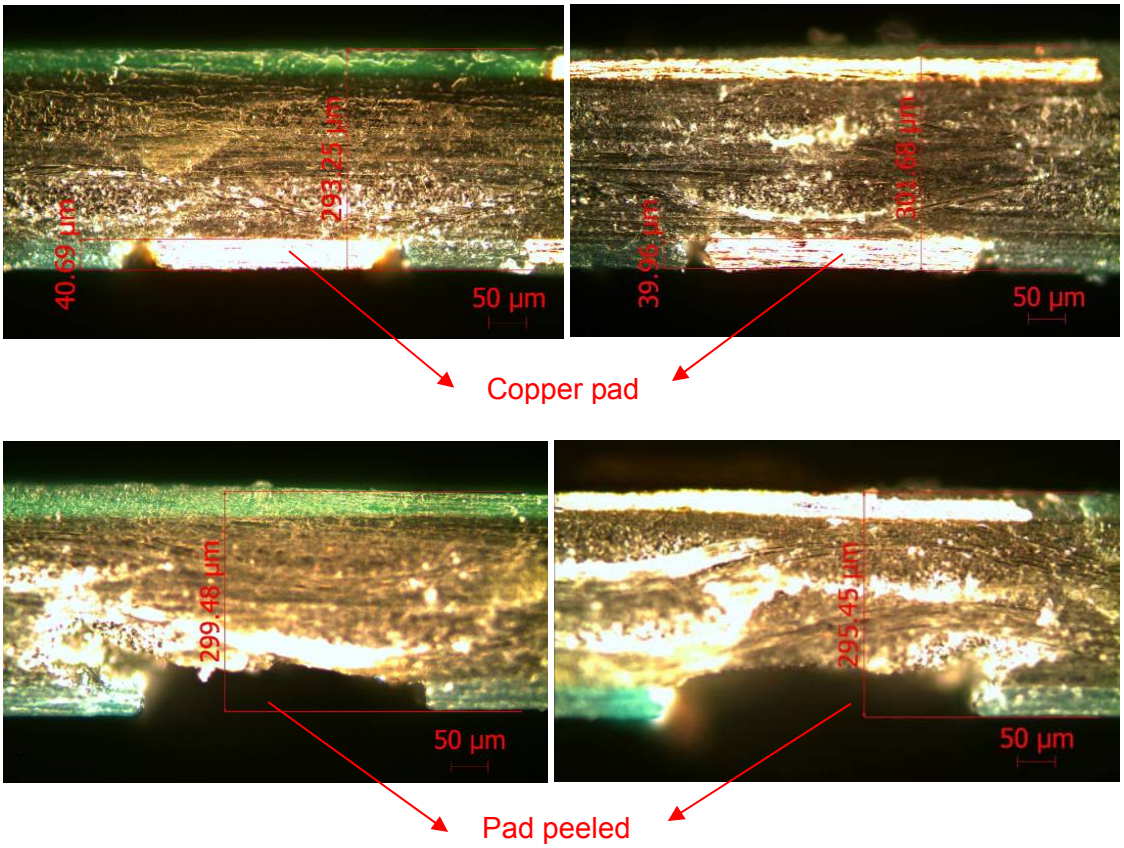

(a) Thickness of BT substrate and embedded copper wire

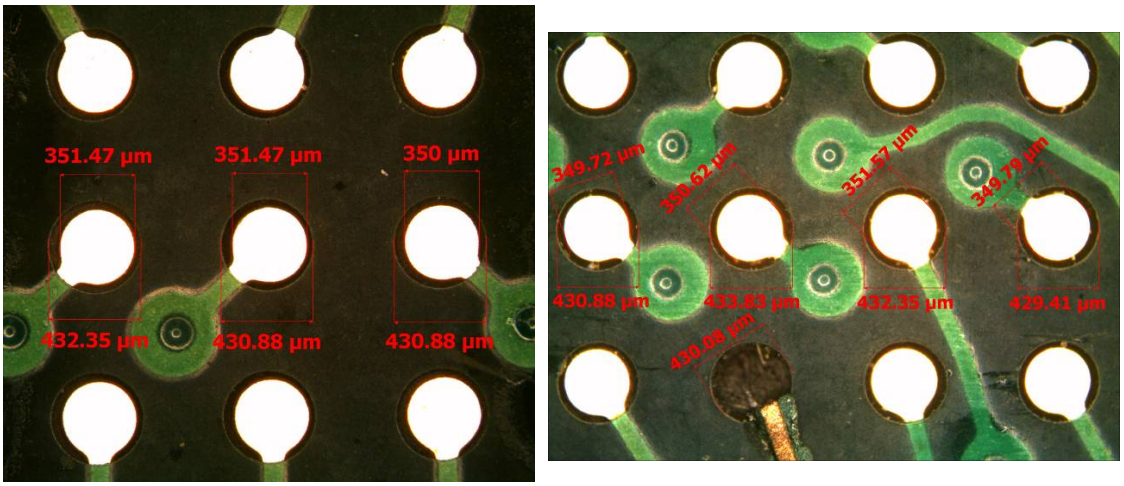

(b) Diameters of the copper pad and solder mask

Fig.4-2 Microscopic images showing characteristic dimensions of BT substrate

Because the solder bump is small and has a curved surface, it is noted that the dimensions may not be correctly measured if the image is not in correct focus. Fig.4-3(a) demonstrates two solder bumps that show changes in the

apparent diameter (D2 or D4) when the focus shifts from the front to a lateral location (dimensions indicated in blue). It is also found that from this viewing angle of the solder bump, it is difficult to focus exactly on the fringe of the solder bump to obtain D2 and D4.

Therefore, the height of solder joints is measured from their front views, as shown in Fig.4-3(b), and the diameters (D2 and D4) are measured from the top view, as shown in Fig.4-3(c) and Fig.4-3(d). From Fig.4-3(b), it is seen that the total solder joint height is around 280μm. By excluding the height of the two cylinder-like flanges (around 40μm) which conceal the copper pads, the stand-off height of the solder bump H3 is found to be around 200μm. In Fig.4-3(c), the focus point is at the perimeter of the round profile and the diameter of solder bump D4 is determined to be around 500μm. In Fig.4-3(d), the focus is at the top surface of the flange, and the diameter D2 shows a variation from around 400μm to 420μm. It is unlikely that the flange is a regular cylinder. The fringe of the flange is not distinct, as it depends on the contact conditions between the molten solder and the solder mask.

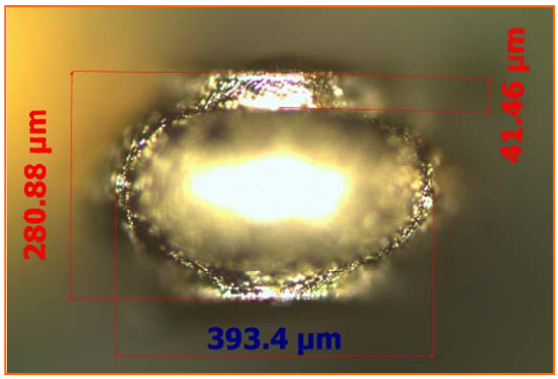

Focus on front site

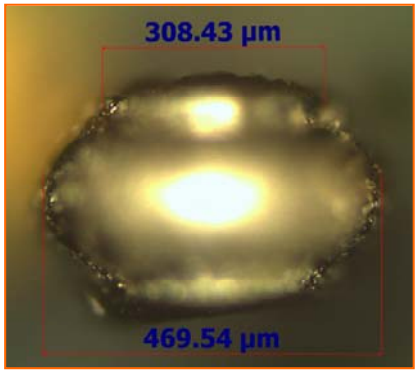

Focus on lateral site

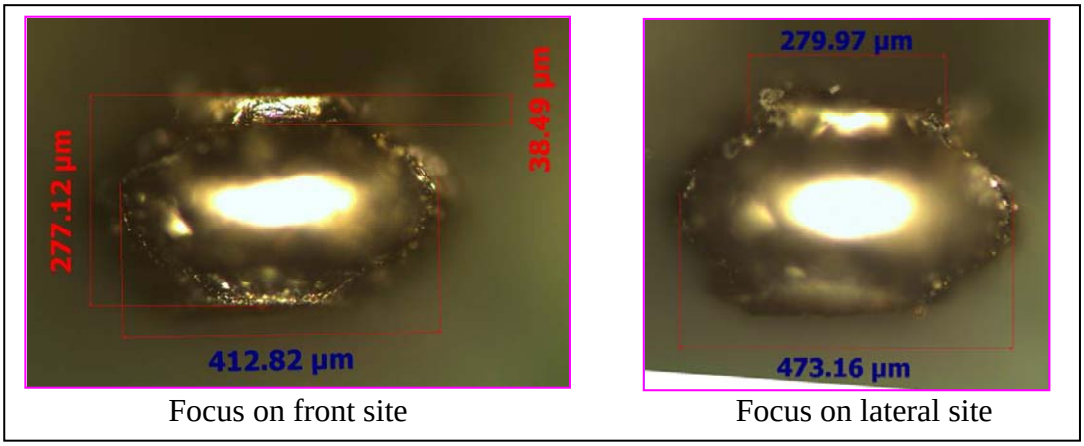

(a) Changes in visually determined diameter with focusing site

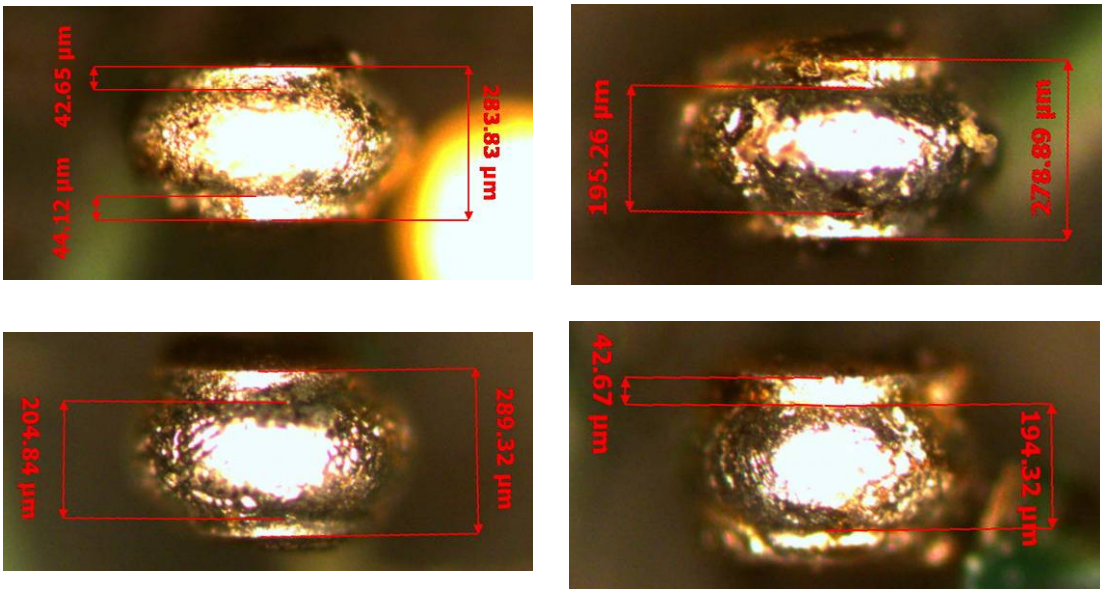

(b) Measurement of height of solder joints from front view

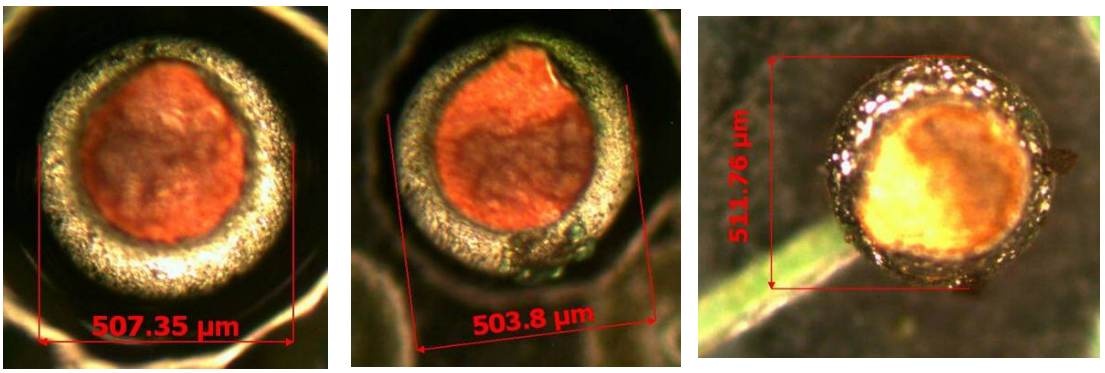

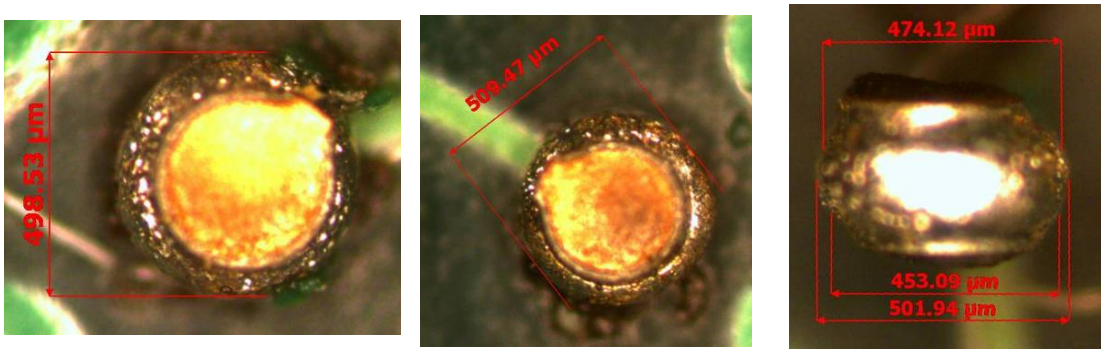

(c) Measurement of diameter of solder joints from plan view

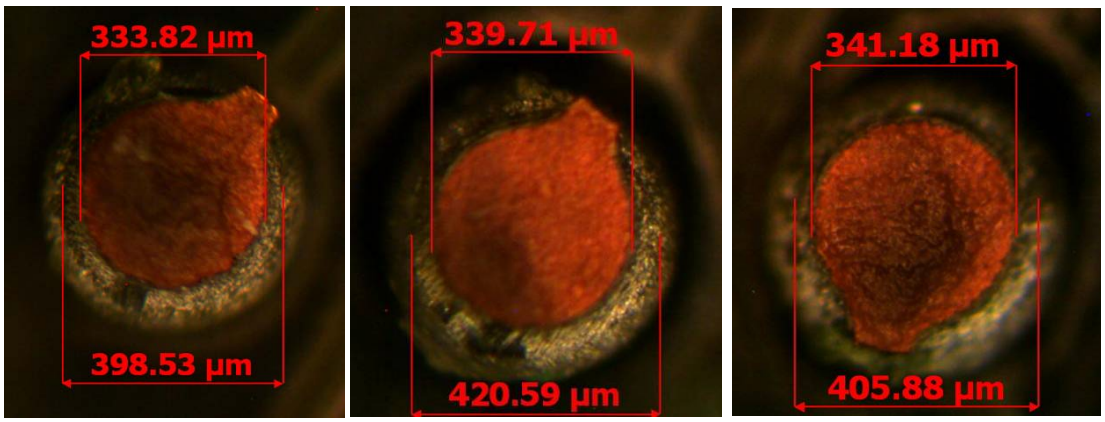

(d) Measurement of diameter of the flange from plan view

Fig.4-3 Microscopic images showing the characteristic dimensions of a solder bump

4.1.2 Finite element model of solder joint

The solder balls studied correspond to the code M705, manufactured by Senju Metal Industry. The balls are 0.42mm in diameter and made of a high reliability lead free solder “Sn96.5Ag3.0Cu0.5” (96.5% Sn, 3.0% Ag and 0.5% Cu). The properties of Sn96.5Ag3.0Cu0.5 alloy, as shown in Table 4-1, can be obtained from the company’s website, and the corresponding properties of the eutectic solder Sn63Pb37 are also listed for comparison. In terms of mechanical properties, it is seen that Sn96.5Ag3.0Cu0.5 alloy has a higher

Young's modulus and a lower yield stress (defined by 0.2% offset strain) and elongation than eutectic solder.

Table 4-1 Properties of M705 alloy compared to eutectic tin-lead alloy (http://www.hin.dk/log/files/web/M705-GRN360K1V_loddepasta.pdf)

		M705	63Sn-Pb
Alloy Composition (%)		Sn96.5-Ag3.0-Cu0.5	Sn63-Pb37
Specific gravity		7.4	8.4
Melting temperature	Solidus	217	183
	Peak	219	
	Liquidus	220	
Tensile strength (MPa)		53.3	56.0
Elongation (%)		46	59
Young's module (GPa)		41.6	26.3
0.2% Yield point (MPa)		39.4	45.8
Coefficient of linear expansion (ppm/C)		21.7	23.5
Vicker Hardness (Hv)		17.9	16.6

In FEM simulations, material stress-strain relationships are described by true (Cauchy) stress (force per current area) and logarithmic strain. Conversion of engineering stress and strain to true values is done via the following:

$$\varepsilon_T = \int \frac{dl}{l} = \ln(\frac{l}{l_0}) = \ln(1+\varepsilon_E) \quad (4\text{-}1)$$

$$\sigma_T = \sigma_E(1+\varepsilon_E) \quad (4\text{-}2)$$

where the subscripts of T and E denote "true" and "engineering" respectively.

Based on these equations, the true stress and true strain for alloy Sn96.5Ag3.0Cu0.5 are obtained, as shown in Fig.4-4, where the bilinear curves are characterized by the yield point and ultimate stress (46% elongation).

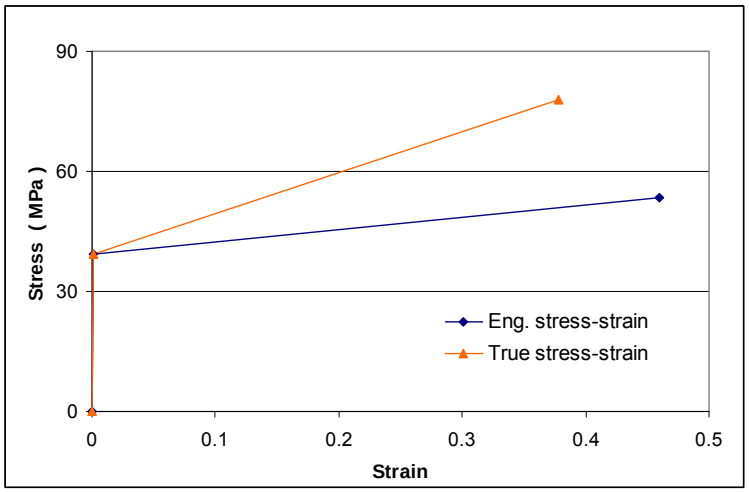

Eng. strain	Eng. stress (MPa)	True strain	True stress (MPa)	True plastic strain
0	0	0	0.000	0.00000
0.00094712	39.4	0.00094667	39.437	0.00000
0.460	53.3	0.37843644	77.818	0.37657

Fig.4-4 Engineering and true stress/strain values of Sn96.5Ag3.0Cu0.5 alloy

Based on experimental measurements, a FEM model is established from the mean values of the characteristic dimensions of actual solder joint specimens, as shown in Fig.4-5. The solder bump between the substrates has a barrel-like profile. The mechanical properties of each component are also listed in the figure, and the properties of the BT substrate are obtained from literature (Lau, et al. 2002), while the mechanical properties of the Pb-free solder bump correspond to Sn96.5Ag3.0Cu0.5 alloy, in terms of true stress and true strain. It should be pointed out that the actual mechanical properties of the solder bump in single solder joint specimens differ from Sn96.5Ag3.0Cu0.5 alloy – this will be discussed latter.

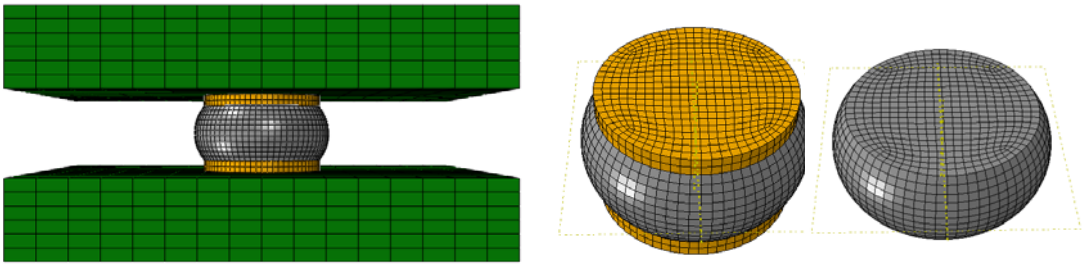

Components	Young's modulus (Gpa)	Yield/Hardening (MPa/ε_p)	Poisson's ratio	Density (Kg/m^3)
Solder (Sn96.5Cu0.5Ag3)	41.659	39.437 , 0 ; 77.818 , 0.377	0.4	7400
Copper pad	120		0.34	8930
BT substrate	26		0.39	2800

Fig.4-5 Barrel profile of a solder joint model based on measured dimensions and material properties of components

4.2 Mechanical properties of solder joints

4.2.1 Combined loading on solder joints

Tensile and compressive tests on single solder joint specimens subjected to combined loading were carried out by applying the load at particular inclinations to the longitudinal axis of the joints. Tests were conducted at two quasi-static and two dynamic speeds. The displacement rate of the Instron micro tester was set to 0.00015mm/s and 0.15mm/s for quasi-static testing and the impact velocities of the striker of the miniature impact tester were around 0.3m/s and 3m/s; a slight variation in velocity exists. The solder joint specimens comprise two substrate, copper pads and solder material. Consequently, the resulting quality and profile of these specimens are not as consistent as that of individual spherical solder balls. For each testing speed, around five valid test results were obtained; the load-deformation response of

solder joint specimens exhibits some scatter compared to that of solder balls. This is illustrated in Fig.4-6, which shows several pure compression test results corresponding to a deformation speed of 0.233m/s. The average of these results is taken to be representative of the overall force-deformation behavior of a single joint.

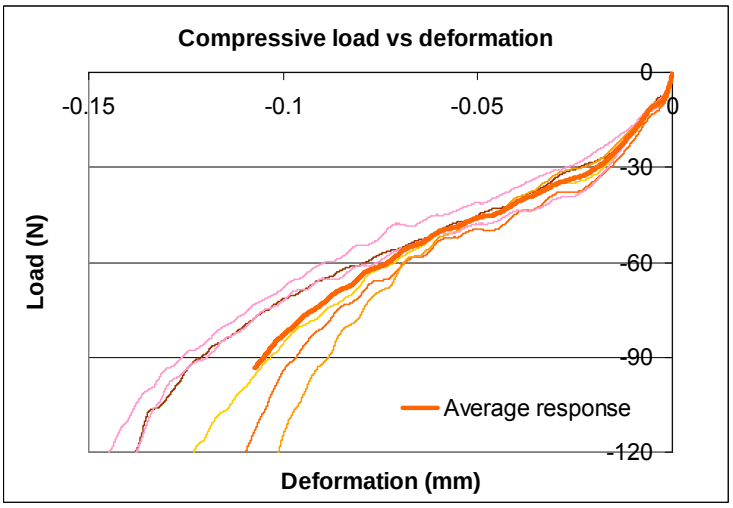

Fig.4-6 Dynamic compressive load-deformation curves at deformation rate of 0.233m/s

The average force-deformation responses for different angles of inclination and deformation rate are shown in Fig.4-7. The angles range from 0^0 to 90^0, at intervals of 15^0 for both compressive and tensile loading. An angle of 0^0 corresponds to pure tension/compression. With an increase in inclination, the shear component of the applied force increases. A 90^0 angle loading corresponds to pure shear. The figure shows the general overall trend of the force-deformation curves with respect to loading angle for different loading speeds. It shows that in general, solder joint strength decreases with an increase in inclination for both tensile and compressive loading.

It is observed that the variation in tensile strength for the four loading speeds is small. However, the compressive and shear strengths increase noticeably with loading speed, especially at higher speeds. For shear, the stress at higher loading speeds increases significantly; this may be due to the geometry of the specimens in this study, whereby the solder joint is constrained between two parallel plates with a constant separation during shearing. Unlike shear testing of single solder balls bonded to only one substrate, if failure of a solder joint constrained between two substrates is by sub-surface cracking between the pad and one of the substrates, a higher force is required to dislodge the solder joint from the polymer substrate at high speeds.

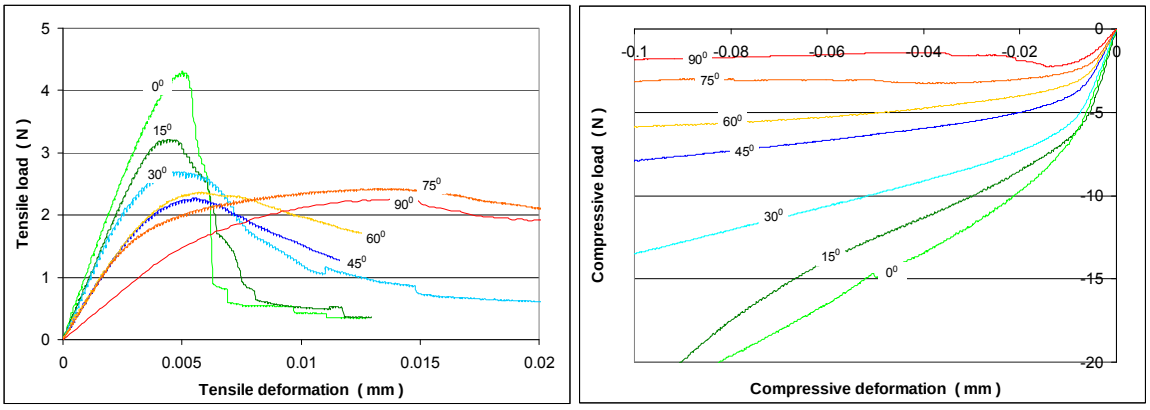

(a) Tensile and compressive response at loading rate of 0.00015mm/s

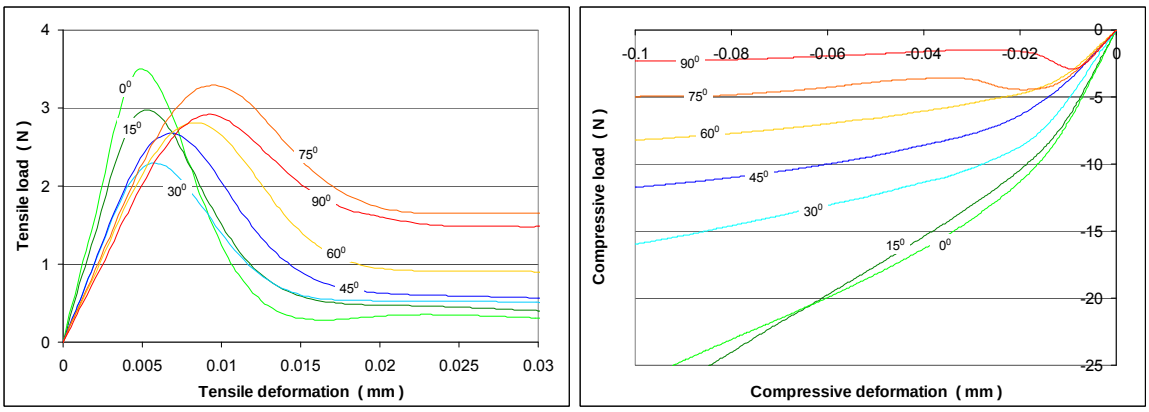

(b) Tensile and compressive response at loading rate of 0.15mm/s

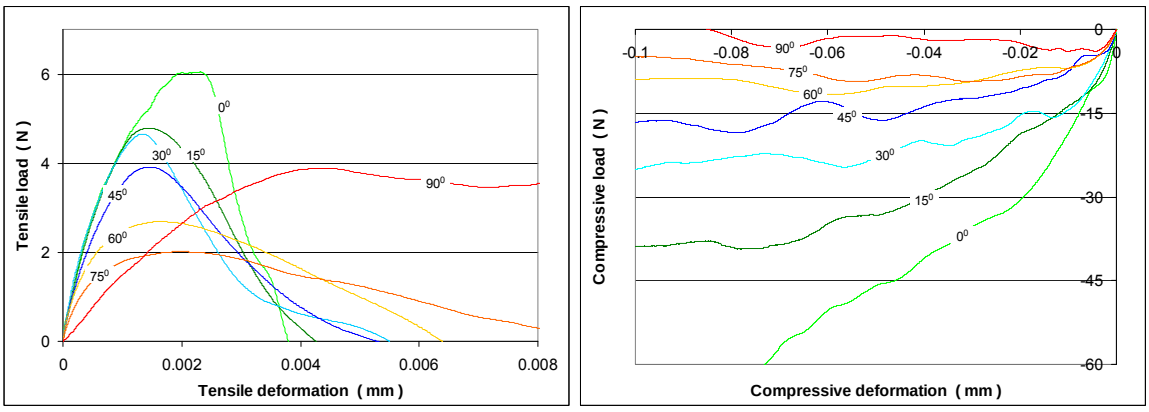

(c) Tensile and compressive response at loading rate of 0.3m/s

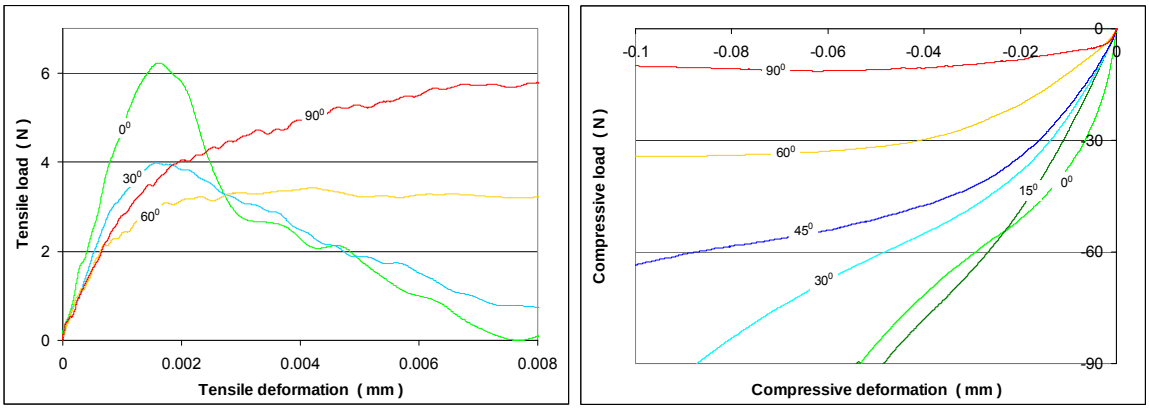

(d) Tensile and compressive response at loading rate of 3m/s

Fig.4-7 Overall average force-deformation responses of single solder joints subjected to inclined tensile and compressive loading at four speeds.

For pure tensile and tensile/shear loading, there is a maximum point on each stress-strain curve. For pure compression and compressive/shear loading, the stress increases with strain without an obvious ultimate strength. As described

in Chapter 2, the failure point on the force-deformation curve is selected as a characteristic reference that indicates commencement of degradation of solder joint mechanical integrity. The failure load is defined by the mid-point of the transition from the linear elastic response to the strain hardening phase of the load-deformation curve for compressive testing. For tensile testing, it is close to the ultimate load. Table A-5 in *Appendix A* lists the average values and standard derivations of the failure load and initial stiffness for single solder joint specimens obtained from individual tests, with respect to inclination angle and test speed. The initial stiffness is obtained from the slope of initial linear portion of the load-deformation curve. The applied load can be resolved into normal and shear components based on the inclination angle α.

According to the values listed in Table A-5, failure force envelopes can be plotted for each loading speed, as shown in Fig.4-8. These plots are in the form of shear load versus normal load, where a positive normal load refers to tensile loading. Standard deviations corresponding to each average value are also shown. Fig.4-9 shows a comparison between the failure force envelopes. Rate sensitivity is observed; this is especially evident for compression/shear loading whereby the failure force increase with loading speed is obvious.

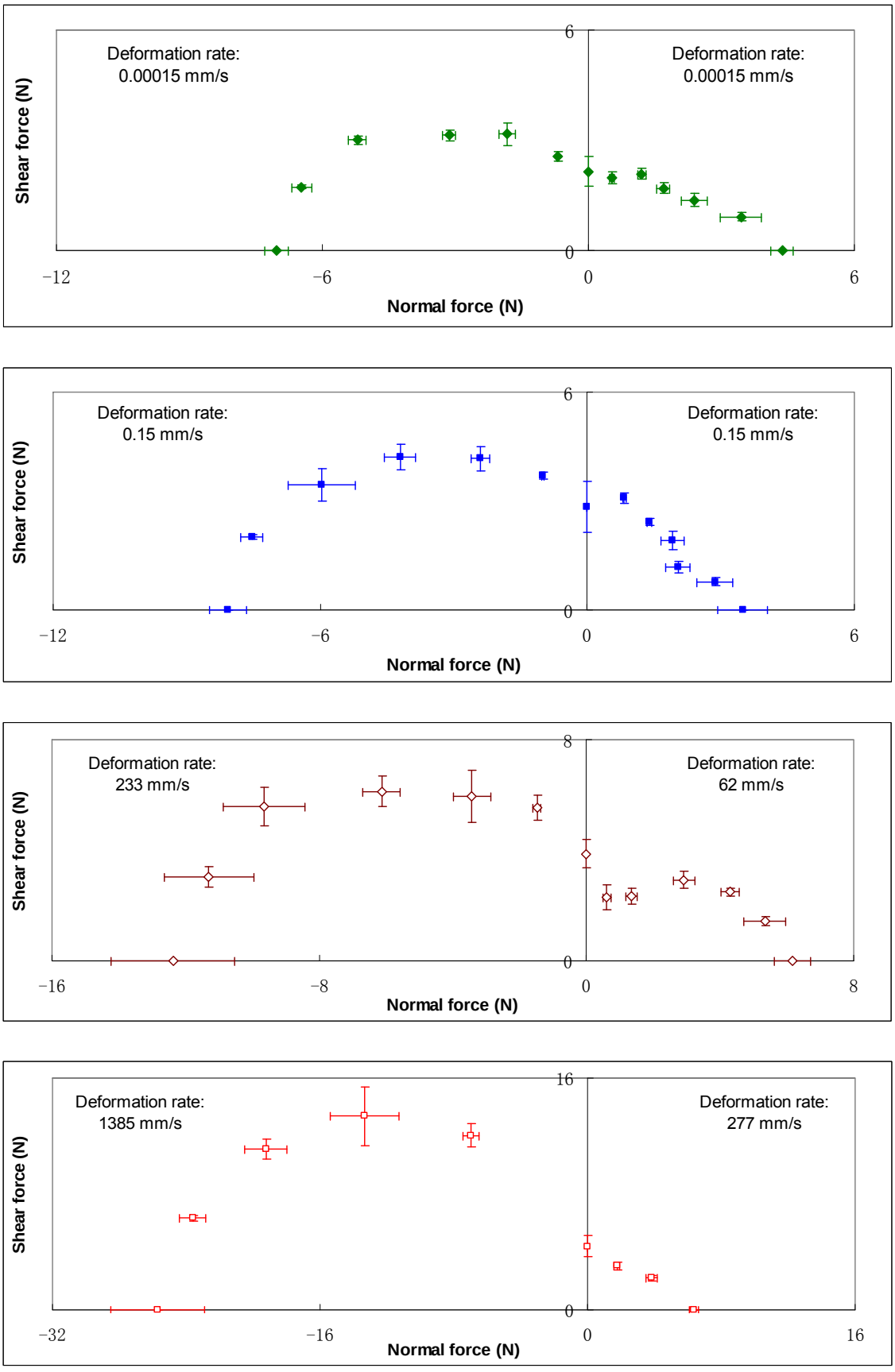

Fig.4-8 Yield envelope of shear and normal load components at different loading speeds

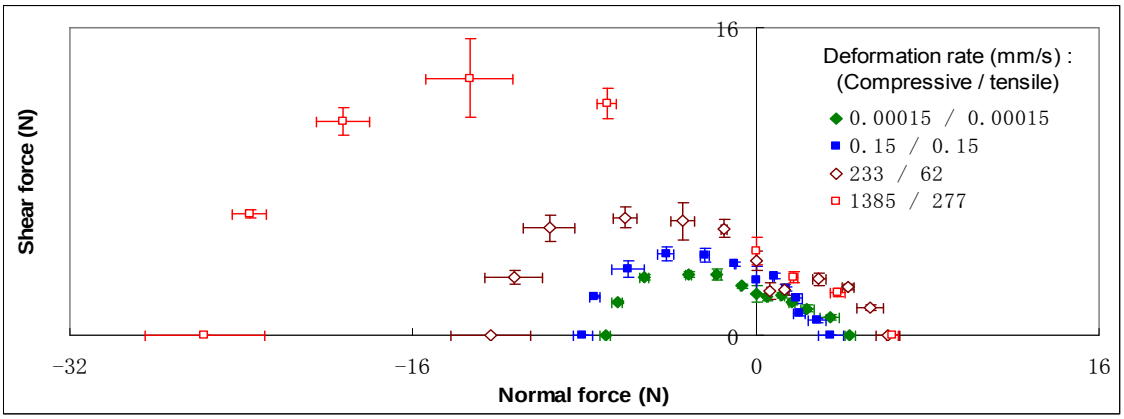

Fig.4-9 Comparison of yield envelopes for different deformation speeds

Previous studies (Tan, et al., 2006; 2009) have shown that the failure force envelope for solder joints is elliptical when plotted with respect to the shear and normal load components. However, the failure force envelopes shown in Fig.4-8 and Fig.4-9 deviate from an elliptical profile. FEM analyses in the following section will show that this arises from the mode of testing, i.e. “laterally unconstrained testing” and “laterally constrained testing”.

4.2.2 Analysis of solder joint forces under different loading modes

(1) Tests without lateral constraints

Fig.4-10(a) depicts the fixture for tensile testing of a solder joint without lateral constraints. An upper adaptor is connected to the crosshead of the tester via a stiff wire. Thus, the resultant force in the specimen is equal to the force in the wire, so that the resultant force direction is aligned with the wire. In this design, the centre of the solder joint should strictly also be in line with the wire

to ensure elimination of bending on the specimen. For compression testing, the configuration of the fixture is more complex than that for tension.

The FEM model for numerical simulation of laterally unconstrained loading for either tensile or compressive loading is shown in Fig.4-10(b). In this model, the surface of the lower substrate is fixed. The upper substrate is not laterally constrained and its upper surface is assigned an upward velocity, e.g. 0.00015mm/s (V_3) for tension, or a downward velocity for compression. The sum of forces and average displacement of nodes on the upper surface are calculated. These correspond to the force and deformation in an actual test.

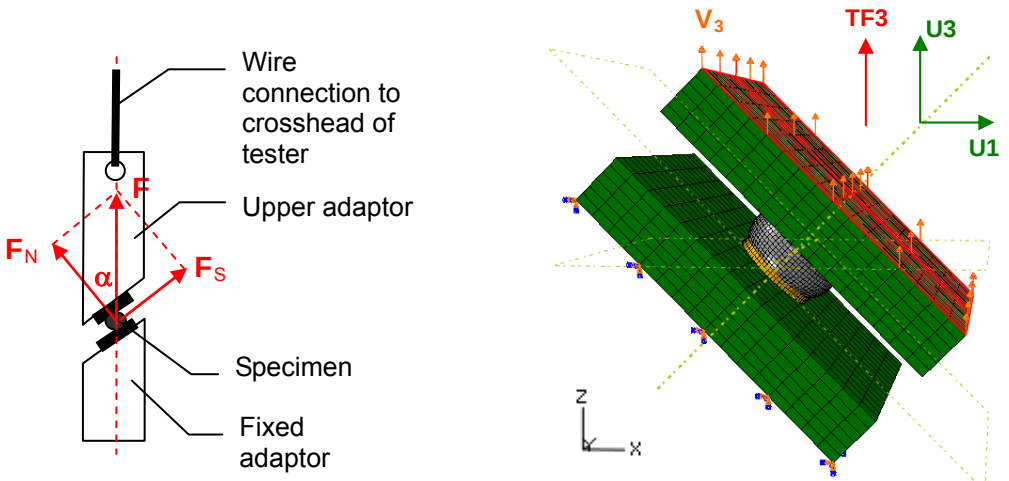

Fig.4-10 Illustration of laterally unconstrained tests and corresponding FEM model

From the simulation, it is found that for laterally unconstrained tests, the upper substrate undergoes both longitudinal (U3) and lateral displacement (U1). The resultant force is only the longitudinal force (TF3) while the lateral force (TF1) is almost equal to zero. Fig.4-11 shows the variation of U1 with U3 for different inclination angles for tensile and compressive tests. It is seen that

loading at a 15^0 incline generates the maximum lateral displacement U1 and is comparable in magnitude to the longitudinal displacement U3. The value of U1 decreases with an increase in inclination, while pure shear testing (90^0 angle), as well as pure normal loading (0^0 angle), has a zero value for U1.

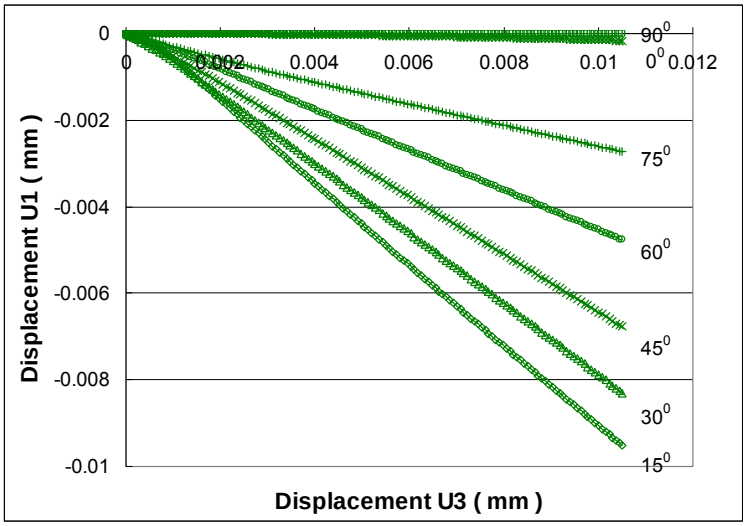

(a)

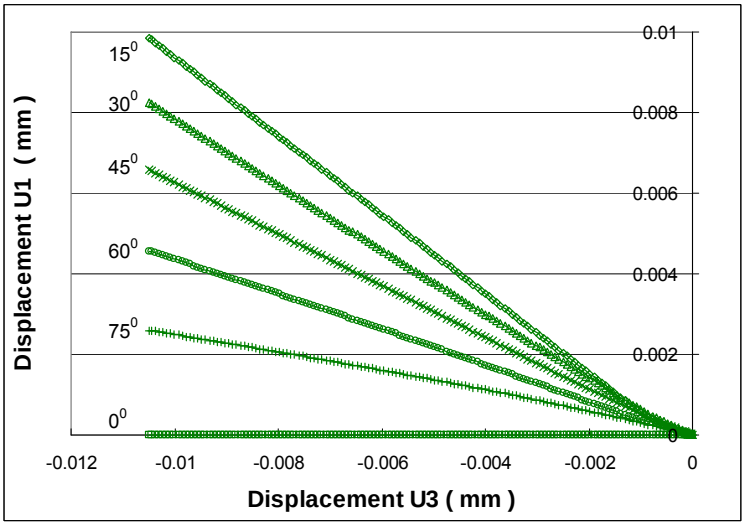

(b)

Fig.4-11 Longitudinal displacement U3 and lateral displacement U1 of upper substrate of single solder joint specimen for laterally unconstrained (a) tensile and (b) compressive testing.

Fig.4-12 shows how the total force (TF3) varies with longitudinal displacement

(U3) for tensile and compression testing at different inclination angles, which correspond to the load-deformation results obtained from actual tests. It is seen that with an increase in inclination, the stiffness and stress decrease, and a particularly large decrease in stiffness occurs for 75^0 and 90^0. For these curves, the failure points are indicated by the red dotted line in the figure.

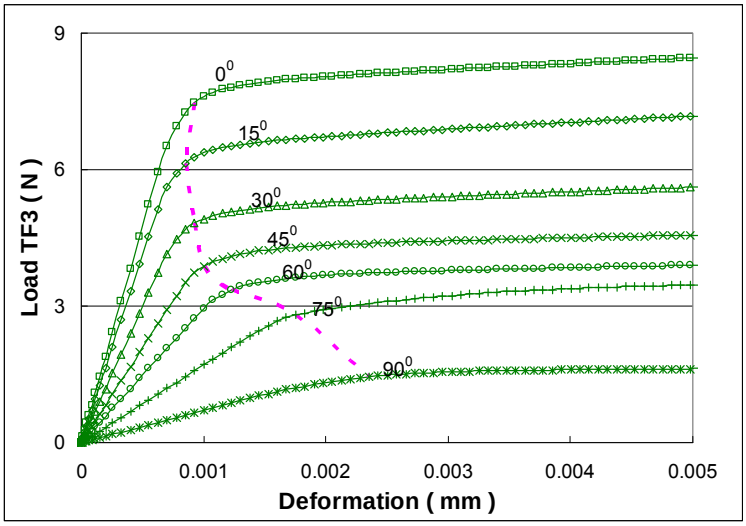

(a)

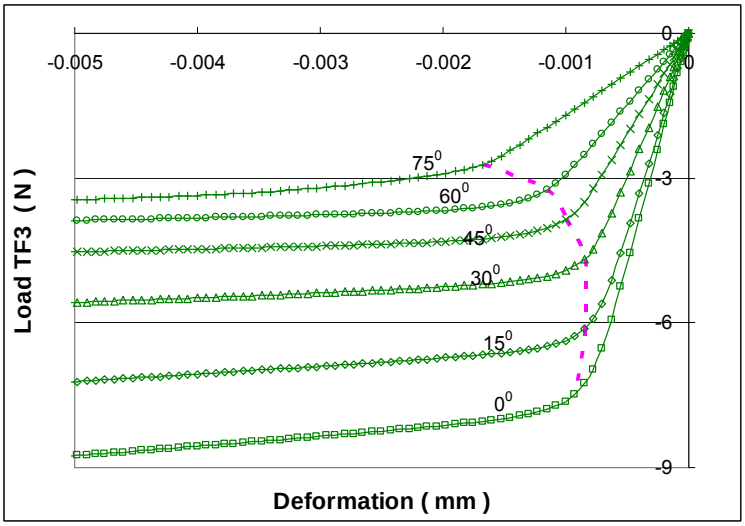

(b)

Fig.4-12 Load (TF3) and deformation (U3) response of single solder joint specimen subjected to laterally unconstrained (a) tensile and (b) compressive loading, and corresponding failure locus.

From the simulation results in Fig.4-12, the initial stiffness and values of the failure point can be determined, as listed in Table 4-2. It is seen that the stiffness decreases with an increase in inclination angle and reaches a minimum for pure shear (90^0 inclination). The resultant force on the specimen, TF3, can be resolved into normal and shear components on the joint, according to the angle α. Fig.4-13 Illustrates the corresponding failure force envelopes according to the values listed in Table 4-2. The failure force envelope resembles an ellipse; however, it is concave for loading around 75^0-90^0. This will be discussed later.

Table 4-2 Values of stiffness and failure force for single solder joint specimen subjected to laterally unconstrained loading.

Test mode (Defromation rate)	Incline angle α	Stiffness	Failure deformation	Failure force TF3 (N)		
	(Degree)	(N/mm)	(mm)	Resultant	Normal	Shear
Tension (0.00015mm/s)	0	9454.7	9.28E-04	7.46	7.46	0.00
	15	8159.8	8.53E-04	6.13	5.92	1.59
	30	5898.1	9.28E-04	4.82	4.18	2.41
	45	4151.8	1.00E-03	3.87	2.74	2.74
	60	2950.6	1.23E-03	3.35	1.67	2.90
	75	1689.4	1.75E-03	2.80	0.72	2.70
Shear	90	677.6	2.35E-03	1.44	0.00	1.44
Compression (0.00015mm/s)	75	1680.1	-1.68E-03	-2.72	-0.70	2.62
	60	2953.7	-1.15E-03	-3.25	-1.63	2.81
	45	4145.8	-1.00E-03	-3.87	-2.73	2.73
	30	5928.0	-8.53E-04	-4.67	-4.05	2.34
	15	8160.7	-8.53E-04	-6.12	-5.91	1.58
	0	9466.0	-9.28E-04	-7.48	-7.48	0.00

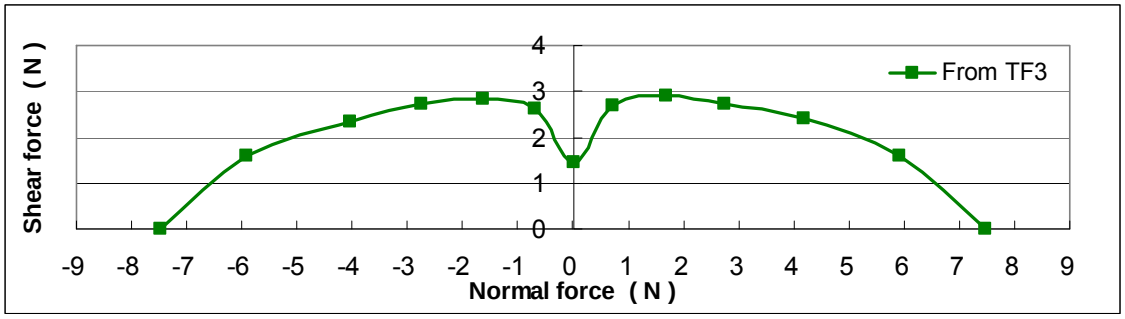

Fig.4-13 Failure force envelope of single solder joint specimens subjected to laterally unconstrained testing

Fig.4-14 shows a comparison between simulation (variation of total load (TF3) with deformation (U3)) and experimental results. In the simulations, no fracture strength between the solder bump and the substrates was specified; failure of the solder joint in a specimen corresponds to deviation from linearity in the load-deformation curves. In actual tests on single solder joint specimens, it is found that failure almost consistently corresponds to peeling of the copper pad from the substrate for tensile or tensile/ shear loading. This explains the large discrepancy between the simulation and the experimental results for tensile loading, and demonstrates that the failure mechanism under tension is not due to yielding of the solder bump in a solder joint. The discrepancy between simulation and experimental results shows the importance of experimental tests in obtaining the mechanical properties of solder joints.

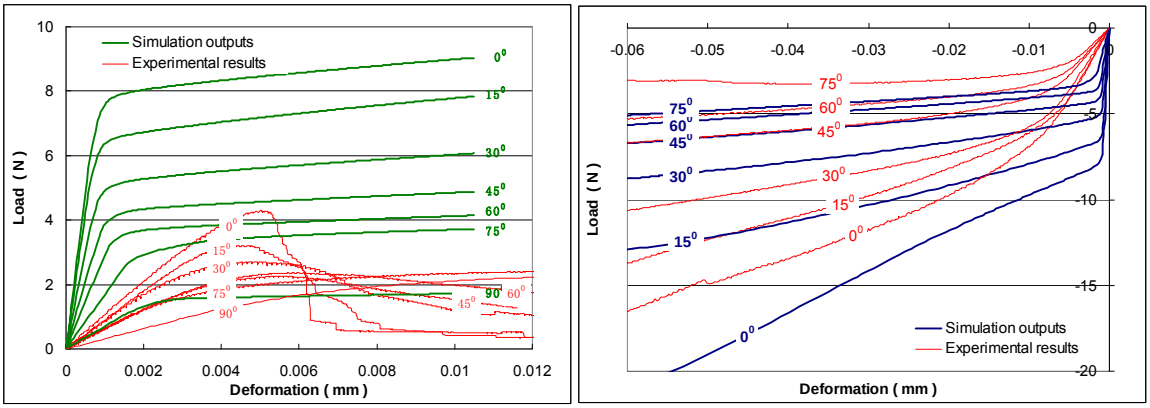

Fig.4-14 Comparison of simulation and experimental results for force-deformation response of single solder joint specimens

(b) Testing with lateral constraints

Fig.4-16(a) shows the fixture for tensile testing with lateral constraints, i.e., the upper adaptor and rod are constrained from lateral displacement. Because the interfaces between the specimen and the adaptors are inclined to the longitudinal direction, a lateral force will be generated at the interface during loading. This force is balanced by the forces on the laterally constrained surface of the rod. However, only the longitudinal force is recorded in each test. Therefore the force recorded is not the total force experienced by the specimen and the actual resultant force on the specimen is not in the longitudinal direction (not at the angle α but an angle β to the normal at the interface), as shown in the figure. However, the displacement of the specimen is only in the longitudinal direction.

Fig.4-16(b) shows the FEM model for simulation of laterally constrained tensile and compressive testing. In the model, the surface of the lower

substrate is fixed. The upper substrate is constrained in the lateral direction while its upper surface is assigned an upward velocity, e.g. 0.00015mm/s for tension, or a downward velocity for compression. The sum of the nodal forces and average nodal displacements of the upper surface of the upper substrate are calculated. These are compared to the force and deformation obtained in actual tests.

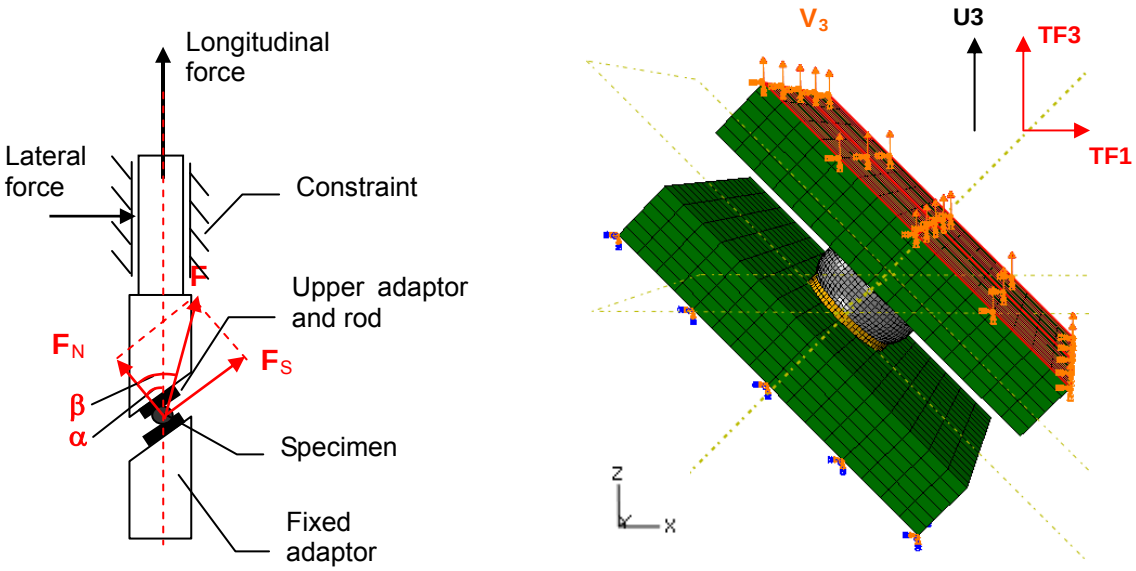

Fig.4-15 Illustration of laterally constrained testing and corresponding FEM model

The force-deformation responses from the simulations are plotted in Fig.4-16 and Fig.4-17 respectively for tensile and compressive testing. Plots of load TF3 versus deformation (U3) correspond to the load-deformation curves obtained from actual tests on single solder joint specimens. Plots of load TF1 versus deformation (U3) show the lateral load on the specimen which could not be recorded in actual tests. It is seen that for a 45^0 inclination, the lateral force is maximum. Existence of the lateral force component demonstrates that the longitudinal force TF3 does not represent the total force experienced by

the specimen. However, the force TF3 does describe the axial force on a specimen for loading in the longitudinal direction. The failure points in the plots of TF3 versus U3 are indicated by a dotted line.

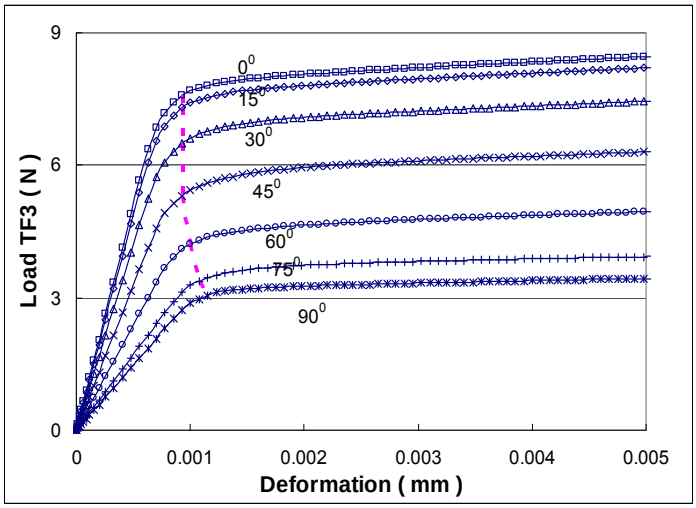

(a)

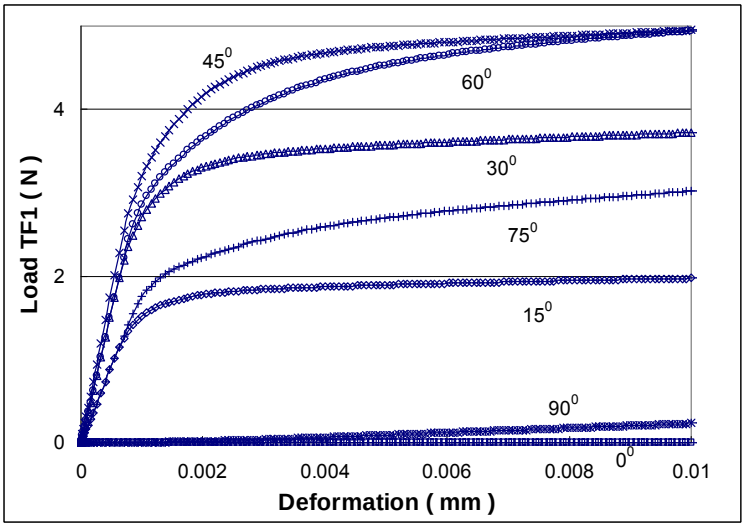

(b)

Fig.4-16 The (a) longitudinal load (TF3) and (b) lateral load (TF1) on single solder joint specimens subjected to laterally constrained tensile testing.

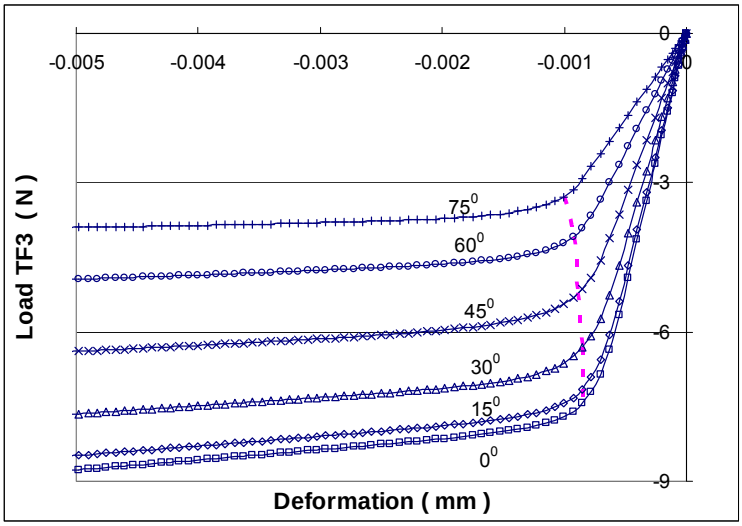

(a)

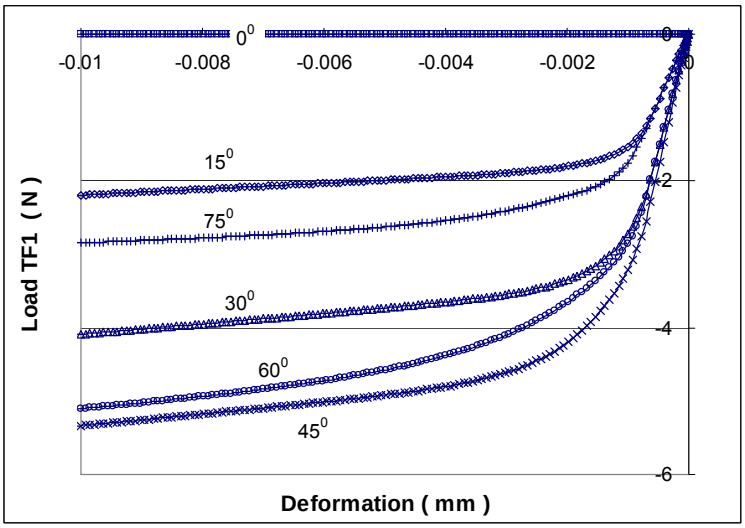

(b)

Fig.4-17 The (a) longitudinal load (TF3) and (b) lateral load (TF1) on single solder joint specimens subjected to laterally constrained compressive testing.

Comparison of the load-deformation responses corresponding to simulation and experimental results are also plotted in Fig.4-18 and Fig.4-19 for tensile and compressive testing respectively. The plots of the longitudinal load TF3 versus deformation U3 show similar discrepancies between simulation and experimental results as those for laterally unconstrained testing. In the figures, the load TF is the resultant of the longitudinal load TF3 and the lateral force

TF1. It is observed that the curves of the resultant total load TF for 0^0 and 90^0 are same as those of the longitudinal load TF1. However, for other inclination angles, the resultant total load TF has a larger value than the corresponding longitudinal load TF3.

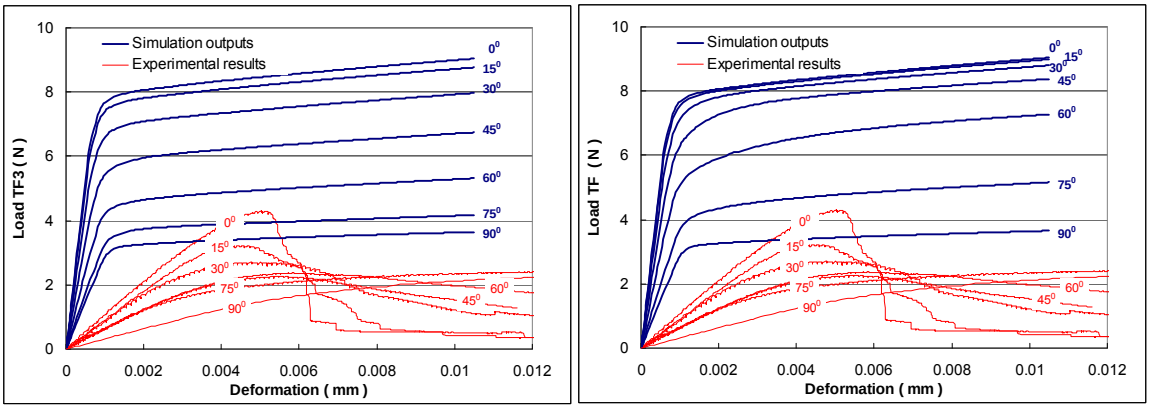

(a) (b)

Fig.4-18 Simulation results for tensile (a) longitudinal load (TF3) and (b) total load (TF) as a function of deformation (U3) and comparison with experimental results.

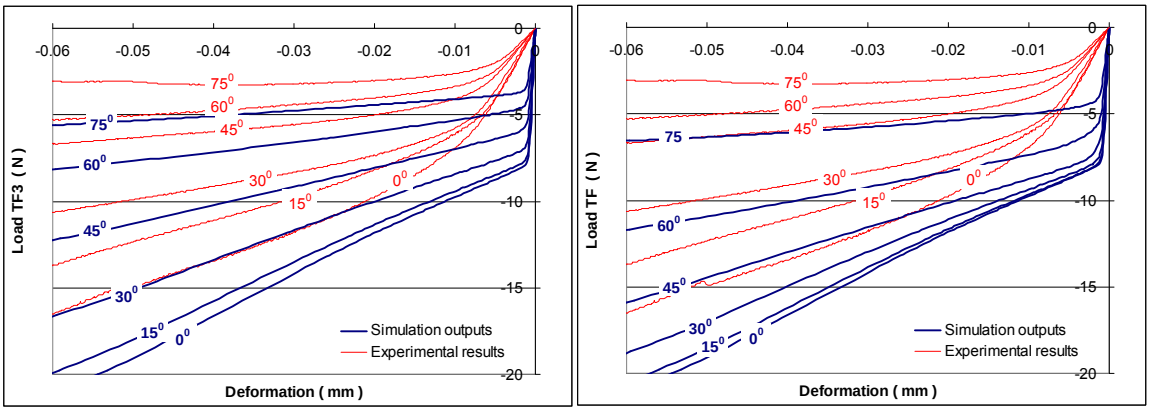

(a) (b)

Fig.4-19 Simulation results for compressive (a) longitudinal load (TF3) and (b) total load (TF) as a function of deformation (U3) and comparison with experimental results.

The failure points determined from the simulated load-displacement curves for laterally constrained tests and the corresponding values of elastic stiffness are

shown in Table 4-3. In actual tests on solder joint specimens, the experimental load-deformation curves correspond to the longitudinal load TF3 and displacement U3 of the simulations. For the purpose of comparison, the corresponding normal and shear components of the resultant force TF3 are obtained for various inclination angle α (as defined in Fig.4-15),

From TF3:

Normal component: $F_{TF3}^{N} = TF3 \cdot \cos(\alpha)$ (4-3)

Shear component: $F_{TF3}^{S} = TF3 \cdot \sin(\alpha)$ (4-4)

As highlighted earlier, the lateral force TF1 is not negligible in comparison with TF3 for laterally constrained testing. Thus, the total force (TF) experienced by a specimen should be the resultant of TF3 and TF1, and the corresponding direction of TF does deviate from the longitudinal direction, as shown in Fig.4-15,

Resultant force TF:

$$TF = \sqrt{(TF1)^2 + (TF3)^2} \quad (4\text{-}5)$$

$$\tan(\beta) = TF1/TF3 \quad (4\text{-}6)$$

where β is the angle between TF and the normal to the specimen (as defined in Fig.4-15). Thus, the corresponding normal and shear force components experienced by specimens in laterally constrained tests should be,

From TF:

Normal component: $F_{TF}^{N} = TF \cdot \cos(\beta) = TF3 \cdot \cos(\alpha) + TF1 \cdot \sin(\alpha)$ (4-7)

Shear component: $F_{TF}^{S} = TF \cdot \sin(\beta) = TF3 \cdot \sin(\alpha) + TF1 \cdot \cos(\alpha)$ (4-8)

Table 4-3 Stiffness and failure force from simulations of laterally constrained testing

Test mode (Defromation rate)	Angle α	Stiffness	Failure deformation	Failure force - TF3 (N)			TF1	Angle β	Failure force - TF (N)			Ratio (TF/TF3)	
	(Degree)	(N/mm)	(mm)	Resultant	Normal	Shear	(N)	(degree)	Resultant	Normal	Shear	Normal	shear
Tension (0.00015mm/s)	0	10126.73	9.28E-04	7.59	7.59	0.00	0.00	0.0	7.59	7.59	0.00	1.00	
	15	9655.05	9.28E-04	7.30	7.05	1.89	1.48	36.0	7.45	7.44	0.46	1.05	0.24
	30	8356.75	9.28E-04	6.49	5.62	3.24	2.61	68.9	6.99	6.92	0.98	1.23	0.30
	45	6565.94	9.28E-04	5.31	3.75	3.75	3.07	94.4	6.13	5.92	1.58	1.58	0.42
	60	4749.84	1.00E-03	4.21	2.11	3.65	2.86	107.4	5.09	4.58	2.22	2.18	0.61
	75	3421.33	1.08E-03	3.38	0.88	3.27	1.82	88.9	3.84	2.63	2.80	3.01	0.86
Shear	90	2949.86	1.15E-03	3.05	0.00	3.05	0.00	0.3	3.05	0.00	3.05		1.00
Compression (0.00015mm/s)	75	3429.50	-1.00E-03	-3.28	-0.85	3.17	-1.75	88.2	-3.72	-2.54	2.71	2.99	0.86
	60	4746.81	-9.28E-04	-4.09	-2.04	3.54	-2.75	106.6	-4.93	-4.43	2.17	2.17	0.61
	45	6507.99	-8.90E-04	-5.22	-3.69	3.69	-3.01	94.1	-6.02	-5.81	1.56	1.58	0.42
	30	8362.37	-8.53E-04	-6.31	-5.47	3.16	-2.50	67.9	-6.79	-6.72	0.99	1.23	0.31
	15	9760.49	-8.53E-04	-7.14	-6.90	1.85	-1.42	35.3	-7.28	-7.27	0.48	1.05	0.26
	0	10256.61	-8.53E-04	-7.43	-7.43	0.00	0.00	0.0	-7.43	-7.43	0.00	1.00	

Based on Table 4-3, the failure force envelope of single solder joint specimens subjected to laterally constrained testing at various inclination angles are plotted in Fig.4-20. It is seen that the profile of the envelope corresponding to the longitudinal force TF3 is different from the one calculated from the total force TF. Only at the points for pure tension, shear and pure compression, do the two envelopes match each other. The direction of the line connecting the data point and the coordinates origin corresponds to the angle α for the envelope obtained from TF3, and angle β for the envelope obtained from TF, as illustrated in Fig.4-20 of the two dot lines corresponding to a test with 45^0 inclination loading. It is seen that the shift of amplitude as well as direction of data point determined by TF3 to the data point determined by TF makes the envelope resemble an elliptical profile.

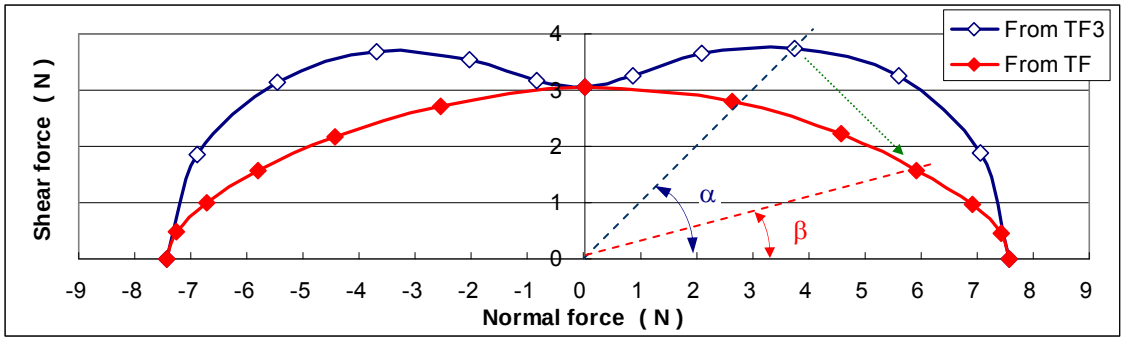

Fig.4-20 Comparison of failure force envelope obtained from longitudinal force TF3 and total force TF for single solder joint specimens subjected to laterally constrained testing.

4.2.3 Failure force envelope of solder joints

The discussion on laterally unconstrained versus constrained tests reveals the differences between these two test modes. In an unconstrained test, there is lateral displacement while constrained tests generate lateral forces in the specimen. The elastic stiffness of specimens subjected to loads at inclined angles was obtained with respect to the longitudinal direction, i.e. in terms of TF3 and U3, for comparison between the two loading modes; Fig.4-21 shows the overall variation stiffness with inclination angle – the amplitude decreases with inclination angle and reaches a minimum for pure shear. Between the laterally unconstrained and constrained modes, the elastic stiffness for constrained tests is always slightly larger.

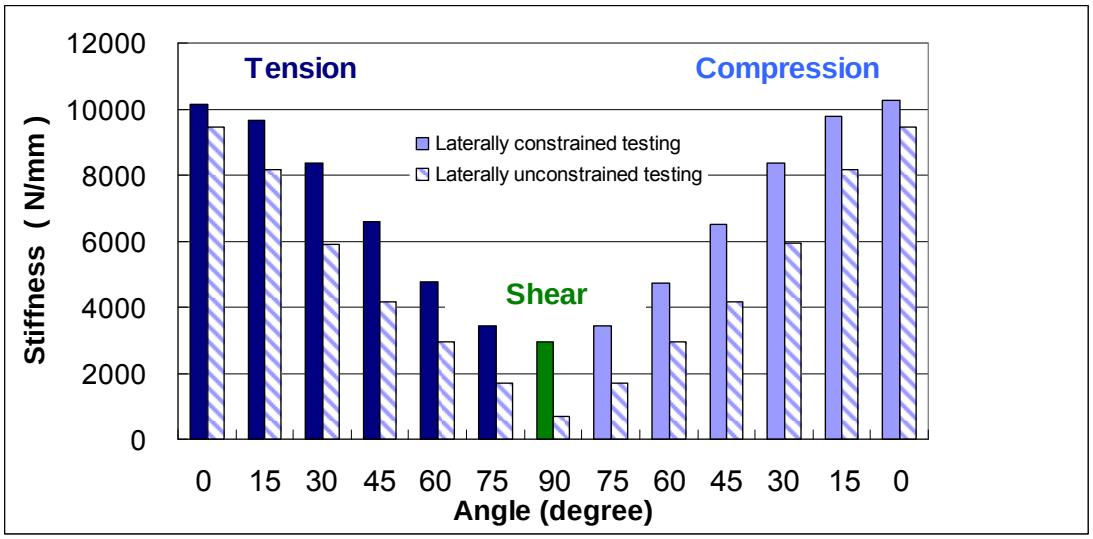

Fig.4-21 Comparison of longitudinal stiffness from simulations of single solder joint specimens subjected to laterally unconstrained and constrained testing.

It is more useful if the failure force of a single solder joint specimen is not coupled to the testing mode, as it is an intrinsic property of the specimen. This is supported by Fig. 4-22, in which the envelope derived from laterally unconstrained testing, based on TF3, and the envelope from constrained testing, based on TF, are coincident. This demonstrates that either test mode can yield the same elliptical failure force envelope if the normal and shear components are derived from the total force that the specimen experiences.

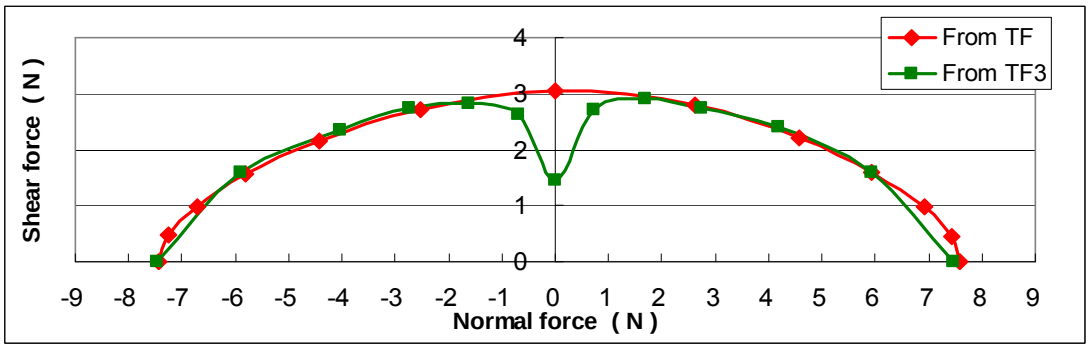

Fig. 4-22 Comparison of failure force envelope derived from TF3 for laterally unconstrained testing and TF for laterally constrained testing.

It is noted that the TF3 envelope for unconstrained testing exhibits a concavity when the inclination angle exceeds 60^0. The strength corresponding to pure shear is also smaller than that derived from TF for constrained testing. This is caused by bending of the specimen, which becomes more significant when the inclination angle increases towards 90^0 (pure shear) in unconstrained testing. As illustrated in Fig.4-23 (for the instants of failure), the resultant displacements of the nodes on the upper substrate are almost all in the same direction, for testing up to 60^0 incline angle, after which, the distribution of resultant displacement on the upper substrate changes gradually and bending becomes obvious for pure shear (90^0).

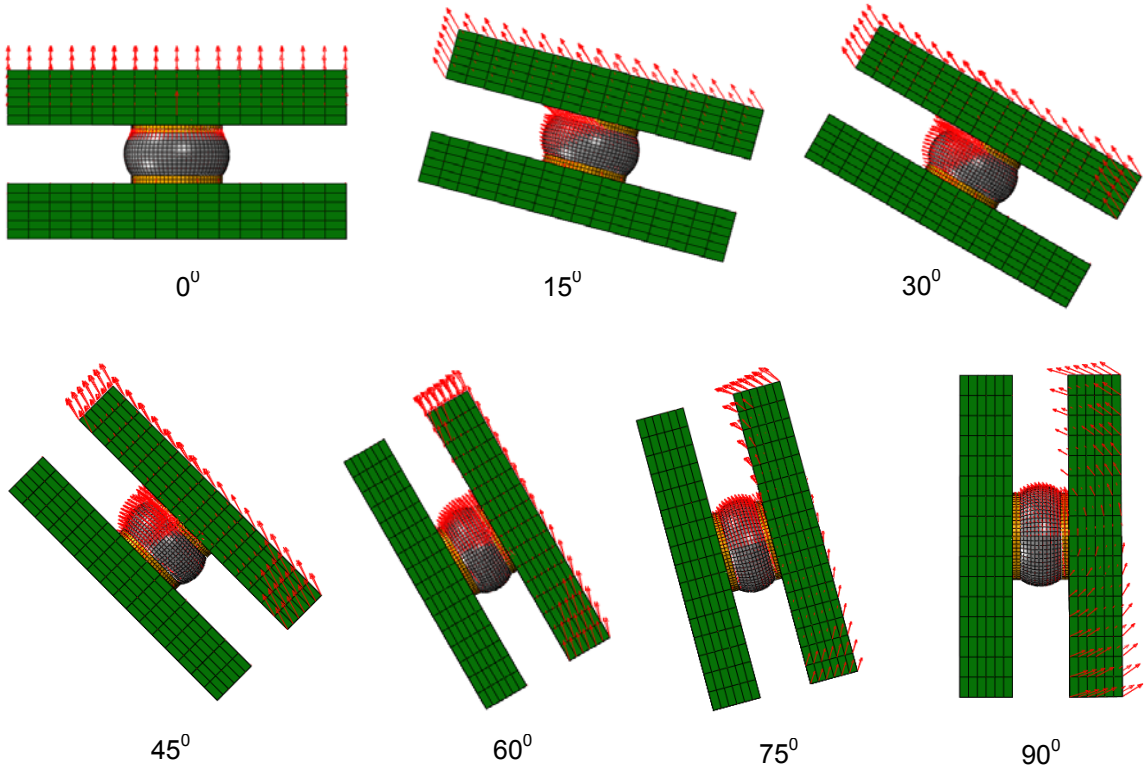

Fig.4-23 Illustration of the direction of resultant displacement in laterally unconstrained testing mode at various incline angles

In this study on single solder joints, the tests corresponded to laterally

constrained conditions. The load-deformation curve is based on the longitudinal load and displacement defined by TF3 and U3 in FEM simulations. An attempt is made to use the failure force envelope corresponding to the longitudinal force from experimental tests to derive the failure force envelope associated with the total force (incorporating the lateral force) that a specimen experiences. The plots in Fig.4-24 show the relationship between the longitudinal load TF3 and the lateral load TF1 for constrained tensile and compressive testing, based on simulation results. The failure point on each curve is also indicated. It is observed that all the plots are almost linear prior to failure, after which the curves become nonlinear. This demonstrates that for each inclination angle, the ratio of TF1 to TF3 for constrained tests ($K(\alpha)$) remains constant until specimen failure commences. Therefore, based on Eqs.(4-3)~(4-8), the following relationships are derived:

$$\frac{F_{TF}^{N}}{F_{TF3}^{N}} = \frac{TF3\cdot\cos(\alpha)+TF1\cdot\sin(\alpha)}{TF3\cdot\cos(\alpha)} = \frac{TF3\cdot\cos(\alpha)+K(\alpha)\cdot TF3\cdot\sin(\alpha)}{TF3\cdot\cos(\alpha)} = \frac{\cos(\alpha)+K(\alpha)\sin(\alpha)}{\cos(\alpha)} = \kappa(\alpha) \tag{4-9}$$

$$\frac{F_{TF}^{S}}{F_{TF3}^{S}} = \frac{TF3\cdot\sin(\alpha)+TF1\cdot\cos(\alpha)}{TF3\cdot\sin(\alpha)} = \frac{TF3\cdot\sin(\alpha)+K(\alpha)\cdot TF3\cdot\cos(\alpha)}{TF3\cdot\sin(\alpha)} = \frac{\sin(\alpha)+K(\alpha)\cos(\alpha)}{\sin(\alpha)} = \kappa'(\alpha) \tag{4-10}$$

This indicates that the ratio of the failure force components (normal and shear) derived from the total force TF and the longitudinal force TF3 is constant for each inclination angle α. Therefore, when the ratio ($\kappa(\alpha)$ and $\kappa'(\alpha)$) for each angle α is obtained, the yield force envelope in terms of F_{TF3}^{N} and F_{TF3}^{S} can be

converted to a yield force envelope in terms of F_{TF}^{N} and F_{TF}^{S}.

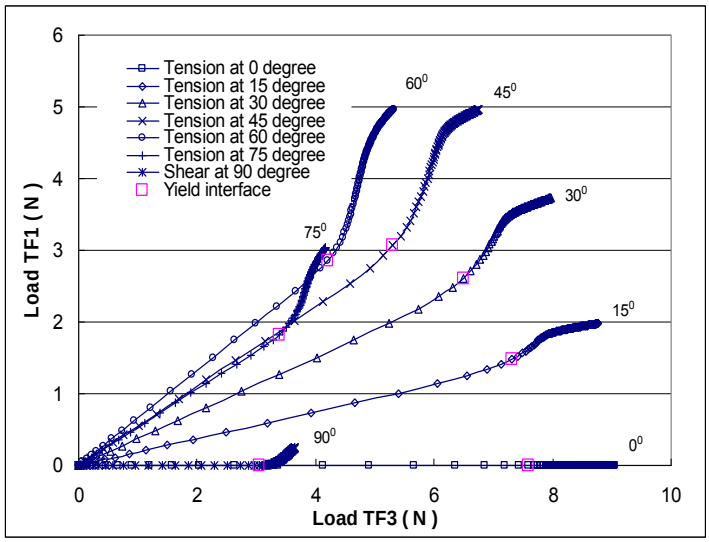

(a)

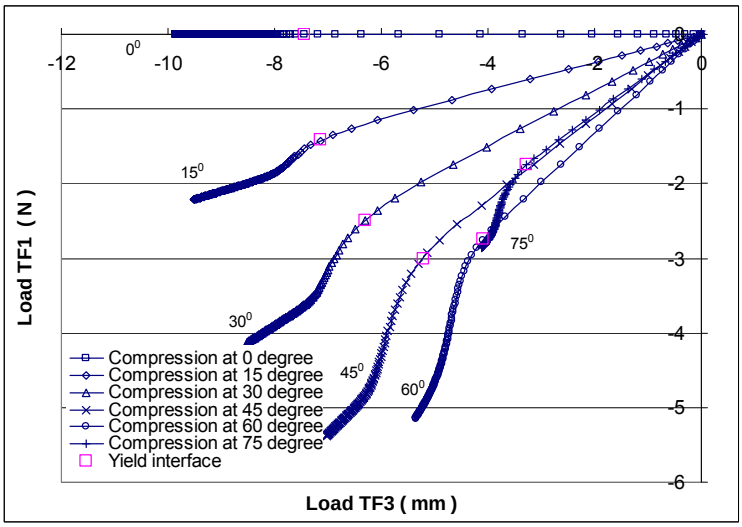

(b)

Fig.4-24 Relationship between longitudinal load (TF3) and lateral load (TF1) for single solder joint specimens subjected to laterally constrained (a) tensile and (b) compressive testing.

Based on the simulation results, the ratios $\kappa(\alpha)$ and $\kappa'(\alpha)$ are calculated for each inclination angle α (Table 4-3). The normal and shear force components obtained from tests (Table A-5 in *Appendix A*) were multiplied by the ratios $\kappa(\alpha)$ and $\kappa'(\alpha)$ respectively. This converts the failure force envelopes in terms

of the measured longitudinal load (Fig.4-9) into failure envelopes with respect to the total load for laterally constrained tests, as shown in Fig.4-25 (the corresponding deformation rates are also indicated).

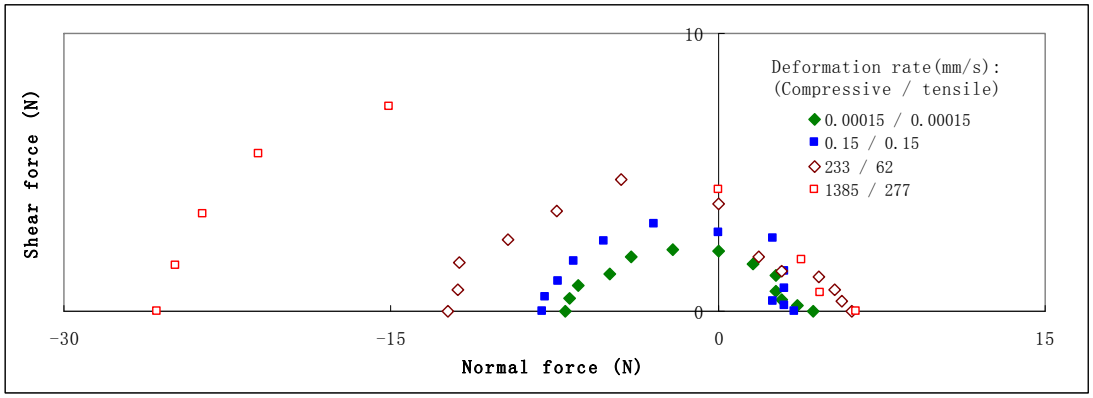

Fig.4-25 Yield force envelope based on total load, converted from experimental results of longitudinal failure force

It is seen that after conversion, the envelopes resemble an elliptical profile more closely, especially in the compression/shear region. For example, Fig.4-26 shows that the fit of an ellipse to the experimental failure force for a deformation rate of 0.00015mm/s results in:

$$\frac{(F_N + 1.89)^2}{5^2} + \frac{(F_S)^2}{2.16^2} = 1 \qquad (4\text{-}11)$$

The fitted profile is an eccentric ellipse; the semi-major and semi-minor axes of the ellipse are 5 N and 2.16 N respectively, and its center corresponds to a normal force of -1.89 N.

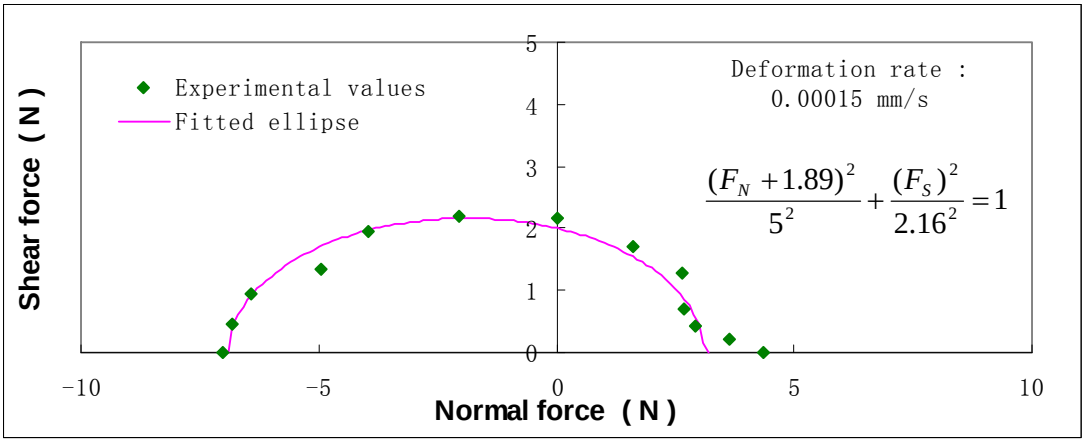

Fig.4-26 Fit of experimental failure force at deformation rate of 0.00015mm/s by an ellipse.

For quasi-static tests conducted using an Instron micro-tester, the deformation rate is equal to the constant speed of the loading rod. However, for dynamic tests using the miniature impact tester, the specimen deformation rate history is not constant (this is common in bar test arrangements, such as a Hopkinson bar system). The deformation rates indicated in Fig.4-25 for dynamic tests are the average deformation rates until the time just before failure. The dynamic deformation rates for tension are different from those for compression; the maximum deformation rate for compressive tests is 1385mm/s, while it is only 277mm/s for tensile tests. Therefore, in establishing the failure envelopes, experimental values from compression tests for a deformation rate of 1385mm/s are excluded due to the lack of matching values from tensile tests.

As the envelopes are ellipse-like, the empirical equation proposed to fit these curves is:

$$\frac{(F_N + R_{N0})^2}{R_N{}^2} + \frac{(F_S)^2}{R_S{}^2} = 1 \qquad (4\text{-}12)$$

where the major semi-axis R_N and minor semi-axis R_S as well as the eccentric distance R_{N0} are deformation rate dependant. It is assumed that the envelopes for different deformation rates are similar; therefore the sizes and positions of these ellipses are determined by the failure forces for pure compression (F_C) and pure tension (F_T),

$$\begin{cases} R_{N0} = (F_C - F_T)/2 \\ R_N = (F_C + F_T)/2 \\ R_S = 2.16R_N/5 \end{cases} \quad (4\text{-}13)$$

The failure forces F_C and F_T for pure compression and tension are then fitted using a power law equation that depends on the deformation rate $\dot{D}$ (*mm/s* in unit),

$$\frac{F}{F_0} = 1 + \left(\frac{\dot{D}}{D}\right)^{1/q} \quad (4\text{-}14)$$

The fitted curves are plotted together with the experimental values, as shown in Fig.4-27, where the constants (F_0, D and q) are also indicated respectively for failure under pure compression and tension.

Test mode	Deformation rate *(mm/s)*	Failure force *(N)*	Fitted failure force *(N)*
Pure tension	0.00015	4.37	4.17
	0.0015	4.12	4.31
	0.015	4.44	4.51
	62	6.16	5.98
	277	6.34	6.46
Pure compression	0.00015	7.03	6.88
	0.0015	6.87	7.13
	0.015	7.60	7.50
	0.15	8.07	8.05
	233	12.38	12.38

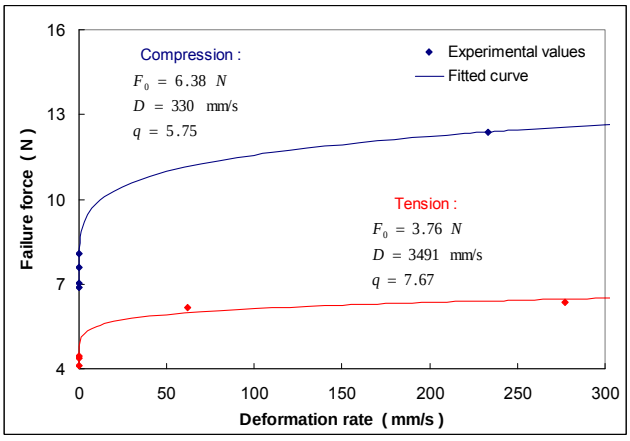

Fig.4-27 Values of failure force of solder joint specimens subjected to pure compression and pure tension, and the corresponding curve fits

Based on the Eqs.(4-12)~(4-14), the failure envelopes for combined normal and shear force are then established in terms of the deformation rate $\dot{D}$ (*mm/s*),

$$\frac{[F_N + (1.251 + 0.579\dot{D}^{0.202})]^2}{1} + \frac{(F_S)^2}{0.187} = 5.1 + 1.779\dot{D}^{0.162} \qquad (4\text{-}15)$$

Fig.4-28 shows a comparison between the failure force envelopes from experimental values and the preceding equation; Fig.4-29a shows a series of envelopes calculated from the preceding equation for deformation rates ranging from 0.0001mm/s to 250mm/s. The curves are plotted as complete envelopes, symmetric about the horizontal axis. The diagram shows clearly that the envelope changes with deformation rate. If a normalized solder joint height is used (e.g. 0.28mm for the specimens in this study), the failure force envelope can be plotted in terms of strain rate. Fig.4-29b shows the envelopes for strain rates corresponding to the deformation rates in Fig.4-29a. It is seen that the range of 0.00036/s to 893/s is sufficiently large to encompass the actual strain rates.

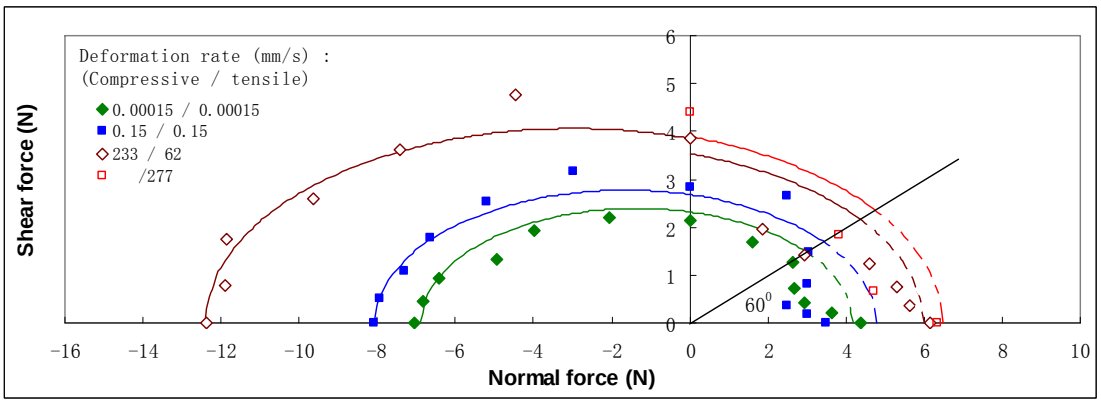

Fig.4-28 Comparison of the fitted failure force envelopes with experimental values for deformation rates experienced by solder joints in tests

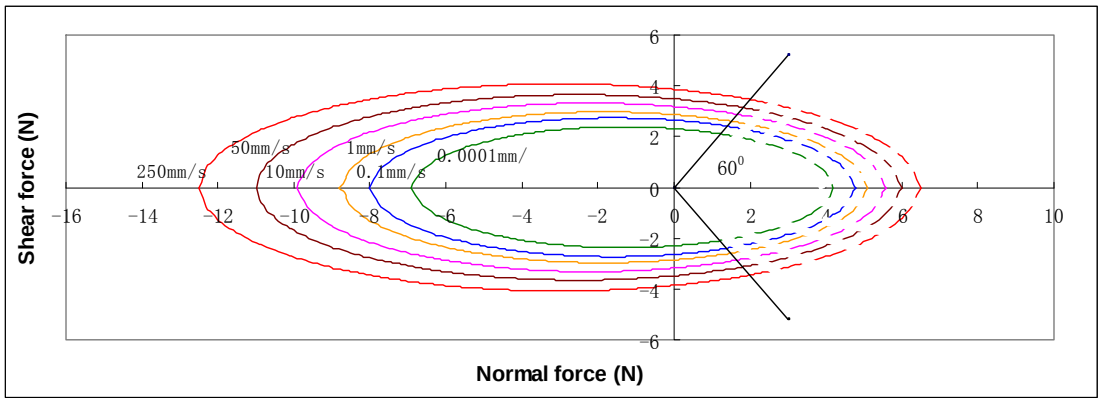

(a) Failure envelopes for different deformation rates

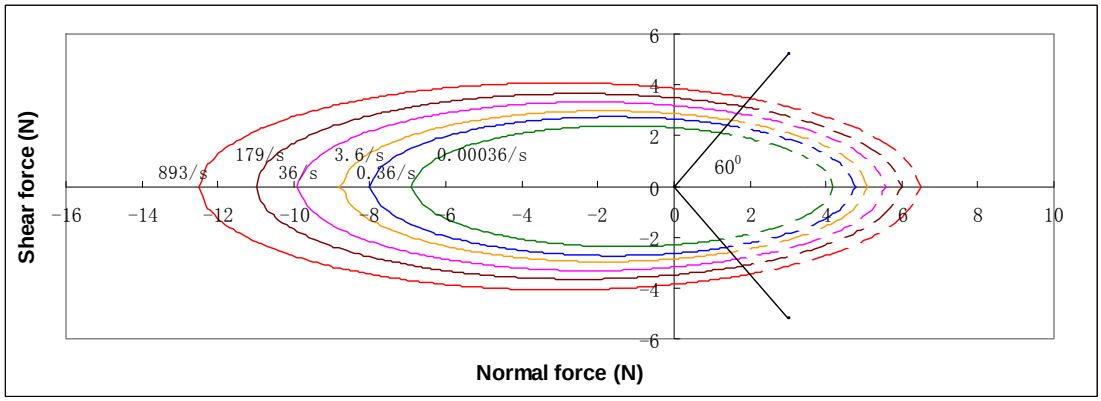

(b) Failure envelopes for different strain rates

Fig.4-29 Elliptical failure force envelopes for single solder joint, in terms of (a) deformation rates from 0.0001mm/s to 250mm/s and (b) corresponding strain rates ranging from 0.00036/s to 893/s, based on the fitted equation

The preceding section describes approximation of the failure envelope for a single solder joint by an ellipse for both tensile and compressive regions. It is observed that the fit for the compression region is better than that for tensile response. This is probably because the failure modes under compression and tension differ. For the solder joints studied, separation between the copper pad and substrate (pad-peel off) is essentially the failure mode under pure tension or combined tension-shear. For compression or compression-shear loading, the failure of solder joints is associated with yield of the solder bump. However, separation of the substrates after compressive testing also causes

pad-peel failure. Thus, microscopic observation of such solder joint failure shows similar images for both tensile and compressively loaded specimens, as illustrated in Fig. 4-30a. Further more, it is observed that the post failue region of the tensile load-deformation curves becomes less steep with the increase of incline angle (Fig. 4-30b). For incline angels great than 60 degree, the post failure region shows somewhat plastic deformation instead of brittle breakge; this shall be associated to the yielding and plastic deformation of solder bulk under such tension-shear loadings. This phenomenon demonstrates that there are a transition of failure mode from pad-peel dominant failure to solder bump yielding dominant failure. Therefore, a straight line was drawn to devide the tensile region into two parts which are associated with the different dominant failure modes. The region with incline angles less than 60 degree is pad-peel failure dominant where elliptical fitting shows somewhat over estimation of solder joint failure strength (plotted in dotted lines).

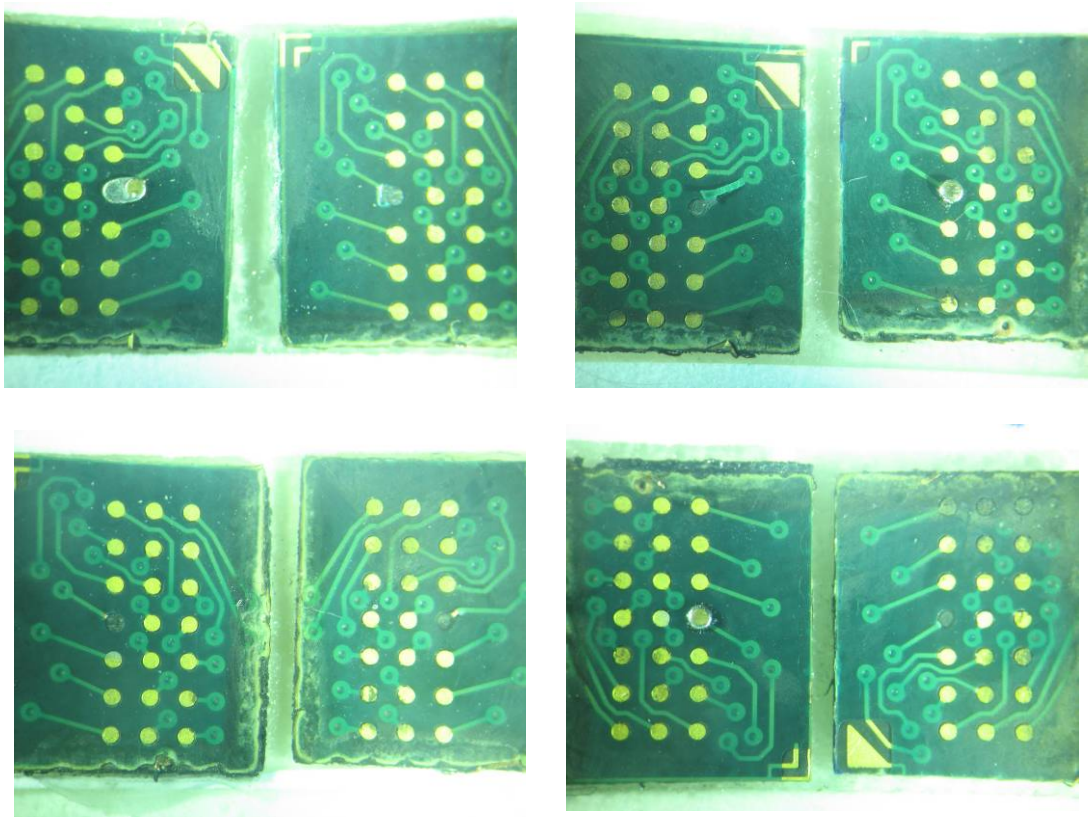

(a)

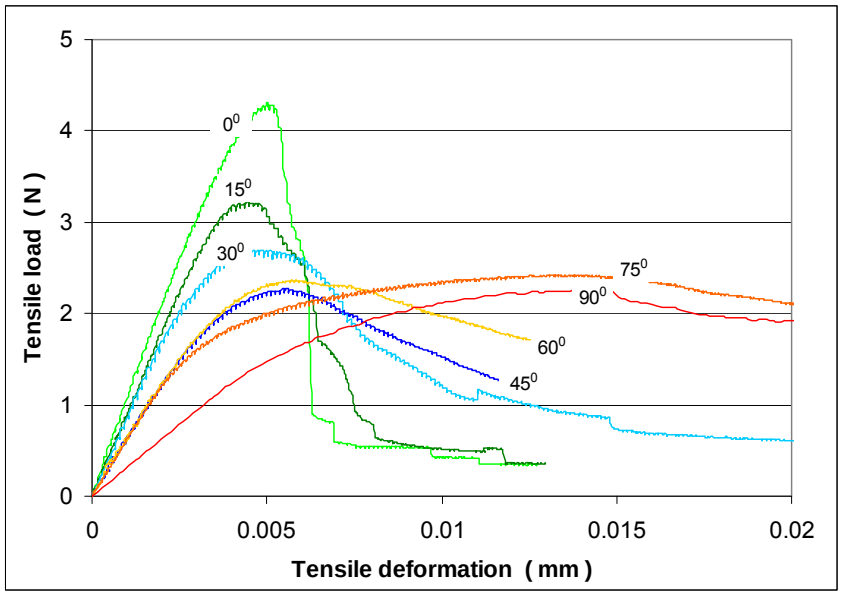

(b)

Fig. 4-30 (a) Post-test microscopic images of (tension and compression) solder joints and (b) illustration of tensile load-deformation curves at different inclination angles at a deformation speed of 0.00015mm/s

4.3 Constitutive and geometrical modeling of solder joints

4.3.1 Variation of load with deformation for uniaxial loading

The mechanical responses of single solder joint specimens for pure uniaxial compression and tension are analyzed and characterized. Dynamic uniaxial compression and tension tests on single solder joint specimens corresponding to two loading speeds are conducted. Quasi-static tests at three rates of deformation are also undertaken using an Instron micro-tester. For each loading speed, the overall average load-deformation response is obtained from five valid tests. Fig.4-31 shows the average load-deformation relationships for single solder joint specimens subjected to static and dynamic tension and compression.

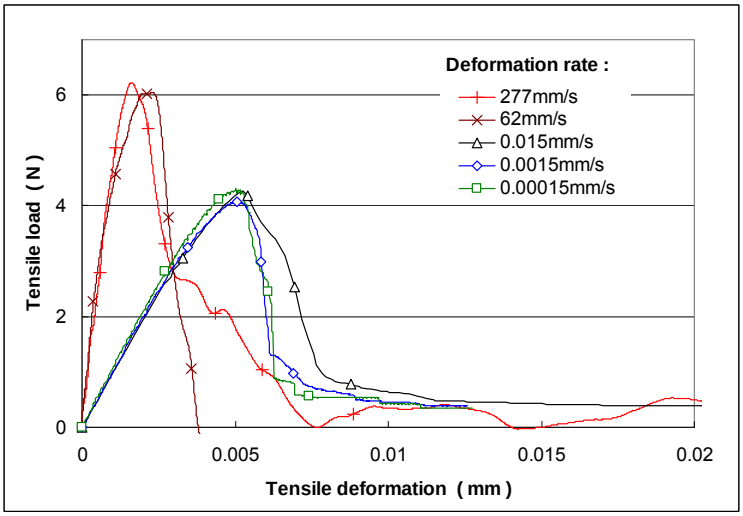

(a)

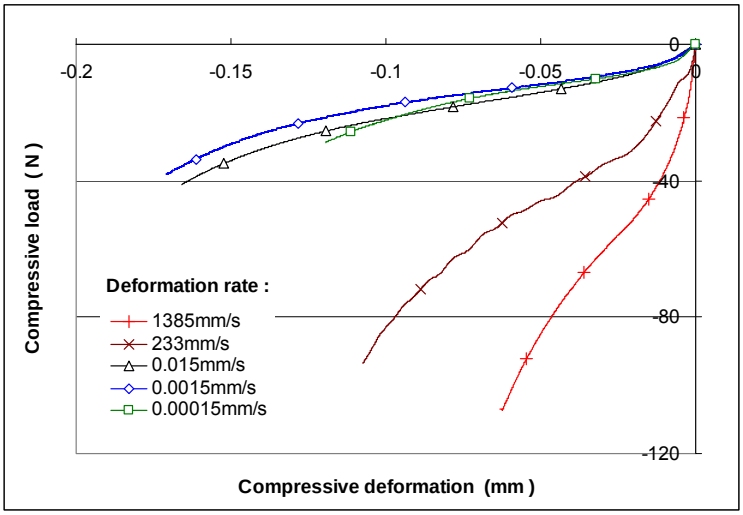

(b)

Fig.4-31 Average load-deformation curves for single solder joints (a) tension; (b) compression

Differences in the quasi-static responses for both tensile and compressive deformation are too small to discern any definite trends with regard to rate sensitivity for deformation speeds of 0.00015mm/s to 0.015mm/s. However, rate sensitivity is obvious when the dynamic results are compared with the quasi-static responses. The data also shows that the degree of rate sensitivity is related to the mode of loading. The compressive load increases significantly with loading speed, particularly at higher speeds. For tensile tests, the maximum point on the load-deformation curve signifies fracture of the joint (which is primarily separation between the Cu pad and the substrate in this study).

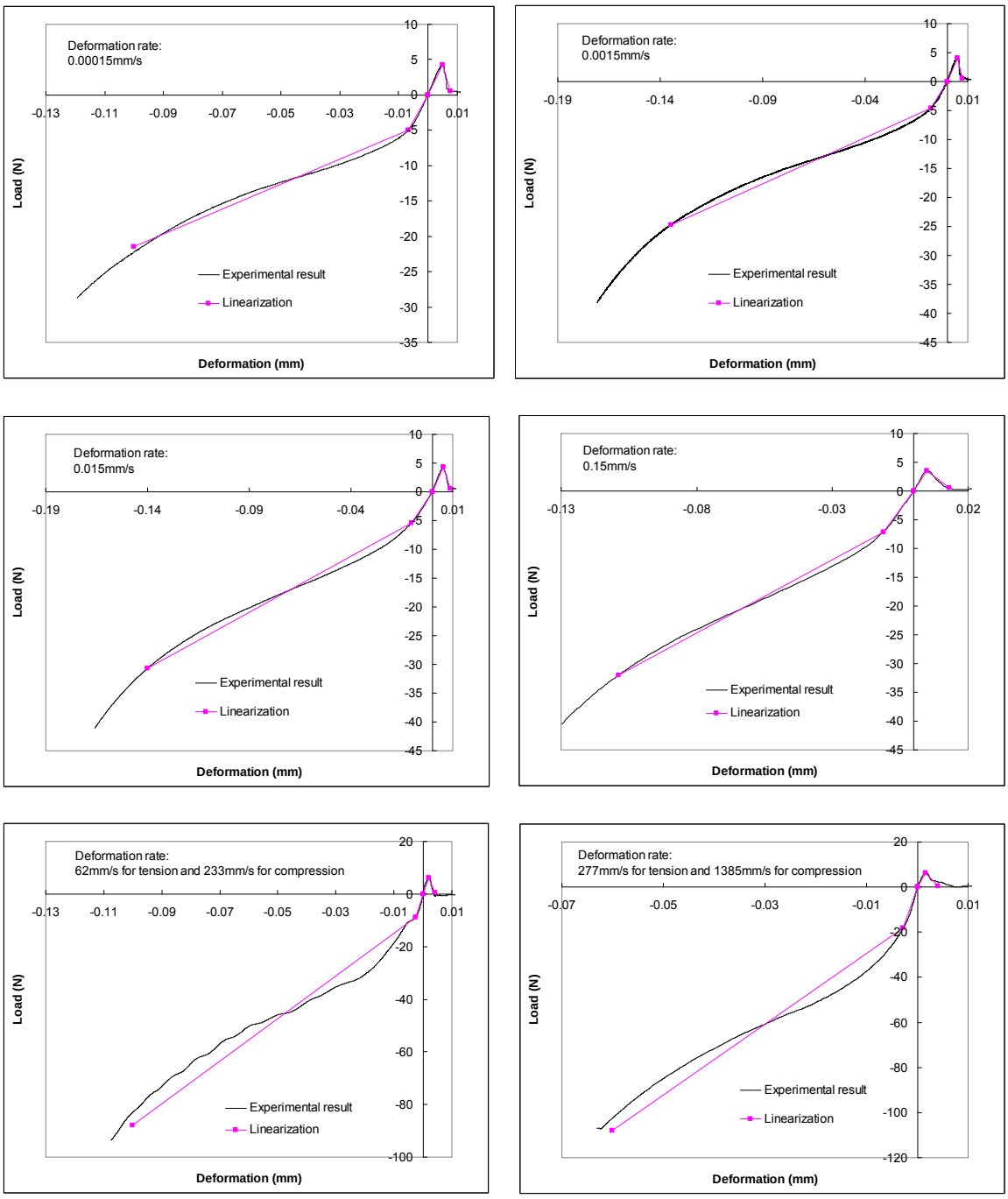

Fig.4-32 Load-deformation curves for pure uniaxial tension and compression, and corresponding bi-linear approximation

In order to incorporate these characteristics in FEM simulations, a simplification of these load-deformation curves is made. Fig.4-32 shows the load-deformation curves for both tensile and compressive tests in terms of deformation rates. It is seen that the initial responses are almost linear and the stiffness is nearly same for both tension and compression. The curve then

either drops quickly due to breakage of the solder joint for tension, or proceeds into post-yield hardening with a lower stiffness for compression. As a solder joint also serves as an electrical connection in IC packages, the breakage of solder joints under tension is more critical than yielding under compression. A bi-linear approximation is made to the solder joint response for both tension and compression. As shown in Fig.4-32, a bi-linear curve adequately represents the initial response of solder joint for tension and compression, which is characterized by linearity. It also approximates the post-yield response for compression.

The initial portion of the bi-linear approximation is from the origin to the yield point of the experimental curve, whereby the yield point is determined from a 0.2% offset strain based on the stand-off height of the solder joints (0.28mm in this study). As illustrated in Fig.4-33, the yield point for tension is quite close to the ultimate load, where solder joint breakage occurs.

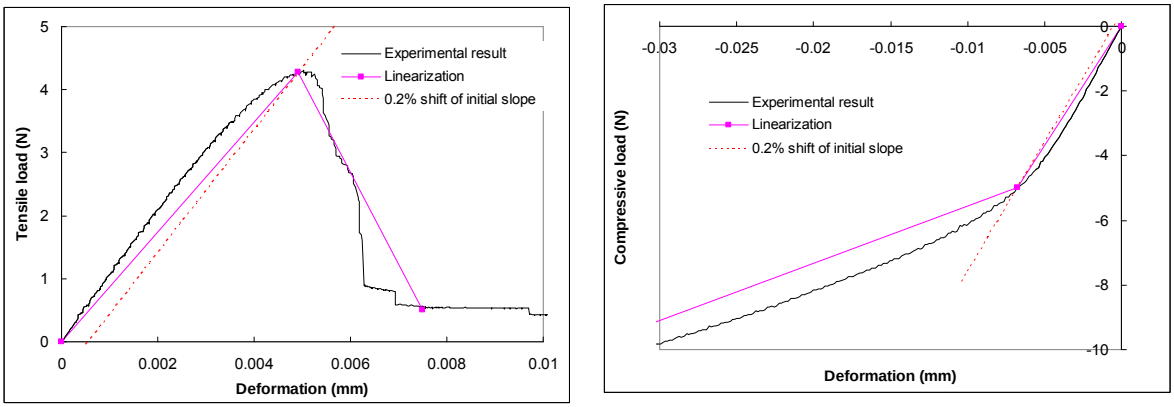

Fig.4-33 Determination of yield points in tensile and compressive load-deformation curves

4.3.2 Simplification of solder joint model

This study involves subjecting single solder joint specimen to quasi-static and dynamic loading, to obtain force-deformation curves. These force-deformation relationships are useful for characterizing the mechanical response and quality of a solder joint. As an actual solder joint has a barrel-like profile, it is not obvious if an equivalent stress-strain relationship can be derived from the force-deformation values for use as material properties in numerical simulations. To examine this, the barrel-like profile of the solder bump in a single solder joint is approximated by a cylinder. This facilitates the conversion of force-deformation data from experiments into equivalent stress-strain responses based on the assumption of a cylindrical profile.

Numerical simulations are conducted to validate this approximation. Fig.4-34 shows the barrel geometry established from microscopic measurements of solder joint dimensions. A cylindrical approximation is made and the solder mask area (0.43mm diameter) and solder bump height (0.2mm) are taken to be the cross-sectional area and height of the cylinder. As this approximation process constitutes a study of methodology, the material properties prescribed for the simulations are based on the quasi-static elastic-plastic response of the BT substrate, Cu and lead free solder (Sn96.5-Ag3.0-Cu0.5), without considering all the actual parameters in a solder joint, such as the inter-metallic layer and the tensile bond strength. For the simulations, the surface of one substrate is constrained, while the other substrate is laterally constrained, and its upper surface is assigned a constant speed

(0.00015mm/s) to deform the solder. The deformation of the solder joint between the two substrate surfaces and the load on the moving surface are calculated. These quantities are similar to what are obtained from experimental tests. The respective predicted load-deformation responses for uniaxial tension, compression and shear loading of the barrel and cylinder models are compared to validate the approximation by a normalized cylindrical solder joint.

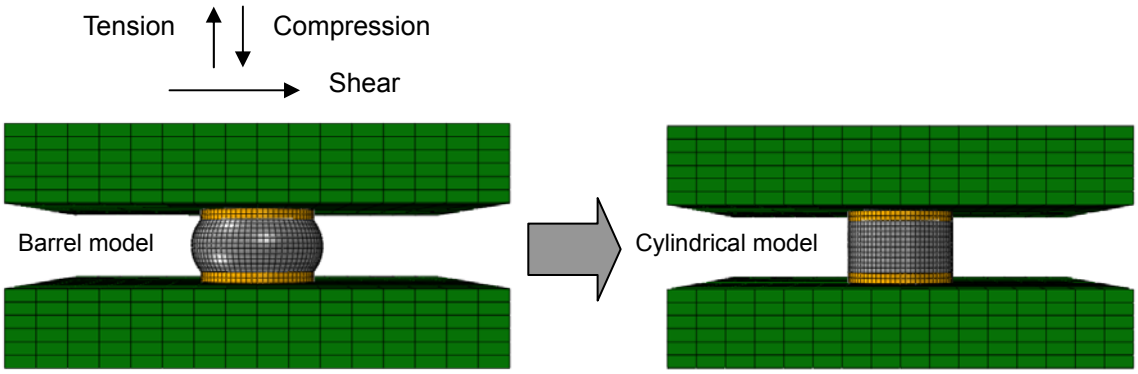

Components	Young's modulus (Gpa)	Yield/Hardening (MPa/ε_p)	Poisson's ratio	Density (Kg/m^3)
Solder (Sn96.5Ag3.0Cu0.5)	41.659	(39.437 , 0) ; (77.818 , 0.377)	0.4	7400
Copper pad	120		0.34	8930
BT substrate	26		0.39	2800

Fig.4-34 Approximation of barrel geometry by a cylinder and prescribed properties of actual joint component materials (BT, Cu and solder)

Fig.4-35 shows simulation results for quasi-static tension, compression and shear of a single solder joint specimen with a barrel and a cylindrical solder bump geometry (based on quasi-static properties of Sn96.5-Ag3.0-Cu0.5). The cylindrical model displays a lower strength than the barrel model for tension, compression and shear after the yield point. This is expected, as the cylinder is essentially a truncation of the bulged surface of the barrel to a straight vertical profile.

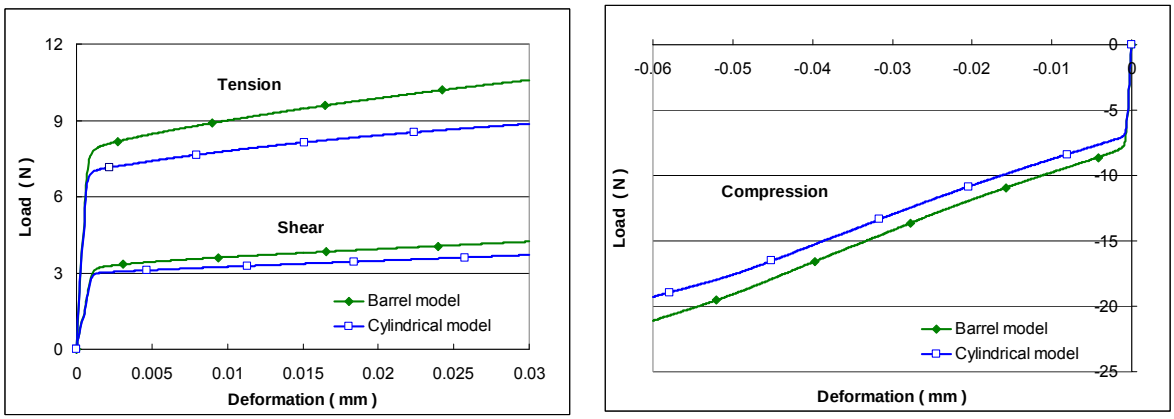

(a) (b)

Fig.4-35 Comparison of load deformation curves for barrel and cylindrical models based on actual properties of component materials (a) tension and shear; (b) compression

One approach to minimize this discrepancy is to adjust and enhance the solder properties in the cylindrical model. A quantitative analysis of the two models is therefore undertaken to determine a factor (*K*) that defines the ratio of the load on the barrel model to that on the cylindrical model for a common deformation, as shown in Fig.4-36. For tensile loading, the ratio increases after yield, while the reverse is observed for compression. The average of the tensile and compressive values is also plotted and this exhibits an approximately constant value after yield. Therefore, a compromise based on this is adopted to generate a stress-strain curve for the solder material properties to be prescribed to the cylindrical model; i.e. the stress-strain curve of the actual solder material is scaled by the ratio corresponding to the approximately constant average value in the post-yield region of the curve (e.g. 1.135 in this case). Tensile, compressive and shear load-deformation curves for the barrel and cylindrical models, based on actual and scaled material properties are presented in Fig.4-37. It shows a significant reduction

in the difference in response between the two model geometries, compared to the results presented in Fig.4-35. For tension and compression, there is close agreement in the initial portion, after which a small degree of divergence appears; for shear, a slight difference is observed in the region after yield, but this reduces with deformation thereafter.

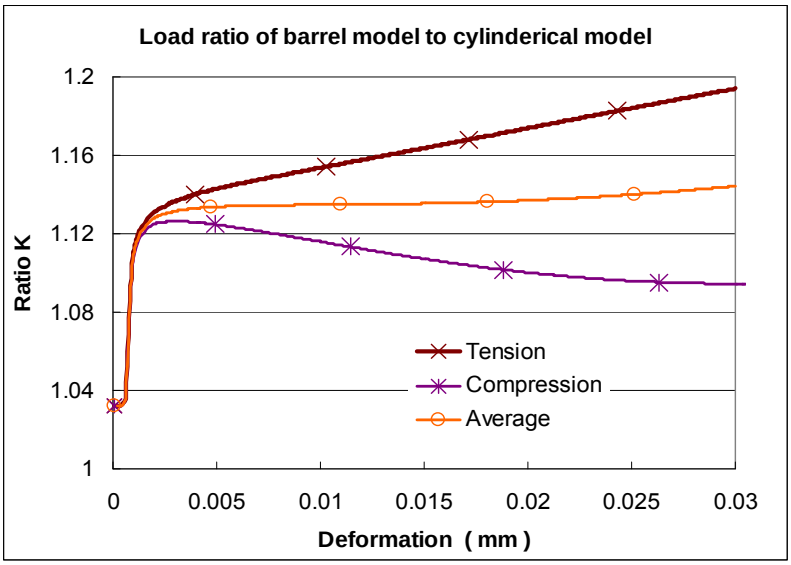

Fig.4-36 Ratio of load on barrel model to that on a cylindrical model, for tension and compression, as well as the average of the two

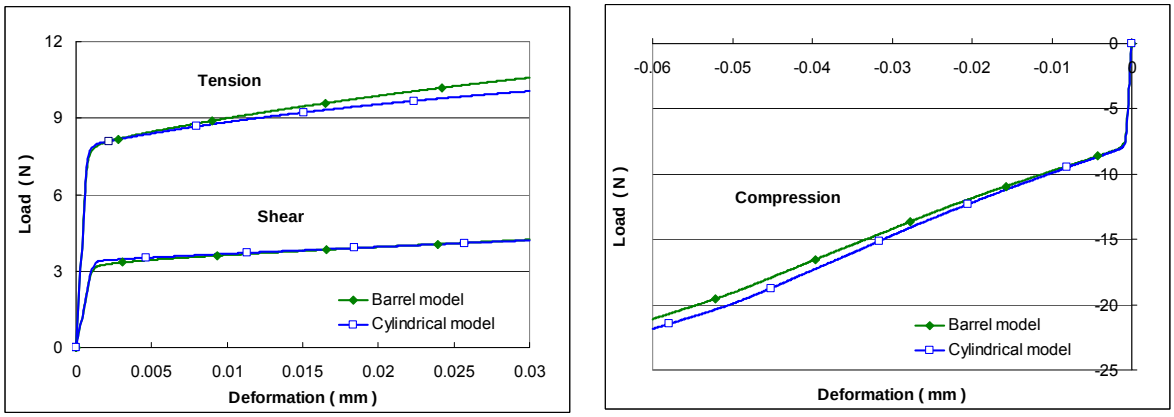

(a) (b)

Fig.4-37 Load-deformation curves for barrel and cylindrical models, based on actual and adjusted solder material properties under (a) tension and shear; (b) compression.

The relative error in load is also determined for the adjusted solder model. This is defined as the difference between load associated with the cylindrical model and that for the barrel geometry divided by the latter; i.e. $(1/K-1)$. Fig.4-38 shows that when actual solder properties are prescribed for both cylindrical and barrel models, the relative error commences with a value of -3% and increases in magnitude to around -11% at yield for tension and compression. For shear, the relative error increases gradually to -12% when the deformation attains a value of 0.03mm. However, when the adjusted solder properties are used for the cylindrical model, the relative error starts from 0.2% and reaches a maximum of only around 2.5% at yield for both tension and compression, while for shear, the relative error increases from 0.8% to a maximum of 5.7%, after which it decrease rapidly with deformation.

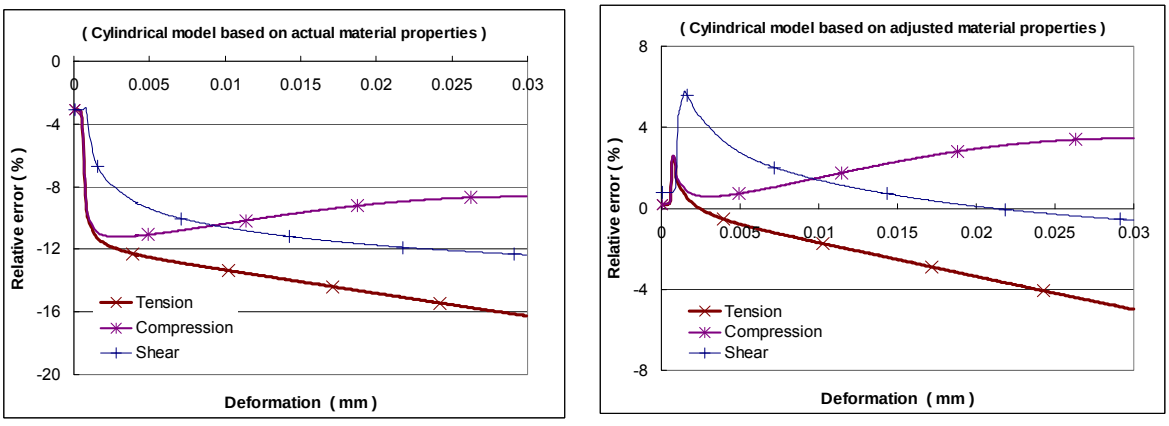

(a) (b)

Fig.4-38 Percentage error in load for cylindrical model relative to barrel model, based on (a) actual and (b) adjusted solder properties

These simulations lead to the conclusion that modification of the solder model geometry from that of a barrel to a cylinder is feasible. However, to maintain

reasonable accuracy, the solder material properties prescribed to the cylindrical model must be modified. An actual solder joint does not possess a prismatic cross-section; consequently, the results of quasi-static and dynamic tests yield only force-deformation responses. The numerical study undertaken, on modifying the profile of a solder joint into a cylindrical approximation, demonstrates that this is a feasible approach if conversion of the force-deformation curve into an equivalent stress-strain response is incorporated. This facilitates FEM modeling of solder joints.

4.3.3 Normalized stress-strain curves for single solder joints

The force-deformation responses of single solder joint specimens subjected to quasi-static and dynamic deformation were obtained from experimental tests. Deformation is defined by the relative displacement between the two outer surfaces of the BT substrates, which includes deformation components contributed by the substrates, copper pads and solder bump. FEM results (Fig.4-39) based on a barrel geometry and actual material properties (BT, Cu and solder) for compression at 0.00015mm/s show that deformation of the copper pads and solder is significantly larger than that of the substrates.

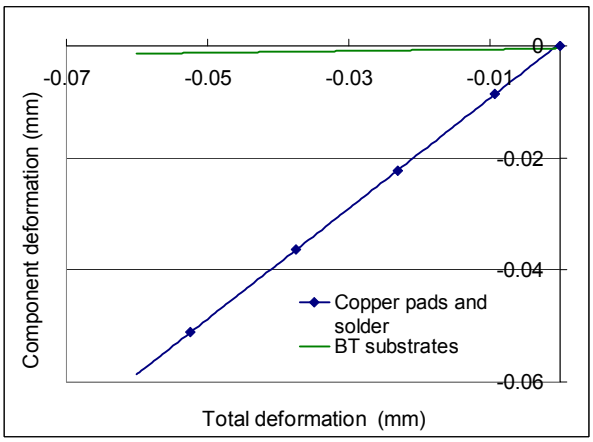

Fig.4-39 Contribution of compressive deformation from BT substrates and combination of copper pads and solder for barrel model of solder joint

Consequently, the solder joint specimen is simplified by approximating it to a cylinder of homogeneous material connected to two substrates. The cylinder captures the response of the two copper pads and solder bump, and represents the stand-off height of the solder joint. The solder mask area (0.43mm diameter) and the total height (0.28mm) between the pad/substrate interfaces are used for the cylinder dimensions. Modified or “normalized” (“equivalent”) engineering stress-strain curves are then derived by converting the force-deformation curves using the initial dimensions of the cylinder, as shown in Fig.4-40. Deformation rates are converted into corresponding strain-rates through the stand-off height of the solder joint. The curves exhibit an initial linear response up to a third or half of the yield strength, after which nonlinearity sets in and this continues to the point of tensile fracture, or when stiffening under compression is attained.

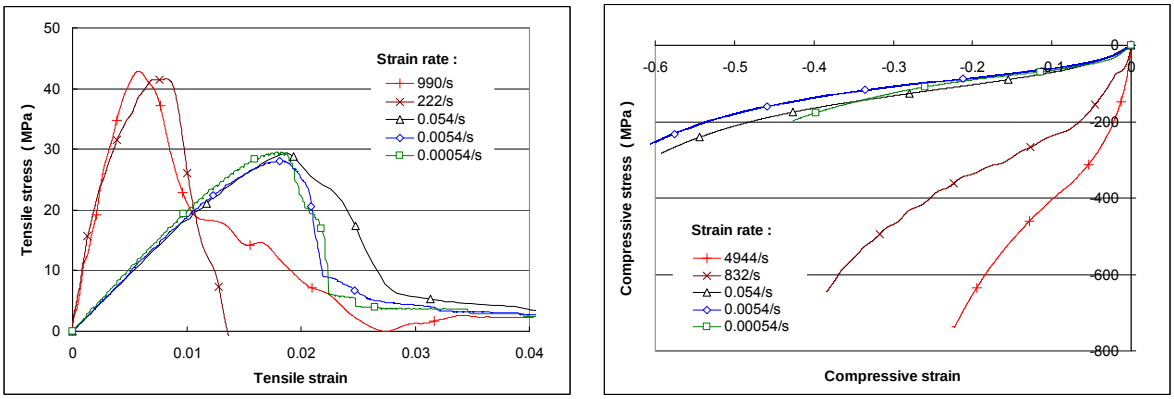

(a) (b)

Fig.4-40 Equivalent stress-strain curves for single solder joints for quasi-static and dynamic loading (a) tensile; (b) compressive.

According to the approximation of the load-deformation response by a bi-linear curve, equivalent stress-strain curves can also be established by this bi-linear approximation. True stress-stain curves are converted from the equivalent stress-strain curves and bi-linear approximations obtained for use in FEM simulation, as shown in Fig.4-41. The yield point is determined from a 0.2% strain offset, based on the initial slope of the stress-strain response (for tension, this is close to the ultimate stress). This value is important, as it is when connection quality in compression starts to degrade or fracture in tension commences. For compression, characterization of these curves with respect to strain rate is directed at the initial modulus, yield stress and hardening modulus.

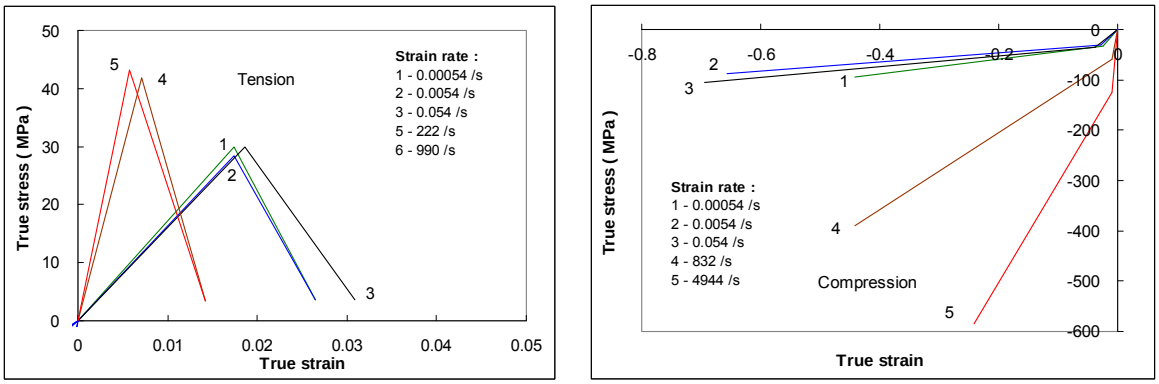

(a) (b)

Fig.4-41 Bi-linear approximation of the true stress-strain curves for single solder joint specimens.

There are a number of equations that have been proposed to describe the plastic behavior of materials as a function of strain rate as well as temperature (as reviewed by Meyers, 1992). The effect of strain rate is usually expressed by $\sigma \propto \ln \dot{\varepsilon}$. The well-known Johnson-Cook model (Johnson and Cook, 1983; Johnson, et al. 1983) has five experimentally-determined parameters to describe the effect of strain rate and temperature,

$$\sigma = \left(\sigma_0 + B\varepsilon^n\right)\left(1 + C\ln\frac{\dot{\varepsilon}}{\dot{\varepsilon}_0}\right)\left[1 - \left(\frac{T - T_r}{T_m - T_r}\right)\right] \qquad (4\text{-}16)$$

where ε_0 and T_r are a reference strain rate and temperature at which σ_0 is measured. The Johnson-Cook equation describes the response of a number of metals fairly well. Additional empirical equations have also been proposed by other investigators, such as the following equation, to describe the shear stress τ and shear strain γ,

$$\tau = \left(\tau_0 \gamma^n\right)\dot{\gamma}_p^m T^{-v} \qquad (4\text{-}17)$$

where n and m are respectively, work-hardening and strain rate sensitivity parameters and v is a temperature softening parameter. Other investigators

favor the equation,

$$\tau = \tau_0 \left(1 + \frac{\gamma}{\gamma_0}\right)^n \left(\frac{\dot{\gamma}}{\dot{\gamma}_r}\right)^m e^{-\lambda(T-T_0)} \tag{4-18}$$

where τ_0 is the yield stress of the material at the reference strain rate $\dot{\gamma}_r$ and the reference temperature T_0. According to Nadai's mathematical analysis (Nadai, 1950), a general relationship between flow stress and strain rate at constant strain and temperature for evaluation of the displacement rate effect for Sn96.5Ag3Cu0.5 solder bump (Kim, et al., 2006) is,

$$\sigma = C\left(\frac{d\varepsilon}{dt}\right)^s \tag{4-19}$$

where s is known as the strain-rate sensitivity and C is a stress coefficient.

In fitting the yield stress with strain rate for single solder joint specimens, the Johnson-Cook model (Johnson, et al. 1983), which utilizes a logarithmic relationship between stress and strain rate, is examined and found to be unsuitable for the current experimental results. The Cowper-Symonds model (Cowper and Symonds, 1957; Wang and Yi, 2002) is found suitable to approximate the variation of yield stress with strain rate,

$$\frac{\sigma}{\sigma_0} = 1 + \left(\frac{\dot{\varepsilon}}{D}\right)^{1/q} \tag{4-20}$$

where D and q are constants and σ_0 is the static yield stress. Fig.4-42 shows how experimental data from tensile and compressive tests fit the Cowper-Symonds model. The initial elastic modulus for tension and compression and the hardening modulus for compression are fitted by a power law equation,

$$E = a + b\dot{\varepsilon}^{c} \tag{4-21}$$

where $a = 1299.49$, $b = 596.98$ and $c = 0.3416$ to fit the initial elastic modulus, and $a' = 165.15$, $b' = 9.13$ and $c' = 0.6448$ for fitting the hardening modulus as shown in Fig.4-43. The results show that the Cowper-Symonds model and the power law constitute reasonable descriptions of the relationship between the yield stress and strain rate, as well as the modulus and strain rate.

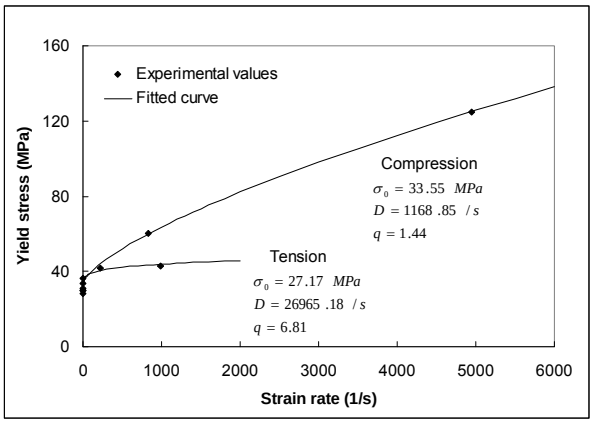

Fig.4-42 Curve fit for variation of yield stress with strain rate for tensile and compressive true stress-strain curves.

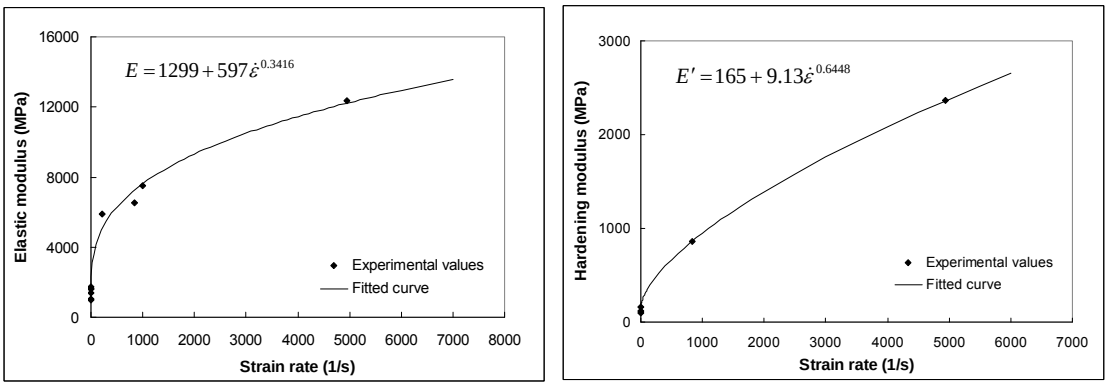

(a) (b)

Fig.4-43 Curve fit of (a) initial elastic modulus and (b) hardening modulus with strain rate

These normalized or equivalent stress-strain relationships can be utilized in numerical simulations to predict the mechanical response of solder joints. Fig.4-44a shows the cylindrical solder joint model subjected to tension, compression and shear, whereby the true stress-strain curve input to ABAQUS is bi-linear for compression and perfectly plastic for tension (Fig.4-44b).

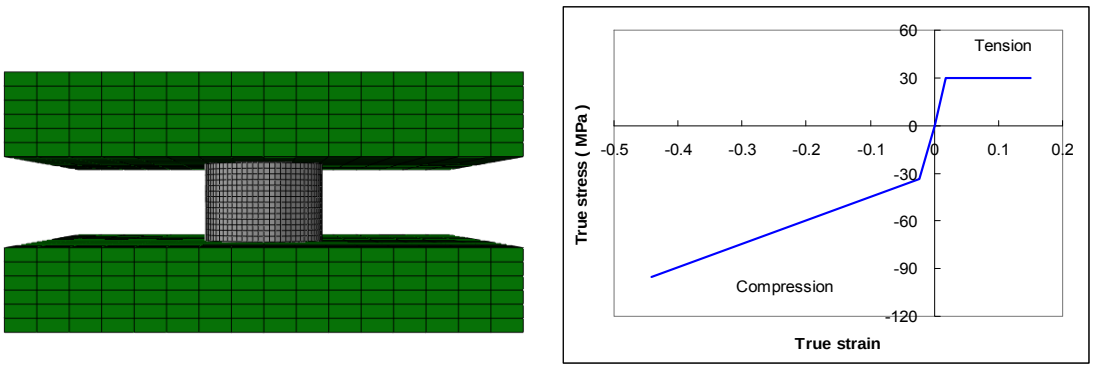

(a) (b)

Fig.4-44 (a) Cylindrical solder joint model and (b) equivalent stress-strain relationship of solder joint prescribed to ABAQUS

Fig.4-45 shows the corresponding results from a preliminary implementation of the stress-strain curve for a strain rate of 5.36×10^{-4}/s in a simulation. The figure also shows the bi-linear approximation of the experimental response, from which the equivalent stress-strain relationship prescribed to ABAQUS was derived, based on idealization of the solder joint by a cylinder. The predicted load-deformation responses are compared with experimental results. Good agreement between the FEM results and experimental data demonstrates that implementation of the normalized stress-strain relationships converted from experimental force-deformation responses for a cylinder solder joint approximation is able to model the behavior of a solder

joint with reasonable accuracy. Fig.4-45 also shows load-deformation simulation results for a barrel-shaped model based on actual solder material (BT, Cu and solder) properties, displaying not only notably higher stress values, especially for tension and shear loading (notwithstanding the fact that no fracture criterion is defined), but also a greater elastic stiffness. This is because the solder properties prescribed to the barrel model does not take into account actual solder joint features, such as its composition of several components and imperfections such as the bond strength and stiffness of the pad-substrate interface, etc. The large discrepancy between the FEM results for the barrel profile model and the experimental results highlights the importance of obtaining the force-deformation response of solder joints from experimental tests as a basis for any modeling or idealization.

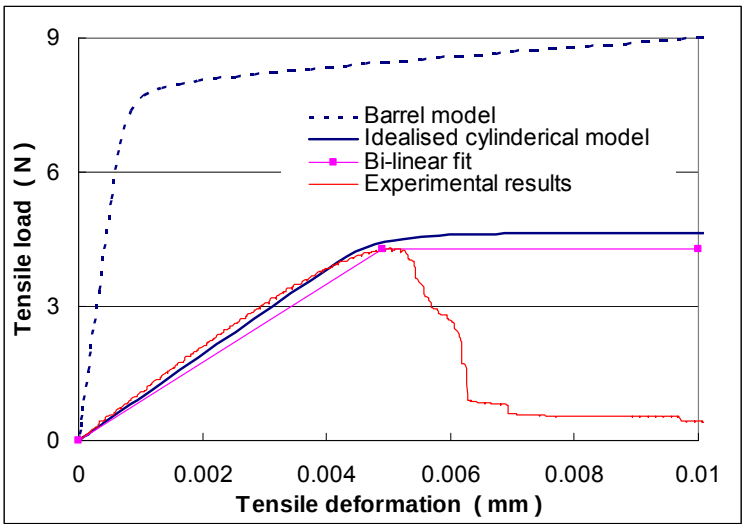

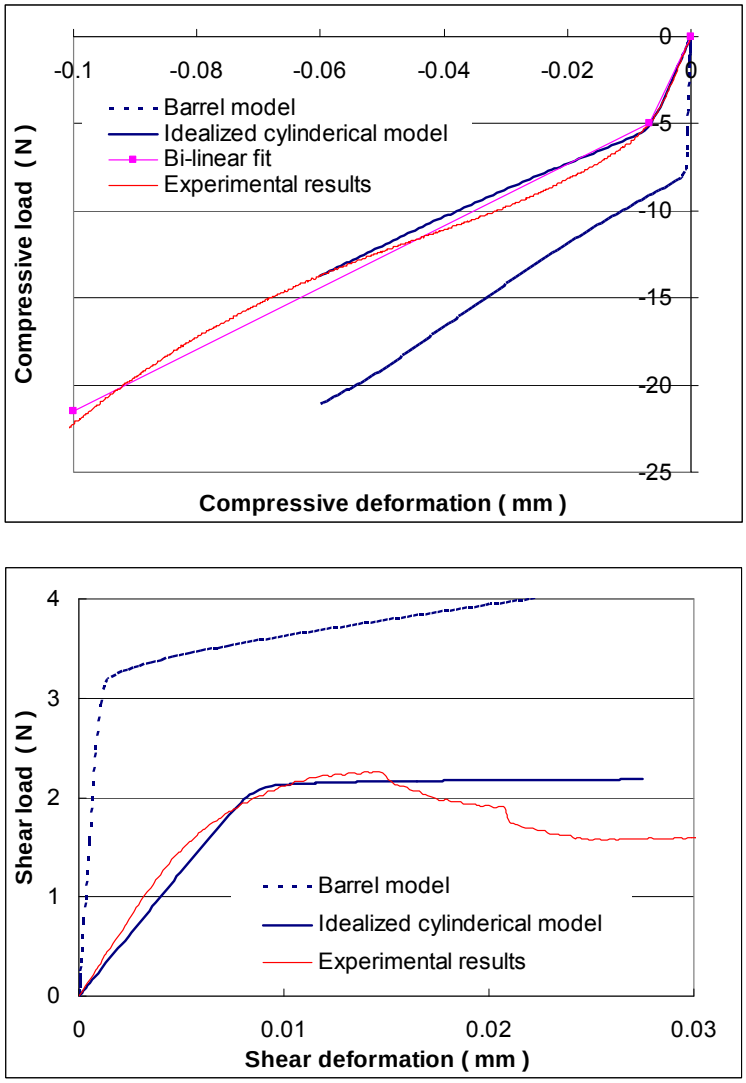

Fig.4-45 Force-deformation response of cylindrical model based on bi-linear solder joint properties (derived from experiments) and comparison with response of barrel model based on actual material properties.

4.4 Beam model representation of solder joint

4.4.1 Establishment of beam model

The idealization of a barrel-like model by a cylindrical model enables the conversion of experimentally obtained force-deformation curves to equivalent stress-strain relationships that can be prescribed to FEM modeling of solder

joints. The barrel model has a curved surface that needs a fine mesh to describe its profiles; this increases the computational cost tremendously, as a PCB board may contain hundreds to thousands of solder joints in IC packages. The cylindrical model facilitates the use of equivalent stress-stain curves derived from the load-deformation curves for FEM modeling. However, the number of elements needed for one solder joint is still large. Therefore,a beam model idealization of a solder joint is investigated. The beam has the same prismatic cross section as the cylindrical model, and is therefore a further simplification of the cylindrical model.

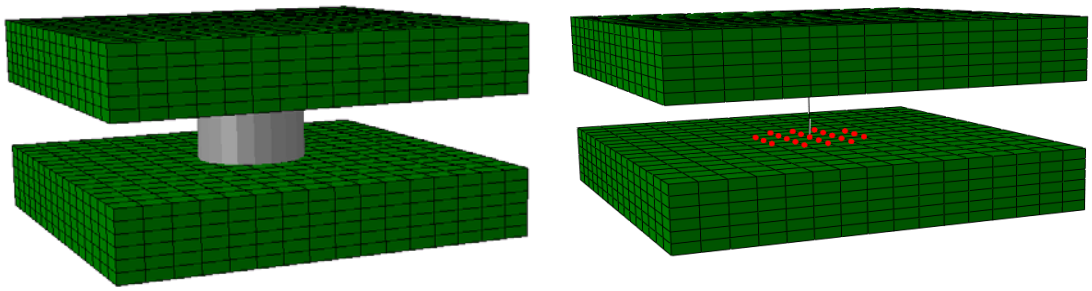

(a) (b)

Fig.4-46 Beam model of solder joint depicted via a (a) 3-D profile and (b) wire connection with an area of influence

Beam theory is essentially a one-dimensional approximation of a three-dimensional continuum. In ABAQUS a beam element is a one-dimensional line element in a three-dimensional space or the X–Y plane; it has a stiffness associated with deformation of the beam “axis”. The deformation consists of axial stretching, curvature change (bending) and torsion. Beam elements offer the additional flexibility associated with transverse shear deformation between the beam axis and the normal to its cross-sections. The main advantage of beam elements is that they are geometrically simple and have few degrees of

freedom. (*ABAQUS Analysis User's Manual, section 24.3.1 "Beam modeling"*). In this study, the beam model for a solder joint comprises two BT substrates linked by a beam that represents the solder joint. A circular cross-section 0.43mm in diameter and 0.28mm in height (same as that in the cylindrical model) is assigned to the beam. Fig.4-46a shows the cylindrical profile of the beam model of a solder joint, whereas in Fig.4-46b, the beam is illustrated as a line connection. The solder joint comprises B32 beam elements (3-node quadratic beams). Connection between the line and the substrates is simulated by a multi-point constraint (kinematic coupling), assigned to the nodes at beam ends and corresponding nodes on the substrates. The node at each end of the beam is the reference node, and nodes on the substrates within the influence region (0.43mm circular area) are coupled nodes that are constrained to have the same motion (translational and rotational degrees of freedom) as the reference node. Fig.4-47 shows a preliminary simulation of a pure compression test at a speed of 0.00015mm/s using the beam model. It shows the contour of Mises stresses for a compression of 0.06mm; the deformation of the beam (copper pad and solder bump) and the two substrates is comparable to the results from the barrel model (Fig.4-39).

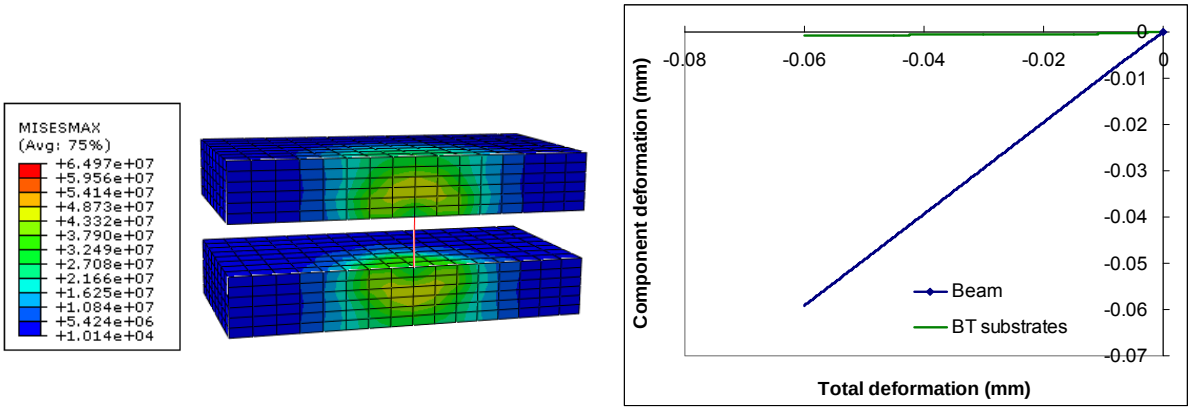

(a) (b)

Fig.4-47 Simulation results for pure compression at speed of 0.00015mm/s using the beam model. (a) von-Mises stress contour at a deformation of 0.06mm and (b) compression of the two BT substrates and the beam

4.4.2 Evaluation of beam model

As the beam model has the same prismatic cross section as the cylindrical model, comparisons are made between the outputs of these two models to evaluate this further simplification of a solder joint. Simulations of tensile and compressive tests at inclination angles ranging from 0^0 to 90^0 at a loading speed of 0.00015mm/s are undertaken. The solder joint material properties prescribed to ABAQUS the same as those shown in Fig.4-44, and the beam is meshed by one element. The force-deformation curves for tension and compression (corresponding to the load-deformation curves recorded in actual tests) are compared for various inclination angles (90^0 corresponds to pure shear) in Fig. 4-48. The simulation outputs based on the beam model are comparable to those from the cylindrical model for the initial portion before yield. However, for tension, there is an increasingly larger strength predicted by the beam model compared to the cylindrical model when the inclination

angle exceeds 60^0. The post-yield portion for compression of the beam model shows some difference with the cylindrical model; this may not be as critical as the discrepancy in the tensile curves, which determine the failure of solder joints.

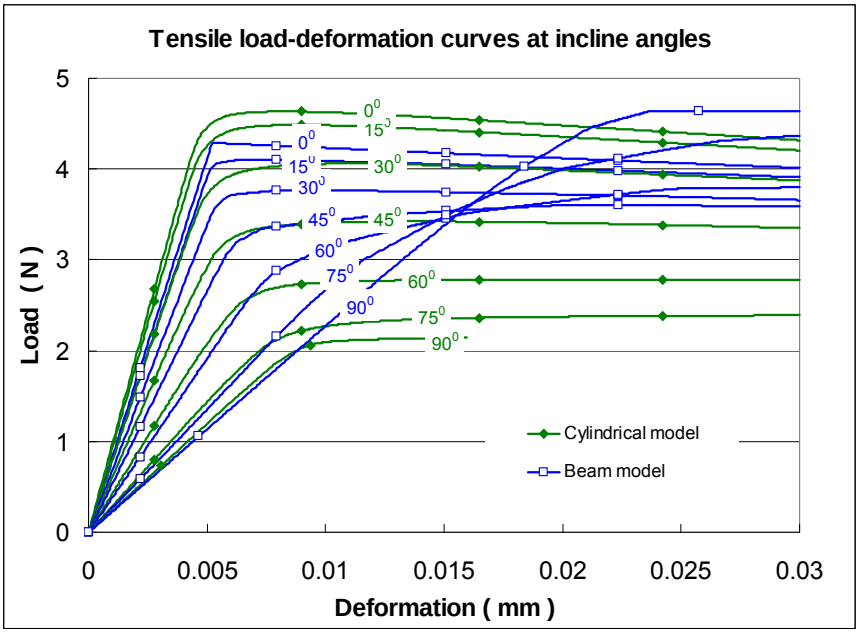

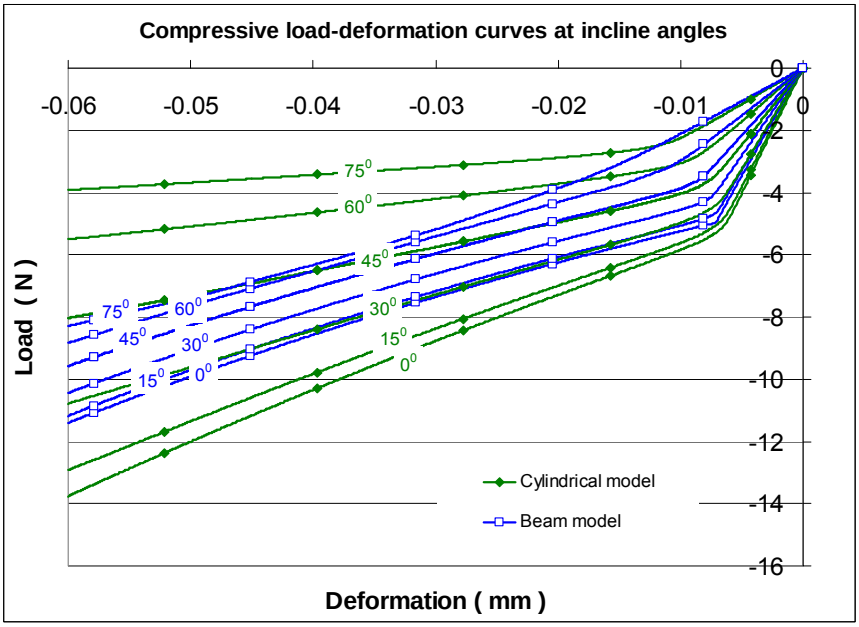

Fig. 4-48 Comparison of simulated load-deformation response for the beam model (meshed by one element) and the cylindrical model, for inclined tension and compression loading

In the beam model, Timoshenko beam elements (B32) are used. They allow for transverse shear deformation and can be used for thick (“stout”) as well as slender beams. As stated in the ABAQUS Analysis User's Manual (Section 24.3.3, on choosing a beam element), “For beams made from uniform material, shear flexible beam theory can provide useful results for cross-sectional dimensions up to 1/8 of typical axial distances or the wavelength of the highest natural mode that contributes significantly to the response. Beyond this ratio the approximations that allow the member's behavior to be described solely as a function of axial position no longer provide adequate accuracy”.

The solder joint in this study has cross-sectional dimensions larger than 1/8 their axial length. Thus, even the use of a thick beam element (Timoshenko beam) cannot guarantee adequate accuracy. Therefore, comparisons between the beam model and the cylindrical model for loading under the full range of inclination angles, from tension/shear to compression/shear, are undertaken to verify whether the approximation is acceptable and to discern the accuracy in implementing this beam model. It is found that when the beam is meshed using more elements, the load-deformation results for a shear dominant mode has a decreasing trend in strength. Fig.4-49 shows the load-deformation curves for the beam model under pure shear (corresponding to 90^0 incline), with the beam meshed using 1 to 6 elements. It demonstrates that the flexibility of the connection increases with the number of elements. Fig. 4-50 presents a complete comparison of the simulation outputs (tension and compression at different inclination angles) from beam models meshed

using 1 and 6 elements. It shows that the elastic region of the curves for tension are almost identical and differences in the curves for compression are small; however, the stress in the post yield region of tensile curves corresponding to inclinations larger than 60^0 is smaller for models meshed by more elements.

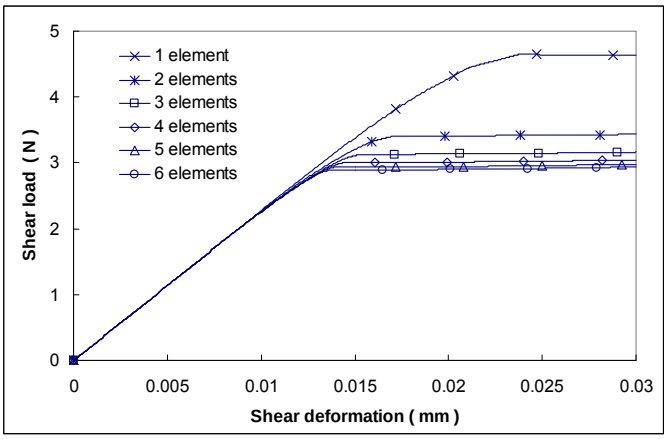

Fig.4-49 Effect of number of beam elements in a solder joint on the shear load-deformation response

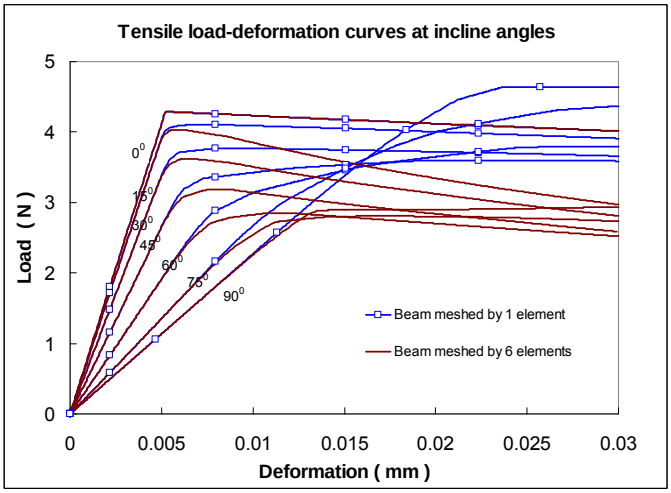

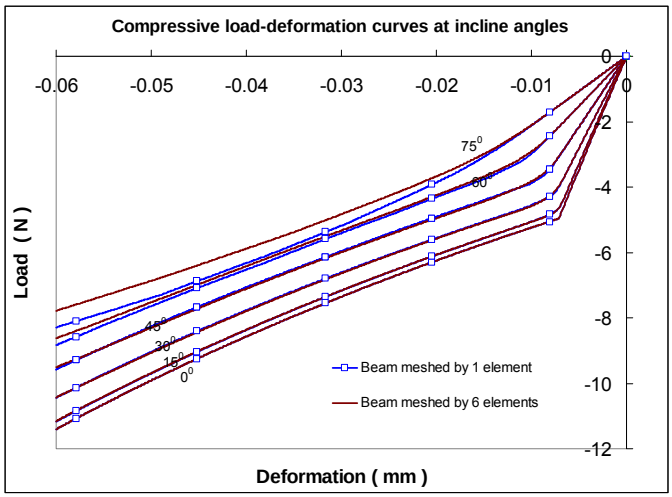

Fig. 4-50 Comparison of simulated load-deformation response of beam models meshed by one and six elements, subjected to inclined tension and compression

A comparison of simulation results with experimental data is shown in Fig.4-51. The simulation results are from the cylindrical and beam models with 6 elements in the beam. It shows that the elastic portions of the simulation results are comparable to the experimental results; however, the simulations for tensile loads show a somewhat larger strength around yield, especially for inclination angles from 15^0 to 75^0. This is attributed to the material properties prescribed to the solder joint; i.e. assumption of perfect plasticity in tension, as shown in Fig.4-44. Actual solder joint breakage is brittle, as shown by the experimental results. The perfect plasticity assumption for tensile loading enables the solder joint to sustain a load after yield and hence delays failure.

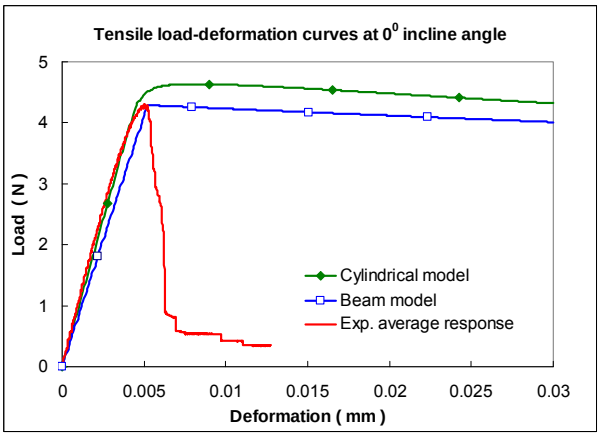
Tensile load-deformation curves at 0⁰ incline angle
Load (N)
Deformation (mm)
Cylindrical model
Beam model
Exp. average response

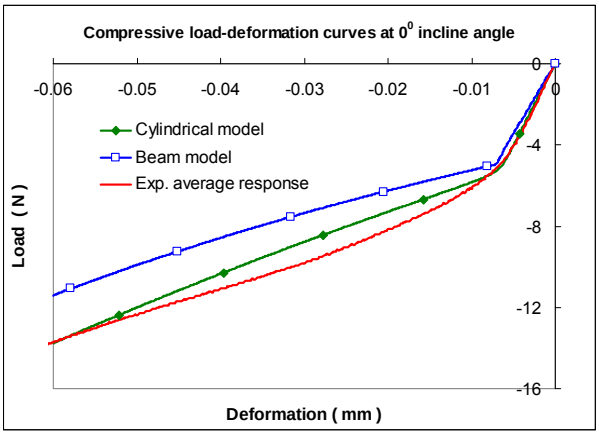
Compressive load-deformation curves at 0⁰ incline angle
Load (N)
Deformation (mm)
Cylindrical model
Beam model
Exp. average response

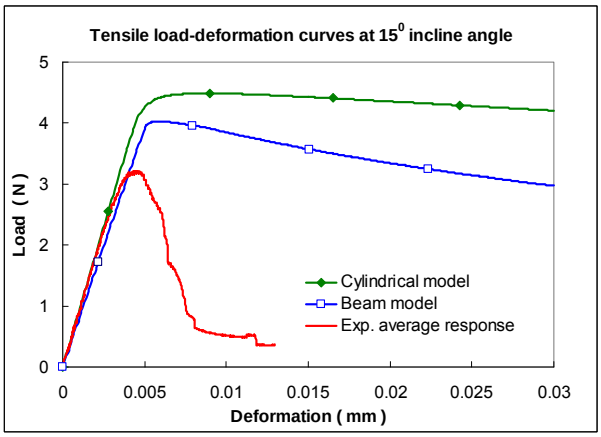
Tensile load-deformation curves at 15⁰ incline angle
Load (N)
Deformation (mm)
Cylindrical model
Beam model
Exp. average response

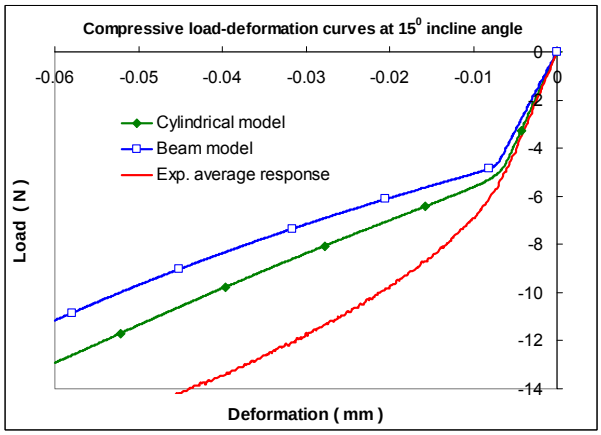
Compressive load-deformation curves at 15⁰ incline angle
Load (N)
Deformation (mm)
Cylindrical model
Beam model
Exp. average response

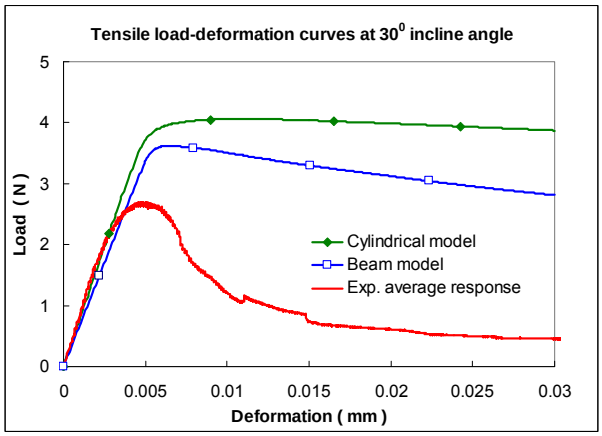
Tensile load-deformation curves at 30⁰ incline angle
Load (N)
Deformation (mm)
Cylindrical model
Beam model
Exp. average response

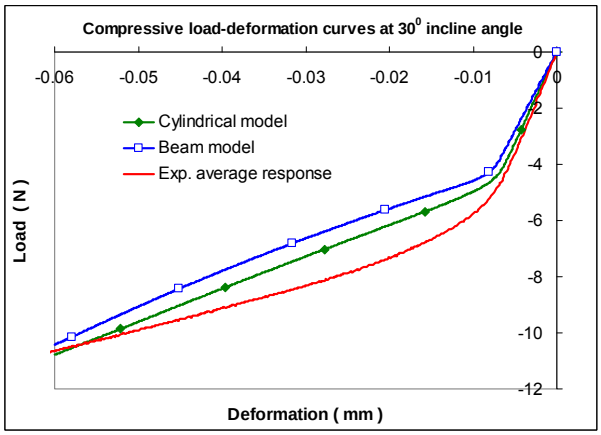
Compressive load-deformation curves at 30⁰ incline angle
Load (N)
Deformation (mm)
Cylindrical model
Beam model
Exp. average response

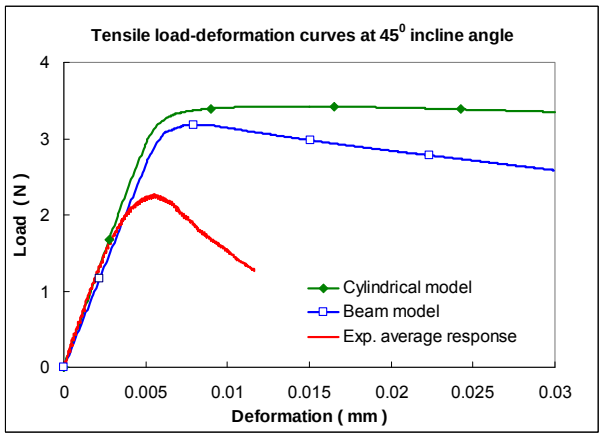
Tensile load-deformation curves at 45⁰ incline angle
Load (N)
Deformation (mm)
Cylindrical model
Beam model
Exp. average response

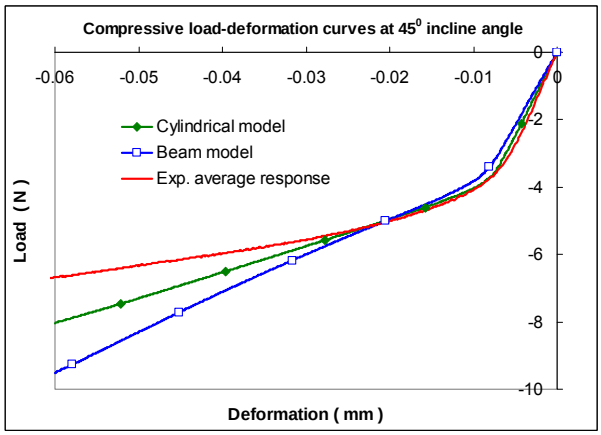
Compressive load-deformation curves at 45⁰ incline angle
Load (N)
Deformation (mm)
Cylindrical model
Beam model
Exp. average response

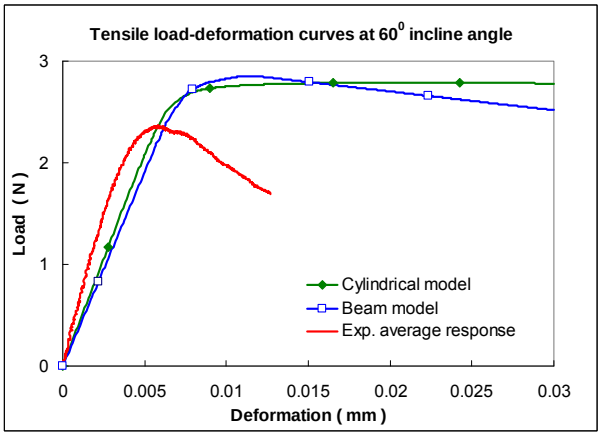

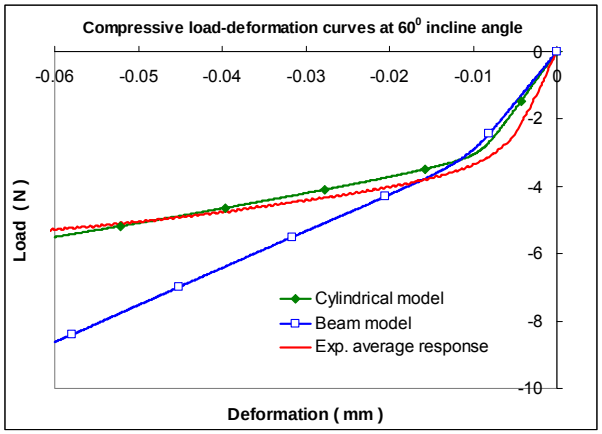

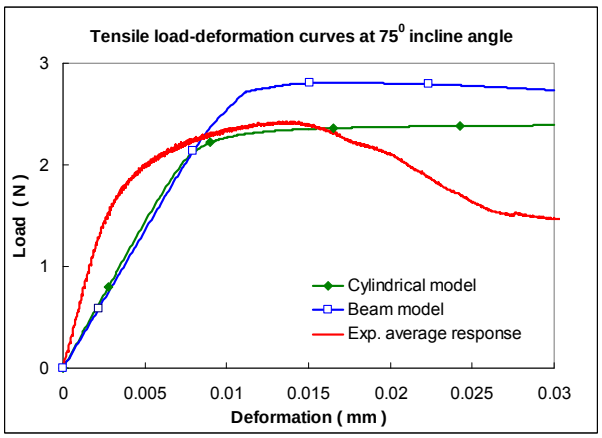

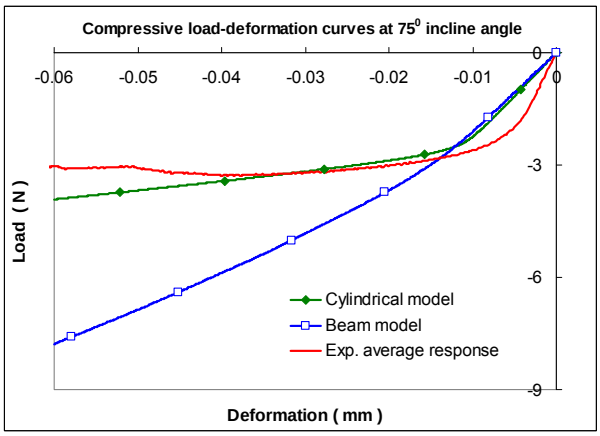

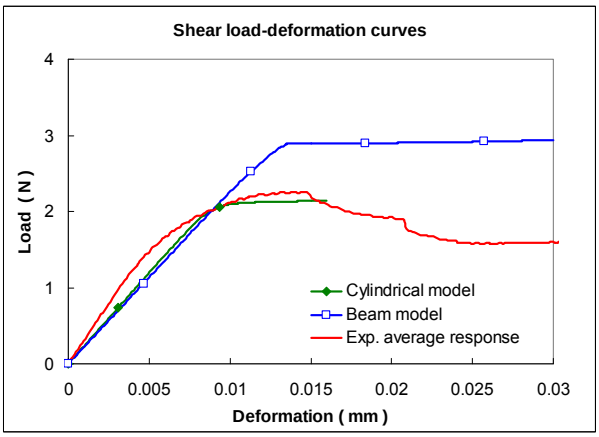

Fig.4-51 Comparison of load-deformation responses in terms of experimental results and simulations based on a solder joint meshed by six beam elements and the cylindrical model, for inclined tension and compression

4.4.3 Beam model based on experimentally obtained properties

As shown in Fig.4-41, the bi-linear relationship can be used to represent the equivalent true stress-strain curves of single solder joint specimens subjected to pure tension and compression, where the post-failure region in a tensile curve is approximated by a negative slope symmetric to its initial elastic response. This approximation is deemed acceptable, as the post-failure behaviour under tension is not critical, since the IC package may fail once the stress in a solder joint reaches the ultimate point. Based on the fitted equations for the elastic, yield and hardening response (Fig.4-42 and Fig.4-43), bi-linear approximations of the true stress-strain responses can be derived in terms of strain rates. An illustration of true stress-strain curves for strain rates from 0.0005/s to 5000/s is shown in Fig.4-52. These bi-linear solder joints responses are prescribed as material properties to ABAQUS.

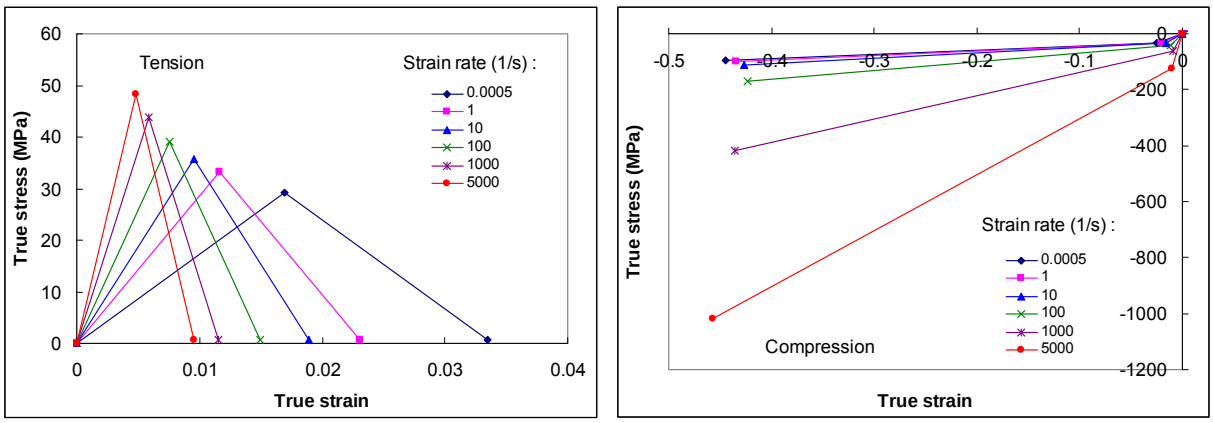

(a) (b)

Fig.4-52 Bi-linear approximations of true stress-strain response for single solder joints at strain rates ranging from 0.0005/s to 5000/s, (a) tensile and (b) compressive

Isotropic elasto-plasticity is commonly used for metal plasticity calculations,

either as a rate-dependent or rate-independent model, and has a particularly simple form. As stated in the *ABAQUS analysis User's Manual* (*Section 19.2.1, "classical metal plasticity"*) - "ABAQUS provides an isotropic hardening model, which is useful for cases involving gross plastic straining or in cases where the straining at each point is essentially in the same direction in strain space throughout the analysis. Although the model is referred to as a "hardening" model, strain softening or hardening followed by softening can be defined". This capability of ABAQUS facilitates the incorporation of the bi-linear tensile curves with post-failure softening to describe solder joint behavior.

Material properties can be defined to be dependent on "field variables" (user-defined variables that represent any independent quantity and defined at nodes, as functions of time). If isotropic hardening is assumed, the yield stress can be input via a table relating plastic strain to strain rate, temperature and/or other field variables. The yield stress at a given state is simply interpolated from the data. For example, material moduli can be functions of weave density in a composite or of phase fraction in an alloy. The number of user-defined field variable dependencies required for many material behaviors can be specified (*ABAQUS Analysis User's Manual, Section 28.6.1, "predefined fields*").

The ABAQUS facility for material property definition enables incorporation of the bi-linear true stress-strain curves (Fig.4-52) for the solder joint beam model. In this study, the solder joint mechanical properties are prescribed as being dependent on a field variable; and the field variable is associated with

the strain rate as a solution-dependent variable, as shown in *Appendix C*.

Timoshenko beam elements (B32) are used for the solder joint in the beam model. As highlighted previously, Timoshenko beam elements can be used for thick (“stout”) beams with cross-sectional dimensions up to 1/8 of typical axial distances; beyond this ratio the approximations may no longer provide adequate accuracy. Therefore, a comparison between the simulation outputs and experimental results for a full range of inclination angles for tension/shear to compression/shear is undertaken to determine the acceptability of the beam model. The force-deformation curves are shown in Fig.4-53. Before yield (tensile and compressive), agreement between simulation outputs and experimental results is acceptable. Because post-failure softening is implemented in the definition of material properties, the simulation output for tension is closer to the experimental values than that when perfect plasticity is assumed. Identification of solder joint failure in tension is more critical than ascertaining commencement of yield in compression.

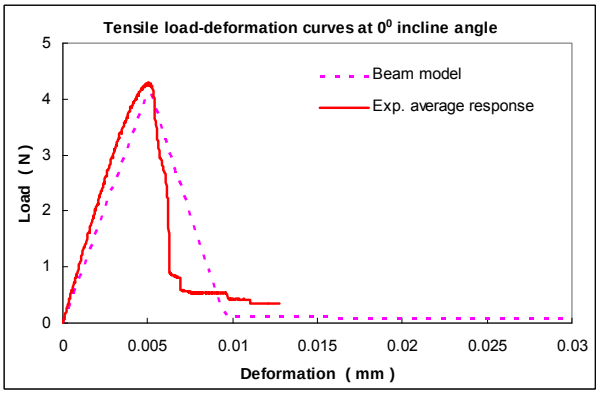
Tensile load-deformation curves at 0⁰ incline angle
Load (N)
Deformation (mm)
Beam model
Exp. average response
0
1
2
3
4
5
0
0.005
0.01
0.015
0.02
0.025
0.03

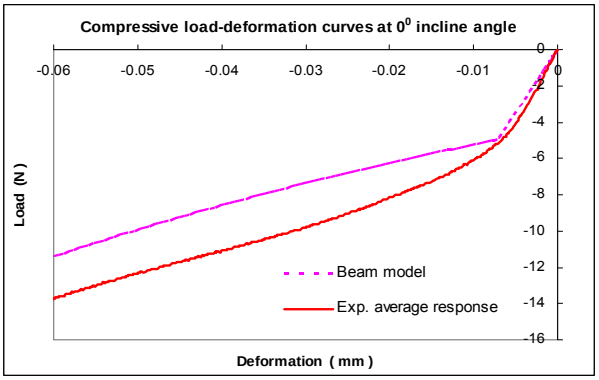
Compressive load-deformation curves at 0⁰ incline angle
Load (N)
Deformation (mm)
Beam model
Exp. average response
-0.06
-0.05
-0.04
-0.03
-0.02
-0.01
0
-2
-4
-6
-8
-10
-12
-14
-16

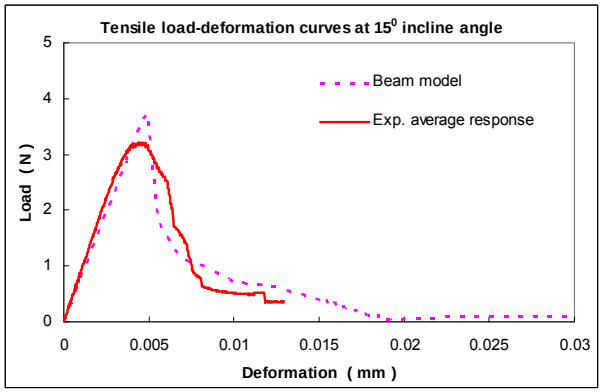
Tensile load-deformation curves at 15⁰ incline angle
Load (N)
Deformation (mm)
Beam model
Exp. average response
0
1
2
3
4
5
0
0.005
0.01
0.015
0.02
0.025
0.03

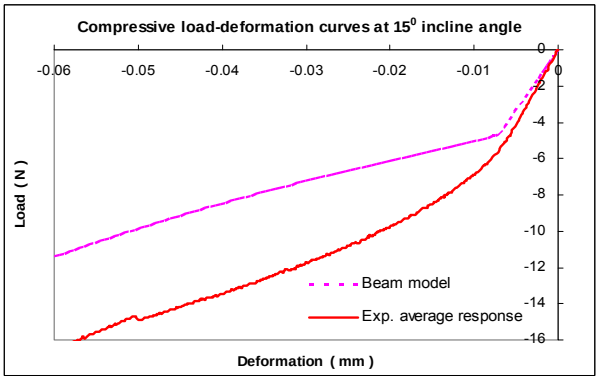
Compressive load-deformation curves at 15⁰ incline angle
Load (N)
Deformation (mm)
Beam model
Exp. average response
-0.06
-0.05
-0.04
-0.03
-0.02
-0.01
0
-2
-4
-6
-8
-10
-12
-14
-16

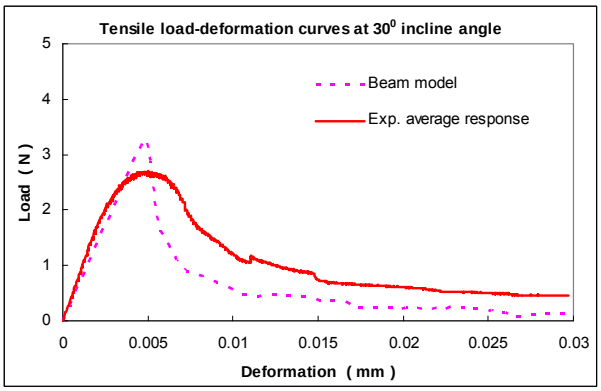
Tensile load-deformation curves at 30⁰ incline angle
Load (N)
Deformation (mm)
Beam model
Exp. average response
0
1
2
3
4
5
0
0.005
0.01
0.015
0.02
0.025
0.03

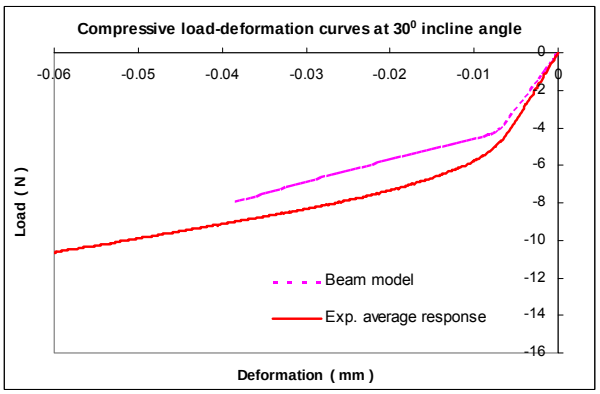
Compressive load-deformation curves at 30⁰ incline angle
Load (N)
Deformation (mm)
Beam model
Exp. average response
-0.06
-0.05
-0.04
-0.03
-0.02
-0.01
0
-2
-4
-6
-8
-10
-12
-14
-16

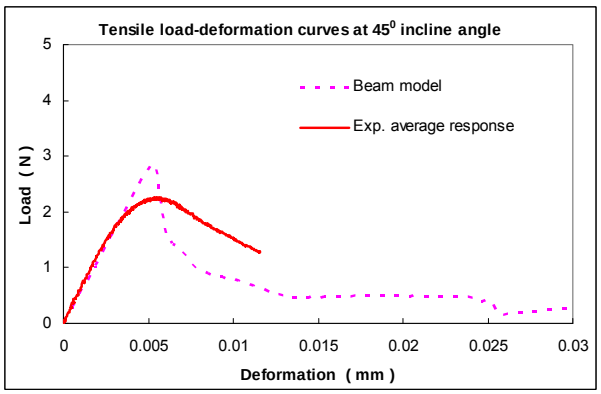
Tensile load-deformation curves at 45⁰ incline angle
Load (N)
Deformation (mm)
Beam model
Exp. average response
0
1
2
3
4
5
0
0.005
0.01
0.015
0.02
0.025
0.03

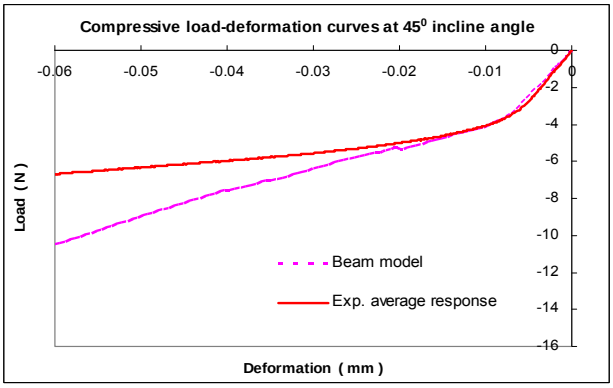
Compressive load-deformation curves at 45⁰ incline angle
Load (N)
Deformation (mm)
Beam model
Exp. average response
-0.06
-0.05
-0.04
-0.03
-0.02
-0.01
0
-2
-4
-6
-8
-10
-12
-14
-16

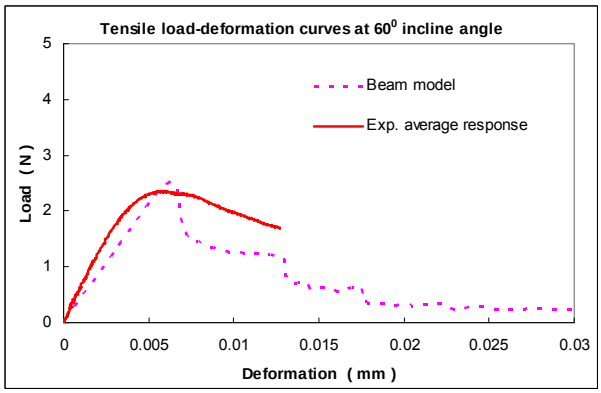

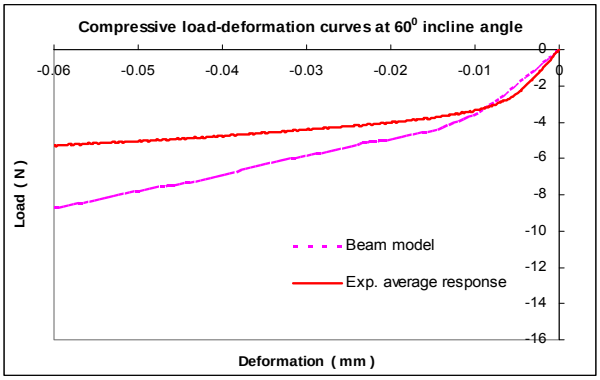

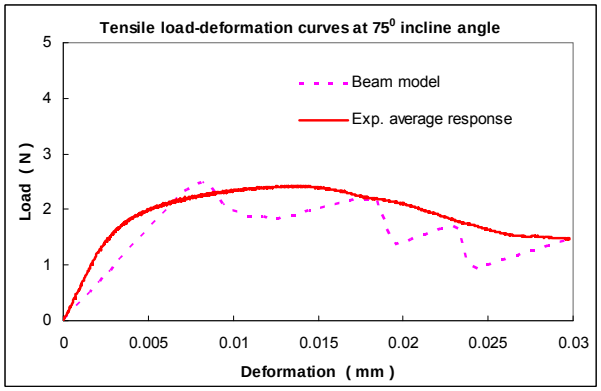

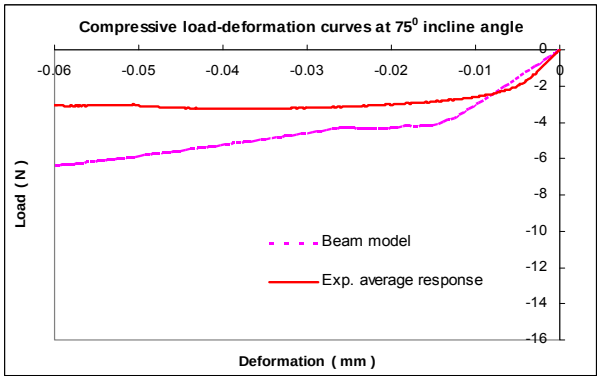

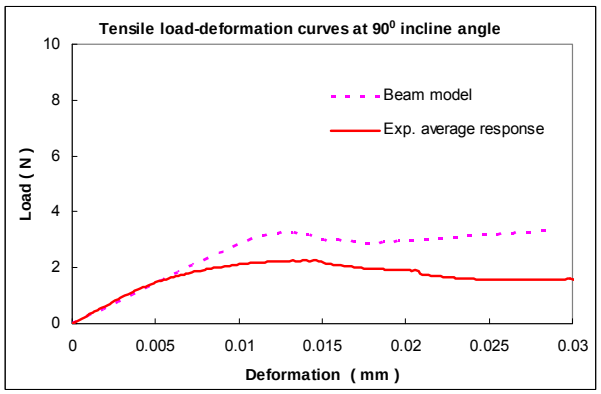

Fig.4-53 Comparison of force-deformation responses of beam model based on experimentally-obtained material properties

The experimental curves in Fig.4-53 are the overall average results of several tests for each loading mode. It shows that the yield forces from simulation of tensile loading are still somewhat larger than the experimental results (e.g. inclinations from 15^0 to 45^0). As described in Chapter 2 and Chapter 3, the load-deformation curves from tests corresponding to each loading mode show some scatter. Therefore, the simulation results may still be within the region of

scatter; this is illustrated in Fig.4-54 for tests corresponding to angles from 15^0 to 60^0, where the group of tensile test curves and average curve are depicted in each diagram.

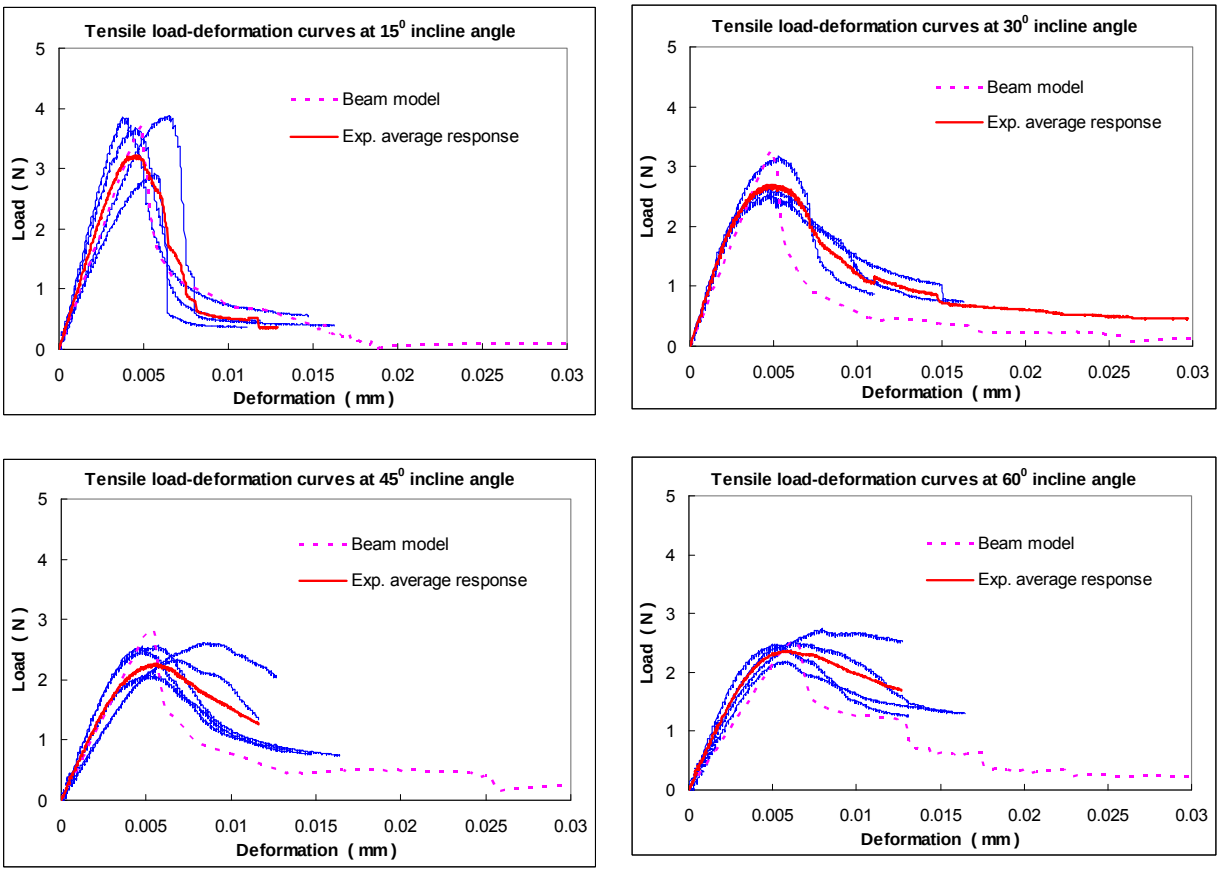

Fig.4-54 Comparison of simulated load-deformation responses with experimental results

Using the beam model, the force components in a solder joint can be extracted from the section force (SF) in ABAQUS. These components are defined by the parameter SFn; for beam elements, n=1 refers to the beam axis and n=2, 3 denotes transverse directions. Fig.4-55 illustrates simulation results for a single solder joint subjected to tensile loading at a 45^0 inclination, and a speed of 0.00015mm/s. The section force components SF1, SF2 and SF3 are plotted and compared with the total force components TF1, TF2 and

TF3, which are the sums of TF of nodes on the upper surface of the substrate. The total force components 1, 2 and 3 refer to directions in the global orthogonal coordinate system. It can be seen that the components SF2 and TF2 are nearly zero; SF1 and SF3 cannot be compared to the TF1 and TF3 curves because of the difference in their definitions. The three components of SF and TF can be converted to normal (beam axis) and shear (transverse to beam axis) components according to the inclination angle α :

$$TF_{shear} = \sqrt{(TF_1 \cdot \cos\alpha + TF3 \cdot \sin\alpha)^2 + (TF_2)^2} \quad (4\text{-}22)$$

$$TF_{normal} = TF_1 \cdot \sin\alpha + TF3 \cdot \cos\alpha \quad (4\text{-}23)$$

$$SF_{shear} = \sqrt{(SF_2)^2 + (SF_3)^2} \quad (4\text{-}24)$$

$$SF_{normal} = SF_1 \quad (4\text{-}25)$$

It is found that the normal and shear force curves derived from TF and SF are identical, as shown in Fig.4-55b. This again shows that the normal-shear failure force envelope obtained from laterally constrained tests should be converted to an envelope corresponding to laterally unconstrained tests, for comparison with the normal and shear forces calculated from section force components.

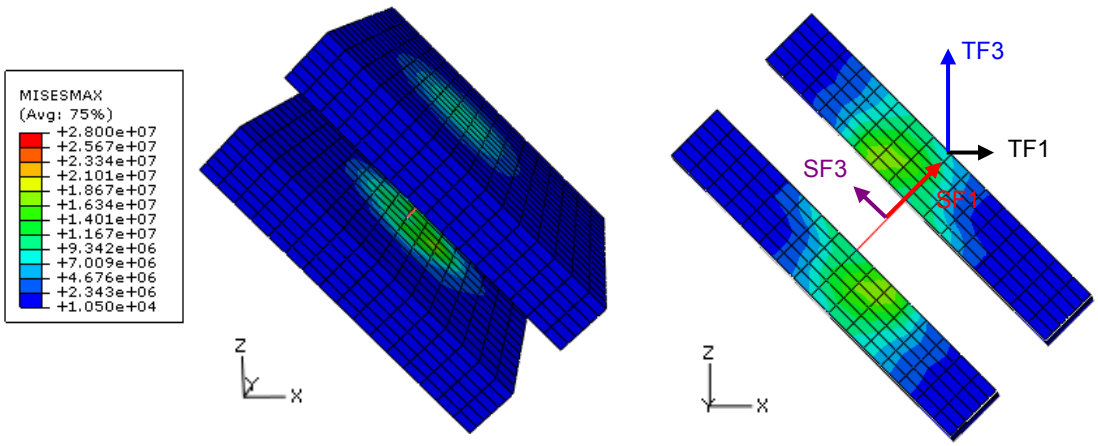

(a) von Mises stress distribution and force components of total force (TF) on the upper substrate, and section forces (SF) in the beam.

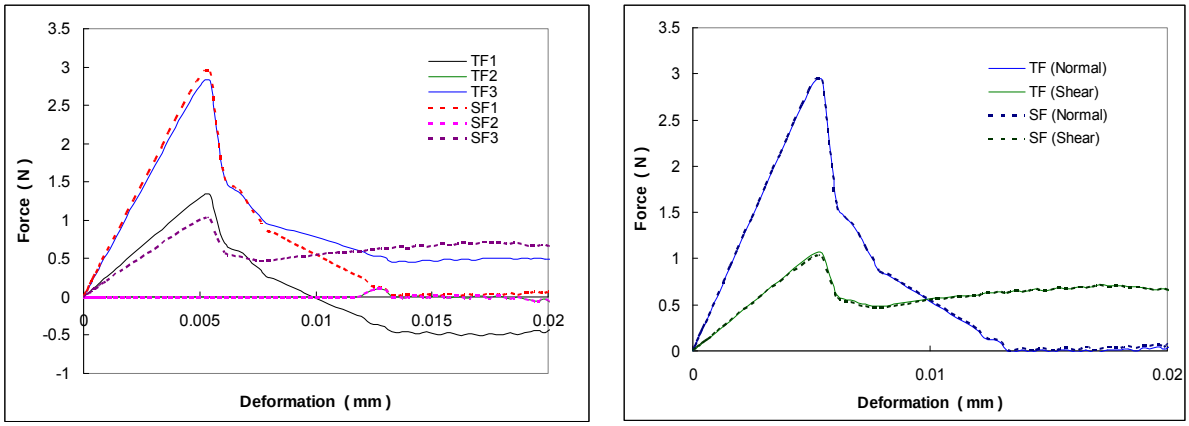

(b) Comparison of force components of TF and SF, and normal and shear components derived from TF and SF

Fig.4-55 Comparison between total force on the substrate (TF) and section forces in a beam (SF) for a solder joint subjected to tension at 45^0 inclination.

CHAPTER 5 EXPERIMENTS AND SIMULATION OF PACKAGE LEVEL SPECIMENS

5.1 PCB bending and drop tests

When a printed circuit board (PCB) with several chips mounted is subjected to mechanical loading, the difference in flexural stiffness of the PCB and the chips attached can cause fractures to develop in the solder joints between a chip and the board. Drop tests involving chip-size BGA packages show that the stress at a solder joint depends on the package structure even if the motherboard strain is the same (Mishiro et al. 2002). Component placement in an electronic product also has effects on solder joint reliability in a BGA package (Alander, et al., 2002). The reliability of electrical devices subjected to mechanical loading is therefore very sensitive to deflection of the PCB.

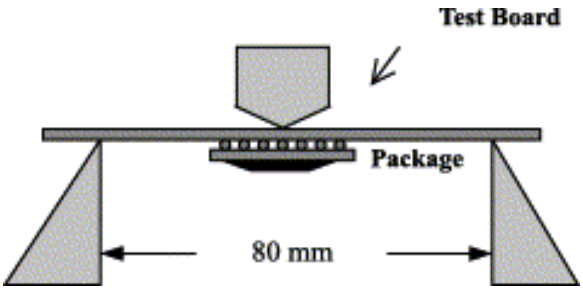

Fig.5-1 Three-point bend test configuration (Wu, et al., 2002)

Three- and four-point bending tests are commonly used for evaluating the reliability of IC packages under flexural loads. For example, second (board)

level reliability testing of a chip scale package by cyclic bending is conducted to evaluate the structural integrity of solder interconnects. The test board is simply supported at both ends and subjected to repetitive deflection in the middle (three-point bend) under cyclic displacement with sinusoidal, triangular or square waveforms (Fig.5-1) to characterize brittle fracture in intermetallic compounds and and the fatigue life (Wu, et al., 2002). Chen et al. (2006) conducted both monotonic and cyclic mechanical four-point bend tests in reliability assessments of BGA components. Deflection in a PCB is usually measured experimentally by techniques involving strain gauges or other sensors. Fig.5-2 shows schematically a three-point bending test under hydraulic cyclic loading and the curvature distribution along the test specimen, as well as the corresponding simulation results in the form of PCB deflection (Shetty and Reinikainen, 2003). The PCB is modeled using elastic orthotropic properties and the simulation results demonstrate that the displacement in the width direction is quite uniform. However, the presence of electronic packages on the PCB causes non-uniform distribution of stress, and the stress near components is higher on the PCB, increasing the possibility of solder joint failure there.

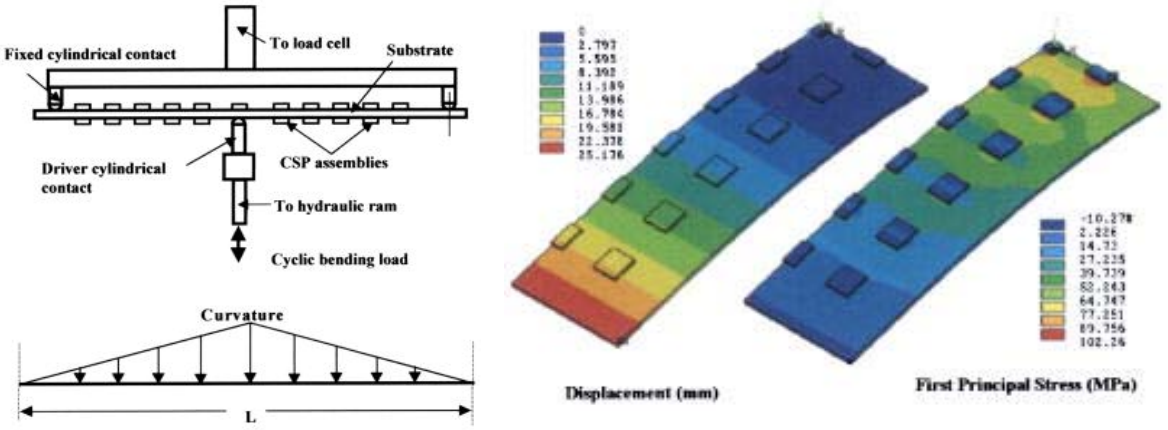

Fig.5-2 Schematic illustration of three-point bending test and curvature distribution in a PCB board; numerical computation of distributions of displacement and first-principal stress on the board (Shetty and Reinikainen, 2003)

Some research has been conducted using FEM simulation of PCBs subjected to impact. For example, Suhir (1992) calculated the theoretical response of a rectangular PCB subjected to impact when its edges are fully clamped, and found that in the case of large shock-induced deflections in PCBs with fixed boundaries, it is important to account for nonlinearity of the PCB vibration. Wang et al. (2006) conducted FEM simulations of a six-layered PCB in order to develop an effective FE model for PCBs subjected to drop-impact testing. The PCB was modeled using four types of materials - isotropic, orthotropic, multi-layer uni-directional fiber and multi-layer fill-warp. Simulations of different models were compared with experimental results (the displacement and acceleration on the PCB were measured respectively by a high speed camera and an accelerometer), as shown in Table 5-1.

Table 5-1 Comparison of experimental and simulation results of different models and comparison of CPU times (from Wang, et al., 2006)

Model	Amplitude of displacement (mm)	Error (%)	Amplitude of acceleration (mm/ms^2)	Error (%)
Experimental	2.55	–	9.81	–
Isotropic fine meshed	2.31	9.41	8.53	13.0
Orthotropic	2.77	8.62	9.75	0.61
Multi-layer uni-directional fiber	2.74	7.45	10.16	3.27
Multi-layer fill–warp	2.58	1.18	9.94	1.33

Material model	CPU time
Isotropic (coarse)	3 min 30 s
Isotropic (fine)	18 min 48 s
Orthotropic	22 min 56 s
Multi-layer uni-directional fiber	1 h 50 min 20 s
Multi-layer fill–warp	2 h 29 min 41 s

Theoretical analysis of deformation of a PCB can only be undertaken for simple cases corresponding to certain boundary and loading conditions. Studies of the dynamic response of a PCB under shock and impact loading are commonly conducted experimentally using board level drop tests. Usually, the entire assembly comprising a PCB and IC packages is dropped from a height via a vertical guide to strike a material which can have its properties adjusted to achieve the desired impact force pulse. Using a beam model for the PCB board, Wong et.al (2002) studied the maximum vertical deflection history at various points along the beam for an impact velocity of 1m/s. The presence of a dominant deflection-time response resembling a sinusoid was clearly evident, as shown in Fig.5-3. Upon impact, very high accelerations (>10000g) were observed near the ends and the solder interconnections near the edge of the chips experience the largest stresses. Fundamental and parametric analyses were conducted for a PCB assembly subjected to a half-sine acceleration by idealizing the PCB as a spring mass system, a beam and a plate respectively (Wong, 2005; Wong et al., 2005)

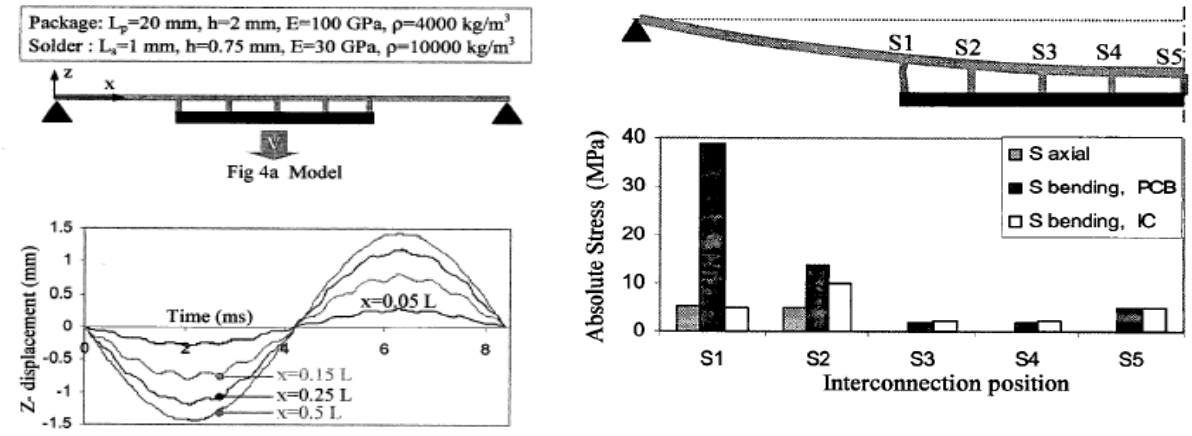

Fig.5-3 Variation of vertical deflection with time at different locations on the PCB and stress magnitudes in solder balls due to PCB curvature (Wong et.al (2002)

During board level drop tests, solder joint failure is induced by the combination of mechanical shock and PCB bending. Tee et al. (2004) studied impact life prediction by drop tests, failure analyses and simulations for TFBGA and VFBGA packages at board level. The critical solder ball is observed to be the outermost corner solder joint, and it fails along the solder and PCB pad interface via a peeling mode. Lai et al. (2006) investigated the board-level drop reliability of chip-scale packages subjected to drop tests with a peak acceleration of 1500G and a pulse duration of 0.5ms (JEDEC drop test condition B) (Fig.5-4a). The effects of SnAgCu or SnPb solder joint compositions, flux and substrate pads with Ni/Au surface finish or OSP coating on the drop reliability of the board-level test vehicle are compared. Luan et al. (2007) conducted dynamic board level drop tests (Fig.5-4b), and studied the effects of drop height, number of PCB mounting screws, tightness of screws, and number of felt layers. Board level drop testing is commonly used to investigate the reliability of electrical packages subjected to impact

loading (Katahira, et al., 2006; Chong, et al., 2006); numerical simulations to predict board-level drop reliability (Yeh, et al., 2006) has also been undertaken.

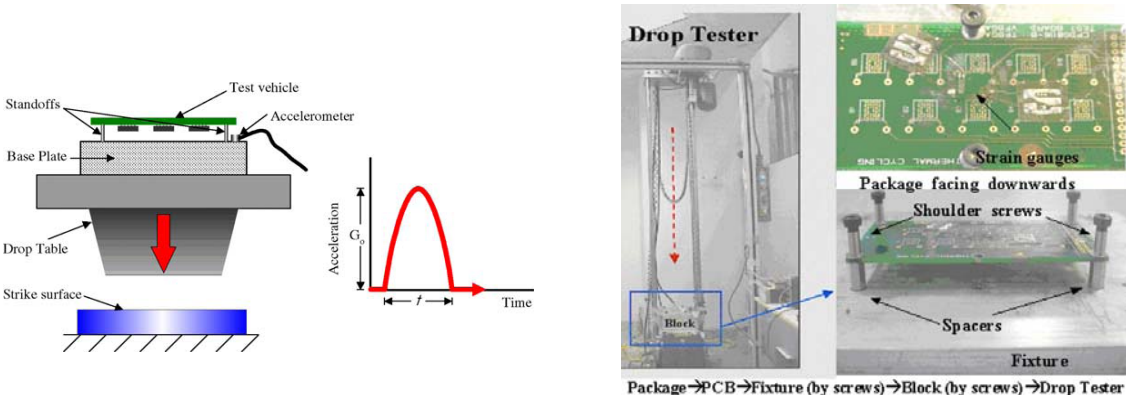

(a) (b)

Fig.5-4 (a) Schematic illustration of JEDEC board-level drop test (from Lai, et al., 2006); and (b) setup of board level drop tester

Three-point bend tests and dynamic drop tests have been widely used for board-level or package-level reliability testing. Therefore, in this study, quasi-static bending and dynamic drop tests are conducted on board level specimens, which comprise a dummy chip bonded on a PCB strip. The objectives of this package level testing are to understand the mechanical response of the IC package under bending and drop impact, and to validate FE simulation employing beam models for solder joints. The experimentally measured values are compared with simulation outputs to demonstrate the ability of FE modeling to predict solder joint failure. Three-point bend tests are first introduced. A study involving FE simulation of PCB board is then undertaken to examine the accuracy of simulating board-level specimens. Finally, experimental tests and numerical simulations are conducted and the results for quasi-static bending and dynamic drop testing of package specimen compared.

5.2 Preliminary study of bending of PCB strip

5.2.1 Static bending of PCB strip

Three point bending tests were performed on PCB strips to obtain load-deflection and strain-deflection curves, and to ascertain the accuracy and repeatability of the test setup. The experimental load and strain information are compared with numerical results in order to verify the simulation techniques. The mechanics of beam bending can be found in many textbooks (Krenk, 2001, Ross, 1996) and the *Appendix D* introduces some concepts related to the three point bending tests conducted.

The PCB strip is 0.75mm thick and 18mm wide. For three-point bending, the maximum bending moment M occurs at the mid-point of the strip (Eq.(D-8), in *Appendix D*). This location experiences the maximum curvature z (Eq.(D-4)), and the maximum longitudinal strain z (Eq.(D-3)). Therefore, a strain gauge is bonded at this location, as shown in Fig.5-5. As this strain value is compared with the numerical output of the node at the centre of the FEM model, a small strain gauge (gauge length 1mm and gauge factor 2.08) is used. The PCB strip is mounted on a three-point bending fixture with a span of 60mm, in conjunction with an Instron Micro-tester. The strain gauge is mounted below the strip and connected to a strain meter and an oscilloscope for data capture.

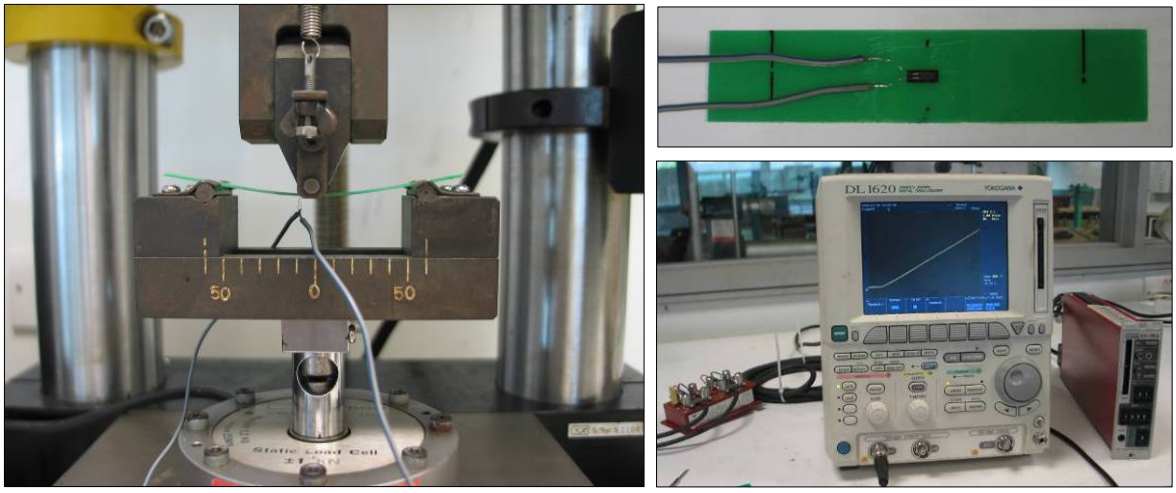

Fig.5-5 Three-point bending of PCB strip

The maximum displacement of the cross-head is set at 5mm and the loading rate used is 0.05mm/s. This corresponds to a 100s test duration. As the beam is quite compliant, an initial gap of around 0.5mm between the loading pin and the beam is proved, in order to ensure that there is no pre-loading in the load-displacement curve. The oscilloscope sampling rate is 100 Hz, the strain meter is operated in DC input mode and the resistance bridge is manually balanced. For three-point bending tests, alignment of the loading pin with the lower part of the fixture is important. As there is no existing fixture to ensure such alignment, a special tool was designed for this purpose. Fig.5-6 shows the load-displacement and strain-displacement curves from five individual tests and the respective average curves, which comprise the initial unloaded portion corresponding to around 0.5mm displacement. These curves display two characteristics; one is that they are quite linear after loading commences, which concurs with the theoretical solution in Eq.(D-10) and Eq.(D-3). The other is that the repeatability is quite good for the five tests, demonstrating that the test setup is acceptable. The average load-deflection and strain-

deflection curves are obtained by omitting the initial zero-load portions from the data.

The experimental curves are then compared with FEM simulation results. A PCB strip is tested instead of a PCB board with IC package for verification purposes because this is a simpler.

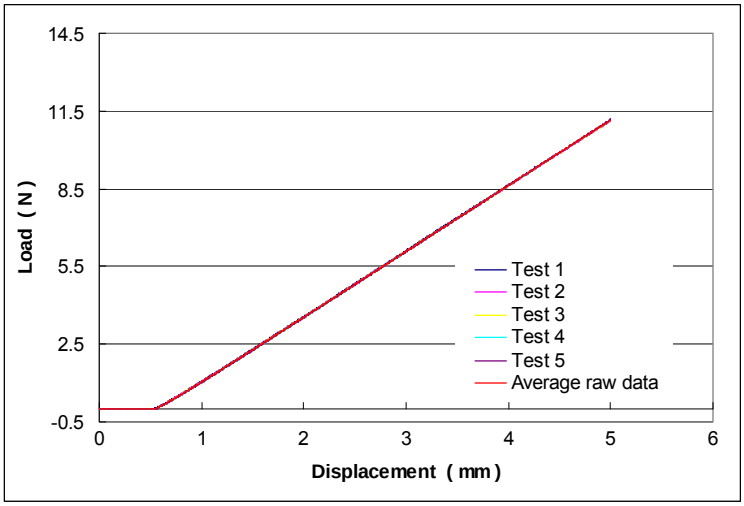

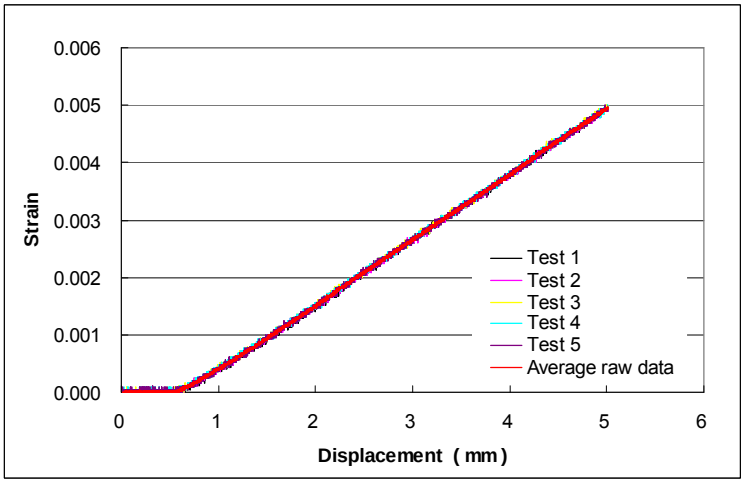

Fig.5-6 Variation of load and strain with beam deflection

5.2.2 FEM simulation of PCB strips

PCB strip specimens for three point bending test measure 0.75mm thick and 18mm wide, with a span of 60mm, and the FEM model was assigned similar dimensions. The coordinate system for the PCB is shown in Fig.5-7. Based on the physical constraints in three-point bending tests, the edges of the PCB model are constrained from moving in the z-direction, and the y-axis center line is assigned a vertical speed of 5mm/s. The total simulation time is 100s, corresponding to a maximum deflection of 5mm at the center line.

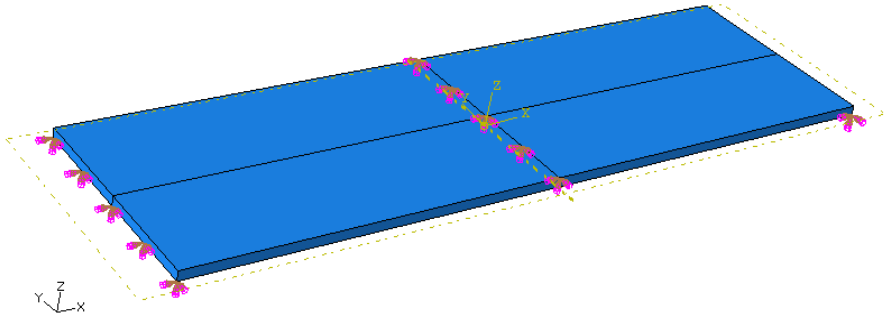

Fig.5-7 FEM model of PCB strip under three-point bending

One simulation consideration is the determination of an appropriate mesh size and element type, which will affect the computational cost and simulation accuracy. Because in the later, a PCB strip with an IC package containing solder joints mounted is subjected to bending and drop tests, and corresponding FEM simulation; direct comparison between the experimental and simulated load and strain histories on a PCB will be a gauge of the simulation accuracy. Therefore, it should be clear how the mesh size and element type for a PCB affect the simulation results.

For this model, the default approximate average size of the mesh assigned by ABAQUS is 1.5mm; this results in one layer of elements along the PCB thickness, as shown in Fig.5-8. As the longitudinal strain is proportional to the distance z from the neutral axis, a single layer of elements is insufficient for generating correct strain values. Therefore the effect of two factors – number of element layers along the z-axis and the global mesh size in the x-y plane – on the simulation results are examined. As shown in Fig.5-8, the sizes of the PCBs investigated are 0.5mm, 1mm, 2mm, 3mm and 4mm; and the number of element layers ranges from 1 to 8.

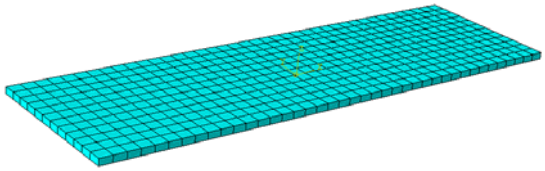

Default: global size 1.5mm, one layer

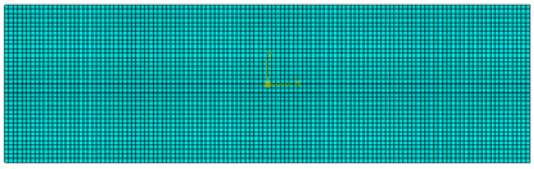

Global size 0.5mm, six layers

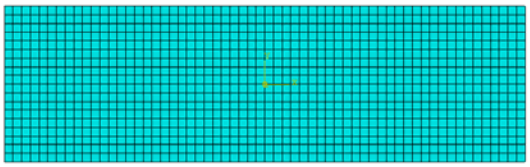

Global size 1mm, six layers

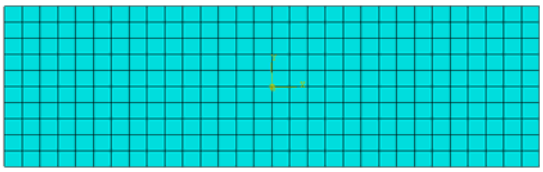

Global size 2mm, six layers

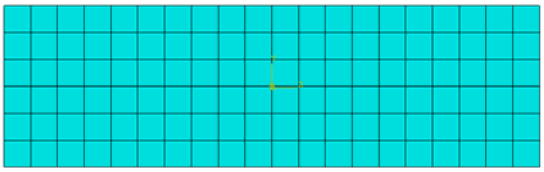

Global size 3mm, six layers

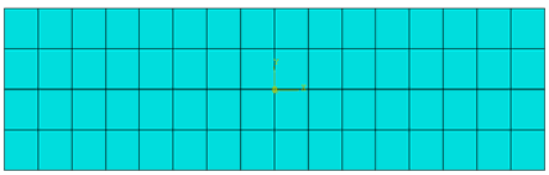

Global size 4mm, six layers

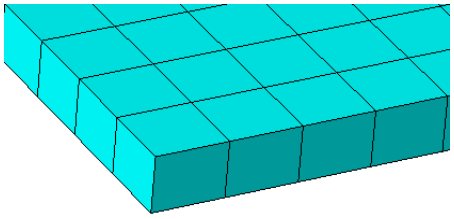

Global size 1mm, one layer

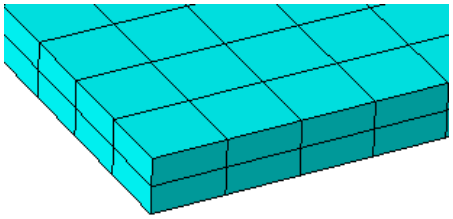

Global size 1mm, two layers

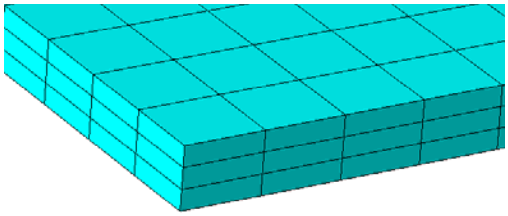

Global size 1mm, three layers

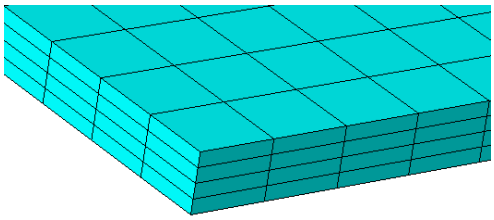

Global size 1mm, four layers

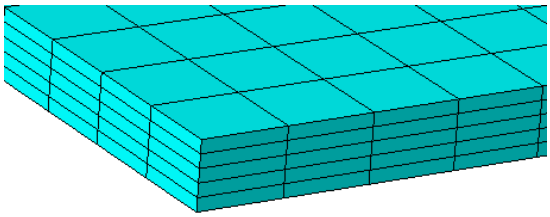

Global size 1mm, five layers

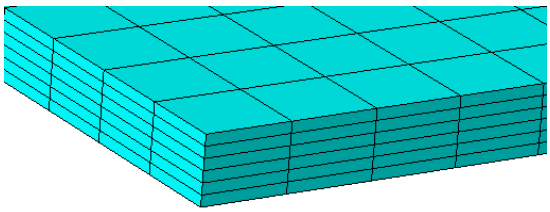

Global size 1mm, six layers

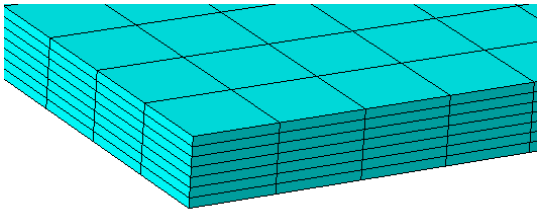

Global size 1mm, seven layers

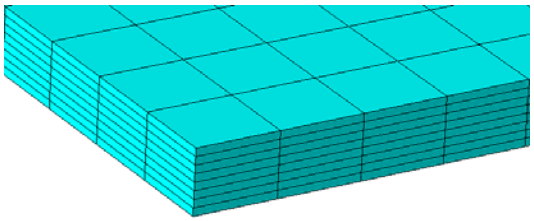

Global size 1mm, eight layers

Fig.5-8 FEM models of PCB investigated

The PCB model comprises 3D hexahedral elements (C3D8R, 8-node linear bricks, with reduced integration and hourglass control) from the ABAQUS/Standard solid element library.

(1) PCB with orthotropic material properties

Microscopic observation of the PCB cross-section is performed, as shown in Fig.5-9. It shows that a PCB is more like an orthotropic material. In ABAQUS, "linear elasticity in an orthotropic material is most easily defined by giving the engineering constants: the three moduli E_1, E_2, E_3; Poisson's ratios v_{12}, v_{13}, v_{23}; and the shear moduli G_{12}, G_{13}, and G_{23} associated with the material's principal directions. These moduli define the elastic compliance according to

$$\begin{Bmatrix} \varepsilon_{11} \\ \varepsilon_{22} \\ \varepsilon_{33} \\ \gamma_{12} \\ \gamma_{13} \\ \gamma_{23} \end{Bmatrix} = \begin{bmatrix} 1/E_1 & -\nu_{21}/E_2 & -\nu_{31}/E_3 & 0 & 0 & 0 \\ -\nu_{12}/E_1 & 1/E_2 & -\nu_{32}/E_3 & 0 & 0 & 0 \\ -\nu_{13}/E_1 & -\nu_{23}/E_2 & 1/E_3 & 0 & 0 & 0 \\ 0 & 0 & 0 & 1/G_{12} & 0 & 0 \\ 0 & 0 & 0 & 0 & 1/G_{13} & 0 \\ 0 & 0 & 0 & 0 & 0 & 1/G_{23} \end{bmatrix} \begin{Bmatrix} \sigma_{11} \\ \sigma_{22} \\ \sigma_{33} \\ \sigma_{12} \\ \sigma_{13} \\ \sigma_{23} \end{Bmatrix}. \quad (5\text{-}1)$$

The quantity v_{ij} has the physical interpretation of the Poisson's ratio that characterizes the transverse strain in j –direction, when the material is stressed in the i –direction. In general, v_{ij} is not equal to v_{ji}, they are related by $v_{ij}/E_i = v_{ji}/E_j$. The engineering constants can also be given as functions of temperature and other predefined fields, if necessary" (from ABAQUS Analysis User's Manual: Material, *Defining orthotropic elasticity by specifying the engineering constants*).

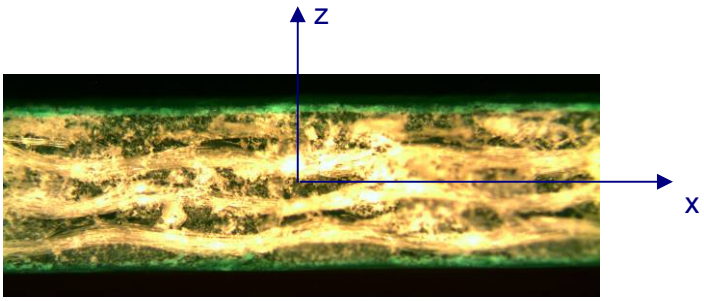

Elastic modulus (GPa)	Yield/Hardening (MPa/ε_p)	Poisson's ratio	Density (kg/m^3)	Dimension (mm)
E_1/E_2: 16.85 E_3: 7.375 G_{12}:3.4 G_{13}/G_{23}:2.25	180,0; 280,0.01; 330,0.02	V_{13}/v_{23}: 0.39 V_{12}: 0.11	2177	Span: 60mm Width: 18mm Thickness: 0.78mm

Fig.5-9 Microscopic image of PCB cross-section and input material properties (orthotropic) for ABAQUS

Fig.5-10 depicts the longitudinal (x-axis) strain distribution in the deformed PCB strip for a vertical deflection of 5mm generated by three-point bending (1mm average mesh size and 6 element layers along the thickness). The results show that the longitudinal strain (LE11) is positive (tension) at the bottom and negative (compression) at the upper surface, and are anti-symmetric with respect to the distance z from the neutral axis. The strain amplitude decreases from the center of the PCB to the two ends. Nodal loads strains are also indicated in Fig.5-10; the values should correspond to the load history recorded by the Instron machine and the strain history recorded by the strain gauge in three point bending tests.

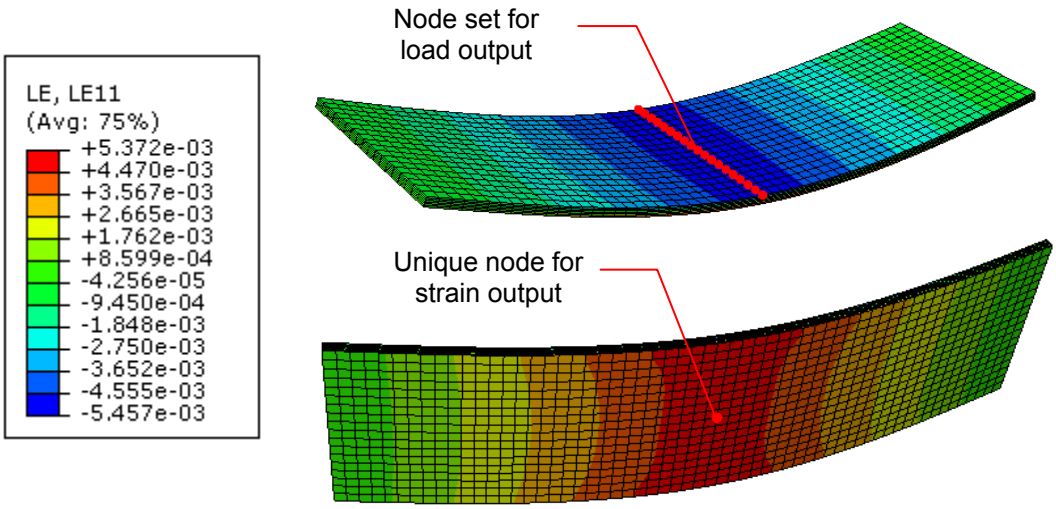

Fig.5-10 Contours of longitudinal strain (LE11) on deformed PCB strip

Comparisons between simulation and experimental results were made. Fig.5-11 shows the effect of mesh size on the load and strain values (the number of element layers is fixed at 6). The simulation results show that the load is not sensitive to mesh size and all the curves coincide with one another, as well as with the average experimental result. For the predicted strain, there is an increase in value when the mesh size is decreased, (i.e. the results with a 0.5mm mesh size are closer to experimental data than that for a 4mm mesh size).

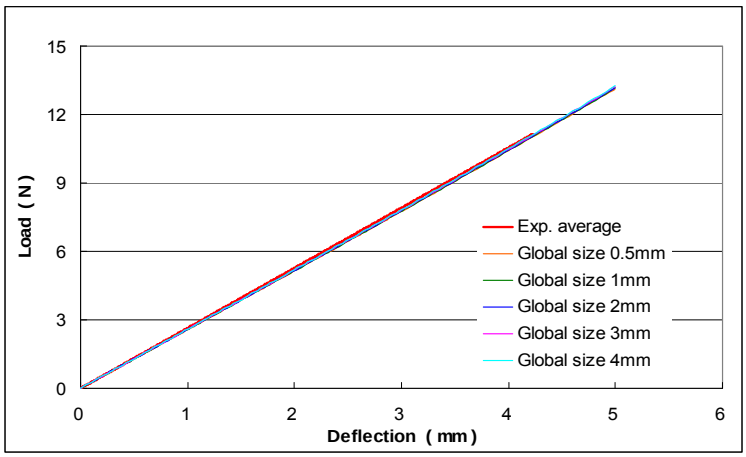

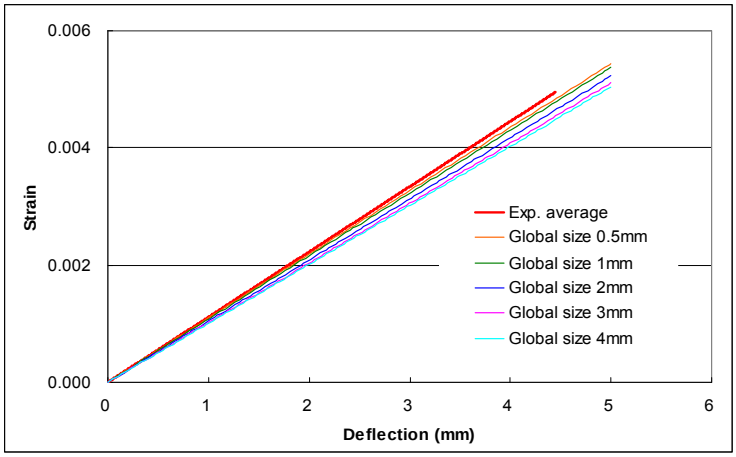

Fig.5-11 Effect of mesh size on simulation load and strain values (3D solid model, orthotropic material properties)

The effect of the number of element layers is much greater than that of the other mesh dimensions, as shown in Fig.5-12. With only one layer, both the load and the strain values are close to 0; with an increase in the number of element layers in the PCB thickness, the load and strain values increase gradually towards the average experimental result. This demonstrates that in order to obtain a meaningful comparison between the numerical and experimental methods, there must be sufficient element layers in the PCB thickness direction.

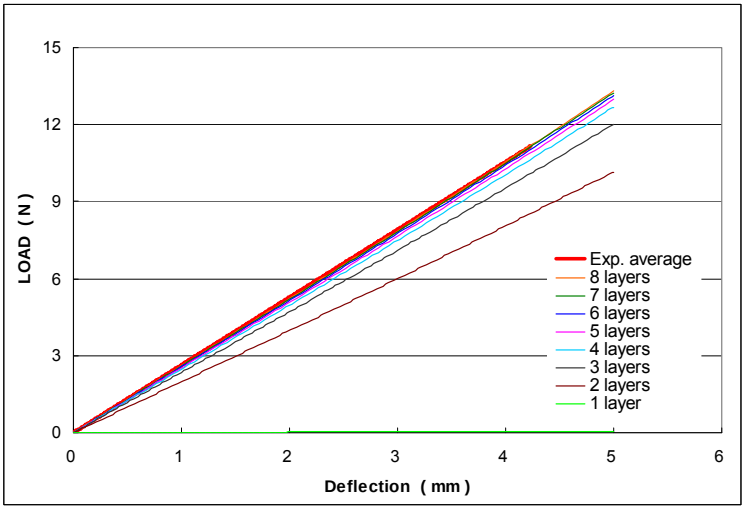

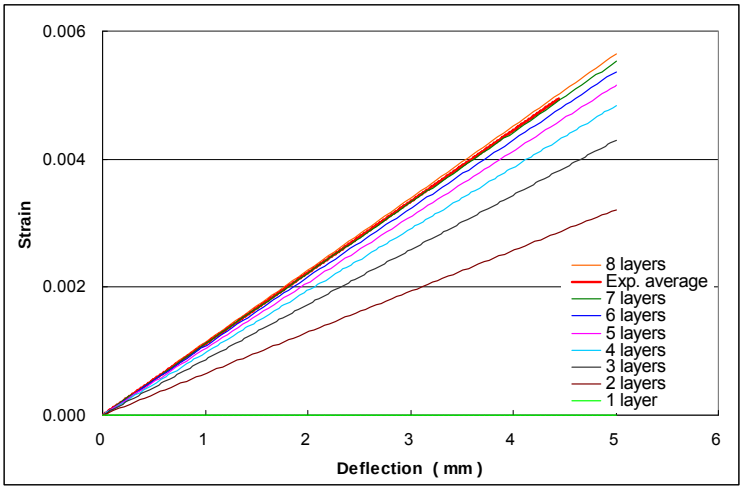

Fig.5-12 Effect of number of element layers on load and strain values of simulation output (3D solid elements with orthotropic material properties)

A fine mesh improves the accuracy of numerical simulation; however, the computational cost will increase correspondingly, and the latter is always a concern. A quantitative study on this is performed, as shown in Table 5-2. The load and strain value at 5mm deflection are noted and listed in the table (as “maximum load” and “maximum strain” respectively) for each of the simulations. As the load-deflection and strain-deflection curves are linear, the slope of each curve can be derived from these maximum values. For clarity, non-dimensional values (percentage) of the load and strain are calculated with respect to corresponding experimental values for 5mm deflection.

Table 5-2 also includes information on the number of elements, total CPU time and wall clock time. The total CPU time is the sum of the user time (i.e., CPU time spent executing ABAQUS) and system time (i.e., the amount of OS kernel CPU time spent by the operating system doing work on behalf of the ABAQUS processes). Wall clock time refers to the actual physical time spent for the analysis process to complete (if the simulation is running on a single

CPU and the job has exclusive access to that CPU, the difference between total CPU time and wall clock time is largely the time taken to perform all I/O requests).

For easy comparison of the numerical results, all values are non-dimensionalized with respect to values from the model with a 0.5mm mesh size and 6 element layers.

Table 5-2 Summary of effect of mesh size and number of element layers on simulation results (3D solid model, orthotropic material properties)

Number of layers	Global size (mm)	Maximum load (N)	*(Percentage)*	Maximum strain	*(Percentage)*	Number of elements	*(Percentage)*	Total CPU time (s)	*(Percentage)*	Wallclock time (s)	*(Percentage)*
Experimental average		13.1828	*100.0%*	*5.56E-03*	*100.0%*						
					Reference number:	25920	*100.00%*	10753	*100.0%*	7157	*100.0%*
6	0.5	13.1389	*99.7%*	5.43E-03	*97.7%*	25920	*100.00%*	10753	*100.0%*	7157	*100.0%*
	1	13.1471	*99.7%*	5.37E-03	*96.5%*	6480	*25.00%*	1976	*18.4%*	1448	*20.2%*
	2	13.1830	*100.0%*	5.23E-03	*93.9%*	1800	*6.94%*	491	*4.6%*	399	*5.6%*
	3	13.2259	*100.3%*	5.11E-03	*91.8%*	720	*2.78%*	205	*1.9%*	177	*2.5%*
	4	13.2482	*100.5%*	5.04E-03	*90.6%*	384	*1.48%*	119	*1.1%*	105	*1.5%*
8	1	13.3111	*101.0%*	5.64E-03	*101.3%*	8640	*33.33%*	3067	*28.5%*	2116	*29.6%*
7	1	13.2468	*100.5%*	5.52E-03	*99.3%*	7560	*29.17%*	2421	*22.5%*	1717	*24.0%*
6	1	13.1471	*99.7%*	5.37E-03	*96.5%*	6480	*25.00%*	1976	*18.4%*	1448	*20.2%*
5	1	12.9827	*98.5%*	5.16E-03	*92.7%*	5400	*20.83%*	1491	*13.9%*	1136	*15.9%*
4	1	12.6802	*96.2%*	4.83E-03	*86.9%*	4320	*16.67%*	1054	*9.8%*	819	*11.4%*
3	1	12.0247	*91.2%*	4.29E-03	*77.1%*	3240	*12.50%*	702	*6.5%*	565	*7.9%*
2	1	10.1610	*77.1%*	3.21E-03	*57.8%*	2160	*8.33%*	462	*4.3%*	379	*5.3%*
1	1	0.0602	*0.5%*	2.99E-09	*0.0%*	1080	*4.17%*	210	*2.0%*	186	*2.6%*

The plots in Fig. 5-13 in terms of the percentage values in Table 5-2 show the variation in the maximum load and strain values, as well as the corresponding total CPU time (in percentage) against mesh size and number of element layers along the PCB thickness; the knee in each curve indicates a transition. The curves of total CPU time show that there is a rapid reduction when the mesh size increase from 0.5mm to 1mm, and the increment in computational time with number of element layers is gradual. Even with 7 or 8 layers of elements (1mm mesh size), the total CPU time is still less than 30% of that for

a 0.5mm mesh (6 layers). Conclusions may be drawn that sufficient layers in the PCB thickness direction are required to optimise simulation accuracy. For three-point bending of PCB strips, the model meshed with 1mm elements and 7 layers appears to be optimal as the predicted load and strain values are 1.005 and 0.993 of the experimental values. If accuracy of strain values is not crucial, the number of layers could be reduced to 6, 5, or even 3, and this still yields 91.2% of the experimental load value, while taking only about 7.9% of total CPU time. Table 5-2 provides a quantitative guide for the balance between simulation accuracy and computational cost.

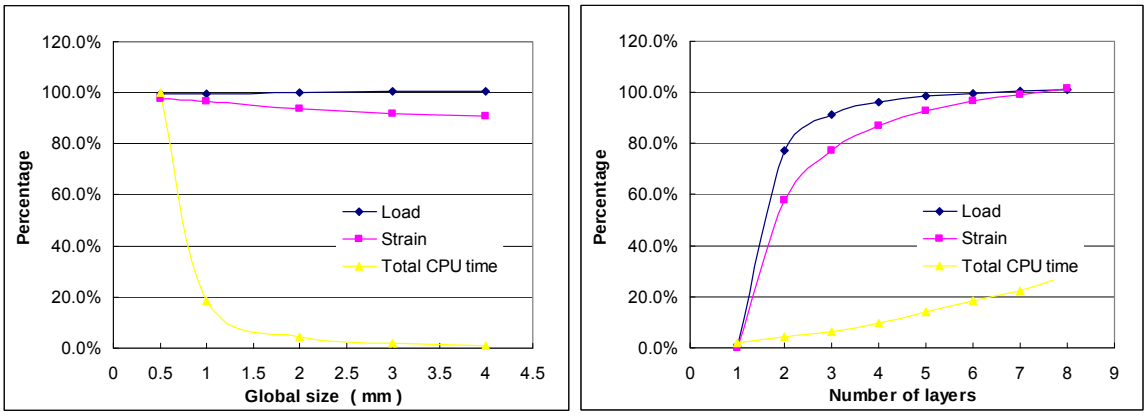

Fig. 5-13 Effect of mesh size and number of element layers on non-dimensionalized load and strain values and total CPU simulation time (3D solid elements with orthotropic material properties)

(2) Use of isotropic material properties

From a review of literature, it is found that there are quite a number of studies that treat PCBs as isotropic and only use a global Young's modulus together with a Poisson's value to describe its elastic mechanical properties.

From three-point bending of a PCB strip, the Young's modulus of an isotropic material can also be determined. From Eq.(D-10), the modulus E can be derived in terms of the load and deflection at the centre of the beam,

$$w(0) = w_{\max} = -\frac{FL^3}{48EI} \quad \Rightarrow \quad E = -\frac{FL^3}{48Iw_{\max}} \tag{5-2}$$

where L is the span (0.06m) and I is the second moment of area of the cross-section about the neutral axis. For a beam of rectangular cross section like the current PCB strip (thickness $h = 0.78mm$ and width $b = 18mm$), the second moment of area of the cross-section (Eq.(D-5)) is

$$I = \frac{1}{12}bh^3 = \frac{1}{12} \times 0.018 \times 0.00078^3 = 7.12 \times 10^{-13} m^3 \tag{5-3}$$

Therefore, the modulus E can be calculated from the load-deflection curve from three-point bend tests:

$$E = -\frac{FL^3}{48Iw_{\max}} = 16.67\, GPa \tag{5-4}$$

Compared with orthotropic material properties (where E_1, E_2 are 16.85 GPa and E_3 is 7.375 GPa), this isotropic elastic modulus E is quite close to the E_1 and E_2 values. For this isotropic material, the Poisson's ratio is selected as 0.39, similar to $v_{13 \text{ and }} v_{23}$ in the orthotropic definition.

A series of simulations is also conducted to investigate how the material properties selected affects the simulation results. Cases of different mesh size and number of layers are studied, similar to that in the preceding section. Fig.5-14 and Fig.5-15 show the variation of load and longitudinal strain with mesh size and number of layers; the trend is similar to the results from the model with orthotropic material properties.

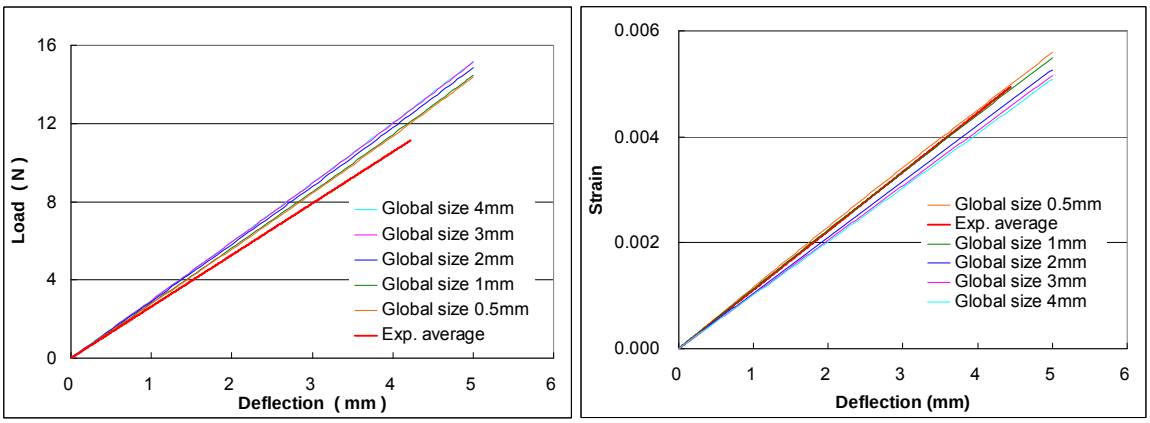

Fig.5-14 Effect of size of mesh on simulation load and strain values (3D solid model, isotropic material properties)

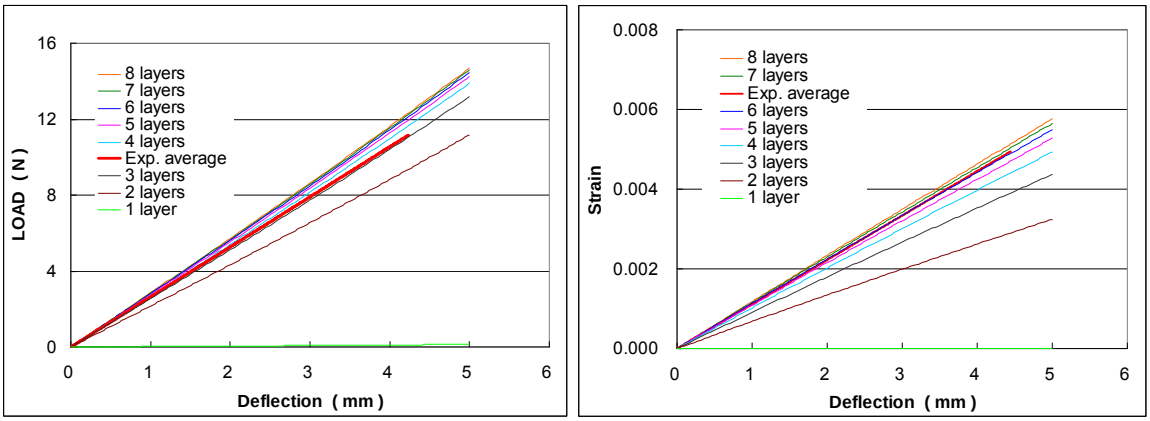

Fig.5-15 Effect of number of element layers on simulation load and strain values (3D solid model, isotropic material properties)

A major difference is that the load based on isotropic material converges to a value higher than the experimental result, with increasing mesh density. This is clearly seen in Fig.5-16, which is a comparison between the two material property definitions for a model with a 1mm mesh and 7 element layers. Fig.5-16 also reveals that the strain LE33 (along the PCB thickness direction) based on the isotropic material model is higher than that corresponding to orthotropic material. This could be caused by the difference between the isotropic modulus E=16.67GPa and the orthotropic value of E_3=7.375GPa, This should be the reason that the load based on isotropic material is larger

than experimental values and values based on orthotropic material.

As with Table 5-2, another quantitative analysis is also conducted and listed in Table 5-3. The reference value for the number of elements and computation time are the same as that in Table 5-2 for purpose of direct comparison. It is seen that the computational cost is approximately the same for the two material definitions.

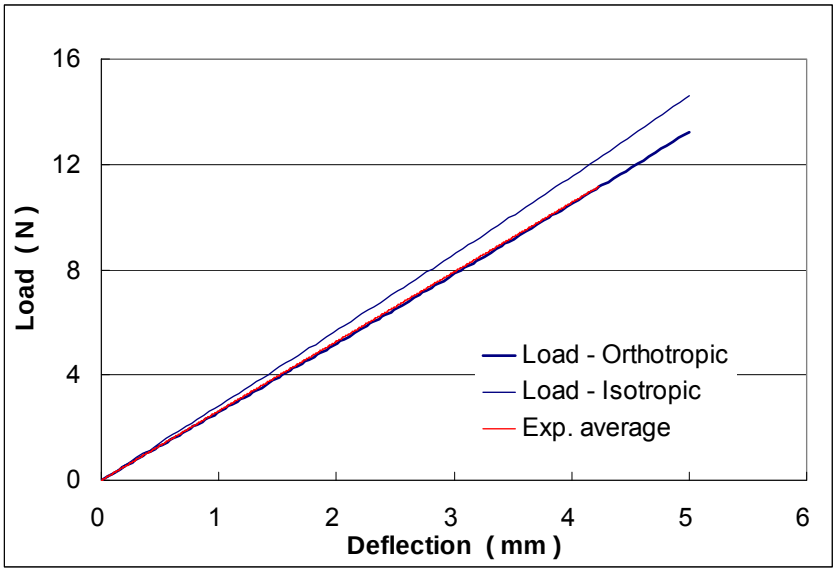

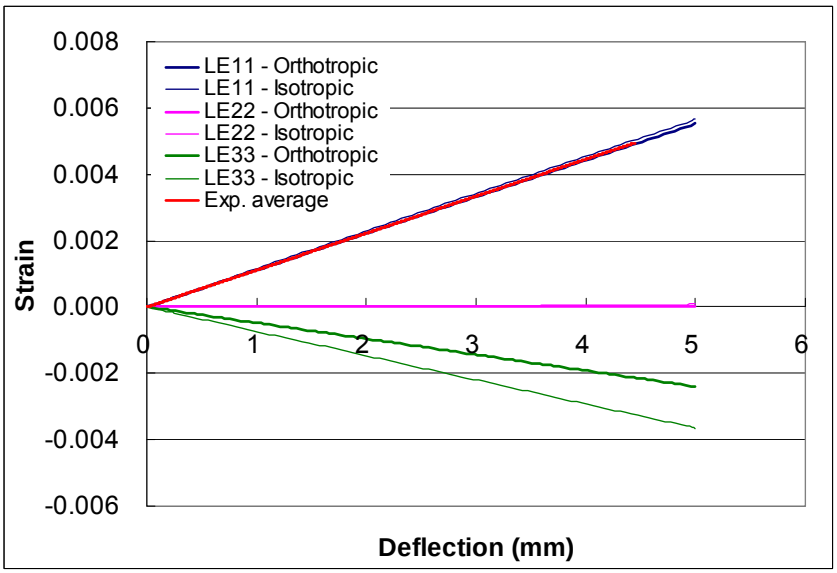

Fig.5-16 Comparison of load and strain FEM results based on orthotropic and isotropic material properties. (3D solid model, 1mm mesh size and 7 element layers in PCB thickness)

Table 5-3 Summary of effect of mesh size and number of element layers on simulation results (3D solid model, isotropic material properties)

Number of layers	Global size (mm)	Maximum load (N)	*(Percentage)*	Maximum strain	*(Percentage)*	Number of elements	*(Percentage)*	Total CPU time (s)	*(Percentage)*	Wallclock time (s)	*(Percentage)*
Experimental average		13.18	*100.0%*	5.56E-03	*100.0%*						
					Reference number:	25920	*100.00%*	10753	*100.0%*	7157	*100.0%*
6	0.5	14.37	*109.0%*	5.60E-03	*100.6%*	25920	*100.00%*	11133	*103.5%*	7211	*100.8%*
	1.0	14.46	*109.7%*	5.49E-03	*98.7%*	6480	*25.00%*	2118	*19.7%*	1512	*21.1%*
	2.0	14.86	*112.7%*	5.27E-03	*94.7%*	1800	*6.94%*	529	*4.9%*	418	*5.8%*
	3.0	15.13	*114.7%*	5.16E-03	*92.7%*	720	*2.78%*	212	*2.0%*	179	*2.5%*
	4.0	15.17	*115.0%*	5.09E-03	*91.5%*	384	*1.48%*	120	*1.1%*	106	*1.5%*
8	1.0	14.69	*111.4%*	5.76E-03	*103.6%*	8640	*33.33%*	3414	*31.7%*	2333	*32.6%*
7	1.0	14.59	*110.7%*	5.65E-03	*101.5%*	7560	*29.17%*	2720	*25.3%*	1979	*27.7%*
6	1.0	14.46	*109.7%*	5.49E-03	*98.7%*	6480	*25.00%*	2118	*19.7%*	1512	*21.1%*
5	1.0	14.26	*108.1%*	5.27E-03	*94.7%*	5400	*20.83%*	1593	*14.8%*	1172	*16.4%*
4	1.0	13.91	*105.5%*	4.94E-03	*88.7%*	4320	*16.67%*	1126	*10.5%*	863	*12.1%*
3	1.0	13.19	*100.0%*	4.37E-03	*78.6%*	3240	*12.50%*	747	*6.9%*	601	*8.4%*
2	1.0	11.17	*84.7%*	3.24E-03	*58.3%*	2160	*8.33%*	472	*4.4%*	384	*5.4%*
1	1.0	0.14	*1.0%*	3.08E-08	*0.0%*	1080	*4.17%*	212	*2.0%*	187	*2.6%*

5.3 Quasi-static bending of PCB with IC packages mounted

5.3.1 Quasi-static bend tests

Three-point bending tests are employed to study the mechanical response of solder joints in IC packages, and the objectives are to verify whether the beam model for solder joints (with mechanical properties obtained from experimental results) can simulate the response of solder joints and predict their failure in IC packages. For this purpose, a dummy IC package is used instead of an actual one. The dummy IC package comprises two pieces of substrate bonded to each other by 24 solder joints arranged in four columns – two inner and two outer columns (Fig.5-17 a). A small square PCB is bonded to one substrate to represent a Silicon chip, and the bend test specimen is a PCB strip (80mm in length and 18mm in width) with the dummy IC package

mounted (Fig.5-17 b). During testing, both the PCB strip and the square PCB will deform due to bending. Solder joint failure will cause only a slight change in the overall strain response of the PCB strip. However, the strain in the Square PCB will drop significantly from its maximum magnitude because of the solder joint pattern in the dummy IC package. Therefore, to detect failure of solder joints during bending tests, a strain gauge (1mm gauge length) is mounted at the center of the square PCB to record the strain history, which is then compared with FEM simulation results to verify the accuracy and validity of the FEM modeling.

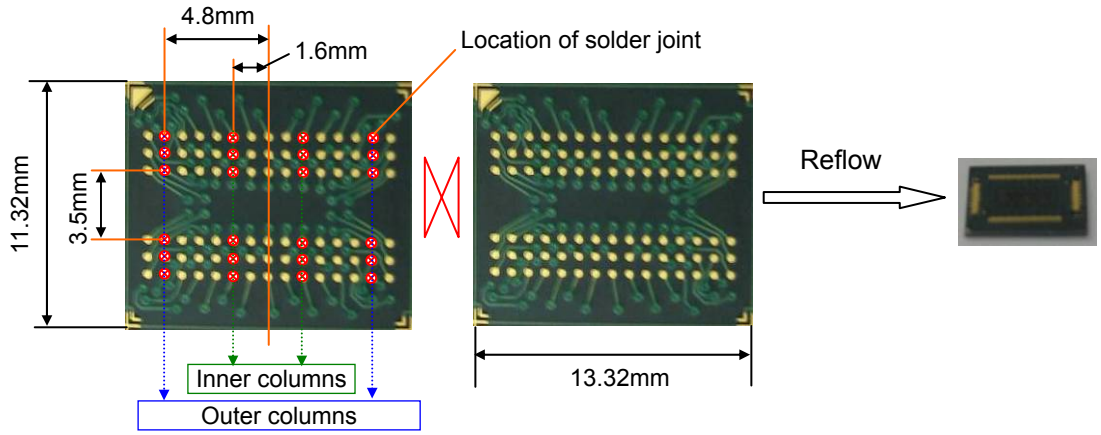

(a) Locations of solder joints (indicated by red circles) in dummy IC package

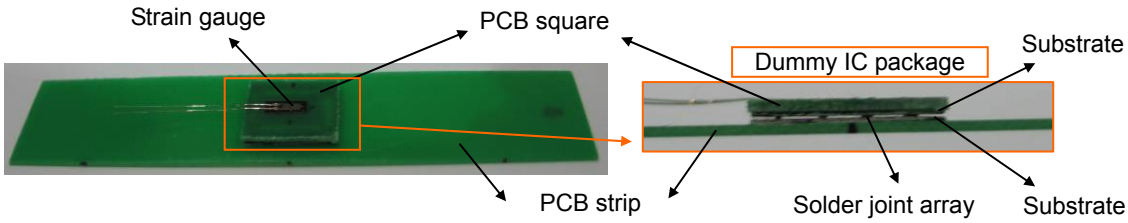

(b) PCB strip with dummy IC package mounted

Fig.5-17 Bending test specimen; (a) locations of solder joints in dummy IC package (b) PCB strip with dummy package mounted and location of strain gauge for detection of solder joint failure

Quasi-static bending tests are conduced on an Instron Micro-tester. The span of the three-point bend set-up is 60mm and specimens are mounted with the dummy package facing downwards (Fig.5-18). The loading rate of the Micro-tester is 0.05mm/s and the total displacement is 5mm. Testing commences with the loading pin 0.5mm above the PCB strip to avoid any preload on the specimen that may degrade the specimen quality. The force-deflection curve is recorded by the Instron machine and the strain history at the center of the square PCB is measured by strain gauges. The two curves are then compared with FEM simulation results.

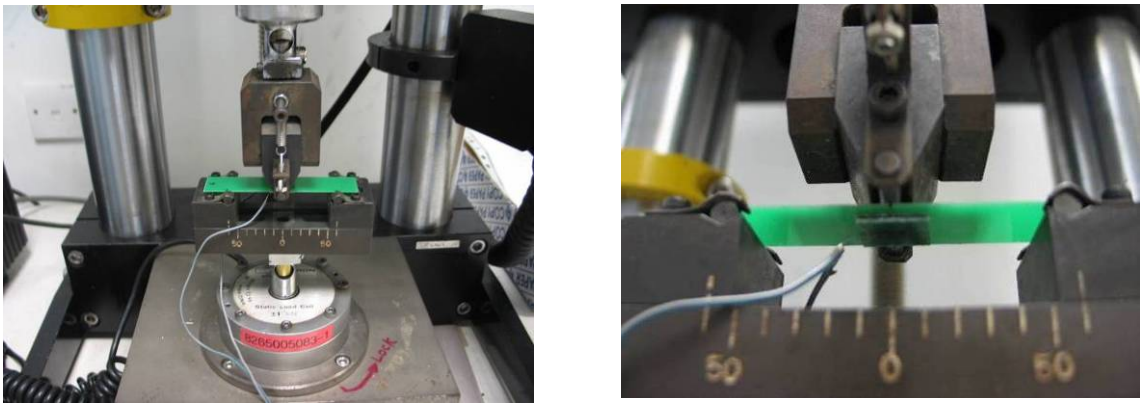

(a) Specimen mounted on Instron micro-tester for three-point bending test

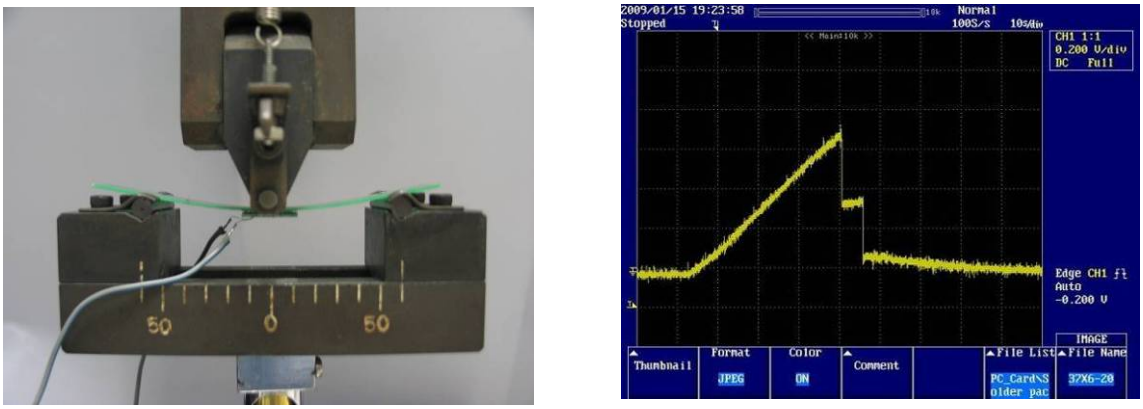

(b) Specimen under bending and example of strain profile displayed on oscilloscope

Fig.5-18 Three-point bending test on PCB strip with dummy IC package mounted

Four specimens are subjected to quasi-static bending tests. The experimental load-deflection and strain-deflection curves are in Fig.5-19. Each specimen was tested three times. For the first test, there are slight sharp drops in the load-deflection curve, illustrating possible occurrence of solder joint damage; the corresponding strain-deflection curve shows significant drops in magnitude which coincide with the drops in the load-deflection curve. After the first test, the dummy package is still connected to the PCB strip and it is not possible to observe solder joint damage inside the package. Therefore, two more bending tests are performed on the same specimen; this is to ensure that the package loses its resistance to bending permanently and to obtain information on the response of the specimen after solder joint damage occurs. The results of the second and third tests are similar, indicating that no further damage occurs. The load-deflection curves are close to that of the first test but without any drops. The corresponding strain-deflection responses from the second and third tests show considerably lower strain values compared to the first test, demonstrating the obvious loss of resistance of the dummy package to bending (these characteristics of the mechanical response before and after solder joint failure are used later to examine whether the solder joints inside such specimens are broken).

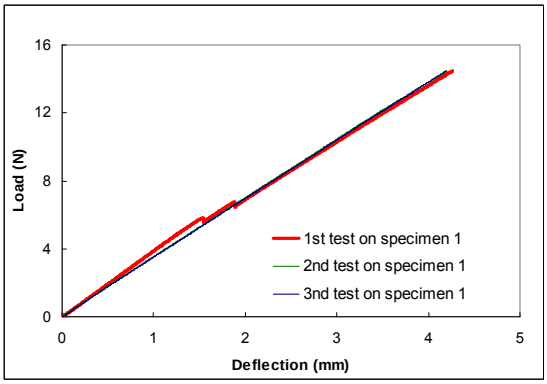

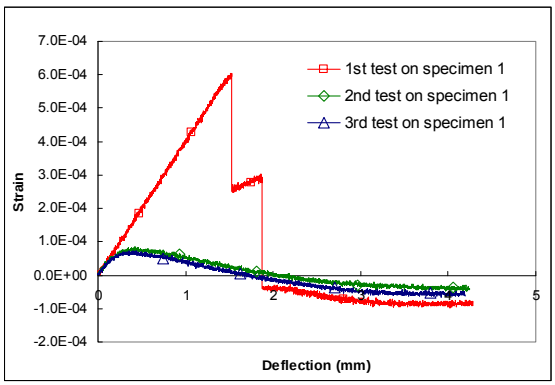

(a) Plots of load and strain against deflection for specimen 1

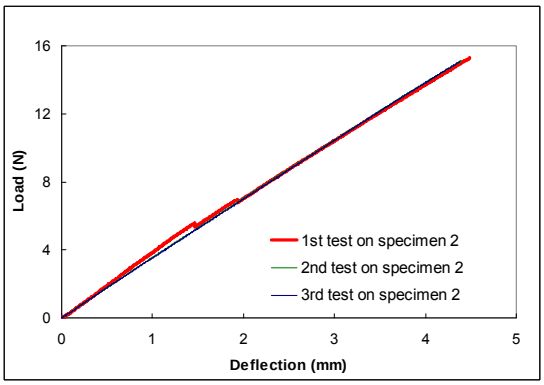

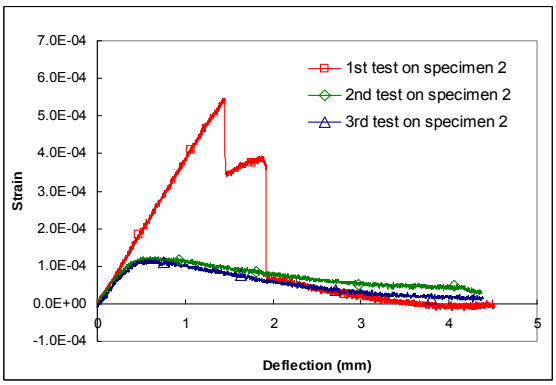

(b) Plots of load and strain against deflection for specimen 2

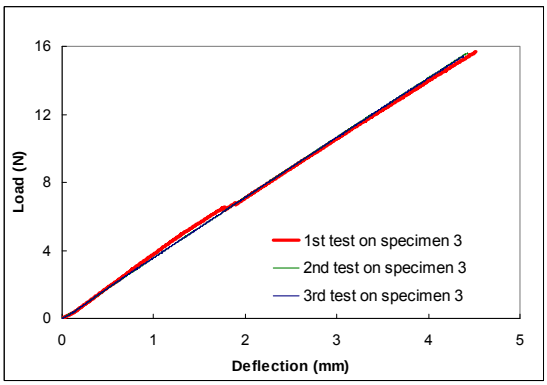

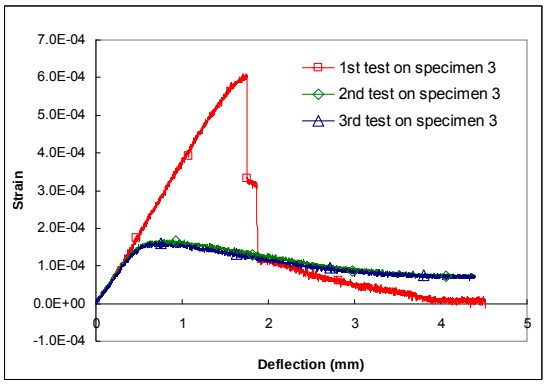

(c) Plots of load and strain against deflection for specimen 3

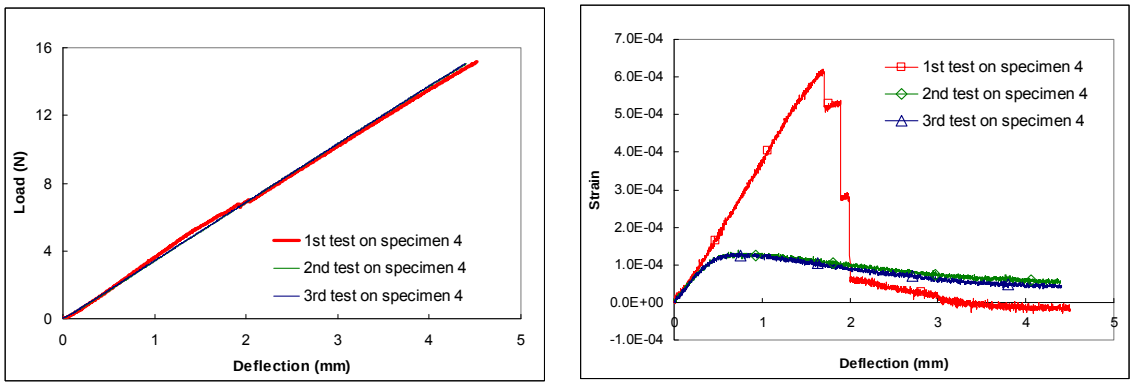

(d) Plots of load and strain against deflection for specimen 4

Fig.5-19 Load-deflection and strain-deflection curves recorded by Instron micron tester and strain gauges in three-point bending tests on four specimens, each conducted three times.

A comparison of the load and strain profiles from the four specimens for the first test is shown in Fig.5-20. Repeatability of the overall load-deflection response is quite good; this is because the magnitude of the load drops induced by breakage of solder joints is small compared to the bending load of the PCB strip. Repeatability of the strain-deflection curves before solder joint breakage is also good. The drops in the strain magnitude are obvious when solder joints break. As in actual tests, it is not possible for the solder joints to break simultaneously. There are two drops in strain (corresponding to breakage of the two outer columns of solder joints in the dummy package), and the instants they occur are arbitrary. Compared with the load-deflection curves, the strain-deflection curves are more sensitive to the breakage of solder joints in the dummy IC package.

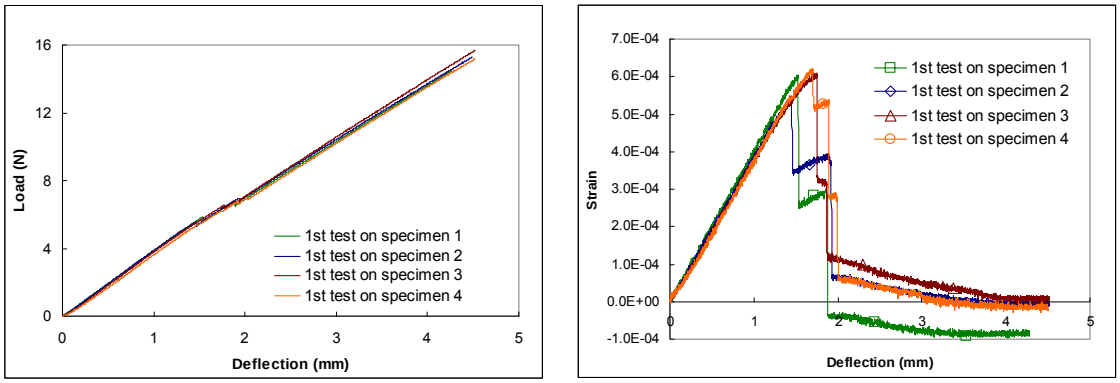

Fig.5-20 Comparison of load and strain profiles for four specimens subjected to bending tests

After the three bending tests for each specimen, the dummy package remains connected to the PCB strip. This demonstrates that the bending process breaks the solder joints in the two outer columns in the first test, but the joints in the two inner columns are not completely broken even after the third test. After testing, the dummy package is dyed with ink and manually peeled apart after the ink is dried. Fig.5-21 shows a pair of the substrates from a dummy package and indicates that the failure mode is pad peel-off. The magnified image shows that the locations corresponding to the outer column are completely covered by ink, indicating complete breakage of the outer solder joints. The locations of the inner column are partially coloured, showing that the bending causes only some degree of cracking in the inner solder joints.

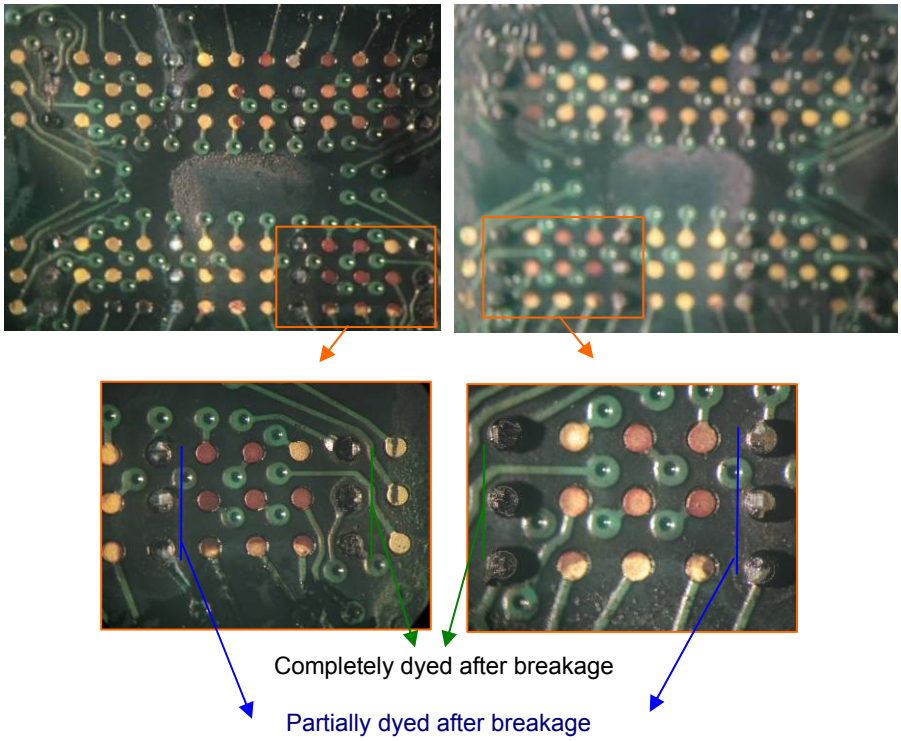

Fig.5-21 Solder joint failure in dummy IC package (specimen was subjected to ink-dye after quasi-static bending)

5.3.2 Numerical simulation of bending of IC packages

Numerical simulations of the bending of PCB strips with a dummy IC package mounted are performed to verify the validity of the beam model in predicting the mechanical response of solder joints under quasi-static loading. Load-deflection and strain-deflection curves from three-point bending experiments are compared with corresponding numerical results; the mechanical response of solder joints was analyzed.

Fig.5-22 shows details of the FEM model of the PCB strip with a dummy IC package mounted. Solder joints are simulated by the beam model with strain-rate dependant mechanical properties incorporated. The PCB is meshed by

seven layers of 3D solid continuum elements through the thickness. Orthotropic material properties are assigned to the PCB material, and the substrates are assigned isotropic material properties.

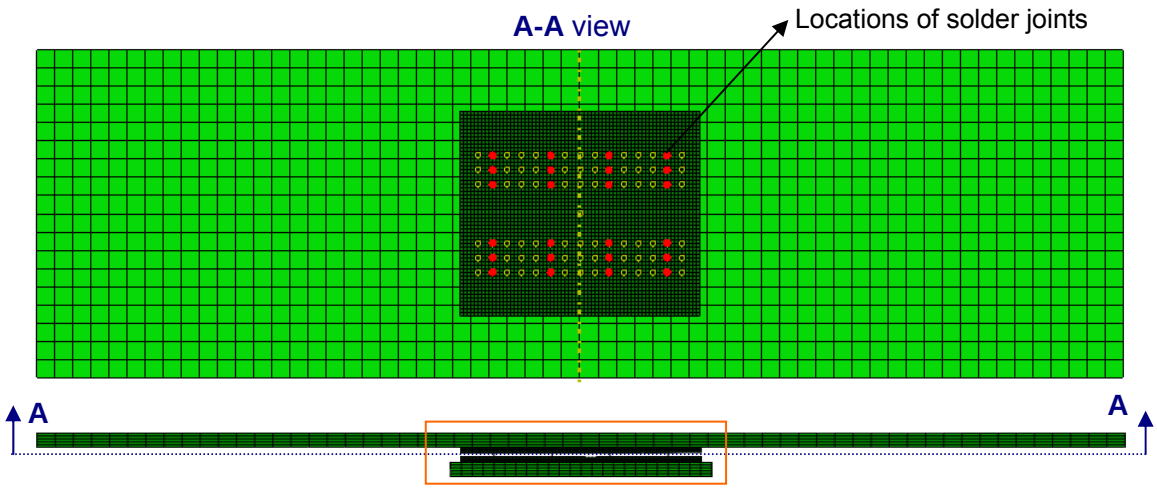

(a) FEM model of PCB strip with dummy IC package mounted

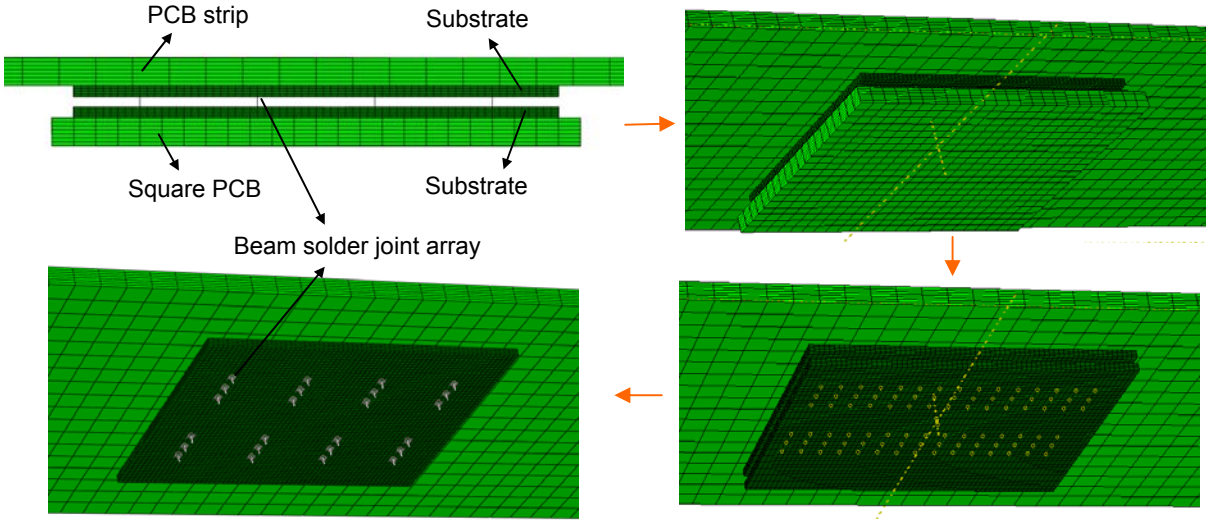

(b) Detailed view of dummy IC package

Fig.5-22 FEM model of PCB specimen for three-point bending tests

To simulate three-point bending, the boundary conditions shown in Fig.5-23a are prescribed. A constant velocity of 0.05mm/s is assigned to the mid-section of the PCB strip, while the two edges at the ends are constrained in the z-

direction (u3=0) throughout the bending process. Nodal values are monitored to obtain load-deflection curves and strain histories (Fig.5-23b).

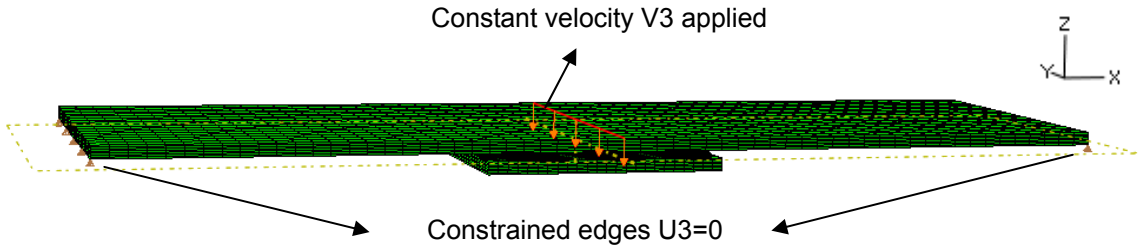

(a) Boundary conditions for simulation of three-point bending

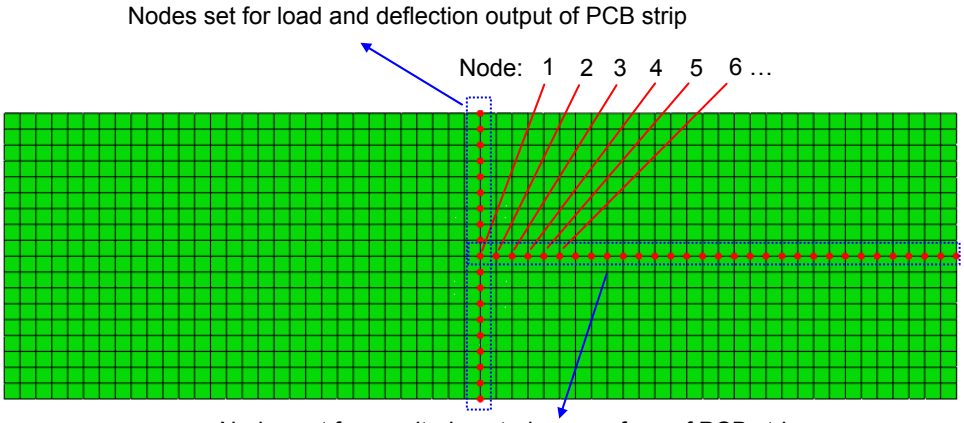

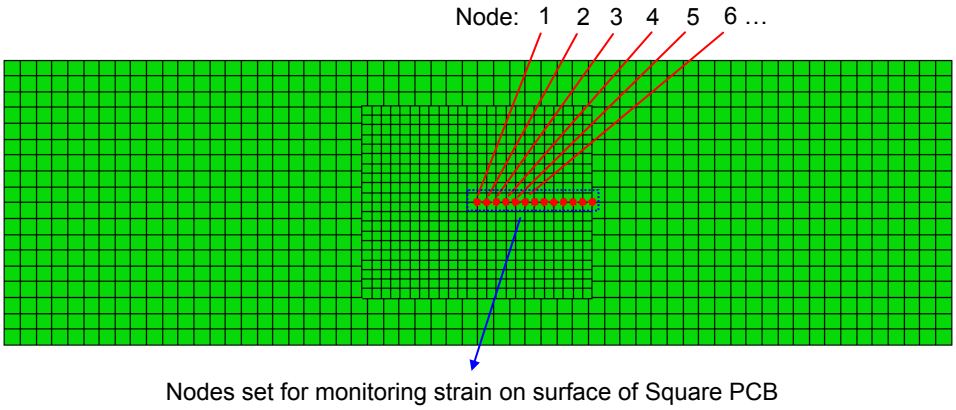

(b) Nodes on the surface of the PCB strip and square PCB for monitoring of force and strain

Fig.5-23 Boundary conditions for three-point bending simulation and nodes sets for simulation output

In three-point bending, the upper surface of the PCB strip undergoes compression while the outer surface of the square PCB undergoes stretching due to the curvature induced. These are reflected by the strain values on the surface of the PCB along the x-direction – the simulation values of longitudinal strain (LE11) at nodes on the PCB strip and square PCB, as shown in Fig.5-24. At the instant of solder joint breakage, the strain values on the square PCB drops significantly; the loss of bending resistance from the dummy package induces an increase in strain in the PCB strip. From Fig.5-24, it is found that the centre point (node 1, on square PCB or PCB strip) yields the highest change in strain value due to solder joint breakage, and the strain on the square PCB drops almost to zero, while the change in strain on the PCB strip is small compared to its final strain magnitude. This demonstrates that bonding of strain gauges at the center of the square PCB is an appropriate approach for monitoring solder joint breakage in the tests undertaken.

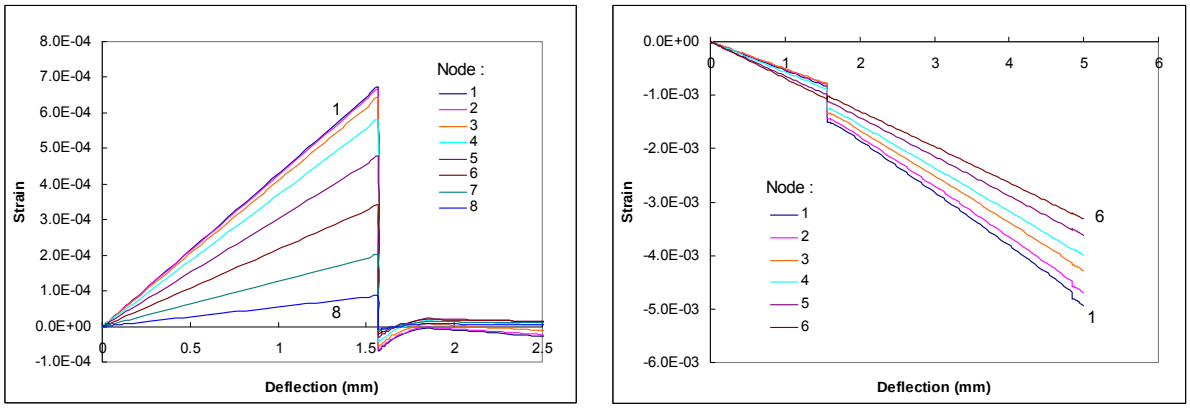

(a) (b)

Fig.5-24 Longitudinal strain (LE11) from node sets on (a) square PCB and (b) PCB strip

Fig.5-25 shows the von Mises stress distribution in the specimen at the instants just before and after the breakage of solder joints, demonstrating that failure of the outer columns of solder joints in the dummy package relieves the Mises stress instantly and almost totally in the square PCB.

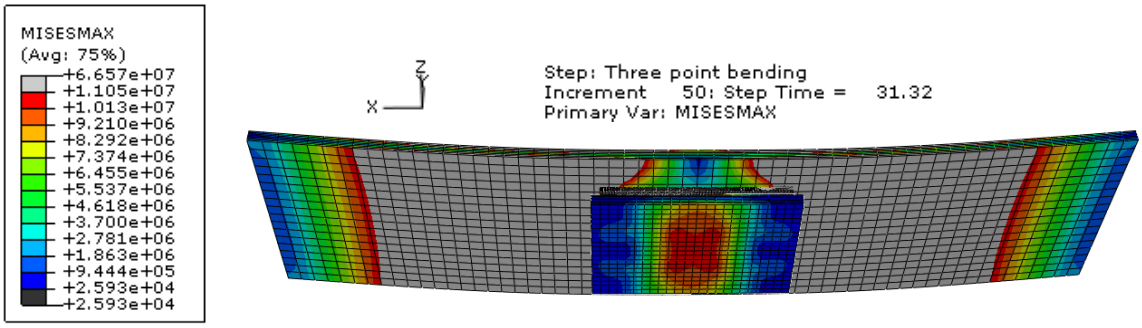

(a)

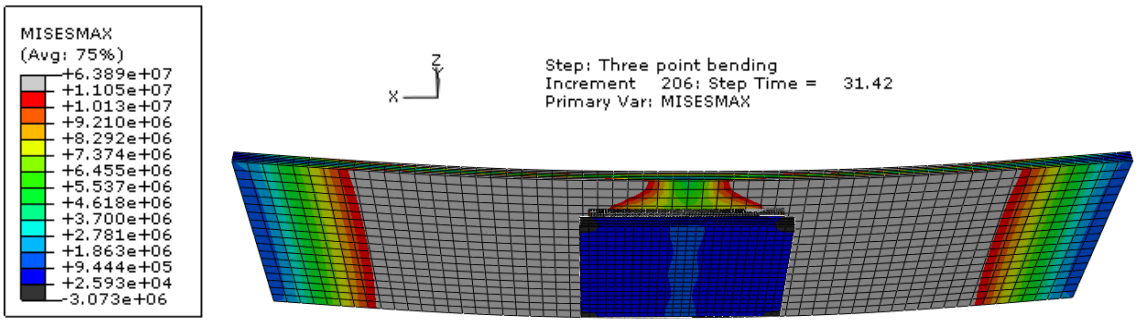

(b)

Fig.5-25 von Mises stress distribution in specimen at instant just (a) before and (b) after breakage of solder joints.

In order to validate the FEM simulation with beam models for solder joints, the simulation load-deflection and strain-deflection curves are compared with experimental results, as shown in Fig.5-26. The load and deflection values are obtained from the node set of the line transverse to the PCB strip at the mid-point; strain values are extracted from the center of the square PCB (Node 1), as indicated in Fig.5-23. The agreement between the simulation and experimental results shows that the beam model can simulate with

reasonable accuracy the failure of solder joints for quasi-static loading.

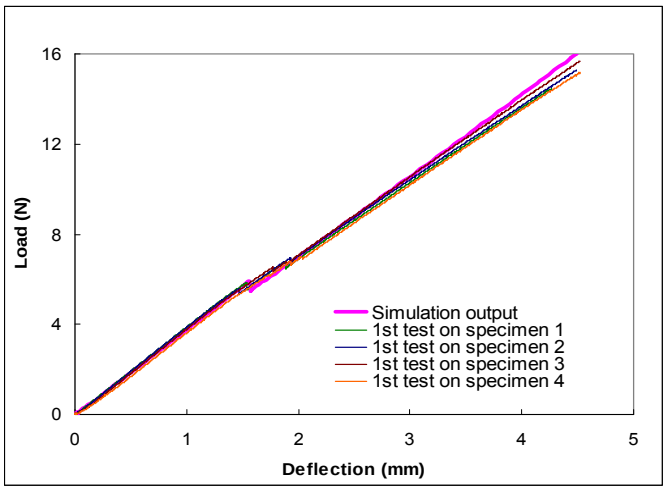

(a) Comparison of simulation and experimental load-deflection response for three point bending

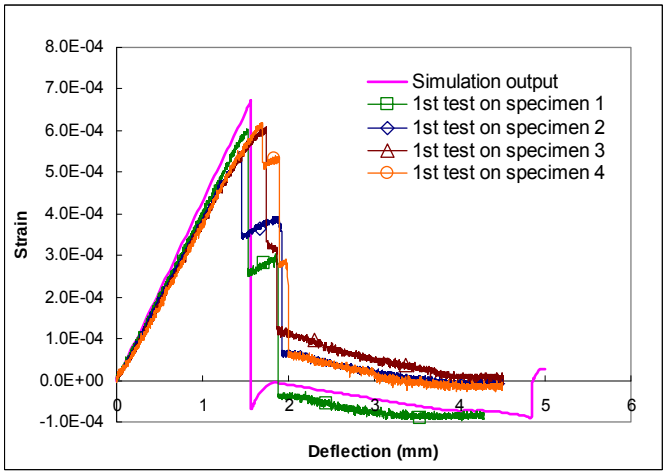

(b) Comparison of strain profile from simulation (node 1) and experimental results from strain gauge on square PCB

Fig.5-26 Comparison of simulation and experimental load and strain response of specimen

As the solder joints are very small and also inside IC packages, there is no experimental means to measure their mechanical responses during testing. Since the validity of the propsed FEM modeling has been verified, the mechanical behavior of solder joints is now elicited through numerical simulation. Various parameters are analyzed for each solder joint, namely the

equivalent plastic strain (PEEQ), section force and strain rate. For the current bending test configuration and solder joint pattern in the dummy IC package, two solder joints, namely 1-7 and 1-3, as shown in Fig.5-27, are selected as representative of the solder joints at the outer and inner columns. The PEEQ curve for solder joint 1-7 shows a sharp increase (at around 1.56mm deflection) followed by a more gradual increase until 40% strain, demonstrating complete breakage of solder joints in the outer column. The PEEQ value of solder joint 1-3 is very small compared to solder joint 1-7; however there is still a sudden increase in the PEEQ of solder joint 1-3 at a deflection close to 5mm, demonstrating that possible minor cracks may have been generated. Two PEEQ contour patterns for the solder joint array are presented for instants just before and after the breakage of solder joints (around 1.56mm deflection). The PEEQ contour shows that the PEEQ values for all solder joints are zero before any joint fails (as indicated by the value of zeros in the scale bar); after that, the PEEQ of all the solder joints in the outer column increases significantly, demonstrating that the solder joints in the outer column are the most critical in this mode of bending.

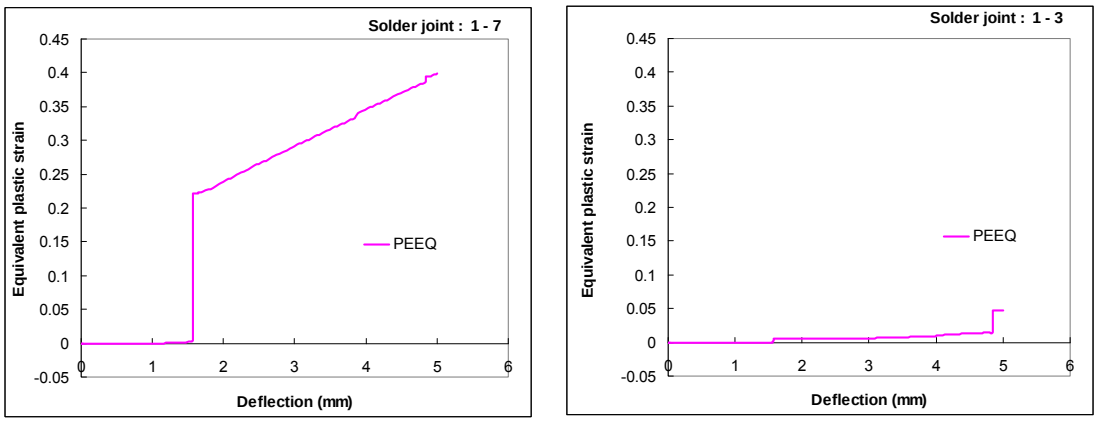

(a)

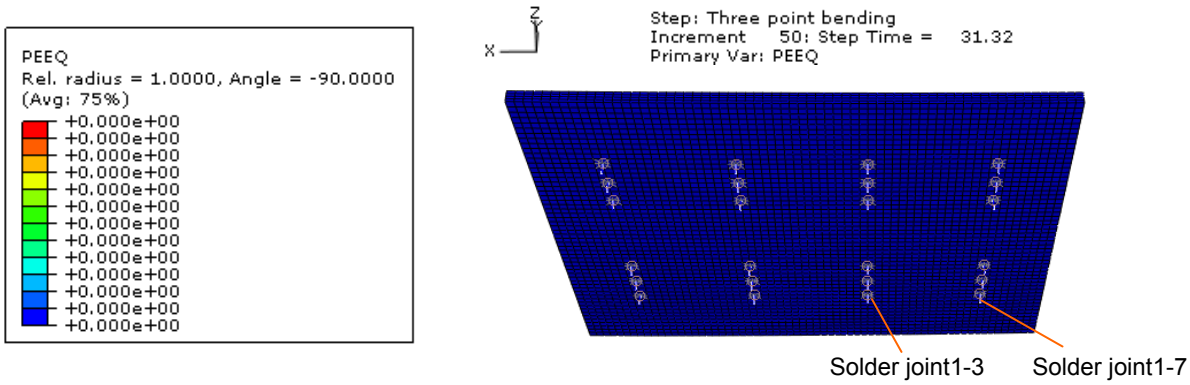

(b)

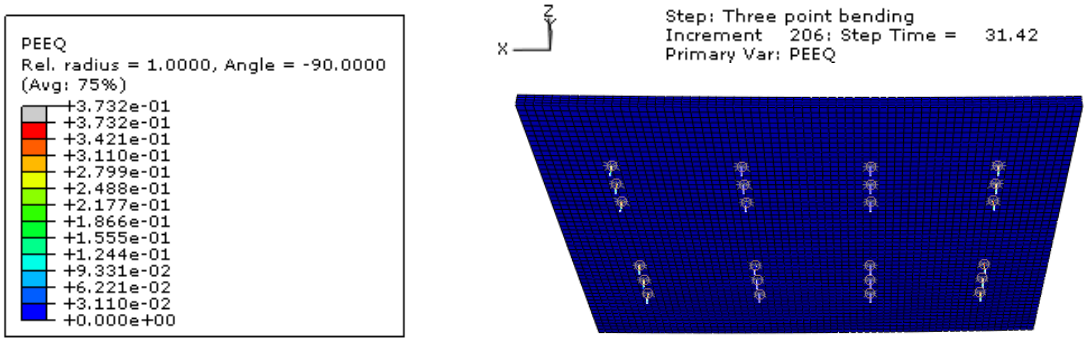

(c)

Fig.5-27 (a) Equivalent plastic strain (PEEQ) profiles for node 1-7 and node 1-3 and distribution of PEEQ in solder joint array just (b) before and (c) after the instant of solder joint failure

The beam section forces (SF1 in the axial direction, and SF2 and SF3 in the transverse directions) for solder joints 1-7 and 1-3 are plotted in Fig.5-28. It shows that during bending the normal (SF1) and shear component (SF3) are tensile and have almost the same magnitude for solder joint 1-7. After breakage of the solder joints in the outer columns, the dominant force transits from the normal force (SF1) to the shear force (SF3) for solder joint 1-3. At almost 5mm deflection, the shear force drops suddenly, demonstrating possible breakage via shear failure. The strain rates experienced by the solder joints before failure are about +/-0.0003/s (Fig.5-29a) under quasi-static loading. The relationship between the normal section force (SF1) and the

shear force (resultant of SF2 and SF3) for solder joints is presented in Fig.5-29b. It shows that solder joint 1-7 experiences a tensile-shear loading corresponding to a 43^0 inclination and solder joint 1-3 experiences a compressive-shear load at a 21^0 inclination before transiting quickly to a shear dominant mode at around 85^0 inclination after solder joint failure in the outer columns.

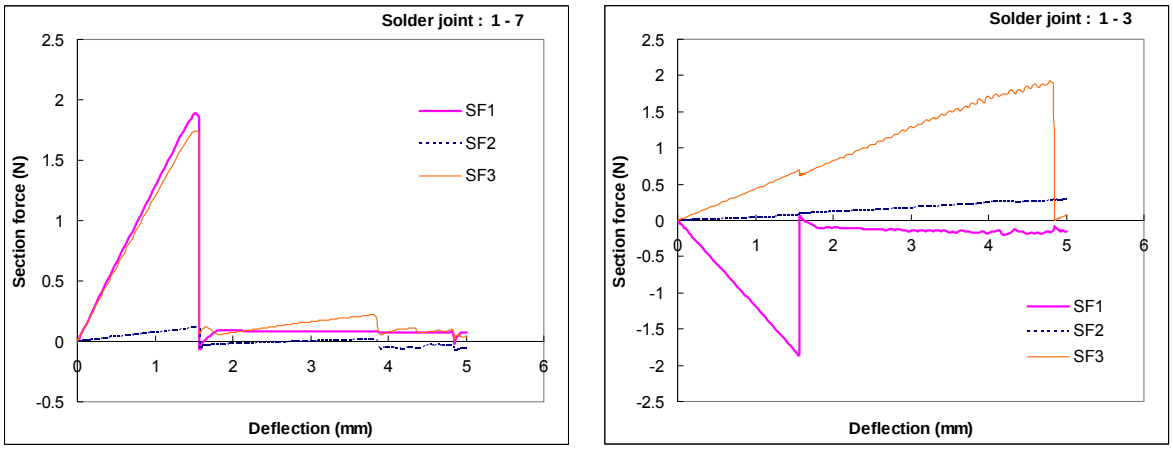

Fig.5-28 Section force SF1 (normal component), SF2 and SF3 (shear components) in beam solder joints 1-7 and 1-3.

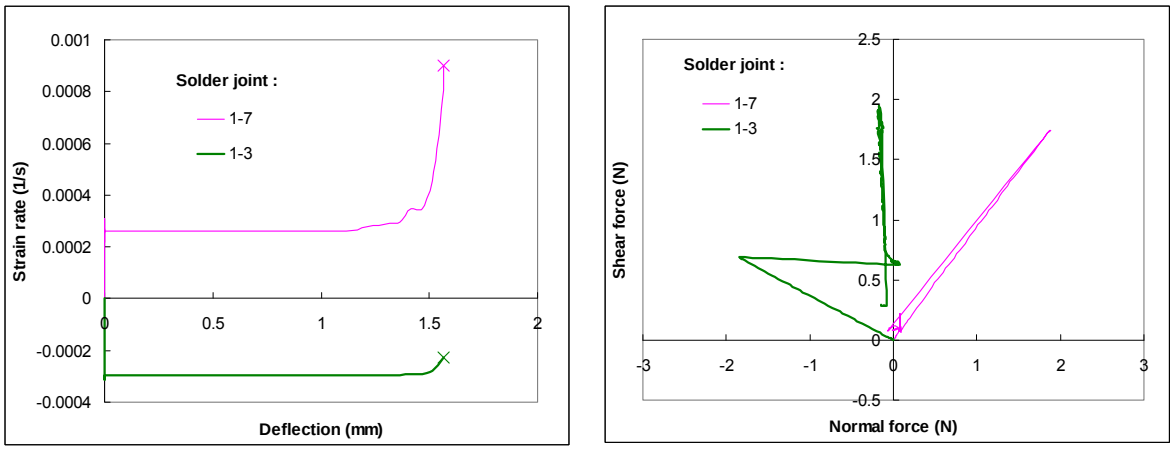

(a) (b)

Fig.5-29 (a) Strain rate histories of solder joints 1-7 and 1-3 before failure and (b) relationship between shear force and normal force in solder joints.

5.4 Response of IC packages to drop impact

5.4.1 Drop test configuration and corresponding FEM model

Drop tests are performed on PCB strips with a dummy IC package mounted, similar to specimens used in quasi-static bending tests. The purpose is to verify the validity of employing the beam model with rate-dependant mechanical properties to simulate solder joints in IC packages subjected to dynamic loading and to examine the mechanical behavior of solder joints in IC packages through FEM simulation. In order to generate combined normal and shear forces in the solder joints, the specimen is placed on the lower part of the three-point bending test fixture. The entire fixture is then mounted on a drop plate and dropped from a given height using the drop tester shown in Fig.5-30. A PCB shock accelerometer (model M350B03) is attached to the drop plate to record the acceleration history and a strain gauge (1mm gauge length) is bonded to the centre of the square PCB to record the strain history, which is compared with FEM simulation results to validate them.

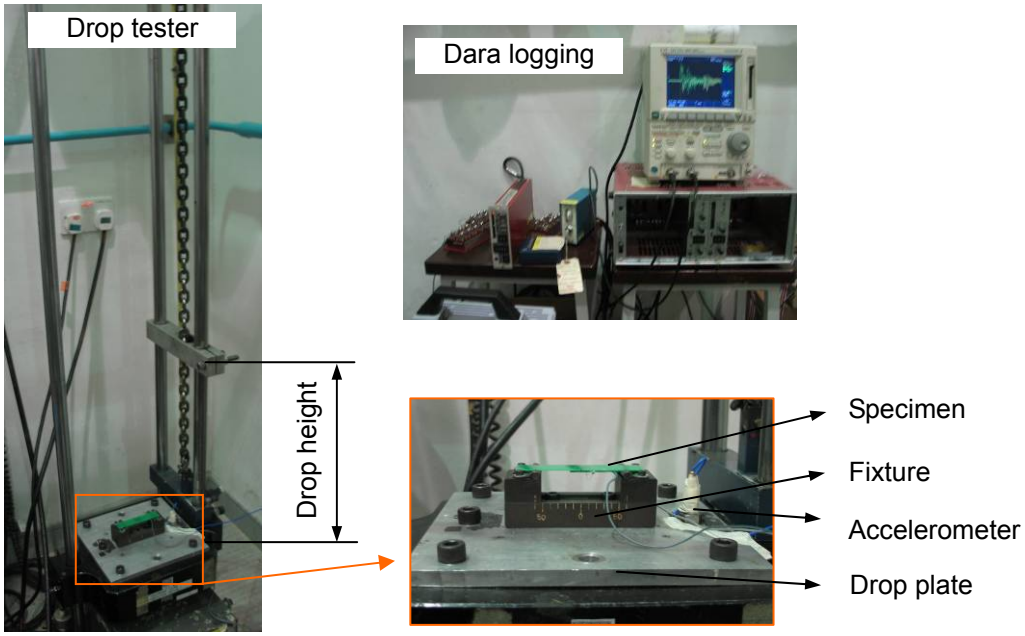

Fig.5-30 Drop tester and recording system

Fig.5-31 shows the FEM model of the specimen. The dimensions and mesh are same as those for simulating quasi-static bending. To simulate the impact process, the boundary conditions shown in Fig.5-31a are prescribed. The entire specimen is assigned an initial velocity field equal to the impact velocity of the drop plate; this can be estimated from the drop height and measured from images captured by a high speed camera. Velocity boundary conditions in the z- direction (V3) are assigned to the two ends of the PCB strip. The velocity-time profile is derived from accelerometer data in tests. Node sets on the PCB strip and square PCB are defined to yield longitudinal strain (LE11) values, and two representative solder joints (1-7 and 1-3) are analyzed in detail (Fig.5-31b).

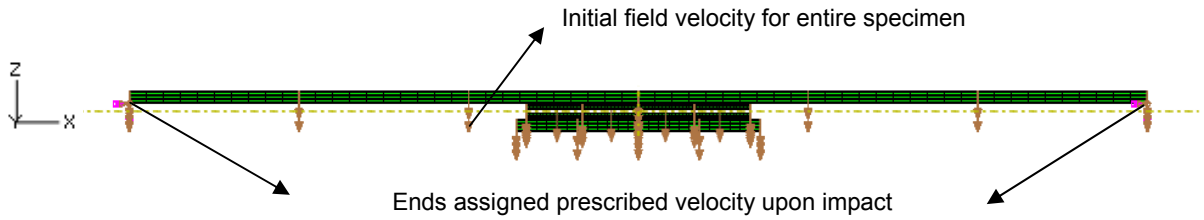

(a) Boundary conditions to simulate dynamic bending tests

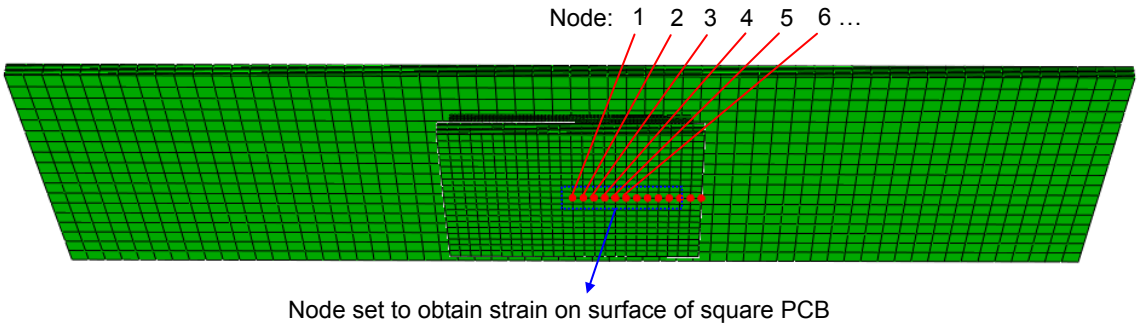

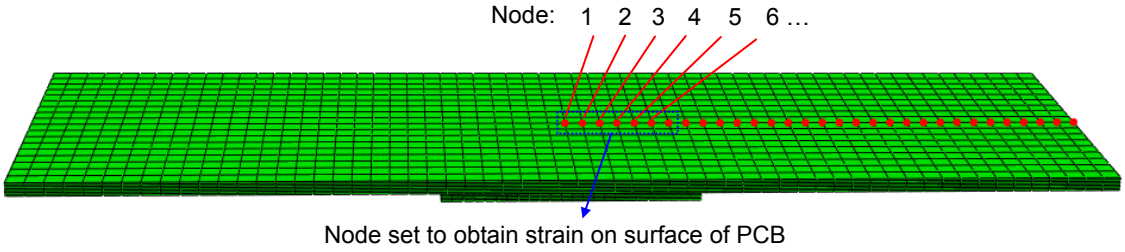

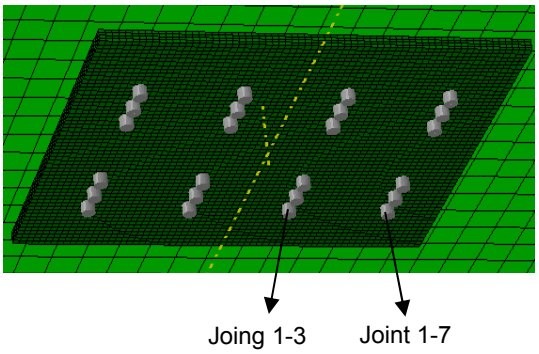

(b) Solder joints to obtain strain and force

Fig.5-31 FEM model for simulation of impact-induced dynamic bending of PCB strip with dummy IC package mounted; (a) boundary conditions and (b) node sets to obtain simulation results.

5.4.2 Experimental and FEM simulation results

Drop tests are first performed with a drop height of 0.9m; this results in all solder joints in the dummy IC package breaking completely. Then tests are then conducted at a lower drop height of 0.3m. Complete breakage of all the solder joints is again noted in both experimental and simulation results. Finally, a 0.1m drop height is selected, and both experimental and simulation results show that the solder joints remain intact. This is later confirmed by experimental quasi-static bending tests on the specimens after subjected to the drop testing. The following descriptions of experimental and simulation results are ordered according to drop height.

(1) 0.9m drop height

Three specimens are tested at the drop height and denoted by DT-9, DT-10 and DT-11. All the strain and acceleration histories recorded by the strain gauge and accelerometer are shown in Fig.5-32. The strain curves display a sharp drop at 1300μs followed by another sharp drop to almost zero, indicating complete loss of strength in the solder joints. The acceleration profiles exhibit large oscillations generated by impact, while the velocity profiles show sharp velocity changes. Coincidence of the responses from tests on the three specimens substantiates the consistency of the experiments.

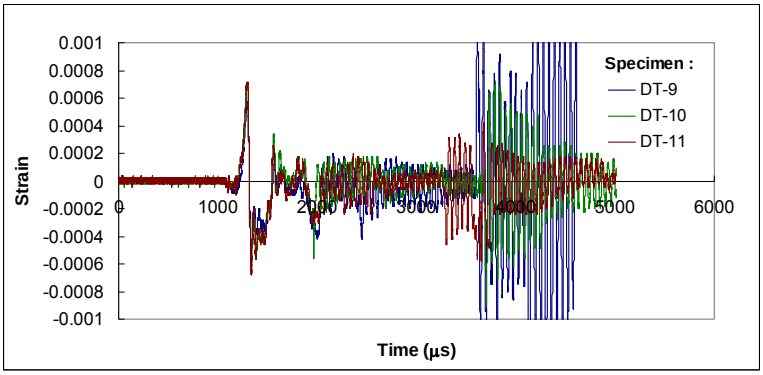

(a) Strain gauge signals

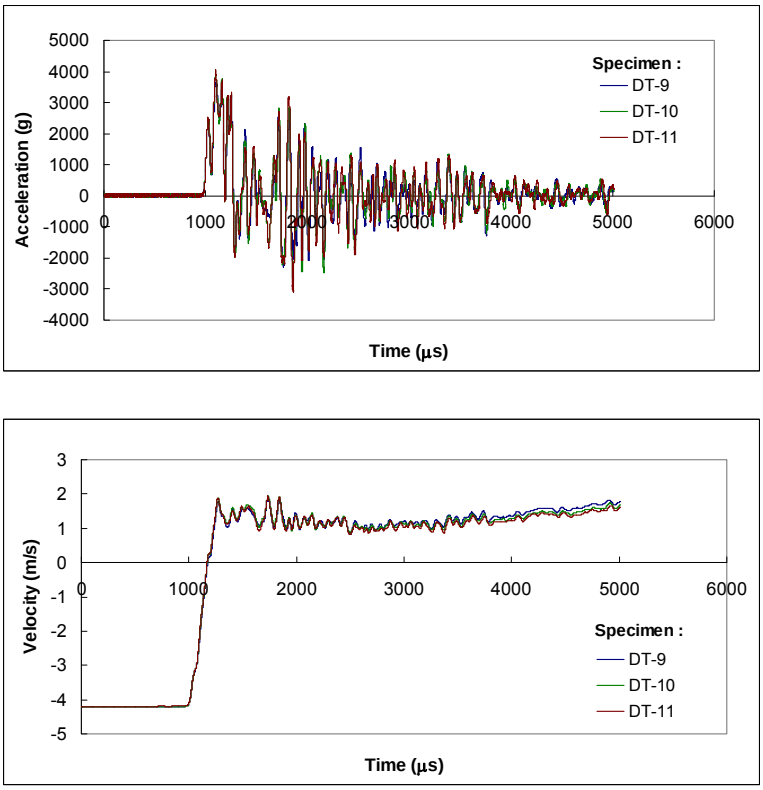

(b) Acceleration profiles from accelerometer and the corresponding velocity history

Fig.5-32 Experimentally-obtained (a) strain at center of the square PCB surface and (b) acceleration and velocity histories of drop platform

Piecewise-linear fits of the velocity profile are undertaken and used as input boundary conditions for the two ends of the PCB strip in FEM modeling (Fig.5-33a). The velocity commences from a constant negative value (-4.2m/s, in the negative z-direction) before the drop plate strikes the ground. Upon impact, the velocity rises quickly to 1.3m/s, in the z-direction (the rebound

velocity). It should be pointed out that the rising slope of the velocity profile during impact is significant, as the slope determines the severity of impact. The simulation results for longitudinal strain (LE11) at node 1 on the square PCB is extracted and compared with experimental data (Fig.5-33b). The strain at node 1 of the PCB strip is plotted for comparison with that at node 1 of the square PCB (Fig.5-33c). In terms of indicating failure of solder joints, the change in the strain-time profile for node 1 of the PCB strip is not as prominent as that from node 1 of the square PCB.

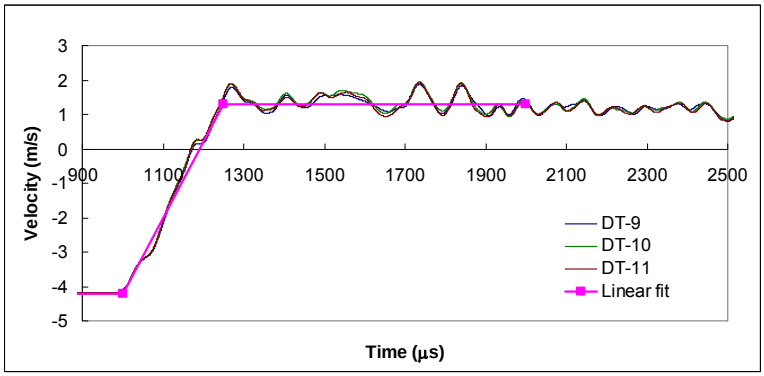

(a) Input boundary conditions for FEM simulation

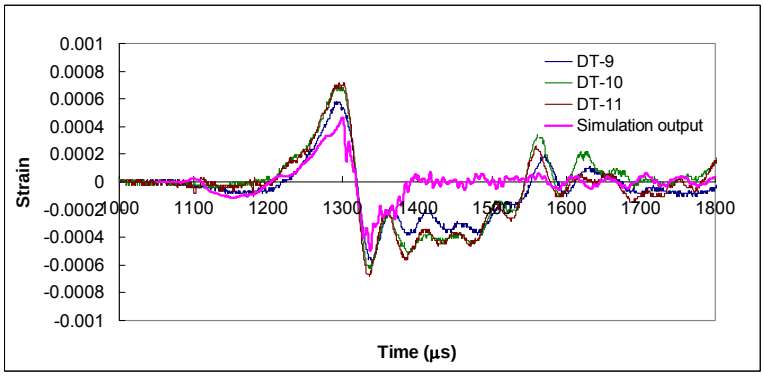

(b) Comparison of strain responses

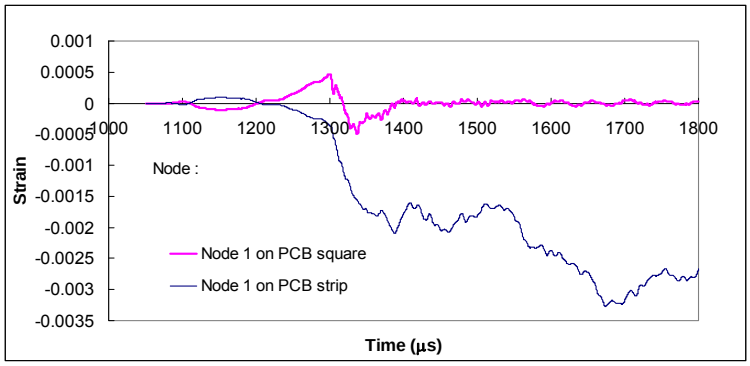

(c) Comparison of simulation strain for node 1 on PCB and node 1 of square PCB.

Fig.5-33 (a) the input velocity boundary for the supporting edges and (b) comparison of strain value at the center of the square PCB between experimental and numerical results and (c) comparison of numerical output of strain at the center of PCB strip and square PCB.

The high speed camera images captured are given in Fig.5-34; they show detachment of the IC package from the PCB strip during impact; however, it is impossible to identify the instant of solder joint failure from the images, because the IC package remains attached to the PCB strip even when the solder joints in the outer columns are broken.

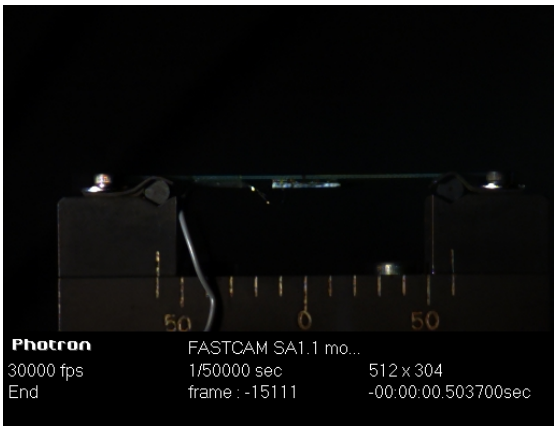

(a)

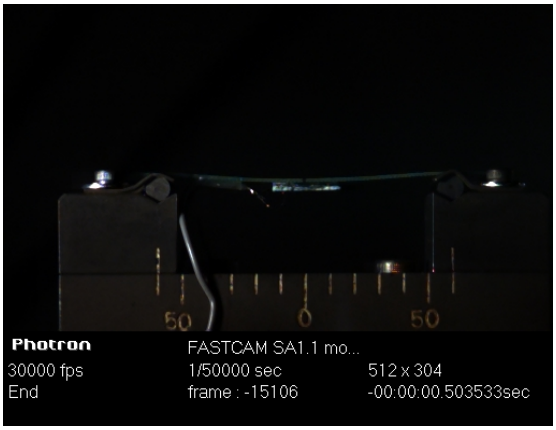

(b)

(c) (d)

Fig.5-34 Sequence of images (a to d) captured by a high speed camera, showing detachment of IC package from PCB strip for a drop height of 0.9m.

The section forces (axial force SF1 and shear force SF2 and SF3) for solder joints 1-7 and 1-3 are plotted in Fig.5-35, together with equivalent plastic strain (PEEQ) histories. The abrupt increase in the PEEQ indicates the instant of solder joint failure and coincides with sudden changes in the section force histories. The strain rate before failure is less than 100/s and the relationship between the normal force (SF1) and shear force (resultant of SF2 and SF3) in the solder joints is shown in Fig.5-36.

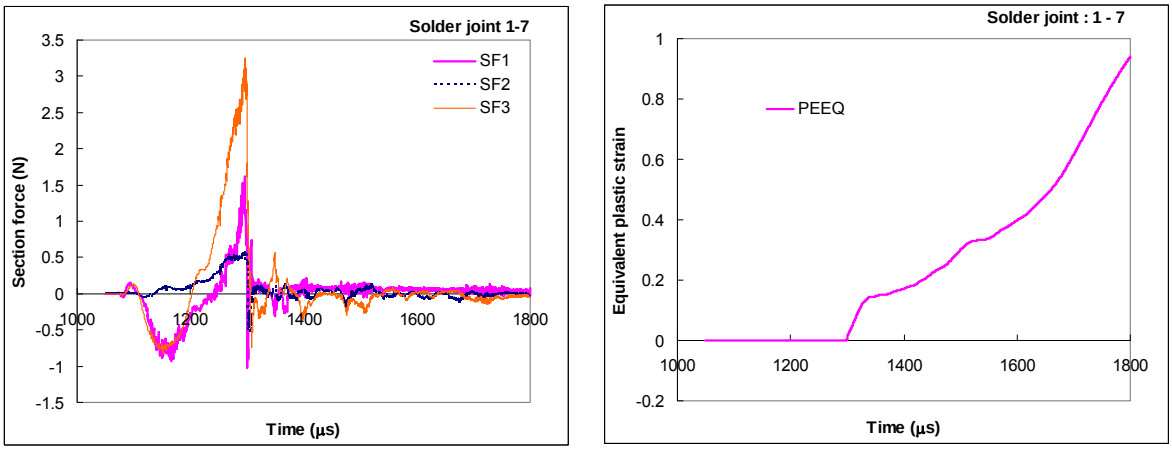

(a) Section force and PEEQ for solder joint 1-7

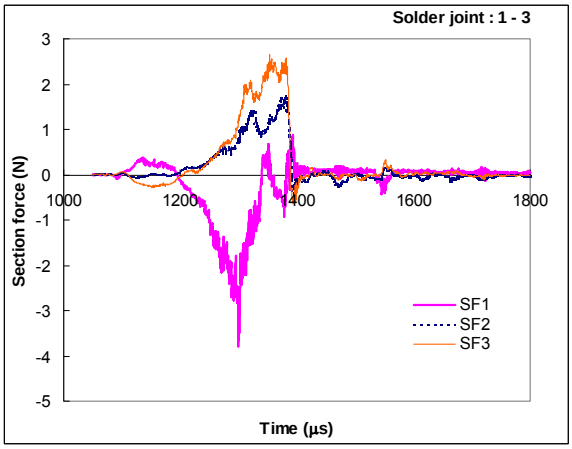

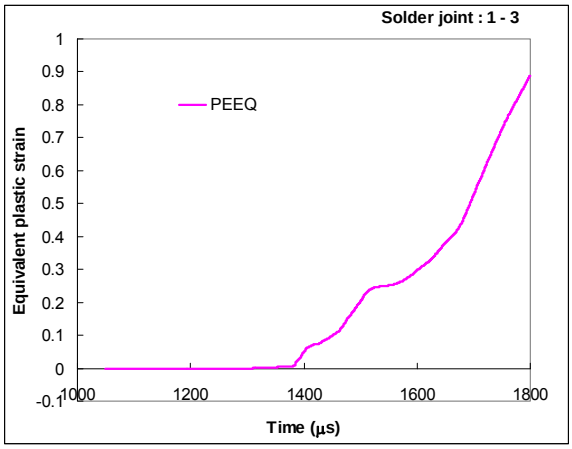

(b) Section force and PEEQ for solder joint 1-3

Fig.5-35 Section force and equivalent plastic strain for (a) solder joint 1-7 and (b) solder joint 1-3

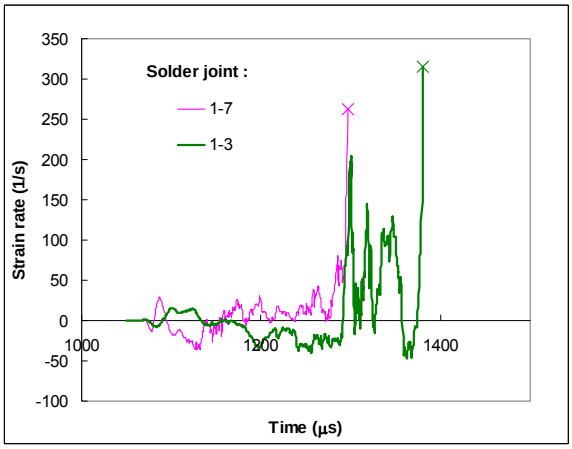

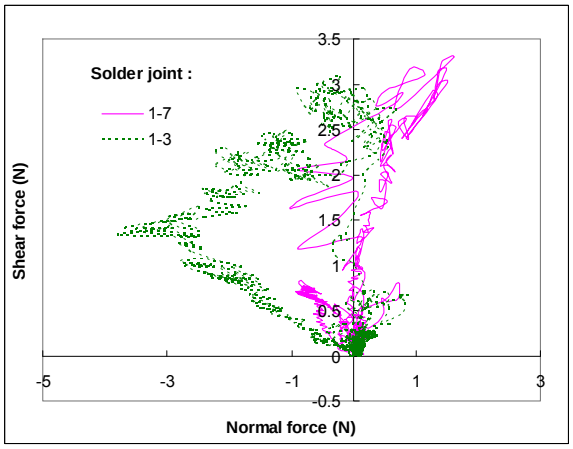

(a) (b)

Fig.5-36 (a) Strain rate histories for solder joints 1-7 and 1-3 before failure and (b) relationship between shear force and normal force in solder joints.

(2) 0.3m drop height

Dropping of specimens from a height of 0.9m results in all the solder joints breaking and the IC package detaching from the PCB strip. Therefore, tests on three specimens are conducted at a reduced drop height of 0.3m, and these are denoted by DT-12, DT-13, DT-14. Fig.5-37 shows the

experimentally measured strain and acceleration, as well as the derived velocity. In terms of strain histories, there is general agreement between simulation (based on simplified piecewise-linear velocity boundary conditions (Fig.5-38a)) and strain gauge readings from the center of the square PCB (Fig.5-38b). Changes in strain at the center of the PCB strip due to breakage of solder joints are not as marked as those for the 0.9m drop height because of fluctuations in the strain readings (Fig.5-38c). The high speed photography images are illustrated in Fig.5-39 and show detachment of the IC package from the PCB strip. However, it is not possible to identify the instant of solder joint failure from the images because the IC package remains attached to the PCB strip. Plots of the section force and PEEQ from FEM simulations show the instant of solder joint failure, and the PEEQ amplitudes are less than those corresponding to the 0.9m drop simulation (Fig.5-40). Fig. 5-41 shows the strain rate experienced by the solder joints before failure and the relationship between the normal (SF1) and shear forces (resultant of SF2 and SF3). The experiments confirm complete breakage of all the solder joints and the simulation results show that the FEM model is able to identify commencement of solder joint failure and the overall response of the specimen under drop impact.

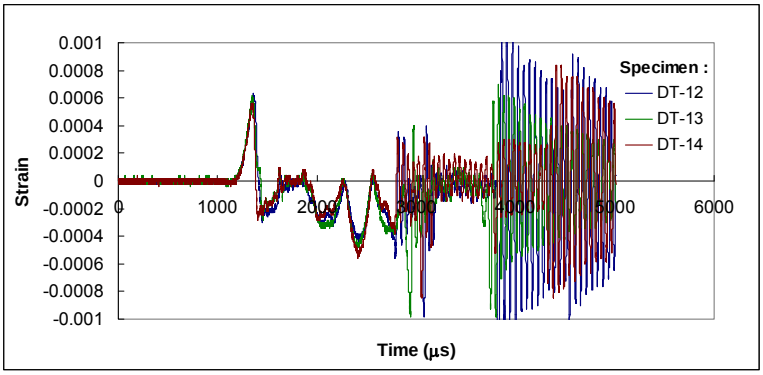

(a) Signals recorded by strain gauge

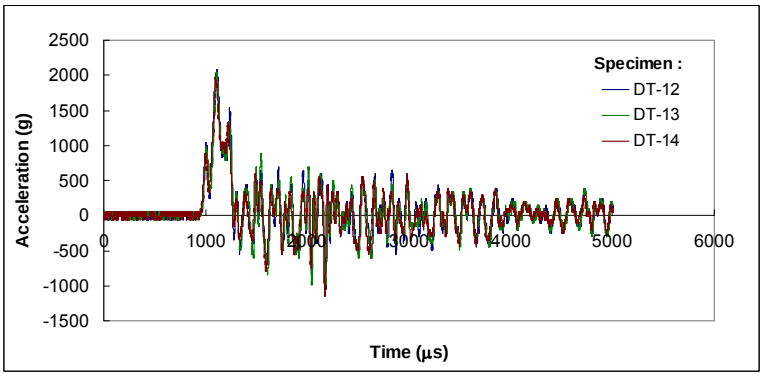

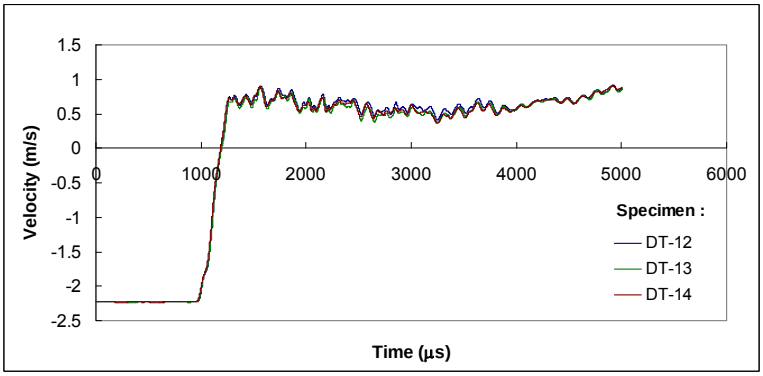

(b) Accelerometer signal and derived velocity history

Fig.5-37 Experimentally obtained (a) strain at the center of the square PCB and (b) acceleration and velocity histories of the drop plate

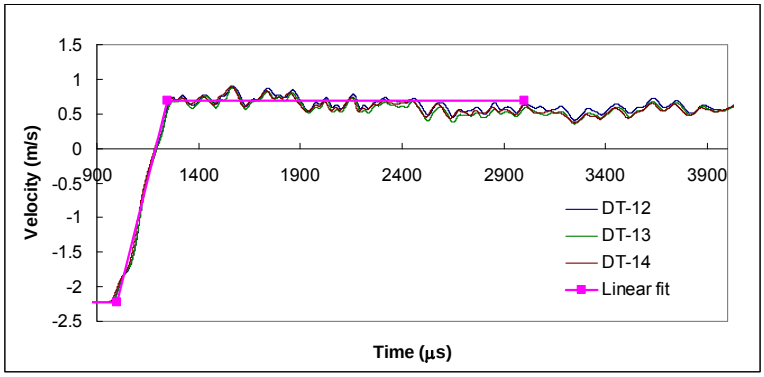

(a) Input boundary condition for FEM simulation

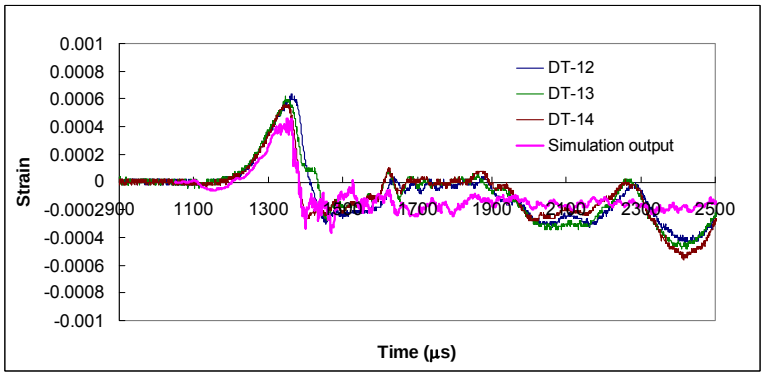

(b) Comparison of strain responses

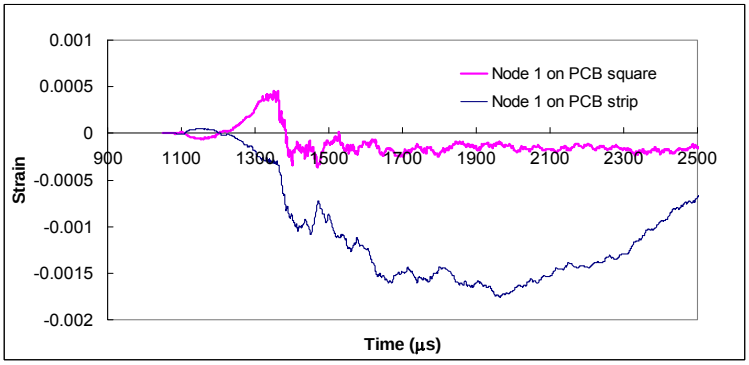

(c) Comparison of strain histories from node 1 on the PCB strip and node 1 on the square PCB.

Fig.5-38 (a) Input velocity boundary conditions for the supporting edges and (b) comparison of experimental and simulation strain histories at the center of the square PCB and (c) comparison of numerical results for strain at the center of the PCB strip and the square PCB

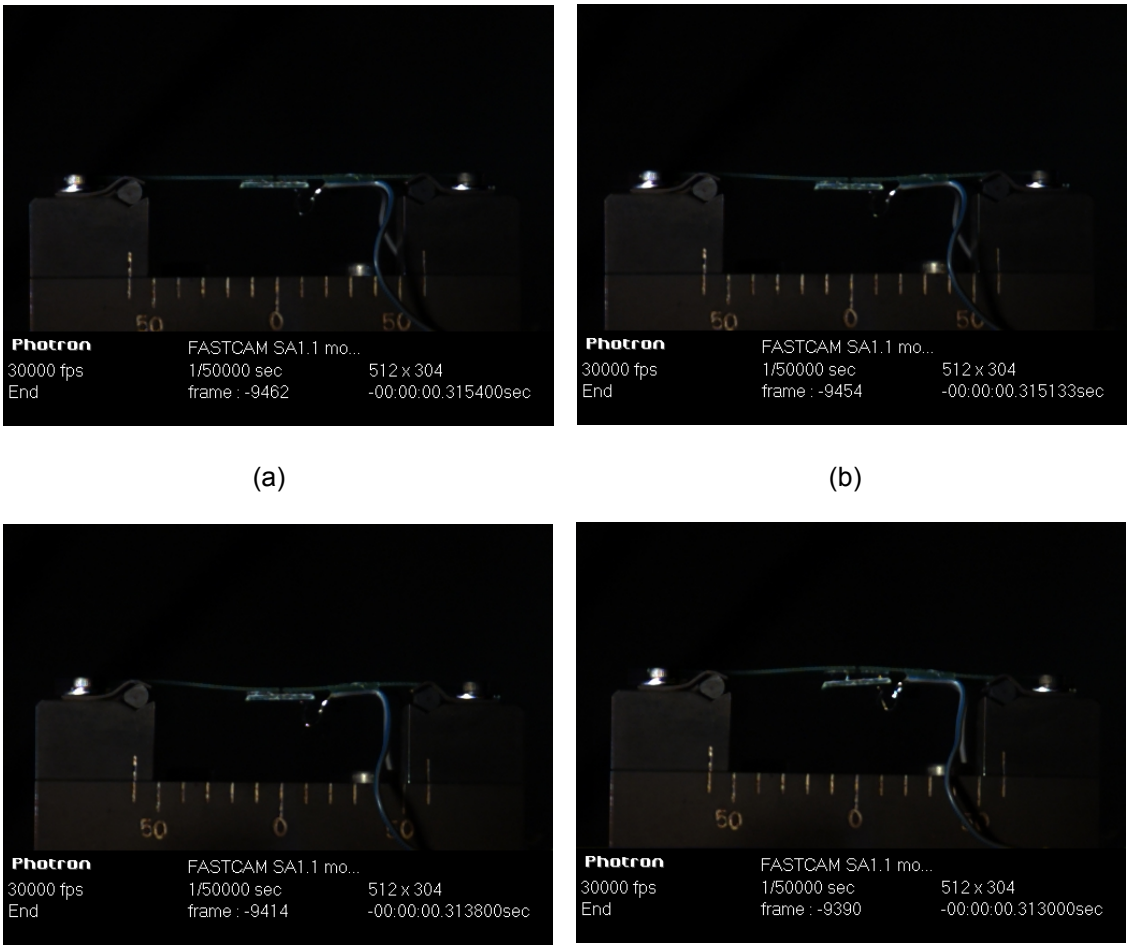

Fig.5-39 High speed camera images (a to d) of specimen (DT-12), showing detachment of the IC package from the PCB strip during drop impact from a 0.3m height.

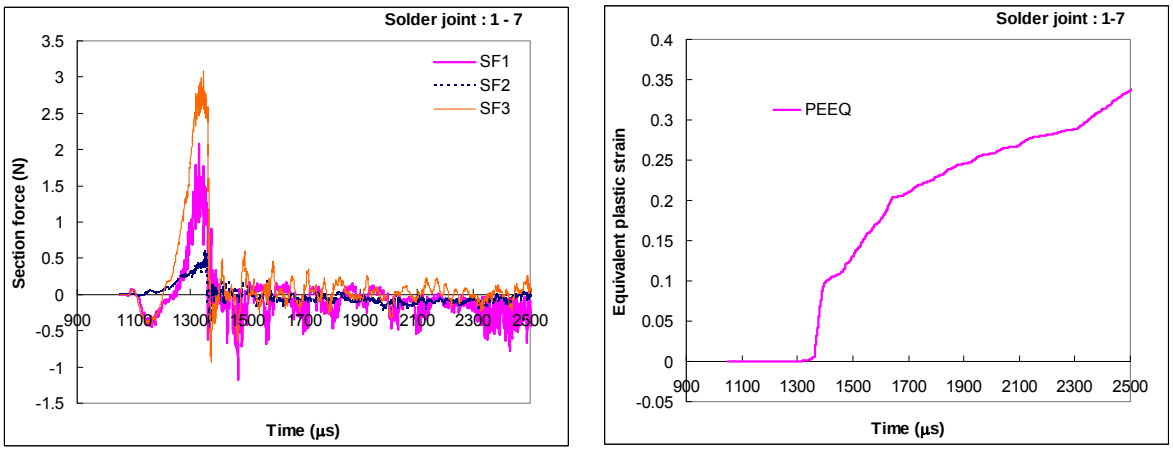

(a) Section force and PEEQ for solder joint 1-7

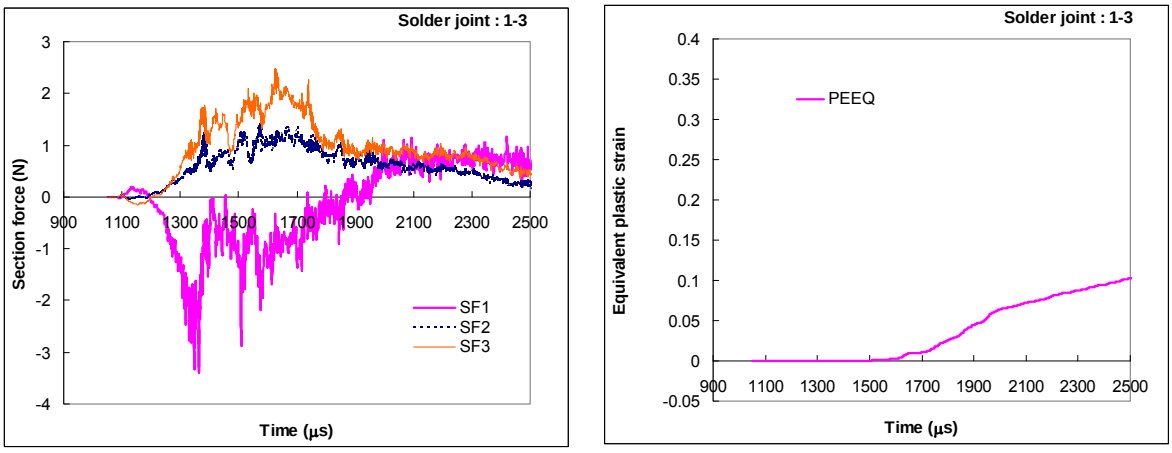

(b) Section force and PEEQ for solder joint 1-3

Fig.5-40 Section force and equivalent plastic strain for (a) solder joint 1-7 and (b) solder joint 1-3

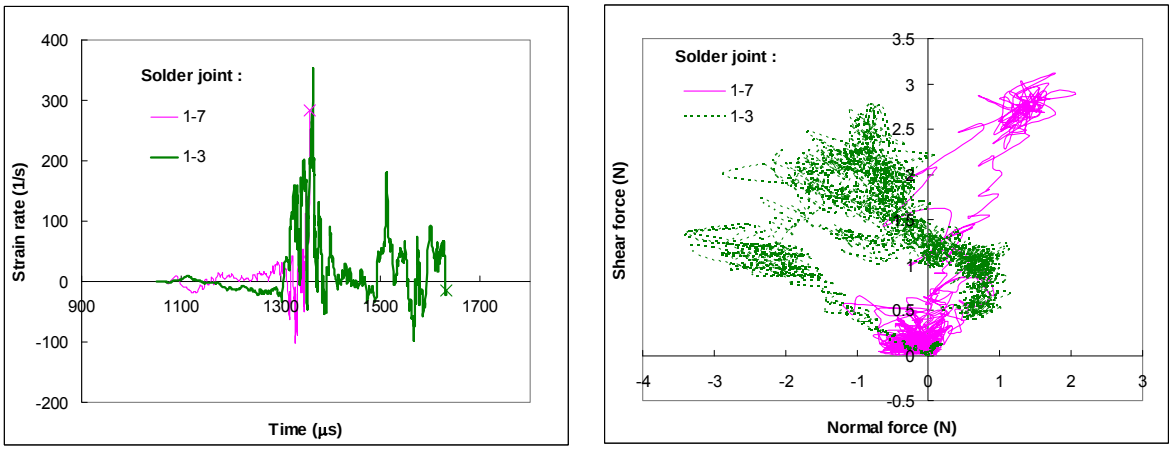

(a) (b)

Fig. 5-41 (a) Strain rate histories for solder joint 1-7 and 1-3 before failure and (b) relationship between shear force and normal force in solder joints.

(3) 0.1m drop height

All the solder joints in the dummy IC package are broken for a drop from 0.3m. The drop height is therefore further decreased to 0.1m for three more test specimens (DT-16, DT-17 and DT-19), and the dummy IC package still

remained connected to the PCB strip after the tests. However, the results have distinct differences with those obtained for drops from 0.9m and 0.3m. The strain gauge signal from the center of the square PCB shows a somewhat sinusoidal profile (Fig.5-42a), demonstrating flexing of the PCB strip on impact, and there is no indication of solder joint breakage via sharp drops in strain values. The strain history from FEM simulation also displays a general profile similar to the experimentally measured results (Fig.5-43b), verifying the validity of the FEM simulation using the beam model. The strain signals from the center of the square PCB and PCB strip show opposite sinusoidal-like profiles (Fig.5-43c). Both experimental and simulation results indicate that the specimen flexes up and down on impact without causing major damage to the solder joints. High-speed camera images reinforce this observation, as shown in Fig.5-44; the time intervals between images correspond to a quarter of the flexural period of the specimen. After the tests, it is found that the dummy IC packages are still intact, with no observable damage. The following description of simulation results on the PEEQ and experimental results from quasi-static bending of specimens after drop tests prove that some minor damages could have been generated in the specimens dropped from a 0.1m height.

Fig.5-45 shows the section force and PEEQ histories in the solder joints. The section force histories for both solder joints 1-7 and 1-3 are sinusoidal and there are no clear signs of solder joint failure. The PEEQ history provides a means to detect degradation of the solder joints; the plot for solder joint 1-7 exhibits an increase at around 4000μs. However, the final PEEQ value is still

too small (only 1%) to indicate any failure in the solder joints. The PEEQ value for solder joint 1-3 is zero throughout the entire duration, demonstrating that its response is still within the elastic region. The strain rate is only around 10/s, and the plot of normal force against shear force shows the transition between compression/shear and tension/shear when the PCB strip flexes upwards and downwards (Fig.5-46).

The strain gauge signals and simulation results in terms of section force and PEEQ value do not show any obvious failure in the dummy IC package after dropping it from 0.1m. After the drop test, the dummy IC package remains connected to the PCB strip. Previous studies on quasi-static bending of the specimen have shown that that there are distinct differences in the strain histories between the first and the second/third bending tests if solder joints fail in the first round of testing. Therefore, in order to examine possible degradation of solder joints in the three specimens after dropping them from 0.1m, three consecutive quasi-static three-point bending tests are conducted on each of the three specimens. The results for each specimen (Fig.5-47) show that the specimen has a greater bending resistance in the first test, compared to the second and third tests. This proves that there is no major failure in the solder joints for specimens after dropped from 0.1m. Comparison of the strain response in the first bending test for the three specimens (Fig.5-48) shows that their behaviour before solder joint failure do not coincide as closely as that for specimens not subjected to drop (Fig.5-20). This indicates that there may have been some minor degradation of the solder joints after a drop from 0.1m. The simulation results for the PEEQ (Fig.5-45a)

also show that a small plastic strain (1%) is generated in solder 1-7 (i.e., at the outer columns of the solder array in the dummy IC package).

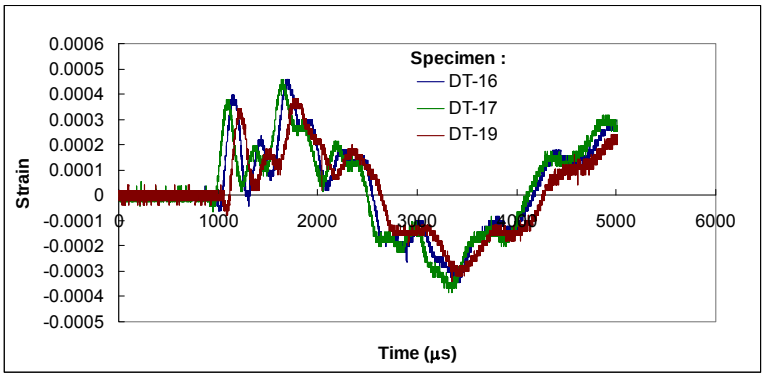

(a) Strain signals recorded by strain gauge

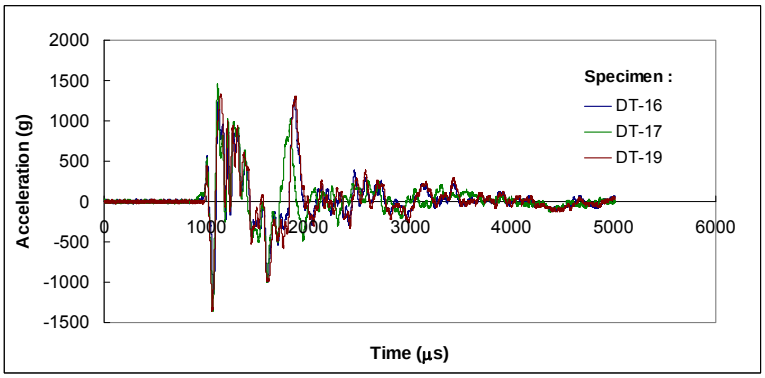

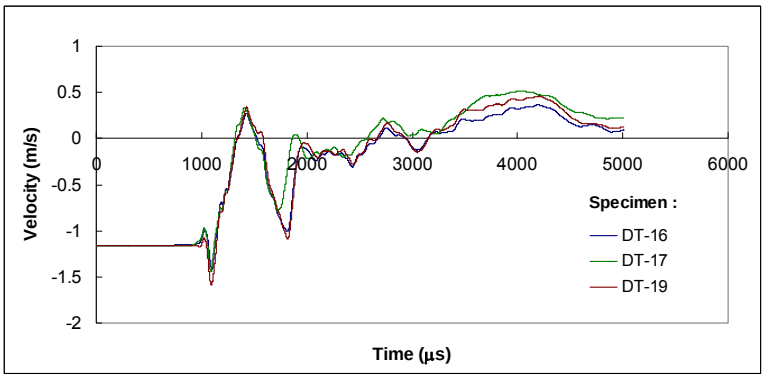

(b) Accelerometer signals and derived velocity history

Fig.5-42 Experimentally obtained (a) strain at the center of the square PCB surface and (b) acceleration and velocity histories of the drop plate

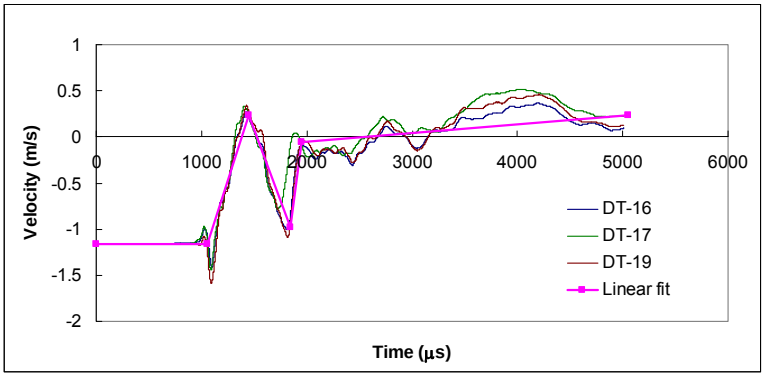

(a) Input boundary condition for FEM simulation

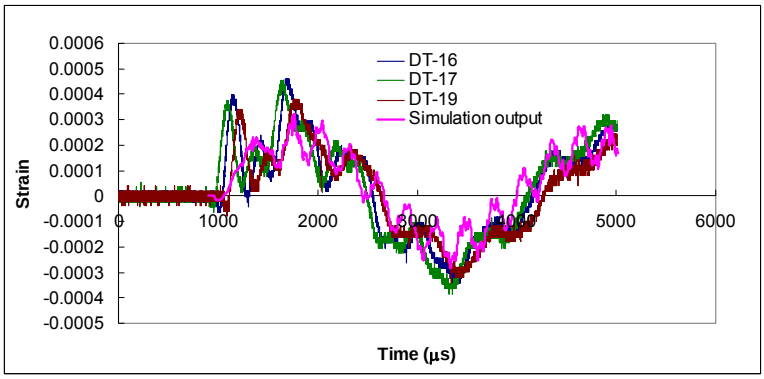

(b) Comparison of strain responses

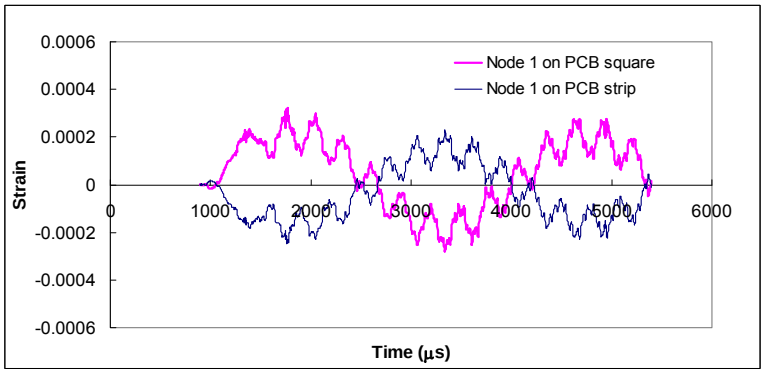

(c) Comparison of simulation output of strain from node 1 on PCB and node 1 on square PCB.

Fig.5-43 (a) Input velocity boundary conditions for the supported edges and (b) comparison of experimental and numerical strain values at the center of the square PCB and (c) comparison of FEM results for strain at the center of the PCB strip and square PCB

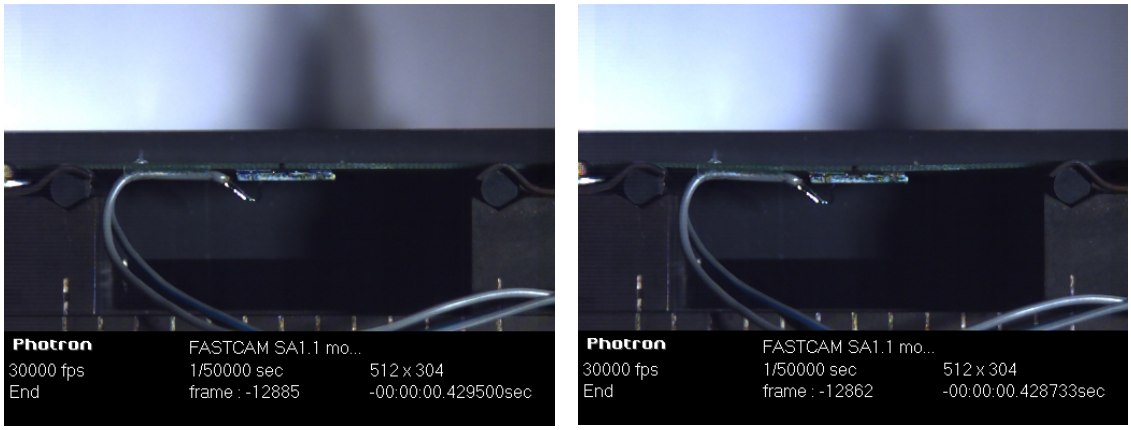

(a) (b)

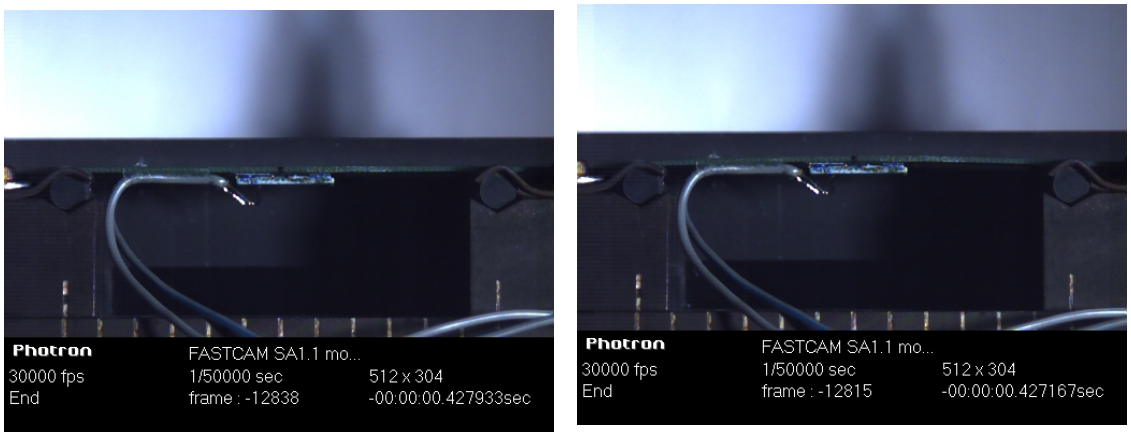

(c) (d)

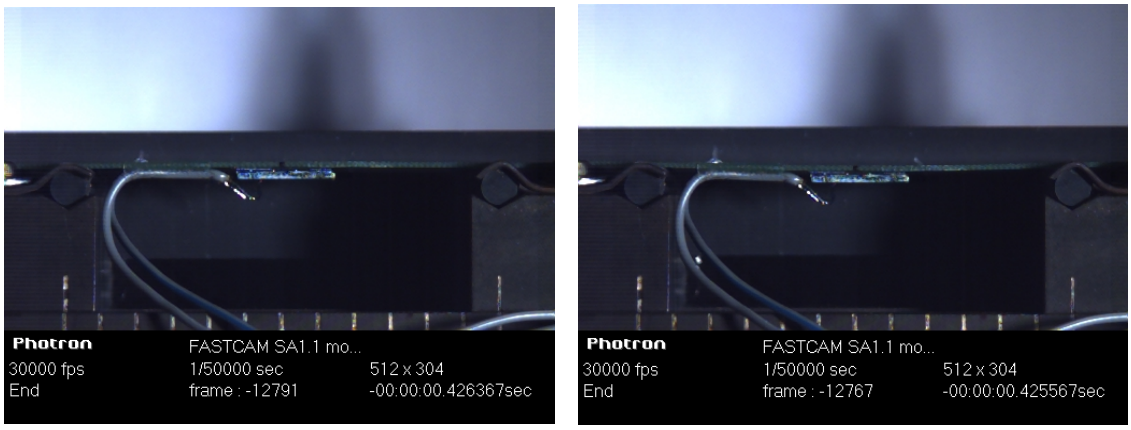

(e) (f)

Fig.5-44 High speed camera image sequence of specimen (DT-16) for drop impact from 0.1m height; time interval between images is 780 micro second (quarter of flexural period).

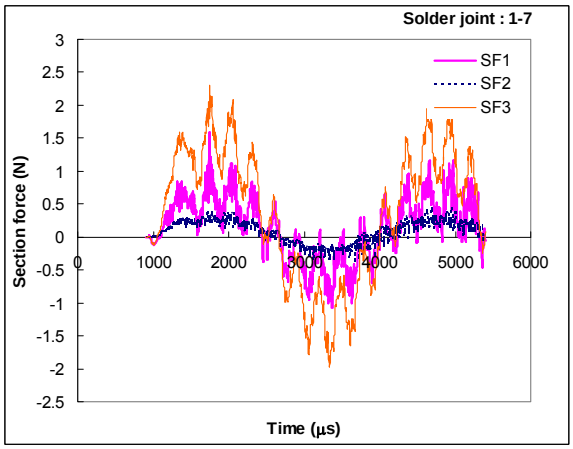

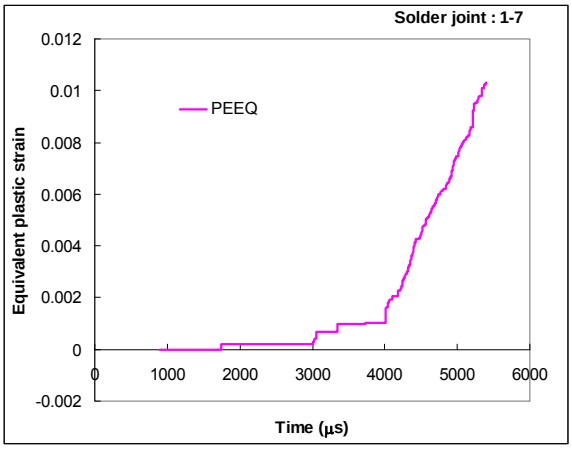

(a) Section force and PEEQ for solder joint 1-7

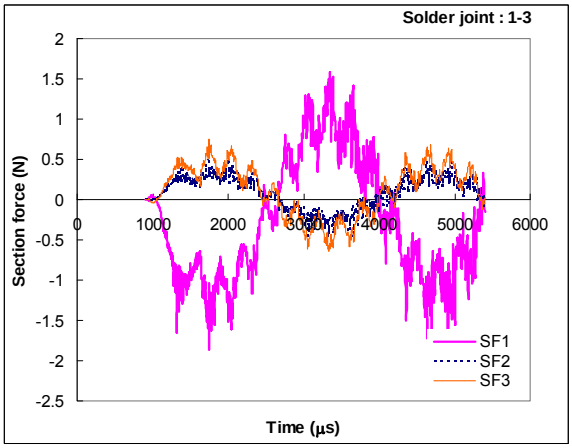

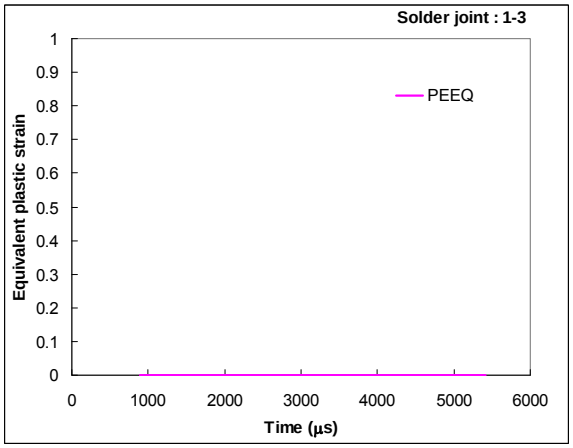

(b) Section force and PEEQ for solder joint 1-3

Fig.5-45 Section force and equivalent plastic strain for (a) solder joint 1-7 and (b) solder joint 1-3

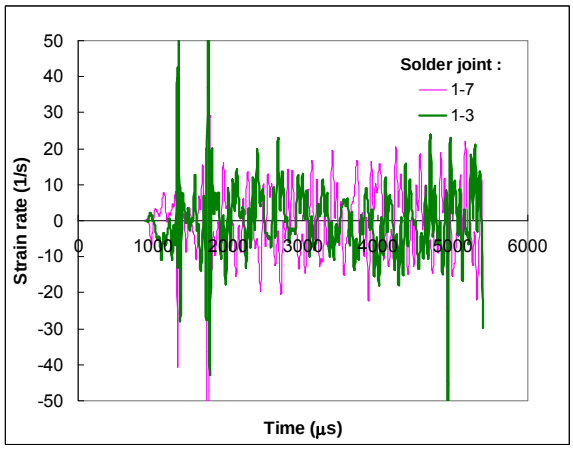

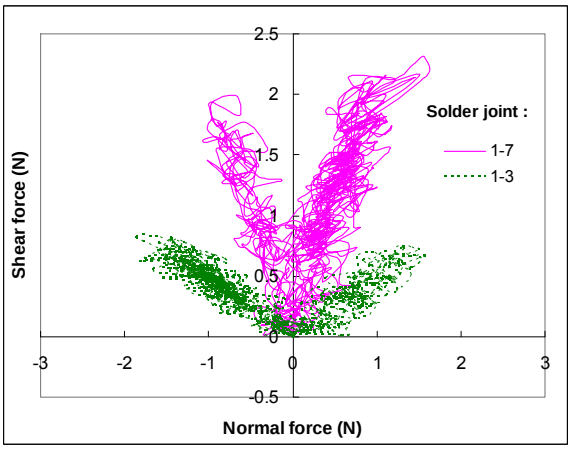

(a) (b)

Fig.5-46 (a) Strain rate histories for solder joints 1-7 and 1-3 before failure and (b) relationship between shear and normal force in solder joints.

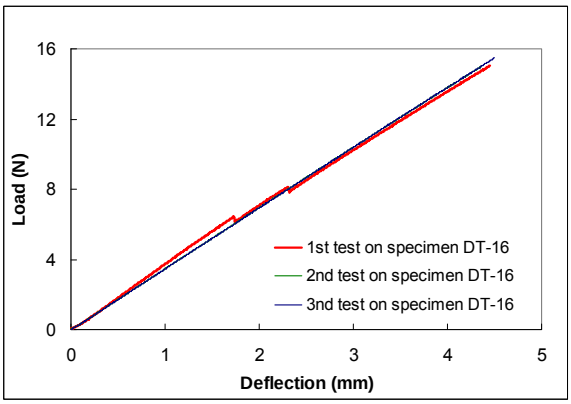

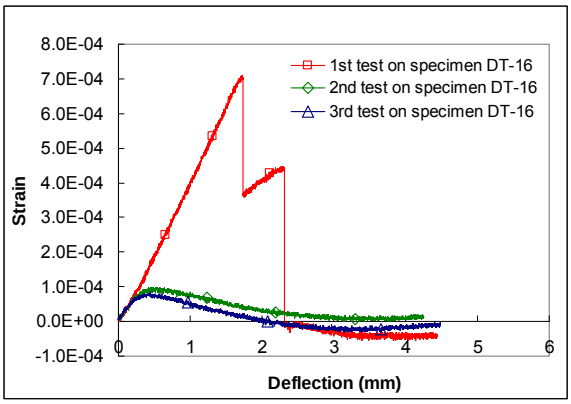

(a)

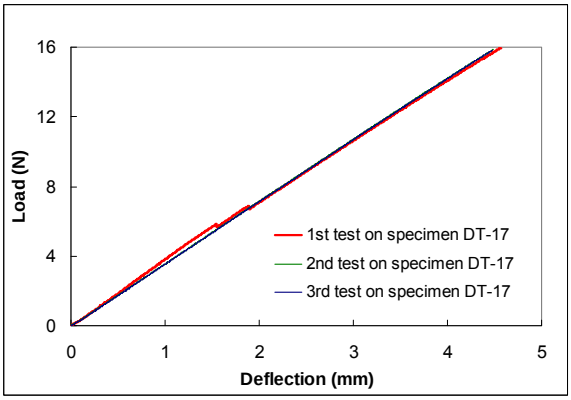

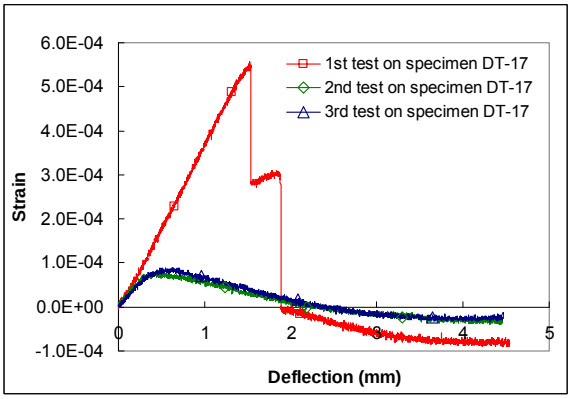

(b)

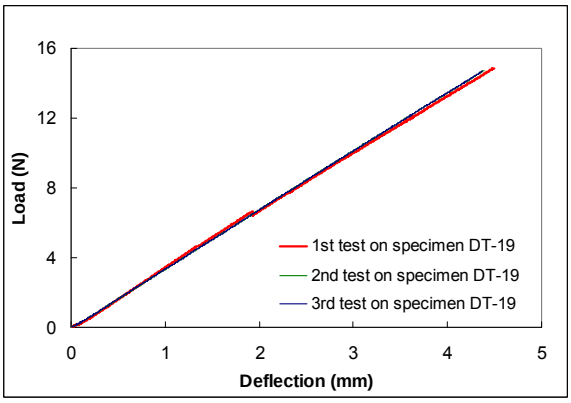

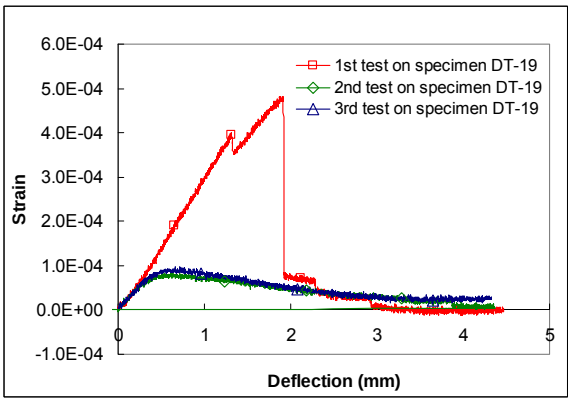

(c)

Fig.5-47 Results of quasi-static three point bending tests to examine possible solder joint degradation after drop tests for specimen (a) DT-16, (b) DT-17 and (c) DT-19

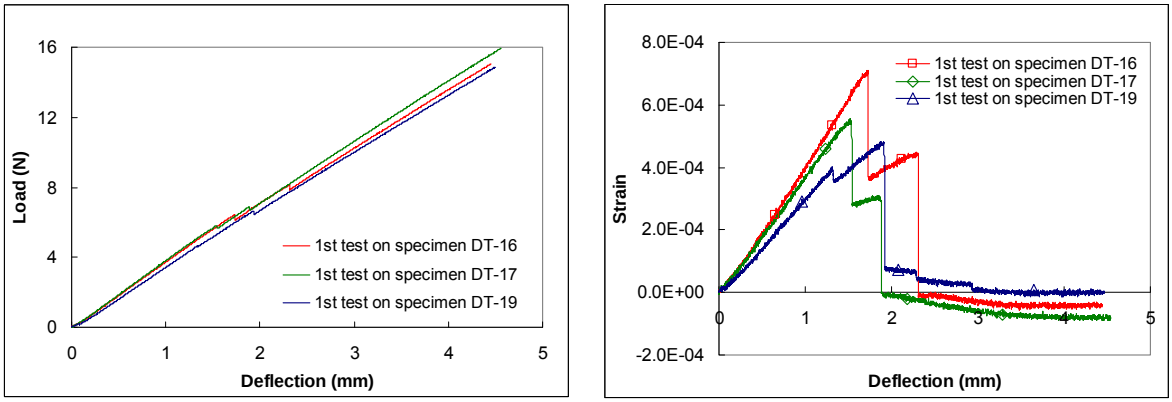

Fig.5-48 Comparison of results of first quasi-static three point bending tests on three specimens after drop test

5.5 Summary and discussion

The mechanical properties (load-deformation response) of actual solder joints are obtained from quasi-static and dynamic tests. Idealization of the actual barrel-like profile of a solder joint by a cylinder is undertaken by deriving equivalent stress-strain relationships for solder joints; this facilitates FEM simulation. Further simplification of the cylindrical solder joint model to a beam model is carried out and results based on the beam model are evaluated and shown to be able to represent the behavior of single solder joints with acceptable accuracy. This chapter has also described the application of the beam model for solder joints in simulation of package level specimens subjected to quasi-static and impact loading. The objectives are to evaluate the ability of the beam model to simulate the response of package level specimens and solder joints in IC packages.

Direct measurement of the mechanical response of solder joints in an IC

package is difficult. Therefore, strain readings from strain gauges bonded to the surface of a PCB are compared with simulation results for strain at the location of the strain gauge to evaluate the accuracy of FEM modeling. It is found that simulation results based on isotropic PCB material (modulus derived from three-point bending test) does not coincide with experimental results as well as simulations based on orthotropic PCB material properties. Another important finding is the influence of the number of element layers in the PCB thickness on the strain values at the PCB surface. It is shown that PCBs meshed by at least 7 layers of elements along its thickness give acceptable results when compared with experiments. Therefore, package level specimen models for quasi-static bending and drop impact had PCBs (PCB strip and square PCB) with 7 element layers in the thickness direction and orthotropic material properties. Fig.5-49 shows an example of quasi-static bending, where the PCB strip and square PCB are meshed with 3 layers; the results deviate considerably from those from a PCB with 7 layers of elements.

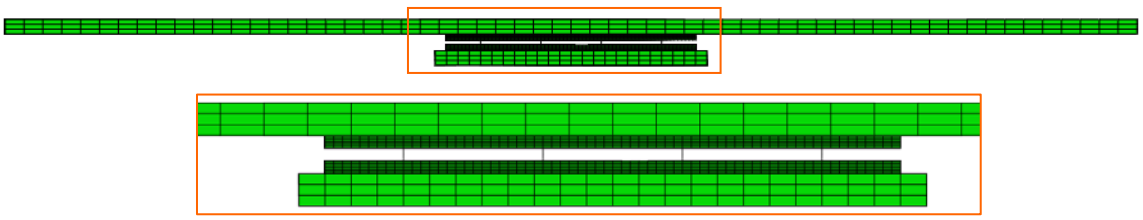

(a) FEM model - PCB with 3 layers of elements

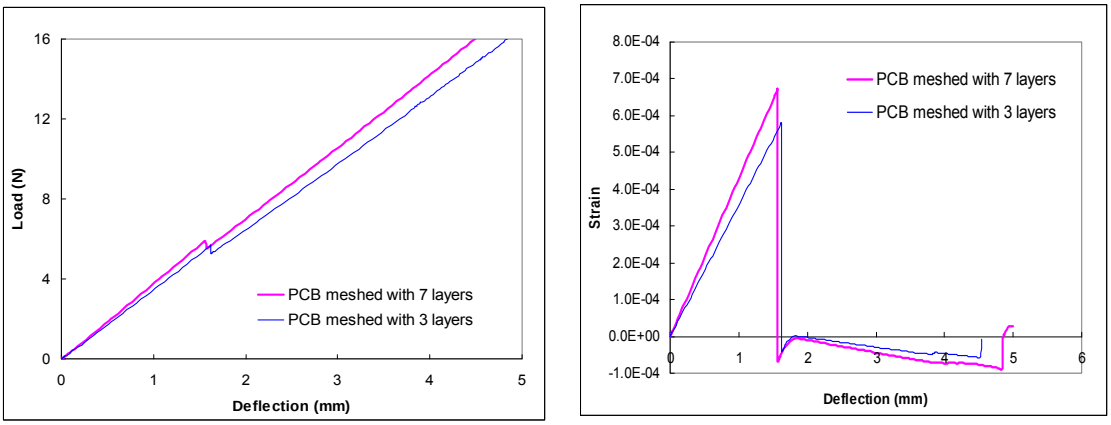

(b) Comparison of simulation output for load and strain

Fig.5-49 Illustration of influence of number of element layers along PCB thickness on simulation results: (a) FEM model - PCB meshed with 3 layers of 3D continuum elements with orthotropic material properties and (b) comparison of predicted variation of load and strain with deflection for models with 7 layers and 3 layers of elements

In drop tests of package level specimens, an accelerometer is used to record the acceleration history during impact and rebound. The velocity is obtained by integrating the acceleration. As the signal recorded by the oscilloscope does not cover the entire acceleration history from commencement of the drop, the initial velocity v_0 just before impact is used to determine the velocity history of the fixture, which is used as the boundary condition in FEM modelling. The initial velocity is estimated from the drop height h via $v_0 = \sqrt{2gh}$. However, the actual initial velocity may deviate from this due to friction. It is noted that this discrepancy in initial velocity has negligible influence on the simulation results. Fig.5-50 illustrates results for a drop from 0.3m. The initial velocity calculated from the drop height (0.3m) is 2.42m/s; however, the actual initial velocity measured from high speed camera images is 2.23m/s. The velocity boundary conditions based on these two initial velocity values and the acceleration history are plotted in Fig.5-50a. The

corresponding strain outputs for the node at the center of the square PCB are seen to be almost identical (Fig.5-50b).

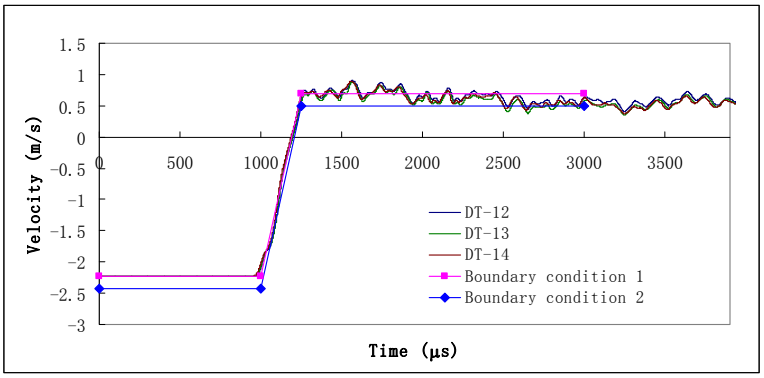

(a) Input velocity boundary condition with the initial velocity based on actual value (boundary condition 1) and calculated from drop height (boundary condition 2)

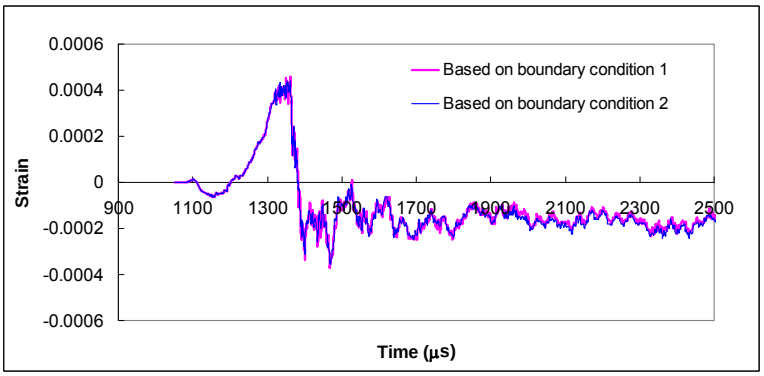

(b) Simulation results for strain from node 1 on square PCB

Fig.5-50 Illustration of the influence of the value of impact velocity on simulation results (results of drop from 0.3m height): (a) input velocity boundary conditions; and (b) corresponding simulation results for strain from node 1 on square PCB.

In simulations of drop testing, the exact value of the initial velocity has negligible influence on the overall simulation results. The velocity history is characterized by the initial velocity, the rebound velocity and the gradient of the rise time. It is noted that the rate of velocity increase during the rise time is critical to the simulation results. Prescribed velocity boundary conditions with an incorrect rise time will result in large errors. Fig.5-51 shows an example

where an instantaneous change from the initial velocity to the rebound velocity is assigned as the input boundary condition for a drop test with a 0.3m drop height; the simulation results for strain at the center of the square PCB is very different from the experimental results, whereas simulation results based on actual boundary conditions match the experimental results well.

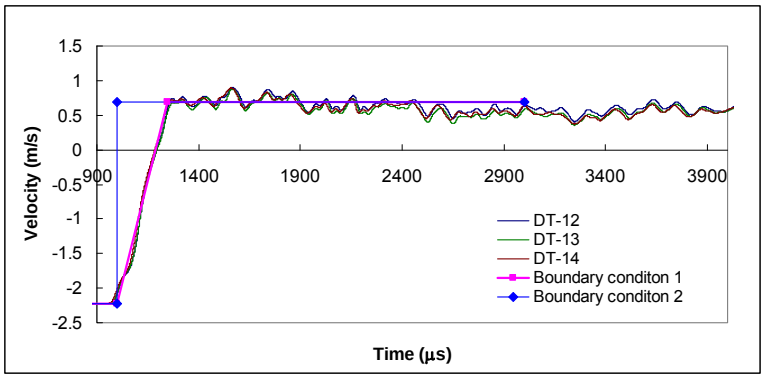

(a) Input velocity following actual rise time (boundary condition 1) and instantaneous change of velocity (boundary condition 2) upon impact

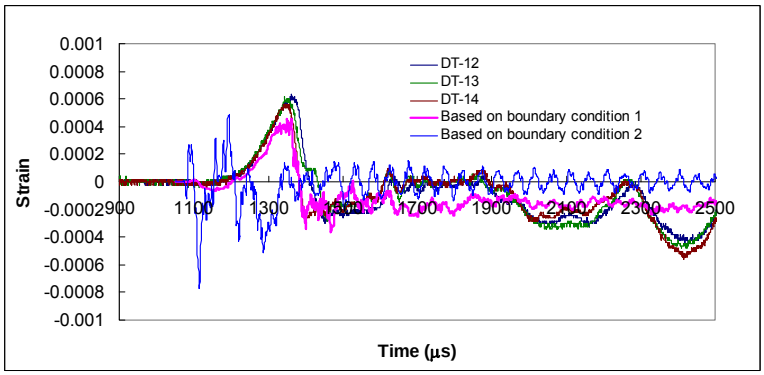

(b) Corresponding simulation results for strain (LE11) compared to experimental strain history recorded by strain gauge at center of square PCB

Fig.5-51 Illustration of influence of rise time in velocity boundary conditions on simulation results (for drop from 0.3m height): (a) input boundary conditions and (b) the corresponding simulation results for strain (LE11).

For the tests described in this chapter, the strain gauges used to record strain changes generated by breakage of solder joints are bonded to the center of

the square PCB. This is an optimal arrangement for the specimens in this study to identify the instant of solder joint breakage, especially in drop tests. Simulation results for strain on the square PCB and PCB strip substantiate this. Fig.5-52a shows the strain at nodes 1 to 6 (distance between nodes is 0.6mm) on the square PCB, and shows an obvious drop in strain upon solder joint failure, even in the results for node 6. Fig.5-52b shows the strains corresponding to nodes 1 to 4 (distance between nodes is 1mm); it is seen that the overall oscillations in the curves overlaid the drops in strain caused by solder joint failure, and it is unlikely to be able to identify the instant of solder joint breakage from the results of node 4.

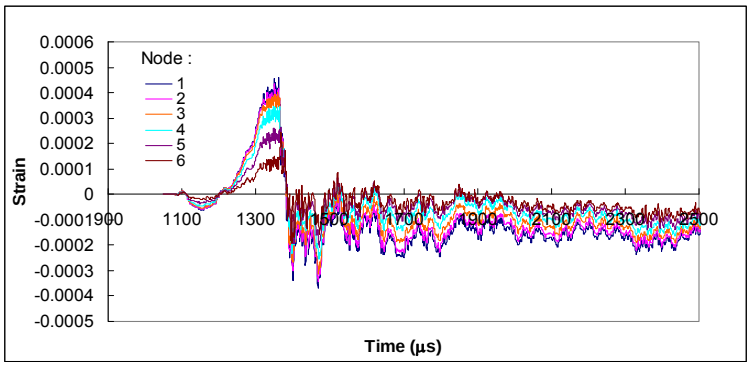

(a) Strain histories from nodes on square PCB (distance between nodes 1 and 6 is 3mm)

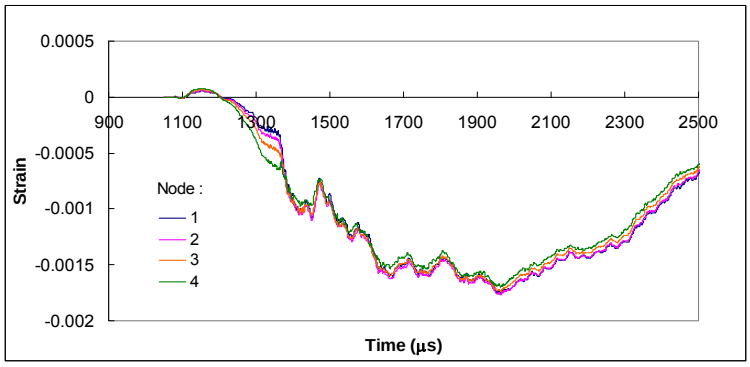

(b) Strain histories from nodes on PCB strip (distance between nodes 1 and 4 is 3mm)

Fig.5-52 Strain histories for nodes on (a) square PCB and (b) PCB strip (simulation results for 0.3m drop height)

It is not possible to directly detect and quantify the failure of solder joints in IC package from experiments. Therefore, analyzing the response of solder joints through FEM modeling is a useful approach when simulation results (e.g. strain at PCB surface) match experimental data. In this chapter, the section forces and the equivalent plastic strain (PEEQ) of the beam model are used to identify the behavior of solder joints during loading. Initiation of PEEQ indicates commencement of failure in solder joints.

In Chapter 4, failure envelopes of normal and shear forces of solder joints are established and described by the equation of an ellipse, which depends on deformation rate. These failure envelopes can also be plotted in terms of strain-rate, as the deformation rates can be converted to stain-rates via normalization with respect to the solder joint height (0.28mm in this study). Fig.5-53 shows a group of failure envelopes for strain rates of 0.001/s, 0.1.s, 1/s, 10/s, 100/s and 500/s (corresponding to deformation rates of 0.00028mm/s, 0.028mm/s, 0.28mm/s, 2.8mm/s, 28mm/s and 140mm/s); the traces of variations of normal force with shear force, based on simulations for solder joint 1-7 and solder joint 1-3 (beam model) are also plotted. For the quasi-static bending tests (Fig.5-53a), the traces of tensile-shear force of solder joint 1-7 nearly touches the failure envelope at strain-rate of 0.01/s, demonstrating the validation of the failure envelope. For the 0.1m height drop test (Fig.5-53b), the normal-shear force trace for solder joint 1-7 touches the failure envelope for a strain-rate of 0.01/s; however, this does not mean that the solder joint will fail because the failure envelope should be compared with the failure envelope for a strain-rate of around 10/s, and the experimental

results show that the solder joints are still intact after the 0.1m height drop test. For the 0.3m and 0.9m height drop tests (Fig.5-53 b and c), failure of the solder joints can be discerned as the normal-shear force traces touch the failure envelopes at corresponding strain rates. The failure envelopes can represent the mechanical quality and strength of a type of solder joints.

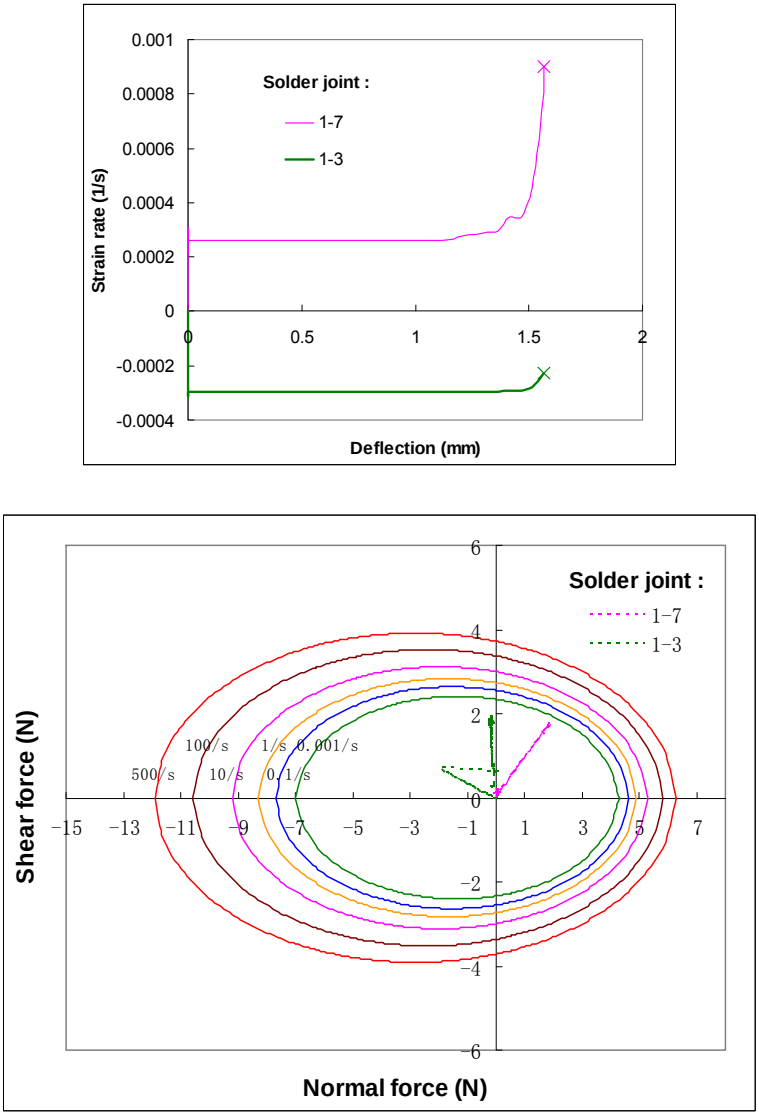

(a) Quasi-static bending

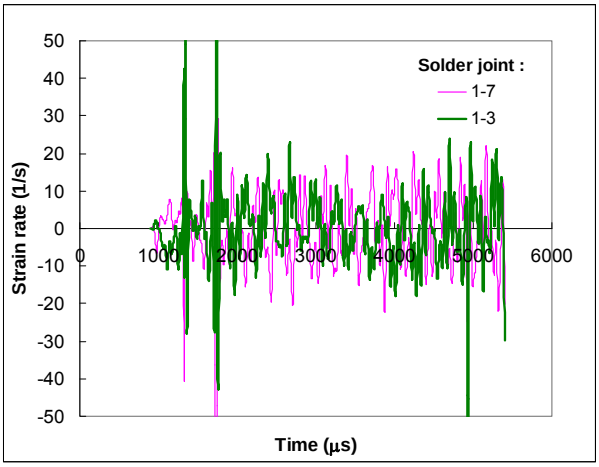

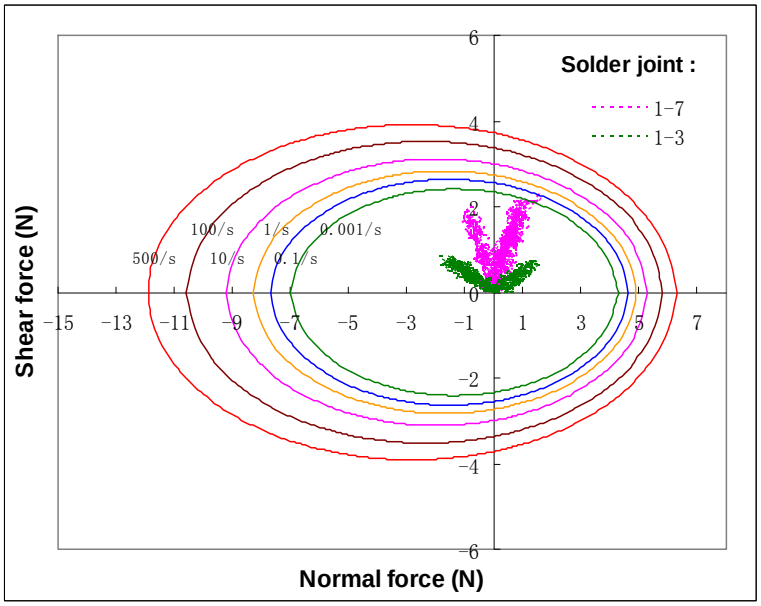

(b) Drop test from 0.1m height

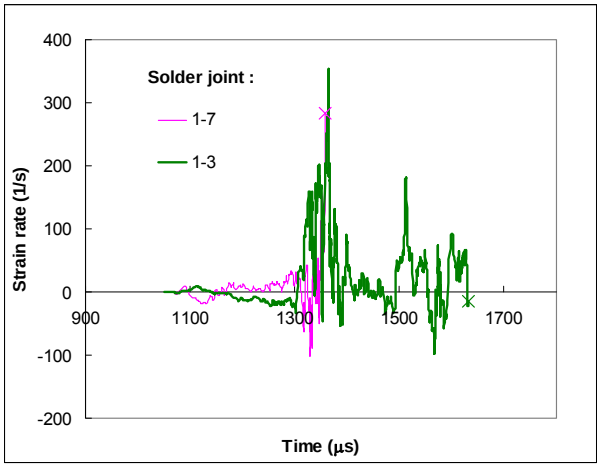

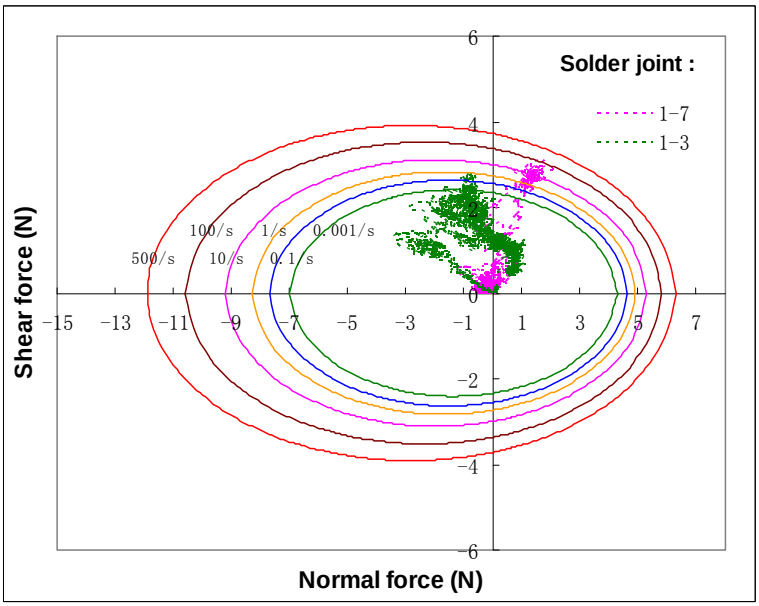

(c) Drop test from 0.3m height

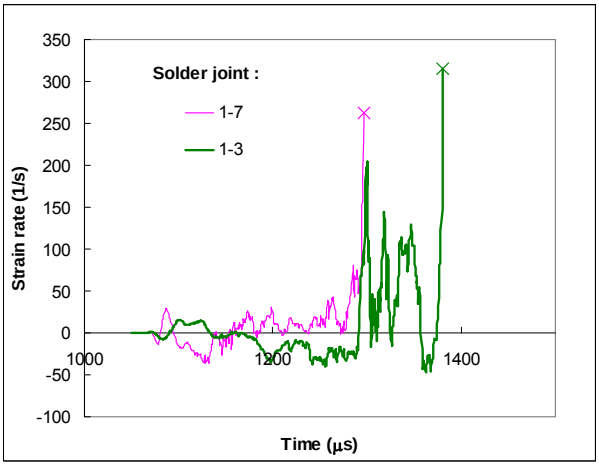

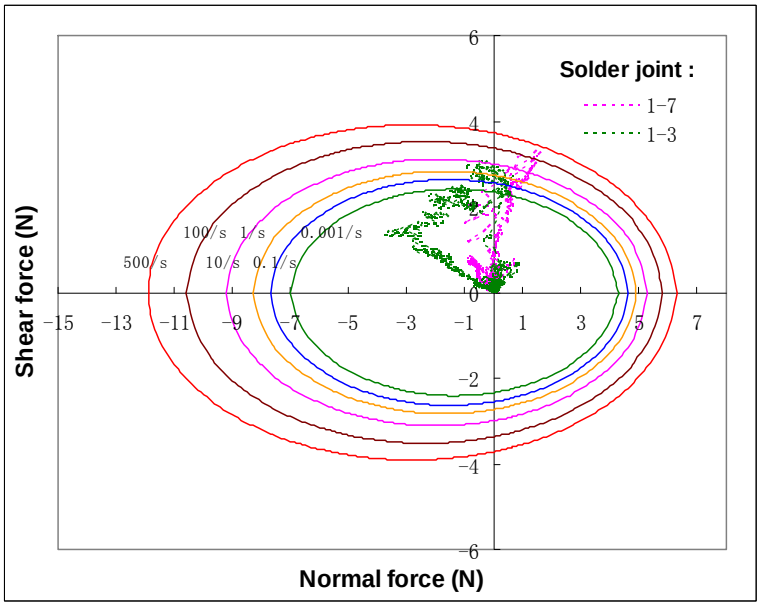

(d) Drop test from 0.9m height

Fig.5-53 Strain rate histories in solder joints, and normal-shear force relationship for solder joints from simulation results for comparison with failure envelopes for (a) quasi-static bending and (b-d) drop tests on PCB strips bonded with dummy IC package mounted.

CHAPTER 6 CONCLUSIONS AND RECOMMENDATIONS FOR FUTURE WORK

Actual solder joints in IC packages have a barrel-like profile and comprise various components – i.e. intermetallic compounds between the solder and the copper pad, impurities, voids, etc. The objective of this study is to characterize the overall behavior of an actual solder joint by experimentally-measured responses, rather than to study the individual material properties of the solder bump, copper pad, substrate, etc. This investigation considers entire single solder joints and how to test the mechanical response of such small specimens. Also examined is the validity of converting experimental force-displacement data from tests on actual solder joints into equivalent stress-strain curves for use in FEM simulation. This avoids the seemingly intractable task of examining a solder interconnection in extremely fine detail to elicit the properties of individual and varying phases/components in order to establish a more exact sub-micro-level model.

In this effort, single solder joint specimens were fabricated from Pb-free solder material, and their mechanical response and failure characteristics under quasi-static and dynamic loading determined and characterized; experimental and numerical approaches were employed. The research undertaken encompassed the following aspects:

- Development of a method to fabricate single solder joint specimens and verification of suitability for eliciting solder joint properties.

- Design of specimen fixtures, together with a series of adaptors incorporating inclined surfaces for quasi-static tests and to apply combined normal and shear loading.

- FEM simulation of SHPB testing on small specimens to validate the feasibility of conducting impact-driven dynamic tests on small solder joints, based on one-dimensional stress wave theory.

- Conceptualization and fabrication of a miniature impact tester to facilitate dynamic tests on single solder joint specimens, and validation of its applicability via numerical simulation and experimental tests.

- Characterization of load-deformation responses for single solder joint specimens at two quasi-static and two dynamic speeds, for seven specimen loading inclinations.

- Establishment of experimental failure force envelope of a solder joint and FEM simulations to discern the force components in “laterally unconstrained” and “laterally constrained” tests. Use of an elliptical locus to fit the failure force envelopes.

- Employment of FEM simulation to validate simplification of the barrel-like geometry of actual solder joints by a cylinder; this enables conversion of experimental force-deformation responses to an equivalent stress-strain relationship for characterizing single solder joint specimens.

- Establishment of a simplified beam element representation of a solder joint and validation through comparison with a three-dimensional cylindrical model as well as experimental results. Application of the beam model for solder joints in FEM simulation of board-level specimens subjected to quasi-static bending and drop impact loading; the simulation results compared well with experimental data, demonstrating that the beam model is acceptable.

(1) An appropriate method of preparing solder joint specimens using BT substrates and 0.42mm diameter lead free (Sn96.5-Ag3.0-Cu0.5) solder balls was established. Electronic package specimens in the form of two parallel square substrates (around 11.3x13.3mm) connected by an array of solder joints were fabricated. As the failure force of a solder joint is very small, single solder joint specimens were laser-cut from an electronic package comprising four solder joints. Each single solder joint specimen extracted comprises a pair of 5x5mm substrates linked by a solder interconnection.

Quasi-static tensile tests on single joint and package specimens were performed to evaluate which is more suitable for eliciting the mechanical properties of single solder joints. Four types of package specimens comprising 4, 8, 16 and 24 solder joints were tested and the results show sequential degradation and damage of individual solder joints in package specimens, resulting in an underestimation of the joint strength. The stiffness derived for one solder joint tends to increase with a smaller number of solder joints in a package, and the data from tests on single solder joint specimens display the highest stiffness. This demonstrates that single solder joint specimens are the most suitable.

(2) Single solder joint specimens possess two characteristics - a very small size and a very low failure force. These introduce difficulties in measuring force-displacement responses for normal, shear and combined normal-shear loading. An Instron micro-tester (model 5548) was found to be suitable for loading the specimens, which were bonded to the loading rods

using a fast curing adhesive (cyanoacrylate). To ensure no pre-loading which may induce initial damage, a special fixture was designed. The fixture facilitates both tensile and compression tests. To define a failure envelope for combined normal and shear loading, adaptors with inclined surfaces were designed for specimens to be loaded at various angles of inclination – 0^0 (for pure tension or compression), 15^0, 30^0, 45^0, 60^0, 75^0 and 90^0 (for pure shear). The failure force components were then used to construct the failure envelope.

(3) The use of a split Hopkinson bar system to determine the dynamic mechanical response of single solder interconnections was examined. Since the solder joints studied are very small, contact between a specimen and the input/output bars results in localized indentation. Numerical simulation of split Hopkinson bar tests on small specimens reveals a non-uniform stress distribution in the bar cross-section at the interface with the specimen, but the stress field attains a one-dimensional plane wave status after propagating sufficiently far from the interfaces – i.e. 75mm for a 5mm diameter bar. Accuracy of the force-deformation responses calculated from wave signals extracted from the mid-points of the input and output bars (the strain gauge locations in actual tests) was examined for several striker speeds and bar diameters, and found to be acceptable for engineering strains as large as 30%-40%. Simulation results supported the feasibility of performing impact tests on small solder joint specimens using a bar system based on one-dimensional stress wave theory.

(4) A miniature impact tester was conceptualized and fabricated for dynamic tests on single solder joint specimens. It comprises an input and an output bar; a tubular striker impinges an impact plate initially in contact with the specimen to generate a tensile or compressive load. Careful alignment is required only for the striker, the impact plate and the ends of the two bars adjacent to the specimen. Strain gauges on both the input and the output bars can be mounted close to the specimen-bar interfaces. Wave dispersion or attenuation has less influence on the results compared to a split Hopkinson bar system. The tester can induce either compression or tension by attaching the impact plate to the end of the input or to the output bar. The force-deformation response of the specimen is derived from the stress waves and this is more accurate than using a load cell which has frequency response limit. The miniature impact tester can also be made portable. FEM simulation was performed to examine the loading wave generated at the impact plate and its planar nature during propagation along the bars was verified. Experimental tests on cylindrical aluminium specimens showed that the results obtained using the miniature impact tester are comparable to those obtained from a split Hopkinson bar system, validating its performance.

(5) Quasi-static tests on single solder joint specimens were undertaken at two loading rates (0.00015mm/s and 0.15mm/s), and dynamic tests were carried out using the miniature impact tester at two striker speeds (around 0.3m/s and 3m/s). Foil strain gauges were used to capture the input wave and semiconductor gauges for the transmitted wave. Quasi-static and dynamic responses of single solder joint specimens under combined shear and tension

or compression were obtained by loading specimens at seven inclinations (from 0^0 to 90^0, at intervals of 15^0). Peeling-off of copper pads from substrates almost always occurred for specimens subjected to tensile loading. The load-deformation curves exhibit an initial linear response followed by a phase of nonlinearity, after which the load drops for tensile loading or enters a post-yield hardening phase for compression. The average responses were obtained from five tests for each type of test and the results indicate that single solder joint specimens exhibit rate-dependent behavior; the degree of rate sensitivity depends on the mode of loading. Variation of the tensile and shear strength for the four loading speeds applied was small. However, the compressive and shear strength increase noticeably with loading speed, especially at higher speeds.

(6) For combined tension/shear and pure shear loading, there is generally an ultimate point in the load-deformation curve after which the load drops quickly, indicating solder joint breakage. However, for combined compression and shear, a solder joint can still sustain loads after yield. Deviation of the load-deformation curve from initial linearity is taken to signify the commencement of solder joint degradation. Therefore, solder joint failure under pure tension or combined tension and shear is defined by the ultimate load. For pure compression or combined compression and shear, failure is defined by the transition from the linear elastic response to the hardening phase. Based on the normal and shear components of the failure load, failure force envelopes for a single solder joint were obtained and plotted. It is noted that the envelopes are not strictly elliptical; the failure force extracted directly

from the load-deformation curves is only part of the total load that a specimen experiences – the component in the direction of the longitudinal axis of loading rods.

An analysis of the force components that a solder joint specimen experiences under loading was carried out, through simulation. Tests were conducted with the loading rods constrained from lateral movement. This results in a specimen experiencing uniaxial displacement but a non-uniaxial force history. Therefore, the load in these “laterally constrained” tests is only a component of the resultant force experienced by a specimen. FEM simulations of a single solder joint specimen with a barrel-like solder bump were performed to simulate loading at various inclination angles. The results show that the failure force envelope constructed from the longitudinal load (TF3) resembles the profiles obtained from experiments. However, the failure force envelope constructed from the total load (resultant of TF1, TF2 and TF3) resembles an ellipse. FEM simulations were also undertaken for a specimen tested under “laterally unconstrained” conditions, whereby the loading rod is not constrained in the lateral direction. In this mode, the force experienced by a solder joint is in the direction of rod axis but the displacement is not constrained to be along the rod axis. The failure force envelope constructed from the longitudinal load (TF3) displays an elliptical profile, but with some concavity around the region for pure shear. This is associated with unstable rotation of the specimen when the inclination angle increases towards pure shear. It is also noted that “laterally unconstrained” tensile tests can be realized via loading the specimen through a stiff wire. However, this is difficult

for compression and not feasible for dynamic testing. Based on the FEM simulation results for “laterally constrained” tests, a relationship between the axial and the transverse load components was established. This was used to reconstruct the failure force envelopes obtained from experiments. The reconstructed elliptical failure force envelopes were elliptical and fitted for various deformation rates.

(7) As actual solder joints have a barrel-like geometry, it is difficult to identify their material properties (e.g. stress-strain relationship) from experimental load-deformation responses. To specify stress-strain information for FEM modeling, a numerical study was undertaken to evaluate the feasibility of simplifying the barrel-like geometry by a cylindrical one. This facilitates the conversion of load-deformation data into equivalent stress-strain curves. Microscopic measurements of actual solder joints dimensions were undertaken. Simulation was employed to examine the load-deformation response of a single solder joint under tension, compression and shear, whereby the solder joint is modelled by a barrel-like geometry similar to actual solder joints, as well as an approximate cylindrical geometry. The results show that the load-deformation curves obtained from the cylinder model can be matched to that of the barrel model when the material properties prescribed to the cylinder model are adjusted by a factor. This validates the simplification of the barrel-like solder joint by a cylinder with a prismatic cross-section to obtain an equivalent stress-strain relationship. Equivalent stress-strain responses corresponding to strain rates ranging from 0.0005/s to 1000/s for uniaxial tension and 0.0005/s to 5000/s for uniaxial compression

were then obtained. The variation of the equivalent yield stress with strain rate was found amenable to modeling by the Cowper-Symonds model. Preliminary implementation of the equivalent stress-strain curve in conjunction with a cylindrical solder model demonstrated the ability to predict the mechanical response of a solder joint in tension, compression and shear, with reasonable accuracy.

(8) Simplification of a barrel-like solder joint by a cylinder also facilitates further simplification to a beam with a uniform cross-section. An equivalent beam model with the equivalent stress-strain properties was then established. Validation of the beam model was done through comparison of the load-deformation responses with that from a 3D cylindrical model and experimental results,for loading at different inclinations.

Package specimens with a dummy IC package mounted on a PCB strip were examined experimentally and numerically. Quasi-static three-point bending tests were undertaken, and a strain gauge bonded to the dummy package provided strain data during bending of the specimen. A sharp drop in the strain indicated solder joint breakage. The drop in strain is more distinct than the drop in the applied load and is therefore a more sensitive indicator of joint breakage. Dynamic drop tests on package specimens for three drop heights were conducted. The strain at the back of the package was monitored as an indicator of solder joint integrity and a parameter for comparison with FEM simulation. FEM simulations of quasi-static bending tests and drop tests were carried out using the beam model for solder joints. Modelling of a PCB strip

with 3D continuum elements was studied and the appropriate mesh size and number of layers along the PCB thickness determined. This facilitates comparison of the load and strain from simulations with experimental values to validate the representation of solder joints by beam elements. The simulation results matched the experiments well in terms of load, strain and breakage pattern of solder joints, demonstrating the validity of employing a beam idealisation for solder joints in conjunction with equivalent stress-strain properties obtained from experimental force-deformation curves.

In summary, this study has established useful methodology for the preparation and testing of single solder joint specimens under quasi-static and dynamic loading. A miniature impact tester was conceptualised and fabricated, and validated for dynamic testing of small specimens. Quasi-static and dynamic load-deformation responses of single solder joints under combined normal/shear loads were obtained and characterized, and failure force envelopes were established and described by empirical equations. FEM models of a solder joint were investigated and the equivalent stress-strain properties of a solder joint derived. Finally, a beam model for solder joints was implemented in FEM simulation of board-level specimens subjected to quasi-static bending and drop impact loading.

Future work

It is noted that the package level quasi-static bending and dynamic drop tests were conducted on specimens with dummy chips mounted. Tests on an actual chip or a dummy chip comprising a silicon die can be conducted to evaluate the ability of FEM simulation to predict solder joint failure.

Microscopic examination of the metallographic structure (intermetallic compounds, etc) in solder joints was not undertaken in this study. The influence of metallographic structure, temperature and aging time on the load-deformation response of solder joints under various quasi-static and dynamic loads could be studied, and how these affect the failure force envelopes.

REFERENCE

Ahmad, M., Hubbard, K., Hu, M., 2005. Solder Joint Shape Prediction Using a Modified Perzyna viscoplastic Model, Journal of Electronic Packaging, Vol.127, pp.290-298

Amagai, M., 2002. Mechanical Reliability in Electronic Packaging, Microelectronics Reliability, Vol.42, pp.607-627

Amagai, M., Watanabe, M., Omiya, M., Kishimoto, K., Shibuya, T., 2002. Mechanical Characterization of Sn-Ag-based Lead-Free Solders, Microelectronics Reliability, Vol. 42, pp.951-966

Akay, H.U., Liu, Y., Rassaian, M., 2003. Simplification of Finite Element Models for Thermal Fatigue Life Prediction of PBGA Packages, Journal of Electronic Packaging, Vol.125, pp. 347-353

Alam, M.O., Chan, Y.C., Hung, K.C., 2002. Reliability study of the electroless Ni-P layer against solder alloy, Microelectronics Reliability, vol.42, pp.1065-1073

Alander, T., Nurmi, S., Heino, P., Ristolainen, E., 2002. Impact of Component Placement in Solder Joint Reliability, Microelectronics Reliability, Vol, 42, pp. 399-406

Arulvanan, P., Zhong, Z.W., Shi, X.Q., 2006. Effects of Process Conditions on Reliability, Microstructure Evolution and Failure Modes of SnAgCu solder Joints, Microelectronics Reliability, Vol46, pp.432-439

Basaran, C., Wen, Y., 2003. Coarsening in BGA solder Balls: Modeling and Experimental Evaluation, Journal of Electronic Packaging, Vol.125, pp. 426-430

Basaran, C., Zhao, Y., Tang, H., Gomez, J., 2005. A Damage-Mechanics-Based Constitutive Model for Solder Joints, Journal of Electronic Packaging, Vol.127, pp.208-214

Bragov, A.M., Lomunov, A.K., 1995. Methodological Aspects of Studying Dynamic

Material Properties Using the Kilsky Method, Int. J. Impact Engng, 16(2), pp.321-330

Cai, X., Chen, L., Zhang, Q., Xu, B., Huang, W., Xie, X., Cheng, Z., 2003. Quantitative Mechanism of Significant Benefits of Underfill in Flip-Chip Assemblies, Journal of Electronic Packaging, Vol.125, pp. 84-92

Chan, Y.W., Ju, T.H., Hareb, S.A., Lee, Y.C., Wu, J.S., Lii, M.J., 2002. Reliability Modeling for Ball grid Array Assembly With a Large Number of Warpage Affected Solder Joints, Journal of Electronic Packaging, Vol.124, pp. 246-253

Chen, K.M. and Chiang, K.N., 2003. Impact of Probing Procedure on Flip Chip Reliability, Microelectronics Reliability, Vol.43, pp.123-130

Chen, W.H., Chiang, K.N., Lin, S.R., 2002. Prediction of Liquid Formation for Solder and Non-solder Mask Defined Array Packages, Journal of Electronic Packaging, Vol.124, pp. 37-44

Chen, Z., He, M., Kumar, A., Qi, G.J., 2007. Effect of Interfacial Reaction on the Tensile Strength of Sn-3.5Ag/Ni-P and Sn-37Pb/Ni-P solder Joints, Journal of Electronic Materials, Vol.36, No.1, pp.17-25

Chen, Z., Kumar, A., Mona, M., 2006. Effect of Phosphorus Content on Cu/Ni-P/Sn-3.5Ag Solder Joint Strength after Multiple Reflows, Journal of Electronic Materials, Vol.35, No.12, pp.2126-2134

Chen, C.M. and Lin, H.C., 2006. Interfacial Reactions and Mechanical Properties of Ball-Grid-Array Solder Joints Using Cu-Cored Solder Balls, Journal of Electronic Materials, Vol.35, No.11, pp.1937-1947

Chen, W.H., Lin, S.R., Chiang, K.N., 2006. Predicting the Liquid formatin for the Solder Joints in Flip Chip Technology, Journal of Electronic Packaging, Vol.128, pp.331-338

Chen, W.M., McCloskey, P., O'Mathuna, S.C., 2006. Isothermal Aging Effects on the Microstructure and Solder bump Shear Strength of Eutectic Sn37Pb and Sn3.5Ag Solders, Microelectronics Reliability, Vol.46, pp.896-904

Chen, B.L., Shi, X.Q., Li, G.Y., Ang, K.H., pickering, J.Pl, 2005. Rapid Temperature Cycling (RTC) Methodology for Reliability Assessment of Solder Interconnection in Tape Ball Grid Array (TGA) Assembly, Journal of Electronic Packaging, Vol.127, pp.466-473

Chen, H.T., Wang, C.Q., Li, M.Y., 2006. Numerical and Experimental Analysis of the Sn3.5Ag0.75cu solder Joint Reliability under Thermal Cycling, Microelectronics Reliability, Vol.46, pp.1348-1356

Chen, Y.S., Wang, C.S., Wang, T.C., Chan, W.H., Chang, K.C., Yuan, T.D., 2007. Solder Joint Reliability Assessment for flip chip ball Grid Array Components with Various Designs in Lead-Free Solder Materials and Solder Mask dimensions, Journal of Electronic Materials, Vol. 36, No.1, pp.6-16

Chiu, T.C., Zeng, K. , Stierman, R., Edwards, D., Ano, K., (2004), Effect of Thermal Aging on Board Level Drop Reliability for Pb-free BGA Packages, Proceeding of Electronic Components and Technology Conference, pp.1256-1262.

Cho, S., Han, b., Joo, J., 2004. Temperatue Dependent Deformation Analysis of Ceramic Ball Grid Array Package Assembly Under Accelerated Thermal Cycling Codition, Journal of Electronic Packaging, Vol. 126, pp.41-47

Chong, D.Y.R., Che, F.X., Pang, J.H.L., Ng, K., Tan, J.Y.N., Low, P.T.H., 2006. Drop Impact Reliability Testing for Lead-free and Lead-Based Soldered IC Packages, Microelectronics Reliability, Vol.46, pp.1160-1171

Chuang, C.M., Shih, P.C., Lin, K.L., 2004. Mechanical Strength of Sn-3.5Ag-Based Solders and Related Bondings, Journal of Electronic Materials, Vol.33, No.1, pp.1-6

Chung, C.L., Fan, J., Huang, M.L., Tsai, F.J., 2002. Study on Failure Mechanism of PCT Reliability for BT Substrate Based CSP (Chip Scale Package), Journal of Electronic Packaging, Vol.124, pp. 334-339

Corbin J.S., 1993. Finite Element Analysis for Solder Ball Connect (SBC) Structural Design Optimisation, IBM J Res Develop, 37(5), pp.585-596

Cotterell, B., Chen, Z., Han, J.B., Tan, N.X., 2003. The Strength of the Silicon Die in

Flip-Chip Assemblies, Journal of Electronic Packaging, Vol.125, pp. 114-119

Cowper, G.R. and Symonds, P.S., 1957. Strain-hardening and Strain-rate Effects in the Impact Loading of Cantilever Beams. Technical report, No.28, Division of Applied Mechanics, Brown University.

Clyens, S., and Campbell, J. D., 1974. Inst. Phys. Conf. Ser. 21, pp.62

Dariavach, N., Callahan, P., Liang, J., fournelle, R., 2006. Intermetallic Growth Kinetics for Sn-Ag, Sn-Cu, and Sn-Ag-Cu Lead-Free Solders on Cu, Ni, and Fe-42Ni Substrates, Journal of Electronic Materials, Vol.35, No.7, pp.1581-1592

Darveaux, R., 2002. Effect of Simulation Methodology on Solder Joint Crack Growth Correlation and Fatigue Life Prediction, Journal of Electronic Packaging, Vol.124, pp. 147-154

Date, M., Shoji, T., Fujiyoshi, M., Sato, K., Tu, K.N., 2004. Impact Feliability of Solder Joints, Proceeding of Electronic Components and Technology Conference, pp.668-674

Davuluri, P., shetty, S., Dasgupta, A., Young, S., 2002. Thermo-mechanical Durability of High I/O BGA Packages, Journal of Electronic Packaging, Vol.124, pp. 266-270

Daya Perera, U., 1999. Evaluation of Reliability of BGA Solder Joints through Twisting and Bending, Microelectronics Reliability, Vol.39, pp.391-399.

Desai, C.S., Wang, Z., Whitenack, R., Kundu, T., 2004. Testing and Modeling of Solders Using New Test Device, Part 1: Models and Testing, Journal of Electronic Packaging, Vol. 126, pp.225-231

Duan, N., Scheer, J., Bielen, J., Kleef, M.V., 2003. The Influence of Sn-Cu-Ni(Au) and Sn-Au-Intermetallic compounds on the Solder Joint Reliability of Flip Chips on Low Temperature co-fired Ceramic Substrates, Microelectronics Reliability, Vol.43, pp.1317-1327

Dudek, r., Döring, R., Michel, B., 2003. Reliability Prediction of Area Array Solder

Joints, Journal of Electronic Packaging, Vol.125, pp.562-568

Dunford, S., Canumalla, S., Viswanadham, P., 2004. Intermetallic Morphology and Damage Evolution under Thermomechanical Fatigue of Lead (Pb) Free Solder Interconnections, Proceeding of Electronic Components and Technology Conference, pp.726-736.

Fan, S.H., Chan, Y.C., Lai, J.K.L., 2003. Open Defects in PBGA Assembly Solder Joints, Journal of Electronic Packaging, Vol.125, pp. 157-162

Fix, A.R., Lōpez, G.A., Brauer, I., 2005. Microstructural Development of Sn-Ag-Cu Solder Joints, Journal of Electronic Materials, Vol. 34, No.2, pp.137-142

Fossum, A.F., Vianco, P.T., Neilsen, M.K., Pierce, D.M., 2006. A Practical Viscoplastic Damage Model for Lead-Free Solder, Journal of Electronic Packaging, Vol.128, pp.71-81

Gama, Lopatnikov, Gillespie Jr, July 2004. Hopkinson bar experimental technique, Appl Mech Rev, Vol 57, No 4

Gu, Yu. and Nakamura, T., 2004. Interfacial Delamination and Fatigue Life Estimation of 3D Solder bumps in Flip-chip Packages, Microelectronics Reliability, Vol.44, pp.471-483

Guilbault, P., Woirgard, E., Zardini, C., Lambert, D., 2002. Reliability Study of the Assembly of a Large BGA on a Build up Board Using Thermo-mechanical Simulations, Microelectronics Reliability, Vol.42, pp.1529-1533

Gupta, P., Doraiswami, R., Tummala, R., 2004, Effect of Intermetallic Compounds on Reliability of Sn-Ag-Cu Flip Chip Solder interconnects for Different Substrate Pad Finishes and Ni/Cu UBM, Proceeding of Electronic Components andTechnology conference, pp.68-74

Guven, I., Kradinov, v., Tor, J.L., Madenci, E., 2004. Strain Energy Density Criterion for reliability Life Prediction of Solder Joints in Electronic Packaging, Journal of Electronic Packaging, Vol. 126, pp.398-405

Gonzalez, M., Vandevelde, b., Hoof, R.V., Beyne, E., 2004. Characterization and FE Analysis on the Shear Test of Electronic Materials, Microelectronics Reliability, Vol.44, pp.1915-1921

Gong, J.C., Malvem, L.E., Jenkins, D.A., 1990. Dispersion Investigation in the Split Hopkinson Pressure Bar, Journal of Engineering Materials and Technology, Vol.112, pp.309-314

Ham, S.J., Lee, S.B., 2003. Measurement of Creep and Relaxation Behaviors of Wafer-Level CSP Assembly Using Moiré interferometry, Journal of Electronic Packaging, Vol.125, pp. 282-288

Han, J.-B., 2001. Flip-Chip BGA Design to Avert Die Cracking, Journal of Electronic Packaging, Vol.123, pp. 58-63

Heffes, M.J. and Nied, H.F., 2004. Analysis of Interfacial Cracking in Flip Chip Packages With Viscoplastic Solder Deformation, Journal of Electronic Packaging, Vol. 126, pp.135-141

Huang, Z., Conway, P.P., Jung, E., Thomson, R.C., Liu, C., Loeher, t., Minkus, M., 2006. Reliability Issues in Pb-free Solder Joint Miniaturization, Journal of Electronic Materials, Vol.35, No.9, pp.1761-1772

Huang, W., Loman, J.M., Sener, B., 2002. Study of the Effect of Reflow Time and Temperature on Cu-Sn Intermetallic Compound Layer reliability, Microelectronics Reliability, Vol.42, pp.1229-1234

Hwang, J.S., 1996. Modern Solder Technology for Competitive Electronics Manufacturing, McGraw-Hill, ISBN 0-07-031749-6

Islam, M.N., Chan, Y.C., Alam, M.O., Sharif, A., 2005. Comparative Study of the Dissolution Kinetics of Electrolytic Ni and Electroless NiP Layers by Molten Sn3.5Ag Solder Alloy, Journal of Electronic Packaging, Vol.127, pp.365-369

Islam, M.N., Chan, Y.C., Sharif, A., Alam, M.O., 2003. Comparative Study of the Dissolution Kinetics of Electrolytic Ni and Electroless Ni-P by the Molten Sn3.5Ag0.5Cu Solder Alloy, Microelectronics Reliability, Vol.43, pp.2031-2037

Islam, M.N., Sharif, A., Chan, Y.C., 2005. Effect of Volume in Interfacial Reaction between Eutectic Sn-3.5% Ag-0.5%Cu Solder and cu Metallization in Microelectronic Packaging, Journal of Electronic Materials, Vol. 34, No.2, pp.143-149

Jang, G.Y. and Duh, J.G., 2006. Elemental Redistribution and interfacial Reaction Mechanism for the Flip Chip Sn-3.0Ag-(0.5 or 1.5) Cu Solder bump with Al/Ni(V)/Cu Under-Bump Metallization During Aging, Journal of Electronic Materials, Vol.35, No.11, pp.2061-2070

Jang, G.Y., Duh, J.G., Takahashi, H., Lu, S.W., Chen, J.C., 2006. Influence of Cu content on Compound Formation near the Chip Side for the Flip-Chip Sn-3.0Ag-(0.5 or 1.5) Cu Solder bump during Aging, Journal of Electronic Materials, Vol.35, No.9, pp.1745-1754

Jang, J.W., Lin, J.K., Frear, D.R., 2007. Failure Morphology after the Drop Impact Test of the Ball grid Array Package with Lead-Free Sn-3.8Ag-0.7Cu on cu and Ni Under-Bump Metallurgies, Journal of Electronic Materials, Vol. 36, No.3, pp.207-213

Johnson, G.R. and Cook, W.H., 1983. Proc. 7th Intern. Symp. Ballistics, Am. Def. Prep. Org. (ADPA), Netherlands

Johnson, G.R., Hoegfeldt, J.M., Lindholm, U.S., and Nagy, A., 1983. Response of various metals to large torsional strains over a large range of strain rates – Part 1: Ductile metals. ASME Journal of Engineering Materials and Technology, 105(1), pp.42

Jonnalagadda, K., 2002. Reliability of via-in-pad structures in mechanical cycling fatigue, Microelectronics Reliability, Vol. 42, pp. 253-258

Joo, J., Cho, S., Han, B., 2005. Characterization of Flexural and Thermo-mechanical behavior of Plastic ball Grid Package Assembly Using moiré Interferometry, Microelectronics reliability, vol.45, pp.637-646

Josell, D., Wallace, W.E., Warren, J.A., Wheeler, D., Powell IV, A.C., 2002. Misaligned Flip-Chip Solder Joints: Prediction and Experimental Determination of Force-Displacement Curves, Journal of Electronic Packaging, Vol.124, pp. 227-233

Katahira, T., Kartio, I., Segawa, H., Takahashi, M., Sagisaka, K., 2006. Vertically high-density Interconnection for Mobile Application, Microelectronics Reliability, Vol.46, pp.756-762

Keser, b., Wetz, L., White, J., 2004. WL-CSP Reliability with Various Solder Alloys and Die Thicknesses, Microelectronics Reliability, Vol.44, pp.521-531

Kim, K.S., Huh, S.H., Suganuma, K., 2003. Effects of Fourth Alloying Additive on Microstructures and Tensile Properties of Sn-Ag-Cu alloy and Joints with Cu, Microelectronics Reliability, Vol.43, pp.259-267

Kim, J.W., Kim, D.G., Jung, S.B., 2006. Evaluation of Displacement Rate Effect in Shear Test of Sn-3Ag-0.5Cu Solder Bump for Flip Chip Application, Microelectronics Reliability, Vol.46, pp.535-542

Kim, K.S., Ryu, K.W., Yu, C.H., Kim, J.M., 2005. The formation and Growth of Intermetallic Compounds and Shear Strength at Sn-Zn Solder/au-Ni-Cu Interfaces, Microelectronics reliability, vol.45, pp.647-655

Kim, J.M., Shin, Y.E., Fujimoto, K., 2004. Dynamic Modeling for Resin Self-alignment Mechanism, Microelectronics Reliability, Vol.44, pp.983-992

Koguchi, H., Sasaki, C., Nishida, K., 2003. Thermo-Viscoelastic Analysis of Deflection in CSP Electronic Device Packages, Journal of Electronic Packaging, Vol.125, pp. 414-419

Kim, J.M., Yasuda, K., Fujimoto, K., 2005. Resin Self-Alignment processes for Self-Assembly Systems, Journal of Electronic Packaging, Vol.127, pp.18-24

Kim, S.W., Yoon, J.W., Jung, S.B., 2004. Interfacial reactions and Shear Strengths between Sn-Ag-based Pb-Free Solder Balls and au/EN/Cu Metallization, Journal of Electronic Materials, Vol.33, No.10, pp.1182-1189

Kolsky, H., 1949. An investigation of the Mechanical Properties of Materials at Very High Rates of Loading. Proceedings of the Physical Society, B62:676-701.

Korhonen, T.M.K. and Henderson, D.W., 2007. Isothermal Fatigue behavior of the Near-Eutectic Sn-Ag-Cu Alloy between -25^{0}C and 125^{0}C, Journal of Electronic Materials, Vol. 36, No.2, pp.173-178

Krenk, S., 2001. Chapter 2: Beams, Mechanics and Analysis of Beams, Columns and Cables, 2nd. Edition, ISBN 3-540-41713-3, Springer-Verlag Berlin Heidelberg New York

Kuo, C.T., Yip, M.C., Chiang, K.N., 2004. Time and Temperature-dependent Mechanical Behavior of Underfill Materials in Electronic Packaging Application, Microelectronics Reliability, Vol.44, pp.627-638

Lai, Y.S., Lee, C.W., and Kao, C.L., 2007. Effect of Test Conditions on Electromigration Reliability of Sn-Ag-Cu Flip-chip Solder Interconnects, Journal of Electronic Packaging, Vol.129, pp. 56-62.

Lai, Y.S., Wang, T.H., Tsai, H.H., Jen, M.H.R., 2007. Cyclic bending Reliability of Wafer-level Chip-scale Packages, Microelectronics Reliability, Vol.47, pp.111-117

Lai, Y.S., Yang, P.F., Yeh, C.L., 2006. Experimental studies of Board-level Reliability of Chip-scale Packages Subjected to JEDEC Drop Test Condition, Microelectronics Reliability, Vol.46, pp.645-650

Lai, Y.S. and Yeh, C.L., 2006. Transient Fracturing of Solder Joints Subjected to Displacement-controlled Impact Loads, Micro Electronics Reliability, Vol.46, pp.885-895

Lai, Y.S., Yeh, C.L., Wang, C.C., 2007. Investigations of Board-level Drop Reliability of Wafer-Level Chip-Scale Packages, Journal of Electronic Packaging, Vol. 129, pp.105-108

Larson, M.C., Verges, M.A., 2003. Extending the Fatigue life of Solder Grid Array (SGA) Electronic Packages, Journal of Electronic Packaging, Vol.125, pp. 18-23

Lau, H. John, (1995), Ball Grid Array Technology, McGraw-Hll, Inc., ISBN 0-07-036608-X

Lau, J.H., 1996. Solder Joint Reliability of Flip Chip and Plastic Ball Grid Array Assemblies under Thermal, Mechanical, and Vibrational Conditions, IEEE Transactions on components, packaging, and Manufacturing Technology-Part B, Vol.19, No.4, pp.728-735

Lau, J.H., 2006. Reliability of Lead-Free Solder Joints, Journal of Electronic Packaging, Vol.128, pp.297-301

Lau, J., Dauksher, W., Ott E., et al., 2004. Reliability Testing and Data Analysis of an 1657CCGA (Ceramic Column Grid Array) Package with Lead-free solder paste on Lead-free PCBs (Printed Circuit Boards), Proceeding of Electronic Components and Technology Conference, pp.718-725

Lau, J. and Dauksher, W., 2005. Reliability of an 1657CCGA (Ceramic Column Grid Array) Package with 95.5Sn3.9Ag0.6Cu Lead-Free Solder Paste on PCBs (Printed Circuit Boards), Journal of Electronic Packaging, Vol.127, pp.96-105

Lau, J.H., Pan, S.H., Chang, C., 2002. Creep analysis of Wafer Level chip Scale Package (WLCSP) With 96.5Sn-3.5Ag and 100In Lead-Free Solder Joints and Microvia Build-Up Printed Circuit Board, Journal of Electronic Packaging, Vol.124, pp. 69-76

Lau, J.H., Pan, S.H., Chang, C., 2002. A New Thermal-Fatigue Life Prediction Model for Wafer Level Chip Scale Package (WLCSP) Solder Joints, Journal of Electronic Packaging, Vol.124, pp. 212-220

Lau, J.H., Lee, S.W.R., Pan, S.H., Chang, C., 2002. Nonlinear-Time-Dependent Analysis of Micro Via-In-Pad Substrates for Solder Bumped Flip Chip Applications, Journal of Electronic Packaging, Vol.124, pp. 205-211

Lee, C.C., Lee, C.C., Ku, H.T., Chang, S.M., chiang, K.N., 2007. Solder Joints layout Design and Reliability Enhancements of Wafer Level Packaging using response Surface Methodology, Microelectronics Reliability, Vol.47, pp.196-204

Li, G.Y., Chan, Y.C., 2002. An Investigation of Intermetallics Formation Between Pd/Ag Metallization and Sn/Pb/Ag Solder, Journal of Electronic Packaging, Vol.124, pp. 305-310

Li, M., Wang, R., Han, M.B., March 1993. A Kolsky Bar: Tension, Tension-Tension, Experimental Mechanics, pp.7-14

Licari, J.J., 1995. Multichip Module Design, Fabrication, and Testing, McGraw-Hill, Inc., ISBN 0-07-037715-4

Lin, Y.C., Chen, x., Liu, X.S., Lu, G.Q., 2005. Effect of Substrate Flexibility on Solder Joint Reliability: Part II: Finite Element Modeling, Microelectronics reliability, vol.45, pp.143-154

Liu, C., Conway, P., Li, D., Hendriksen, M., 2004. Journal of Electronic Packaging, Vol. 126, pp.359-366

Liu, J.F., Shim, V.P.W., Tan, V.B.C., Lee, T.K., 2007. Dynamic Testing of Solder Joint Strength under compression, Tension and Shering, 9th electronics Packaging Technology Conference, pp.380-385

Liu, X., Sooklal, V.K., verges, M.A., Larson, M.C., 2006. Experimental Study and Life Prediction on High Cycle Vibration Fatigue in BGA Packages, Microelectronics Reliability, Vol.46, pp.1128-1138

Liu, S., Ume, I.C., 2002. Vibration Analysis Based Modeling and Defect Recognition for Flip-Chip Solder-Joint Inspection, Journal of Electronic Packaging, Vol.124, pp. 221-226

Liu, X., Xu, S., Lu, G., Dillard, D.A., 2002. Effect of Substrate Flexibility on Solder Joint Reliability, Microelectronics Reliability, Vol.42, pp.1883-1891

Lu, H.Y., Balkan, H., Ng, K.Y.S., 2006. Microstructure Evolution of the Sn-Ag-y%Cu Interconnect, Microelectronics Reliability, Vol.46, pp.1058-1070

Lu, H., Shi, H., Zhou, M., 2006. Thermally Induced Deformation of Solder joints in real Packages: Measurement and Analysis, Microelectronics Reliability, Vol.46, pp.1148-1159

Luan, J., Tee, T.Y., Pek, E., Lim, C.T., Zhong, Z.W., 2007. Dynamic Responses and

Solder Join Reliability under Board level Drop Test, Microelectronics Reliability, Vol.47, pp.450-460

Mattila, T.T. and Kivilahti, J.K., 2005. failure Mechanisms of Lead-Free Chip Scale Package Interconnections under Fast Mechanical Loading, Journal of Electronic Materials, Vol. 34, No.7, pp.969-976

Maveety, J.G., Liu, P., Vijayen, J., Hua, F., Sanchez, E.A., 2004. Effect of Colling Rate on Microstructure and Shear Strength of Pure Sn, Sn-0.7Cu, Sn-3.5Ag, and Sn-37Pb Solders, Journal of Electronic Materials, Vol.33, No.11, pp.1355-1363

McDowell, D. L., Miller, M.P., Brooks, D.C., 1994. A Unified Creep-Plasticity Theory for Solder Alloys, Fatigue of Electronic Materials, ASTM STP 1153, S.A. Schroeder and M.R. Mitchell, eds., American Society for Testing and Materials, Philadelphia, pp.42-59

Mercado, L.L., Phillips, b., Sahasrabudhe, S., Sedillo, J.P., Bray, D., Monroe, E., 2004. Use-condition-based Cyclic Bend Test Development for Handheld Components, Electronic Components and Technology Conference, pp.1279-1287

Meyer, L.W. 1992. In Shock-Wave and High-Strain-Rate Phenomena in Materials, eds. Meyers, M.A., Murr, L.E. and Staudhammer, K.P., Dekker, New York.

Mirman, B., 2002. Impact of Low Temperatures on Solder Joint Failures, Journal of Electronic Packaging, Vol.124, pp. 135-137

Mishiro, K., Ishikawa, S., Abe, M., Kumai, T., Higashiguchi, Y., Tsubone, K., 2002. Effect of the drop impact on BGA/CSP package reliability, Microelectronics Reliability, Vol.42, pp.77-82

Müller, W.H., 2004. Morphology Changes in Solder Joints – Experimental Evidence and Physical Understanding, Microelectronics Reliability, Vol.44, pp.1901-1914

Nadai, A., 1950. Theory of flow and fracture of solids, New York: McGraw-Hill

Nagaraj, B., 1997. Drop Impact Simulation of a Custom Pager Product, Advances in Electronic Packaging, Vol.19, pp.539-547

Nose, H., Sakane, M., Tsukada, Y., Nishimura, H., 2003. Temperature and Strain Rate Effects on Tensile Strength and Inelastic Constitutive Relationship of Sn-Pb solders, Journal of Electronic Packaging, Vol.125, pp. 59-66

Nurmi, S., Sundelin, J., Ristolainen, E., Lepistö, T., 2004. The effect of solder Paste Composition on the Reliability of SnAgCu Joints, Microelectronics Reliability, Vol.44, pp.485-494

Obaid, A.A., Sloan, J.G., Lamontia, M.A., Paesano, A., Khan, S., Jr., J.W.G., 2005. Test Method Development to Quantity the In Situ elastic and Plastic Behavior of 62%Sn-36%Pb-2%Ag Solder Ball Arrays in Commercial Area Array Packages at -40^{0}C, 23^{0}C, and 125^{0}C, Journal of Electronic Packaging, Vol.127, pp.483-495

Obaid, A.A., Sloan, J.G., Lamontia, M.A., Paesano, A., Khan, S., Jr., J.J.G., 2005. Experimental in Situ characterization and Creep Modeling of Tin-Based Solder Joints on Commercial Area Array Packages at -40^{0}C, 23^{0}C, and 125^{0}C, Journal of Electronic Packaging, Vol.127, pp.430-439

Ogawa, T., Kaga, R., Ohsawa, T., 2005. Microstructure and Mechanical properties predicted by Indentation Testing of Lead-Free Solders, Journal of Electronic Materials, Vol. 34, No.3, pp.311-317

Ogawa, K., June 1984. Impact-tension compression Test by Using a split-Hopkinson Bar, Experimental Mechanics, pp.81-86

Okura, J.H., Dasgupta, A., Caers, J.F.J.M., 2002. Hygro-Mechanical Durability of Underfilled Flip-Chip-on-Board (FCOB) Interconnects, Journal of Electronic Packaging, Vol.124, pp. 184-187

Park, J.E., Jasiuk, I., Zubelewicz, A., 2003. Stresses and Fracture at the Chip/Underfill Interface in Flip-Chip Assemblies, Journal of Electronic Packaging, Vol.125, pp. 44-52

Pang, J.H.L., Xu, L., Shi, X.Q., Zhou, W., Ngoh, S.L., 2004. Intermetallic Growth Studies on Sn-Ag-Cu Lead-free Solder Joints, Journal of Electronic Materials, Vol.33, No.10, pp.1219-1226

Pendse, R.D., Zhou, P., 2002. Methodology for Predicting Solder Joint Reliability in Semiconductor Packages, Microelectronics Reliability, Vol. 42, pp. 301-305.

Peng, C.T., Kuo, C.T., Chiang, K.N., 2004. Experimental Characterization and Mechanical Behavior Analysis on Intermetallic Compounds of 96.5Sn-3.5Ag and 63Sn-37Pb Solder Bump with Ti-Cu-Ni UBM on Copper Chip, Proceeding of Electronic Components and Technology Conference, pp.90-97.

Peng, C.T., Kuo, C.T., Chiang, K.N., Ku, T., Chang, K., 2006. Experimental Characterization and Mechanical Behavior Analysis of Intermetallic Compounds of Sn-3.5Ag lead-free Solder bump with Ti/Cu/Ni UBM on Copper chip, Microelectronics Reliability, Vol.46, pp.523-534

Pucha, R.V., Tunga, K., Pyland, J., sitaraman, S.K., 2004. Accelerated Thermal Cycling Guidelines for Electronic Packages in Military Avionics Thermal Environment, Journal of Electronic Packaging, Vol. 126, pp.256-264

Ratchev, P., Vandevelde, b., De Wolf I., 2004. Reliability and failure Analysis of SnAgCu Solder Interconnections for PSGA Packages on Ni/Au Surface Finish, IEEE Trans Dev Mater Reliab, Vol.4, No.1

Rayasam, M., Subbarayan, G., 2006. A Three-Dimensional Solder Shape Model Incorporating top Pad Inclination and Misalignment, Journal of Electronic Packaging, Vol.128, pp.291-293

Rayasam, M., Thompson, T.B., Subbarayan, G., Gurumurthy, C., Wilcox, J.R., 2006. A Model for Assessing the Shape of Solder Joints in the Presence of PCB and Package Warpage, Journal of Electronic Packaging, Vol.128, pp.184-191

Roellig, M., dudek, R., Wiese, S., Boehme, B., wunderle, B., Wolter, K.J., Michel, B., 2007. Fatigue Analysis of Miniaturized Lead-free solder Contacts Based on a Novel Test concept, Microelectronics Reliability, Vol.47, pp.187-195

Ross, C.T.F., 1996. Chapter 4: Beam deflections due to bending, Mechanics of Solids, ISBN 0-13-237778-0(pbk), Printed and bound in Great Britain by Redwood Books Limited, Trowbridge, Wiltsire.

Saha, S.K., Mathew, S., Canumalla. S., (2004), Effect of Intermetallic Phases on Performance in a Mechanical Drop Environment: 96.5Sn3.5Ag Solder on Cu and Ni/Au Pad Finishes", Proceeding of Electronic Components and Technology Conference, pp.1288-1295.

Salalha, W., Zussman, E., Bar-Yoseph, P.Z., 2004. Investigation of Flip-Chip bonding for MEMS Applications, Journal of Electronic Packaging, Vol. 126, pp.48-51

Sasaki, K., Ohguchi, K., Ishikawa, H., 2001. Viscoplastic Deformation of 40Pb/60Sn Solder Alloys – Experiments and Constitutive Modeling, Journal of Electronic Packaging, Vol.123, pp. 379-387

Shah, K.R., Mello, M., 2004. Ball Grid Array Solder Joint Failure Envelope Development for Dynamic Loading, Proceeding of 54th Electronic Components and Technology Conference, pp. 1067-1074.

Shakya, S., Heinrich, S.M., Lee, P.S., 2004. An Improved Analytical Model for Time-Dependent Shearing Deformation in Area-Array Interconnects, Journal of Electronic Packaging, Vol. 126, pp.74-81

Sharif, A. and Chan, Y.C., 2005. Comparative Study of Interfacial Reactions of Sn-Ag-Cu and Sn-Ag Solders on Cu Pads during Reflow Soldering, Journal of Electronic Materials, Vol. 34, No.1, pp.46-52

Shetty, S. and Reinikainen, T., 2003. Three- and Four-Point Bend Testing for Electronic Packages, Journal of Electronic Packaging, Vol.125, pp.556-561

Shi, X.Q., Pang, H.L.J., Zhang, X.R., 2004. Investigation of Long-term Reliability and Failure Mechanism of Solder Interconnections with Multifunctional Micro-moiré Interferometry System, Microelectronics Reliability, Vol.44, pp.841-852

Shi, X.Q., Wang, Z.P., Zhou, W., Pang, H.L.J., Yang, Q.J., 2002. A New creep Constitutive Model for Eutectic Solder Alloy, Journal of Electronic Packaging, Vol.124, pp. 85-90

Shim, v.P.W., Liu, J.F., Lee, V.S., 2006. A Technique for Dynamic Tensile Testing of

Human Cervical Spine Ligaments, Experimental Mechanics, Vol.46, pp.77-89

Shohji, I., Mori, h., Orii, Y., 2004. Solder Joint reliability Evaluation of Chip Scale Package Using a Modified Coffin-Manson Equation, Microelectronics Reliability, Vol.44, pp.269-274

Siviour, C.R., Walley, S.M., Proud, W.G., Field, J.E., 2005. Mechanical Properties of SnPb and lead-free solders at high rates of strain, Journal of Physics D: Applied Physics, Vol.38, pp.4131-4139

Spraul, M., Nüchter, W., Möller, A., Wunderle, b., Michel, B., 2007. Reliability of SnPb and Pb-free flip-chips under Different Test conditions, Microelectronics Reliability, Vol.47, pp.252-258

Steenberge, N.V., Limaye, P., Willems, G., vandevelde, B., Schildermans, I., 2007. analytical and finite Element Models of the Thermal Behavior for Lead-free Soldering Processes in Electronic Assembly, Microelectronics Reliability, Vol.47, pp.215-222

Stepniak, F., 2002. Failure Criteria of Flip Chip Joints During Accelerated Testing, Microelectronics Reliability, Vol.42, pp.1921-1930

Stolkarts, V., Keer, L.M., Fine, M.E., 2001. Constitutive and Cyclic Damage Model of 63Sn-37Pb Solder, Journal of Electronic Packaging, Vol.123, pp. 351-355

Strauss, R., 1994. Surface Mount Technology, Butterworth-Heinemann Ltd, ISBN 0-7506-1862-0

Su, B., Lee, Y.C., Dunn, M.L., Die cracking at Solder (In60-Pb40) Joints on Brittle (GaAs) Chips: Fracture Correlation Using Critical Bimaterial Interface Corner Stress Intensities, Journal of Electronic Packaging, Vol.125, pp. 369-377

Suhir, E., (Dec. 1992), Nonlinear Dynamic Response of a Printed Circuit Board to Shock Loads Applied to its Support Contour, Transactions of the ASME, Vol.114, pp.368-377.

Suganuma KI, 2004. Lead-free Soldering in Electronics, Marcel Dekker, Inc. New York. Basel, ISBN 0-8247-4102-1

Suhir, E., 2002. Could Shock Tests Adequately Mimic Drop Test Condition?, Journal of Electronic Packaging, Vol.124, pp. 170-177

Sundelin, J.J., Nurmi, T., Lepistö, T.K., Ristolainten, E.O., 2006. Microstructure, Creep Properties and Failure Mechanism of SnAgCu Solder Joints, Journal of Electronic Materials, Vol.35, No.7, pp.1600-1606

Tan, L.B., Tan, V.B.C., Zhang, X.W., Lim, C.T., 2006. Joint Failure Prediction of BGAs via Failure Force Mapping, 2006 Electronics Packaging Technology Conference, pp.1-9

Tan, L.B., Zhang, X.W., Lim, C.T., Tan, V.B.C., 2009. Mapping the Failure Envelope of Board-level Solder Joints, Microelectronics Reliability, Vol.49, pp.397-409

Tan, V.B.C., Tong, M.X., Lim, K.M., Lim, C.T., Sep. 2005. Finite Element Modeling of Electronic Packages Subjected to Drop Impact, IEEE Transactions on Components and Packaging Technologies, Vol.28, No.3, pp. 555-560

Tang, H., Basaran, C., 2003. A Damage Mechanics-Based fatigue Life Prediction Model for Solder Joints, Journal of Electronic Packaging, Vol.125, pp. 120-125

Tay, A.A.O., 2005. Modeling of Interfacial Delamination in Plastic IC Packages under Hygrothermal Loading, Journal of Electronic Packaging, Vol.127, pp.268-275

Tropea, P., Mellal, A., botsis, J., 2003. Deformation and Damage of a Solder-Copper Joint, Microelectronics Reliability, Vol.43, pp.1791-1796

Tee, T.Y., Ng, H.S., Lim, C.T., Pek, E., Zhong, Z.W., 2004. Impact Life Prediction Modeling of TFBGA Packages under Board Level Drop Test, Microelectronics Reliability, Vol.44, pp.1131-1142

Tee, T.Y., Ng, H.S., Yap, d., Baraton, X., Zhong Z.W., 2003. Board Level Solder Joint Reliability Modeling and Testing of TFBGA Packages for Telecommunication Applications, Microelectronics Reliability, Vol.43, pp.1117-1123

Tee, T.Y., Ng, H.S., Yap, D., Zhong Z.W., 2003, Comprehensive board-level Solder

Joint Reliability Modeling and Testing of QFN and PowerQFN packages, Microelectronics Reliability, Vol.43, pp.1329-1338

Tee, T.Y., Kho, C.L., Yap, D., Toh, E., Baraton, X., Zhong, Z., 2003. Reliability Assessment and Hygroswelling Modeling of FCBGA with No-flow Underfill, Microelectronics Reliability, Vol.43, pp.741-749

Tee, T.Y. and Zhong, Z.W., 2004. Board Level Solder Joint Reliability Analysis and Optimization of Pyramidal Stacked Die BGA Packages, Microelectronics Reliability, Vol.44, pp.1957-1965

Towashiraporn, P., Subbarayan, G., McIlvanie, B., Hunter, B.C., Love, D., Sullivan, B., 2004. The Effect of Model Building on the Accuracy of Fatigue Life Predictions in Electronic Packages, Microelectronics Reliability, Vol.44, pp.115-127

Tsai, M.Y., chen, C.H., Lin, C.S., 2006. Test Methods for Silicon Die Strength, Journal of Electronic Packaging, Vol.128, pp.419-426

Vandevelde, B., Beyne, E., Zhang, K., Caers, J., vandepitte, D., Baelmants, M., 2003. Parameterized Modeling of Thermomechanical Reliability for CSP Assemblies, Journal of Electronic Packaging, Vol.125, pp. 498-505

Vandevelde, B., Degryse, D., Beyne, E., Roose, E., Corlatan, D., Swaelen, G., Willems, G., Christiaens, F., Bell, A., Vandepitte, D., Baelmans, M., 2003. Modified Micro-macro Thermo-mechanical Modeling of Ceramic ball Grid Array Packages, Microelectronics Reliability, Vol.43, pp.307-318

Vandevelde, B., Gonzalez, M., Limaye, P., Ratchev, P., Beyne, E., 2007. Thermal cycling Reliability of SnAgCu and SnPb Solder Joints: A Comparison for Several IC-packages, Microelectronics Reliability, Vol.47, pp.259-265

Varghese, J. and Dasgupta, A., 2007. Test Methodology for durability Estimation of surface Mount Interconnects under Drop Testing Conditions, Microelectronics Reliability, Vol.47, pp.93-103

Variyam, M., Chiu, T.C., Sundararaman, V., Edwards, D., 2003. Effect of Package and Board Characteristics on Solder Joint Reliability of Microstar BGA, Electronic

Components and Technology Conference, pp. 583-588.

Vianco, P.T., Rejent, J.A., Hlava, P.F., 2004. Solid-state Intermetallic compound Layer Growth Between copper and 95.5Sn-3.9Ag-0.6Cu Solder, Journal of Electronic Materials, Vol.33, No.9, pp.991-1004

Wang, F.J., Gao, F., Ma, X., Qian, Y.Y., 2006. Depressing Effect of 0.2wt.%zn Addition into Sn-3.0Ag-0.5cu Solder Alloy on the Intermetallic growth with Cu Substrate during Isothermal Aging, Journal of Electronic Materials, Vol.35, No.10, pp.1818-1824

Wang, D. and Panton, R.L., 2006. Experimental study of void formation in Eutectic and Lead-Free Solder bumps of flip-Chip Assemblies, Journal of Electronic Packaging, Vol.128, pp.202-207

Wang, J., 2002. Underfill of Flip Chip on Organic Substrate: Viscosity, Surface Tension, and Contact Angle, Microelectronics Reliability, Vol. 42, pp.293-299

Wang, J., Lim, H.K., Lew, H.S., Saw, W.T., Tan, C.H., 2004. A Testing Method for Assessing Solder Joint Reliability of FCBGA Packages, Microelectronics Reliability, Vol.44, pp.833-840

Wang, Y.Q., Low, K.H., Pang, H.L.J., Hoon, K.H., che, F.X., Yong, Y.S., 2006. Modeling and Simulaiton for a Drop-impact Analysis of Multi-layered Printed Circuit Boards, Microelectronics Reliability, Vol.46, pp.558-573

Wang, D., and Panton, R.L., 2005. Experimental Study of void Formation in High-Lead Solder Joints of Flip-Chip Assemblies, Journal of Electronic Packaging, Vol.127, pp.120-126

Wang, B. and Yi, S. 2002. Dynamic Plastic Behavior of 63 wt% Sn 37 wt% Pb Eutectic Solder under High Strain Rates, Journal of Materials Science Letters, 21, pp.697-698

Wang, H.F., Zhao, M., Guo, Q., 2004. Vibration Fatigue Experiments of SMT Solder Joint, Microelectronics Reliability, Vol.44, pp.1143-1156

Wang, L.L., Labibes, K., Azari, Z., Pluvinage, G., 1994. Generalization of Split Hopkinson Bar technique to use viscoelastc Bars, Int. J. Impact Engng, 15(5), pp.669-686

Wei, Y., Chow, C.L., Lau, K.J., vianco, P., Fang, H.E., 2004. Behavior of Lead-Free Solder Under Thermomechanical Loading, Journal of Electronic Packaging, Vol. 126, pp.367-373

Wiese, S. and Meusel, E., 2003. Characterization of Lead-free Solders in Flip Chip Joints, Journal of Electronic Packaging, Vol.125, pp.531-538

Wiese, S. and Rzepka, S., 2004. Time-independent Elastic-plastic Behavior of Solder Materials, Microelectronics Reliability, Vol.44, pp.1893-1900

Wiese, S. and Wolter, K.J., 2004. Microstructure and Creep Behavior of Eutectic SnAg and SnAgCu Solders, Microelectronics Reliability, Vol.44, pp.1923-1931

Wiese, S. and Wolter, K.J., 2007. Creep of Thermally Aged SnAgCu-solder Joints, Microelectronics Reliability, Vol.47, pp.223-232

Williamson, D.M., Field, J.E., Palmer, S.J.P., Siviour, C.R., 2007. Rate dependent strengths of some solder joints, Journal of Physics D: Applied Physics Vol.40, pp.4691–470

Wong, E.H., 2005. Dynamics of board-Level Drop Impact, Journal of Electronic Packaging, Vol.127, pp.200-207

Wong, E.H., Lim, K.M., Lee, N., Seah S., et al., (2002), Drop impact test-mechanics & physical, Proceeding of Electronics Packaging Technology Conference, pp.327-333.

Wong, E.H., Mai, Y.W., Seah, S.K.W., 2005. Board Level Drop Impact – Fundamental and Parametric Analysis, Journal of Electronic Packaging, Vol.127, pp.496-502

Wu, C.M.L., Li, R.K.Y., Yeung, N.H., 2002. Impact Resistance of SM Joints formed with ICA, Journal of Electronic Packaging, Vol.124, pp. 374-378

Wu, J.D., Ho, S.H., Huang, C.Y., Liao, C.C., Zheng, P.J., Hung, S.C., 2002. Board Level Reliability of a Stacked CSP Subjected to Cyclic Bending, Microelectronics Reliability, Vol. 42, pp.407-416

Wu, J.D., Huang, C.Y., Liao, C.C., 2003. Fracture Strength Characterization and Failure analysis of Silicon Dies, Microelectronics Reliability, Vol.43, pp.269-277

Xiao, Q. and Armstrong, W.D., 2005. Tensile Creep and Microstructural Characterization of bulk Sn3.9ag0.6Cu Lead-free Solder, Journal of Electronic Materials, Vol. 34, No.2, pp.196-211

Xiao, Q., Bailey, H.J., Armstrong, W.D., 2004. Aging Effects on Microstructure and tensile Property of Sn3.9Ag0.6Cu Solder Alloy, Journal of Electronic Packaging, Vol. 126, pp.208-212

Xie, H., Asundi, A., Boay, C.G., Lu, Y., Yu, J., Zhong, Z., Ngoi., B.K.A., 2002. High Resolution AFM Scanning Moiré Method and its Application to the Micro-deformation in the BGA Electronic Package, Microelectronics Reliability, Vol.42, pp. 1219-1227

Xu, L. and Pang, J.H.L., 2006. Nanoindentation on SnAgCu Lead-Free Solder Joints and Analysis, Journal of Electronic Materials, Vol.35, No.12, pp.2107-2115

Xu, L., Pang, J.H.L., Ren, F., Tu, K.N., 2006. Electromigration Effect on Intermetallic Growth and Young's Modulus in SAC Solder Joint, Journal of Electronic Materials, Vol.35, No.12, pp.2116-2125

Xu, B., Cai, X., Huang, W., Cheng, Z., 2004. Research of Underfill Delamination in Flip Chip by the J-Integral Method, Journal of Electronic Packaging, Vol. 126, pp.94-99

Yang, S.Y., Jeon, Y.D., Lee, S.B., Paik, K.W., 2006. Solder Reflow Process Induced Residual Warpage Measurement and its Influence on Reliability of flip-Chip Electronic Packages, Microelectronics Reliability, Vol.46, pp.512-522

Yang, D.G., Liang, J.S., Li, Q.Y., Ernst, L.J., Zhang, G.Q., 2004. Parametric Study on flip chip package with Lead-free solder Joints by using the Probabilistic Designing

Approach, Microelectronics Reliability, Vol.44, pp.1947-1955

Yang, x.J., Luo, Y., Gao, Q., 2007. Constitutive Modeling on Time-Dependent Deformation Behavior of 96.5Sn-3.5Ag solder Alloy Under Cyclic Multiaxial Straining, Journal of Electronic Packaging, Vol. 129, pp.41-47

Yao, Q., Qu, J., 2002. Interfacial Versus Cohesive Failure on Polymer-Metal Interfaces in Electronic Packaging – Effects of Interface Roughness, Journal of Electronic Packaging, Vol.124, pp. 127-134

Ye, H., Hopkins, D.C., Basaran, C., 2003. Measurement of High Electrical Current Density Effects in Solder Joints, Microelectronics Reliability, Vol.43, pp.2021-2029

Yeh, C.L. and Lai, Y.S., 2006. Transient Fracturing of Solder Joints Subjected to Displacement-controlled Impact Loads, Microelectronics Reliability, Vol.46, pp.885-895

Yeh, C.L., Lai, Y.S., Kao, C.L., 2006. Evaluation of board-level reliability of Electronic Packages under consecutive Drops, Microelectronics Reliability, Vol.46, pp.1172-1182

Yeh, C.L. and Lai, Y.S., 2007. Design Guideline for ball Impact Test Apparatus, Journal of Electronic Packaging, Vol. 129, pp.98-104

Yi, S., Luo, G., Chian, K.S., 2002. A Viscoplastic Constitutive Model for 63Sn37Pb Eutectic Solder, Journal of Electronic Packaging, Vol.124, pp. 91-96

Yunus, M., Srihari, K., Pitarresi, J.M., Primavera, A., 2003. Effect of Voids on the Reliability of BGA/CSP Solder Joints, Microelectronics Reliability, Vol.43, pp.2077-2086

Zhang, L., Arora, v., Nguyen, L., Kelkar, N., 2004. Numerical and Experimental Analysis of Large Passivation Opening for Solder Joint reliability Improvement of Micro SMD Packages, Microelectronics Reliability, Vol.44, pp.533-541

Zhang, Q., Dasgupta, A., Haswell, P., 2005. Isothermal Mechanical Durability of Three Selected PB-Free Solders; Sn3.9Ag0.6Cu, Sn3.5Ag, and Sn0.7Cu, Journal of

Electronic Packaging, Vol.127, pp.512-522

Zhang, Q., Dasgupta, A., Nelson, D., Pallavicini, H., 2005. Systematic Study on Thermo-Mechanical Durability of Pb-free Assemblies: Experiments and FE Analysis, Journal of Electronic Packaging, Vol.127, pp.415-429

Zheng, P.J., Lee, J.Z., Liu, K.H., Wu, J.D., Hung, S.C., 2003. Solder Joint Reliability of TFBGA Assemblies with Fresh and Reworked Solder balls, Microelectronics Reliability, Vol.43, pp.925-934

APPENDIX A TABLES OF MECHANICAL PROPERTIES OF SINGLE SOLDER JOINT SPECIMENS

Table A-1 Initial stiffness and load/deformation values at failure for tests at deformation rate of 0.00015mm/s

Test mode	Incline angle α (degree)	Initial stiffness (N/mm)	Deformation at failure (mm)	Load at failure (N)		
				Resultant	Normal	Shear
Tension (0.00015 mm/s)	0	1153.4	0.005500	4.717	4.717	0.000
		1034.7	0.005499	4.279	4.279	0.000
		1087.0	0.005125	4.341	4.341	0.000
		930.0	0.006000	4.138	4.138	0.000
	15	1082.2	0.004625	3.658	3.534	0.947
		1179.6	0.004125	3.895	3.762	1.008
		786.0	0.006500	3.851	3.719	0.997
		673.4	0.006000	2.851	2.754	0.738
	30	941.4	0.004750	2.645	2.291	1.322
		888.0	0.005125	2.481	2.149	1.240
		853.6	0.005625	3.138	2.718	1.569
	45	455.4	0.009000	2.585	1.828	1.828
		457.7	0.007000	2.316	1.638	1.638
		729.6	0.004875	2.492	1.762	1.762
		564.2	0.005375	2.060	1.456	1.456
		760.3	0.005000	2.518	1.780	1.780
	60	556.6	0.007000	2.569	1.284	2.225
		539.6	0.005625	2.146	1.073	1.858
		718.9	0.005500	2.448	1.224	2.120
		598.6	0.006250	2.498	1.249	2.163
	75	651.4	0.005500	2.093	0.542	2.022
		668.1	0.005375	1.918	0.496	1.852
		607.8	0.007000	2.290	0.593	2.212
		519.8	0.005375	1.910	0.494	1.845
Shear 0.00015mm/s	90	154.6	0.011000	1.672	0.000	1.672
		421.4	0.007875	2.408	0.000	2.408
		334.2	0.011500	2.373	0.000	2.373

Compression (0.00015 mm/s)	75	466.3	0.008125	2.637	-0.683	2.547
		550.0	0.008375	2.532	-0.655	2.446
		516.7	0.013500	2.837	-0.734	2.740
		267.0	0.014250	2.703	-0.700	2.611
		341.7	0.011750	2.558	-0.662	2.471
	60	603.3	0.008500	3.550	-1.775	3.075
		272.9	0.018380	3.321	-1.661	2.876
		476.8	0.020130	3.385	-1.693	2.932
		414.7	0.012370	3.907	-1.954	3.384
		661.4	0.012500	4.140	-2.070	3.585
	45	710.8	0.009875	4.504	-3.185	3.185
		662.3	0.011130	4.643	-3.283	3.283
		321.4	0.020130	4.370	-3.090	3.090
		474.6	0.013500	4.565	-3.228	3.228
		628.6	0.008750	4.124	-2.916	2.916
	30	740.2	0.011130	6.110	-5.291	3.055
		673.1	0.012880	5.948	-5.151	2.974
		830.0	0.010880	5.648	-4.891	2.824
		801.4	0.010000	6.240	-5.404	3.120
		713.0	0.013250	6.149	-5.325	3.074
	15	543.5	0.013500	6.670	-6.443	1.726
		946.0	0.009750	6.947	-6.710	1.798
		1005.3	0.007870	6.467	-6.247	1.674
	0	978.3	0.010250	6.751	-6.751	0.000
		1008.2	0.010500	6.925	-6.925	0.000
		769.3	0.017750	7.077	-7.077	0.000
		930.5	0.011000	7.378	-7.378	0.000

Table A-2 Initial stiffness and load/deformation values at failure for tests at deformation rate of 0.15mm/s

Test mode	Incline angle α (degree)	Initial stiffness (N/mm)	Deformation at failure (mm)	Load at failure (N)		
				Resultant	Normal	Shear
Tension (0.15 mm/s)	0	750.4	0.006750	2.940	2.940	0.000
		949.5	0.006875	3.800	3.800	0.000
		863.8	0.006750	3.125	3.125	0.000
		1003.2	0.006999	4.130	4.130	0.000
	15	703.9	0.007625	2.942	2.842	0.761
		689.9	0.007250	2.762	2.668	0.715
		890.7	0.008000	3.455	3.337	0.894
		637.5	0.007250	2.693	2.601	0.697
		690.0	0.007875	3.145	3.038	0.814
	30	479.5	0.007750	2.134	1.848	1.067
		532.4	0.006750	2.109	1.827	1.055
		489.2	0.008250	2.290	1.983	1.145
		566.2	0.008625	2.906	2.517	1.453
		545.2	0.007250	2.303	1.994	1.151
	45	589.8	0.007750	2.722	1.925	1.925
		558.4	0.007750	2.510	1.774	1.774
		502.8	0.009125	2.867	2.027	2.027
		432.6	0.008125	2.232	1.579	1.579
		570.7	0.009125	3.181	2.250	2.250
	60	492.8	0.009625	2.819	1.410	2.442
		448.3	0.010130	2.962	1.481	2.565
		398.0	0.011250	2.762	1.381	2.392
		410.4	0.010380	2.670	1.335	2.312
		516.2	0.008875	2.730	1.365	2.365
	75	453.3	0.012250	3.271	0.847	3.160
		496.3	0.011130	3.361	0.870	3.246
		454.3	0.010630	3.036	0.786	2.933
		487.9	0.010630	3.120	0.807	3.013
Shear (0.15 mm/s)	90	433.9	0.011500	2.964	0.000	2.964
		572.9	0.010750	3.755	0.000	3.755
		283.9	0.011500	2.082	0.000	2.082
		356.1	0.010990	2.595	0.000	2.595

Compression (0.15 mm/s)	75	445.2	0.011380	3.933	-1.018	3.799
		290.5	0.017000	3.714	-0.961	3.588
		374.6	0.014250	3.840	-0.994	3.709
	60	424.6	0.018250	5.341	-2.670	4.625
		421.6	0.015880	4.817	-2.408	4.171
		374.2	0.017250	4.375	-2.188	3.789
		159.5	0.031630	4.705	-2.352	4.074
	45	372.1	0.020800	6.100	-4.313	4.313
		288.8	0.025500	5.380	-3.804	3.804
		443.5	0.018800	6.310	-4.462	4.462
		677.0	0.012200	6.360	-4.497	4.497
		386.4	0.025000	6.320	-4.469	4.469
		391.7	0.028000	5.230	-3.698	3.698
	30	485.5	0.019000	7.270	-6.296	3.635
		491.1	0.015000	5.850	-5.066	2.925
		628.0	0.013500	6.050	-5.239	3.025
		553.2	0.017000	7.690	-6.660	3.845
		675.9	0.014700	7.570	-6.556	3.785
	15	910.6	0.012000	8.130	-7.853	2.104
		950.7	0.011300	7.870	-7.602	2.037
		828.7	0.012300	7.580	-7.322	1.962
		657.0	0.015800	7.610	-7.351	1.970
	0	641.3	0.016100	7.850	-7.850	0.000
		708.2	0.015100	8.326	-8.326	0.000
		796.3	0.013600	7.850	-7.850	0.000
		458.3	0.020600	7.650	-7.650	0.000
		911.7	0.013000	8.670	-8.670	0.000

Table A-3 Initial stiffness and load/deformation values at failure for tests at impact speed around 0.3m/s

Test mode	Incline angle α	Initial stiffness	Deformation at failure	Load at failure (N)		
	(degree)	(N/mm)	(mm)	Resultant	Normal	Shear
Tension (62 mm/s)	0	2982.5	0.002810	6.188	6.188	0.000
		4547.2	0.002190	6.915	6.915	0.000
		3625.7	0.002640	6.644	6.644	0.000
		8213.6	0.001820	6.577	6.577	0.000
		6418.3	0.001680	5.682	5.682	0.000
		4634.1	0.001910	5.562	5.562	0.000
	15	6304.1	0.001700	5.949	5.746	1.540
		4889.8	0.001750	5.146	4.971	1.332
		4313.9	0.001970	5.396	5.212	1.397
		4138.9	0.001990	4.875	4.709	1.262
		7350.2	0.001410	6.650	6.423	1.721
		3652.1	0.002080	5.220	5.042	1.351
	30	4572.4	0.001670	4.810	4.165	2.405
		8899.8	0.001310	5.063	4.385	2.532
		8444.7	0.001210	4.924	4.264	2.462
		4935.9	0.001880	5.464	4.732	2.732
		4974.9	0.001420	4.640	4.018	2.320
	45	3389.8	0.001600	3.504	2.478	2.478
		4367.3	0.001470	4.320	3.055	3.055
		5467.4	0.001500	4.526	3.201	3.201
		4099.4	0.001460	4.180	2.956	2.956
	60	2236.8	0.001880	2.536	1.268	2.196
		8636.8	0.007350	2.600	1.300	2.252
		3266.5	0.001810	2.987	1.493	2.587
		5491.0	0.001340	3.006	1.503	2.603
		3660.0	0.001080	2.170	1.085	1.879
		3232.9	0.001720	2.938	1.469	2.545
	75	3373.2	0.002030	2.442	0.632	2.358
		4279.9	0.002290	3.012	0.780	2.909
		2100.0	0.001980	2.065	0.534	1.995
		2772.0	0.001890	1.987	0.514	1.919

Shear (62 mm/s)	90	1675.9	0.002960	3.206	0.000	3.206
		1388.2	0.003850	3.924	0.000	3.924
		1833.9	0.003680	4.451	0.000	4.451
		1504.9	0.004420	3.879	0.000	3.879
Compression (233 mm/s)	75	1152.0	0.005750	6.410	-1.659	6.192
		1888.4	0.004850	5.800	-1.501	5.602
		2257.3	0.003910	5.750	-1.488	5.554
		1871.0	0.003540	5.090	-1.317	4.917
		1524.8	0.004070	5.650	-1.462	5.457
	60	913.8	0.015600	6.390	-3.195	5.534
		1090.1	0.016400	5.490	-2.745	4.754
		2340.9	0.007440	7.560	-3.780	6.547
		1194.9	0.007180	6.511	-3.256	5.639
		2076.6	0.005340	8.300	-4.150	7.188
	45	712.0	0.001770	9.200	-6.505	6.505
		8097.3	0.002350	7.860	-5.558	5.558
		1089.3	0.009210	9.480	-6.703	6.703
		193.3	0.042600	8.110	-5.735	5.735
	30	3668.4	0.003740	11.900	-10.306	5.950
		1009.1	0.007870	9.530	-8.253	4.765
		2401.9	0.005750	12.000	-10.392	6.000
	15	2300.4	0.005840	12.300	-11.881	3.183
		2783.6	0.004010	10.100	-9.756	2.614
		3602.9	0.004070	12.700	-12.267	3.287
	0	7462.9	0.005630	13.590	-13.590	0.000
		4338.0	0.007900	14.650	-14.650	0.000
		3948.1	0.005190	10.100	-10.100	0.000
		4362.0	0.006670	12.490	-12.490	0.000
		3238.1	0.005770	11.050	-11.050	0.000

Table A-4 Initial stiffness and load/deformation values at failure for tests at impact speed around 3m/s

Test mode	Angle α	Initial stiffness	Deformation of linearity limit	Load of linearity limit (N)		
	(degree)	(N/mm)	(mm)	Resultant	Normal	Shear
Tension (277 mm/s)	0	4225.6	0.001740	6.450	6.450	0.000
		4339.7	0.001550	5.889	5.889	0.000
		4839.4	0.001610	6.224	6.224	0.000
	30	2950.4	0.001730	4.212	3.648	2.106
		4111.6	0.001480	5.030	4.356	2.515
		3787.1	0.002110	4.548	3.938	2.274
		4141.8	0.001250	4.270	3.698	2.135
		3654.4	0.001810	4.020	3.481	2.010
	60	1630.8	0.003730	3.827	1.913	3.314
		2113.2	0.003100	3.450	1.725	2.988
		2633.9	0.003740	3.851	1.925	3.335
		3884.5	0.002140	3.298	1.649	2.856
		5822.1	0.001030	3.070	1.535	2.659
Shear (277 mm/s)	90	5274.9	0.001750	4.688	0.000	4.688
		3341.7	0.001830	4.170	0.000	4.170
		3245.0	0.001570	3.550	0.000	3.550
		2921.7	0.001820	4.140	0.000	4.140
		1679.3	0.006100	5.420	0.000	5.420
Compression (1385 mm/s)	60	828.5	0.011500	13.400	-6.700	11.605
		896.0	0.014800	14.980	-7.490	12.973
		1011.0	0.010100	13.370	-6.685	11.579
	45	1349.2	0.014700	22.680	-16.037	16.037
		2019.2	0.007830	19.200	-13.576	13.576
		2045.9	0.006880	17.960	-12.700	12.700
		1844.4	0.006440	15.740	-11.130	11.130
	30	2626.5	0.007320	22.618	-19.588	11.309
		1663.1	0.011000	21.710	-18.801	10.855
		1959.9	0.011400	23.960	-20.750	11.980
		2213.5	0.007330	20.560	-17.805	10.280
	15	2389.8	0.009540	25.120	-24.264	6.502

		2291.9	0.009660	23.700	-22.892	6.134
		2529.0	0.009020	25.200	-24.341	6.522
		3267.3	0.006420	23.800	-22.989	6.160
	0	10481.3	0.002690	22.600	-22.600	0.000
		6472.6	0.008720	27.080	-27.080	0.000
		8050.3	0.003580	24.300	-24.300	0.000
		6547.1	0.007700	28.880	-28.880	0.000

Table A-5 Average and standard deviations of initial stiffness and load/deformation at failure for single solder joint specimens subjected to quasi-static and dynamic loading at different incline angles

Test mode	Incline angle α		Initial stiffness	Deformation at failure	Load at failure (N)		
	(degree)		(N/mm)	(mm)	Resultant	Normal	Shear
Tension (0.00015 mm/s)	0	Avg	1051.3	0.005531	4.369	4.369	0.000
		Stdev	*94.3*	*0.000359*	*0.247*	*0.247*	*0.000*
	15	Avg	930.3	0.005313	3.564	3.442	0.922
		Stdev	*239.5*	*0.001120*	*0.486*	*0.469*	*0.126*
	30	Avg	894.3	0.005167	2.755	2.386	1.377
		Stdev	*44.2*	*0.000439*	*0.342*	*0.296*	*0.171*
	45	Avg	593.4	0.006250	2.394	1.693	1.693
		Stdev	*145.6*	*0.001757*	*0.212*	*0.150*	*0.150*
	60	Avg	603.4	0.006094	2.415	1.208	2.091
		Stdev	*80.9*	*0.000688*	*0.186*	*0.093*	*0.161*
	75	Avg	611.8	0.005813	2.053	0.531	1.983
		Stdev	*66.4*	*0.000794*	*0.179*	*0.046*	*0.173*
Shear	90	Avg	303.4	0.010125	2.151	0.000	2.151
		Stdev	*136.1*	*0.001965*	*0.415*	*0.000*	*0.415*
Compression (0.00015 mm/s)	75	Avg	428.3	0.011200	2.653	-0.687	2.563
		Stdev	*120.0*	*0.002843*	*0.123*	*0.032*	*0.118*
	60	Avg	485.8	0.014376	3.661	-1.830	3.170
		Stdev	*154.2*	*0.004775*	*0.351*	*0.176*	*0.304*
	45	Avg	559.5	0.012677	4.441	-3.140	3.140
		Stdev	*159.8*	*0.004525*	*0.204*	*0.144*	*0.144*
	30	Avg	751.5	0.011628	6.019	-5.212	3.009
		Stdev	*64.0*	*0.001383*	*0.233*	*0.201*	*0.116*
	15	Avg	831.6	0.010373	6.695	-6.467	1.733
		Stdev	*251.3*	*0.002866*	*0.241*	*0.233*	*0.062*
	0	Avg	921.6	0.012375	7.033	-7.033	0.000
		Stdev	*106.5*	*0.003597*	*0.266*	*0.266*	*0.000*

Test mode	Incline angle α		Initial stiffness	Deformation at failure	Load at failure (N)		
	(degree)		(N/mm)	(mm)	Resultant	Normal	Shear
Tension (0.15 mm/s)	0	Avg	891.7	0.006844	3.499	3.499	0.000
		Stdev	*110.3*	*0.000119*	*0.560*	*0.560*	*0.000*
	15	Avg	739.4	0.007500	2.970	2.869	0.769
		Stdev	*133.6*	*0.000433*	*0.422*	*0.407*	*0.109*
	30	Avg	522.5	0.007725	2.348	2.034	1.174
		Stdev	*37.0*	*0.000752*	*0.324*	*0.281*	*0.162*
	45	Avg	530.8	0.008375	2.703	1.911	1.911
		Stdev	*63.8*	*0.000702*	*0.359*	*0.254*	*0.254*

	60	Avg	453.1	0.010052	2.789	1.394	2.415
		Stdev	*51.1*	*0.000883*	*0.111*	*0.055*	*0.096*
	75	Avg	473.0	0.011160	3.197	0.827	3.088
		Stdev	*22.4*	*0.000764*	*0.146*	*0.038*	*0.141*
Shear	90	Avg	411.7	0.011185	2.849	0.000	2.849
		Stdev	*123.7*	*0.000377*	*0.704*	*0.000*	*0.704*
Compression (0.15 mm/s)	75	Avg	370.1	0.014210	3.829	-0.991	3.699
		Stdev	*77.5*	*0.002810*	*0.110*	*0.028*	*0.106*
	60	Avg	345.0	0.020753	4.809	-2.405	4.165
		Stdev	*125.8*	*0.007316*	*0.401*	*0.200*	*0.347*
	45	Avg	426.6	0.021717	5.950	-4.207	4.207
		Stdev	*132.5*	*0.005736*	*0.510*	*0.361*	*0.361*
	30	Avg	566.7	0.015840	6.886	-5.963	3.443
		Stdev	*83.9*	*0.002169*	*0.871*	*0.754*	*0.435*
	15	Avg	836.8	0.012850	7.798	-7.532	2.018
		Stdev	*130.1*	*0.002011*	*0.257*	*0.248*	*0.067*
	0	Avg	703.1	0.015680	8.069	-8.069	0.000
		Stdev	*170.3*	*0.003009*	*0.418*	*0.418*	*0.000*

Test mode	**Incline angle α**		**Initial stiffness**	**Deformation at failure**	**Load at failure (N)**		
	(degree)		**(N/mm)**	**(mm)**	**Resultant**	**Normal**	**Shear**
Tension (62 mm/s)	0	Avg	5070.2	0.002175	6.161	6.161	0.000
		Stdev	*1929.1*	*0.000461*	*0.548*	*0.548*	*0.000*
	15	Avg	5108.2	0.001817	5.539	5.351	1.434
		Stdev	*1427.9*	*0.000248*	*0.651*	*0.629*	*0.169*
	30	Avg	6365.5	0.001498	4.980	4.313	2.490
		Stdev	*2117.7*	*0.000274*	*0.312*	*0.270*	*0.156*
	45	Avg	4331.0	0.001508	4.133	2.922	2.922
		Stdev	*862.6*	*0.000064*	*0.442*	*0.313*	*0.313*
	60	Avg	4420.7	0.002530	2.706	1.353	2.344
		Stdev	*2324.3*	*0.002381*	*0.332*	*0.166*	*0.287*
	75	Avg	3131.2	0.002048	2.376	0.615	2.295
		Stdev	*925.6*	*0.000172*	*0.468*	*0.121*	*0.452*
Shear	90	Avg	1600.7	0.003728	3.865	0.000	3.865
		Stdev	*195.2*	*0.000602*	*0.510*	*0.000*	*0.510*
Compression (233 mm/s)	75	Avg	1738.7	0.004424	5.740	-1.486	5.544
		Stdev	*418.0*	*0.000882*	*0.470*	*0.122*	*0.454*
	60	Avg	1523.3	0.010392	6.850	-3.425	5.932
		Stdev	*640.6*	*0.005191*	*1.093*	*0.547*	*0.947*
	45	Avg	2523.0	0.013983	8.663	-6.125	6.125
		Stdev	*3734.3*	*0.019375*	*0.797*	*0.564*	*0.564*
	30	Avg	2359.8	0.005787	11.143	-9.650	5.572
		Stdev	*1330.2*	*0.002065*	*1.398*	*1.211*	*0.699*
	15	Avg	2895.6	0.004640	11.700	-11.301	3.028
		Stdev	*658.4*	*0.001040*	*1.400*	*1.352*	*0.362*
	0	Avg	4669.8	0.006232	12.376	-12.376	0.000
		Stdev	*1626.1*	*0.001077*	*1.844*	*1.844*	*0.000*

Test mode	Incline angle α		Initial stiffness	Deformation at failure	Load at failure (N)		
	(degree)		(N/mm)	(mm)	Resultant	Normal	Shear
Tension (277 mm/s)	0	Avg	4468.2	0.001633	6.338	6.338	0.000
		Stdev	*326.5*	*0.000097*	*0.283*	*0.283*	*0.000*
	30	Avg	3729.1	0.001676	4.416	3.824	2.208
		Stdev	*482.7*	*0.000328*	*0.392*	*0.339*	*0.196*
	60	Avg	3216.9	0.002748	3.499	1.750	3.030
		Stdev	*1681.3*	*0.001161*	*0.338*	*0.169*	*0.293*
Shear	90	Avg	3292.5	0.002614	4.394	0.000	4.394
		Stdev	*1291.7*	*0.001952*	*0.701*	*0.000*	*0.701*
Compression (1385 mm/s)	60	Avg	911.8	0.012133	13.917	-6.958	12.052
		Stdev	*92.2*	*0.002413*	*0.921*	*0.460*	*0.798*
	45	Avg	1814.7	0.008963	18.895	-13.361	13.361
		Stdev	*322.9*	*0.003869*	*2.901*	*2.051*	*2.051*
	30	Avg	2115.7	0.009263	22.212	-19.236	11.106
		Stdev	*408.1*	*0.002243*	*1.438*	*1.245*	*0.719*
	15	Avg	2619.5	0.008660	24.455	-23.622	6.329
		Stdev	*442.7*	*0.001519*	*0.816*	*0.788*	*0.211*
	0	Avg	7887.8	0.005673	25.715	-25.715	0.000
		Stdev	*1875.5*	*0.002982*	*2.804*	*2.804*	*0.000*

APPENDIX B FORMULATION OF DYNAMIC TESTING METHODOLOGY AND THE MINIATURE IMPACT TESTER

FIELD OF THE INVENTION

This invention relates to the dynamic testing of small specimens to obtain force-displacement and strain-stress responses.

BACKGROUND OF THE INVENTION

To obtain the dynamic mechanical properties of a material, a dynamic mechanical tester is usually employed to apply tension or compression and obtain force-displacement readings. For low speed dynamic tests, measurement devices such as a load cell and LVDT are capable of detecting the mechanical response of a specimen, assuming that the loading duration is sufficiently long to satisfy the frequency response of the system. A commonly used piece of equipment for dynamic testing is the split Hopkinson bar; it is based on one-dimensional stress wave theory, and can be used for high speed impact testing due to its high frequency response. A split Hopkinson bar system comprises three cylindrical bars (a striker and, input/output bars) which are required to be straight and aligned coaxially. For specimens of small cross sectional area, the input/output bars in a split Hopkinson bar system should be thin enough to be compatible to the size of the specimen. However,

it is difficult to ensure the alignment of such thin bars, especially when long bars are required for long loading durations. In addition, flexural waves may be generated in such bars and superpose on the longitudinal waves. An example of a small specimen is a solder joint in a BGA IC package, measuring less than 0.5mm. A review of literature shows that dynamic testing of a solder joint has been undertaken using a load cell to measure the strength; however, the loading speed is limited to ensure the accuracy of load cell readings. This invention proposes an experimental method for dynamic testing of small specimens and the establishment of a miniature impact tester.

OBJECT OF THE INVENTION

The primary objective of this invention is to establish dynamic testing methodology to facilitate measurement of the force-displacement or strain-stress response of small specimens. This invention enables convenient employment of ultra thin bars for high speed testing of small specimens, without the requirement of exact alignment of the entire long bars in the system. It employs the use of a heavy striker to produce a long loading pulse. Based on one-dimensional wave theory, the force-deformation or stress-strain response obtained has accuracy comparable to a split Hopkinson bar system.

The invention comprises a compact launch unit to accommodate the striker, a specimen and the ends of the input and out bars; this is the short region that requires straightness and good alignment compared to that for a split Hopkinson bar system, in which the requirement must be fulfilled throughout.

Therefore, this facilitates the establishment of a portable impact tester for research, laboratory or industrial applications related to dynamic testing of small specimens. Conversion between compressive and tensile loading can be conveniently done through re-positioning of a few components.

Other objects, features and advantages of the present invention will become apparent from the detailed description which follows, or may be learned by practice of the invention.

SUMMARY OF THE INVENTION

1. The invention proposes a new methodology for establishment of an impact tester for dynamic testing of small specimens, based on one-dimensional wave theory. Figure B-1a illustrates the configuration of the mechanism for compressive testing. A specimen is sandwiched between two bars, an impact plate is attached to the end of the input bar and a striker is propelled to impinge on the impact plate to generate dynamic compression on the specimen. One-dimensional wave propagation in the bars and stress equilibrium in the specimen are assumed, as is done for a split Hopkinson bar system. The method of data processing to calculate the stress-strain response from the recorded stain gauge signals differs from that for a split Hopkinson bar system. In this invention, the overall average deformation rate of a specimen, $v_s(t)$, is calculated from the input strain wave $\varepsilon_i(t)$ (recorded by stain gauges on the input bar) and the transmitted strain wave $\varepsilon_t(t)$ (recorded by strain gauges on the output bar),

$$v_s(t) = C_0\left[\varepsilon_i(t) + \varepsilon_t(t)\right] \quad \text{(B-1)}$$

where C_0 is the elastic wave speed in the bars. The overall average force experienced by the specimen, F_s, is derived from the transmitted strain wave $\varepsilon_t(t)$,

$$F_s = AE_0\varepsilon_t(t) \quad \text{(B-2)}$$

where A is the cross-sectional area and E_0 the elastic modulus of the bars. From the deformation rate history of the specimen ($v_s(t)$), the deformation history of the specimen ($d_s(t)$) can be derived,

$$d_s(t) = \int_0^t v_s(t)dt \quad \text{(B-3)}$$

The engineering strain history $\varepsilon_s(t)$ of the specimen is obtained by factoring in the specimen initial length L_s,

$$\varepsilon_s(t) = d_s(t)/L_s \quad \text{(B-4)}$$

The specimen engineering stress history $\sigma_s(t)$ can be calculated by noting of the specimen initial cross-sectional area A_s,

$$\sigma_s(t) = F_s(t)/A_s \quad \text{(B-5)}$$

2. Conversion from a compressive to a tensile configuration is easily effected by just attaching the impact plate to the other bar (or by exchanging the two bars), as illustrated in Fig.B-1b.

3. When the material and cross-sectional area of the striker are the same as that of the input bar, the loading wave generated has a wave length twice the length of the striker.

4. A thick and heavy (larger in cross-sectional area or density) but short striker can be employed to generate long loading wave in the bars (Fig.B-2a and Fig.B-2b); this allows the launch unit to be dimensionally compact, resulting in a small portable impact tester.

5. Strain gauges can be mounted close to the bar-specimen interfaces, as long as the stress waves become uniform across the bar cross-sections at those locations. As waves propagating away from the strain gauges are not used data processing, good coaxial alignment is only required for the striker, impact plate and the bar segments between the strain gauges. This enables very long and thin bars to be used, and exact alignment of the entire bar length is not strictly necessary. Moreover, wave dispersion has minimal influence on the results, compared to a split Hopkinson bar system, because the strain gauges are sited close to the specimen/bar interfaces.

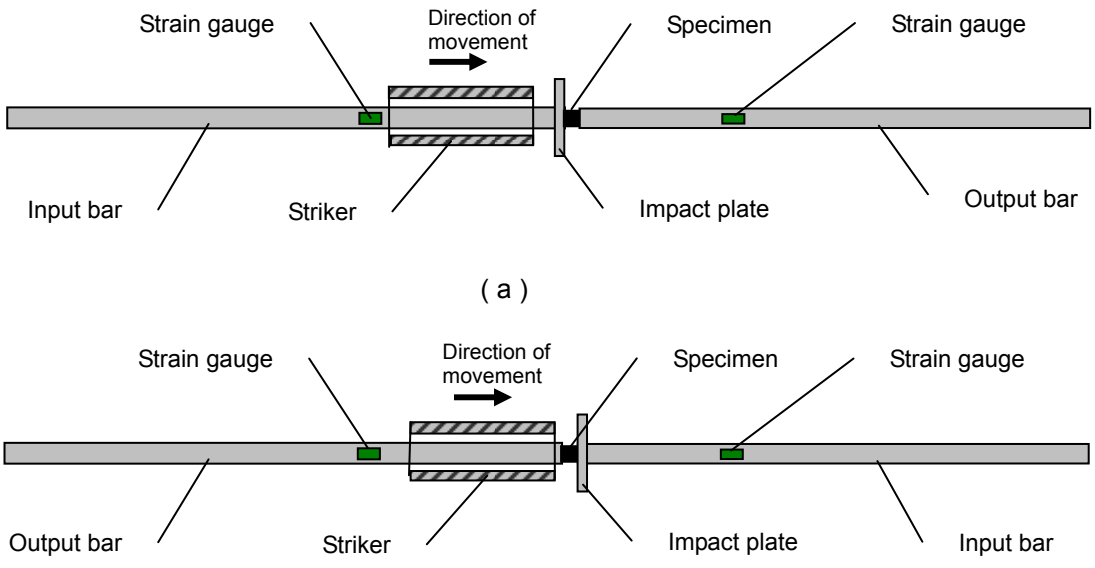

Fig.B-1 Illustration of configuration for (a) dynamic compressive and (b) dynamic tensile testing

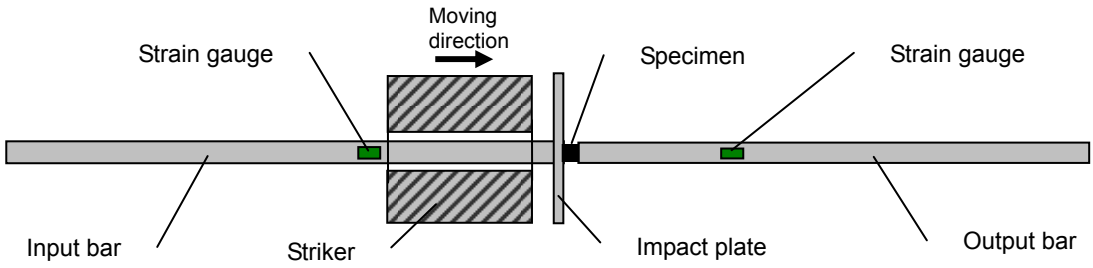

(a)

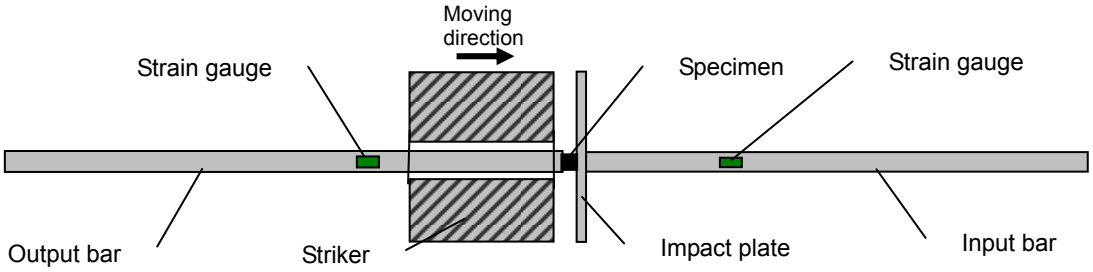

(b)

Fig.B-2 Illustration of configurations for (a) dynamic compressive and (b) dynamic tensile testing using a thick and heavy striker

DETAILED DESCRIPTION OF THE PREFERRED EMBODIMENTS

A miniature impact tester was fabricated as a preferred embodiment of this invention. The accompanying drawings (Fig.B-3 to Fig.B-5) which are incorporated into and constitute a part of the description of the invention, illustrate the preferred embodiment of the invention and serve to implement the principles of the invention into practice. It is to be understood, however, that the drawings are designed for purpose of illustration only, and not as a definition of the limits of the invention for which reference should be made to the claims appearing at the end of the description.

Figure B-3 is an isometric view of the embodiment of the miniature impact

tester constructed according to the present invention.

Figure B-4 shows the front views of the miniature impact tester assembled for tension and compression modes.

Figure B-5 illustrates major components of the miniature impact tester.

Figure B-6 presents detailed sketches of the major components.

The miniature impact tester shown in Fig.B-3 is a simple and cost-effective design that uses a spring to propel a striker. The configuration illustrated in Fig.B-4a is for a tension mode, which can be converted to a compression mode simply by attaching the impact plate 13 to the other bar (Fig.B-4b).

Base plate 1 is a solid plate with threaded holes to position and for connection with other components. This cost-effective design uses arrays of holes to position components at suitable locations.

A guide tube 15 is attached to the guide tube support 5; one end of the guide tube is threaded in order that a thick screw cap 19 can be screwed to compress the spring 18; the end of the striker has a flange that is restrained by a sliding catch 4 when spring 18 is compressed. A spring length indicator 2 is used to indicate the position of the screw cap 19.

By pushing the sliding catch 4 downwards, the striker 17 is propelled by the

compressed spring 18, to move towards the impact plate 13; the velocity of the striker 17 is measured by the trigger pin 16 which cuts an array of laser beams from laser emitters 14. The striker 17 then impacts the impact plate 13, and generates an input wave in the slender bar 10, which is then recorded by strain gauges 11. The tensile force generated then propagates into the other slender bar 21 through the specimen and this is recorded by strain gauges 20.

If the impact plate 13 is attached to the bar 21 instead, the striker 17 will impinge on the impact plate 13 and generate compression in the specimen. The input wave is recorded by strain gauges 20 and the transmitted wave is recorded by strain gauges 11. An adapter sleeve 12 is used to mount the slender bars onto the bar supports; this takes the form of a hollow cylinder or a linear bearing.

MODIFICATIONS OF THE PREFERED EMBODIMENTS

Many modifications and variations may be made to the miniature impact tester without departing from the spirit and scope of the invention described. For example, the striker is propelled by a compressed spring in this arrangement - a simple and inexpensive design. An alternative maybe to use compressed air to propel the striker; this requires a more complex launch mechanism, but results a high striker speed with low mechanical noise. In addition, the striker can also be designed to slide within the guide tube.

CLAIMS

1. A dynamic mechanical testing methodology based on one-dimensional wave theory, which makes it convenient to employ two long slender bars for impact/dynamic testing of small specimens.

2. A miniature impact tester that is designed as a preferred embodiment of the invention as claimed in Claim 1, characterized by the mechanism including the spring propulsion unit, guide tube, striker, release mechanism and stop block, etc.

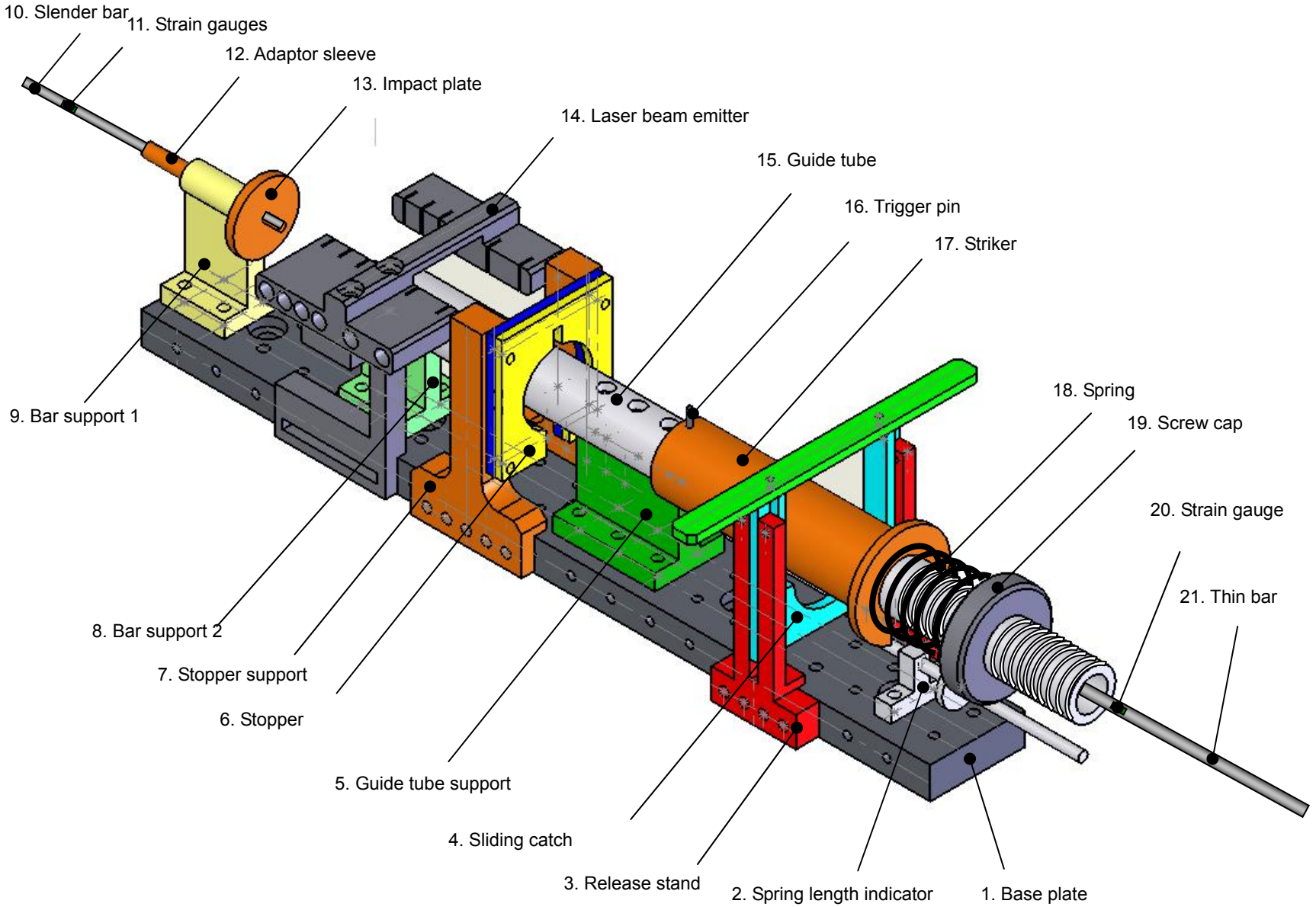

Fig.B-3 Isometric view of an embodiment (illustrated construction is the miniature tensile impact tester) constructed according to the present invention

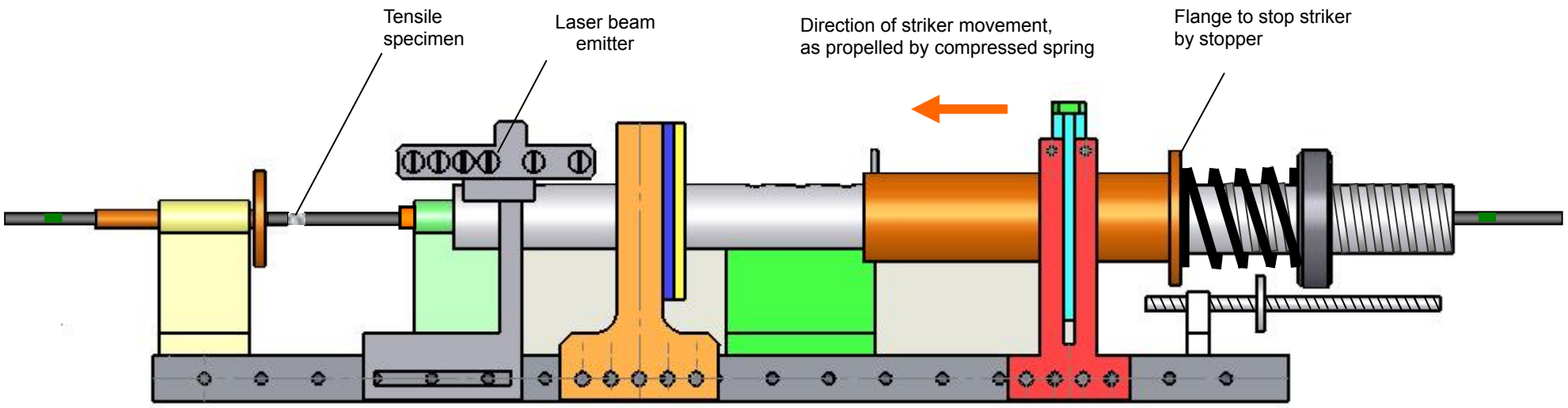

Fig.B-4a Front view of miniature impact tester for tensile loading

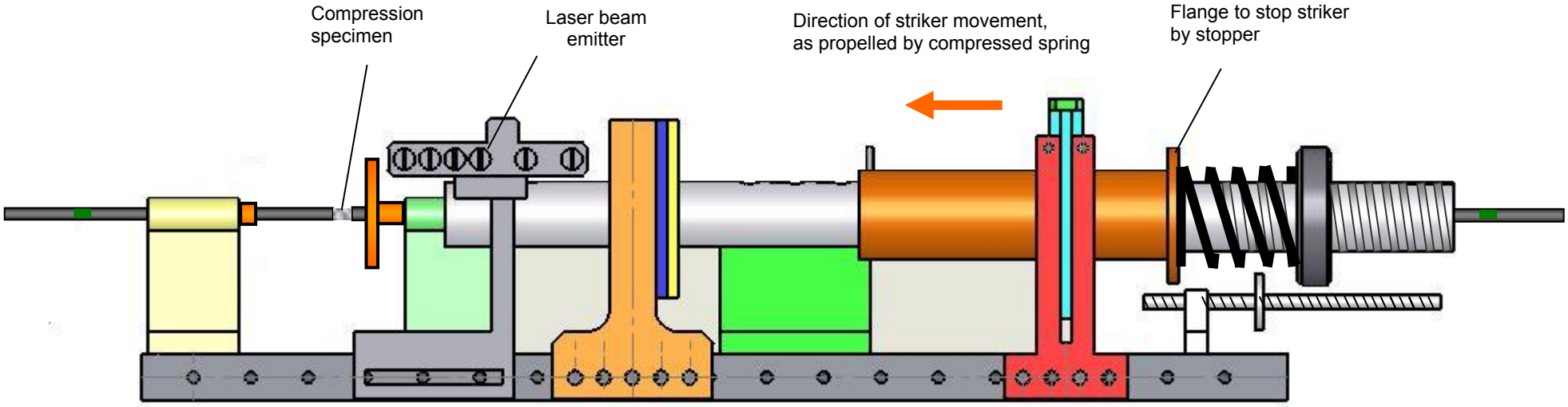

Fig.B-4b Front view of miniature impact tester for compressive loading

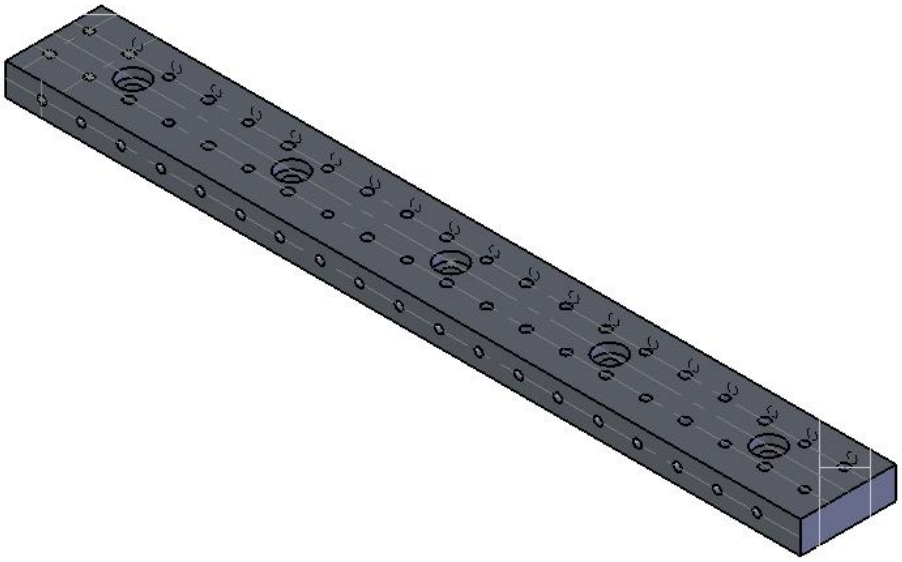

Base plate (1)

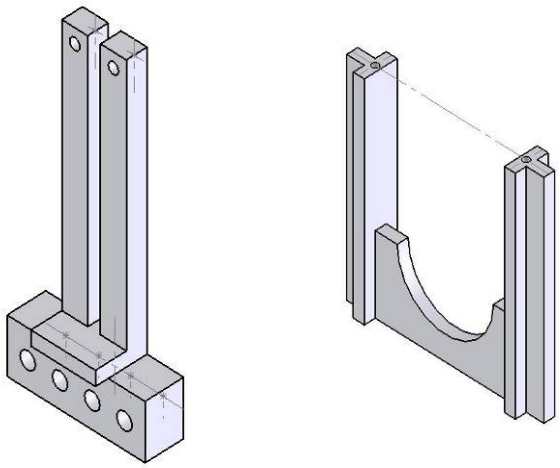

Release stand (3) and sliding catch (4)

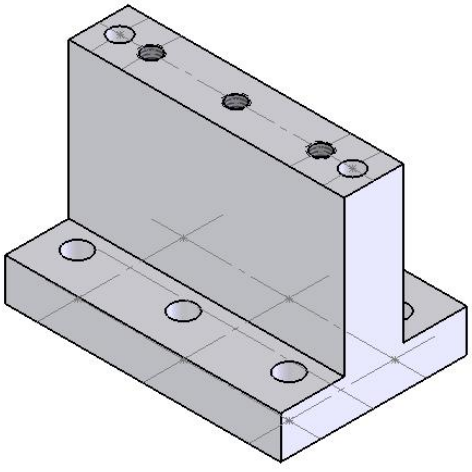

Guide tube support (5)

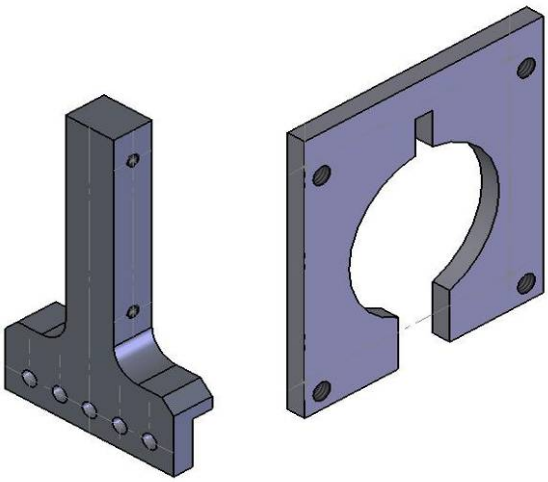

Stopper support (7) and stopper (6)

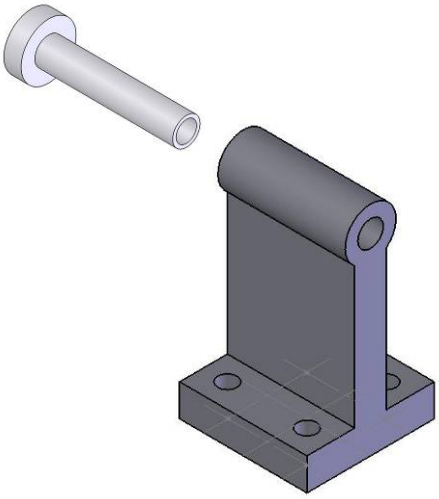

Adaptor sleeve (12) and bar support (8, 9)

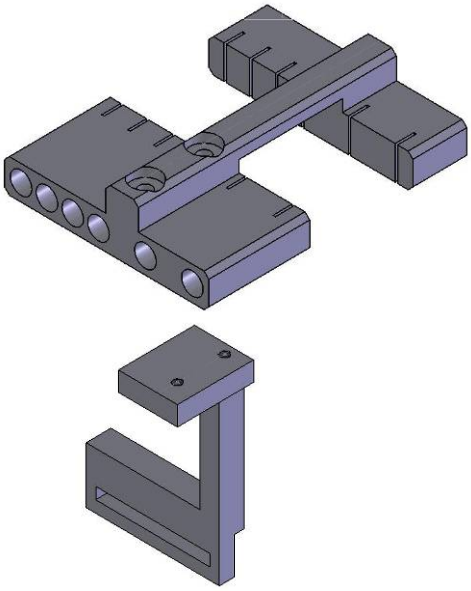

Laser emitter mounting frame (14)

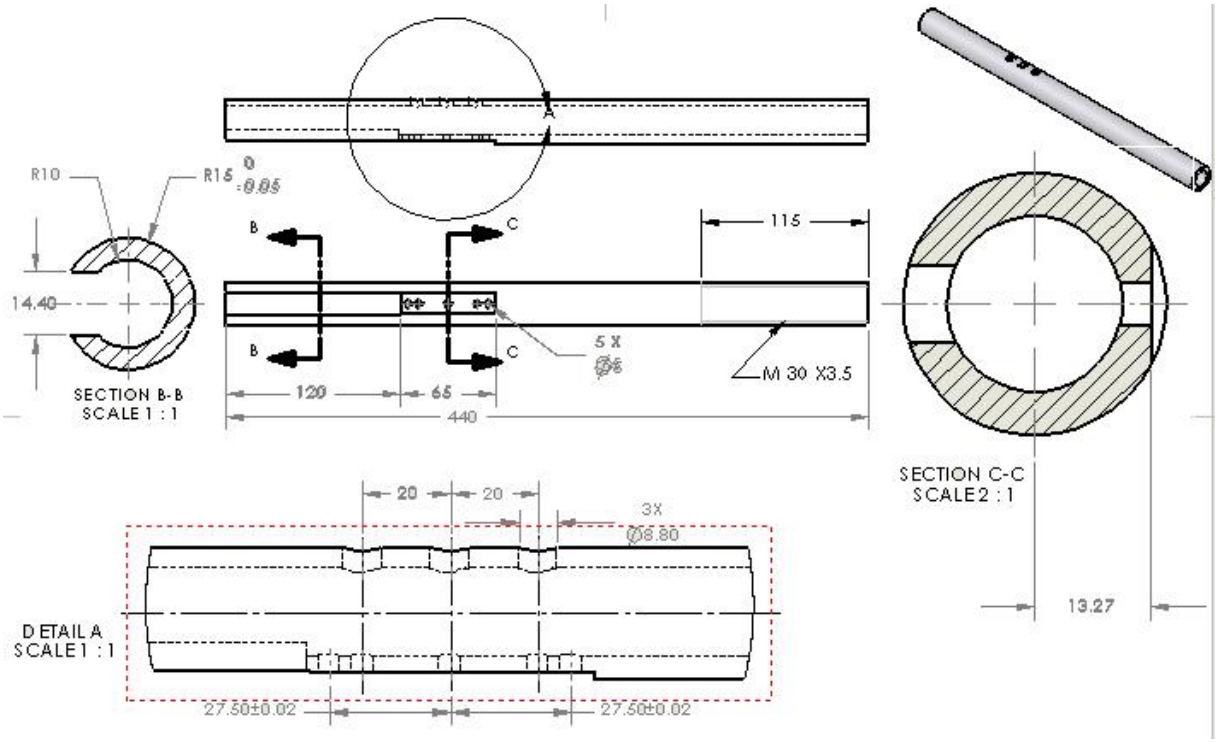

Guide tube (15)

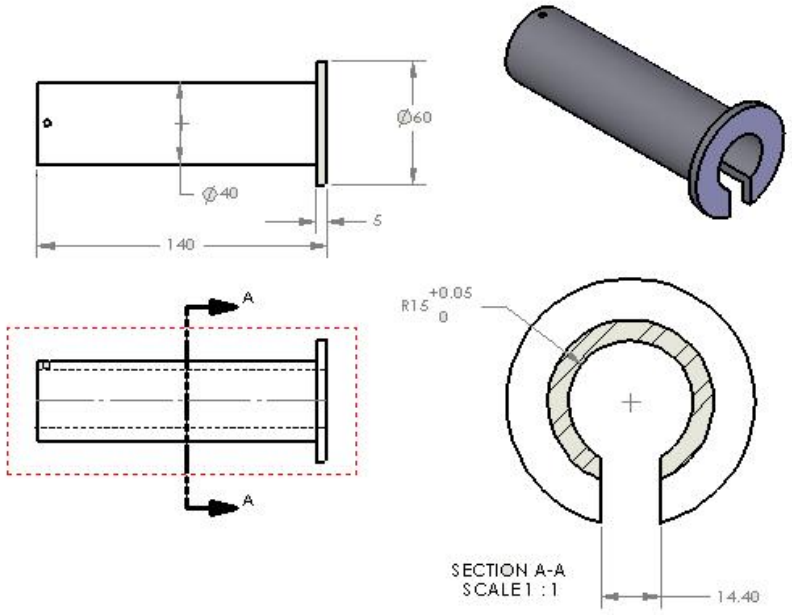

Striker (17)

Fig.B-5 Major components of the miniature impact tester.

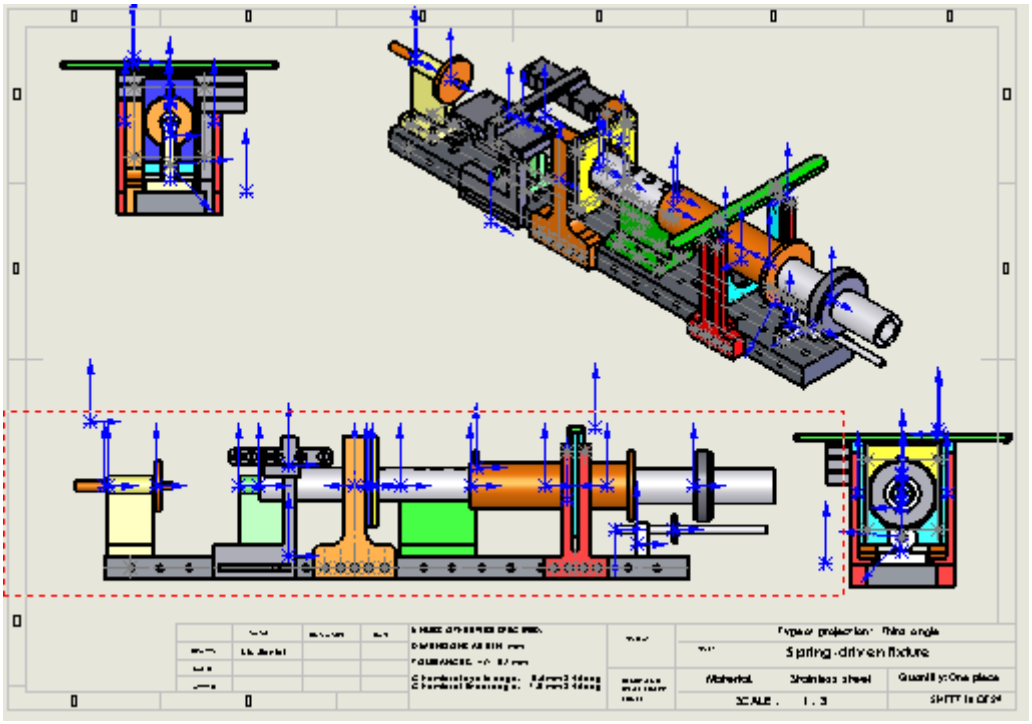
Spring-driven fixture

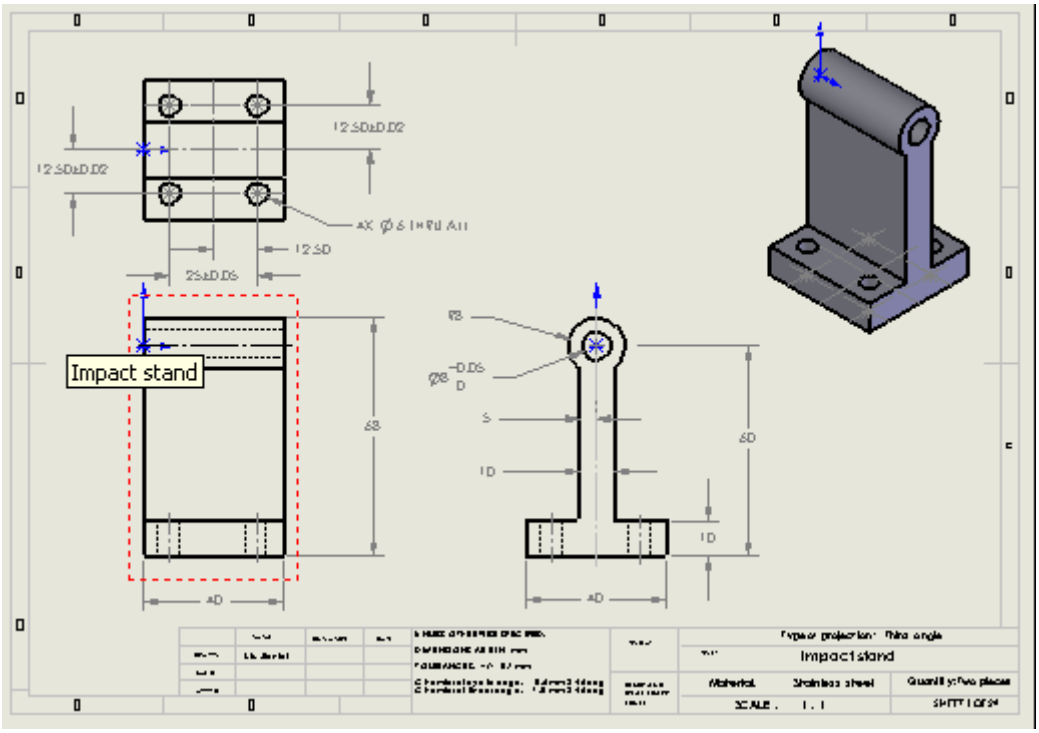
Impact stand
Impact stand

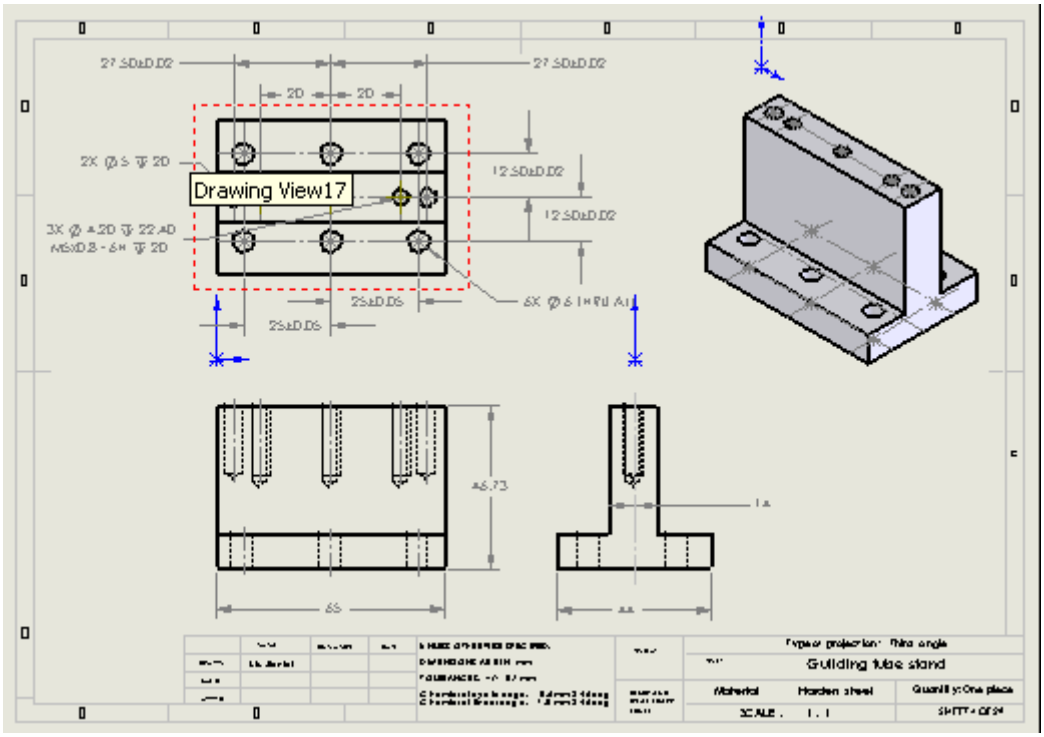
Drawing View17
Guiding tube stand

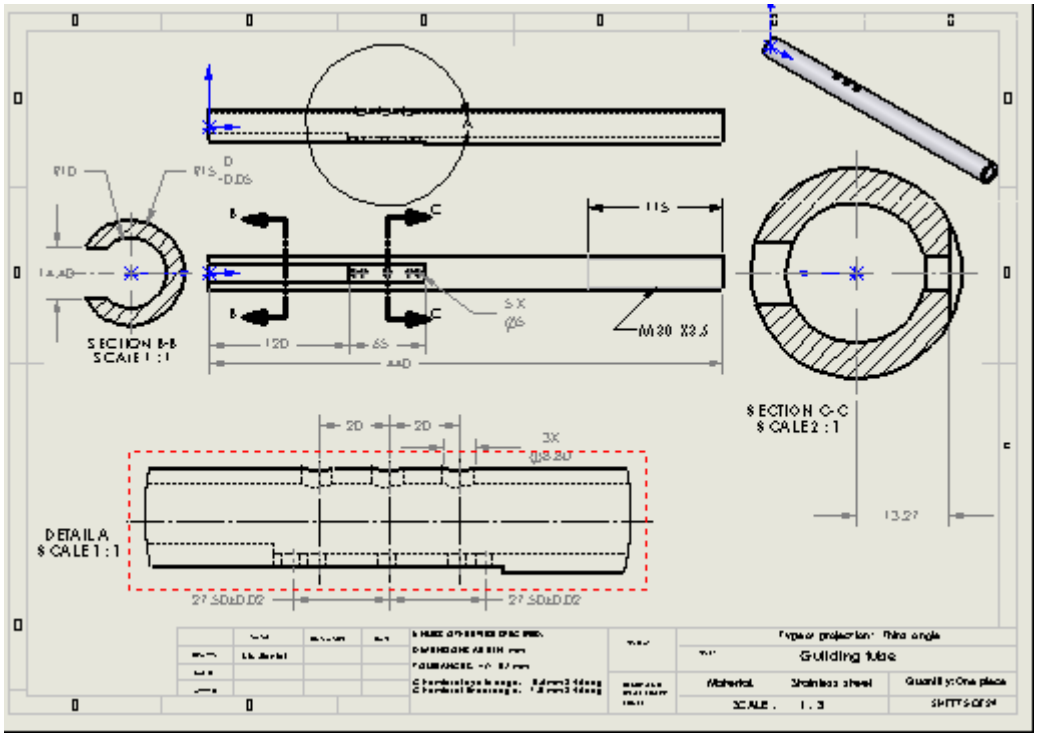
SECTION B-B
SCALE 1 : 1
SECTION C-C
SCALE 2 : 1
DETAIL A
SCALE 1 : 1
M30 X3.5
Guiding tube

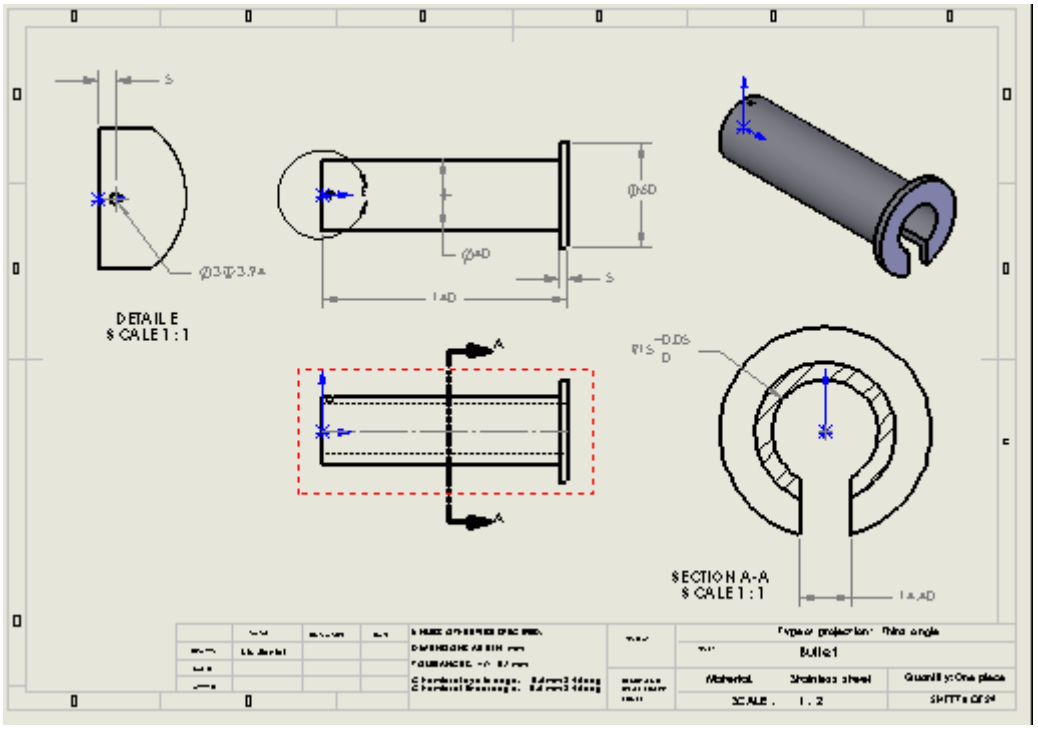
DETAIL E
SCALE 1 : 1
SECTION A-A
SCALE 1 : 1
Bullet
Material
Stainless steel
SCALE . 1 . 2

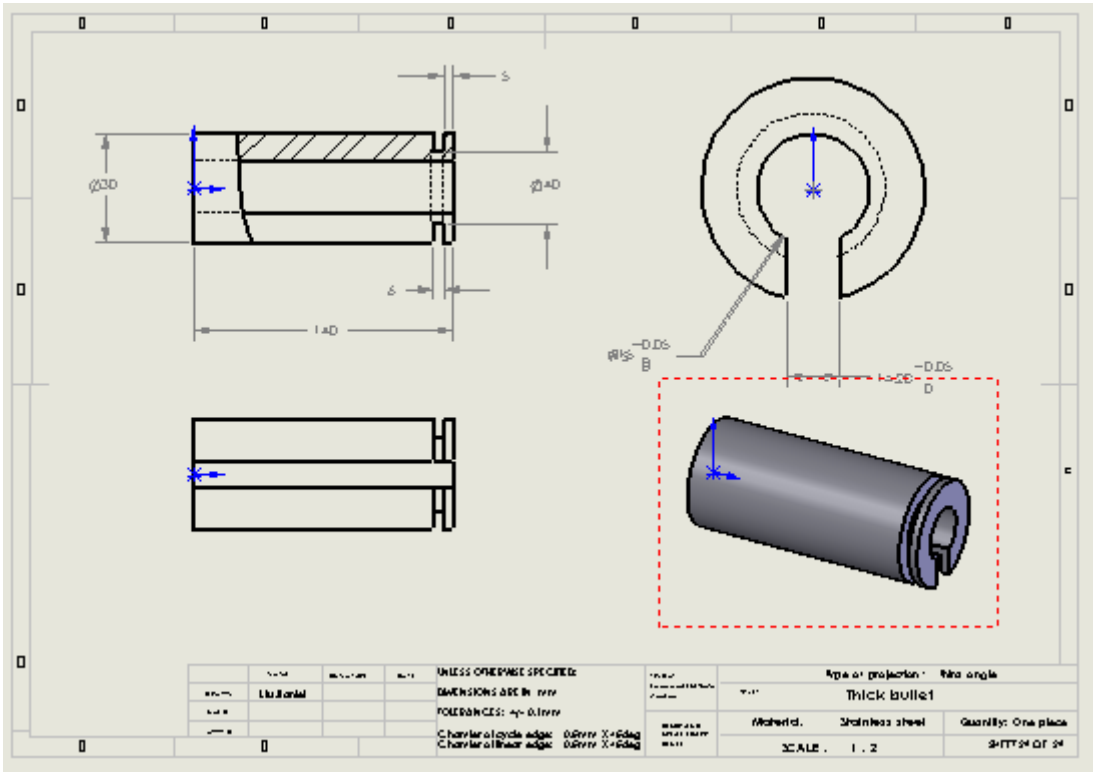
Thick bullet
Material
Stainless steel
SCALE . 1 . 2

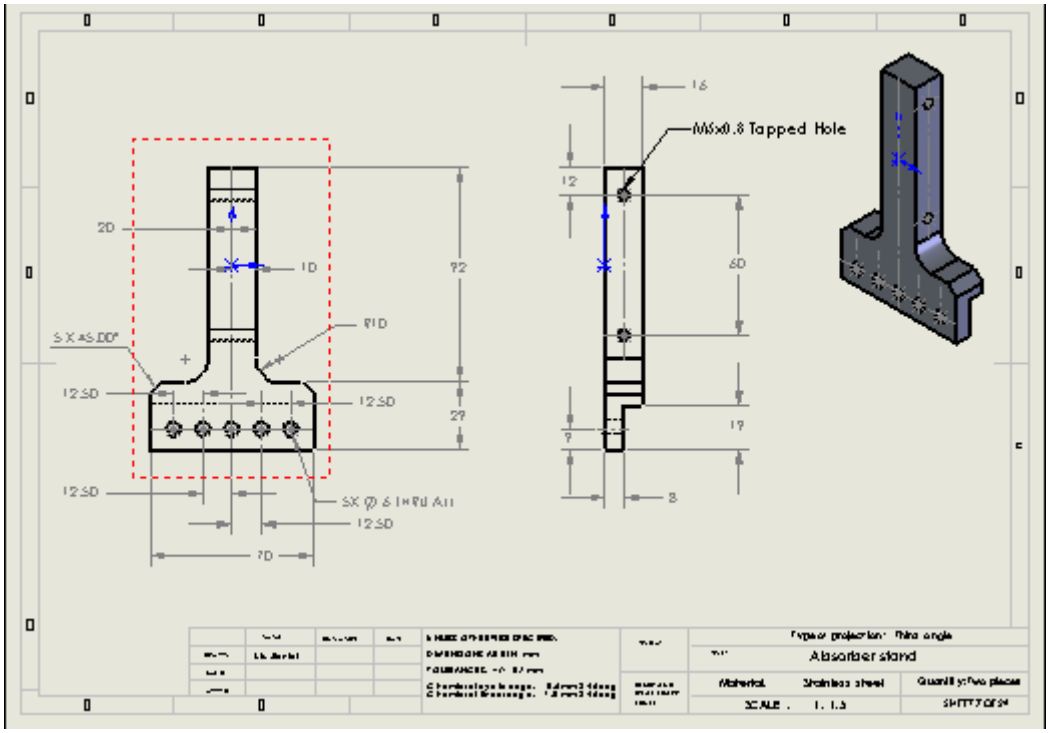
M6x0.8 Tapped Hole
Absorber stand
Material
Stainless steel
Quantity:Two places
SCALE : 1 : 1.5

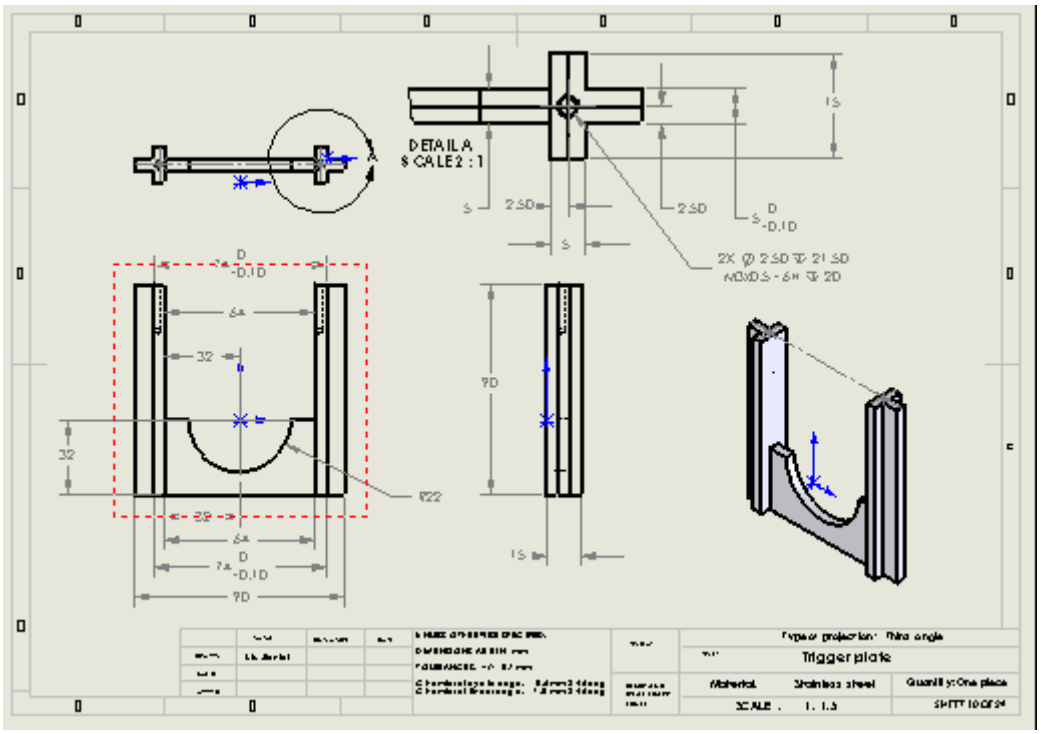
DETAIL A
SCALE 2 : 1
Trigger plate
Material
Stainless steel
Quantity:One place
SCALE : 1 : 1.5

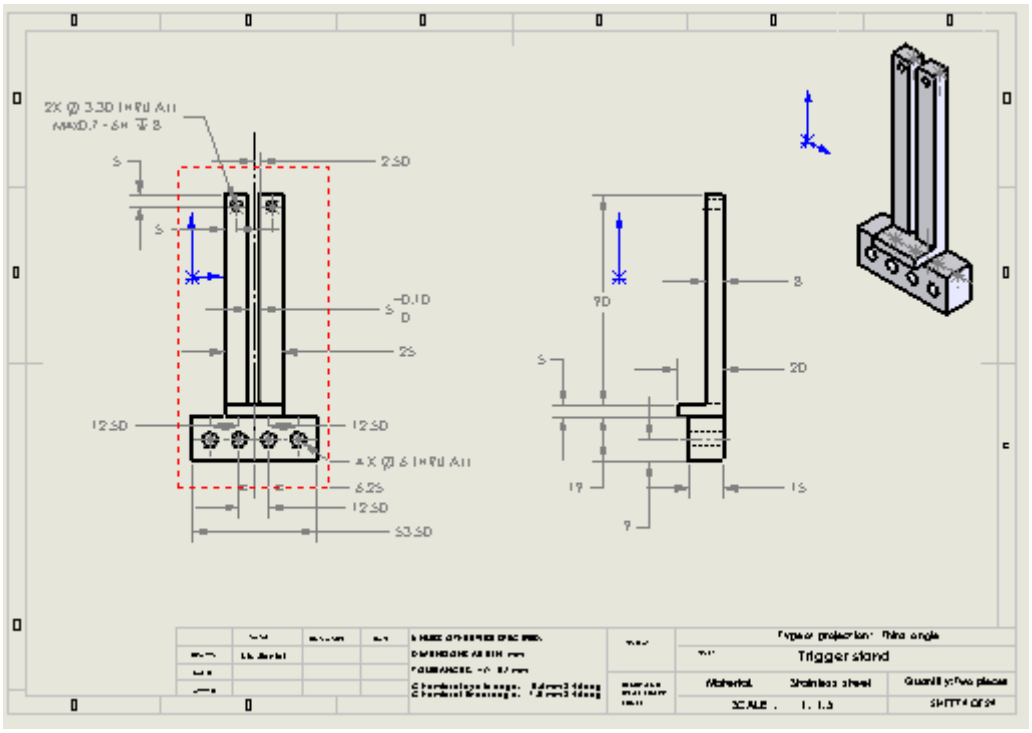
Trigger stand
Material
Stainless steel
SCALE 1 : 1.5

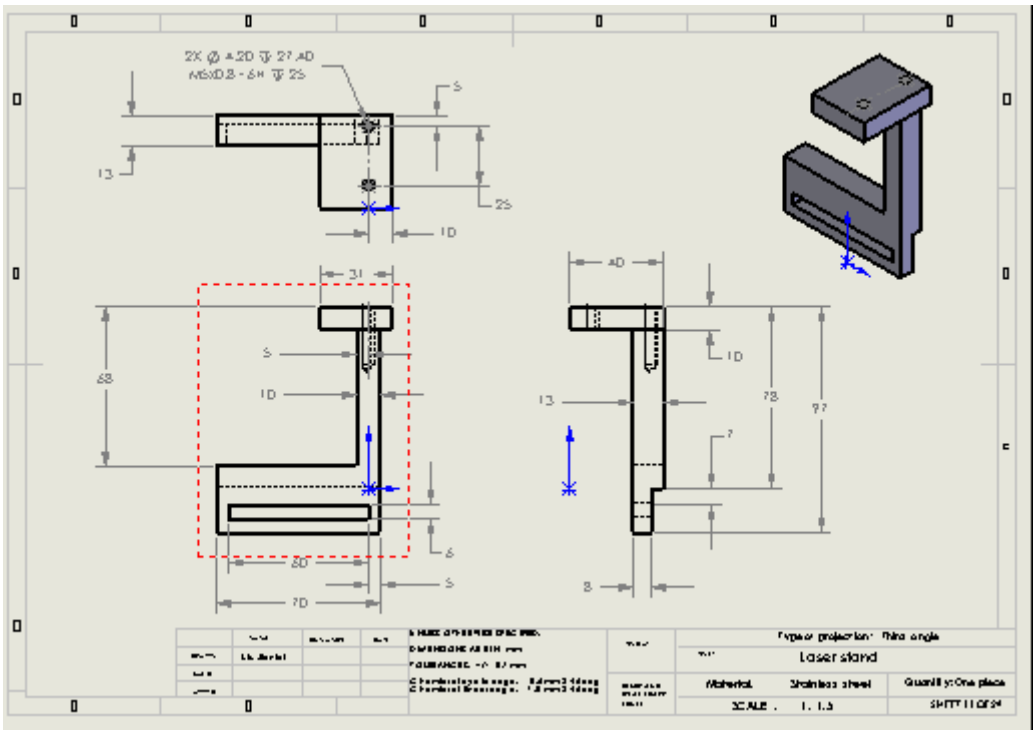
Laser stand
Material
Stainless steel
SCALE 1 : 1.5

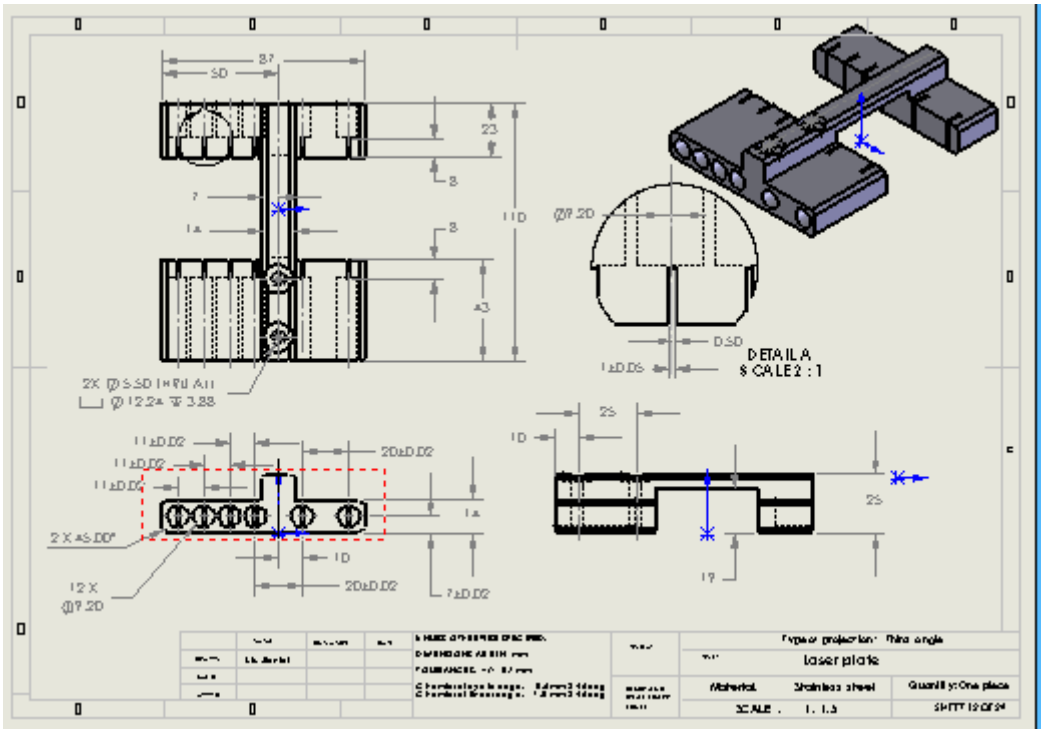
DETAIL A
SCALE 2 : 1
Laser plate
Stainless steel
Quantity:One place

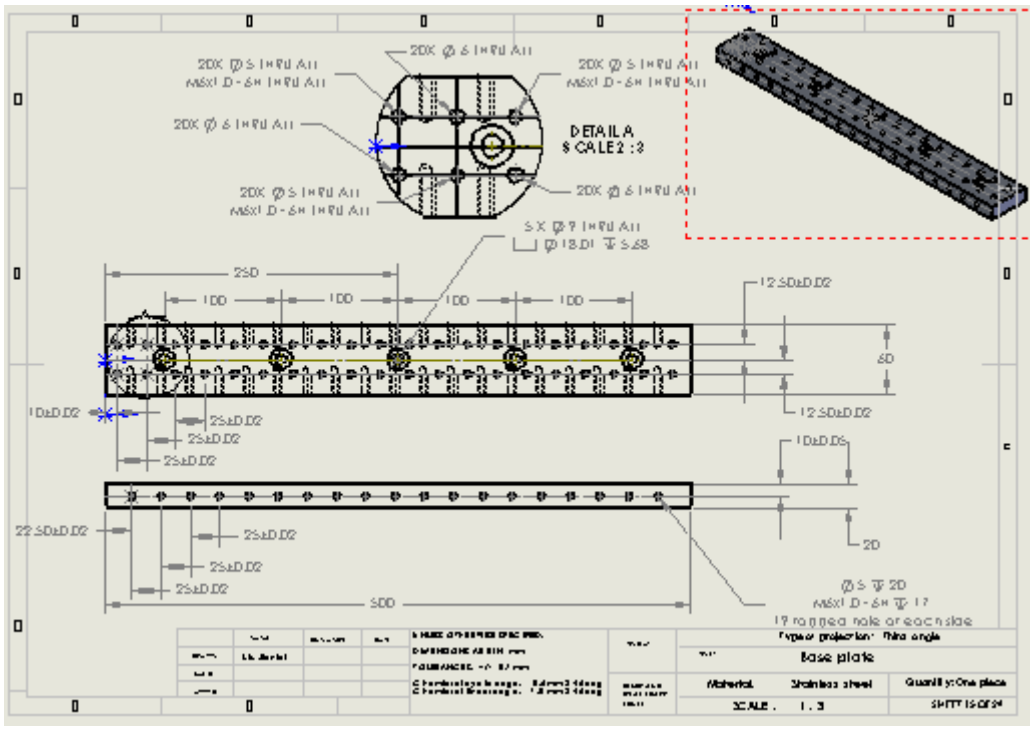
DETAIL A
SCALE 2 : 3
Base plate
Stainless steel
Quantity:One place

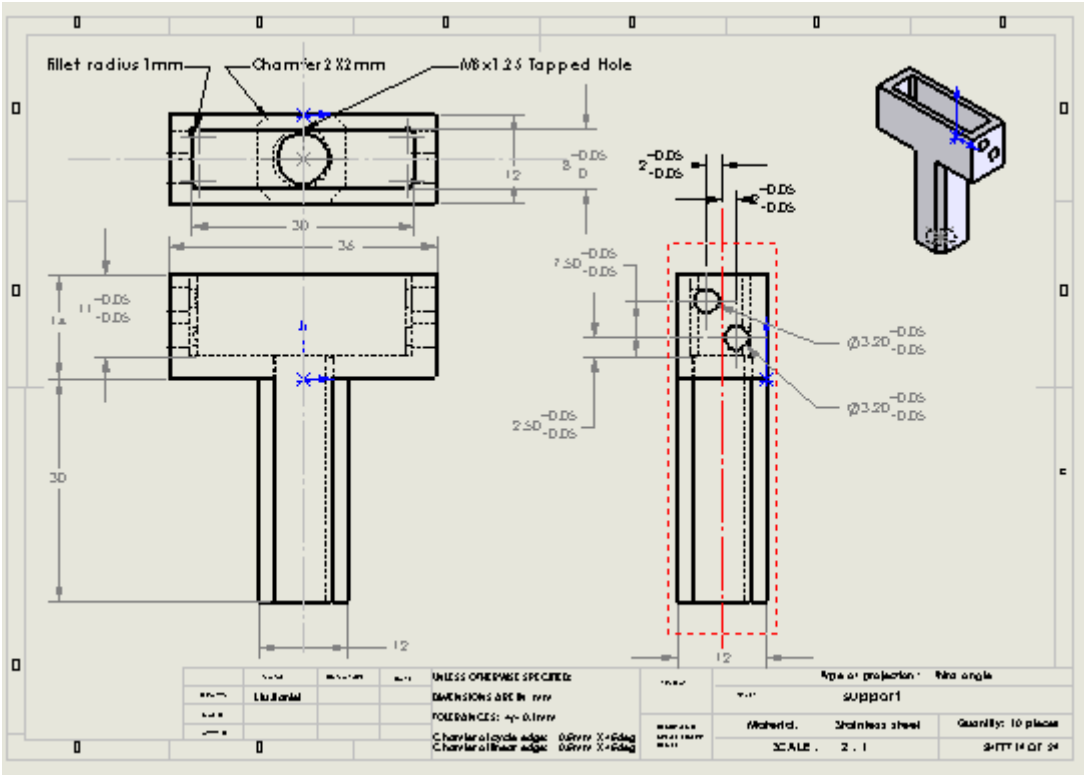

Fig.B-6 Sketches of main parts of the miniature impact tester

APPENDIX C DEFINITION OF MATERIAL PROPERTIES IN DEPENDENCE ON FILED VARIABLES

In ABAQUS, material properties can be defined to be dependent on “field variables” (user-defined variables that represent any independent quantity and defined at nodes, as functions of time). For example, material moduli can be functions of weave density in a composite or of phase fraction in an alloy. The number of user-defined field variable dependencies required for many material behaviors can be specified (*ABAQUS Analysis User's Manual, Section 28.6.1, “predefined fields*”). For instance, *Section 17.1.2* in the *ABAQUS Analysis User's Manual* on *“material data definition*, *specifying material data as functions of temperature and independent field variables”*, states that “Material data are often specified as functions of independent variables such as temperature. Material properties are made temperature dependent by specifying them at several different temperatures”. An example is given in the manual, illustrating temperature-dependent linear isotropic elasticity (Fig.C-1). In this case, six sets of values are used to specify the material description, as shown in the figure. “For temperatures that are outside the range defined by θ_1 and θ_6, ABAQUS assumes constant values for E and ν. The dotted lines on the graph represent the straight-line approximations that will be used for this model. In this example only one value of the thermal expansion coefficient is given, α_1 , and it is independent of temperature”.

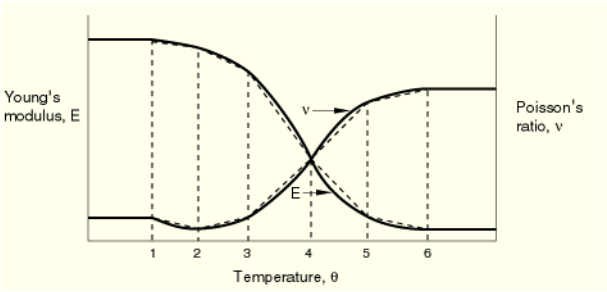

Elastic Modulus	Poisson's Ratio	Temperature
E_1	ν_1	θ_1
E_2	ν_2	θ_2
E_3	ν_3	θ_3
E_4	ν_4	θ_4
E_5	ν_5	θ_5
E_6	ν_6	θ_6

Fig.C-1 Example of material definition of a a simple, isotropic, linear elastic material, showing the Young's modulus and Poisson's ratio as functions of temperature (*ABAQUS analysis user's manual, figure 17.1.2–1*).

Another example in the *ABAQUS analysis user's manual* (*section 17.1.2, "material data definition"*), shows an elastic-plastic material for which the yield stress is dependent on the equivalent plastic strain and temperature (Fig.C-2). "In this case the second independent variable (temperature) must be held constant, while the yield stress is described as a function of the first independent variable (equivalent plastic strain). Then, a higher value of temperature is chosen and the dependence on equivalent plastic strain is given at this temperature. This process, as shown in the following table, is repeated as often as necessary to describe the property variations in as much detail as required".

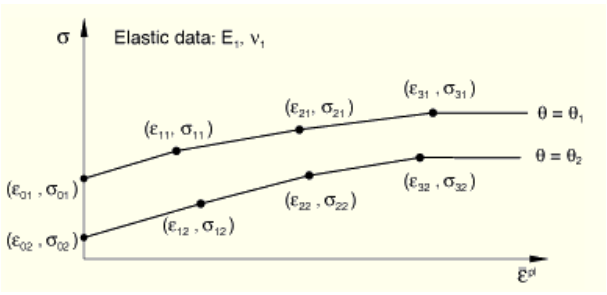

Yield Stress	Equivalent Plastic Strain	Temperature
σ_{01}	ε_{01}	θ_1
σ_{11}	ε_{11}	θ_1
σ_{21}	ε_{21}	θ_1
σ_{31}	ε_{31}	θ_1
σ_{02}	ε_{02}	θ_2
σ_{12}	ε_{12}	θ_2
σ_{22}	ε_{22}	θ_2
σ_{32}	ε_{32}	θ_2

Fig.C-2 Example of material definition with two independent variables for elastic-plastic material (*ABAQUS analysis user's manual, figure 17.1.2–2*)

A material property can be defined as a function of variables calculated by ABAQUS. Material data can be specified as functions of solution-dependent

variables with a user subroutine. The user subroutine USDFLD is needed to define field variables at a material point as functions of time, of the available material point quantities, and of material directions. Material properties defined as functions of these field variables may thus be dependent on the solution. The user subroutine USDFLD is called at each material point for which the material definition includes a reference to the user subroutine.

The ABAQUS facility for material property definition enables incorporation of the bi-linear true stress-strain curves for the solder joint beam model. In this study, the solder joint mechanical properties are prescribed as being dependent on a field variable; and the field variable is associated with the strain rate as a solution-dependent variable, as shown in Fig.C-3.

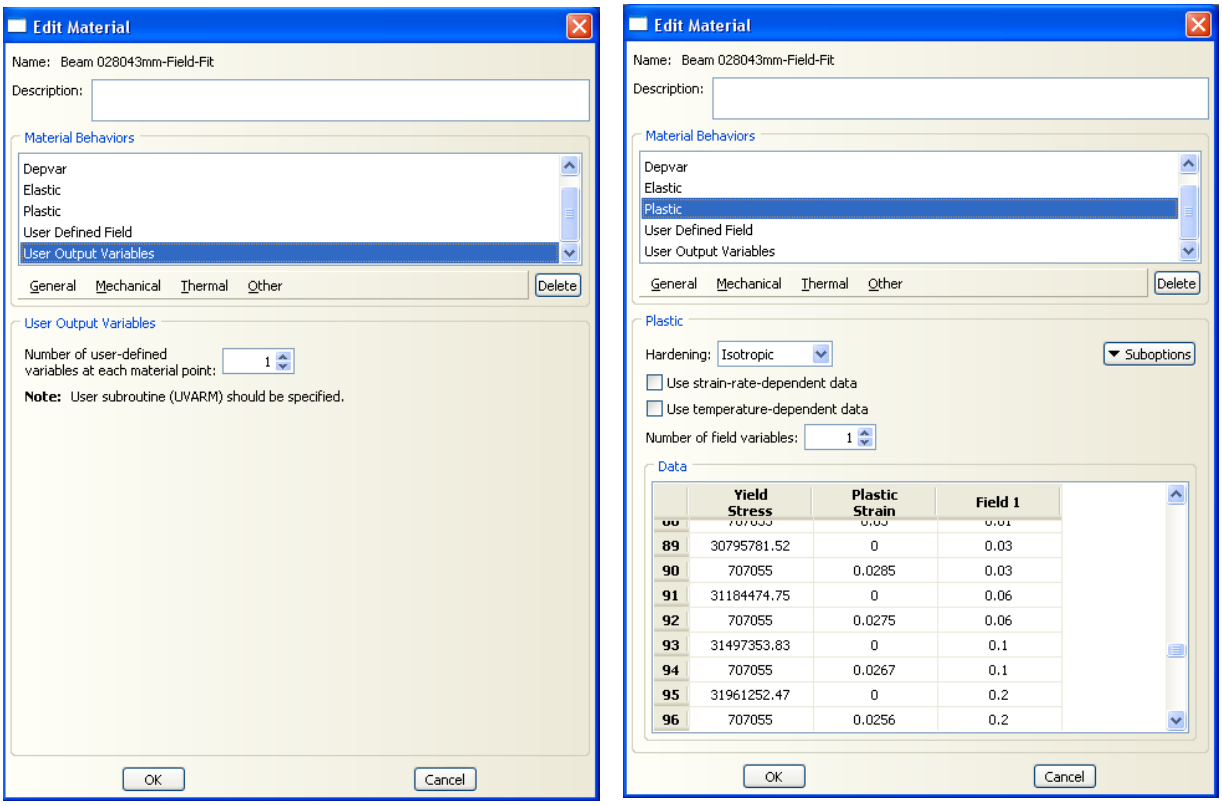

Fig.C-3 Illustration of solution dependent variable and field variable in material definition for solder joint beam model

APPENDIX D MECHANICS OF THREE POINT BENDING TEST

Consider a simply supported beam. A uniform cross-section beam of length L and constant elastic modulus E is subjected to a centrally applied concentrated load F, as shown in Fig.D-1. The XY plane is the plane of symmetry of the beam and the x axis coincides with the neutral axis in the undeformed state. The mechanics of beam bending can be found in many textbooks (Krenk, 2001, Ross, 1996) and the following introduces some concepts related to the three point bending tests conducted.

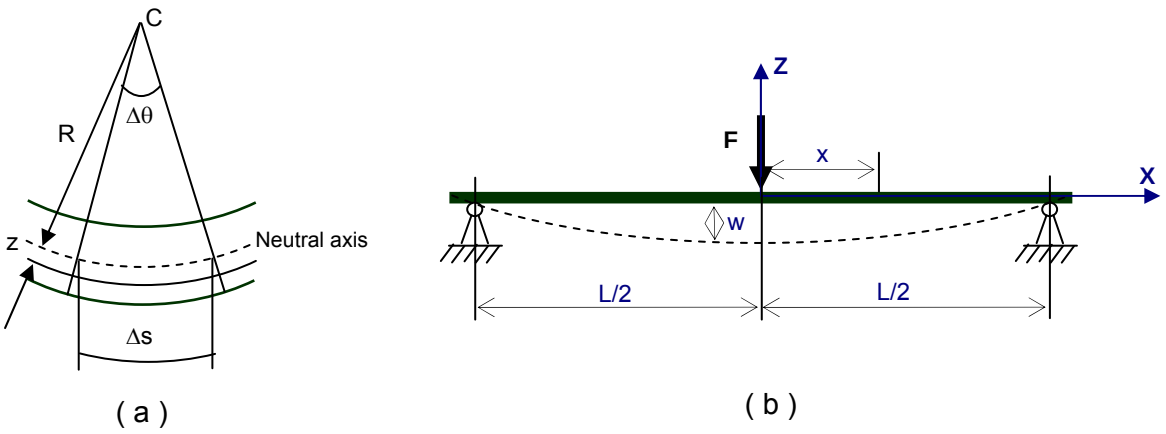

Fig.D-1 Three-point bending of a rectangular beam

With reference to the beam segment with initial length Δs in Fig.D-1a, the curvature of the neutral axis in the deformed state is

$$\kappa = \frac{1}{R} = \frac{\Delta\theta}{\Delta s} \qquad \text{(D-1)}$$

where $\Delta\theta$ is the angle between the two end cross-sections. If a fiber located at a distance z below the neutral axis has an initial length Δs, its length after

deformation is

$$\Delta s' = (R+z)\cdot\Delta\theta = (R+z)\cdot\kappa\cdot\Delta s \qquad \text{(D-2)}$$

Therefore, the longitudinal strain corresponding to this elongation is proportional to the curvature κ and to the distance z from the neutral axis,

$$\varepsilon = \frac{\Delta s' - \Delta s}{\Delta s} = \kappa\, z \qquad \text{(D-3)}$$

If the beam material is linear elastic (modulus E), the bending moment M is determined by integrating the contributions from the stress at each point of the cross-section A, multiplied by its distance z from the neutral axis,

$$M = \int_A \sigma z dA = \int_A E\varepsilon\cdot z dA = E\left(\int_A z^2 dA\right)\kappa = EI\kappa \qquad \text{(D-4)}$$

where I is the 2nd moment of inertia about the neutral line. For a cross section of a rectangular beam of thickness h and width b, the second moment of area is

$$I = \int_A z^2 dA = b\int_{-h/2}^{h/2} z^2 dz = \frac{1}{12}bh^3 \qquad \text{(D-5)}$$

In most cases where the deflection $w(x)$ caused by bending moment is small, the rotation θ and curvature κ are given by,

$$\theta \approx \frac{dw(x)}{dx} \quad , \quad \kappa \approx \frac{d\theta(x)}{dx} \approx \frac{d^2 w(x)}{dx^2} \qquad \text{(D-6)}$$

Therefore, the bending moment can be expressed in terms of the second derivative of the displacement,

$$M = EI\kappa = EI\frac{d^2 w(x)}{dx^2} \qquad \text{(D-7)}$$

This is an important expression for the bending of beam. For three-point bending of a rectangular beam (Fig.D-1b), an expression relating the concentrated load F and the deflection $w(x)$ can be derived. In this case,

there is a discontinuity in the slope of bending moment distribution at mid-span. Applying the bending moment equation to the beam between x=0 and x=L/2 gives,

$$M = EI\frac{d^2w(x)}{dx^2} = \frac{F}{2}\cdot(\frac{L}{2}-x) \tag{D-8}$$

$$\Rightarrow EI\frac{dw(x)}{dx} = \frac{F}{4}\cdot(\frac{L}{2}-x)^2 + C_1$$

$$\Rightarrow EIw(x) = \frac{F}{12}\cdot(\frac{L}{2}-x)^3 + C_1(\frac{L}{2}-x) + C_0$$

At $x = L/2$, $w(x) = 0$; therefore $C_0 = 0$

At $x = 0$, $\theta = \frac{w(x)}{dx} = 0$; therefore $C_1 = -\frac{FL^2}{16}$

Therefore,

$$w(x) = \frac{F}{EI}\left[\frac{(L/2-x)^3}{12} - \frac{L^2(L/2-x)}{16}\right] \tag{D-9}$$

The maximum deflection occurs at $x = 0$, where

$$w(0) = w_{\max} = -\frac{FL^3}{48EI} \tag{D-10}$$